Engineering Materials

Nishar Hameed
Jaworski C. Capricho
Nisa Salim
Sabu Thomas *Editors*

Multifunctional Epoxy Resins

Self-Healing, Thermally and Electrically Conductive Resins

Springer

Engineering Materials

This series provides topical information on innovative, structural and functional materials and composites with applications in optical, electrical, mechanical, civil, aeronautical, medical, bio- and nano-engineering. The individual volumes are complete, comprehensive monographs covering the structure, properties, manufacturing process and applications of these materials. This multidisciplinary series is devoted to professionals, students and all those interested in the latest developments in the Materials Science field, that look for a carefully selected collection of high quality review articles on their respective field of expertise.

Indexed at Compendex (2021)

Nishar Hameed · Jaworski C. Capricho ·
Nisa Salim · Sabu Thomas
Editors

Multifunctional Epoxy Resins

Self-Healing, Thermally and Electrically Conductive Resins

Springer

Editors
Nishar Hameed
School of Engineering
Swinburne University of Technology
Hawthorn, Victoria, Australia

Jaworski C. Capricho
School of Engineering
Swinburne University of Technology
Hawthorn, Victoria, Australia

Nisa Salim
School of Engineering
Swinburne University of Technology
Hawthorn, Victoria, Australia

Sabu Thomas
School of Chemical Science
Mahatma Gandhi University
Kottayam, India

ISSN 1612-1317 ISSN 1868-1212 (electronic)
Engineering Materials
ISBN 978-981-19-6037-6 ISBN 978-981-19-6038-3 (eBook)
https://doi.org/10.1007/978-981-19-6038-3

This Springer imprint is published by the registered company Springer Nature Singapore Pte Ltd.
The registered company address is: 152 Beach Road, #21-01/04 Gateway East, Singapore 189721, Singapore

Contents

About the Editors

Assoc. Prof. Nishar Hameed is the Group Leader of Smart Materials Lab, School of Engineering, Swinburne University of Technology. Nishar's research is focused on the novel and faster processing of next generation 'smart' polymers and composite materials. He has published more than 100 high impact journal papers, 6 book chapters, 3 edited books and 2 patents. His several achievements include many "firsts" in the field, inspiring many follow-up studies. Nishar recently developed a new method to produce flexible, toughened, and fast cure resins that can be integrated to make formable and rapid cure fibre reinforced composites, concrete preforms and graphene nanocomposites. His research has also led to the development of a new, environmentally processing route to make plastics films and fibres from natural polymers (cellulose, wool, silk) and biomass. Nishar won many awards as he advanced his research career including AINSE (Australian Institute of Nuclear Science and Engineering) Post Graduate Research Award, Smart Geelong Early Researcher Award, Young Tall Poppy Award, Phillip Law Award and Deakin's Best Doctoral Thesis Award. He has been awarded several prestigious fellowships including the highly esteemed Victoria Fellowship, Famelab State Finalist and two Endeavour Fellowships. He has held visiting appointments at Rice University, University of California Los Angeles, University of Southern Mississippi, University of Kentucky, CNRS Montpellier, Indian Institute of Technology Madras and Indian Institute of Science Bangalore.

Dr. Jaworski C. Capricho is a Research Scholar at Swinburne University of Technology. Jaworski is a research scientist within the Smart Materials Lab at the School of Engineering, Swinburne University of Technology Australia. Jaworski is a licensed chemist in the Philippines, science author, and inventor. He has laboratory and project management experience in both research and industry in Asia, New Zealand, and Australia and led several research and development studies involving polymers and biomaterials. He is an inventor of a patent family applied worldwide; three have been granted in Australia, Japan, and Brazil as of this time. In 2018, he joined the research group of A/Prof Nishar Hameed and Prof Bronwyn Fox at Swinburne University of

Technology. He is a recipient of the ARC (Australian Research Council) PhD Scholarship and Tuition-Free Scholarship from Swinburne University and a former Visiting Scientist of CSIRO (Commonwealth Scientific and Industrial Research Organization) and Guest Researcher at the ANSTO-HZB Neutron School in Sydney. In July 2019 and 2020, ANSTO awarded two of his proposals entitled "Spectral imaging of polynitroxyl radical epoxy thermosets via infrared polariscopy with focal point array detection" to use the IRM (Infrared Microscopy) beamline in the Australian Synchrotron, valued close to AUD $200,000 in relation to his current work on the development of thermoset resins exhibiting multifunctional behavior with their associated Industry 4.0 potential. He has published in leading chemistry, polymer, and materials journals and presented his work as an invited speaker at the ICCM22 (22nd International Conference on Composite Materials) and the 37th Australasian Polymer Symposium; and a poster in the 2019 Carbon Innovation Conference, ICCM22, the 2019 Emerging Polymer Technologies Summit and several HDR Graduate Symposiums at Swinburne University.

Dr. Nisa Salim is a Vice Chancellors Initiative Senior Research Fellow, School of Engineering, Swinburne University of Technology. She is currently a Vice-Chancellor's Initiative Senior Research Fellow who received her Ph.D. from Deakin University in Materials in Engineering. Her research activities have been on multifunctional carbon-based materials product developments, based on scalable formulations of carbon materials, their structure and function. Her expertise includes the synthesis, functionalization and fabrication of functional polymers and carbon materials for energy, and sensor applications. She has published over 65 high-impact journal papers, 5 book chapters and 1 patent. Her research has been presented at conferences on more than 40 occasions and she has been an invited speaker at local, interstate and international venues. She has received more than 15 awards and fellowships for her research innovation and impact, starting with a highly prestigious Gold Medal from the Australian Institute of Nuclear Science and Engineering (AINSE) for Excellence in Research in 2014. The awarding bodies include scientific organisations, professional associations, and federal and state governments. This includes Smart Geelong Early Researcher Award, Victoria Fellowship, Endeavour Fellowship, Alfred Deakin Fellowship and many more even with a career break of more than 2 years. Her vision is to develop multifunctional, engineered materials that are enablers for sustainable, next generation technologies. She is currently an Editorial board member (ECR) for Chemical Engineering Journal, Elsevier.

Prof. Dr. Sabu Thomas is a Vice Chancellor and Professor of Nanoscience and Polymer Science, Mahatma Gandhi University, Priyadarshini Hills PO, Kottayam, Kerala, 686 560 India. He is currently Vice Chancellor of Mahatma Gandhi University and the Founder, Director and Professor of the International and Inter-university Centre for Nanoscience and Nanotechnology. He is also a full professor of polymer science and engineering at the School of Chemical Sciences, Mahatma Gandhi University, Kottayam, Kerala, India. Professor Thomas is an outstanding leader with sustained international acclaims for his work in nanoscience, polymer science

and engineering, polymer nanocomposites, elastomers, polymer blends, interpenetrating polymer networks, polymer membranes, green composites, nanocomposites, nanomedicine and green nanotechnology. His ground-breaking inventions in polymer nanocomposites, polymer blends, green bio-nanotechnological and nano-biomedical sciences have made transformative differences in the development of new materials for the automotive, space, housing and biomedical fields. In collaboration with India's premier tyre company, Apollo Tyres, his group invented high-performance barrier rubber nanocomposite membranes for inner tubes and inner liners for tyres. He has received a number of national and international awards, which include: Fellowship of the Royal Society of Chemistry, London FRSC, Distinguished Professorship from Josef Stefan Institute, Slovenia, MRSI Medal, Nano Tech Medal, CRSI Medal, Distinguished Faculty Award, Dr APJ Abdul Kalam Award for Scientific Excellence-2016, Mahatma Gandhi University Award for Outstanding Contribution-2016, Lifetime Achievement Award of the Malaysian Polymer Group, Indian Nano Biologists Award 2017 and the Sukumar Maithy Award, for the best polymer researcher in the country. He is in the list of most productive researchers in India and holds the position of No. 5. Recently, because of outstanding contributions to the field of nanoscience, polymer science and engineering, he has been conferred with Honoris Causa (D.Sc) Doctorate by the University of South Brittany, Lorient, France and the University of Lorraine, Nancy, France. Very recently, he has been awarded Senior Fulbright Fellowship to visit 20 universities in the USA and the most productive faculty award in the domain of materials sciences. Professor Thomas has published over 1000 peer-reviewed research papers, has co-edited 165 books, and has 15 patents. His H-index is 122, and he has more than 72,000 citations.

Introduction to Multifunctional Epoxy Composites

Camille A. Issa

Abstract This chapter delves into the importance of understanding epoxy resins and the task of preparing epoxy nanocomposites. The most recent up-to-date multifunctional epoxy nanocomposites with electrically conductive, magnetic, thermally conductive, shape-memory, self-healing, and flame-retardant features are reviewed. Epoxy nanocomposites are used in aeronautic, automotive, anti-corrosive coatings, high voltage, and structural applications. The information offered will aid understanding and promote the use of epoxy resins and encourage the development of new applications.

Keywords Self-healing · Shape memory · Magnetic · Thermal and Electrical Conductivities · Flame Retardancy

In lightweight and high-strength applications, it is clear that a predominant tendency has led to a growth in the substitution of conventional materials with polymer composites during the previous couple of decades. Its excellent strength-to-weight ratio, toughness, and thermal stability account for this. Filler qualities, filler shape, filler-matrix interactions, matrix properties, filler orientation in the matrix, and the volume fraction of the filler are all directly related to composite performance. The thermoplastic, thermoset, or rubber matrix component of composites can be used because of their versatility and exceptional performance; thermosetting polymers are commonly employed in engineering goods. Since its introduction in the late 1940s, epoxy resin has been widely used in a variety of industrial and commercial applications. Its improved stiffness, low shrinkage, high corrosion and chemical resistance, outstanding adhesive capabilities, creditable thermomechanical properties, creditable dielectric strength, and other characteristics brand it ideal for engineering uses. Epoxy, dissimilar to polyester resins, is able to maintain mechanical and physical qualities while being exposed to strong solvents. Epoxy resin can also be used to connect practically any material, including glass, wood, stone, ceramics, plastics, and metals.

C. A. Issa (✉)
Department of Civil Engineering, Lebanese American University, Byblos, Lebanon
e-mail: cissa@lau.edu.lb

N. Hameed et al. (eds.), *Multifunctional Epoxy Resins*, Engineering Materials,
https://doi.org/10.1007/978-981-19-6038-3_1

1 Introduction

Due to its desirable mechanical properties, solvent resistance, thermal stability, and creditable thermal insulation [1–3], epoxy is the most widely used thermosetting plastic with extensive manufacturing applications, including adhesives [4–7], electronic gadgets [8], laminates [9], encapsulations [10, 11], coatings [12–14], aquatic systems [5–17], and aerospace components [18–21]. Liquid epoxy resins, a family of highly reactive prepolymers with low molecular weight oligomers that include oxirane structures as an epoxy activity, can include aromatic, aliphatic, and/or heterocyclic backbone architectures [22]. Epoxy resins have a variety of physical properties due to their varied backbone architectures. A short-chain aliphatic epoxy resin, for example, possesses a low viscosity, whereas an aromatic epoxy resin has excellent thermal properties, such as a high glass transition temperature [23]. The most productive epoxy resin for industrial settings is the diglycidyl ether of bisphenol-A (DGEBA) [23]. Epoxy resins outperform polyester, phenolic, and melamine resins due to their low shrinkage and harmless loss during the curing process, as well as their inertness and chemical resistance, as well as their diversity in curing agents and circumstances [24]. A cross-linking reaction is a curing phase, or solidification of liquid epoxy resins with hardeners known as curing agents or catalysts, such as alcohols, acids or acid anhydrides, polyfunctional amines, thiols, and phenols, produce a stiff, insoluble, and infusible epoxy [25]. The qualities of the final epoxy finish are said to be influenced by the resins and curing chemicals used. In general, the high-temperature cured epoxy system achieves better stiffness, tensile strengths, and glass transition temperatures than the low-temperature cured epoxy method [26].

Epoxy nanocomposites have recently gained popularity owing to their distinctive physicochemical qualities that result from combining the individual properties of epoxy and nanoparticles in a single unit [27, 28]. The combination of better structural behavior with intelligent qualities such as sensing, actuation capabilities, and strain monitoring is termed novel multifunctional epoxy nanocomposites [29]. Numerous nanostructural materials, such as carbon nanofibers [5], iron and iron oxide nanoparticles [30], graphene [31, 32], carbon nanotubes [33, 34], silica [35, 36], nano clay [37, 38], polyaniline [39], alumina [40], zinc oxide [41–43], and were utilized to formulate epoxy nanocomposites to enhance the mechanical properties and realize new functionalities such as magnetic, electrical conductivity, and optical characteristics. Thus resulting into an epoxy with distinctive electrical [43, 44], anticorrosive [45], magnetic characteristics [46], and optical [47] capabilities. Although numerous broad assessments exist concerning the thermal combustion, decomposition, and flame retardancy of epoxy nanocomposites with surface-modified silicon dioxide nanoparticles [23] and epoxy systems [22], there is a paucity of publications about multifunctional epoxy nanocomposites. The challenges and potential resolutions for creating epoxy nanocomposites are discussed in this chapter. The multifunctional epoxy nanocomposites and their usage are explored to present the necessary fundamental knowledge that might help expand their utilization in creative industrial applications.

2 Multifunctional Properties

2.1 Self-healing

Self-healing epoxy are epoxy materials capable of automatic recovery when damaged. They are inspired by biological systems such as the human skin, which are naturally able to heal itself. Existing self-healing epoxy can be classified into three groups: capsule-based, vascular, and intrinsic self-healing materials [48]. In capsule-based self-healing materials, small capsules comprising a liquid capable of filling and closing cracks are embedded under the material surface. In case the material is damaged, cracks trigger some capsules to rupture, releasing the liquid and closing the gap. For vascular self-healing materials, the capsules are substituted by a vascular structure comparable to a tunnel network, in which numerous functional liquids flow. These functional liquids will also fill the gap when a crack appears and breaks the vascular network. The material contained inside a capsule or a vascular network is known as a healing agent. The mechanism and behavior of healing agents are essential to the recovery process and restoration of mechanical properties.

Intrinsic self-healing materials heal through the inherent reversibility of chemical or physical bonding instead of structure design [49], such as the swelling of shape-memory polymers [50], the melting and solidification of thermoplastic materials [51], and increasing viscosities of pH-sensitive micro-gels [52]. Consequently, the healing mechanisms of intrinsic self-healing materials are fundamentally different from those of capsule-based and vascular self-healing composites.

Capsule-based and vascular self-healing structures are the main routes to building autonomous self-healing structures. Healing mechanisms, healing performance, and fabrication techniques for producing capsules and building vascular networks have been summarized and analyzed. Capsule-based self-healing materials can heal small cracks, while vascular systems are more suitable for healing larger damaged areas. The healing performance varies from 24 to 121% depending on the types of healing agents, different healing, and damage conditions.

2.2 Shape Memory

Shape-memory epoxy resins are an emergent category of polymers with applications covering numerous areas of daily life. Some of these applications include, for example, smart fabrics [53, 54], heat-shrinkable tubes for electronics or films for packaging [55], self-deployable sun sails in spacecraft [56], self-disassembling mobile phones [57], intelligent medical devices [58], or implants for minimally invasive surgery [59, 60]. These examples cover only a tiny number of the possible applications of shape-memory technology, which shows potential in numerous other applications.

Shape-memory epoxy resins are dual-shape materials belonging to the group of 'actively moving' polymers [61]. They can actively adjust from a shape A to a shape B. Shape A is a temporary shape that is obtained by mechanical deformation and subsequent fixation of that deformation. This procedure also defines the change of shape shift, resulting in shape B, which is the permanent shape. In shape-memory polymers stated so far, heat or light has been employed as the stimulus. Using irradiation with infrared light, application of electric fields, alternating magnetic fields, or immersion in water, indirect actuation of the shape-memory effect has also been realized. The shape-memory effect only depends on the molecular architecture and does not necessitate a specific chemical structure in the repeating units. Therefore, intrinsic material properties, e.g., mechanical properties, can be altered to the need of specific applications by variation of molecular parameters, such as the type of monomer or the comonomer ratio.

2.3 Magnetic

Magnetic epoxy nanocomposites are typically created by incorporating magnetic nanoparticles into the epoxy matrix. Consequently, epoxy is widely used in microwave adsorption [62–64], magnetic resonance imaging [65], flexible electronics [66], and electromagnetic interference shielding [66]. Owing to their distinctive physicochemical properties, such as high coercivity and integral active chemical catalysis with their minute size and high specific surface area, magnetic nanoparticles, such as cobalt, iron, nickel, and their alloys among them or others, have recently attracted significant consideration in various chemical and physical domains [67], owing to their distinctive physicochemical properties containing high coercivity and integral active chemical catalysis with their minute size and high specific surface area, which are unlike the bulk materials [68]. In magnetic hysteresis loops, the intensity of the applied external magnetic field is essential to return the material to zero magnetization once it has become saturated, and the remnant magnetization is the magnetization that remains after the applied external magnetic field has been detached. Diverse magnetic domains, wherein atoms' magnetic moments are aligned in an identical direction, make up bulk magnetic materials. However, when the size of a magnetic substance shrinks, the number of magnetic domains shrinks as well, perhaps to only one. These nanoparticles' magnetic characteristics are no longer consistent with bulk magnetic materials [69]. Magnetic nanoparticles have added proficient interactions with the polymer matrix on the nanoscale, which influences the surface energy at the interface between the magnetic nanoparticles and the matrix [70]. Magnetite (Fe_3O_4) is the strongest magnetic substance of all-natural minerals on Earth [71], out of all the magnetic nanoparticles. Park et al. [72] studied the magnetic characteristics and wear rates of silane-modified Fe_3O_4/epoxy nanocomposites. The modified Fe_3O_4/epoxy nanocomposites' saturation magnetization was found to be higher than that of the unmodified Fe_3O_4/epoxy nanocomposites. However, because pure magnetic metal nanoparticles are easily oxidized and flammable in air, the

majority of reported magnetic nanocomposites are based on magnetic metal oxide [73].

2.4 Thermal and Electrical Conductivities

The unprecedented growth of the semiconductor electronic sector, particularly wireless telecommunication, necessitated the development of new multifunctional nanocomposites to meet the demands of electronic gadgets [74]. As a result of their ecologically acceptable and cost-effective process/materials and ease of large-scale fabrication adaptation, epoxy-based nanocomposites with electrical and thermal conductivities have advanced [75]. Nanoparticles are typically superior to micron-sized particles in electrically and thermally conductive applications because they have a higher specific surface area, which improves electrical and thermal properties, such as a lower percolation threshold and increased electrical and thermal conductivity [76]. Epoxy materials with good thermal conductivity can effectively reduce heat and solve heat dissipation issues in electronic devices [77].

Because of their exceptional conductivity [78] and extensive range of applications in electronics [79], supercapacitors [80], electrodes for electrodeposition [81], and conducting polymers have gotten increased attention in recent decades. A doping procedure can usually be used to adjust the conductivity of conducting polymers [82]. Zhang and Guo et al. [83, 84] have produced pure conducting polymers as conducting nanofillers to increase the electrical conductivity of epoxy. The addition of a 10.0% (w/w) loading of nanofiller to the epoxy resulted in the electrical conductivity rise by 5–6 orders of magnitude.

The extremely mobile electrons in pure metallic nanoparticles result in outstanding electrical conductivity. Nevertheless, because of their easy oxidation and flammability in air, it is difficult for metal oxide nanoparticles to be extensively utilized in production, and most of the indicated effort focuses on them [73]. To maintain pure iron nanoparticles, Zhu and Zhang et al. proposed a protective shell made of metal oxide [31] and carbon [70] thin layers. In conclusion, the electrical conductivity of metallic nanoparticle/epoxy nanocomposites might be up to seven orders of magnitude greater than pure epoxy, which might be advantageous for the manufacture of electrically conductive epoxy nanocomposites in large quantities.

Owing to its great adhesive strength, low cost, and good chemical and corrosion resistance, epoxy is now one of the most extensively utilized electrically conductive adhesives for microelectronic packaging such as printed circuit board to flip-chip integrated circuit package assembly [84]. Electrically conductive adhesives typically contain an organic polymeric binder as well as conductive fillers. Epoxy acts as a mechanical link between the interconnections, while the conductive fillers offer electrical conductivity by making physical contact with each other. Silver, gold, nickel, copper, and other carbon compounds could be employed as conductive fillers [74, 85, 86]. Silver flakes are the utmost utilized and commercially obtainable filler due to the nature of their conductive oxides and their high electrical conductivity. Although

nickel and copper are budget-wise, they can be oxidized easily at high humidity and temperatures. These issues decline the behavior of the device interconnections [87]. Electrically conductive adhesives possess several benefits compared with standard solder technology, including mild processing conditions, environmental friendliness, lightweight, and low stress on substrates. Nevertheless, numerous obstacles are to be addressed involving the minute and reduced conductivity at high temperatures and elevated humidity.

2.5 Flame Retardancy

Despite the fact that epoxy is the most common technical polymer, untreated epoxy is exceedingly flammable, severely limiting its applications. As a result, modifying epoxy to increase its flame retardancy is critical [88]. Reduced polymer flammability is usually achieved by combining intrinsically flame-retardant polymers with the chemical modification of existing polymers [89].

Nitrogen-, phosphorus-, and silicon-based materials [89] have been discovered to have flame-retardant characteristics in material compounds in recent decades. Green products are flame-retardants that are less harmful to the environment than halogenated chemicals [88, 90]. Silicon can normally enhance char formation in the condensed phase while trapping active radicals in the gas phase. The produced stable molecular compounds might prevent combustible gases from escaping due to breakdown caused by the nitrogen. Phosphorus could disrupt exothermic activities in the gas phase and promote char formation on the material surface as a barrier in the condensed phase [89]. The flame retardancy behavior of epoxy after mixing with various morphologies as nanofillers was investigated using these principles [83, 91]. The nanofiber morphology was shown to reduce the peak heat release rate of the epoxy in excess of the nanosphere morphology, owing to the increased specific surface area. Gu et al. [21] said that the phosphorus component has a role in the flame-retardant behavior of epoxy materials, implying that phosphorus can stimulate char yield production in the condensed phase.

Graphene is also considered a suitable halogen-free flame-retardant for epoxy, owing to the graphitized and layered structure. The graphene acts as a physical barrier to adsorb the degradation products and facilitate the development of char [92]. Due to its fragile thermal oxidation stability, obtained graphene usually decays in combustion, reducing its flame-retardant property. As a result, some modifications to the produced graphene are required in order to provide a desired flame-retardant property [93].

3 Applications

3.1 Aeronautics

The materials used in aerospace applications are typically subjected to harsh climatic situations such as high humidity, wide temperature swings, and a variety of mechanical loads such as tension, creep, compression, and torsion. Traditional materials such as titanium, steel, and aluminum are acceptable materials that meet all standards, but they have a significant disadvantage when it comes to the fundamental goal of low weight limits [94]. For efficient weight reduction, revolutionary polymer composites in aeronautic production have recently amplified dramatically as load-carrying elements of the innovative generation of adaptable airplanes [95]. Due to their outstanding mechanical behavior, electrical and chemical resistance, and low shrinkage on curing, epoxy-based thermosetting nanocomposites are one of the predominantly utilized aerospace materials in the aeronautical industry [18]. Multifunctionality has also become an important part of aircraft technology. The aerospace industry requires multifunctional epoxy nanocomposites with better mechanical and thermal properties as well as sensing/actuating capabilities [96]. For example, the electrical conductivity of structural sections for airplane fuselages must exceed 1–10 s/m [94] to effectively disperse lightning currents without the usage of conductive metal fibers or metal screens. As a result, new sophisticated epoxy nanocomposites with extra capabilities must be explored without jeopardizing structural integrity. Paipetis and Kostopoulos have written a comprehensive evaluation of the current state of the art in the aerospace composites industry [96].

3.2 Automotive

Epoxy resin is the predominant thermosetting resin in natural fiber composites for automotive applications because it has excellent performance and resilience to environmental deterioration [97]. In the automotive industry, epoxy-based matrix composites are commonly used as automobile bumper beams [98], the power transmission drive shaft [99], dashboards, headliners, seat backs, door panels, package trays, and interior parts [100], as well as an electrically conductive adhesive between a silicon chip and a package lead frame, and as a heat conductive adhesive between a silicon die and a lead frame or substrate [10]. Low-density natural fiber epoxy composites can often reduce the weight of a car by 10–30%. It is projected that a 25% reduction in automobile weight is equivalent to saving 250 million barrels of crude oil annually [98].

Natural fiber-epoxy composites, on the other hand, have low prices, reduced tool wear rates, low manufacturing energy needs, reduced safety and health risks, and good formability. They are less vulnerable than metals to the effects of stress concentration [101]. Carbon nanofibers and glass fibers were recently integrated into natural

fiber composites to produce hybrid fiber-reinforced epoxy composites, thus offering improved fatigue features because micron cracks in the resin will not spread easily like in metals and instead discontinue at the strong hybrid fibers [101]. Characteristics such as stacking sequences, fiber orientation angles, layer number, and layer thickness must be changed to achieve the required performance for automotive use [99].

3.3 Anti-corrosion Coatings

Epoxy resins are utilized in aquatic systems, the erection of new vehicular and pedestrian bridges, the strengthening and rehabilitation of structurally deficient bridges, as structural materials, and as anti-corrosion coatings in addition to aerospace and automotive applications [95]. Steel [102], iron [46], aluminum [14], and magnesium alloys [103] are now commonplace in automobiles, cellular phones, household appliances, guided weapons, large constructions, and computer industries. Metal corrosion, on the other hand, has become a growing problem in the metal finishing sector [104]. According to NASA [105], corrosion-related maintenance expenditures in the USA are estimated to be between 70 and 120 billion dollars per year. As a result, several efforts and inventive deterrence strategies to avert rusting were developed [106].

Lately, epoxy coatings have enticed much consideration because of their excellent adhesion, corrosion resistance, and environmental friendliness [107]. Epoxy coatings, in general, operate as a physical obstacle to keep harmful species at bay [108]. Nonetheless, pure epoxy cannot provide long-term anti-corrosive performance due to cavities and imperfections over the coating surface, subsequently to the curing progression, which causes them to be permeable to water, oxygen, and corrosive ions [109]. Inorganic nanofillers [110] and nanoclay [111] have recently been added into epoxy matrices to build epoxy nanocomposites and adjust the epoxy barrier effect to improve the epoxy coating's anti-corrosive qualities. According to reports, nanoparticles can fix cavities, micron fractures, and other imperfections of epoxy coatings, resulting in enhanced anti-corrosive behavior [112, 113].

3.4 High Voltage

Because of its superior electrical and mechanical qualities, excellent processability, and chemical stability, epoxy resin is one of the most often used thermosets in high-voltage equipment such as printed circuit boards, high-voltage capacitors, motors, generators, and transformers as insulation [114, 115]. When constructing epoxy insulation materials, the dielectric voltage breakdown strength is usually the essential peak metric [116]. As a result, increased heat stability is required for superior epoxy insulating materials to avoid electrical breakdown [117, 118]. As a result

of their extraordinary dielectric breakdown voltage and higher dielectric strength, epoxy composites reinforced with micron-sized inorganic fillers such as alumina, silica, and others have emerged as the ideal insulating materials for high voltage applications compared with pure epoxy [119]. Since nanocomposite insulation can offer higher performances such as reduced dielectric losses and elevated dielectric strength, tracking and erosion resistance, and surface hydrophobicity compared to traditional micro-sized epoxy composites [120], there has been a lot of interest in using nano-sized fillers as additives in epoxy matrices to form nanocomposites [121]. Over a wide range of frequencies, the dielectric permittivity of epoxy nanocomposites was lower than that of pure epoxy and epoxy with the micro-sized filler at low concentrations (depending on the filler type and size) [122]. Meanwhile, it has been discovered that the dielectric property of insulation is also highly connected to the accumulation of surface charge [123]. Nano-sized fillers on the surface of epoxy materials may cause fluctuations in electrical characteristics at the surface and prevent surface charge buildup, resulting in reduced dielectric behavior [124, 125].

4 Conclusion

This chapter provides a comprehensive summary of the characterization, manufacture, and properties of epoxy composites. Due to their exceptional heat and solvent resistance, high specific strength, high thermomechanical properties, lightweight, good adhesiveness, and reduced cost, epoxy composites are widely used in a variety of manufacturing industries, including aeronautic, automotive, aquatic, construction, and oil and gas. Epoxy composites are also used in electromagnetic shielding, printed circuit boards, supercapacitors, and other applications. Fibers, organic fillers, and inorganic fillers are commonly used in composites to obtain excellent performance. Furthermore, the addition of thermoplastic copolymers may cause the epoxy composites to phase split into multiple phase morphologies, allowing the performance of the epoxy composites to be tailored.

References

1. Akatsuka, M., Takezawa, Y., Amagi, S.: Polymer **42**, 3003–3007 (2001)
2. Jyotishkumar, P., Koetz, J., Tiersch, B., Strehmel, V., O¨zdilek, C., Moldenaers, P., H¨assler, R., Thomas, S.: J. Phys. Chem. B **113**, 5418–5430 (2009)
3. Gu, H., Tadakamalla, S., Zhang, X., Huang, Y., Jiang, Y., Colorado, H.A., Luo, Z., Wei, S., Guo, Z.: J. Mater. Chem. C **1**, 729–743 (2013)
4. Hsiao, K.-T., Alms, J., Advani, S.G.: Nanotechnology **14**, 791–793 (2003)
5. Zhu, J., Wei, S., Ryu, J., Budhathoki, M., Liang, G., Guo, Z.: J. Mater. Chem. **20**, 4937–4948 (2010)
6. Zhang, X., He, Q., Gu, H., Colorado, H.A., Wei, S., Guo, Z., Appl, A.C.S.: Mater. Interfaces **5**, 898–910 (2013)

7. Zhang, X., Alloul, O., He, Q., Zhu, J., Verde, M.J., Li, Y., Wei, S., Guo, Z.: Polymer **54**, 3594–3604 (2013)
8. Tunce, E., Sauers, I., James, D.R., Ellis, A.R., Paranthaman, M.P., Aytu˘g, T., Sathyamurthy, S., More, K.L., Li, J., Goyal, A.: Nanotechnology 18, 025703 (2007)
9. Agubra, V.A., Mahesh, H.V., J. Polym. Sci., Part B: Polym. Phys. **52**, 1024–1029 (2014)
10. Gromala, P., Muthuraman, B., Ozturk, B., Jansen, K., Ernst, L.: Thermal, mechanical and multi-physics simulation and experiments in microelectronics and microsystems (EuroSimE). In: 2015 16th International Conference (2015)
11. Jin, H., Mangun, C.L., Stradley, D.S., Moore, J.S., Sottos, N.R., White, S.R.: Polymer **53**, 581–587 (2012)
12. Shi, X., Nguyen, T.A., Suo, Z., Liu, Y., Avci, R.: Surf. Coat. Technol. **204**, 237–245 (2009)
13. Acebo, C., Fern´andez-Francos, X., Messori, M., Ramis, X., Serra, A.: Polymer **55**, 5028–5035 (2014)
14. Abdollahi, H., Ershad-Langroudi, A., Salimi, A., Rahimi, A.: Ind. Eng. Chem. Res. **53**, 10858–10869 (2014)
15. Zhang, B., Asmatulu, R., Soltani, S.A., Le, L.N., Kumar, S.S.A.: J. Appl. Polym. Sci. **131**, 40286 (2014)
16. Tian, W., Liu, L., Meng, F., Liu, Y., Li, Y., Wang, F.: Corros. Sci. **86**, 81–92 (2014)
17. Wang, X.-L., Yang, Y.-Y., Chen, H.-J., Wu, Y., Ma, D.-S.: Tetrahedron **70**, 4571–4579 (2014)
18. Toldy, A., Szolnoki, B., Marosi, G.: Polym. Degrad. Stab. **96**, 371–376 (2011)
19. Liu, Y.Y., Wei, H., Wu, S., Guo, Z.: Chem. Eng. Technol. **35**, 713–719 (2012)
20. Guo, J., Zhang, X., Gu, H., Wang, Y., Yan, X., Ding, D., Long, J., Tadakamalla, S., Wang, Q., Khan, M.A., Liu, J., Zhang, X., Weeks, B.L., Sun, L., Young, D.P., Wei, S., Guo, Z.: RSC Adv. **4**, 36560–36572 (2014)
21. Gu, H., Guo, J., He, Q., Tadakamalla, S., Zhang, X., Yan, X., Huang, Y., Colorado, H.A., Wei, S., Guo, Z.: Ind. Eng. Chem. Res. **52**, 7718–7728 (2013)
22. Levchik, S.V., Weil, E.D.: Polym. Int. **53**, 1901–1929 (2004)
23. Sprenger, S.: J. Appl. Polym. Sci. **130**, 1421–1428 (2013)
24. Plueddemann, E.P.: J. Adhes. Sci. Technol. **5**, 261–277 (1991)
25. Lee, H., Neville, K.: Handbook of Epoxy Resins. McGraw-Hill, New York (1967)
26. Azeez, A.A., Rhee, K.Y., Park, S.J., Hui, D.: Compos. B **45**, 308–320 (2013)
27. Gu, H., Guo, J., Wei, H., Yan, X., Ding, D., Zhang, X., He, Q.,Tadakamalla, S., Wang, X., Ho, T.C., Wei, S., Guo, Z.: J. Mater. Chem. C **3**, 8152–8165 (2015)
28. Guo, J., Gu, H., Wei, H., Zhang, Q., Haldolaarachchige, N.S., Li, Y., Young, D.P., Wei, S., Guo, Z.: J. Phys. Chem. C **117**, 10191–10202 (2013)
29. Paipetis, A., Kostopoulos, V.: Carbon Nanotube Enhanced Aerospace Composite Materials: A New Generation of Multi-functional Hybrid Structural Composites. Springer Science & Business Media (2012)
30. Zhu, J., Wei, S., Ryu, J., Sun, L., Luo, Z., Guo, Z., Appl, A.C.S.: Mater. Interfaces **2**, 2100–2107 (2010)
31. Rafiee, M.A., Rafiee, J., Wang, Z., Song, H., Yu, Z.-Z., Koratkar, N.: ACS Nano **3**, 3884–3890 (2009)
32. Qing, Y., Wang, X., Zhou, Y., Huang, Z., Luo, F., Zhou, W.: Compos. Sci. Technol. **102**, 161–168 (2014)
33. Cui, L.-J., Geng, H.-Z., Wang, W.-Y., Chen, L.-T., Gao, J.: Carbon **54**, 277–282 (2013)
34. Park, I., Peng, H.-G., Gidley, D.W., Xue, S., Pinnavaia, T.J.: Chem. Mater. **18**, 650–656 (2006)
35. Liu, Y.-L., Hsu, C.-Y., Wei, W.-L., Jeng, R.-J.: Polymer **44**, 5159–5167 (2003)
36. Park, J.H., Jana, S.C.: Macromolecules **36**, 2758–2768 (2003)
37. Wang, K., Wang, L., Wu, J., Chen, L., He, C.: Langmuir **21**, 3613–3618 (2005)
38. Jang, J., Bae, J., Lee, K.: Polymer **46**, 3677–3684 (2005)
39. McGrath, L.M., Parnas, R.S., King, S.H., Schroeder, J.L., Fischer, D.A., Lenhart, J.L.: Polymer **49**, 999–1014 (2008)
40. Li, Y.-Q., Fu, S.-Y., Mai, Y.-W.: Polymer **47**, 2127–2132 (2006)
41. Sun, D., Sue, H.-J., Miyatake, N.: J. Phys. Chem. C **112**, 16002–16010 (2008)

42. Liu, Y., Lin, Z., Lin, W., Moon, K.S., Wong, C.P., Appl, A.C.S.: Mater. Interfaces **4**, 3959–3964 (2012)
43. Bao, C., Guo, Y., Song, L., Kan, Y., Qian, X., Hu, Y.: J. Mater. Chem. **21**, 13290–13298 (2011)
44. Guo, J., Long, J., Ding, D., Wang, Q., Shan, Y., Umar, A., Zhang, X., Weeks, B.L., Wei, S., Guo, Z.: RSC Adv. **6**, 21187–21192 (2016)
45. Olad, A., Barati, M., Behboudi, S.: Prog. Org. Coat. **74**, 221–227 (2012)
46. Wang, D., Kou, R., Choi, D., Yang, Z., Nie, Z., Li, J., Saraf, L.V., Hu, D., Zhang, J., Graff, G.L., Liu, J., Pope, M.A., Aksay, I.A.: ACS Nano **4**, 1587–1595 (2010)
47. Gonzalez-Campo, A., Orchard, K.L., Sato, N., Shaffer, M.S.P., Williams, C.K.: Chem. Commun. 4034–4036 (2009)
48. Blaiszik, B.J., Baginska, M., White, S.R., Sottos, N.R.: Autonomic recovery of fiber/matrix interfacial bond strength in a model composite. Adv. Func. Mater. **20**, 3547–3554 (2010). https://doi.org/10.1002/adfm.201000798
49. Chen, X.X., Wudl, F., Mal, A.K., Shen, H.B., Nutt, S.R.: New thermally remendable highly cross-linked polymeric materials. Macromolecules **36**, 1802–1807. https://doi.org/10.1021/Ma0210675
50. Habault, D., Zhang, H., Zhao, Y.: Light-triggered self-healing and shape-memory polymers. Chem. Soc. Rev. **42**, 7244–7256 (2013). https://doi.org/10.1039/C3CS35489J
51. Selver, E., Potluri, P., Soutis, C., Hogg, P.: Healing potential of hybrid materials for structural composites. Compos. Struct. **122**, 57–66 (2015)
52. Zheng, C., Huang, Z.: Microgel reinforced composite hydrogels with pH-responsive, self-healing properties. Colloids Surf. A Physicochem. Eng. Aspects **468**, 327–332 (2015). https://doi.org/10.1016/j.colsurfa.2014.12.060
53. Hu, J., et al.: J. Dong Hua University Engl. Ed. **19**, 89 (2002)
54. Mondal, S., Hu, J.L., Indian, J.: Fibre Textile Res. **31**, 66 (2006)
55. Charlesby, A.: Atomic Radiation and Polymers, p. 198. Pergamon Press, New York (1960)
56. Campbell, D., et al.: Elastic memory composite material: an enabling technology for future furable space structures. In: 46th AIAA/ASME/ASCE/AHS/ASC Structures, Structural Dynamics, and Materials Conference, Austin, Texas (2005_
57. Hussein, H., Harrison, D.: Investigation into the use of engineering polymers as actuators to produce 'automatic disassembly' of electronic products. In: Bhamra, T., Hon, B., (eds.) Design and Manufacture for Sustainable Development 2004, Wiley-VCH, Weinheim (2004)
58. Wache, H.M., et al.: J. Mater. Sci.: Mater. Med. **14**, 109 (2003)
59. Lendlein, A., Langer, R.: Science **296**, 1673 (2002)
60. Metcalfe, A., et al.: Biomaterials **24**, 491 (2003)
61. Behl, M., Lendlein, A.: Soft Matter **3**, 58 (2007)
62. Guo, Z., Park, S., Hahn, H.T., Wei, S., Moldovan, M., Karki, A.B., Young, D.P.: J. Appl. Phys. **101**, 09M511 (2007)
63. Guo, Z., Lee, S.E., Kim, H., Park, S., Hahn, H.T., Karki, A.B., Young, D.P.: Acta Mater. **57**, 267–277 (2009)
64. Zhu, J., Wei, S., Haldolaarachchige, N., Young, D.P., Guo, Z.: J. Phys. Chem. C **115**, 15304–15310 (2011)
65. Guo, Z., Henry, L.L., Palshin, V., Podlaha, E.J.: J. Mater. Chem. **16**, 1772–1777 (2006)
66. Gu, H., Tadakamalla, S., Huang, Y., Colorado, H.A., Luo, Z., Haldolaarachchige, N., Young, D.P., Wei, S., Guo, Z., Appl, A.C.S.: Mater. Interfaces **4**, 5613–5624 (2012)
67. Hao, R., Xing, R., Xu, Z., Hou, Y., Gao, S., Sun, S.: Adv. Mater. **22**, 2729–2742 (2010)
68. Pan, Y., Du, X., Zhao, F., Xu, B.: Chem. Soc. Rev. **41**, 2912–2942 (2012)
69. Colombo, M., Carregal-Romero, Casula, S.M.F., Guti´errez, L., Morales, M.P., B¨ohm, I.B., Heverhagen, J.T., Prosperi, D., Parak, W.J., Chem. Soc. Rev. **41**, 4306–4334 (2012)
70. Zhang, X., Alloul, O., Zhu, J., He, Q., Luo, Z., Colorado, H.A., Haldolaarachchige, N., Young, D.P., Shen, T.D., Wei, S., Guo, Z.: RSC Adv. **3**, 9453–9464 (2013)
71. Gu, H., Huang, Y., Zhang, X., Wang, Q., Zhu, J., Shao, L., Haldolaarachchige, N., Young, D.P., Wei, S., Guo, Z.: Polymer **53**, 801–809 (2012)
72. Park, J., Rhee, K., Park, S.: Appl. Surf. Sci. **256**, 6945–6950 (2010)

73. Guo, Z., Lei, K., Li, Y., Ng, H.W., Hahn, H.T.: Compos. Sci. Technol. **68**, 1513–1520 (2008)
74. Gu, J.W., Lv, Z.Y., Wu, Y.L., Zhao, R.X., Tian, L.D., Zhang, Q.Y.: Compos. A **79**, 8–13 (2015)
75. Gu, J., Lv, Z.Y., Yang, X.T., Wang, G.E., Zhang, Q.Y.: Sci. Adv. Mater. **8**, 972–979 (2016)
76. Gu, J., Li, N., Tian, L.D., Lv, Z.Y., Zhang, Q.Y.: RSC Adv. **5**, 36334–36339 (2015)
77. Gu, J., Du, J.J., Dang, J., Geng, W.C., Hu, S.H., Zhang, Q.Y.: RSC Adv. **4**, 22101–22105 (2014)
78. Gu, H., Guo, J., Zhang, X., He, Q., Huang, Y., Colorado, H.A., Haldolaarachchige, N.S., Xin, H.L., Young, D.P., Wei, S., Guo, Z.: J. Phys. Chem. C **117**, 6426–6436 (2013)
79. Stoyanov, H., Kollosche, M., Risse, S., Wach´e, R., Kofod, G.: Adv. Mater. **25**, 578–583 (2013)
80. Wei, H., Zhu, J., Wu, S., Wei, S., Guo, Z.: Polymer **54**, 1820–1831 (2013)
81. Wang, D., Ye, Q., Yu, B., Zhou, F.: J. Mater. Chem. **20**, 6910–6915 (2010)
82. Gu, H., Guo, J., Yan, X., Wei, H., Zhang, X., Liu, J., Huang, Y., Wei, S., Guo, Z.: Polymer **55**, 4405–4419 (2014)
83. Zhang, X., He, Q., Gu, H., Colorado, H.A., Wei, S., Guo, Z., Appl, A.C.S.: Mater. Interfaces **5**, 898–910 (2012)
84. Rosca, I.D., Hoa, S.V.: Compos. Sci. Technol. **71**, 95–100 (2011)
85. Guan, Y., Chen, X., Li, F., Gao, H.: Int. J. Adhes. Adhes. **30**, 80–88 (2010)
86. Wu, H.P., Wu, X.J., Ge, M.Y., Zhang, G.Q., Wang, Y.W., Jiang, J.: Compos. Sci. Technol. **67**, 1182–1186 (2007)
87. Li, Y., Moon, K.-S.J., Wong, C.: Nano-conductive Adhesives for Nano-electronics Interconnection. Springer (2010)
88. Hergenrother, P.M., Thompson, C.M., Smith, J.G., Jr., Connell, J.W., Hinkley, J.A., Lyon, R.E., Moulton, R.: Polymer **46**, 5012–5024 (2005)
89. Bourbigot, S., Duquesne, S.: J. Mater. Chem. **17**, 2283–2300 (2007)
90. Shi, Y., Kashiwagi, T., Walters, R.N., Gilman, J.W., Lyon Chum, R.E., Sogah, D.Y.: Polymer **50**, 3478–3487 (2009)
91. Zhang, X., Yan, X., Guo, J., Liu, Z., Jiang, D., He, Q., Wei, H., Gu, H., Colorado, H.A., Zhang, X., Wei, S., Guo, Z.: J. Mater. Chem. C **3**, 162–176 (2015)
92. Liu, S., Yan, H., Fang, Z., Wang, H.: Compos. Sci. Technol. **90**, 40–47 (2014)
93. Hong, N., Zhan, J., Wang, X., Stec, A.A., Hull, T.R., Ge, H., Xing, W., Song, L., Hu, Y.: Compos. A **64**, 203–210 (2014)
94. Guadagno, L., Raimondo, M., Vittoria, V., Vertuccio, L., Naddeo, C., Russo, S., De Vivo, B., Lamberti, P., Spinelli, G., Tucci, V.: RSC Adv. **4**, 15474–15488 (2014)
95. Sugita, Y., Winkelmann, C., La Saponara, V.: Compos. Sci. Technol. **70**, 829–839 (2010)
96. Paipetis, A., Kostopoulos, V.: Carbon Nanotube Enhanced Aerospace Composite Materials: A New Generation of Multi-functional Hybrid Structural Composites (2012)
97. Ghassemieh, E.: Materials in Automotive Application, State of the art and Prospects. INTECH Open Access Publisher (2011)
98. Davoodi, M., Sapuan, S., Ahmad, D., Ali, A., Khalina, A., Jonoobi, M.: Mater. Des. **31**, 4927–4932 (2010)
99. Badie, M., Mahdi, E., Hamouda, A.: Mater. Des. **32**, 1485–1500 (2011)
100. Holbery, J., Houston, D.: JOM **58**, 80–86 (2006)
101. Talib, A.A., Ali, A., Badie, M.A., Lah, N.A.C., Golestaneh, A.: Mater. Des. **31**, 514–521 (2010)
102. Behzadnasab, M., Mirabedini, S., Kabiri, K., Jamali, S.: Corros. Sci. **53**, 89–98 (2011)
103. Qiao, Y., Li, W., Wang, G., Zhang, X., Cao, N.: RSC Adv. **5**, 47778–47787 (2015)
104. Hosseini, M., Jafari, M., Najjar, R.: Surf. Coat. Technol. **206**, 280–286 (2011)
105. Chang, C.-H., Hsu, M.-H., Weng, C.-J., Hung, W.-I., Chuang, T.-L., Chang, K.-C., Peng, C.-W., Yen, Y.-C., Yeh, J.-M.: J. Mater. Chem. A **1**, 13869–13877 (2013)
106. Hollamby, M.J., Fix, D., D¨onch, I., Borisova, D., Mohwald, H., Shchukin, D.: Adv. Mater. **23**, 1361–1365 (2011)
107. Atta, A.M., El-Saeed, A.M., El-Mahdy, G.M., Al-Lohedan, H.A.: RSC Adv. **5**, 101923 (2015)
108. Pour-Ali, S., Dehghanian, C., Kosari, A.: Corros. Sci. **85**, 204–214 (2014)

109. Popovi´c, M., Grgur, B., Mi˘skovi´c-Stankovi´c, V.: Prog. Org. Coat. **52**, 359–365 (2005)
110. Rostami, M., Rasouli, S., Ramezanzadeh, B., Askari, A.: Corros. Sci. **88**, 387–399 (2014)
111. Tomi´c, M.D., Dunji´c, B., Liki´c, V., Bajat, J., Rogan, J., Djonlagi´c, J.: Prog. Org. Coat. **77**, 518–527 (2014)
112. Yu, Z., Di, H., Ma, Y., Lv, L., Pan, Y., Zhang, C., He, Y.: Appl. Surf. Sci. **351**, 986–996 (2015)
113. Issa, C.A., Salem, G.: Cons. Bldg. Mat. **42**(5), 48–52 (2013)
114. Kochetov, R., Andritsch, T., Morshuis, P., Smit, J.: 2010 Annual Report Conference on Electrical Insulation and Dielectric Phenomena (CEIDP) (2010)
115. Xia, Y., Wang, W., Tao, C., Li, C., He, S., Chen, W.: Electrical Insulation Conference (EIC), 2015 IEEE (2015)
116. Mohanty, A., Srivastava, V.: Mater. Des. **47**, 711–716 (2013)
117. Siddabattuni, S., Schuman, T.P., Dogan, F.: Mater. Sci. Eng., B **176**, 1422–1429 (2011)
118. Wang, Q., Chen, G.: Adv. Mater. Res. **1**, 93–107 (2012)
119. Meyer, L., Cherney, E., Jayaram, S., Elect, I.E.E.E.: Insul. Mag. **20**, 13–21 (2004)
120. Green, C., Vaughan, A., Elect, I.E.E.E.: Insul. Mag. **24**, 6–16 (2008)
121. Iyer, G., Gorur, R., Richert, R., Krivda, A., Schmidt, L.: IEEE Trans. Dielectr. Electr. Insul. **18**, 659–666 (2011)
122. Singha, S., Thomas, M.J.: IEEE Trans. Dielectr. Electr. Insul. **15**, 12–23 (2008)
123. Du, B., Zhang, J., Gao, Y.: IEEE Trans. Dielectr. Electr. Insul. **19**, 755–762 (2012)
124. Mohamad, A., Chen, G., Zhang, Y., An, Z.: IEEE Trans. Dielectr. Electr. Insul. **22**, 101–108 (2015)
125. Wang, Q., Chen, G., Alghamdi, A.S.: Solid Dielectrics (ICSD), 10th IEEE International Conference on 2010 (2010)
126. Gu, H., Guo, J., Wei, H., Yan, X., Ding, D., Zhang, X., He, Q., Tadakamalla, S., Wang, X., Ho, T.C., Wei, S., Guo, Z.: J. Mater. Chem. C **3**, 8152–8165 (2015)

Basics of Self-healing Epoxy Systems—General Concepts, Behavior, and Mechanism

Shalini Parihar and Bharti Gaur

Abstract Epoxies are the most versatile thermoset resins and are considered to be the hallmark of thermoset industries. The demand for epoxy resins is predicted to grow at a compound annual growth rate of 6.32% by 2030. The self-healing nature of synthetic material is an emerging field of research as it can prolong the service life of the material and thus can possess a broader range of applications. The development of self-healing epoxy resins has been inspired by the natural repairing system wherein the damage initiates autonomic healing of the wound. This chapter covers the fundamentals of the self-healing system as well as the mechanism and main approaches of self-healing, which are further divided depending on the healing chemistries involved and the type of vessels used to store the healing agent. The benefits and drawbacks of various self-healing techniques have been discussed. This chapter also reviews the existing self-healing epoxy systems published in the last decade. Lastly, the research opportunities in the near future and the challenges are discussed.

Keywords Self-healing · Epoxy resins · Intrinsic · Extrinsic · Microcapsules · Thermo-reversible crosslinks

1 Introduction

Epoxy resins are the prepolymers containing three-membered epoxy rings with an oxygen atom bonded to two interconnected carbon atoms and thus possess considerable ring strain, making them highly reactive. These epoxy rings are usually terminal, though they may lie within the chain of the molecule. The thermoset epoxy resins are a fusion of both epoxy resin and curative agent. Because of the existence of electron-rich oxygen and electron-deficient carbon atoms in the oxirane rings, the epoxide resins can undergo both electrophilic as well as nucleophilic addition reactions. Thus, epoxy resins can cross-link with one another or with a variety of hardeners/curatives

S. Parihar · B. Gaur (✉)
Department of Chemistry, National Institute of Technology Hamirpur (H.P.), Hamirpur, India
e-mail: bhartigaur@nith.ac.in

N. Hameed et al. (eds.), *Multifunctional Epoxy Resins*, Engineering Materials,
https://doi.org/10.1007/978-981-19-6038-3_2

such as alcohols, thiols, phenols, amines, anhydrides, amides, and acids, resulting in three-dimensional cross-linked thermosetting polymers. The cross-linking density of the epoxy thermosets is responsible for the mechanical, thermal, and many other properties of the material. The process of fusion of the oxirane group and hardener is termed as curing of epoxy, and the cured epoxy thermoset resin contains no or relatively very few epoxide groups.

Epoxy resin thermosets possess excellent properties such as adhesive strength, thermal stability, chemical resistance, electrical insulation, mechanical strength, processability, flame retardance, and water tightness. These properties enable a wide range of thermosetting resin applications in aerospace and recreation industries, coatings and adhesives, printed circuit boards, potting materials for electronics, high tension electrical insulators, fiber-reinforced plastic materials, and lightweight automobile parts. Epoxy thermosets can also improve the decorative/aesthetic performance of the material. An increase in the functionality of these resins increases their reactivity and thus promotes their binding with various substrates/fibers. The epoxy resin thermosets are employed as a matrix material for fiber-based composites in renewable energy and aerospace industries. Thus, epoxy resins are important, commercially available, multipurpose thermosetting materials with high strength and firmness.

However, epoxy resin thermosets have an imperfection, as they are brittle, and minor cracks are more likely to form during their service life. These microcracks are difficult to detect because they are deep within the structure, and if not repaired, they can progress to macrocracks, causing the entire system to fail. Traditional damage repair techniques (welding and patching) are restricted to visible cracks only, are not instantaneous or autonomous, and demand a thorough inspection of the material. Epoxy systems are difficult to recycle at the end of their lives due to their highly cross-linked network architectures and thus may cause health and environmental difficulties. The epoxy resin's service life can be extended either by preventing the microcracks formation in the epoxy matrix or by repairing microcracks as soon as they form. Hence to reduce the cost of damage repair and to prolong the service life of the material, there is a need to upgrade the material to be self-healing. Over the past few decades, successful attempts have been made to synthesize epoxy-based self-healing materials, and this has attracted the interest of many researchers and scientists.

Self-healing may be defined as the material's ability to recover from damages/cracks on its own. The inspiration for self-healing in materials is derived from nature's wound and cut repairing ability in living organisms. Every living species can release the healing agents to the site of injuries and thus repair the damage by sealing and then healing the wounds. Even the plants can restore the mechanical properties along with the wound closure. The self-healing materials are supposed to imitate the capability of biotic materials to repair the wound and restore mechanical integrity.

This chapter represents an overview of the general concept of self-healing approaches, discusses various healing mechanisms along with the benefits and drawbacks of the various methods, and studies the behavior of epoxy systems with self-healing ability.

2 Approaches of Self-healing

There are numerous self-healing approaches, which are primarily classified into two categories: extrinsic self-healing and intrinsic self-healing. In these two approaches, the self-healing chemistries that the polymeric material undergoes during the crack repairing process are different. However, the mobile phase is required in both self-healing approaches so that it can flow to the site of damage and fill the crack during the healing process. In the extrinsic self-healing approach, the crack in the network structure is repaired by the release of the healing agents from the containers, which are already embedded in the polymer matrix and allow them to flow to the site of damage. The cross-linking of the healing agent results in the repair of the crack. Because the damage itself triggers the release of the healing agent from the containers, this extrinsic self-healing approach is also known as autonomous self-healing as no external intervention, such as heat, light, or moisture, is required to initiate the repair mechanism.

On the other hand, in the case of the intrinsic self-healing approach, the self-healing process is driven by the chemical bonding of the matrix. Thus, the material is designed with the inherent potential to restructure after impairment in the presence of external triggers such as heat, light, or chemicals. No stored healing agent or catalyst is required in its self-repairing chemistry. The intrinsic self-healing mechanism is considered non-autonomous, as external stimuli are required to initiate the healing process. The following sections summarize the development of self-healing polymeric materials for these two categories.

2.1 Extrinsic Self-healing Mechanism

In extrinsic self-healing, the resin matrix is not healable on its own. The repairing agent-filled micro-containers are dispersed within the matrix system in advance. When exposed to fracture, the micro-containers rupture, thereby releasing the healing agent, which travels through capillary action to the site of damage, where it is cured by the polymerization reaction, restoring the material's damage and surface integrity [1]. The healing agent must be stable for a long duration inside the micro-containers and should be able to reach the crack site via capillary action, i.e., lower viscosity. It should react quickly to seal the crack in a reasonable amount of time and have no harmful effects on the polymer matrix. The added catalyst and the curing agents present in the polymer matrix must be chemically stable within the matrix but rapidly

react when they come in contact with the healing agent. The catalyst must be stable over a wide range of applications and temperatures and well dispersed within the matrix.

This self-healing mechanism is not repeatable, and the scratch at a specific location can be healed only once [2]. The healing performance and self-healing ability of the material depend on structural and dynamic factors such as size, shape, and distribution pattern of micro-containers, flow, and incorporation of healing agents into micro-containers. In this self-healing approach, the research is mainly focused on the fracture process, repairing agent, kneading process, and matrix formulation techniques. Based on the type of micro-containers embedded within the matrix, the extrinsic self-healing technique is further divided into categories such as microencapsulation, microvascular networks, hollow fibers, or nanoparticles, which are described in detail in the upcoming sections.

2.1.1 Healant Loaded Capsules/Containers

In this mechanism of self-healing, capsules of micro-size are used as containers for the healing agent. Some researchers have also developed dual capsule-based self-healing systems in which both the healing agent as well as the curative agent or hardener are encapsulated and dispersed within the polymeric system. Many researchers have worked on developing epoxy-based self-healing coatings and studying their healing capabilities as well as other mechanical properties; a few of the research articles are listed below.

Self-healing System Having Capsule and Catalyst

Epoxy resins with capsule-based self-healing ability were first reported by White et al. [3] in 2001, which involved the use of a monomer, dicyclopentadiene (DCPD), stored in urea-formaldehyde microcapsules. A progressive crack ruptures the microcapsules, and the healing agent is released into the cracked location by capillary action, where it comes in contact with dispersed Grubb's catalyst and initiates the polymerization reaction resulting in crack repairing and restoring the material's surface integrity as shown in Fig. 1. Here, the repairing process occurs through a living ring-opening metathesis polymerization (ROMP) reaction. In terms of toughness, the healing efficiency of the material was found to be 75%. This is an autonomically self-healable material because no external stimulus is needed to initiate the repairing process as it is triggered by the propagating crack itself. DCPD is widely used as a healing agent in self-healing materials [4–6], and Grubb's catalyst is used as a catalyst in the ROMP of DCPD. White et al. made use of first-generation Grubb's catalyst, but due to low chemical and thermal stability, its applications are limited in microcapsule-based self-healing polymeric materials. To overcome this difficulty, Moore et al. [7] made use of second-generation Grubb's catalyst, Hoveyda Grubb's second-generation catalyst, and with first-generation Grubb's catalyst to compare

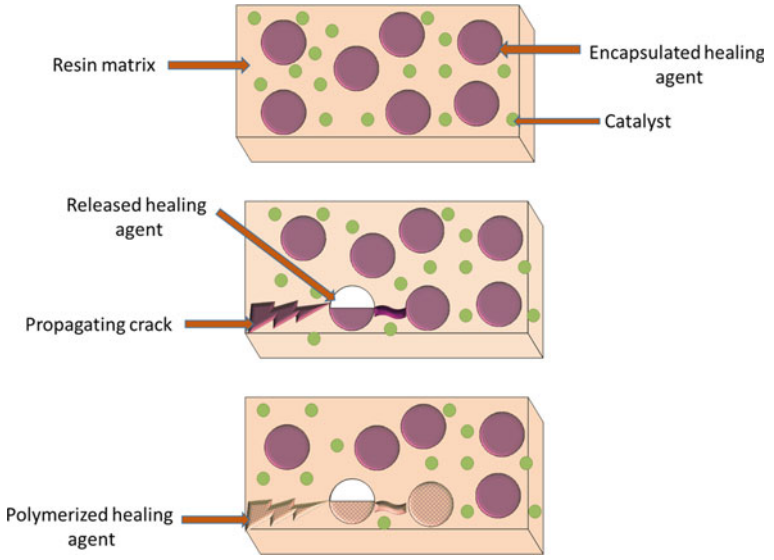

Fig. 1 Autonomic healing process for self-healing material with an embedded encapsulated healing agent and the catalyst dispersed within the composite matrix

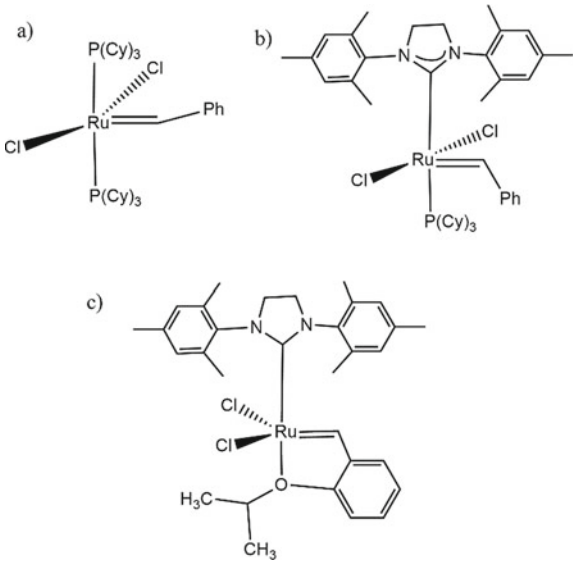

Fig. 2 Molecular structures of **a** Grubb's first-generation catalyst, **b** Grubb's second-generation catalyst, and **c** Hoveyda Grubb's second-generation catalyst

their thermal, chemical, and catalytic properties. Figure 2 represents the structures of various Grubb's catalysts.

The second-generation Grubb's catalyst was discovered to have excellent healing efficiency and thermal stability at elevated temperatures. To withstand harsh

conditions such as mechanical shear, high temperatures, and so on, the capsule's robustness must be greatly enhanced. Caruso et al. [8] created double-walled microcapsules made of PU/UF polyurethane/poly(urea-formaldehyde) microcapsules for this purpose. These double-walled microcapsules outperformed single-walled urea-formaldehyde capsules in terms of thermal stability and mechanical properties. Jin et al. [9] used a rubber toughened structural epoxy adhesive to further their research on self-healing. The self-healing ability of embedded microcapsules filled with DCPD monomer and Grubb's catalyst was demonstrated by high-temperature curing at 110 °C for 3 h. The fracture toughness of the rubber adhesive was investigated by using a width tapered double cantilever beam (WTDCB) test specimen. For 6.6 wt% of DCPD microcapsules and 10 mg of the catalyst, the healing efficiency was found to be 58%.

The poor catalytic dispersion and activation/deactivation of the catalyst, which may reduce the healing ability of the matrix, are some concerns with this capsule catalyst-based self-healing system. Thus, to preserve the catalytic reactivity of the catalyst, a wax-coated Grubb's catalyst can be used [10]. A glass-reinforced self-healing epoxy composite system can also be prepared by using DCPD capsules and paraffin wax microspheres having 10 wt% Grubb's catalyst [11]. The self-healing ability in such case accessed using a low-velocity impact test revealed that the crack length was reduced to 51% after the repair observed through fluorescent labeling.

In a very recent study, Romero-Sabat et al. [12] reported the synthesis of an extrinsic self-healing composite material with a healing efficiency of more than 100% at low or ultra-low temperatures. It is based on the ring-opening metathesis polymerization (ROMP) of 5-ethylidenenorbornene/dicyclopentadiene (ENB/DCPD) blends that can flow even at −70 °C and can react with Grubb's third-generation catalyst. The monomers, ENB/DCPD, were encapsulated within the polyurea (PU) capsules and dispersed into three commercially available epoxy resins, and there was no need to shield the metathesis catalyst. The fracture toughness analysis with tapered double cantilever beam (TDCB) for all different epoxy systems reveals that the healing efficiency was found to be more than 100% at cryogenic temperatures (−20 °C).

Dual Capsule-Based Self-healing Systems

The microcapsule catalyst-based systems have some disadvantages, such as improper dissolution of the catalyst, disruption of the catalyst by the epoxy of the matrix system, the low compatibility of the DCPD and Grubb's catalyst with the matrix, and insufficient interactions of the healing agent with the catalyst. The dual capsule-based self-healing systems have been investigated to overcome these disadvantages. Here, in this category, both the healing agent and the hardener are encapsulated separately into the microcapsules, which are then dispersed evenly into the polymer matrix system. When a fracture occurs, the microcapsules rupture and the healing agent gets polymerized when it comes in contact with the hardener, thus repairing the damage. For this purpose, in 2007, Rong et al**.** synthesized an epoxy amine-based resin system in

which the DGEBA epoxy resin and imidazole hardener were both encapsulated separately and dispersed into the matrix system [13]. In this case, no catalyst is required for the polymerization reaction. The microcapsules shell wall for epoxy resin has been prepared from poly(urea-formaldehyde) PUF by the oil in water emulsion, and PUF encapsulated imidazole served as the hardener for the epoxy. The healing efficiency was accessed by the fracture toughness test and was found to be around 106%. The heat resistance self-healing epoxy composite system had also been developed by Yuan et al. using diglycidyl ether of bisphenol A (EPON 828) as a healing agent and a catalyst 2,4,6-tris(dimethylaminomethyl)phenol (DMP-30) [14]. The material used to prepare the microcapsule shell wall was poly(maleimide-formaldehyde) (PMF). The employed epoxy resin is thermally stable, and DMP-30 has low volatility, making the system self-healable and can survive in high-temperature curing conditions. The composite system showed a high level of self-repairing ability below 200 °C and healing efficiency of 72–86% even on exposure to a high temperature of 250 °C.

Li et al. [15] developed a self-healing epoxy-based system using DGEBA diglycidyl ether bisphenol A as the active ingredient. The epoxy resin and polyetheramine hardener were encapsulated in a poly(methyl methacrylate) (PMMA) shells using a water-in-oil emulsion technique. The ratio and content of microcapsules had an impact on healing efficiency. When 5 wt% of the microcapsules were dispersed within the resin system, and curing was carried out at room temperature for 24 h, the healing efficiency was found to be 43.5%. It was increased to 84.5% when the microcapsule content was raised to 15 wt%.

Our group [16] has recently developed a dual capsule-based self-healing material using a bio-based epoxy and an imidoamine curing agent. An in situ polymerization technique was used to develop melamine-formaldehyde (MF) microcapsule containers. The average size of epoxy-filled microcapsules was 83 μm, while that of hardener-filled microcapsules was 95 μm. The mild steel specimens served as coating substrates, and the self-healing coatings were prepared by using epoxy/imidoamine with 10 and 20 wt% epoxy microcapsules and both 10 wt% epoxy and 10 wt% hardener-filled microcapsules. The solvent wash analysis was used to determine the stability of microcapsules, which was found to be 98.2 and 87.5% for epoxy microcapsules-based and dual capsule-based coatings, respectively. SEM confirmed the surface morphology and the self-healing ability. The salt spray, mechanical analysis, and adhesion testing were performed on coated specimens with and without microcapsules. The self-healing coatings with both 10 wt% epoxy and 10 wt% curing agent-filled microcapsules exhibited excellent properties.

Wang [17] synthesized an epoxy composite with self-healing capabilities. Here also, the dual capsules of diglycidyl1,2-cyclohexanedicarboxylate (DGCHD) and an aliphatic amine hardener (HB-1618) were prepared. The polyetherimide was used as the shell wall material for the amine hardener microcapsules. The healing efficiency varies with the capsule concentration. With a 15% capsule concentration (6 wt% epoxy-containing and 9 wt% hardener-containing microcapsules), the efficiency was 65.6%. The hollow glass bubbles can also be used to encapsulate the epoxy and amine solutions, and a dual-part epoxy amine-based self-healing polymer

was developed by Zhang et al. [18]. The epoxy and amine solutions were encapsulated in etched, hollow glass bubbles (HGBs) and dispersed in the matrix system. The micro-compression tests were performed on a single HGB to determine its mechanical robustness and cracking ability. The HGBs were found to be much brittle as well as stronger than the PUF or PU microcapsules. The incorporated ratio of epoxy to amine HGBs was optimized to 4:1. The material showed the best healing efficiency of 62% when cured at 50 °C for 24 h, and the total HGBs content was 12.5–15.0 wt%. The healing efficiency was found to increase with increasing curing time at 50 °C, which was attributed to promote cross-linking over time as well as good diffusion of higher molecular weight chains. Corrosion-resistant, dual capsule-based self-healing epoxy coatings using epoxy resin and an amine hardener have also been reported [19], wherein the poly(styrene-*co*-acrylonitrile), SAN, was used as a shell wall material for microcapsules. Commercially available Bisphenol F epoxy resin and cycloaliphatic polyamine (EPIKURE F205-Hexion) were used as the core materials, and the material used to prepare the coating matrix was bisphenol A epoxy resin (EPON 828) and polyamidoamine curing agent (Merginamide A280). The core material was encapsulated by using the emulsion electrospray technique. Three coating samples based on microcapsule content in ratios 1, 5, and 10 wt% (in 1:1 molar ratio of epoxy and amine hardener) were dispersed within the matrix. The healing efficiency was determined with the help of electrochemical impedance spectroscopy (EIS). The coating sample with 1 wt% of microcapsule showed the best corrosion resistance with 99% self-healing efficiency.

High-temperature cured epoxy resins have a wide range of applications as structural adhesives and structural composites due to their chemical and mechanical properties. Ghazali et al. [20] studied the self-healing behavior of a dual capsule-based, high-temperature cured epoxy resin system. DGEBA resin and mercaptan hardener were loaded into the dual capsules, and 2,4,6-tris (dimethylaminomethyl)phenol (DMP-30) was used as a catalyst. The microcapsules were synthesized from poly(melamine-formaldehyde) (PMF) by in situ polymerization reaction. The mechanical behavior and self-healing abilities of the tapered double cantilever beam (TDCB) epoxy specimens were examined using mode I fracture toughness testing. When heated to 70 °C, the epoxy system recovered up to 111% of its original fracture toughness. At higher temperatures, the healant with a lower viscosity showed excellent healing ability.

The self-healing capsules are mostly made up of synthetic polymers, which can cause environmental as well as health issues. Thus, self-healing bio-capsules for encapsulating the monomers can eliminate these concerns. These bio-capsules can be prepared using alginate biopolymer. Hia et al. [21] used the electro-spraying method in order to encapsulate the epoxy (DGEBA) as well as a hardener (mercaptan/tertiary amine), respectively. The diameter of these encapsulated bio-capsules was reported to be in the range of 300–400 μm, and shell wall thickness varied from 3 to 6 μm. The core content of the epoxy and hardener microcapsules was found to be 74% and 59%, respectively. The use of scandium (III) triflate was also explored as a catalyst in the same resin system. The self-healing abilities of the two systems were accessed through the Charpy impact test. The healing efficiency of these systems was tested

by subjecting these to multiple healing cycles and was found to be in the range of 68–85% even after three/four healing cycles. The multicore internal structure of the microcapsules controls the release of the repairing agent and thus was attributed to multiple healing of the material, which is otherwise not possible in a capsule-based system.

Mono Capsule-Based Self-healing System

The dual capsule system may result in poor microcapsule distribution and clustering, both of which can reduce the material's mechanical strength [22]. A new kind of self-healing system was designed wherein the solvents like methanol and ethanol are used as healing agents to repair the damage of thermoplastic polymers. This self-healing system is similar to the capsule-based healing system, where the implanted solvent capsules break during damage allowing the liquid solvent to fill the scratches and repair to occur. Caruso et al. [23] had synthesized a thermoset polymer with self-healing ability by incorporating the solvent-filled microcapsules into the epoxy composite. The solvent inside the capsules would act as a wetting agent on the surface of the polymer, resulting in swelling of the polymeric material, thus interlocking the chains across the fractured surfaces, which seal the crack and restore the mechanical properties.

The cerium nitrate is supposed to exhibit corrosion inhibition properties, and it is found that cerium ions cause the precipitation of cerium oxides or hydroxides, which obstruct the cathodic reduction reaction of metallic coatings. However, the cerium nitrate is consumed over time if it is mixed with the epoxy before being applied to the metal surfaces and thus is not in a position to recover the induced fracture during the service life of the coating. Farzi [24] made use of cerium nitrate in their self-healing epoxy-based coating system. The authors had encapsulated the cerium nitrate into the poly(urea-formaldehyde) PUF microcapsules through a two-step polymerization process, which were then embedded into the epoxy-based coating system. The self-healing performance of the system was accessed by using EIS tests in 0.6 M NaCl solutions. The EIS findings reveal that whenever the damage occurs, cerium nitrate is released from the microcapsules and results in effective healing of the cracks as the precipitates of oxide and hydroxides in the damaged region form a passive layer that inhibits the corrosion. The healing efficiency of the coatings containing 10 wt% of microcapsules was observed to be the highest, but it decreases the adhesive strength of the coatings.

The metal complexes with imidazole can be prepared easily and can be used as the latent curing agents for one-pack epoxy-based self-healing systems. The latent hardeners react with the epoxy resin on heating and do not react at room temperature. Tripathi et al. [25] synthesized a self-healing system based on microcapsules with latent curing agent functionality, wherein the latent curing agent is dispersed within the matrix phase. The epoxy resin was encapsulated in poly(urea-formaldehyde) shell-walled microcapsules. The Ni and Cu-imidazole complexes were prepared by complexation reactions of Ni and Cu chlorides with 2-methyl imidazole and were

used as latent curing agents. The epoxy composites were prepared by ultrasonication, dispersing the varying amount of epoxy-filled microcapsules (5–30 wt%) and fixed amounts of latent hardeners (1 wt%) triethylenetetramine (TETA). They were added to cure the resin at 30 °C for 24 h. The 100% healing efficiency was attained with 30 wt% of the microcapsules, but the mechanical properties of the matrix deteriorated with an increase in the capsule loading. Ma et al. [26] prepared an epoxy oxide-based (E-51) self-healing system for 4D printing. The melamine-formaldehyde (MF) microcapsules were prepared by in situ polymerization. Herein, the bisphenol A-based epoxy resin (E-51) was used as a healing agent, $Cu(MI)_4Br_2$ as a latent curing agent, and graphene oxide (GO) acted as a reinforcing phase that increased the tensile strength of the materials. The microcapsules and the latent curing agent were uniformly distributed in the matrix. The scratch healing efficiency of the material was found to be 87.22%, and the broken healing efficiency was 89.97%.

Linseed oil (LO) can act as a healing agent as it is environment friendly, shows some lubricating properties, and is economically viable. Moreover, it is air drying in nature and can polymerize with oxygen resulting in a flexible and water repellent coating layer [27]. Thus, linseed oil can provide self-healing and self-lubricating properties to the material, thus making it resistant to damage and could repair scratches after damage. Suryanarayana et al. [28] investigated the effectiveness of linseed oil as a repairing agent. The linseed oil was encapsulated within the urea-formaldehyde shell walls using the in situ polymerization technique. LO was found to be able to repair the crack and thus protect the underlying substrate from corrosion. Yang et al. [29] extended the work with linseed oil and encapsulated LO into polyurethane shell walls rather than potentially hazardous UF shells. The LO-filled polyurethane microcapsules were prepared by interfacial polymerization. Epikote 862, a commercially available epoxy resin, serves as the matrix material, and Epikure 205, a low viscosity modified cycloaliphatic amine curing agent, serves as the epoxy curing agent. The self-repairing and the self-lubricating properties of the coatings were determined by electrochemical impedance spectroscopy (EIS), salt spray analysis, and friction wear test methods. The friction wear test results revealed that the coating performance was enhanced when the microcapsule concentration reached up to 10 wt% or more. The friction coefficient was reduced to 86.8% compared to the pure epoxy coating without microcapsules.

The increased lubricating property and the wear resistance with self-healing ability can significantly extend the material's service life. To improve the mechanical damage and the wear resistance tendency of the material, the work with linseed oil has been further extended, and the self-healing ability of a polymer composite embedded with bifunctional microcapsules was also investigated [30]. The organic solvent dibutyl phthalate (DBP) and linseed oil (LO) were encapsulated into urea-formaldehyde microcapsules by in situ polymerization in an oil in water emulsion. The synthesized microcapsules possessed a dense and intact surface structure with an average size of 1.4 μm. The healing efficiency of the polymeric materials can be accessed by various characterization techniques such as AFM and 3D-scratch instrument [30]. The improved mechanical properties and repairing mechanism of the composite material were attributed to bifunctional microcapsules and lubricating

particles (LO). The material's friction coefficient was decreased by 92%, and the healing efficiency was found to be more than 96% by volume.

The mono capsule self-healing systems possess great advantages as they eliminate concerns regarding catalyst dissolution, activation/deactivation, cost, etc. However, chain mobility is essential within the cured epoxy matrix, which is difficult to achieve for a low-temperature curing system.

2.1.2 Healant Loaded Pipeline Type Containers

The disadvantage associated with the microcapsule-based self-healing mechanism is the amount of the healing agent. In achieving multiple healing with limited material, whether the healing agent has been consumed entirely or not after the first healing cycle cannot be detected. Multiple healing is possible only if a sufficient amount of healing agent remains available after a one-time scratch repair event. Thus, to attain multiple self-healing in extrinsic mechanisms, a reservoir that can store and deliver a larger amount of the healing agent should be developed. This healant loaded mechanism of self-healing uses brittle pipeline type containers filled with a polymerizable medium that should be fluid, at least at healing temperature. When the polymerizable material flows into the cracked site, it heals the crack through polymerization. Depending on the type of pipeline type containers, this type of mechanism can be further classified into two categories, viz. hollow glass tubes/glass fibers and microvascular networks, which are described in the following sections.

Hollow Glass Fibers

The incorporation of the self-healing functionality to the fiber-reinforced composites will make the materials scratch resistant, corrosion resistant, self-healable, and provide high strength. The various containers used as a reservoir for the healing agents in the composite materials are hollow nanofibers, carbon nanotubes, halloysite nanotubes (HNT), hollow glass fibers, and titanium dioxide nanotubes (TNTs). The internal diameter and the wall roughness of the containers are responsible for the flowing tendency of the healing agent within the containers. The large-sized vessels are very convenient for repairing large damage zones. The epoxy-based chemicals are used as healing agents for this type of mechanism as they can flow easily on heating and can be cured by epoxy hardeners. The smart composites of hollow glass fibers can be produced using two approaches, viz. (1) the whole fiber is filled with one-part curing resin and (2) a two-part system with hardener filling fiber and resin filling fiber. The pipeline type containers filled with both healing agent and the hardener are dispersed within the matrix system, and the self-healing process is depicted in Fig. 3.

The hollow fibers can be used as containers for the healing agent and the structural reinforcement for the matrix. The hollow fibers are also commercially available. Self-healing HGF/epoxy reinforced composites with smaller diameters (internal diameter

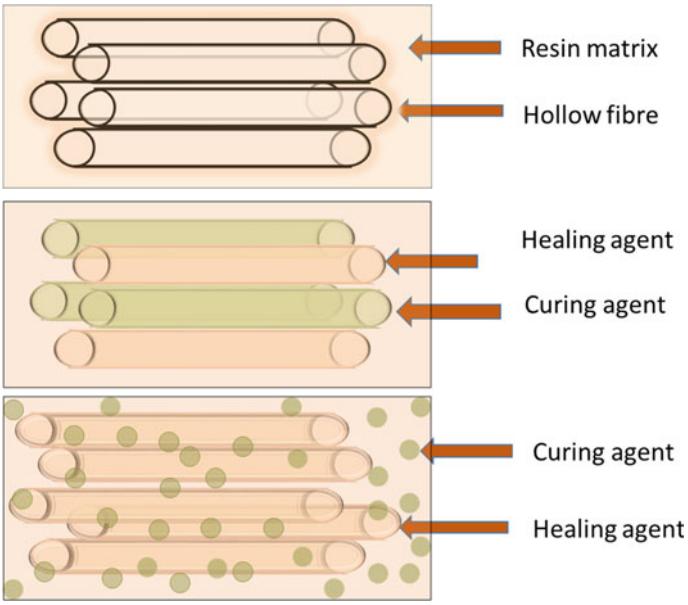

Fig. 3 Hollow fiber/pipeline type containers for the healing agent and hardener

of 5 μm and outer diameter of ca. 15 μm) have been reported [31]. The commercially available (Hollex S2 glass fiber) HGFs act as both containers and structural reinforcement material. The laminates of a thickness of 6.5 mm were prepared by the unidirectional prepreg material. The epoxy resin was incorporated in one fiber direction and the hardener in the other direction. Before encapsulation, hardener and epoxy resin are mixed with acetone so that the viscosity of the material can be reduced and it can flow easily to the site of damage where the curing takes place. Inorganic nanomaterials such as mesoporous silica SBS-15 and TiO_2 nanotubes (TNTs) have been reported in the preparation of self-healing epoxy coatings [32]. The epoxy healing agent was encapsulated within TiO_2 nanotubes, and the amine hardener was encapsulated in the mesoporous silica. The encapsulation techniques used for epoxy and the hardener are vacuum loading processes and shaking incubation for 24 h. The containers were dispersed within the epoxy matrix and then coated on a carbon steel substrate. The self-healing potential of the matrix was investigated by using electrochemical impedance spectroscopy (EIS), and the material's anticorrosive property was recovered to 57% within 5 days. Zhu et al. [33] prepared a self-pressurized healing system of glass fiber/epoxy composite by using plastic polypropylene (PP) tubes as containers for epoxy/mercaptan healing and foaming agents. On decomposition at 70 °C, the foaming agent produces gas within the sealed PP tubes, increasing the pressure inside the tubes. Whenever there is damage to the composite, the pressurized fluid inside the PP tubes bursts out and thus spreads out over a large cracked plane. The author reported an enhanced repairing efficiency compared to the case

without pressurization and gives details of the factors such as tube spacing, forming time, and forming agent on healing performance. A multifunctional nanocomposite coating was reported in 2019 [34], where the epoxy resin matrix was reinforced by the halloysite nanotubes (HNTs). The linseed oil was encapsulated into urea-formaldehyde microcapsules that served as the repairing agent, and the added sodium nitrate acted as a corrosion inhibitor. The Doctor's blade method was used to apply the nanocomposite epoxy coatings on mild steel specimens. The coating material could effectively restore its mechanical integrity, and the quick release of the healing agent and inhibitor in response to external stimuli results in good healing efficiency as well as the corrosion resistance of the steel specimen. This multifunctional epoxy nanocomposite coating system finds its application in the oil and gas industries as a corrosion protector.

The polyester resins can also be used as healing agents and, thus, filled within the hollow glass fibers (HGFs). The Polimal 1058 (a polyester resin) has been reported to work as a healing agent by Kling et al. [35]. They prepared a damage detection and self-healing epoxy composite embedded with thin hollow glass fibers of an internal diameter of 56 μm. A UV fluorescent dye was used as a visual indicator for damage detection under UV illumination. The composites were fabricated by two different methods, viz. hand layup (HLU) and vacuum-assisted resin transfer molding (VARTM). The falling weight impact testing machine damaged the prepared samples to investigate the repairing process. The damaged HLU and VARTM samples were heated at 60 and 23 °C for 12 and 120 h, respectively, for the repairing process. When compared to a reference sample without healing, the sample with the embedded healing agent showed a 20% enhancement in the bending properties after repair.

Some advantages of the hollow fiber approach of self-healing include the higher volume of repairing agent available to heal the damages, visual inspection of the damage sites, easy mixing, and tailoring of the hollow fibers with the conventional reinforcing fiber. On the other hand, some of the disadvantages include a requisite multistep fabrication and the need for low viscosity resins during fiber infiltration.

Vascular Network

The biomimetic approach of incorporating microvascular networks into composite materials develops a new type of self-healing materials. Here, in this microvascular approach of self-healing, the repairing agent is stored within the hollow channels or brittle vessels or a network of capillaries that are interconnected in 1D, 2D, or 3D. The healing agent-filled networks are distributed throughout the resin matrix as shown in Fig. 4. When the smaller vessels are damaged, they rupture and release the repairing agent, which flows to the site of damage and eventually fills the crack. The main advantage of this approach is the availability of a large quantity of repairing agents and thus the ability to repair large damaged areas. Multiple healing can be achieved by this approach because the damaged region has multiple connectivities to the healing agent. The disadvantage of this approach is that during the repairing process, the cross-linked material may jam up the micro-pipes from the damaged

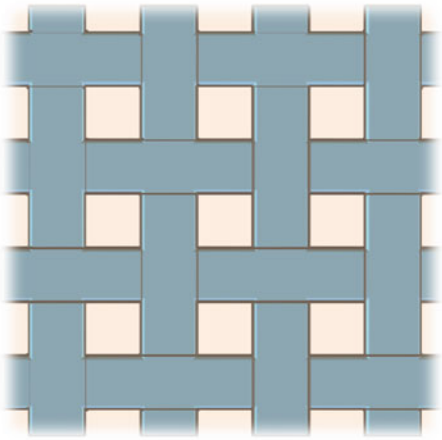

Fig. 4 Microvascular system with self-healing ability having single network specimen

region and become disconnected from the rest of the vascular system. Moreover, this network is complicated by the multistep fabrication process, and its manufacturing is more expensive than the microencapsulation technique. In 2007, Toohey et al. [36] mimicked human skin architecture and developed a first of this type, microvascular composite material by using the familiar healing combination of liquid DCPD as the repairing agent and the Grubb's catalyst, which was incorporated into a thick epoxy coating applied on the top surface of a microvascular substrate. The 200 μm wide channels were filled with DCPD healing agent. The maximum healing of 70% was attained with 10 wt% of the catalyst in the epoxy topcoat. Up to seven repeated healing cycles were demonstrated. The amount of catalyst in the top epoxy coat did not influence the healing efficiency. However, it can be a limiting factor for healing as if the catalyst is exhausted; then no healing is possible even with a continuous supply of the healing agent.

Carbon fiber-reinforced composites (CFRCs) have potential applications in aerospace and offshore wind turbines. The incorporation of self-healing ability to CFRCs may protect them from delamination. Wang et al. [37] designed self-healing CFRCs that can restore their mechanical properties by repairing the structural fibers after delamination. The short carbon fibers SCFs serve as the structural fibers here. The hollow vessels filled with the liquid healing agent were mixed with SCFs and were embedded within the material. Upon damage, the structural fiber ruptures, breaking the nearby vessels and releasing the healing agent that flows to fill the gap between the damaged surfaces. The author has compared the tensile strength of the system having pure epoxy resin as a healing agent and the epoxy resin with 13.8vol% of short carbon fibers. The tensile strength of the system with SCFs after the damage was found to be restored to 47.3% of the original tensile strength. In self-healing composites, the microvascular networks are in the in-plane direction and are normally used to transport the repairing agent into the fractured sites. The

self-healing system, where microvascular channels in the through-thickness direction are introduced into the matrix, has also been prepared [38]. The effectiveness of the through-thickness channels was evaluated by injection testing and mechanical testing. The delamination filling test, tensile test, and four-point bending test can be used to estimate the effect of microchannels on materials' strength and feasibility. The composite stiffened panels were repaired after indentation loading, and the compression testing technique was used to determine the healing ability. The compression strength of the repaired sample after indentation loading was recovered to 96% compared to the virgin specimen.

The healing efficiencies of the materials can be enhanced by using MWCNTs epoxy nanocomposite as the repairing agent for the vascular GFRPs [39]. The viscosity of the nano-modified healing agent was adjusted by using ethyl phenylacetate (EPA) solvent. The healing efficiency of the system and the effect of MWCNTs on the interlaminar fracture toughness were investigated by quasi-static mode I interlaminar fracture toughness tests. The healing efficiencies of the composite materials were found to be increased to 192% compared to the neat epoxy. The presence of the MWCNTs in the damage site may not only restrict the crack propagation after repairing but can provide reinforcement at the time of fracture toughness studies and thus is attributed to the increased healing efficiencies of the composites.

2.2 Intrinsic Self-healing Mechanism

The intrinsic self-healing materials have latent self-healing functionalities in their structures, and there is no need to store the healing agents in micro-containers. This mechanism of self-healing involves the use of some external stimuli such as photochemical, thermal, solvent, electrochemical and moisture activation to initiate the healing process, which involves the bond breaking and bond reformation of the bonds. The materials with inherent self-healing ability can repair the scratches by temporarily increasing the movement of the polymeric chain at the site of damage, allowing the material to flow to the damaged area and can repair the cracks.

Various mechanisms, such as the recombination of chain ends, reversible bond formation, molecular interdiffusion, photothermal metal-ligand complexation, host–guest interactions, and photochemical self-healing, can be used to carry out intrinsic self-healing of materials. Self-healing properties have been studied extensively in a variety of thermoplastic materials, including semicrystalline, amorphous, fiber-reinforced composites, and block copolymers. This self-healing technique requires no monomer/healing agent or catalyst, is simpler than the extrinsic technique, and is more competitive in terms of production and applications of end products.

The main advantage associated with the intrinsic self-healing mechanism is that repeated healing is possible at the same injured site of the coatings. Moreover, the self-healing functionality does not include any foreign or encapsulated healing agent. In spite of the advantages, the intrinsic system may be associated with some drawbacks, such as the flowability of the material, which improves the healing rate by eliminating

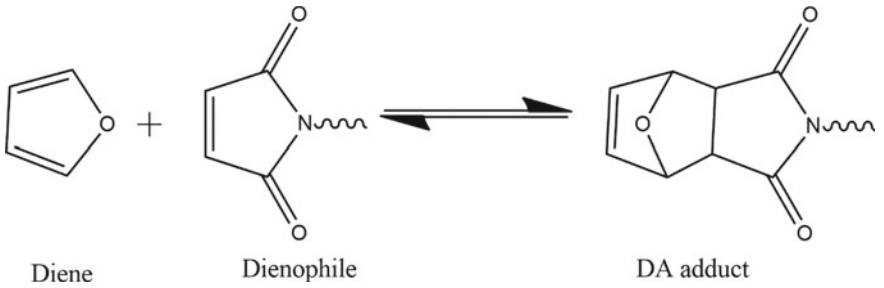

Fig. 5 Reversible Diels-Alder reaction of a diene and dienophile

the effect of damage. However, most materials with intrinsic self-healing ability are associated with higher viscosities. A high temperature is needed to overcome viscosity. Moreover, this approach is confined to small damage zones only and thus has a limited range of applications.

The different approaches to intrinsic self-healing, depending upon the type of stimuli provided to initiate the healing mechanism, are discussed in the following sections of this chapter.

2.2.1 Reversible Bond Self-healing

In most intrinsic self-healing systems, the healing is attained through reversible bonds such as Diels-Alder reactions, disulfide metathesis, hydrogen bonding, and metal-ligand bonding that have been introduced into the polymeric material.

Thermo-Reversible Cross-Links

The well-known thermally reversible cross-linking reactions are widely used in the field of polymer for the synthesis of self-mending materials. The DA cross-links are most widely used for the construction of thermo-reversible intrinsic self-healing materials due to mild reaction conditions, high yield, and excellent thermal reversibility of the DA cross-links.

The Diels-Alder reaction in Fig. 5 was discovered in 1928 and is a [4 + 2] cycloaddition reaction between the diene and dienophile through an unsymmetrical transition state.

The cycloaddition product formed by the DA reaction exhibits both *endo* as well as *exo* isomer. When heated to a higher temperature, the DA adduct regenerates the original diene and dienophile moieties via retro-DA reaction. These broken chain lengths decrease the molecular weight and viscosity of the material at elevated temperatures, resulting in the material flow to the site of damage. When the temperature decreases to room temperature, the DA adduct's reformation occurs, and thus the cracks are sealed. These DA and retro-DA reactions can occur multiple times by decreasing or

increasing the temperature; thus, the material can undergo multiple healing cycles at the same injured site. Researchers have developed various self-healing materials with intrinsic self-healing ability using dienes such as anthracene, fulvene, pyrone, cyclopentadiene, and a maleimide unit. Nevertheless, most of the research has been focused on the Diels-Alder reaction between furan and maleimide groups. Wudl et al. [40] prepared a self-repairable epoxy polymeric material using polyfuran and polymaleimide through Diels-Alder reactions. Here, the retro-DA reaction (disconnection of the linked sites) occurs above 120 °C, and the disconnected cross-links reconnect while cooling. Wang et al. [41] synthesized a cross-linker/curing agent for the epoxy resin with diamine Diels-Alder adduct. The structure and properties of the epoxy resin with repeated self-healing ability were also analyzed. The thermo-reversible gels can also be prepared by mixing bismaleimide {1,1'-(methylenedi-4,1-phenylene)} with furfurylamine and DGEBA oligomers, as reported in [42]. This gel served as a repairing agent for epoxy amine thermosetting materials and was applied directly on the crack surface of epoxy material. The healing mechanism was controlled by the DA reaction, where heating liquifies the secondary gel that flowed to the site of damage, and cross-links were formed upon cooling and fixed the epoxy network structure.

Novolac epoxy resins, due to their excellent integrated properties, have many applications in the field of electronic packaging, and their area of applications can be broadened by introducing the self-healing functionality to the novolac epoxy resins. A new novolac epoxy resin with pendant furan groups has been reported by Li et al. [43]. The commercially available novolac epoxy resin (DEN431) had been used as the matrix material and was modified with furfuryl alcohol. The bifunctional BMI (*N*,*N*-(4,4-methylenediphenyl) dimaleimide) was used as the cross-linker for the modified novolac. The higher storage modulus and the excellent thermal stability were associated with the cross-linked epoxy resin. The thermo-reversible nature and self-repairing properties of the materials can be studied by using SEM, DSC, thermal re-solution, and gel-solution-gel transition experiments [51].

Photo-Reversible Cross-Links

Photo-reversible reactions play an important role in polymer chemistry and have excellent applications in the field of self-healing materials. This approach of self-healing is cost effective, can take place under the sunlight as no thermal treatment is needed to initiate the healing process, and can heal the repeated cracks at the same location within the polymeric material. As shown in Fig. 6, when irradiated with UV radiations of suitable wavelength, olefinic compounds such as anthracene and coumarin undergo a photo-reversible dimerization, resulting in a cyclobutene-like structure. When irradiating with UV light of a shorter wavelength, these cross-links can be reverted to the olefinic compounds. The concept of this photo-reversible cyclization/dimerization has been used by many researchers and thus prepared many polymeric materials with self-healing functionalities.

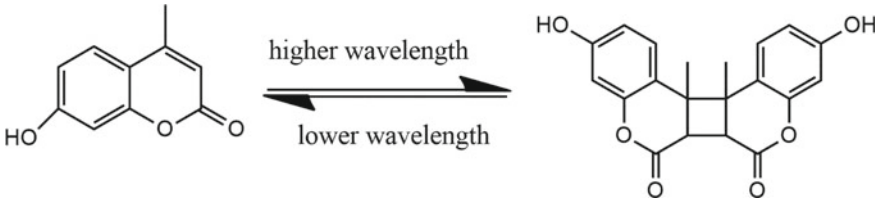

Fig. 6 Photo-reversible dimerization reaction

Simone et al. [44] synthesized a photo-curable epoxy resin with photoactive anthracene moieties by dissolving the photoactive monomer in a low viscosity epoxy derivative. The reversible bond formation and the cross-linking kinetics of the synthesized epoxy-based resin were analyzed by spectroscopic and DMA analysis. The fluorescence microscopy analysis showed that the mechanical stress causes the free anthracene moieties to diffuse on the cracked surface. The photo-reversible polymerization repairs the microscopic damages when exposed to UV light radiations ($I > 300$ nm). However, to ensure the viscoelastic flow and the polymeric chains' diffusion in the cracked zone of the material, additional heating at 60 °C was needed. The healing efficiency of the material was found to be within 84% to 100% after the first repair step. Recently, Tezel [45] synthesized a dual capsule photo-curable self-healing coating formulation based on epoxy-polyester acrylate resin. The author has encapsulated a commercial epoxy and a polyethylenimine (PEI) into microcapsules made up of poly(urea–formaldehyde) PUF and a poly(maleimide-urea–formaldehyde) PMUF shell wall materials. The sizes of the epoxy and PEI-filled microcapsules were determined with the help of a Zeta sizer and were found to be 185 and 377 nm, respectively. About 2 wt% of the microcapsules content (in 1:1 molar ratio for epoxy and PEI microcapsules) was dispersed within the coating formulation and was applied to the plexiglass substrate surface. Artificial scratches were made on the coating surfaces before exposing them to UV light for curing purposes. The scratches healed on their own after an exposure time of 48 h. This system permits the low-temperature repairing of the damages. Zhen et al. [46, 47] synthesized epoxy acrylate self-healing composite by introducing reversible dynamic host–guest chemistry into the resin structure. A β-CD/azobenzene inclusion complex (6-GMA-β-CD/AAAB) with C=C was synthesized, and the epoxy acrylate was cross-linked with this complex through free radical copolymerization by the facile UV curing process. As the complex is light responsive, upon exposure to UV radiations, the cross-linking points were unlocked, and chain mobility increased, which provided better healing abilities to the epoxy resin. Moderate heating was needed to increase the chain movement at the site of damage and initiate the host–guest interactions. The epoxy acrylate film showed excellent mechanical properties along with self-healing ability. The tensile strength of the scratched sample was recovered to 63.3% of the original value. Multiple healing is possible due to the reversible dynamic host–guest chemistry.

2.2.2 Dynamic Disulfide Bond Self-healing System

The disulfide bonds are versatile and thus gain significant attention in the self-healing chemistry due to their relatively easy implementation in the existing networks. The conventional epoxy thermosets have been synthesized with aliphatic disulfide chains obtained from thiol precursors at mild healing temperatures. Using tri-*n*-butylphosphine as a catalyst, Zang et al. [48] created an epoxy polymer of diethylenetriamine-cured polysulfide diglycidyl ether. The cross-linked epoxide polysulfides were self-repaired at room temperature without external intervention, as demonstrated by the restoration of tensile strength. The glass transition temperature of this epoxy resin was low, and thus the polymer has limited composite applications.

Vitrimers are an emerging class of polymers having many attractive material processing properties such as healing, reshaping, and recycling. de Luzuriaga et al. [49] synthesized a dynamic epoxy vitrimer based on the reversible exchange of aromatic disulfides by using DGEBA as the epoxy monomer and AFD (4-aminophenyl disulfide) as the dynamic hardener. This system was easily applicable to fiber-reinforced polymer composites (FRPCs), as the starting materials are easily available. The synthesized FRPCs showed comparable mechanical strength in addition to new properties such as recyclability, healing ability, and re-processability when compared with reference epoxy counterparts. Zhou et al. [50] synthesized a new type of vitrimers (BDSER) having thermosetting dynamic epoxy network with double disulfide bonds. Here, the reaction between difunctional epoxy monomer having disulfide bonds and 4,4'disulfanediyldianiline (4-AFD) took place. The relaxation time of the vitrimer at 200 °C was found to be 9 s. Moreover, there was no significant loss in the chemical and thermodynamic properties of the vitrimer after three continuous cycles of breaking and compression molding.

Huang et al. [51] synthesized epoxy vitrimers by using disulfide chemistry. They made the epoxy resin system by reacting DGEBA with AFD (4-aminophenyldisulfide). The surface of the nanoparticles of silica was pre-modified either with an epoxy resin or by a thiol compound MPTMS (3-mercaptopropyltrimethoxysilane) and 3-glycidoxypropyltrimethoxysilane (GPTMS). The pre-modified nanoparticles were mixed with the resin system and were used as nanofillers. A good matrix reinforcement effect was observed with the pre-modified nanoparticles when compared with the unmodified ones. The epoxy-modified silica composites possess higher T_g values when compared to the thiol-modified silica composites. It was found that the thiol-modified nanoparticle composites possess a much faster stress relaxation rate than epoxy-modified silica composites. This may be attributed to the faster exchange rate of thiol-disulfide reactions and thus showed efficient self-healing behavior verified by the time-dependent healing experiment. The mechanical properties of the material were found to increase with an increased amount of thiol-modified silica fillers.

Li et al. [52] also investigated the self-repairing ability of the epoxy resins having exchangeable disulfide dynamic bonds. The resin material was synthesized by polymerizing two epoxies with an amine having a disulfide bond. The soft and rigid components used were poly-(ethylene glycol) diglycidyl ether (DER736), and

DGEBA. The self-healing materials with different flexibilities were obtained by tuning the content of the soft segment within the resin system. The greater the flexibility of the polymer, the lower the activation energy, glass transition temperature, and poor mechanical strength of the material, but it could possess better self-healing properties. The specimens were optimized, and the optimal specimen showed good mechanical properties as well as self-healing efficiency.

Supramolecular Self-healing

For the past few decades, supramolecular chemistry has been used for the development of self-healing polymeric materials. The rate of dynamic bond breaking and reformation via supramolecular chemistry is fast under ambient conditions. The other factors, such as chain relaxation time and bonding directionality, also have an impact on the healing efficiency of the material. The cracks in the material rupture the non-covalent bonds as they are much easier to break than covalent bonds. The damage can generate new fragments with unbonded non-covalent interactions. These fragments can further recombine by non-covalent interactions, close the cracks, and repair the damage. Depending upon the type of non-covalent bonding and supramolecular interactions involved, the healing ability of the materials may be classified into self-healing via (1) H-bonding, (2) metal-ligand interactions, (3) host-guest interactions, and (4) Π-Π stacking interactions. Nevertheless, in most of the research articles, it has been reported that one self-healing material may combine with more than one type of non-covalent interactions, deliberately or accidentally; thus, it is difficult to categorize the supramolecular healing chemistry on the basis of the interactions involved.

Significant attention has been attributed to enhancing the strength of hydrogen bonds as it is important for self-healing as well as mechanical properties of the materials. Chai et al. [53] prepared an epoxy resin with higher impact resistance by introducing the toughening agent quadruply hydrogen-bonded supramolecular polymer into the bisphenol A-based epoxy resin. The supramolecular polymer consists of poly-(propylene glycol) bis(2-aminopropyl) ether chains and 2-ureido-4[1H]-pyrimidinone (UPy) moieties. The spherical microphase-separated domains were prepared by physical blending of epoxies with the supramolecular monomers before curing. The amount of UPy supramolecular monomers strongly influences the size of the microdomain. The mechanical studies revealed that supramolecular blending could be a method for toughening epoxy resins. A significant improvement was observed in the impact strength (by 300%) of the blended epoxy compared with the neat epoxy.

Host-guest interactions result in targeted binding of dimensionally matching molecular segments. Biological systems are found to have naturally occurred host–guest interactions. These have applications in sensing, drug delivery, surface recognition, and stimuli-responsive hydrogels. The cyclodextrins (CDs), crown ethers, pillar[*n*]arenes, calixarenes (CAs), etc., are generally employed host molecules. Cyclodextrins exhibit the properties such as multi-responsiveness, water solubility,

most desired dissociation/re-association dynamics, and biocompatibility, and thus CD-modified host polymers are of significant importance.

Supramolecular elastomers were also prepared using diethylenetriamine, urea, and small carboxylic acids such as citric acid and sebacic acid [54]. The synthesized phase-separated polymers having H-bonding interactions among amide alkyl-urea and imidazolidone moieties possess self-healing ability at room temperature within 8–72 h, and the healing efficiency was found to be 31–99%. The material is non-cytotoxic and thus may have potential applications in the biomedical field.

The carboxylated cellulose nanocrystals (C-CNC) and chitosan (CT) modified epoxy natural rubber (ENR) latex are used to develop multiple hydrogen bonding bond interactions and thus can provide self-healing properties to the polymeric materials [55]. The developed material was converted into a self-healing sensor by assembling the nanostructural polymer network with carbon nanotubes. The nanostructured supramolecular self-healing sensor possesses repeatable and extremely fast self-healing ability with a high healing efficiency of 93% for the third healing cycle.

The H-bonding plays an important role in the development of supramolecular self-healing materials as the reformation of the broken bonds can take place at room temperature. However, the reformation of H-bonding has a poor tolerance for moisture, and materials healing efficiency decreases significantly in a humid environment.

3 Conclusion

With advancements in science and technology, the field of self-healing has progressively expanded over time. A large number of novel self-healing systems have been emerging with enhanced self-healing capabilities. The self-healing materials possess a broad range of applications in the food industry, agriculture, transportation, medicine, recycling, and upcycling. The developed self-healing systems showed higher healing efficiencies and thus broadening the application field of these materials. However, there are many drawbacks associated with these self-healing systems, some of which are listed below:

The main concern with the self-healing system is the harsh repairing conditions, as the material requires heating to certain temperatures, and the self-healing under normal temperature conditions is inaccessible. Moreover, the physical properties of the materials, such as flexibility, conductivity, and transparency post healing, are not very good. Thus, most of them are limited to the field of theoretical research and have no direct implementation.

The research should emphasize more on the solutions to the aforementioned shortcomings during the course of future research. Researchers should focus on developing self-healing materials by selecting low-cost starting materials, mild reaction conditions, small/simple synthetic steps, fast repairing rate, high healing efficiency, and excellent mechanical properties to be used in real-world applications.

In summary, self-healing materials have a wide array of potential applications. It may be predicted that the continuous progress in polymeric design and preparation technology of smart materials in the future will play an important role in the broader field.

References

1. Gurumurthy, B.M., Shivaprakash, Y.M., Hiremath, A., Gowrishankar, M.C., Jayashree, P.K.: Self healing materials: a new era in material technology: a review. Int. J. Appl. Eng. Res. **11**, 1373–1378 (2016)
2. Zwaag, S. Van Der, Grande, A.M., Post, W., Garcia, S.J., Bor, T.C.: Review of current strategies to induce self-healing behavior in fibre reinforced polymer based composites. Mat. Sci. Technol. **30**, 1633–1641 (2014). https://doi.org/10.1179/1743284714Y.0000000624
3. White, S.R., Sottos, N.R., Geubelle, P.H., Moore, J.S., Kessler, M.R., Sriram, S.R., Brown, E.N., Viswanathan, S.: Erratum: correction: autonomic healing of polymer composites. Nature **415**, 817–817 (2002). https://doi.org/10.1038/415817a
4. Mauldin, T.C., Rule, J.D., Sottos, N.R., White, S.R., Moore, J.S.: Self-healing kinetics and the stereoisomers of dicyclopentadiene. J. R. Soc. Interface. **4**, 389–393 (2007). https://doi.org/10.1098/rsif.2006.0200
5. Rule, J.D., Moore, J.S.: ROMP reactivity of endo- and exo-dicyclopentadiene. Macromolecules **35**, 7878–7882 (2002). https://doi.org/10.1021/ma0209489
6. Mercy, J.L., Prakash, S., Sandeep, K.S., Praveen, D.S.: Characterisation of dicyclopentadiene filled microcapsules for self-healing composite materials. Appl. Mech. Mater. **766–767**, 3–7 (2015). https://doi.org/10.4028/www.scientific.net/amm.766-767.3
7. Wilson, G.O., Caruso, M.M., Reimer, N.T., White, S.R., Sottos, N.R., Moore, J.S.: Evaluation of ruthenium catalysts for ring-opening metathesis polymerization-based self-healing applications. Chem. Mater. **20**, 3288–3297 (2008). https://doi.org/10.1021/cm702933h
8. Caruso, M.M., Blaiszik, B.J., Jin, H., Schelkopf, S.R., Stradley, D.S., Sottos, N.R., White, S.R., Moore, J.S.: Robust, double-walled microcapsules for self-healing polymeric materials. ACS Appl. Mater. Interfaces. **2**, 1195–1199 (2010). https://doi.org/10.1021/am100084k
9. Jin, H., Miller, G.M., Pety, S.J., Griffin, A.S., Stradley, D.S., Roach, D., Sottos, N.R., White, S.R.: Fracture behavior of a self-healing, toughened epoxy adhesive. Int. J. Adhes. Adhes. **44**, 157–165 (2013). https://doi.org/10.1016/j.ijadhadh.2013.02.015
10. Rule, J.D., Brown, E.N., Sottos, N.R., White, S.R., Moore, J.S.: Wax-protected catalyst microspheres for efficient self-healing materials. Adv. Mater. **17**, 205–208 (2005). https://doi.org/10.1002/adma.200400607
11. Patel, A.J., Sottos, N.R., Wetzel, E.D., White, S.R.: Autonomic healing of low-velocity impact damage in fibre-reinforced composites. Compos. Part A Appl. Sci. Manuf. **41**, 360–368 (2010). https://doi.org/10.1016/j.compositesa.2009.11.002
12. Romero-Sabat, G., Gago-Benedí, E., Roa Rovira, J.J., González-Gálvez, D., Mateo, A., Medel, S., Tolentino Chivite, A.: Development of a highly efficient extrinsic and autonomous self-healing polymeric system at low and ultra-low temperatures for high-performance applications. Compos. Part A Appl. Sci. Manuf. **145** (2021). https://doi.org/10.1016/j.compositesa.2021.106335
13. Rong, M.Z., Zhang, M.Q., Zhang, W.: A novel self-healing epoxy system with microencapsulated epoxy and imidazole curing agent. Adv. Compos. Lett. **16**, 167–172 (2007). https://doi.org/10.1177/096369350701600502
14. Yuan, Y.C., Ye, X.J., Rong, M.Z., Zhang, M.Q., Yang, G.C., Zhao, J.Q.: Self-Healing Epoxy Composite with Heat-Resistant Healant, pp. 4487–4495 (2011)

15. Li, Q., Siddaramaiah, Kim, N.H., Hui, D., Lee, J.H.: Effects of dual component microcapsules of resin and curing agent on the self-healing efficiency of epoxy. Compos. Part B Eng. **55**, 79–85 (2013). https://doi.org/10.1016/j.compositesb.2013.06.006
16. Thakur, T., Gaur, B., Singha, A.S.: Bio-based epoxy/imidoamine encapsulated microcapsules and their application for high performance self-healing coatings. Prog. Org. Coatings. **159**, 106436 (2021). https://doi.org/10.1016/j.porgcoat.2021.106436
17. Wang, H.-P., Zhu, Y.-Q., Li, M.-Q.: Self-healing Epoxy with Epoxy-amine Dual-capsule Healing System, vol. 110, pp. 246–250 (2017). https://doi.org/10.2991/ame-17.2017.42
18. He Zhang, Pengfei Wang, J.Y.: Self-healing epoxy via epoxy-amine chemistry in dual hollow glass bubbles He. Territ. E Caracter. Da Popul. Adscrita Da Equipe Saúde Da Família 905. Compos. Sci. Tech. 3, 1–46 (2014)
19. Safdari, A., Khorasani, S.N., Neisiany, R.E., Koochaki, M.S.: Corrosion Resistance Evaluation of Self-Healing Epoxy Coating Based on Dual-Component Capsules Containing Resin and Curing Agent. Int. J. Polym. Sci. (2021). https://doi.org/10.1155/2021/6617138
20. Ghazali, H., Ye, L., Amir, A.N.: Microencapsulated healing agents for an elevated-temperature cured epoxy: influence of viscosity on healing efficiency. Polym. Polym. Compos. **29**, S1317–S1327 (2021). https://doi.org/10.1177/09673911211045373
21. Hia, I.L., Chan, E.S., Pasbakhsh, P.: Biocapsules for self-healing epoxy composites. ECCM 2016 Proc. 17th Eur. Conf. Compos. Mater. (2016)
22. Huang, H., Ye, G.: Numerical Studies of the Effects of Water Capsules on Self-Healing Efficiency and Mechanical Properties in Cementitious Materials. Adv. Mater. Sci. Eng. (2016). https://doi.org/10.1155/2016/8271214
23. Caruso, M.M., Delafuente, D.A., Ho, V., Sottos, N.R., Moore, J.S., White, S.R.: Solvent-promoted self-healing epoxy materials. Macromolecules **40**, 8830–8832 (2007). https://doi.org/10.1021/ma701992z
24. Farzi, G., Davoodi, A., Ahmadi, A., Neisiany, R.E., Anwer, K., Aboudzadeh, M.A.: Encapsulation of Cerium Nitrate within Poly (urea-formaldehyde) Microcapsules for the Development of Self-Healing Epoxy-Based Coating (2021). https://doi.org/10.1021/acsomega.1c04597
25. Taylor, P., Tripathi, M., Dwivedi, R., Kumar, D., Roy, P.K.: Polymer-Plastics Technology and Engineering Thermal Activation of Mendable Epoxy through Inclusion of Microcapsules and Imidazole Complexes. https://doi.org/10.1080/03602559.2015.1070866
26. Ma, B., Zhang, Y., Wei, Y., Li, M., Li, D.: Graphene oxide-modified microcapsule self-healing system for 4D printing. Front. Mater. **8**, 1–10 (2021). https://doi.org/10.3389/fmats.2021.657777
27. Lang, S., Zhou, Q.: Synthesis and characterization of poly(urea-formaldehyde) microcapsules containing linseed oil for self-healing coating development. Prog. Org. Coatings. **105**, 99–110 (2017). https://doi.org/10.1016/j.porgcoat.2016.11.015
28. Suryanarayana, C., Rao, K.C., Kumar, D.: Preparation and characterization of microcapsules containing linseed oil and its use in self-healing coatings. Prog. Org. Coatings. **63**, 72–78 (2008). https://doi.org/10.1016/j.porgcoat.2008.04.008
29. Yang, H., Mo, Q., Li, W., Gu, F.: Preparation and properties of self-healing and self-lubricating epoxy coatings with polyurethane microcapsules containing bifunctional linseed oil. Polymers (Basel). **11** (2019). https://doi.org/10.3390/polym11101578
30. Zhang, L., Wang, H., He, F., Chen, H., Xie, G., Wei, B., Luo, J., He, B., Wu, Z.P.: Wear in-situ self-healing polymer composites incorporated with bifunctional microcapsules. Compos. Part B Eng. **232**, 1–9 (2022). https://doi.org/10.1016/j.compositesb.2021.109566
31. Bleay, S.M., Loader, C.B., Hawyes, V.J., Humberstone, L., Curtis, P.T.: A Smart Repair System for Polymer Matrix Composites, vol. 32 (2001)
32. Vijayan, P.P., Al-maadeed, M.A.S.A.: TiO_2 nanotubes and mesoporous silica as containers in self-healing epoxy coatings. Nat. Publ. Gr. 1–9 (2016). https://doi.org/10.1038/srep38812
33. Zhu, Y., Ji, X., Zhi, M., Qiu, M.: Self-healing glass fi ber/epoxy composites with polypropylene tubes containing self-pressurized epoxy and mercaptan healing agents. Compos. Sci. Technol. **135**, 146–152 (2016). https://doi.org/10.1016/j.compscitech.2016.09.020

34. Habib, S., Khan, A., Nawaz, M., Sliem, M.H., Shakoor, R.A., Kahraman, R., Abdullah, A.M., Zekri, A.: Self-healing performance of multifunctional polymeric smart coatings. Polymers (Basel). **11**, 1–19 (2019). https://doi.org/10.3390/polym11091519
35. Kling, S., Czigány, T.: Damage detection and self-repair in hollow glass fibre fabric-reinforced epoxy composites via fibre filling. Compos. Sci. Technol. **99**, 82–88 (2014). https://doi.org/10.1016/j.compscitech.2014.05.020
36. Toohey, K.S., Sottos, N.R., Lewis, J.A., Moore, J.S., White, S.R.: Self-healing Materials with Microvascular Networks, pp. 581–585 (2007). https://doi.org/10.1038/nmat1934
37. Wang, Y., Edgell, J., Graham, N., Jackson, N., Liang, H., Pham, D.T.: Self-healing of structural carbon fibres in polymer composites. Cogent Eng. **7** (2020). https://doi.org/10.1080/23311916.2020.1799909
38. Kato, Y., Minakuchi, S., Ogihara, S., Takeda, N.: Self-healing composites structure using multiple through-thickness microvascular channels. Adv. Compos. Mater. **00**, 1–18 (2020). https://doi.org/10.1080/09243046.2020.1744228
39. Bekas, D.G., Baltzis, D., Paipetis, A.S.: Nano-reinforced polymeric healing agents for vascular self-repairing composites. JMADE. **116**, 538–544 (2017). https://doi.org/10.1016/j.matdes.2016.12.049
40. Chen, X., Dam, M.A., Ono, K., Mal, A., Shen, H., Nutt, S.R., Sheran, K., Wudl, F.: A thermally re-mendable cross-linked polymeric material. Science **295**(80), 1698–1702 (2002). https://doi.org/10.1126/science.1065879
41. Kuang, X., Liu, G., Dong, X., Wang, D.: Correlation between stress relaxation dynamics and thermochemistry for covalent adaptive networks polymers. Mater. Chem. Front. **1**, 111–118 (2017). https://doi.org/10.1039/c6qm00094k
42. Peterson, A.M., Jensen, R.E., Palmese, G.R.: Room-temperature healing of a thermosetting polymer using the diels-alder reaction. ACS Appl. Mater. Interfaces. **2**, 1141–1149 (2010). https://doi.org/10.1021/am9009378
43. Li, J., Zhang, G., Deng, L., Jiang, K., Zhao, S., Gao, Y., Sun, R., Wong, C.: Thermally reversible and self-healing novolac epoxy resins based on Diels-Alder chemistry. J. Appl. Polym. Sci. **132**, 1–7 (2015). https://doi.org/10.1002/app.42167
44. Radl, S., Kreimer, M., Griesser, T., Oesterreicher, A., Moser, A., Kern, W., Schlögl, S.: New strategies towards reversible and mendable epoxy based materials employing [4πs + 4πs] photocycloaddition and thermal cycloreversion of pendant anthracene groups. Polymer (Guildf). **80**, 76–87 (2015). https://doi.org/10.1016/j.polymer.2015.10.043
45. Tezel, Ö., Beyler Çiğil, A., Kahraman, M.V.: Dual microcapsules based epoxy/polyethylenimine autonomous self-healing system for photo-curable coating. Polym. Adv. Technol. **32**, 553–563 (2021). https://doi.org/10.1002/pat.5109
46. Hu, Z., Liu, Y., Xu, X., Yuan, W., Yang, L., Shao, Q., Guo, Z., Ding, T., Huang, Y.: Efficient intrinsic self-healing epoxy acrylate formed from host-guest chemistry. Polymer (Guildf). **164**, 79–85 (2019). https://doi.org/10.1016/j.polymer.2019.01.010
47. Hu, Z., Zhang, D., Lu, F., Yuan, W., Xu, X., Zhang, Q., Liu, H., Shao, Q., Guo, Z., Huang, Y.: Multistimuli-responsive intrinsic self-healing epoxy resin constructed by host-guest interactions. Macromolecules **51**, 5294–5303 (2018). https://doi.org/10.1021/acs.macromol.8b01124
48. Lei, Z.Q., Xiang, H.P., Yuan, Y.J., Rong, M.Z., Zhang, M.Q.: Room-temperature self-healable and remoldable cross-linked polymer based on the dynamic exchange of disulfide bonds. Chem. Mater. **26**, 2038–2046 (2014). https://doi.org/10.1021/cm4040616
49. Ruiz De Luzuriaga, A., Martin, R., Markaide, N., Rekondo, A., Cabañero, G., Rodríguez, J., Odriozola, I.: Epoxy resin with exchangeable disulfide crosslinks to obtain reprocessable, repairable and recyclable fibre-reinforced thermoset composites. Mater. Horizons. **3**, 241–247 (2016). https://doi.org/10.1039/c6mh00029k
50. Zhou, F., Guo, Z., Wang, W., Lei, X., Zhang, B., Zhang, H., Zhang, Q.: Preparation of self-healing, recyclable epoxy resins and low-electrical resistance composites based on double-disulfide bond exchange. Compos. Sci. Technol. **167**, 79–85 (2018). https://doi.org/10.1016/j.compscitech.2018.07.041

51. Huang, Z., Wang, Y., Zhu, J., Yu, J., Hu, Z.: Surface engineering of nanosilica for vitrimer composites. Compos. Sci. Technol. **154**, 18–27 (2018). https://doi.org/10.1016/j.compscitech.2017.11.006
52. Li, Z., Zhong, J., Liu, M., Rong, J., Yang, K., Zhou, J., Shen, L., Gao, F.: Investigation on Self-healing Property of Epoxy Resins Based on Disulfide Dynamic Links (2020)
53. Chai, Z.Y., Xie, Z., Zhang, P., Ouyang, X., Li, R., Gao, S., Wei, H., Liu, L.H., Shuai, Z.J.: High impact resistance epoxy resins by incorporation of quadruply hydrogen bonded supramolecular polymers. Chinese J. Polym. Sci. **34**, 850–857 (2016). https://doi.org/10.1007/s10118-016-1809-1
54. Liu, L., Pan, C., Zhang, L., Guo, B.: A novel and non-cytotoxic self-healing supramolecular elastomer synthesized with small Molecular biological acids. Macromol. Rapid Commun. **37**, 1603–1610 (2016). https://doi.org/10.1002/marc.201600300
55. Cao, J., Lu, C., Zhuang, J., Liu, M., Zhang, X., Yu, Y., Tao, Q.: Multiple hydrogen bonding enables the self-healing of sensors for human-machine interactions. Angew. Chemie Int. Ed. **56**, 8795–8800 (2017). https://doi.org/10.1002/anie.201704217

Diffusion in Epoxy Oligomers and Polymers

A. E. Chalykh, N. Yu. Budylin, and A. V. Shapagin

Abstract According to one of the currently developed mechanisms of self-healing of epoxy protective coatings, an important role in the process is played by the diffusion migration stage of the composition components to the crack network defects, on the one hand, by swelling of the pore walls, on the other hand, and by their adhesive interaction, on the third. PART 3.1; 3.2, and 3.3 of this chapter summarize the results of our investigations performed at the Laboratory of Structural and Morphological Research of the Institute of Physical Chemistry of the Russian Academy of Sciences concerning the translational mobility of epoxy oligomers, epoxy-amine adducts as model systems for investigation of curing processes of epoxy oligomers and phase equilibrium and structure formation during curing of epoxy compositions. It seems that the presented experimental and methodological material will make it possible to significantly advance our understanding of the details of the self-curing mechanism.

Keywords Epoxy oligomer · Adduct · Epoxy curing · Epoxy matrix modification · Phase equilibrium · Interdiffusion · Self-diffusion · Interdiffusion · Epoxy oligomers · Epoxy polymers · Translational mobility of the macromolecules · Activation energy · Pulsed magnetic field gradient · Interferometry

1 Translational Mobility of Epoxy Oligomers. Influence of Molecular Weight and Thermal Prehistory

The results of the study of self-diffusion and interdiffusion in melts of individual epoxy oligomers and their mixtures of different molecular weights are summarized. The results on the concentration dependences of interdiffusion coefficients and partial coefficients of self-diffusion and diffusion activation energies are presented for the first time. The effect of end groups on the parameters of molecular weight dependence of transfer coefficients of oligomers diffusion is described. In the investigated

A. E. Chalykh (✉) · N. Yu. Budylin · A. V. Shapagin
Frumkin Institute of Physical Chemistry and Electrochemistry Russian Academy of Sciences (IPCE RAS), Moscow, Russia
e-mail: chalykh@mail.ru; chalykh@phyche.ac.ru

N. Hameed et al. (eds.), *Multifunctional Epoxy Resins*, Engineering Materials,
https://doi.org/10.1007/978-981-19-6038-3_3

molecular weight range of Eos, there is a linear dependence of $D - M^b$ with b, depending on the temperature: for $T < 433$ K $- b = 2.4$ and for $T > 433$ K $b = 2.0$. This dependence differs from the previously obtained data for several polymer melts at $M < M_{cr}$, for which in the oligomeric region $b < 2$.

1.1 Introduction

It is known [1, 2] that the problem related to the influence of the molecular weight (MW) and molecular weight distribution (MWR) of oligomers and polymers on the translational mobility of their macromolecules has several solutions. The simplest solution to this problem can be analyzed in the framework of the Einstein-Stokes model. According to this model, the translational diffusion coefficient of any molecule and macromolecule is unambiguously related to their geometric dimensions R and friction coefficient by the following relation:

$$D = \frac{kT}{\zeta} \tag{1}$$

Usually, for spherical non-solvated molecules and ellipsoidal or wand-like particles, it is written as

$$\zeta = 6\pi\eta_O R \text{ or } \zeta = 6\pi\eta_O\left(\frac{3Mv}{4\pi N_A}\right)^{\frac{1}{3}} \tag{2}$$

$$\zeta = 6\pi\eta_O\left(\frac{3v}{4\pi}\right)\varphi \text{ and } \zeta = 6\pi\eta_O\left(\frac{3v}{4\pi}\right)\chi(p). \tag{3}$$

respectively [3]. Here, k is the Boltzmann constant, v is the molar volume of the link, N_A is the Avogadro number; η_O is the effective viscosity or microviscosity of the matrix related to the local friction coefficient experienced by the moving molecule in this or that diffusion medium; M is the molecular weight of diffusing molecules or macromolecules; φ is the form factor, and $\chi(p)$ is the function characterizing the degree of particle asymmetry.

These relations are widely enough used in the practice of physicochemical research. For example, in [4], monomer and solvent diffusion coefficients are used to calculate the monomer friction coefficients of polymers and oligomers. In [2], the MW of spherical, ellipsoidal, and bubble-shaped non-solvated particles is determined by Eq. (2) and the diffusion coefficient of macromolecules in a viscous solvent. In [5], using the viscosity coefficients of oligomer melts, the values of their partial diffusion coefficients are estimated using Eq. (1).

Therefore, it follows that if the diffusion process in a binary system in which the molecules of component "1" are used as a diffusant, the effect of the molecular weight of the oligomers that form the diffusion medium (let us denote it by index

"2") will manifest itself in the value of the diffusion coefficient through its monomer friction coefficient, which, in turn, is related to the local mobility of the oligomer chain fragments.

If the interdiffusion process is realized in another region of solutions, when oligomers of different MW are the diffusant and another oligomer or polymer is the diffusion medium, i.e., $\zeta_1 = \text{const}$, „ the influence of the MW of the oligomers on (D_{21} ($2 \rightarrow 1$)) is associated with a change in the contour length of the molecules, on the one hand, and a change in their conformational state, on the other hand.

From this point of view, polymer self-diffusion ((D_{22}^{*})) takes a special place in the study of translational mobility of macromolecules since two parameters simultaneously change when comparing diffusion coefficients of oligomers and polymers of different MW: both the monomer friction coefficient and the size of the diffusing molecule.

Thus, to characterize the influence of MW oligomers on their translational mobility to the full extent, it is necessary to obtain detailed information on the diffusion properties of oligomer solutions and melts: to describe the concentration and temperature dependences of interdiffusion and self-diffusion coefficients and to determine activation energies characterizing elementary acts of motion of macromolecule fragments and chains as a whole.

It should be noted that, at present, epoxide oligomer (EO) melts are most often considered associative liquids, which naturally impose specific difficulties on the interpretation of the experimental data. However, the nature of associates, the morphology, the thermal stability, and the kinetic stability are still open. The data obtained by methods of turbidity spectrum, NMR, light scattering, infrared spectroscopy, and viscometers are ambiguous and contradictory. First of all, it concerns the results of rheological investigations, which are frequently used as basic information for the formation of representations about the structural organization of EO melts [5–8]. According to Aleman's data [9, 10], viscous flow activation energy (E_η) of epoxy oligomers measured in the temperature interval from 400 to 450 K is constant, $E = 130$ kJ/mol, and slightly depends on the molecular mass of oligomers. In [11, 12], the E_η was measured in a slightly larger temperature range from 350 to 450 K, decreases with increasing temperature from 90 to 45 kJ/mol, and changes continuously with changes in the molecular weight of EO. In [13, 14], the extreme dependence of E_η of the viscous flow with temperature was described. The ambiguity of these results encourages researchers to continuously search for new information on the properties of epoxy oligomers melts. In this connection in the present work, we studied the self and mutual diffusion of epoxy oligomers in a wide range of temperatures and molecular weights.

1.2 Experimental Section

The article summarizes the results of research on epoxy oligomers of different brands: domestic—ED-20, ED-40, ED-44, ED-49, and ED-5 and resins of foreign firms—Epikote 1009—Shell (USA), Araldite GT 6610, Ciba (Switzerland), YD-128—Toto Kasei Co. (Japan), and DER-664 by DAU Chemical. Along with individual EOs, their mixtures were also studied. The molecular weights of oligomers were determined by gel permeation chromatography (Table 1).

The self-diffusion coefficients of EO molecules were measured in the temperature range from 353 to 483 K by NMR with a pulsed magnetic field gradient (IGMP NMR), with a proton resonance frequency of 60 MHz and the amplitude of the maximum magnetic field gradient of 56 Tl/m. A two-pulse stimulated echo sequence technique was used in the range of diffusion times from 3 ms to 1 s [17, 18]. The accuracy of the D^* measurement was 10%.

Interdiffusion was studied by the optical wedge method on the ODA-2 interferometer (IPC RAS Moscow, Russia). The measurement technique did not differ from the traditional one [19, 20]. A higher molecular weight EO was placed in a wedge-shaped capillary of a diffusion cell and brought into optical contact with the surface of metalized quartz plates at $T \geq T_g$. The assembled cell was placed in a thermostatted cuvette preheated to the preset temperature. Then, the cell was filled with liquid oligomers. The moment of contact of oligomers was observed visually on the monitor screen and considered the beginning of the interdiffusion process. The resulting interference pattern characterizing the concentration distribution profile in the interdiffusion zone was used to plot the composition distribution curves and calculate the interdiffusion

Table 1 Characteristics of epoxy oligomers

EO	M_n	M_w	T_g*, K	ρ, g/cm^3	Epoxy grades**, %	Designation
DGEBA	340	340	–	–	22–24	EO 1
YD-128	380	–	–	–	22–24	–
ED-20	390	420	255	1.197	20–22	EO2
ED-16	480	540	260	1.210	16.0–18.0	EO3
E40	600	–	275	1.245	12–16	EO4
E44	1770	2664	313	1.242	6–8	EO5
E49	1860	2500	310	1.240	2.0–4.5	EO6
DER	2568	3154	323	1.242	2–3	EO7
Araldite 6610	3964	6665	343	1.240	1.5–2	EO8
E-O5	2840	3500	340	1.237	1.8–2.8	EO9
Epikote 1009	3367	7151	344	1.238	1.3–2	EO10

* The glass transition temperatures of the oligomers were obtained by refractometry and DSC methods [15]

** Epoxide numbers were determined by direct titration with hydrogen bromide (Durbetaki method) [16]

coefficients by the Matano-Boltzmann method. Microphotographs illustrating the interdiffusion process are presented in Sects. 1.2 and 1.3.

1.3 About the Course of Mass Transfer Processes

A study of the self-diffusion process in melts of epoxy oligomers and their mixtures has shown that two dependences of diffusion damping $A - g^2$ are observed for these compounds: exponential and no exponential (Fig. 1). We observed the second, non-exponential one, as a rule, for EO mixtures with bi- or polymodal MWR and, as a consequence, a set of exponential modes with self-diffusion coefficients D_i^*:

$$A = \sum P_i \exp\left(-\gamma^2 g^2 \delta^2 t_d D_i^*\right) \tag{4}$$

where P_i is the population of components with self-diffusion coefficients D_i^*.

The no exponential course of diffusion damping was also described earlier in [21–23]. The authors of these studies made various assumptions about the possible reasons for this fact. For example, in [21], the no exponential form of diffusion damping was attributed to the presence of macromolecule associations in EO melts, which, as the authors believed, arise due to entanglements between macromolecules

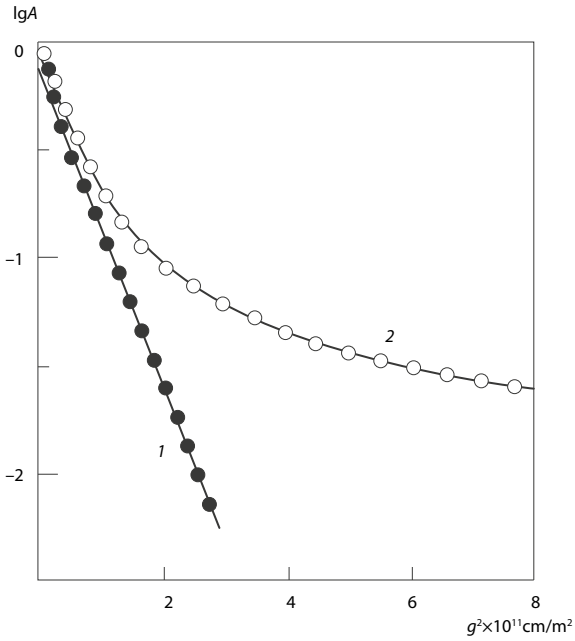

Fig. 1 Magnetization amplitude dependence on the magnetization field gradient for EO-2 (1) and EO-2/Epikote 1009 mixture (2) at 413 K. The diffusion time is 150 ms

and have finite lifetimes. Other papers [22, 23] associated c with molecular-mass heterogeneity of industrial EO grades.

The analysis of experimental data on diffusion in binary epoxy systems, the components of which differ from each other only by molecular masses, showed that all the studied systems in the temperature range from T_g to $T_g + 180$ K, where the T_{II}-transition temperature is also situated [13], belong to the systems with unlimited mutual solubility of components. The spontaneous mixing of the epoxy oligomers brought in contact follows the purely diffusive regularities; that is, each isoconcentration plane situated inside the diffusion zone with respect to any reference system (Hittorff, laboratory, mass-fixed, or volume-fixed) moves with a constant rate in the $X - t^{1/2}$ coordinate system, where X is the coordinate of the plane and t is the observation time. It is of fundamental importance that the kinetic constants of the mixing process are well reproduced when the figurative point of the system moves both up and down the temperature scale. This means, first, that no changes in the molecular weight characteristics of the components in the studied temperature range occur in the EO melts during the process, in contrast to the effects in EO-elastomer systems described in [24, 25]. Second, the associative nature of EO melts does not appear in traditional diffusion experiments. This is possible when the diffusion relaxation time of the local concentration gradient is longer or comparable to the lifetime of associates of EO macromolecules.

1.4 Concentration Dependence of Diffusion Coefficients

Typical concentration dependences of interdiffusion coefficients $D_V - \varphi_1$ for some binary EO systems are shown in Figs. 2, 3 and 4. It can be seen that $D_V - \varphi_1$ dependences are uniform. The value of D_V changes smoothly and monotonically at the transition from one component to another, i.e., from one limiting value of the coefficient of interdiffusion $D_{12} \equiv D_V$ at $\varphi_1 \to 0$, to another $D_{21} \equiv D_V$ at $\varphi_1 \to 1$. Here, index "2" denotes a high-molecular-weight oligomer and index "1" denotes a low-molecular-weight oligomer.

In this case, the difference in the values of the limiting diffusion coefficients $\Delta D = \lg[D_{12}/D_{21}]$, characterizing the intensity of the change in the translational mobility of molecules with composition, decreases from 2.0 at 353 K to 0.3 at 473 K. In some systems with close MW values of the components, the concentration dependence of D_V degenerates.

Analysis of the effect of temperature on the character of the concentration dependences of the interdiffusion coefficient in EO mixtures allowed us to distinguish two temperature regions:

– (region I) $T < 443$ K, which is characterized by a marked increase in D_V with a change in system composition,

– (region II) $443 < T < 503$ K, where D_V weakly changes with a change in concentration.

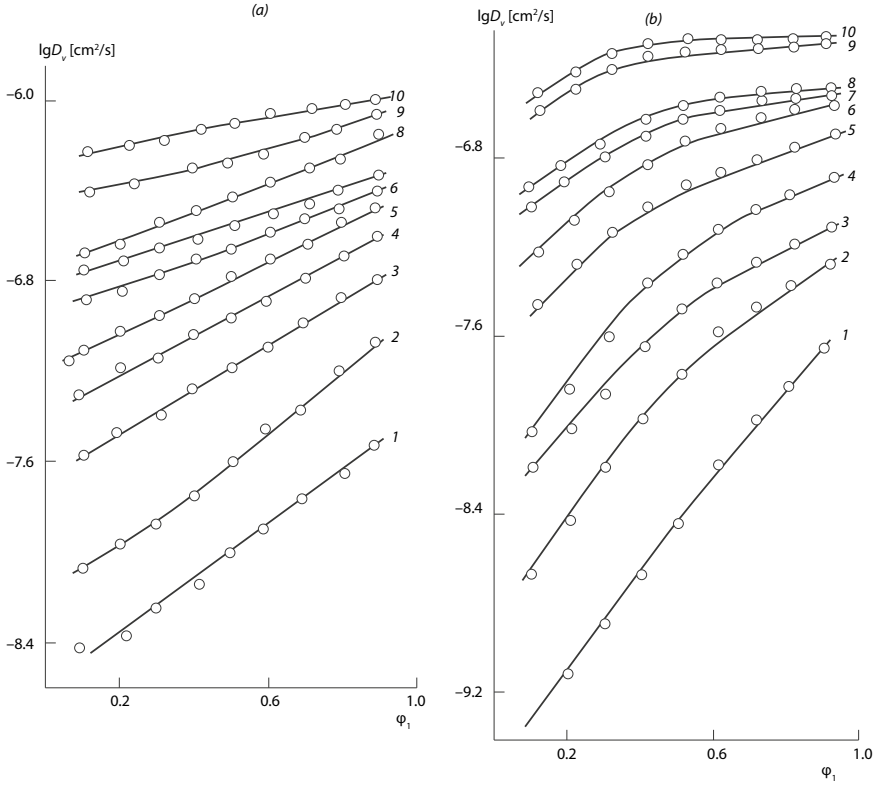

Fig. 2 Concentration dependence of interdiffusion coefficients in the system EO-2/EO-4 (**a**) EO-2/EO-9 (**b**) at temperatures 353 (1), 373 (2), 393 (3); 413 (4), 423 (5), 433 (6), 443 (7), 463 (8), 483 K (9), and 495 K (10)

Figure 4 shows the data for the case when the diffusion medium is the same (Epikote 1009) and diffusants are different: DGEBA, ED-20, E40, and E44. As the MW of the diffusant M_1 increases or the M_2/M_1 ratio decreases (M_2 corresponds to the molecular weight of EPIKOTE 1009), the concentration dependence of D_V (1) degenerates against the background of a general decrease in the absolute values of diffusion coefficient.

1.5 Temperature Dependence of Diffusion Coefficients

Notably, in the analysis of the experimental data on the self-diffusion coefficients of melts, the translational mobility of molecules in ED melts, and mutual diffusion has been studied in the temperature range, which covers the areas from the glass transition temperature to the temperature above the ll-transition. Note that earlier measurements

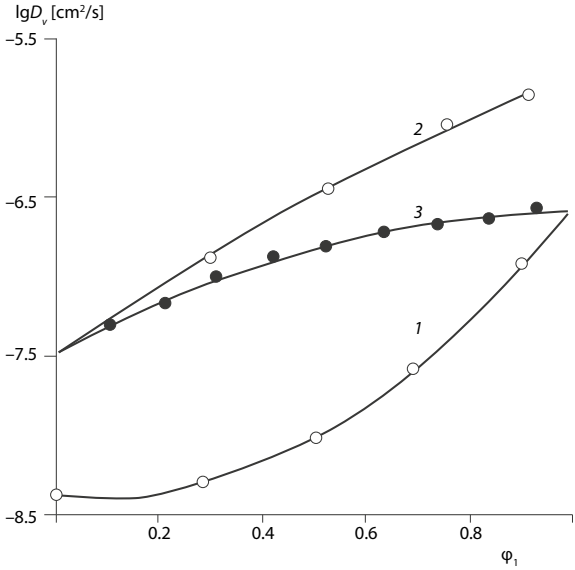

Fig. 3 Dependences of the partial self-diffusion coefficients of EO-8 (1) and EO-1 (2) and mutual diffusion coefficient (3) on the EO-1/EO-8 system composition at 433 K

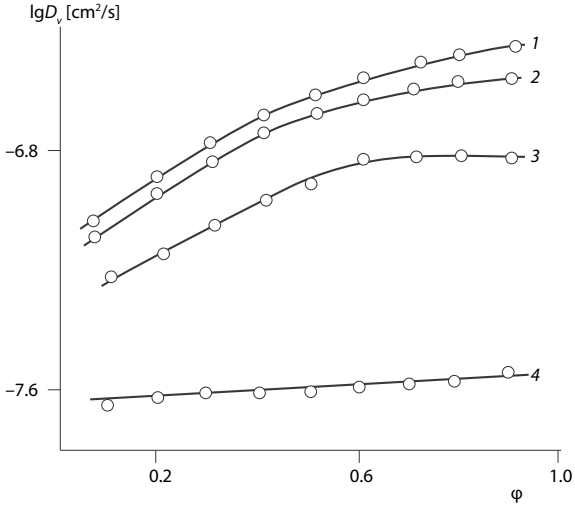

Fig. 4 Dependences of interdiffusion coefficients on the composition of C-systems EO-9/EO-1 (1), EO-9/EO-2 (2); EO-9/EO-4 (3); and EO-9/EO-5 (4) at 493 K

were performed only for some low-molecular-weight oligomers—ED-20, ED-16, and DGEBA [26].

Figure 5 shows the temperature dependences of self-diffusion coefficients in the coordinates of the Arrhenius equation:

$$D^* = D^*(0)\exp\left(-E^*/kT\right) \tag{5}$$

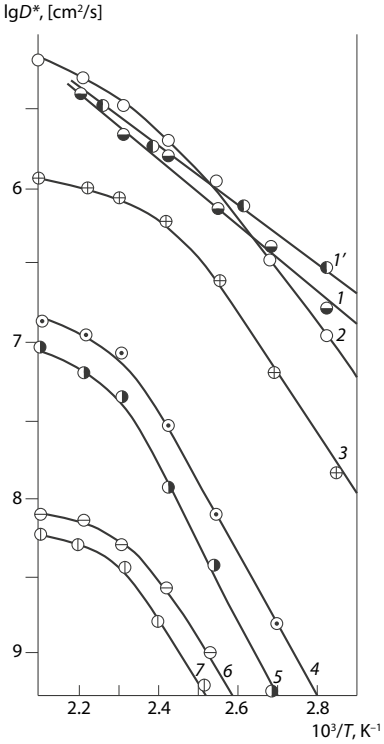

Fig. 5 Temperature dependences of self-diffusion coefficients of EO: 1 and 1′—DGEBA, 2—ED-20 and YD-128, 3—E40, 4—E44, 5—DER, 6—Araldite 6610, 7—Epikote 1009

where E^* is the apparent activation energy of self-diffusion.

One can see that the coefficient values for EO-2 and YD-128 coincide since their molecular masses have close values, while for DGEBA, they lie below the D^* values of the oligomers whose mass is greater than that of DGEBA. For comparison, the dotted line shows the D^* values of DGEBA extracted from [19]. It can be seen that these values are close to those obtained by us.

The self-diffusion coefficients of EO decrease with increasing molecular weight over the entire temperature range. The intensity of the decrease is different for temperatures near T_g and T_{ll}. For all epoxy oligomers, the Arrhenius dependences can be approximated by two linear (first approximation) sections characterized by different slope angles, E^* and E^{**}. The first section corresponds to the temperature range from 353 to 423–433 K (E^*) and the second from 433 to 493 K (E^{**}). It should be noted that the breakpoint temperature (T^* 433 K) is close to the ll-transition temperature in epoxy oligomers identified by infrared spectroscopy and relaxation spectrometry [28].

This character of the dependence is reproduced by repeated cycles of “rise and fall” temperature. Special experiments have shown that the appearance of a kink

Table 2 Activation energy of self-diffusion EO

EO	lgM_w	Activation energy of self-diffusion, kJ/mol		lgD^*, [cm^2/s] at T_g
		E^*	E^{**}	
DGEBA	2.53	48.5	28.4	–10.90
ED-20	2.62	46.8	19.2	–10.90
YD-128	2.62	46.8	19.2	–10.90
ED-40	2.78	74.4	19.6	–10.80
ED-44	3.43	85.3	21.7	–11.20
DER	3.50	100.7	24.7	–11.10
Araldite 6610	3.82	85.7 ± 13.1	23.8	–10.80
Epikote 1009	3.85	85.7 ± 13.1	19.2	–10.95

in the $lgD^* - 1/T$ dependence is associated neither with chemical reactions (self-crosslinking), which could take place at high temperature nor with polymer degradation. On the one hand, this was confirmed by refractometric studies [29] and, on the other hand, by gel chromatography data. The chromatograms of epoxy compounds preheated at 473 K coincide with those obtained for EO not subjected to heat treatment. In addition, according to DTA data, thermal decomposition of EO is observed at temperatures above 573 K.

Table 2 and Fig. 6 present the values of activation energy calculated from the dependence $lgD^* - 1/T$ for each of the indicated temperature intervals. The values of $D^*(T_g)$ obtained by extrapolation of the first part of this dependence to T_g are also given there. It can be seen that $D^*(T_g)$ are quite close for all EO regardless of their molecular weight and, on average, reach ~12 × 10^{-11} cm^2/s.

For most of the systems studied, with the exception of those cases where the diffusion media were DGEBA and ED-20, a single trend of changes in the DE diffusion coefficients with temperature is observed (Fig. 7).

1.6 Interdiffusion of Epoxy Oligomers

For most investigated systems, except for the cases when the diffusion media were DGEBA and ED-20, the same tendency of changes of DE diffusion coefficients with temperature was observed. It can be seen that the temperature dependence of the limiting interdiffusion coefficient D_{12} can also be approximated by two linear sections characterized by different slope angles, namely E_I (correlation coefficient 0.98) and E_{II} (correlation coefficient 0.96). As in the case of self-diffusion, the first section corresponds to the temperature region 353–433 K and the second to the interval 455–493 K. It should be noted that the position of the kink in the temperature dependences on the coefficient of interdiffusion of EO (455 K) is also close to the temperature of T_{II}-transition in EO (433 K), that is, this temperature does not depend

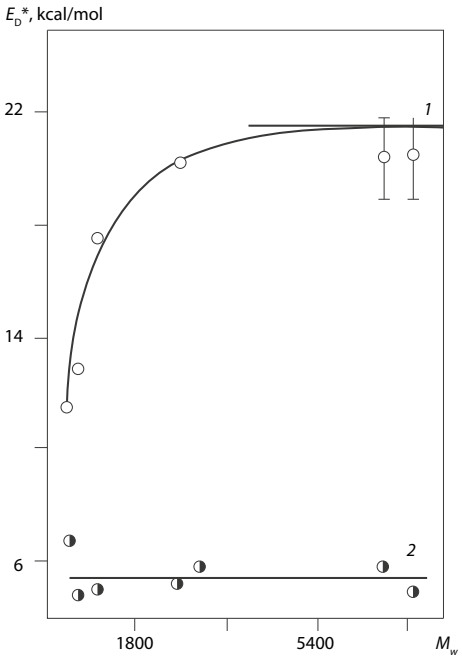

Fig. 6 Dependence of the activation energy of EO self-diffusion on the molecular weight for $T <$ 433 K (1) and $T >$ 433 K (2)

on the way of measuring the translational mobility of oligomers but is a characteristic value of the matrix in which mass transfer occurs.

Numerical values of apparent activation energies E_I and E_{II} are given in Table 3. Their concentration dependence is shown in Fig. 8. For all systems, regardless of the EO being a diffusant, $E_I > E_{II}$. In this case, if the E_I value depends on concentration and occupies an intermediate position between the activation energies of self-diffusion of components $E_{II} \leq E_I \leq E^*_{22}$, then E_{II} is practically independent of the co-stock and satisfies the condition $E_{II} \cong E^*_{11} \cong E^*_{22}$.

Figure 8 shows that E_I, as E^*, is a function of the molecular weight of the diffusion medium, increasing slightly in the transition from ED-20 to EPIKOTE 1009. For E_{II}, this dependence is weakly expressed.

A comparison of the activation energies of E_{II} translational mobility with the activation energies characterizing the segmental and group mobility of oligomer macromolecules showed that it is close to the activation energy and α-transitions ~71.06 and 50.16 kJ/mol, respectively, and agrees with the activation energy—transitions ~16.72 kJ/mol [30]. It means that in the temperature range $T <$ 438 K, large-scale motions of macromolecule fragments forming the diffusion medium are responsible for the translational mobility of epoxy oligomers molecules. At $T >$ 433 K—small-scale movements of macromolecule fragments and monomer units (CH_3-, OH-groups).

It appears that such a temperature dependence of diffusion coefficients in ED melts is related to the formation of "hole vacancies" of extended sizes in diffusion media at

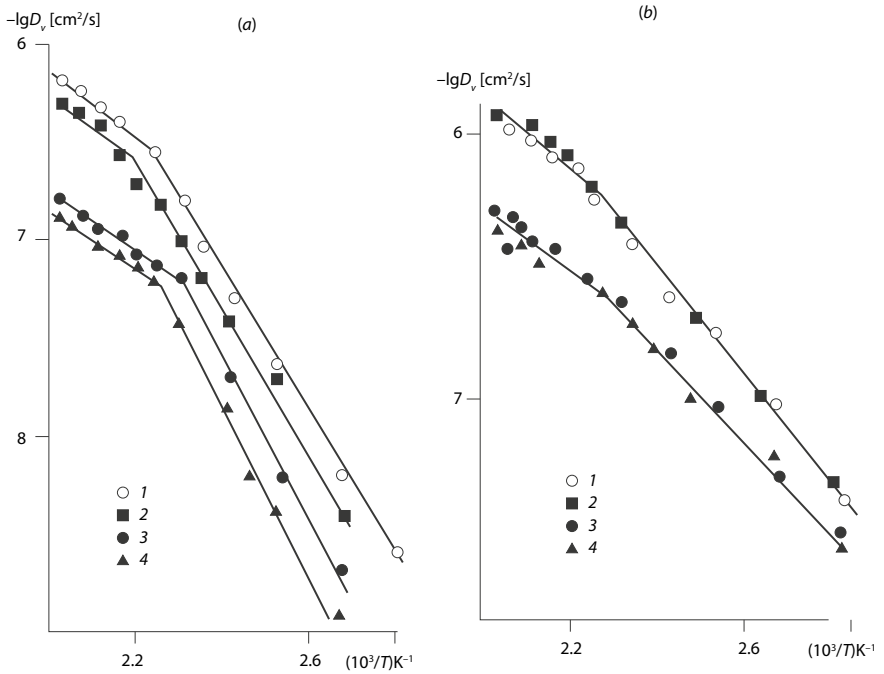

Fig. 7 Temperature dependences of the limiting coefficient of interdiffusion of EO-2 **a** in matrices EO-5 (1), EO-6 (2), EO-8 (3), and EO-9 (4); and **b** marginal coefficient of interdiffusion of oligomers of EO-5 (1), EO-6 (2), EO-8 (3), and EO-9 (4) in the matrix EO-2

Table 3 Interdiffusion activation energy in epoxy oligomers

EO	E_{12}, kJ/mol		E_{21}, kJ/mol	
	$T < T_{ll}$	$T > T_{ll}$	$T < T_{ll}$	$T > T_{ll}$
ED-44	62.2	24.0	43.1	22.0
ED-49	72.3	24.8	41.9	23.0
Araldite 6610	75.2	26.5	40.5	23.5
Epikote 1009	74.5	26.4	42.5	24.4

E_{12}—activation energy of diffusion of ED-20 into oligomers; E_{21}—activation energy of oligomers diffusion into ED-20

high temperatures ($T_g + 150$) in the so-called free volume flicker clusters whose lifetime exceeds the time of the diffusion jump of the oligomer molecule (displacement of its center of gravity). Obviously, under these conditions, the contribution to the activation energy of the work of micro-cavity formation becomes minimal, and the value of the activation energy is determined only by the energy costs associated with overcoming the intermolecular interaction and the friction forces in the movement of the molecule along the surface of the free volume cluster. At low temperatures

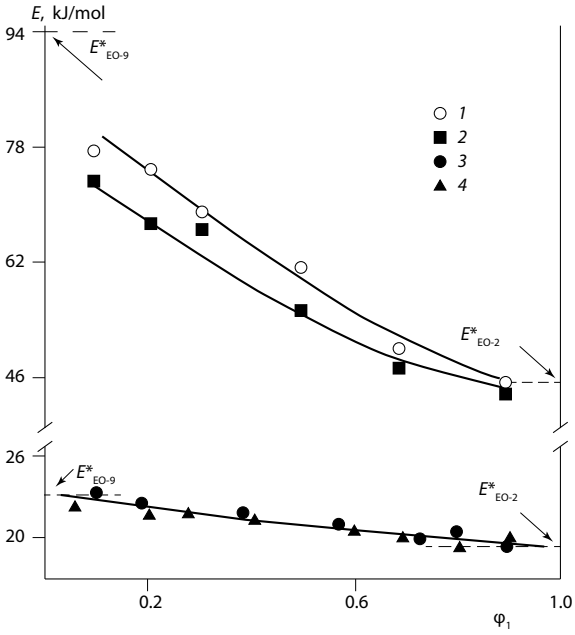

Fig. 8 Concentration dependences of apparent activation energies of interdiffusion in the EO-2/EO-9 system (1.3) and EO-2/EO-5 system (2.4) at temperatures $T < T_{ll}$ (1, 2) and $T > T_{ll}$ (3, 4)

($T < T_{ll}$), the main contribution to the mechanism of translational motion of EO molecules in melts is related to the formation of micro-cavity of necessary size near them.

1.7 The Influence of the Molecular Weight of Oligomers

According to the existing theories of translational mobility of macromolecules [18, 19], two groups of systems are distinguished when considering the dependence of self-diffusion coefficients on molecular mass. The first refers to monodisperse or close to monodisperse melts, while the second group refers to systems with a broad molecular-mass distribution. For the first group of systems for which the theoretical analysis is described in [24, 25], the relations $D^* \cong M^{-1}$ at $M < M_{cr}$ and $D^* \cong M^{-2}$ at $M > M_{cr}$. M_{cr} is the critical molecular mass at which a net of physical links between macromolecules develops.

However, the results of experimental studies are different. For example, $D^* \cong M^{-1.7}$ was obtained for PEG and PDMS in [3], and both $D^* \cong M^{-1}$ and $D^* \cong M^{-2.7}$ were found for polystyrene melts [3]. A detailed analysis of the molecular weight dependence of the self-diffusion coefficient of PEG melts is given in a monograph [32]. According to these authors, the dependence of D^* on M_n has two characteristic regions and is described by the relation $D^* \cong M_n^{-b}$, where $b \sim 1$ for $M_n \leq 10^3$ and $b \sim 2$ for $M_n > 3 \times 10^3$.

The systematic experimental investigations have not been practically carried out for the second group of systems, though these systems are of the most significant interest. There are only separate attempts to analyze the translational mobility of these systems within the concept of the self-diffusion and cooperative diffusion coefficient spectra [32, 33].

Before proceeding to the analysis of the diffusion characteristics of EO with different molecular weight distributions, we note that we will refer to the data on the diffusion of individual EO to their weight-average molecular weight M_w, and we will choose the equation as the basis for their relationship with the translational mass transfer coefficients:

$$D^* \cong D_0 M_{\mathrm{w}}^{-b} \tag{6}$$

where D_0 is the diffusion coefficient corresponding to the diffusion coefficient of the monomer. In works [1–3], D_0 is identified with diffusion coefficients of "monomer," "segment in diffusion medium," "monomer friction coefficient," and friction coefficient of blob with the environment.

The complex nature of the temperature dependence of the self-diffusion coefficients of epoxy oligomers required the analysis of the dependence of $D^* - M_{\mathrm{w}}$ for different temperatures. The following intervals were chosen: $T < 433$ K (393 K, 413 K) and $T > 433$ K (453, 473 K).

It has been established (Fig. 9) that in the investigated range of molecular masses, linear dependence of $\lg D - \lg M_{\mathrm{w}}$ (the correlation coefficient is 0.97) with a temperature-dependent slope: for $T < 433$ K $b = 2.4$, and for $T > 433$ K $b = 2.0$ really takes place. This clearly differs from the data obtained earlier for a number of polymer melts at $M < M_{\mathrm{cr}}$, for which, in the oligomeric region, $b < 2$.

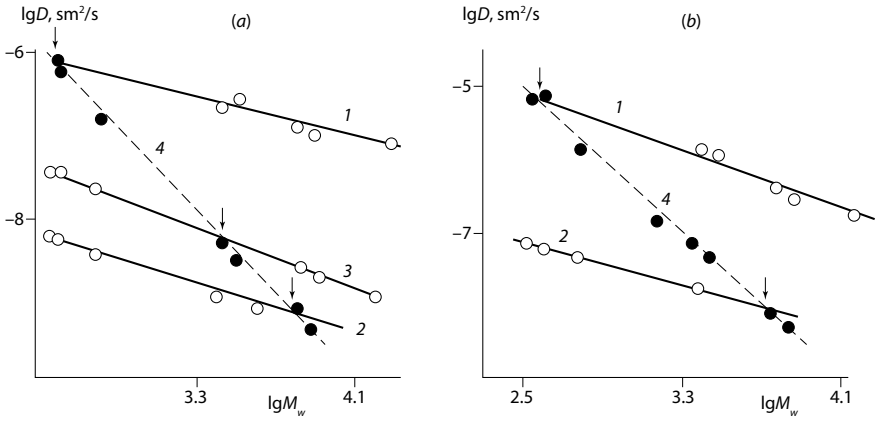

Fig. 9 Dependence of the limiting coefficients of interdiffusion (1–3) and self-diffusion (4) on the molecular weight of EO. $T = 393$ K (**a**) and 493 K (**b**). The arrows indicate the self-diffusion coefficients and the MW of the oligomers forming the diffusion media

It should be noted that, for epoxide oligomers, in this temperature interval, one can observe anomalies in the dependence of Newton viscosity on the molecular weight: b varies from 2.7 (403 K) to 3.5 (343 K).

Figure 9 shows some dependences of D_{ij} on the molecular mass M_i of EO diffusing into the medium of EO with a constant molecular mass M_j. Three cases are given: when the MW of the diffusing molecules is less than the MW of the diffusing medium ($M_i < M_j$); when $M_i > M_j$, and when the M_j of the diffusing medium is within the MW interval corresponding to the homologous series of diffusing EO molecules. It is seen that for all cases at different temperatures, the experimental points in the coordinates lie on straight lines (the correlation coefficient is 0.98), crossing the dependences at the points corresponding to the MW and self-diffusion coefficient of EO molecules that compose the diffusion medium (arrows mark these points in Fig. 9).

The exponent of Eq. (6), the value of which is commonly used to determine the diffusion mechanism [31, 34, 35], varies in the rather narrow range of 0.90 ± 0.06. Importantly, it does not depend on temperature, in contrast to the factor b calculated from self-diffusion data. This means that the M_w^{-b} multiplier in Eq. (6) is really a structural characteristic of diffusing unchained molecules, whose mono-dimensional friction coefficient is determined by D_0.

We experimentally determined the multiplier D_0 as the limiting diffusion coefficient of ED-20. Dependences of D_0 on MW of EO molecules forming the diffusion medium M_{cr} are shown in Fig. 10. As M_{cr} increases, the monomeric diffusion coefficient decreases, asymptotically approaching some constant value of $D_{0\infty} \cong D_0$ at $M_{cr} \to \infty$. This type of $D_0 - M_{cr}$ dependence is observed at all temperatures and for any other diffusant. The specificity of each diffusant is evident in the values of D_0 and M_{cr}. Thus, for ED-20, it is 1×10^4, for dibutyl phthalate $M_{cr} = 7 \times 10^3$, for cyclohexanone—6×10^3.

Experimental dependences $D_0 - M_{cr}$ at degrees of polymerization of epoxy oligomer $N > 5$ are satisfactorily described by the empirical equation

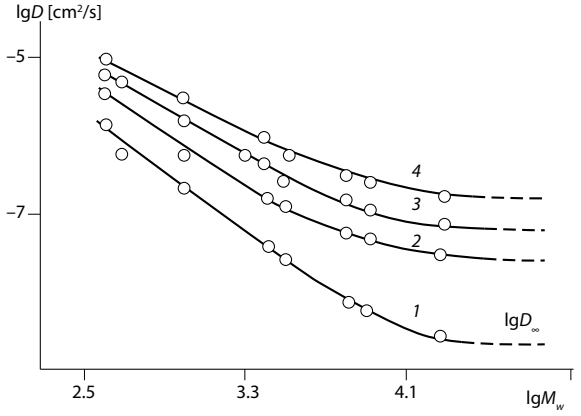

Fig. 10 The dependence of the diffusion coefficients of EO-2 (1–4) in epoxy oligomers on the MW of the oligomer medium. $T =$ 393 K (1), 433 K (2), 443 K (3), and 494 K (4)

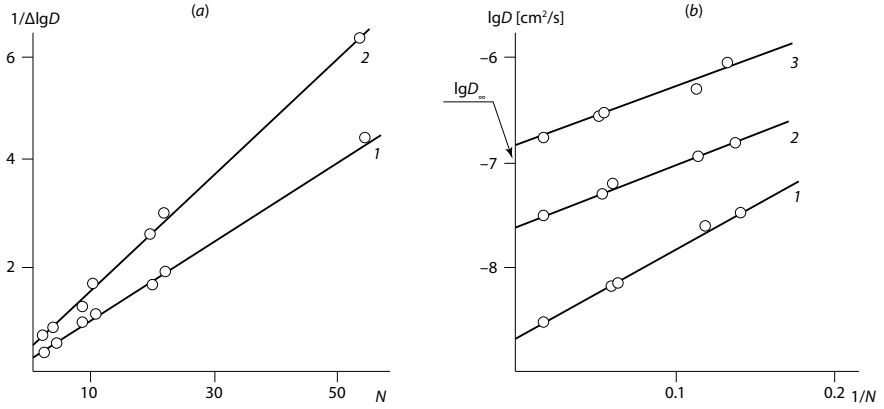

Fig. 11 Dependence of diffusion coefficients of EO-2 in epoxy oligomers on their degree of polymerization in the coordinates of Eq. (7). $T = 393$ K (1), 433 K (2), and 494 K (3)

$$\lg D_0 = \lg D_{0\infty} + \frac{k}{N} \tag{7}$$

where k is a constant (Fig. 11). We used these dependences in determining $D_{0\infty}$.

In the whole range of polymerization degrees (N), the dependences $D_0 - M_{\text{cr}}$ are described by the equation:

$$\left(lg\frac{D_0}{D_{0\infty}}\right)^{-1} = \frac{2.3 f_\infty}{B} + \frac{f_\infty^2}{Ba} N \tag{8}$$

f_∞ is the free volume fraction of EO at $M \to \infty$, B is a constant close to unity; a is a constant related to the local free volume of links and end groups of macromolecules). Note that the coefficient of thermal expansion of the free volume of polyhydroxy ethers calculated (under assumption $B \cong 1$) along the segments f_∞/B, segmented by straight lines on the ordinate axis, is $(5 \pm 0.1) \times 10^{-4}$ and is close to the standard value of 4.8×10^{-4} [2, 4].

Thus, the presented experimental material clearly shows that the monomeric diffusion coefficient (friction) D_0 depends on the MW of the diffusion medium. It is obvious that this effect should be taken into account when interpreting the dependence of the self-diffusion coefficient on MW. Therefore, it can be stated that Eq. (8) is valid for the analysis of translational mobility of unchained macromolecules only when the MW of diffusing molecules changes and the MW of macromolecules forming the diffusion medium remains unchanged. Probably, in this case, it can be assumed that for unchained molecules $b \cong 1$.

When describing self-diffusion in oligomer melts, relation (7) should be written in the form:

$$D = D_0(M) \cdot M^{-b} \tag{9}$$

which takes into account explicitly the contribution to the self-diffusion coefficient made by end groups, whose concentration continuously changes during the transition from one polymer homologue to another.

1.8 Conclusion

Coefficients of mutual and self-diffusion of epoxy oligomers of different molecular weights were determined by NMR spectroscopy (spin-echo) and optical interferometry. The dependences of diffusion coefficients on temperature and concentration of binary systems are presented. It was found for the first time that for all EO, the Arrhenius temperature dependences of the coefficients of the self and interdiffusion can be approximated by two linear sections characterized by different activation energies—E_{I} and E_{II}. The first section corresponds to the temperature range from 353 to 423–433 K, and the second from 433 to 493 K. The kink temperature ($T^* \cong 433$ K) of the Arrhenius temperature dependences is close to the temperature ll-transition of EO identified by infrared spectroscopy and relaxation spectrometry.

It has been established that in the investigated range of molecular masses there is a linear dependence $D \cong M^b$ with a temperature-dependent slope angle: for $T <$ 433 K – $b \cong 2.4$, and for $T > 433$ K – $b \cong 2.0$. This clearly differs from the previously obtained data for a number of polymer melts at $M < M_{\mathrm{cr}}$, for which in the oligomeric region $b < 2$.

2 Epoxy-Amine Adducts as Model Systems for Investigation of Curing Processes of Epoxy Oligomers

A method for studying the process of obtaining polymer composite materials through the use of special objects—adducts, partially cured epoxy resins—is proposed. The paper describes the method of obtaining adducts on the basis of industrial epoxy resin ED-20 and curing agent—diaminodiphenylsulfone. Preliminary studies have established the mutual solubility of these components, the rate of their mutual mixing, and the temperature range of the chemical reaction. The dependence of the molecular weight characteristics of the obtained adducts on the degree of conversion as well as their glass transition temperatures was traced. The obtained adducts were combined with thermoplastics—polyetherimide and polymethylmethacrylate—and the mixing processes were observed by optical interferometry. The evolution of phase state diagrams of thermoplastic-reactoplastic mixtures and changes in interdiffusion coefficients in these systems during the chemical curing reaction were traced in this work.

2.1 Introduction

At the present time, many methods of obtaining materials based on epoxy resins with self-healing properties have been described in the literature. At the same time, the recovery process of the epoxy matrix after a crack has sprouted in it can occur by different mechanisms, for example, both thorough wetting of the fracture surface by the adhesive released from the previously introduced microcapsules and through the realization of complex chemical reactions or interdiffusion processes between the composite material components [36–44]. In the latter case, a number of difficulties arise for the study since the mass transfer processes take place practically in the matrix, which is in the glassy state. In our opinion, this complexity can be circumvented by investigating the behavior of the system during the chemical curing reaction at different stages.

One of the effective experimental approaches allows to study of the change of translational mobility of components during curing (formation of the spatial mesh of reactoplastic), tracing the evolution of boundary curves of the phase diagram, and evaluating the kinetics and mechanism of mutual diffusion, and solubility at different stages of structure formation is related to the study of mass transfer in the epoxy oligomer adducts (aER)—thermoplastics systems. It is assumed that a set of adducts with different conversion rates (α) allows adequate modeling of the process of formation of spatially cross-linked structures of composite binders at different stages of the reactoplastic curing process.

In the present work, we summarize the results of our studies of the kinetics of hardener dissolution in a dian epoxy oligomer; the partial translational diffusion coefficients are determined and their changes with changes in the oligomer curing degree are traced; the apparent activation energies of interdiffusion are calculated. Note that in our experiments, thermoplastics act as macromolecular probes whose partial mass transfer coefficients will make it possible to estimate the influence of the parameters of the spatially cross-linked structures on their translational migration in oligomer solutions at different curing stages.

2.2 Objects and Methods of Research

The following objects were used as objects of research: ED-20 dian epoxy resin ($M_n = 380$ g/mol), curing agent—diaminodiphenylsulfone (DADPS), thermoplastic polymers: polyetherimide (PEI, Ultem 1000, $M_w = 62{,}000$ g/mol) and polymethylmethacrylate (PMMA, Aldrich, $M_w = 996{,}000$ g/mol); epoxy oligomer adducts (aER) of various degrees of conversion (α).

When synthesizing adducts with different degrees of conversion of epoxy groups, the ratio of the component oligomers: hardener was taken as a multiple of the stoichiometric ratio 10:3 by mass [16]. So, for an adduct corresponding to the conversion degree $\alpha = 0.1$, for 100 mass parts of the oligomer, there were 3 mass parts

of the hardener, for $\alpha = 0.2 - 6$ mass parts, etc. After the components were combined and thoroughly mixed, the mixtures were heated and thermostatted for 6 h at 453 K. The complete conversion of reactive groups during the curing reaction was confirmed by infrared spectroscopy. Preliminary measurements by differential scanning calorimetry (Netzsch Phoenix DCS 204F1) determined the optimum temperature interval for curing EO (433–453 K), selected high-temperature curing agent DADPS (Fig. 12).

It was assumed that each of the epoxy groups of the oligomer would react with the terminal-NH_2 DADPS (Fig. 13), the amount of which is sufficient to form, eventually, a continuous network of chemical bonds in the mixture.

The content of epoxy and amine groups during the curing of each adduct was determined by infrared spectroscopy in the frequency range of 400–4000 cm^{-1} using

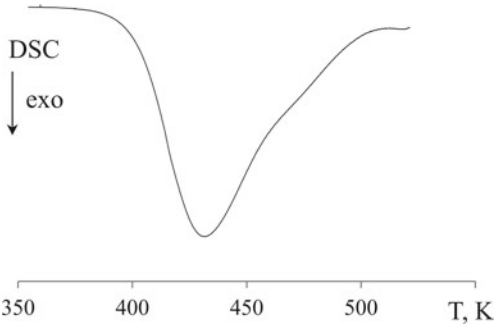

Fig. 12 Curing thermogram of DADPS epoxy oligomer at stoichiometric ratio

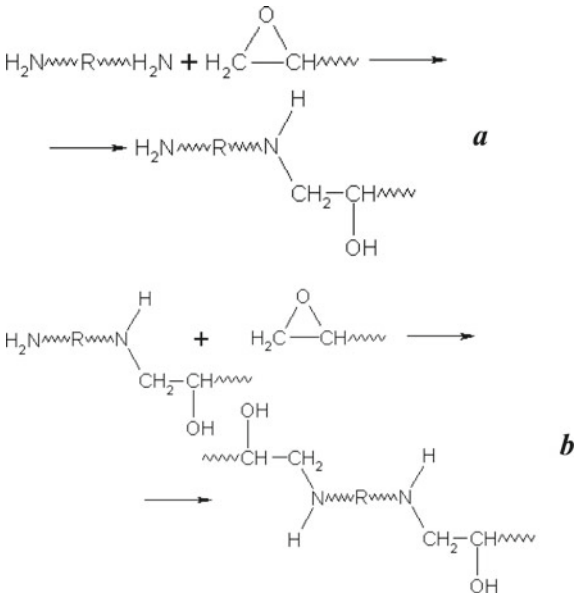

Fig. 13 The reaction of the interacting functional groups of the epoxy oligomer with the amine hardener (**a**) and macromolecule growth (**b**)

an IFS 66v Fourier infrared spectrophotometer with a high-temperature cell. After careful mixing of the components, the compositions were applied to a KBr tablet, which was covered with the same tablet on top, thus forming an adduct layer with a thickness of ~20 μm. The tablets were placed in the spectrometer cell holder, and IR spectra were recorded at curing temperature every 15 min. The spectra were processed using a standard OPUS program. The main absorption bands, the intensity of which changes during curing, are the broad band of valence vibrations of hydroxyl groups in the region of 3200–3700 cm^{-1}, and bands of strain vibrations of the epoxy cycle and primary amino groups in the regions of 880–950 cm^{-1} and 1629 cm^{-1}, respectively. Absorption bands [45] at 1510 cm^{-1} and 1374 cm^{-1}, caused by valent vibrations of the >C=C< bond in the aromatic ring and strain vibrations of methyl groups at the carbon atom, respectively, were used as "internal standards." Based on the values of the optical density of the epoxide group absorption bands and the "internal standards" in accordance with the Lambert–Beer law, the concentrations of epoxide groups in the curing amino-epoxide compositions were calculated.

Molecular weight characteristics of aER were determined by gel permeation chromatography. The samples of epoxy oligomers and oligomer adducts were analyzed on a Waters (USA) high-pressure gel chromatograph with a 264 nm UV detector and Styragel HR 4E columns 300 mm long and 7.8 mm in diameter. Tetrahydrofuran was used as the solvent. The elution rate was 1 ml/min, polymer concentration in the solvent was 1 mg/ml, and the sample volume was 10 μl. Column and injector thermostat temperature was set to 298 K. Calibration of the chromatographic system was carried out with reference polystyrene samples from "Waters" company, which have monodisperse molecular weight distribution ($M_w/M_n = 1.03$). Samples of reference polystyrene and the analyzed polymer were dissolved in THF at room temperature and then transferred to the injector of the chromatograph.

Figure 14 shows a typical chromatogram of the initial epoxy oligomer ED-20. It can be seen that it is formally polymodal. On the chromatogram, at least three molecular fractions A1, A2, and A3 can be distinguished. However, the proportion of fractions A2 and A3 is small, so processing the chromatogram by standard methods gives the value of the molecular weight distribution equal to 1.09, which allows us to refer to the oligomer chosen for the study as monodisperse.

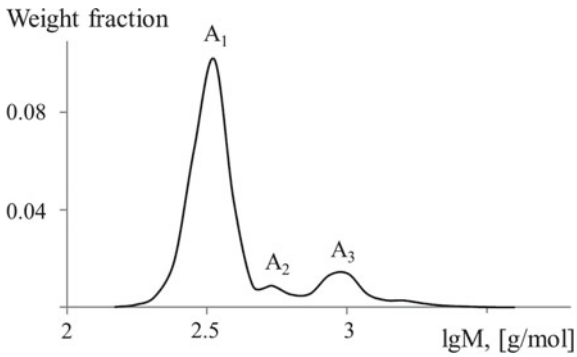

Fig. 14 The molecular weight distribution of ED-20 epoxy oligomer

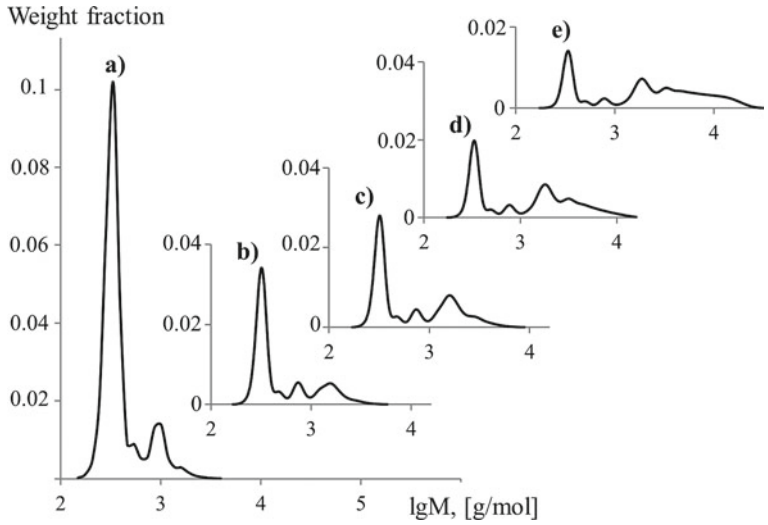

Fig. 15 Molecular weight characteristics of aER. Conversion degrees α: **a** 0, **b** 0.05, **c** 0.10, **d** 0.20, **e** 0.30

The chromatograms of the synthesized adducts are shown in Fig. 15. We can see that the number and proportion of peaks falling on higher molecular weight fractions increase with growth α, i.e., the polydispersity of the adducts increases. At the same time, peaks corresponding to initial oligomer fractions decrease both in intensity and area, indicating a decrease in the number of initial epoxy units. It was found that the growing peaks correspond to MW multiples of the initial oligomer MW.

At low conversion rates ($\alpha \leq 0.30$), an increase in the MW of the initial oligomer occurred due to the reaction of attachment of the hardener molecules and lengthening of the MW of the initial oligomer (Fig. 13). At higher ($\alpha \geq 0.35$), the formation of the so-called microgel structures occurred, and the appearance of which was accompanied by an increase in pressure of the elution solution when feeding it into the chromatographic column, which did not allow us to obtain correct information on the MW aER in this way (Fig. 16).

Additional information on the evolution of the molecular weight characteristics of the adducts was obtained by chromatogram decomposition in the ORIDGEN 7 program. It was found that the content of the monomeric fraction of EE in the adduct decreased from 76 to 25 wt%, the dimer from 14 to 6 wt%. Whereas the tetramer content in aER with a conversion rate of 0.1 reaches 24 wt%. It is interesting to note that the tetramer content in samples with conversion rates of 0.1–0.3 changes little, whereas, in the adducts, the share of molecular fractions with $M = 3150$ appears and grows. The greatest changes in molecular weight characteristics occur at $\alpha \geq 0.3$. It is under these conditions that microgels and mesh fragment particles appear. In Fig. 16, this state of the adducts, which can be called transitional, is indicated by the dotted line. A further increase in the content of the hardener in the mixtures

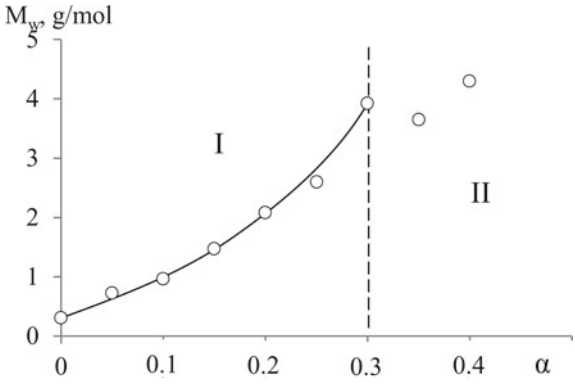

Fig. 16 Dependence of the average molecular weight of aER on the degree of conversion. Region I corresponds to the formation of long-branched macromolecules of aER, and region II corresponds to the formation of microgel particles

and, consequently, the degree of conversion led to the formation of a high-molecular-weight "tail" in the chromatograms as a result of the reaction of copolymerization of di- and trimers.

Additional information about the MW of the adducts of various degrees of hardening, including $\alpha \geq 0.35$, was obtained using their glass transition temperatures, which were determined by DSC. Figure 17 shows typical thermograms of the temperature dependences of the heat capacity of aERs in their glass transition region.

It can be seen that the Cp–T dependences Δ are S-shaped, and the aER glass transition temperature increases and reaches its maximum value at a sharp $\alpha \rightarrow 1$. Increase in the glass transition temperature (Fig. 18) is associated with the formation of a spatial bonding network. For this area of adducts, the MW aER value calculated from the Nielsen equation [46] characterizes the value of the molecular mass of the reactant between the nodes of the mesh (see Table 4).

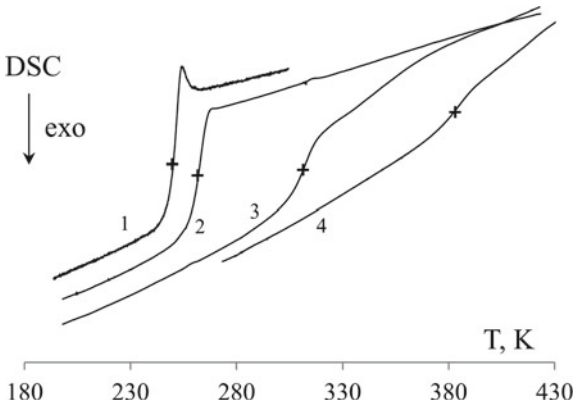

Fig. 17 DSC thermograms of the adducts. Conversion degrees α: ED-20—0% (1), 0.2 (2), 0.6 (3), and stoichiometric component ratio (4)

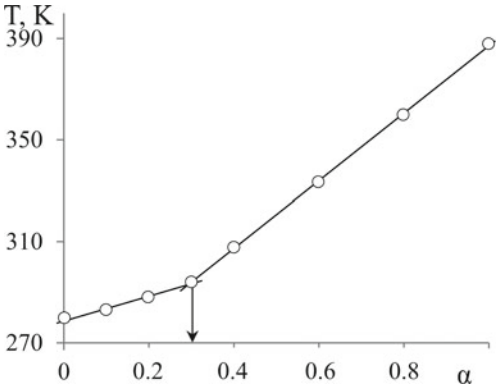

Fig. 18 Dependence of the glass transition temperature of aER-DADPS on the degree of conversion

Table 4 Comparative MW values of adducts of epoxy oligomers

α	GPC		
	M_n	M_w	MMW
0.1	495	997	2.01
0.2	672	2034	3.02
0.3	908	3918	4.31

Subsequently, these values of the molecular weight characteristics of the adducts were used to analyze the behavior of polymer-oligomer mixtures at various stages of the chemical curing reaction.

To study solubility, interdiffusion, and construction of phase diagrams in binary systems thermoplastic-ER and thermoplastic-aER, we used the optical wedge interferometer ODA-2 method (IPC RAS). The methodology of the experiments did not differ from the traditional one [19]. A pre-pressed thermoplastic film was placed inside the interference cell, heated in a thermal furnace to a temperature higher than the thermoplastic glass transition temperature, and brought into optical contact with the surface of glass plates of the wedge capillary. After the assembled cell was thermostatted at the experimental temperature, a diffusant (epoxy oligomer or adduct) was introduced into the wedge gap between the plates. The moment of contact between the components was observed visually on the monitor screen and was taken as the beginning of the interdiffusion process. Interferograms of interdiffusion zones were recorded periodically at intervals of ~110 min depending on the diffusion rate and resolution of interference fringes. Studies of interdiffusion were carried out in isothermal mode. For plotting phase state diagrams, a step mode of temperature rise and fall with step 20/30 K in the temperature range 293–553 K was used. At each stage, the system was thermostatted from 20 to 60 min, depending on its lability. The concentration distribution profiles obtained by the Matano-Boltzmann method were used to calculate the interdiffusion coefficients; the positions of points on the binodal curves of the phase state diagrams were determined by concentration jumps at the interphase boundaries.

Phase and relaxation transition temperatures in homopolymers and decomposition temperatures were obtained by differential scanning calorimetry (Netzsch Phoenix DCS 204F1) at scanning speeds of 10 K/min.

2.3 *Phase Equilibrium and Interdiffusion in the Epoxy Oligomer–Curing Agent System*

In the production technology of composite materials based on thermosetting binders, the correct choice of temperature-time homogenization mode of the epoxy-hardener mixture and curing parameters of the composition is of great importance [26]. Naturally, it is of interest to determine under what conditions the dissolution process of hardener particles in the oligomer melt occurs and what kinetic constants describe this process.

The figure shows typical interferograms obtained by combining ER with DADPS both in the isothermal holding mode, used to obtain data on mass transfer processes (Fig. 19). The step heating/cooling mode is used to build a phase state diagram (PSD) of the system. It was found that the phase equilibrium of the ER/DADPS system is characterized by a phase state diagram with crystalline equilibrium (Fig. 20). In accordance with the obtained data at low temperature, there is a partial dissolution of DADPS. In this case, near the crystal surface, the concentration of the saturated solution is established, which changes with temperature. At $T \geq T_m$ (Fig. 20b), the system is homogenized. The interferograms of the interdiffusion zone are characterized by a continuous change in the refractive index in the transition from one component to another.

Along with the component's dissolution in the diffusion zone at elevated temperatures, the curing reaction of ED-20 proceeds, manifested in the interferograms by

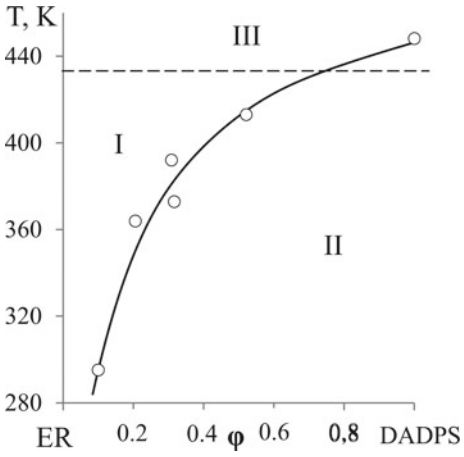

Fig. 19 Phase state diagram of the ED-20−DADPS system. Areas I, II, and III are the true solution-melt, crystalline state of DADPS, and chemical reaction, respectively. The diagram was constructed according to the compositions of coexisting phases established near the phase boundary (Fig. 20), determined by the interferometric method

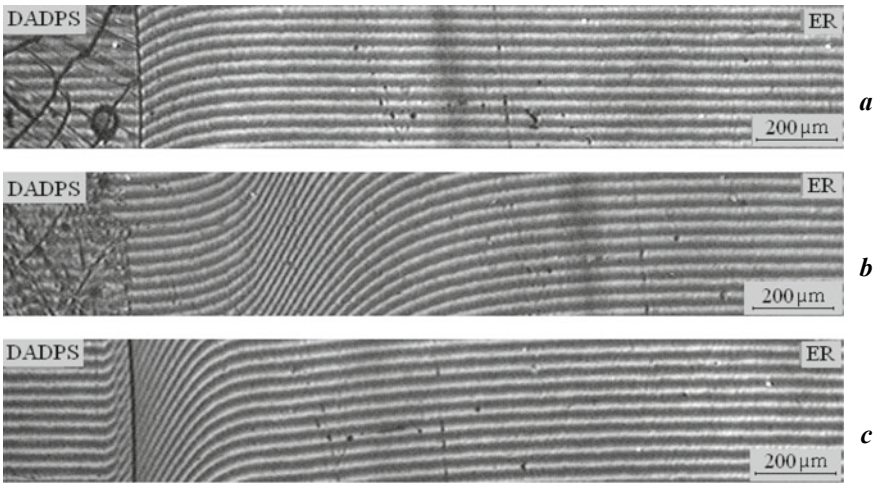

Fig. 20 Interferograms of interdiffusion zones of the DADPS−ED-20 system at temperatures: **a** 363 K ($T \leq T_m$), **b** and **c** 453 K (explanations in the text)

thickening the interference bands in the mixing region and an increase in the total number of bands in the system (Fig. 20c). We were able to identify two states of the system, which are characterized by different kinetic parameters of the diffusion of the ingredients (Fig. 21). At the initial part of the mixing process, a linear dependence of the position of the isoconcentration planes coordinate X on time $t^{1/2}$ is observed, indicating a diffusion mechanism of mixing. In the course of further mass-exchange processes, transfer rates slow down due to copolymerization of the components, growth of the molecular weight of oligomers, and then practically stop due to the formation of a network of spatial bonds, which is reflected in the change in the slope angles of the dependencies $X - t^{1/2}$.

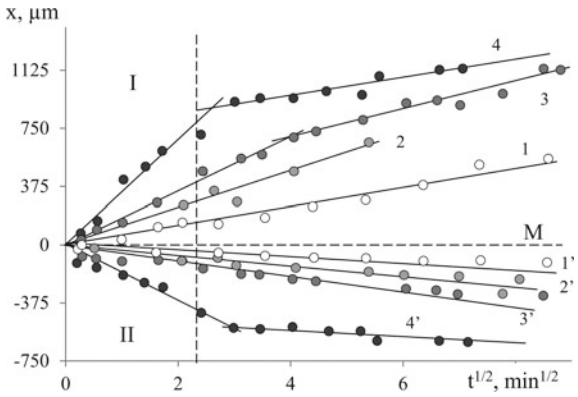

Fig. 21 Kinetic dependences of the movement of isoconcentration planes in the system DADPS−ED-20 at temperatures of 363 K (1, 1'), 373 K (2, 2'), 413 K (3, 3'), and 453 K (4, 4'). I and II are the diffusion regions of DADPC in ER and ER in DADPS, respectively

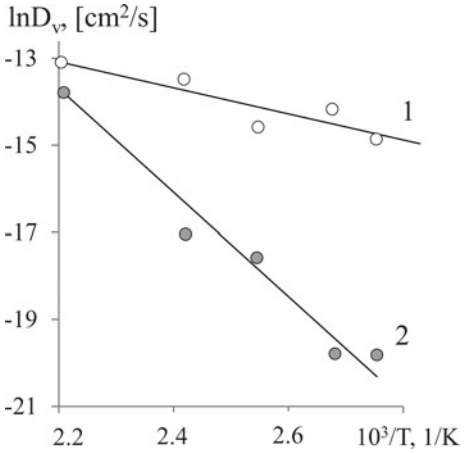

Fig. 22 Temperature dependences of coefficients of mutual diffusion of DADPS in ER (1) and ER in DADPS (2)

The calculated values of diffusion coefficients for the extreme concentrations of the systems (dissolution of DADPS in ER and ER in DADPS) are shown in Fig. 22. The apparent activation energies calculated from the values presented are 24.1 and 92.8 kJ/mol for the diffusion of DADPS into ER and ER into DADPS, respectively.

Thus, it can be argued that the dissolution kinetics of DADPS in ER obeys diffusion patterns up to the temperature of the beginning of the chemical reaction of the epoxy oligomer curing.

2.4 Phase Equilibria and Interdiffusion in Adducts of Epoxy Oligomers

Figure 23 shows typical interferograms illustrating the spontaneous formation of interdiffusion zones during conjugation of thermoplastics with aERs of different compositions. It was found that at low degrees of conversion, $\alpha \leq 0.15$, which corresponds to the initial stages of curing of epoxy oligomers, in the whole temperature-concentration range, the blends are homogeneous at any ratio of components despite the gradient nature of compositions distribution.

As the degree of conversion increases, which is identical to the increase in the molecular weight of oligomers and the formation of branched molecular structures, the same structural and morphological changes are observed in all systems, regardless of the nature of the homopolymer monomer links. Starting from a certain degree of transformation of epoxy groups in the diffusion zone, enriched with aER, a phase boundary appears, separating the areas of dissolution of the adduct in the thermoplastic and thermoplastic in the adduct.

Increasing the degree of curing leads, on the one hand, to the formation of a phase boundary in the region of more concentrated solutions (Fig. 24b) for both

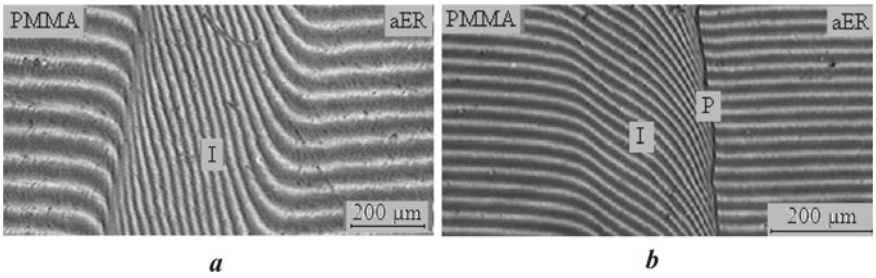

Fig. 23 Interferograms of interdiffusion zones at 453 K of the PMMA—aER system $\alpha = 0.1$ (**a**) and $\alpha = 0.2$ (**b**), where I is the interdiffusion zone, P is the phase boundary

PEI and aER, and, on the other hand, to a shift in the homogenization temperature (binodal dome) to a higher temperature region. Note that for such systems, two optical boundaries are identified on the concentration distribution profile.

The moment of phase boundary formation was most clearly recorded in the PEI–aER system. It was found that regardless of how the interdiffusion process was organized—under isothermal conditions, stepwise increase and/or decrease in temperature, as the temperature approached 373 K in the mixture of PEI with aER in the diffusion zone enriched with adduct ($\alpha = 0.1$), a phase boundary appeared (Fig. 24), separating the regions of aER solutions in PEI from aER solutions of PEI. As the temperature increases, the phase boundary degenerates, and the diffusion gradient

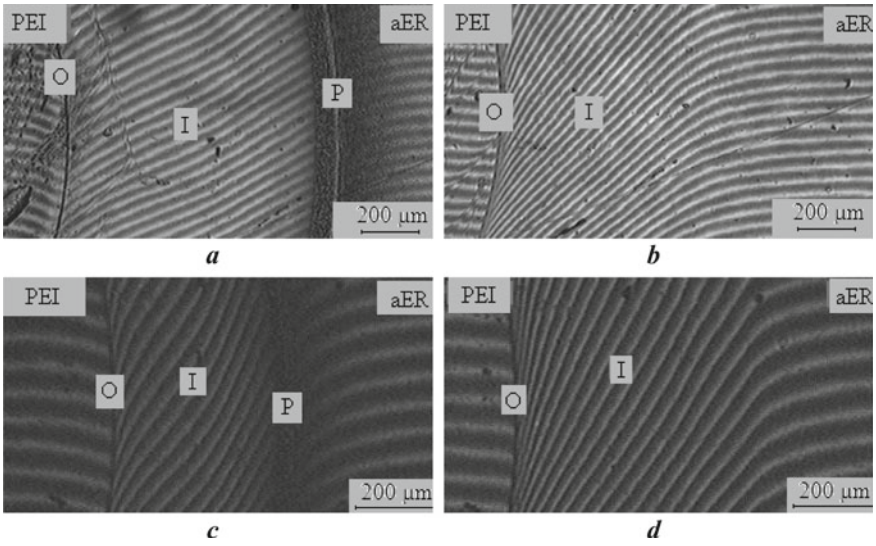

Fig. 24 Interferograms of interdiffusion zones at 293 K (**a**, **c**) and 493 K (**b**, **d**) of the PEI–aER system: $\alpha = 0.1$ (**a**, **b**), (0.2 **c**, **d**), where I is the interdiffusion zone, P is the phase boundary, O is the optical boundary

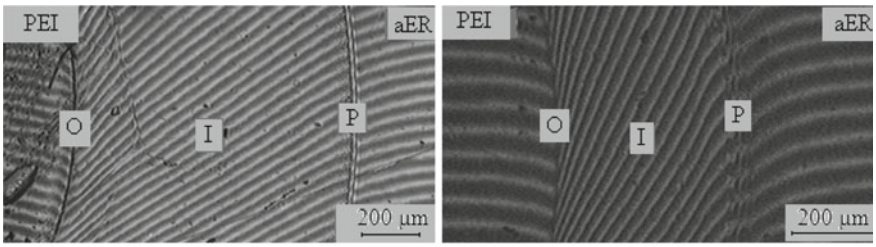

Fig. 25 Interferograms of interdiffusion zones at 373 K of the PEI–aER system $\alpha = 0.1$ (**a**) and at 408 K $\alpha = 0.2$ (**b**), where O is the optical boundary, I is the interdiffusion zone, P is the phase boundary

zone is again in the single-phase region. This means that the epoxy oligomer does not form a continuous network of spatial bonds at this degree of curing (Fig. 25).

It should be noted that in the PEI–aER system up to a conversion degree of 0.3, the formation and dissolution of heterogeneous structures occur as a result of cyclic cooling and heating, while starting from $\alpha > 0.35$, a network of chemical bonds is formed in the aER, which prevents dissolution of thermoplastic in aER and promotes swelling of the adduct. Fundamental changes in the PEI–aER system occur for adducts with $\alpha > 0.3$. In this case, a phase boundary is formed, and the solubilities of PEI in aER and aER in PEI decrease sharply. Nevertheless, the composition distribution profiles in the interdiffusion zone are reproduced in the heating–cooling cycles. At $\alpha > 0.35$, a network of chemical bonds is formed in the ER adduct, which prevents the dissolution of thermoplastic macromolecules in the epoxy polymer. The sol fraction of the adduct continues to dissolve in PEI.

Note that the processes of interdiffusion in partially cured epoxy oligomers have a common character both with thermoplastics and linear oligomers, solvents, and plasticizers. Specificity is observed only in quantitative values of diffusion constants and compositions of coexisting phases.

Thus, in all of the systems studied, partial compatibility of the components occurs mainly due to the dissolution of the adduct fraction in the thermoplastic, while the solubility of the thermoplastic in aER is negligible. Note that this information is of fundamental importance when modifying epoxy oligomers with thermoplastics and thermoplastics with epoxy resins. An increase in the degree of conversion leads to an expansion of the heterogeneous region, mainly due to a decrease in the solubility of the adduct in the thermoplastic and a decrease in the sol fraction in the epoxy polymer composition.

We should add to the above that in the mixtures of epoxy oligomer adducts with thermoplastics, the movement of isoconcentration planes occurred by the diffusion mechanism in strict accordance with the law $X - t^{1/2}$ (Fig. 26).

Binodal curves of phase state diagrams of systems for adducts with different degrees of conversion of epoxy groups were plotted according to the compositions of coexisting phases (Figs. 27 and 28). It can be seen that all partially cured mixtures

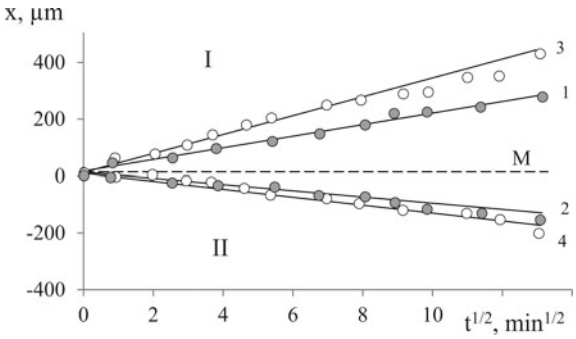

Fig. 26 Kinetics of motion of the PEI front in aER (I) and aER in PEI (II) α: −0.2 (1, 2), 0.1 (3, 4) in diffusion coordinates. The temperature of the experiments was 453 K

are characterized by amorphous stratification diagrams. The increase in solubility with increasing temperature allows them to be attributed to the class of systems with UCST. It was experimentally possible to fix UCST directly only in the PEI-aER system at conversion degrees 0.1 and 0.2.

As was shown earlier, as the degree of conversion; hence the molecular weight of the adduct increases, the mutual solubility of polymers deteriorates mainly due to a decrease in the solubility of aER in the thermoplastic. This fact is clearly illustrated by isothermal cross-sections of phase state diagrams. In this case, the two-phase state regions of polymer mixtures are within the zone bounded by solubility isotherms. Extrapolation of these dependences to $\alpha \rightarrow 1$ shows that the system disintegrates into coexisting phases with compositions close to the pure components when fully solidified (Fig. 29). The dome of solubility isotherms, to which the critical parameters correspond (critical concentration and degree of conversion and, consequently, molecular weight at a particular temperature) is constructed taking into account that the initial systems are either completely compatible, as in the case of PMMA

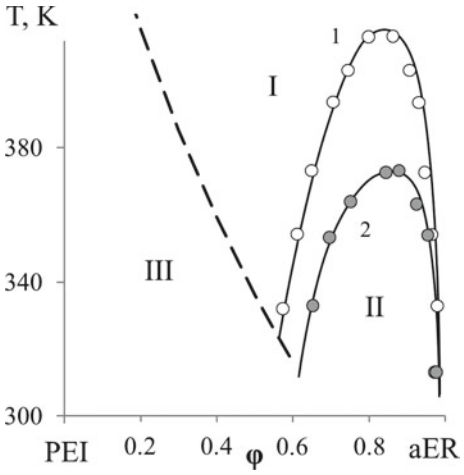

Fig. 27 Phase state diagrams of the PEI-aER system during curing of ED-20. (1, 2)—binodal curves at different stages of the curing reaction. Conversion degree: 1—0.1, 2—0.2, the dashed line shows glass transition temperature of PEI–aER mixtures. Areas in the diagram: I—homogeneous, II—heterogeneous, III—vitrified

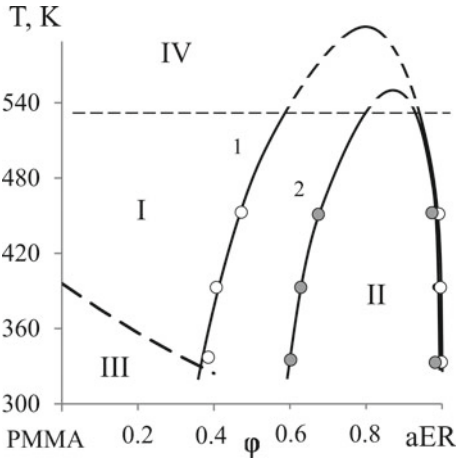

Fig. 28 Phase state diagrams of PMMA-aER system during curing of ED-20. (1, 2)—binodal curves at different stages of the curing reaction. Conversion degree: 1—0.2, 2—0.3, the temperature of glass transition of PMMA–aER mixtures is shown with a dashed line. Areas in the diagram: I—homogeneous, II—heterogeneous, III—vitrified, IV—zone of thermodegradation of components

mixtures, or partially compatible as in the mixture of PEI with initial ER, where already at 293 K phase boundary formation was observed.

Figures 30, 31 and 32 show the concentration dependences of the mutual diffusion coefficients for mixtures of PEI and PMMA with aER of various degrees of conversion. For comparison, the concentration dependences of diffusion coefficients corresponding to the systems with initial linear oligomers are plotted.

One can see that the general tendency of change of interdiffusion coefficients with composition in spatially cross-linked systems is similar to linear solutions of oligomers and thermoplastics. All concentration curves $D_v - \varphi$ are convex, and the

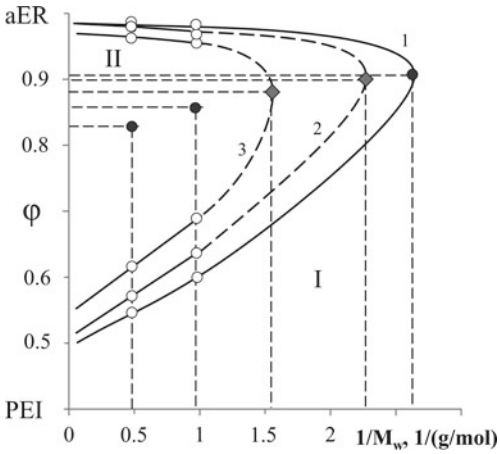

Fig. 29 Isothermal cross-sections of DPS of the system aER-PEI (dependence of the solubility of components in the system aER–PEI on the molecular weight of aER) at temperatures: 1—293, 2—313, and 3—353 K. Regions: I—homogeneous, II—heterogeneous. Gray rhombuses indicate the calculated critical points

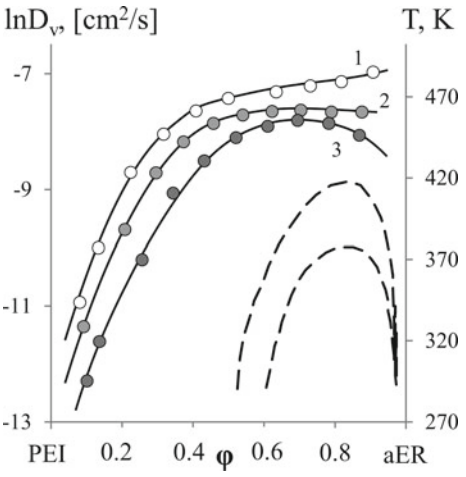

Fig. 30 Concentration dependences of interdiffusion coefficients (1–3) of the PEI–aER system at 453 K, where 1 corresponds to the initial ER, and 2 and 3 to ER adducts with $\alpha = 0.1$ and 0.2

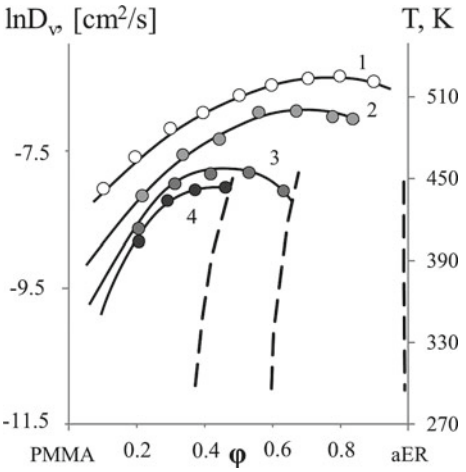

Fig. 31 Concentration dependences of interdiffusion coefficients (1–4) of the PMMA–aER system at 453 K, where 1 corresponds to the initial aER, and 2, 3, and 4 to the ER adducts with $\alpha = 0.1$, 0.2, and 0.3, respectively

values of interdiffusion coefficients change smoothly with a change in the composition of solutions. As the degree of conversion increases, the absolute values of interdiffusion coefficients in the region of true solutions of the diagram decrease. It is interesting to note that the transition from linear oligomers to spatially cross-linked adducts at $\alpha > 0.35$ is accompanied by a decrease in their translational diffusion coefficients by 4 decimal orders of magnitude, from 10^{-7} to 10^{-11} cm/s^2. As the temperature increases, the diffusion coefficients increase, and the range of solution compositions within which they can be determined expands.

A specific feature of this class of systems is the behavior of translational diffusion coefficients in the region of dilute thermoplastic solutions in adducts of epoxy oligomers. This peculiarity is related to the fact that in this temperature-concentration region, there are boundary curves, zones of two-phase state and labile solutions, and

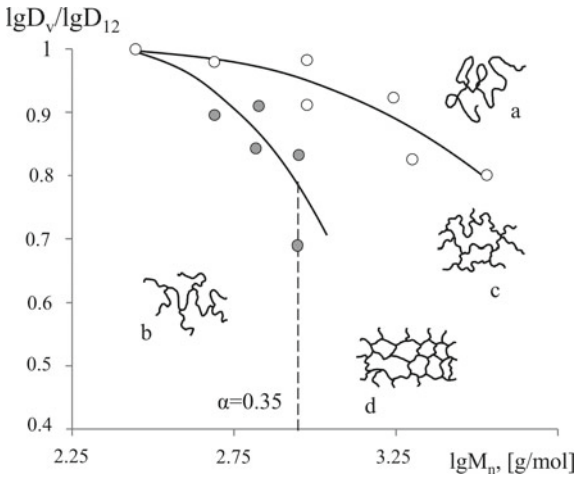

Fig. 32 Molecular weight dependences of reduced diffusion coefficients characterizing the rate of penetration of macromolecules of oligomers (1) and adducts (2) into the volume of thermoplastics, determined at 453 K. (Schematic representation of macromolecules is taken from [8], some additional points are taken from [15]). Structures: **a** flexible ball, **b** statistical long branches, **c** sparsely cross-linked, **d** densely cross-linked

domes of binodales. The appearance of heterogeneous temperature-concentration zones at certain degrees of conversion leads, for quite understandable reasons [35], to a break in the concentration dependences of interdiffusion coefficients and a decrease in their values in the region of compositions close to those of coexisting phases, in the region of the so-called Frenkel heterophase states.

Note that all of the diffusion coefficient dependences shown in Figs. 30 and 31 and concentration dependences contain very limited information about the limiting partial diffusion coefficients of thermoplastics in epoxy oligomers adducts (the right branch of the binodal curve is adjacent to the adduct axis).

At the end of this section, we tried to perform a comparative analysis of the translational diffusion coefficients of linear epoxy oligomers and their adducts. For this purpose, we used the dependences of the translational diffusion coefficients on the values of the molecular masses of the macromolecules of linear oligomers and their adducts (Fig. 32).

One can see that in the entire MW range, the diffusion coefficients of linear oligomers are higher than the translational diffusion coefficients of adducts. This effect is related, as it seems to us, to the branching of the adduct macromolecules. The nonlinearity of the dependences excludes any traditional analysis [2] in terms of conformational behavior of the pre-converted epoxy oligomer macromolecules during their diffusion in the volume of thermoplastics.

2.5 Conclusion

Thus, we can expect that in the thermoplastic solutions we studied, three stages of the process will be realized in the formation of the reactoplastic phase structure: first, the stage of evolution or "migration of the binodal curve," or rather the dome of the binodal curve, into the temperature-concentration region, where the figurative point of a given system is located; responsible for this stage is the kinetics of the increase in the molecular weight of the initial oligomer; secondly, the stage of solution macro-dissolution, formation, and growth of disperse phase particles of thermoplastic saturated with epoxy oligomer adducts; and finally, the stage of secondary phase decomposition occurs in the area of high degrees of transformation of the epoxy oligomer. At this stage, we should expect the formation of nanosized particles of dispersed phase distributed in the volume of thermoplastic macrophase and at their periphery in the matrix of the cured thermoplastic.

3 Phase Equilibrium and Structure Formation During Curing of Epoxy Compositions

Consideration of self-healing of epoxy curing materials should include the peculiarities of creating modern structural materials associated with the widespread use of a modification of thermoset resins with thermoplastic polymers. The phase structure created as a result of the formation of a spatial network of chemical bonds in the modified systems can not only determine the final performance characteristics but also influence the principles and processes of self-healing.

3.1 Introduction

A modern and, apparently, long-term trend in the creation of new structural polymeric materials is the use of mixed compositions based on thermoset resins modified with thermoplastics: polysulfone, polyethersulfone, polyetherimides, etc. [47–65]. The creation of new engineering plastics based on such polymer blends is of fundamental importance and determines the ways of development of structural polymeric materials with high mechanical and adhesive properties, thermal and electrical properties, chemical resistance, and good technological characteristics.

Now, it is impossible to consider blends only as a direction in polymer modification to expand the range of existing material grades and applications. In fact, polymer–polymer compositions form their own class of materials with diverse, sometimes specific properties and specific structural-morphological and phase organization, providing their wide application.

In order to obtain composite materials possessing a complex of required physical and mechanical characteristics, it is necessary to form a given phase structure. For the controlled course of the processes of "self-assembly of macromolecules" into micro- and macro-dimensional phase formations initiated by curing reactions of thermoset resins, information on phase equilibria, diffusion transfer coefficients, the evolution of boundary curves of phase diagrams at different stages of mesh structure formation becomes in demand [62–67].

The analysis of the technology of engineering structural materials in general and on the basis of thermo- and thermosetting plastics mixtures, in particular, showed that the synthesis of structural materials is multistage, and the stages are separated in space and time. Traditionally, there is a stage of binder preparation, i.e., mixing the components; a stage of prepreg formation, i.e., impregnation of the fiber filler with the binder; and, finally, a stage of binder curing in a given product. It is at this stage that the main chemical and phase transformations take place, and the required structural and morphological organization of the material as a whole is formed.

At first sight, it seems that each stage of synthesis technology is connected with different physical and chemical processes; so, mixing—with the kinetics of dissolution of polymer particles in the oligomer, impregnation—with the viscous flow of solution in the porous structure of fiber filler and its adsorption interaction with filler surface, curing—with the kinetics of the reaction of spatial grid formation in a binder and so on. However, from the fundamental point of view, the most important thing is the information about phase diagrams, translational diffusion coefficients, thermodynamic parameters of interaction of components at different stages of preparation, and chemical transformation of the reactive component. It is this information, as will be shown below, that allows one to quantitatively describe and predict all the structural-morphological transformations occurring with mixtures, solutions, and dispersions during the entire technological cycle of the preparation of structural materials based on thermo- and thermosetting plastics in a general form.

3.2 Phase Equilibria and Interdiffusion in the Epoxy Oligomers—Thermoplastics Systems

3.2.1 Dissolution Kinetics

Among the methods for studying the kinetics of polymer dissolution, the simplest informative method is the optical wedge or multi-beam microinterferometry [19, 65, 68]. This method is used to record the kinetics of changes in the distribution profile of the refractive index (concentration) spontaneously occurring in the interface zone of the oligomer and thermoplastic phases. Figure 33 shows typical interferograms of interdiffusion zones of homogeneous (Figs. 33a and 34a), two-phase amorphously stratified (Fig. 33b), and two-phase crystallizing mixtures (Fig. 34b). It can be seen that at temperatures above the critical and melting temperatures, the concentration

distribution profiles are determined in the entire range of compositions from one component to the other. At temperatures below the melting point of the thermoplastic (in this case, polyethylene glycol (PEG)), only a portion of the concentration profile corresponding to the dissolution of crystallites in the oligomer is observed (Fig. 34b). At temperatures below the upper critical solution temperature (UCST) in the diffusion zone, there is a phase interface separating oligomer solutions in thermoplastic from thermoplastic solutions in the oligomer. Concentrations corresponding to compositions of coexisting phases are established near the interface for systems with amorphous and crystalline equilibrium. Special thermokinetic studies of the concentration distribution in the diffusion zones have shown that the compositions of coexisting phases do not depend on the observation time and are quantitatively reproduced in the heating and cooling modes. This indicates the equilibrium and reversibility of the boundary concentrations measured in this way.

The character of the concentration profile shows that the movement of isoconcentration planes within the interdiffusion zones obeys the law $X(\varphi) - \sqrt{t}$, which indicates a diffusion mechanism of mixing epoxy oligomers (EO) with thermoplastics at all temperatures and regardless of the phase and physical state of polymers.

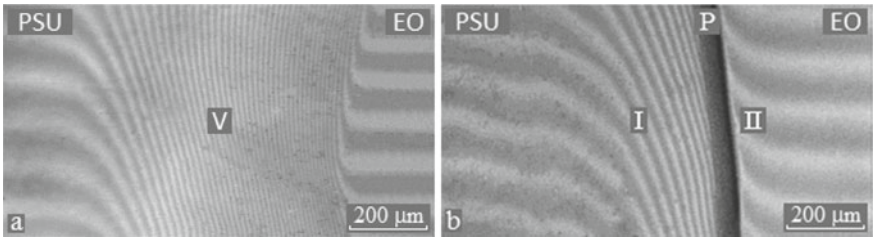

Fig. 33 Interferograms of interdiffusion zones of ED-20–PSU (**a**) and E44–PSU (**b**) systems at 220 °C. V—diffusion zone, P—phase boundary, I—diffusion zone of EO in PSU, II—diffusion zone of PSU in EO. Diffusion time 64 min. E44–EO with $M_n = 1.9$ kDa

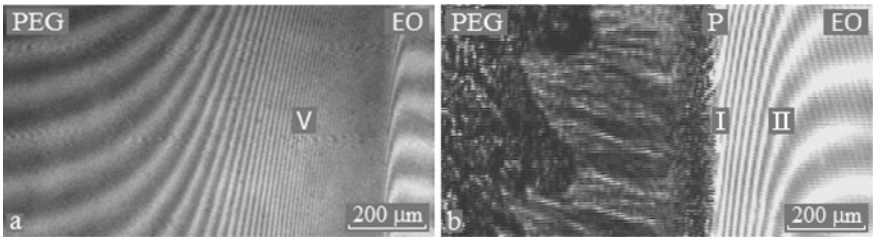

Fig. 34 Interferograms of interdiffusion zones of the E44–PEG systems at 120 (**a**) and 40 °C (**b**). M_n PEG = 10 kDa. The notations correspond to Fig. 33

Phase diagrams

Binodal curves and liquidus lines of phase diagrams for mixtures of thermoplastics with EO of different molecular weights were constructed using the temperature dependences of the compositions of coexisting phases. Using the methods for analyzing phase equilibria described in [69], generalized diagrams of the phase and physical states of the systems were constructed using fragments of the binodal curves (Fig. 35).

The influence of the molecular weight (MW) of epoxy oligomers on their compatibility with thermoplastics is most clearly demonstrated by isothermal cross-sections of phase diagrams (Fig. 36). In the coordinates $\varphi_i - 1/M_n$ (φ_i is the composition of the *i*th coexisting phase), the experimental points form two lines framing the two-phase state region of the systems and intersecting at the critical point. It is shown that

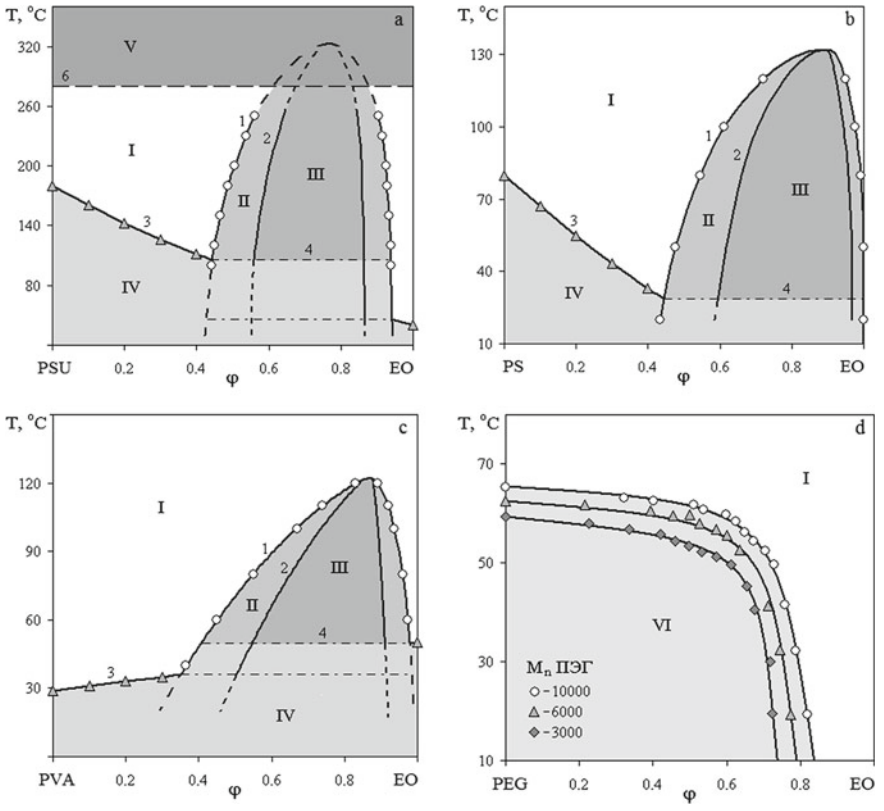

Fig. 35 Generalized phase diagrams of EO—thermoplastic systems: E44–PSU (**a**), ED-20–PS $M_{nPS} = 35$ kDa (**b**), E49–PVA (**c**), E44–PEG (**d**); 1—binodal curve, 2—spinodal curve, 3—change of glass transition temperature by Fox equation, 4—phase glass transition temperature, 5—liquidus. Areas: I—true solutions (solutions-melts), II—metastable states, III—labile solutions zone, IV—glassy state, V—thermal destruction, VI—crystalline state

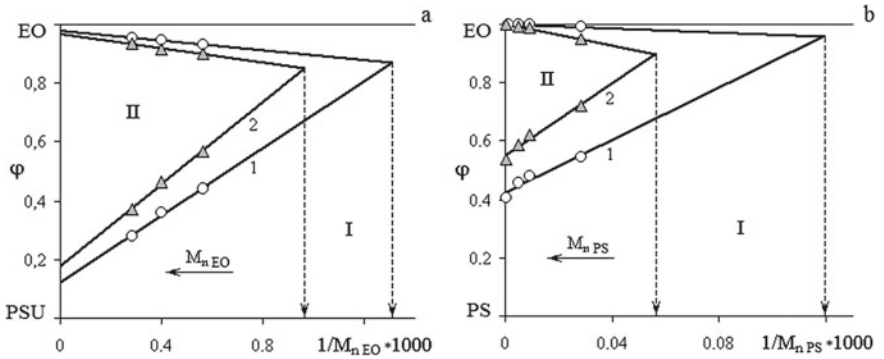

Fig. 36 Dependence of component solubility in the systems: E44–PSU on the molecular weight of EO at 1–100, 2–250 °C (**a**) and ED-20–PS on the molecular weight of PS at 1–80, 2–120 °C. The arrows indicate the molecular weights of loss of compatibility at these temperatures

this construction of the phase diagrams makes it possible to determine the critical composition of the mixture and the molecular weight of the oligomer and polymer.

As the MW of the components increases for all systems, the heterogeneous region expands. It is important that complete loss of solubility of thermoplastic in epoxy oligomer occurs earlier than oligomer in thermoplastic.

The position of the critical point of the phase diagrams with amorphous stratification we estimated using Alexeev's diameter. It was found that the critical concentration (φ_{cr}), as the molecular weight of EO or thermoplastic increases, shifts to the region of compositions enriched with a lower molecular component in full accordance with the equation

$$\varphi_{cr2} = \frac{\sqrt{r_1}}{\sqrt{r_1} + \sqrt{r_2}} \tag{10}$$

following from the classical Flory–Huggins-Scott theory of polymer solutions [47]. Here, r_i is the degree of polymerization of the ith component. It is shown that using experimentally found value φ_{cr} and having information about the molecular mass of one of the components, it is possible to solve the inverse problem—to estimate the value of the degree of polymerization and, consequently, the molecular weight of the second unknown component.

Based on the compositions of the coexisting phases, we calculated the paired parameters of the interaction of the components, the temperature dependences of which we used to calculate the critical temperatures (the calculation scheme is shown in Fig. 37). The critical value of χ was calculated using the equation

$$\varphi_{cr2} = \frac{1}{2}\left(\frac{1}{\sqrt{r_1}} + \frac{1}{\sqrt{r_2}}\right)^2. \tag{11}$$

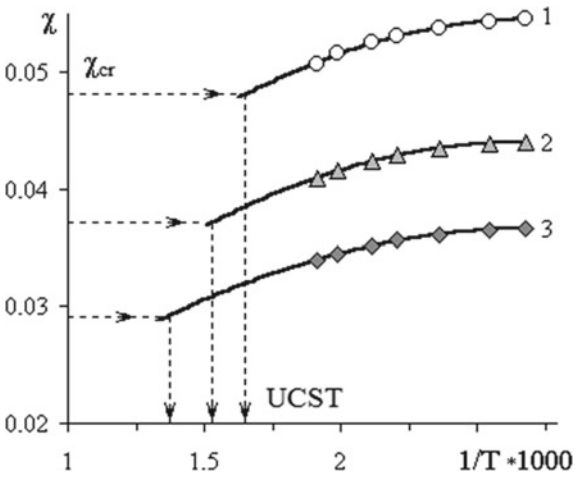

Fig. 37 Temperature dependences of the paired interaction parameter for the EO–PSU systems. EO: 1—1.9, 2—2.9, 3—5.1 kDa. The arrows show the UCST

We also used the values of χ extrapolated to high temperatures to construct a dome of phase diagrams in the region of upper critical solution temperatures (dotted curves in Fig. 35a).

It was found that the dependence of the critical temperature and the Flory–Huggins parameter on the molecular weights of the components for all the systems studied are linear.

3.2.2 Interdiffusion

The concentration dependences of interdiffusion coefficients (D_v) (Fig. 38) are determined by two parameters: the distance of figurative points of the systems from the critical temperature and the ratio of the molecular weights of the components. Figurative point is a point on the phase diagram corresponding to the investigated system of a certain composition at a certain temperature. Thus, at a temperature above UCST and the molecular weight of the oligomer is much less than the molecular weight of the thermoplastic, the change in the diffusion coefficient with a change in the composition occurs according to the curves with a maximum (Fig. 38a). Near the critical point, a minimum appears on the concentration dependences, the position of which coincides with the position of UCST (Fig. 38b). A further decrease in temperature (below the UCST) leads to the appearance of a break in the concentration dependence of interdiffusion coefficients. At these temperatures, a decrease in the coefficient is observed as the solution composition approaches the binodal curve (Fig. 38c). The reasons for such behavior of the diffusion coefficients are associated with a change in the chemical potential of the solutions as the figurative point of the system approaches the spinodal concentration.

An increase in MW of the components generally leads to a decrease in D_v, except for the EO–PS system, wherein the area of concentrated and moderately concentrated

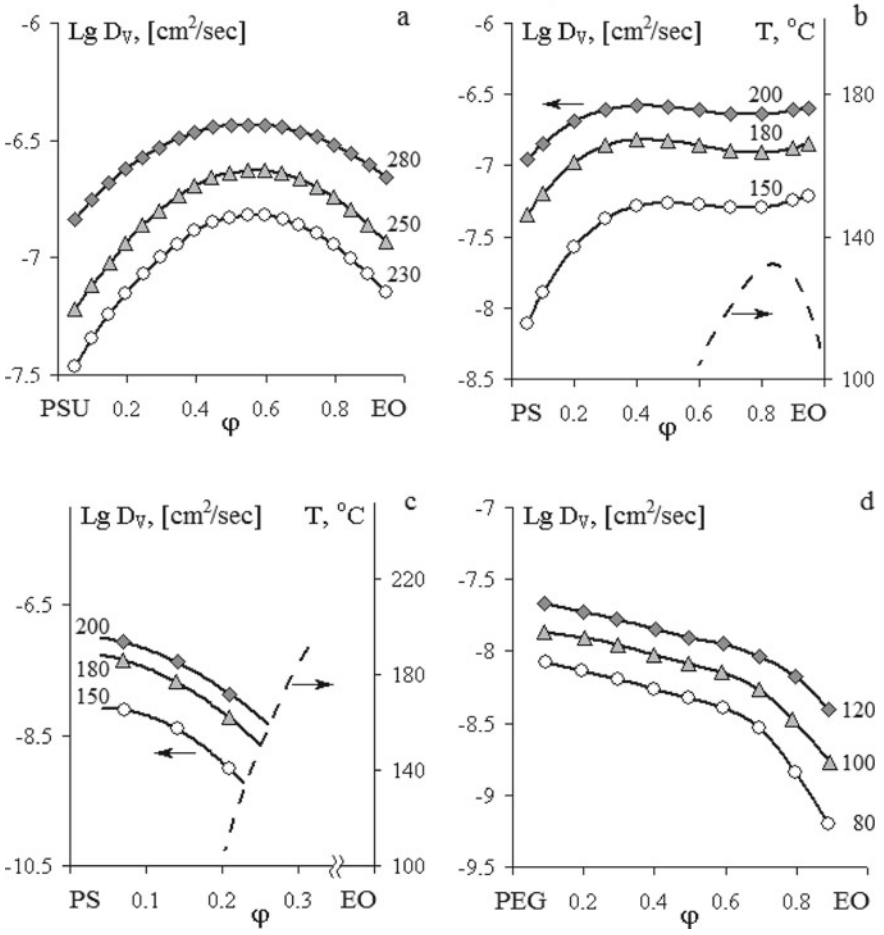

Fig. 38 Concentration dependences of interdiffusion coefficients for the systems: E40–PSU (**a**), ED-20–PS $M_{nPS} = 35$ kDa (**b**), E40–PS (**c**), E44–PEG $M_{nPEG} = 10$ kDa (**d**). Diffusion temperatures are indicated next to the corresponding curves. Dotted lines are binodal curves of phase diagrams. ED-20 (MW = 0.36 kDa), E40 (MW = 0.48 kDa)

solutions of polystyrene in the epoxy oligomer, the diffusion coefficients do not depend on MW of the high-molecular-weight component.

In the region of dilute and semi-dilute solutions, the translational mobility of dissolved polystyrene macromolecules in epoxy oligomer is described by the equation $D_v = D_0 M^{-b}$ with exponent $b = 0.5$, which indicates a small deviation of the system from Θ-conditions.

The increase in the molecular weight of polyglycols also leads to a decrease in the interdiffusion coefficient. In this case, on the dependence $\lg D_v - \lg M_n$, there is a kink, and the index of degree changes from 0.5 to 1, which indicates the formation

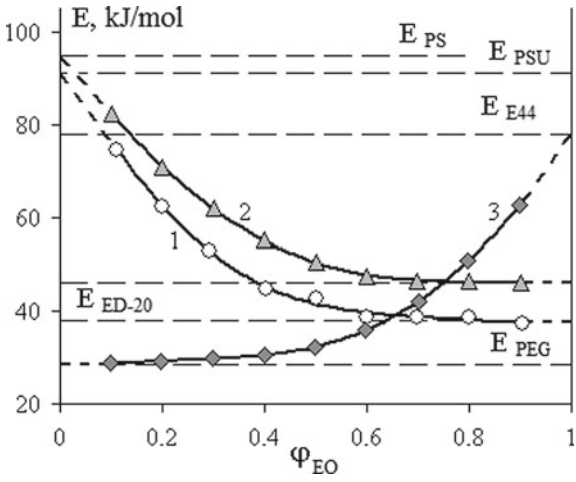

Fig. 39 Concentration dependences of apparent activation energies (E) of interdiffusion of the systems: ED-20–PSU, ED-20–PS, E44–PEG. Dotted line marks E of self-diffusion of individual components

of a mesh of meshes in the solution. For PEG, the molecular weight between the meshing nodes is ≈5000, which agrees with the literature data.

The temperature dependences of the coefficients of interdiffusion in the coordinates of the Arrhenius equation are linear throughout the temperature range studied. The exception is the system E44–PEG ($\varphi_{EO} \rightarrow 1$), for which a kink is observed at the temperature of the T_{ll}-transition. The concentration dependences of the apparent activation energies of interdiffusion (Fig. 39) are located between the activation energies of self-diffusion of the diffusion system components.

Thus, it has been established that all initial systems are characterized either by amorphous stratification diagrams with the UCST or by crystalline equilibrium. Generalized phase and physical diagrams have been constructed, which allow predicting a priori the structural-morphological and relaxation state of mixtures of any composition in a wide range of temperatures and molecular weights of the components. It is shown that the mechanism of mixing epoxy oligomers with thermoplastics is diffusive. Diffusion coefficients in the region of temperatures where operations of mixing of components and prepreg production are traditionally performed vary in the range of values from 10^{-7} to 10^{-8} cm^2 s^{-1}. Using these values of diffusion coefficients, it is also possible to estimate a priori the time of diffusion relaxation—the dissolution of the thermoplastic particle in the epoxy oligomer matrix.

Note that in [63, 65], the authors discuss the problem of the influence of mutual solubility of oligomers and polymers on the structure and phase state of the cured composition in sufficient detail. In the framework of the information described above, this problem is reduced to the determination of the position of the figurative point on the temperature-concentration field of the phase diagram.

3.3 Phase Equilibria and Interdiffusion in the Systems Thermoplastics—Epoxy Oligomers Adducts

This section summarizes the results of modeling studies in which an attempt was made to obtain information about the evolution of phase equilibria and translational mobility of components during the formation of spatially cross-linked structures in mixtures of thermoplastics with thermoset resins. A set of epoxy oligomer adducts (ad.EO, aEO) of different degrees of conversion (α) obtained in ED-20 curing reactions with diamine curing agent was used as one of the mixture components whose content in the reaction system was less than stoichiometric. In each case, the completeness of the amino-group conversion was identified by infrared spectroscopy. At present, this method of modeling curing reactions is generally accepted in the practice of polymer materials science.

3.3.1 Mixing Kinetics

During the transition from linear EO to their adducts in the interdiffusion zones, which spontaneously arise at the conjugation of thermoplastic and adduct phases and characterize the process of their dissolution (Fig. 40), one observes the same type of concentration-morphological changes. First, starting from a certain degree of precursor conversion, there appears a clearly identifiable phase boundary separating the areas of diffusion dissolution of the adduct in thermoplastic (I) and thermoplastic in partially cured EO (II). Second, it was found that before the formation of spatially cross-linked structures in adducts ($\alpha < \alpha_{gel}$, here α_{gel} is the degree of precursor transformation corresponding to gel formation), the phase interface is observed only in a limited temperature range. As a rule, for this adduct state, it degenerates when the critical solution temperature of the components is reached in the process of increasing temperature. After the formation of gel structures (gel) in EO adducts, however, the phase interface remains unchanged at all temperature and time conditions of the interdiffusion process up to the temperatures of epoxy polymer decomposition. Thus, by scanning the interdiffusion zone by temperature, the points of true gel formation in the matrices of EO adducts were determined. It was found that, within the error range, the gel varies in the range from 0.35 to 0.45 and depends little on the nature of the thermoplastic, i.e., it is a characteristic of the cured oligomer.

Thirdly, an increase in the degree of conversion of the adduct $\alpha > \alpha_{gel}$ leads to a decrease in solubility of both thermoplastic macromolecules in the cross-linked precursor phase and the sol fraction of ad.EO in the polymer matrix. At high conversion rates $\alpha > 0.7$, zone I degenerates. For such adducts in the interdiffusion zone, only the phase interface and the area of dissolution of thermoplastic macromolecules in the spatially cross-linked phase of the epoxy polymer are observed. Obviously, in this case, we can speak only about “one-side” diffusion or about the swelling of cross-linked EO in the thermoplastic melt.

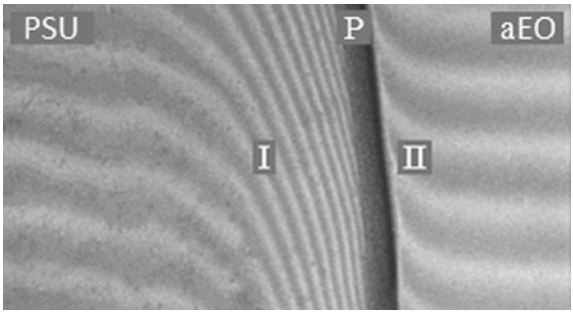

Fig. 40 Interferogram of the interdiffusion zones of the system aEO–PEG. Adduct conversion rate $\alpha = 0.65$, process temperature $T = 100$ °C, observation time 64 min. P—phase boundary, I—diffusion zone of aEO into thermoplastic, II—diffusion zone of thermoplastic into aEO. The curing agent is DETA

It has been noted that the described processes of interdiffusion in EO adducts are of a general character both for their mixtures with thermoplastics and solvents, plasticizers, and oligomers. The specificity of the systems is manifested only in quantitative parameters of the process: the size of interdiffusion zones, the rate of movement of isoconcentration planes, numerical values of compositions of coexisting phases, and the initial phase state of the mixture.

Of principal importance for all these systems is the fact that the compositions of coexisting phases, which are established near the interphase boundaries, and the isothermal kinetics of the movement of isoconcentration planes in the adduct and thermoplastic phases are quantitatively reproduced in the stepwise temperature increase and decrease modes. This allows us to speak, first, about the reversibility of the information obtained and, second, to use it to construct generalized phase equilibrium diagrams of the adduct-thermoplastic systems.

It should also be noted that in EO adducts, the sizes of interdiffusion zones change with time in strict accordance with the $X - \sqrt{t}$ law, i.e., the diffusion mechanism of mixing the polymers brought into contact is also realized in these systems at different degrees of curing.

3.3.2 Phase Diagrams

Binodal curves of amorphous separation diagrams for mixtures of ad.EO with PSU, PS, PVA, and amorphous-crystalline equilibrium diagrams for ad.EO–PEG mixtures, modeling the phase separation at different stages of the precursor crosslinking (Fig. 41a–d), were plotted using the compositions of coexisting phases. It can be seen that the solubility of ad.EO in thermoplastics, as well as in the initial linear systems, increases with increasing temperature, i.e., these systems also belong to the kind of systems with UCST. However, it is possible to directly register the UCST position only for adducts with a low degree of conversion, up to 0.25. At $\alpha > 0.3$,

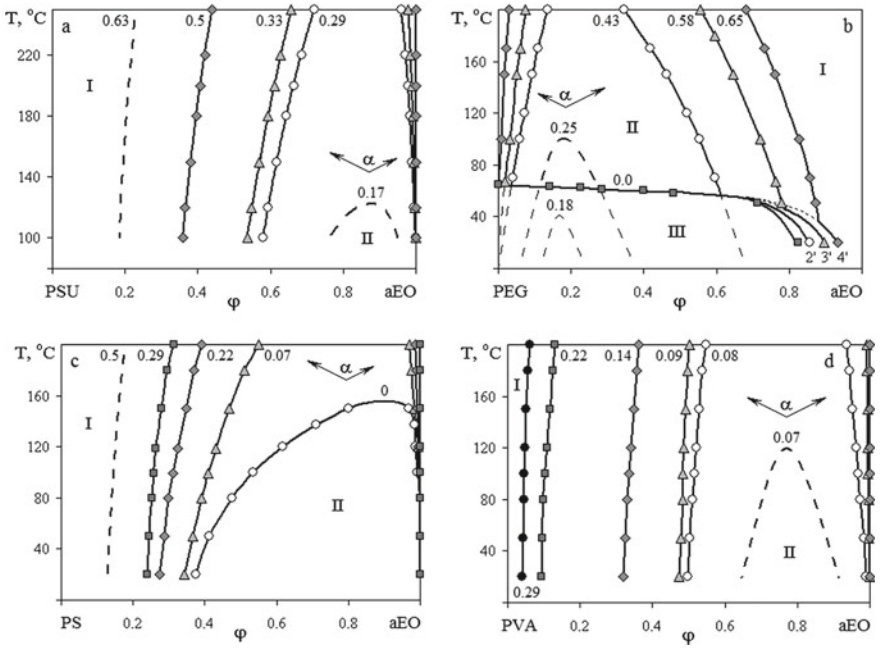

Fig. 41 Phase diagrams of aEO–PSF (**a**), aEO–PEG (**b**), aEO–PS (**c**), and aEO–PVA (**d**) systems. 1—liquidus lines, 2—binodal curves. The curing agent is DETA. Dotted line marks the calculated phase diagrams. Numbers in the curves correspond to the degree of conversion of the adduct. I and II—regions of true solutions and heterogeneous state, respectively. The arrows indicate the direction of the evolution of the phase diagram with increasing degree of conversion

the UCST of the systems appears in the region of thermodegradation of the epoxy component. It is interesting to note that the nature of the curing agent has little effect on the position of the binodal curves of the adherent-epoxy-thermoplastic systems.

As the degree of transformation of EO increases, the size of the heterogeneous state region in the amorphous stratification diagrams increases, and the mutual solubility of the components of the mixtures decreases. This is manifested to a greater extent at the position of the left branch of the binodal curve, corresponding to the solubility of ad.EO in thermoplastics. The solubility of homopolymers in ad.EO (the right branch of the binodal curve) changes to a much lesser extent.

Obviously, this fact should be taken into account when choosing the conditions of structure formation in these temperature-concentration regions of the phase diagrams.

The change in the mutual solubility of adducts in thermoplastics as a function of the conversion degree is most pronounced in the isothermal sections of the phase diagrams (Fig. 42). The dome of solubility isotherms (dotted lines), to which the critical system parameters (α_{cr}, φ_{cr}, UCST) correspond, is constructed taking into account the fact that the initial systems are either completely or partially compatible. It can be seen that the critical value of the degree of adduct transformation corresponding to the beginning of the phase separation of the solutions is significantly

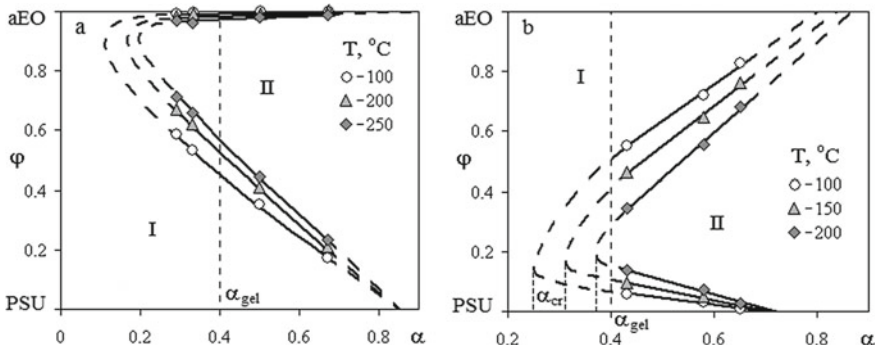

Fig. 42 Isothermal cross-sections of phase diagrams for systems of aEO with PSU (**a**) and PEG (**b**)

lower than the gelation degree. This means that the phase separation of the precursor and thermoplastic adduct solutions may begin before a continuous network of cross-links is formed in the precursor and curing agent phase. In fact, this is the specifics of the intermolecular interaction between epoxy oligomers and polymers.

Extrapolation of these dependencies to $\alpha \rightarrow 1$ shows that at the content of the curing agent in the compositions close to stoichiometric (at 100% degree of conversion of epoxy and amine groups), one should expect complete stratification of the system into coexisting phases whose composition is close to the cured epoxy polymer and thermoplastic.

The above data on the solubility diagrams of precursor adducts and linear thermoplastics can be used to estimate their average molecular weight. Using the method of critical compositions [see Eq. (10)] and numerical values of the parameters of the critical points of specific systems, the molecular weight of the adducts of epoxy oligomers was calculated (Fig. 43). One can see that as the degree of conversion increases, the effective molecular weight of ad.EO increases quite rapidly, reaching a value of ≈40 kDa during gelation. It is interesting to note that the numerical values of the effective molecular weight of ad.EO do not depend on the nature and molecular weight of the reference polymer, i.e., thermoplastic. The proposed technique makes it possible to obtain quantitative information on the molecular weight of adducts, which is so necessary for theoretical analysis of the evolution of phase equilibria in curing reactions.

The obtained fragments of phase diagrams of the systems ad.EO—thermoplastics can be used for predicting the UCST of cured epoxy polymers in the region of high temperatures, where the operation of engineering structural plastics is possible. For this purpose, it is possible to take advantage of the construction of temperature dependences of the dimensions of the sections connecting the intersection points of the isotherms with the binodal curves $\Delta\varphi(T)$ (corresponding to the distance between the compositions of coexisting phases) and their extrapolation to the zero value of $\Delta\varphi$ (Fig. 44). Figure 45 shows that the critical temperatures thus obtained change with changes in the degree of precursor transformation according to linear dependences,

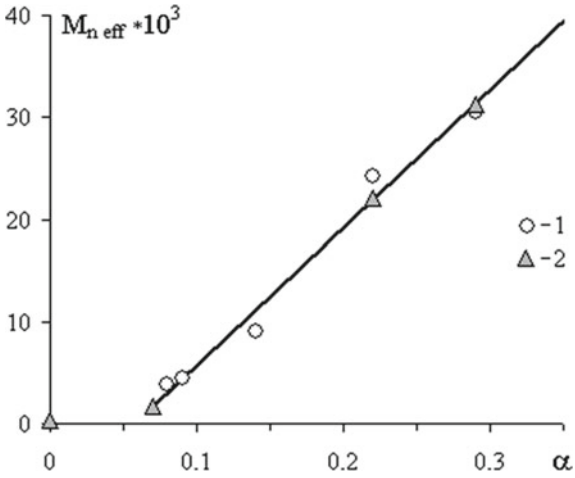

Fig. 43 Dependence of the effective molecular weight of the adducts on the degree of conversion. Systems: 1—aEO–PVA, 2—aEO–PS

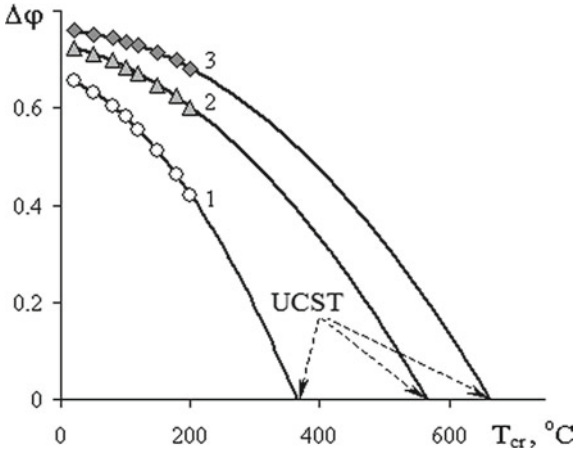

Fig. 44 Temperature dependence for aEO–PS systems: 1—0.07, 2—0.22 и 3—0.29

which can be extrapolated in the region of low and high degrees of curing, and low and high temperatures.

3.3.3 Interdiffusion

Since the area of compositions with high precursor content is of the greatest interest when modifying thermoset resins, particularly epoxy polymers, we focused our attention on determining the so-called limiting diffusion coefficients characterizing the translational mobility of dissolved thermoplastic macromolecules in a partially cured oligomer matrix (Fig. 46). One can see that as spatially cross-linked structures form in the epoxy oligomer matrix, homopolymer diffusion coefficients decrease. The

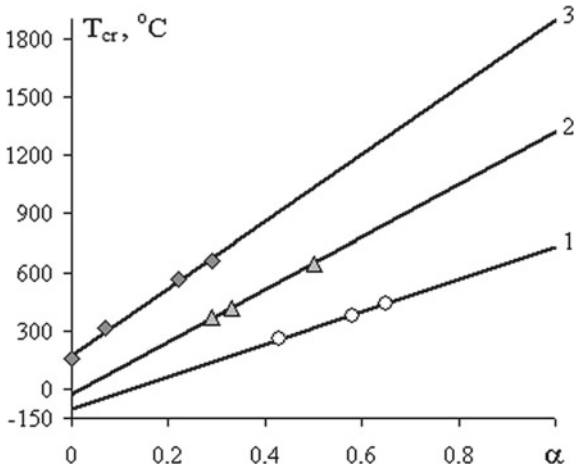

Fig. 45 Dependence of critical temperatures on the degree of conversion for mixtures of aEO with PEG (1), PSU (2), and PS (3)

most intense decrease of thermoplastics diffusion coefficients occurs in the region of gel formation in the epoxy oligomer matrix. For PS, PSU, and PVA macromolecules, diffusion coefficients reach values 10^{-11}–10^{-12} cm^2 s^{-1}, typical for translational mobility of macromolecules near the glass transition temperature [47].

Some difference in the dependences of thermoplastic diffusion coefficients on the degree of curing of the oligomer is related to the position of the figurative point of the system relative to the "expanding" binodal curve. According to the phase diagrams (Fig. 41), during the curing of the epoxy oligomer, the binodal curve gradually shifts toward the infinitely diluted thermoplastic solutions in the epoxy oligomer adduct, approaching the figurative point of the system located on the isoconcentration plane, by the movement of which we determined the diffusion coefficient value. This leads

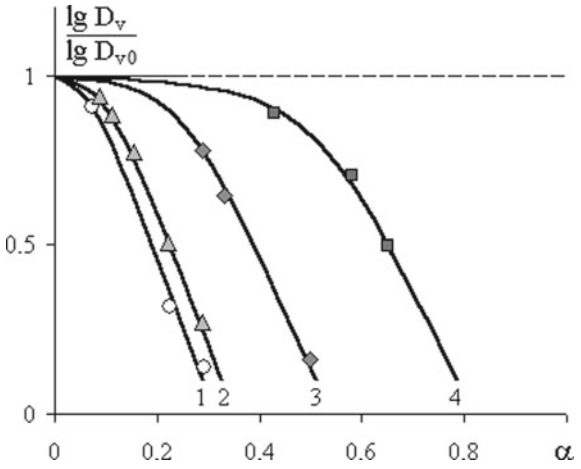

Fig. 46 Dependence of the relative thermoplastic diffusion coefficient into the EO adduct on the degree of conversion for aEO with PS (1), PVA (2), PSU (3), and PEG (4) systems

to an increase in the contribution of thermodynamic non-ideality of the solution and, as a consequence, to a drop in the diffusion coefficient.

Thus, it can be argued that the phase disintegration of EO solutions, curing agent, and linear polymers, initiated by the reactions of formation of the spatial bonding network in the epoxy oligomer matrix, in the growth and formation of thermoplastic disperse phase particles, will occur in conditions with continuously decreasing translation diffusion coefficient of macromolecules and continuously increasing oversaturation both in the particle volume and in the dispersion environment surrounding it.

3.4 Structure Formation During Curing of Mixtures of Epoxy Oligomers with Thermoplastics

In contrast to the previous chapters, which analyzed the phase and diffusion characteristics of blends of thermoplastics with epoxy oligomers and epoxy polymers whose chemical nature remained unchanged during the measurement process, this section presents the results of structural-morphological, optical, rheological, thermochemical, and phase studies of the same systems, but recorded during the formation of cross-linked structures in the epoxy oligomer matrix. In this section, we tried to answer the question of how widely the results of "static" measurements can be used in the transition to the kinetics of the structure formation process initiated by chemical reactions of the formation of spatial reticulated structures.

Despite the obvious importance of quantitative information on the phase equilibria of the initial systems and systems at different stages of their transformations, only fragments of phase diagrams (mainly in the region of the binodal curve dome) are found in the literature, and the proposed models of boundary curve evolution are based not on specific experimental data but are created by analogy with epoxy-rubber systems. Such models have been proposed mainly for systems with amorphous stratification, characterized either by UCST (Fig. 47a) or low critical solution temperature (LCST) (Fig. 47b) [65]. Obviously, in the form presented in Fig. 47, they allow us to speak only about the most general trends in changes in the phase state of the reaction mixture. It is impossible to obtain comprehensive information on the changes in the compositions and volumes of the coexisting phases, dispersity and nature of the inclusion particles and matrix phase, state of the interphase transition zones, and presence of macro- and microcomposite inhomogeneities in the system from the materials of such studies.

Below, by the example of two systems characterized by amorphous PSU–EO stratification and complex amorphous-crystalline PEG–EO equilibrium, the current state of this area of phase transformations of polymer systems is considered.

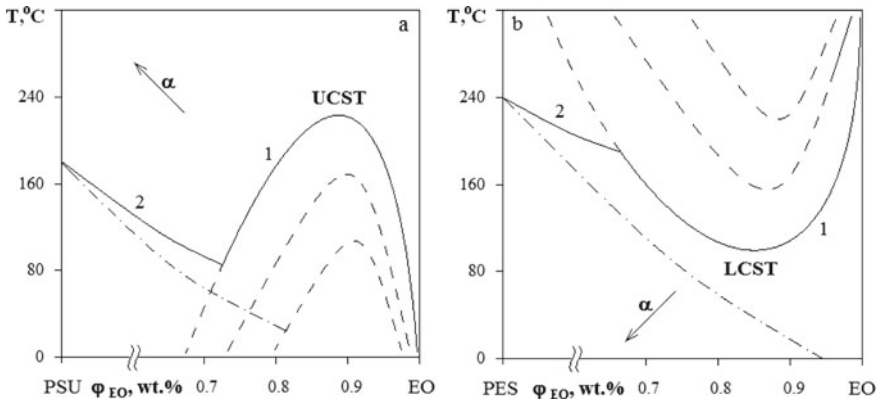

Fig. 47 Evolution models of the boundary curves of phase diagrams with UCST and LCST during curing of thermoset: 1 and dashed lines—model binodal curves, 2 and dotted lines—concentration dependences of glass transition temperature for mixtures of PSU and PES with adducts. The arrows indicate the directions of the shift of the binodal curves with an increasing degree of conversion [65]

3.4.1 General Remarks

The starting point for building a model of the structure formation process in our case is the information of the phase diagrams of the EO–PSU, ad.EO–PSU, PEG–EO, and PEG–ad.EO systems and the experimental fact of constancy of the selected mixture compositions and reaction temperature during the entire curing process.

As an example, Fig. 48 shows in the temperature-concentration field of the diagram the position of some figurative points of mixtures of EO with PSU, which further investigated the kinetics of structure formation during curing of ED-20. It can be seen that at the beginning of the process, the initial mixtures of all selected compositions (5, 10, and 15 wt.% PSU) are in the area of true solutions of the phase diagram. Estimates from the dependences of the critical temperatures on the degree of conversion (Fig. 45) showed that their distance from the UCST reaches ~200 °C.

When spatially cross-linked structures are formed in such solutions as a result of the interaction of functional groups of the oligomer and curing agent molecules, the thermodynamic compatibility of the components deteriorates [63], which manifests itself in the approach of the binodal curves to the figurative points of the mixtures (shown by arrows in Fig. 48). At the degree of transformation ~0.2, the dome of the binodal curve reaches and then crosses the process isotherm (160 °C). Thus, figurative points of given compositions appear under binodal curves in areas of labile and metastable states, which, naturally, leads PSF solutions in EO to stratification. The specific mechanism of delamination—spinodal or nucleation—depends on the ratio of the critical point composition to the given mixture composition.

Further growth of the mesh density in the epoxy oligomer matrix will be accompanied by a shift of the left branch of the binodal curve to the region of dilute solutions of EO reaction products in PSU and the right branch to the ordinate of the epoxy

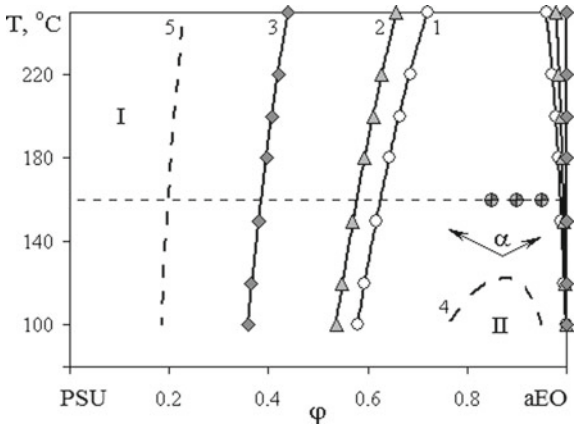

Fig. 48 Phase diagrams of ad.ED-20–PSU systems. α: 1—0.29; 2—0.33; 3—0.5; 4—0.17; 5—0.63. The curing agent is PEPA. Dotted line indicates the calculated phase diagrams. ⊕—figurative points of the systems under study. I and II are the regions of true solutions and heterogeneous state, respectively. The arrows indicate the directions of phase diagram evolution with increasing α

three-dimensional polymer. Obviously, the degree of supersaturation of such solutions with an increasing degree of oligomer conversion should increase, thus creating the necessary conditions for further (secondary) phase separation of mixtures. It is essential that these processes occur in the heterogeneous region of the phase diagram.

It can be assumed with a high degree of probability that after the system reaches the glass transition of the epoxy matrix, the chemical processes of formation of spatially cross-linked structures will slow down and, as a consequence, the phase separation rate will decrease.

The phase diagram (Fig. 48) also follows the trend of changes in the compositions of the coexisting phases of the matrix and dispersed inclusions, the proportion of the dispersed phase, which can be estimated by the lever rule. It is interesting to note that, since the right branch of the binodal curve shifts insignificantly with increasing degree of conversion, the main changes in the phase structure should be expected in changes in the composition of dispersed phases.

In contrast to the system considered above, mixtures of EO and PEG in the initial state are characterized only by crystalline equilibrium; more precisely, one can assume that the UCST for the solutions of these polymers is below the liquidus line. The situation is different for the adducts of epoxy oligomers. The formation of a network of chemical bonds leads to the fact that UCST is higher than T_m, and the phase diagram of such systems is characterized by a complex amorphous-crystalline equilibrium (Fig. 49). Obviously, this imposes a certain imprint on the patterns of phase transformations, which can proceed differently in different zones of the phase diagram. Thus, Fig. 49 shows that mixtures containing 15 wt.% PEG at all temperatures (20, 60, 80, and 120 °C) at the beginning of the process are in the region of true polymer melt solutions. After the beginning of the curing reaction, the binodal curve crosses the liquidus line, the region of the two-phase state of the mixtures

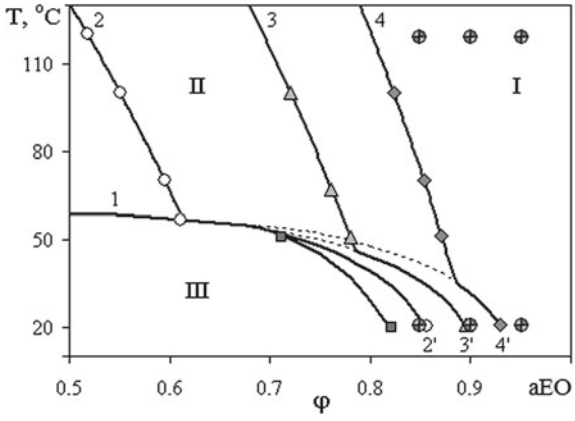

Fig. 49 Phase diagrams of the ad.ED-20–PEG systems. 1, 2', 3', 4'—liquidus lines. 2, 3, 4—binodal curves. The curing agent is DETA. α: 1—0; (2, 2')—0.43; (3, 3')—0.58; (4, 4')—0.65. ⊕–figurative points of the systems; I, II, III—regions of true solutions, amorphous stratification, and crystalline state, respectively

increases in size, and the right branch of the binodal curve gradually approaches the figurative point of the given mixture. Finally, it crosses it, which creates conditions for amorphous stratification of the system.

It is interesting to note that in the region of low temperatures (below the PEG melting point), one should expect a phase disintegration associated with the intersection of figurative points with the liquidus line, i.e., with the release of the PEG crystal phase also initiated by the chemical crosslinking reaction of linear oligomer molecules.

3.4.2 Kinetics of Structure Formation

The methods of photocolorimetry, viscosity, and DSC revealed that in all systems at different curing temperatures, the optical density of the mixtures changes according to S-curves (Figs. 50 and 51). Regardless of the phase nature of the disperse phase particles (particles of amorphous PSU or crystallites of PEG), the following is clearly identified: the induction period τ_{ind}, the stage of a rapid increase in turbidity (the phase separation of the solution itself), and the stage of the steady state of the system when the optical density of mixtures does not change.

The parameters of the kinetic curves are significantly influenced by the temperature and the thermoplastic content of the composition. As a rule, with increasing temperature and concentration of PSU and PEG, the duration of the induction period decreases.

The duration of the induction period can be considered as a characteristic kinetic parameter of the system since, during this time, such molecular-chemical changes occur in the solutions, which lead to a shift of the dome of the binodal curve to the area of the figurative points of the mixtures. Indeed, the temperature dependence of τ_{ind}, like any kinetic parameter, is described by the exponential dependence $\tau_{ind} = B\exp(E/RT)$, where B is a constant and E is the effective activation energy, reflecting the set of different phenomena associated with the beginning of the phase separation

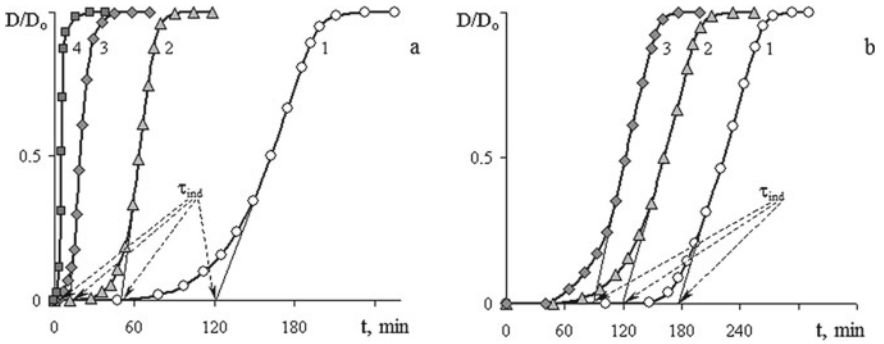

Fig. 50 Kinetic dependences of relative optical density of curing system EO-20–PSU with PSU = 10 wt.% and T_{cur}: 1—80, 2—100, 3—120, and 4—160 °C (**a**) and T_{cur} = 80 °C and PSU: 1—5, 2—10, and 3—15 wt.% (**b**)

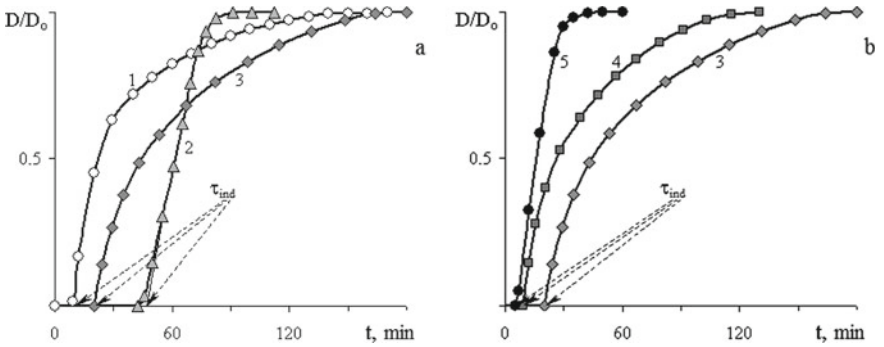

Fig. 51 Kinetic dependences of the relative optical density of the curing system ED-20–PEG with PEG = 15 wt.% and T_{cur}: 1—20, 2—40, 3—60, 4—80, and 5—120 °C. The curing agent is MFDA

of the mixture. The experimental points for all the systems studied in ln τ_{ind} − 1/T form a single straight line (Fig. 52), and the effective activation energy of the process calculated from these data of 48 kJ mol^{-1} (PSU), 42 kJ mol^{-1} (PEG), and 45 kJ mol^{-1} (PVA) is close to the activation energy of curing of MFDA epoxy oligomers, which according to various authors varies in the range from 45 to 62 kJ mol^{-1} [3]. These facts clearly indicate a single mechanism of structure formation in mixtures of epoxy polymer—thermoplastic, the limiting stage of which is the kinetics of change in the molecular weight characteristics of the epoxy oligomer during its curing.

Figures 53 and 54 compare kinetic curves of changes in the optical density of solutions, the relative viscosity of mixtures, and the degree of conversion calculated from DSC data. It can be seen that the course of the dependence $\eta/\eta_0(t)$, presented in the coordinates of the equation $\eta/\eta_0 = Rt^n$, is similar to that described for many other curing oligomeric compositions in the monograph [3]. The viscosity growth curve can be approximated by three linear sections with different values of *n*. Following

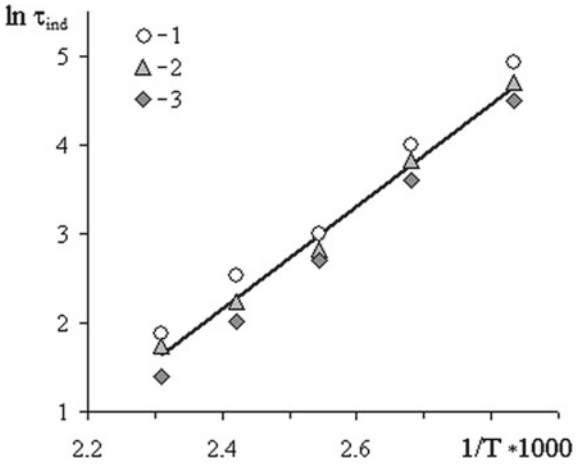

Fig. 52 Temperature dependence of the induction period time of phase separation of the EO-PSU system in the coordinates of the Arrhenius equation. PSU concentration: 1—5, 2—10, and 3—15 wt.%

the concept outlined in [3], it can be assumed that in the initial rather short section ($n \approx 0.5$), linear growth of the molecular weight of macromolecules prevails. At the second stage ($n \approx 3$), the process of formation of fragments of three-dimensional structures begins to play a major role, as a result of which the system rather quickly reaches the point of gel formation (t^*) (at $t > t^*$ $n \approx 10$).

Comparison of kinetic curves of changes in optical density, viscosity, and degree of conversion clearly shows that the phase disintegration of the EO–PSU system occurs already at the first stage of the process at $\alpha_{cr} < 0.15$. Gel formation occurs at $\alpha_{gel} \approx 0.4$, when the system is in the two-phase state. A change in the composition of the mixtures affects the length of the induction period. Thus, at the PSU content of more than 10% (corresponds to the critical composition of the system), the phase disintegration occurs already at the first stage of the process, whereas in mixtures with a small PSU content of ~5% ($\varphi < \varphi_{cr}$)—near the gelation point.

Thus, the onset time of phase separation, and hence the molecular-kinetic state of the system, is determined by the radius of curvature of the binodal curve dome, the critical composition, and the difference between the curing temperature and the critical temperature of the initial system. The difference in these temperatures determines the degree of conversion of the onset of phase separation. The higher this difference, the higher the influence of the chemical bonding network on the formation and growth of dispersed phase particles.

It is known that under isothermal conditions, the kinetics of mesh formation in EO can be satisfactorily described in the coordinates of the Avrami equation [70]

$$\frac{1}{1-X} = \exp\left(kt^n\right) \tag{12}$$

where X is the fraction of the substance transferred to the new phase during time t and k is the parameter that takes into account all temperature-dependent terms. It was shown that the Avrami degree index (n) in the EO—curing agent systems

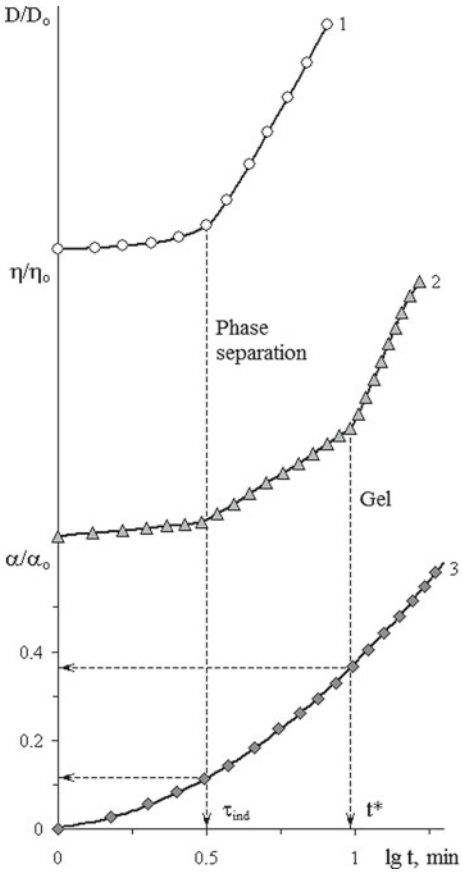

Fig. 53 Dependence of relative optical density (1), relative viscosity (2), and relative degree of conversion (3) on curing time for ED-20–PSU system with a concentration of PSU = 15 wt.% and T_{cur} = 120 °C. See details in the text

varies in the range from 0.95 to 2.0, depending on the nature of the reagents and reaction conditions [26]. The authors of these works attributed the obtained result to the nucleation of microgel structures in the oligomer during its curing, which formed a continuous network of transverse bonds in the final product.

An attempt was made to analyze the kinetics of curing epoxy oligomer in a mixture with thermoplastics according to DSC data and the kinetics of phase separation of the same systems according to changes in optical density (Figs. 55 and 56) in the framework of Avrami approach. It can be seen from the figures that the experimental points are satisfactorily described by Eq. (12).

It is interesting to note that the kinetic curves of changes in the degree of conversion are characterized by the Avrami degree indices close to $n = 1$ and are not sensitive to changes in temperature, mixture composition, or the type of phase separation of the system. This fact complements the results obtained above on the effective activation energies of the curing process calculated from the extent of the induction period of the optical density change curves. Now, it can be stated that the mechanism of the

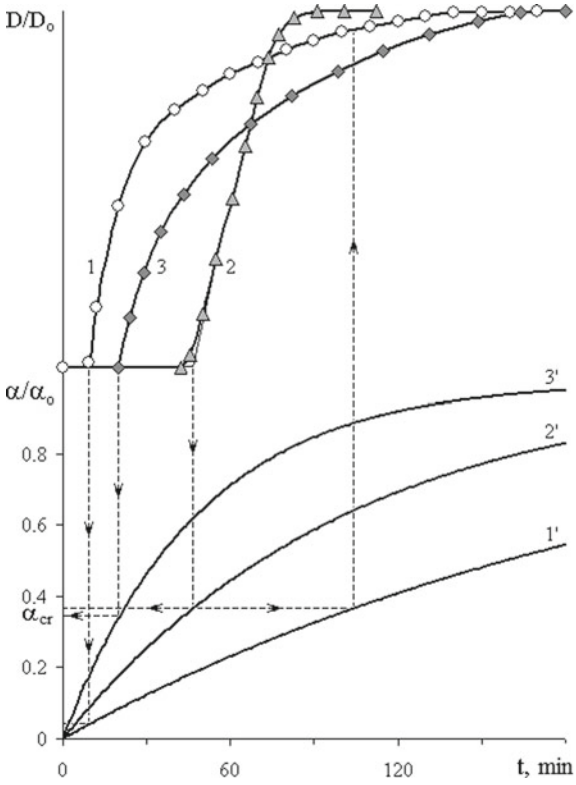

Fig. 54 Kinetic curves of changes in relative optical density (1–3) and relative degree of conversion (1'–3') for ED-20–PEG system. Concentration of PEG = 15 wt.%, T_{cur}: 1 and 1'—20, 2 and 2'—40, 3 and 3'—60 °C

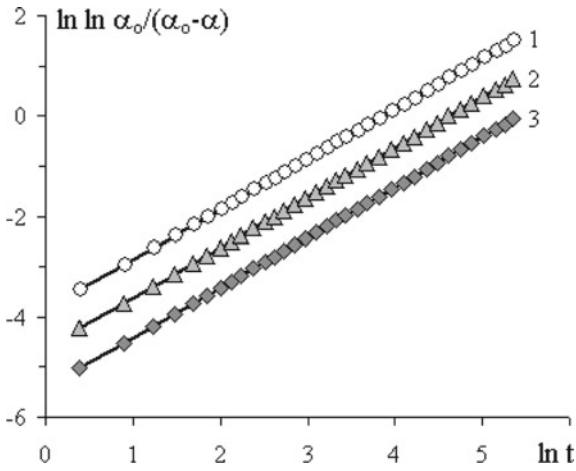

Fig. 55 Kinetics of change in the degree of conversion in the coordinates of the Avrami equation of the system ED-20–PEG. Concentration of PEG = 15 wt.%, T_{cur}: 60 (1), 40 (2), 20 °C (3)

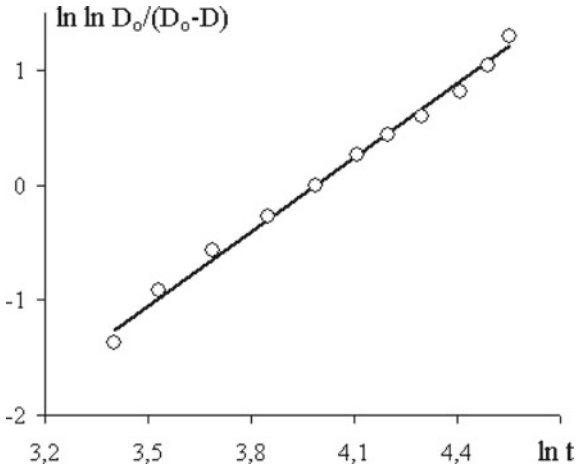

Fig. 56 Kinetics of changes in optical density in the coordinates of the Avrami equation of the system ED-20–PEG. Concentration of PEG = 15 wt.%, T_{cur} = 60 °C

chemical reaction of epoxy oligomer curing with amine curing agent does not change when transitioning to mixtures of EO with thermoplastics.

The Avrami degree indices for the phase separation curves obtained from optical density measurements vary from 1.7 to 5.8. The correlation coefficient reaches values of 0.96.

The kinetic curves of changes in optical density reflect the total process associated with both the formation of the chemical bond network and the formation of the dispersed structure of samples. Nevertheless, it can be argued that the kinetics of the structure formation process in mixtures of epoxy oligomers with thermoplastics can be quantitatively described within a unified approach accepted in the chemistry and physics of mesh polymers [26].

3.4.3 Structure of Cured Systems

Typical SEM images illustrating the structural and morphological organization of the cured epoxy polymer-thermoplastic systems are shown in Figs. 57 and 58.

It can be seen that all of them are characterized by a "matrix-inclusion" type structure. The specifics of each system are related to the size of the particles, their size distribution, the volume fraction of the dispersed phase, and the mutual arrangement of the particles of the dispersion medium.

At low thermoplastic content (less than 5 wt.%), practically for all compositions, uniform distribution of spherical polymer particles over the volume of cured epoxy polymer is observed (Fig. 57a). Particle distribution curves are unimodal; the average particle size varies in the range of 0.5–2 μm. According to X-ray microanalysis data for EO–PSU mixtures, the matrix consists mainly of epoxy polymer and inclusion—polysulfone.

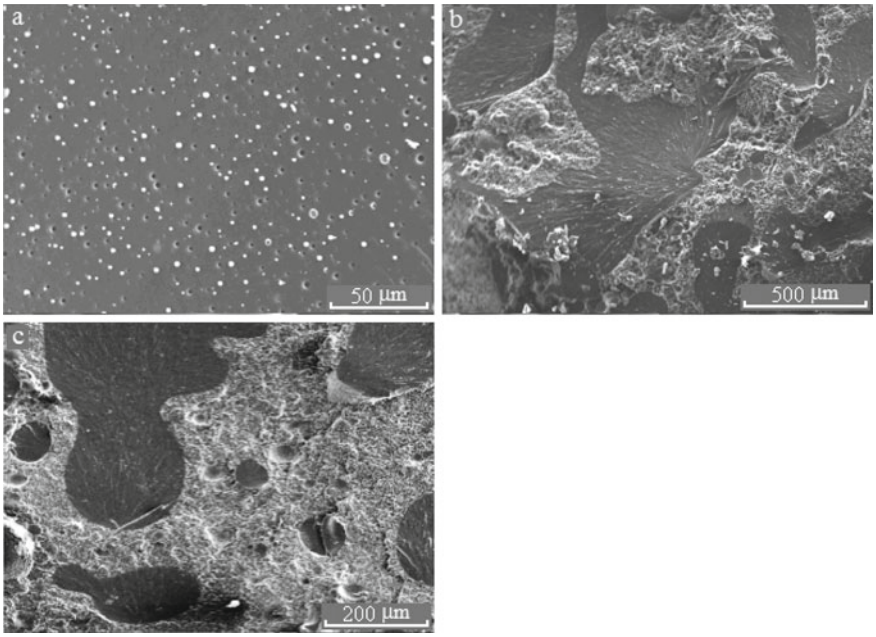

Fig. 57 Morphology of ED-20–PSU system. Chipping of the sample. Concentration of PSU: 5 (**a**), 10 (**b**), and 15 wt.% (**c**)

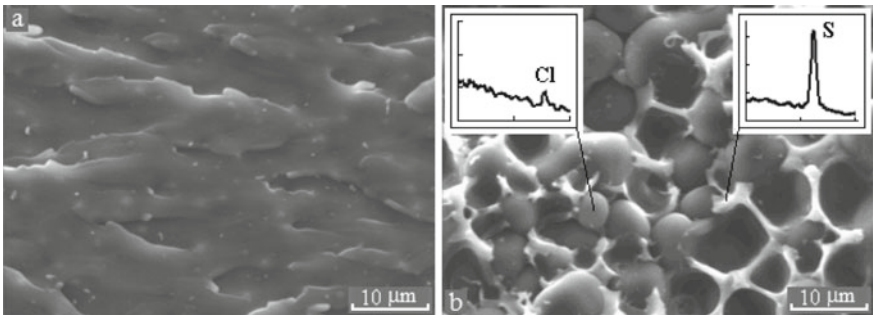

Fig. 58 Morphology of ED-20–PSU blend. Chipping of the sample. Concentration of PSU 10 wt.%. The insets show fragments of the spectra of the characteristic X-ray emission of the microphases

A fundamentally different structure is formed in compositions with a high content of thermoplastics. For example, in mixtures with PSF content of more than 10 wt.% (Fig. 57b) at low magnifications, it is clearly seen that the system is macro heterogeneous and, despite the relatively small thermoplastic content, is in the region of phase inversion. Elemental analysis of the cross-sectional chip surface of each macrophase showed that the "dark" phase (by secondary electron contrast) is depleted in PSU (6%), while the "light" phase is enriched in it (20%).

Under higher magnification, we can see that the "dark" macrophase (Fig. 58a) has a structure similar to that of the mixture shown in Fig. 57a. The "light" macrophase (Fig. 58b) contains the dispersed phase in the form of spherical particles. Local microanalysis showed that the spherical inclusions contained mostly epoxy polymer, while the dispersed medium was polysulfone (≈94%).

Such a complex multilevel structure of the mixture makes it possible to reconstruct the evolution of phase separation during the curing of the epoxy oligomer. For this purpose, information on the compositions of the coexisting phases for the macro- and microlevels was plotted on the phase diagram (Fig. 59). It can be seen that the phase containing 5 wt.% PSU is near the right branch of the binodal curve, where the continuous phase is the epoxy polymer, and the PSU-enriched phase is the inclusions. In contrast, the mixture containing more than 10 wt.% PSU is in the middle region of compositions, which coincides with the region of phase inversion. The presence of extended macro phases for this system indicates that their formation took place in conditions of low viscosity and high translational mobility of components (D_v 3×10^{-7} cm^2 s^{-1}), which determined a high rate of phase growth (estimated time of formation of particles with a radius of 50 μm in these conditions ~200 s), that is, this structure was formed at the early stages of phase separation. Indeed, the ratio of macrophase volumes calculated from microphotographs and determined from compositions of coexisting phases and figurative point of the system coincide (Figs. 60 and 61).

The phase diagrams (Figs. 48 and 59) show that the compositions of the coexisting phases on the isotherm change differently during curing. The right branch of the

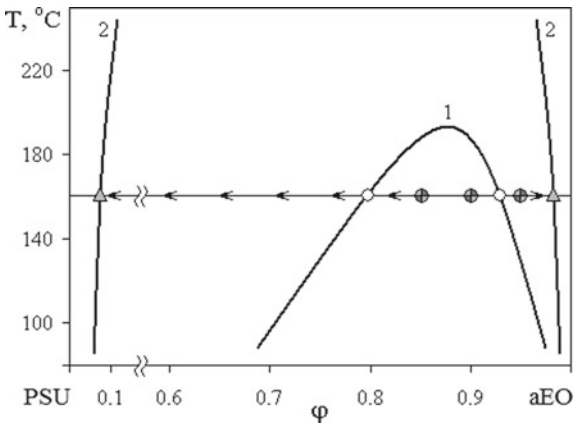

Fig. 59 Schematic of the phase separation of the EO–PSU system during curing. ⊕–figurative points of the initial systems (5, 10, and 15 wt.% PSU), ○—concentrations of coexisting phases in the initial stages of curing (at loss of mobility), △—concentrations of coexisting phases at the end of curing. 1—Suggested binodal curve of loss of mobility, 2—Binodal curve of epoxy polymer-PSU. The points were obtained by processing of morphological patterns, according to local X-ray microanalysis, and by shifting the glass transition temperature of phases enriched with PSU and epoxy polymer

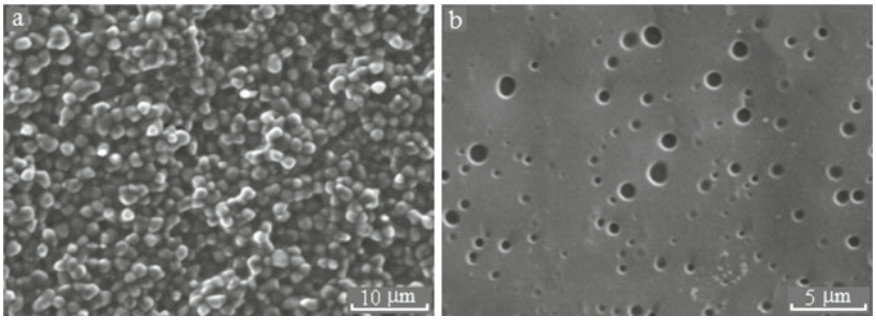

Fig. 60 Morphology of ED-20—PVA blend. Chipping of the sample. Concentration of PVA: 15 (**a**) and 5 wt.% (**b**), $T_{cur} = 30$ °C

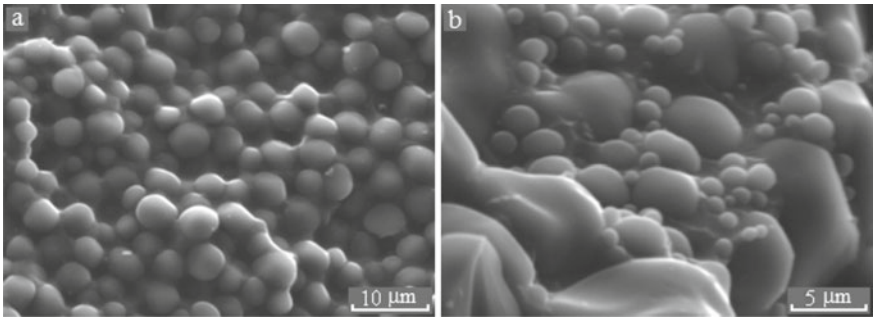

Fig. 61 Morphology of ED-20–PVA mixture. Chipping of the sample. Concentration of PVA: 15 wt.%, $T_{cur} = 60$ °C. **a**—in the volume, **b**—in the near-surface layers

binodal curve (solubility of PSU in the epoxy adduct matrix) changes little, while the left branch (solubility of EO adducts in the PSU matrix) changes significantly. This leads to the fact that in the macrophase formed in the initial stages of phase separation and enriched with PSU, supersaturation rapidly grows, which causes secondary phase separation.

This phase separation occurs at a relatively low translational mobility of macromolecules in the epoxy polymer network (D_v 10^{-9} cm^2 s^{-1}), which suppresses particle growth (the estimated time of particle formation with a radius of 5 μm under these conditions is ~1500 s) and leads to the formation of dispersed spherical microphase of small size (up to 1 μm), enriched in epoxy polymer with component concentrations close to the right branch of the binodal curve and dispersion medium enriched in PSU (94%).

Similar structures were obtained in the compositions with PVA and PEG. It was found that in mixtures with a small PVA content (less than 15%), structures characterized by a bimodal distribution of particle sizes were observed on the surface (Figs. 60 and 61). At that, small particle fractions (~0.2–2 μm), as a rule, are concentrated at the periphery of large ones (~30–40 μm). Specific features of this system

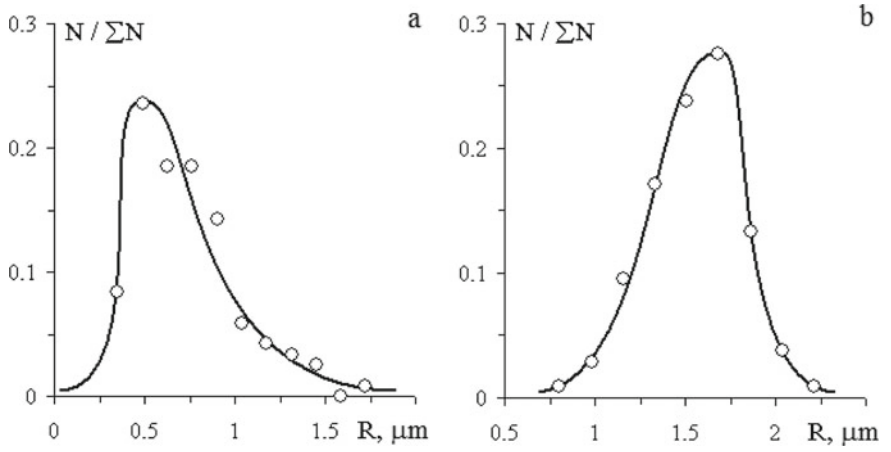

Fig. 62 Particle size distribution in the ED-20–PVA mixture cured at 30 °C. Concentration of PVA: 5 (**a**), 15 wt.% (**b**)

should include the fact of non-uniform distribution of the dispersed phase across the sample. As a rule, the surface layer is enriched with particles of the dispersed phase in comparison with the volume. As we approach the sample surface, structures with bimodal particle size distribution are more often found (Fig. 61b). All this allows us to assume that the formation of gradient structures (from the phase and concentration points of view) is associated with the processes of macro-dissociation of mixtures caused, probably, by "displacement" of thermoplastic by the network of chemical bonds forming in the matrix (Fig. 62).

The secondary phase separation is most clearly manifested in the EO–PEG system (Fig. 63). It can be seen that there are large phase formations of rounded shape in the matrix. Around these particles, there are concentrated microphase separations whose size is two decimal orders of magnitude smaller than the size of macroparticles. This bimodal particle size distribution (Fig. 64) is most often observed at low curing temperatures (below the PEG melting point).

In Fig. 63b, there is an interesting fragment of the secondary phase separation localized near the interfacial boundary of a large particle. The microparticles are located exactly along the perimeter of the macroparticle at some small distance from its surface. Along with that, there are observed particles of intermediate size, which are distant from the interphase boundary of the large particle. It can be concluded that the phase separation proceeds in several stages. Initially, large particles are formed, then at a greater distance from the smaller particles, and, finally, at large degrees of conversion, the smallest ones are formed.

Summarizing the experimental material on the phase behavior of mixtures of epoxy oligomers and polymers with thermoplastics obtained by us and described in the literature, we can unequivocally state that the mechanism of formation of heterogeneous structures is determined by the mutual positioning of critical points of solutions-melts of linear oligomers and their adducts with thermoplastics and

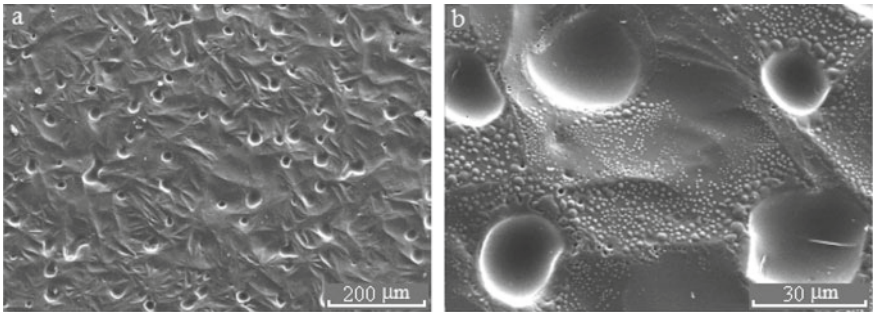

Fig. 63 Morphology of ED-20–PEG mixture. Surface of the sample. Concentration of PEG = 15 wt.%. $T_{cur} = 20$ °C

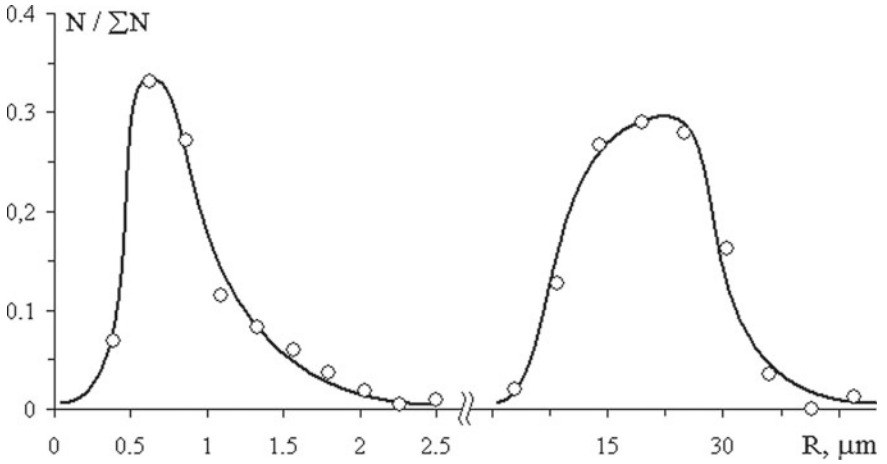

Fig. 64 Particle size distribution in the ED-20–PEG mixture cured at 20 °C. Concentration of PEG = 15 wt.%

figurative points of specific mixtures on the phase diagram field, on the one hand, and the value of translation diffusion coefficients of macromolecules of thermoplastics dissolved initially in epoxy.

It follows from the generalized phase diagrams that during the curing process, the UCST and binodal curves change their position so that the heterogeneous state region increases in size and the figurative points of specific mixtures fall into the two-phase state zone. At this stage of the structure formation process, phase separation and particle growth occur under conditions of high partial translational mobility of thermoplastic molecules. According to the formal theory of phase transformations, the growth rate of particles and the distance between them are determined by the diffusion coefficient and supersaturation in the middle of the distance coordinate

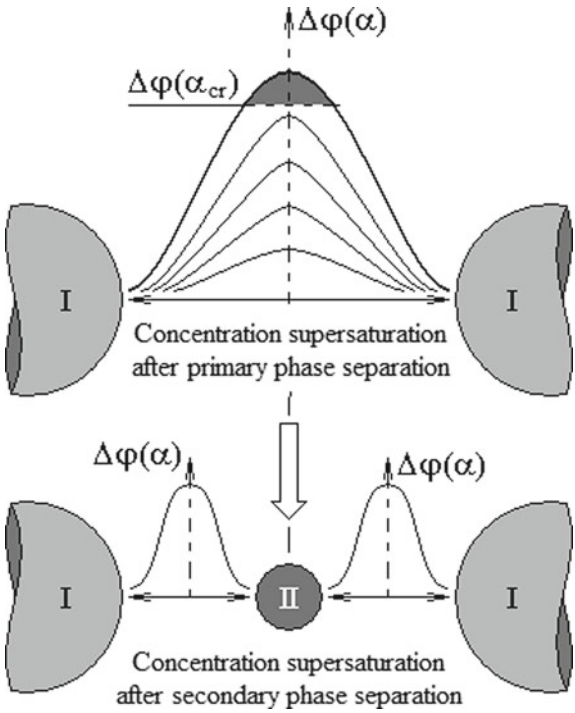

Fig. 65 Schematic of the secondary phase separation in the epoxy-thermoplastic mixture matrix and the concentration distribution profiles occurring at different curing stages. Double arrows indicate zones of diffusion outflow. I and II—dispersion particles formed during primary and secondary phase decomposition, respectively

(Fig. 65). The specificity of systems during the curing process is that both thermodynamic (compositions of coexisting phases) and kinetic (diffusion coefficients) parameters are continuously changing as a result of the formation of the chemical bonding network.

This leads to a gradual imbalance between the growth of concentration supersaturation at the periphery of the particles and the flow of thermoplastic macromolecules to the growing particle. In other words, the growth rate of supersaturation exceeds the diffusion rate of concentration flux to the particles of the dispersed phase.

At the same time, the balance between the growth of supersaturation with respect to the dissolved epoxy oligomer in the thermoplastic and the rate of its flow to the inner surface of the particle is also disturbed inside the particle. Thus, both in the dispersed phase and in the dispersion medium, conditions for secondary phase separation are created.

At this stage of phase separation, the formation of dispersed phase particles whose composition corresponds to the composition of coexisting phases on the phase diagrams is localized in one case in the matrix, but near the surface of the macroparticle, in the second case inside the macroparticle. Note that the secondary phase separation inside the particles, in contrast to the matrix, also depends on their sizes since the diffusion relaxation time is related to this parameter. It can be expected that under these conditions (inside the particles of dispersed phases), it will be realized

at large degrees of conversion when the diffusion coefficients reach extremely low values.

Thus, the proposed mechanism of phase decomposition of mixtures of reactive oligomers with thermoplastics qualitatively explains the whole set of experimental data obtained. Naturally, the specific parameters of the phase structure of the mixtures are determined by the specific numerical values of the diffusion coefficients, the UCST position, the activation energy, and the reaction constants of the formation of the mesh structures.

Acknowledgements Part of this work was supported by the Ministry of Science and Higher Education of the Russian Federation (project 122011300052-1), and another one was supported by Russian Foundation for Basic Research (project No. 20-03-00722).

References

1. Pascault, J.P., Williams, R.J.J.: Epoxy Polymers: New Materials and Innovations, p. 387, 1st edn. Wiley-VCH (2010). ISBN-13: 978-3527324804
2. Tsvetkov, V.N., Eskin, V.E., Frenkel, S.Ya.: Structure of Macromolecules in Solutions, p. 720. Nauka, Moscow (1964) (In Russian)
3. Malkin, A.Ya., Isayev, A.I.: Rheology. Concepts, methods and applications. Appl. Rheol. **16**(5), 240–241 (2006). https://doi.org/10.1515/arh-2006-0039
4. Ferry, J.D.: Viscoelastic Properties of Polymers, p. 499. John Wiley and Sons, Inc., New York (1961)
5. Nechitailo, L.G., Gerasimov, I.G., Batog, A.E., Zaitsev, Y.S.: Dependence epoxydiane oligomer viscosity on temperature and molecular mass. Ukr. Khim. Zh. **53**(9), 997–1000 (1988)
6. Gerasimov, I.G., Nechitailo, L.G., Batog, A.E., Zaitsev, Y.S.: Isothermal relaxation of viscosity of epoxydian oligomers. Ukr. Khim. Zh. **55**(10), 1093–1095 (1989)
7. Zhavoronok, E.S.: Reactive Rubber-Epoxy Compositions, p. 163. Ph.D. Thesis, Frumkin Institute of Physical Chemistry and Electrochemistry Russian Academy of Sciences (IPCE RAS), Moscow, Russia (2002)
8. Irzhak, V.I.: Architecture of Polymers, p. 368. Nauka, Moscow (2012). ISBN 978-5-02-038459-0 (In Russian)
9. Aleman, J.V.: Flow properties of epoxide prepolymers. J. Polym. Sci. Part A Polym. Chem. **18**(8), 2567–2575 (1980). https://doi.org/10.1002/pol.1980.170180815
10. Aleman, J.V.: Flow instabilities of epoxide prepolymers. Polym. Eng. Sci. **23**(4), 177–182 (1983). https://doi.org/10.1002/pen.760230402
11. Markevich, M.A., Rytov, B.L., Vladimirov, L.B., Shashkin, D.P., Shiryaev, P.A., Solovev, A.G.: Structural organization in epoxydiane oligomers and polymers. Vysokomol. Soedin. Ser. A **28**(8), 1595–1602 (1986)
12. Markevich, M.A.: Viscosity of epoxydiane oligomer solutions. Vysokomolekulyarnye Soedineniya Seriya B. **27**(11), 838–842 (1985)
13. Ghijsels, A., Groesbeek, N., Raadsen, J.: Temperature-dependence of the zero-shear melt viscosity of oligomeric epoxy-resins. Polymer **25**(4), 463–466 (1984). https://doi.org/10.1016/0032-3861(84)90203-9
14. Venediktov, E.A., Rozhkova, E.P.: Kinetic relationships of metal filling of epoxy resin by in situ reduction of silver nitrate. Russ. J. Appl. Chem. **86**(6), 928–932 (2013). https://doi.org/10.1134/S1070427213060244

15. Budylin, N.Yu.: Phase Equilibria and Interdiffusion in Reactoplastics—Thermoplastics Systems, p. 180. Ph.D. Thesis, Frumkin Institute of Physical Chemistry and Electrochemistry Russian Academy of Sciences (IPCE RAS), Moscow, Russia (2014)
16. Kochnova, Z.A., Zhavoronok, E.S., Chalykh, A.E.: Epoxy Resins and Hardeners: Industrial Products, p. 200. OOO "Paint-Media", Moscow (2006). ISBN 5-902904-03-X (In Russian)
17. Lantsov, V.M., Pakter, M.K., Irzhak, V.I., Abdrakhmanova, L.A., Abramova, Y.I., Zakirov, I.N., Vasilev, G.I., Paramonov, Y.N., Zaitsev, Y.S.: Kinetic Heterogeneity of epoxide oligomers. Vysokomol. Soedin. Ser. A **29**(11), 2297–2301 (1987)
18. Maklakov, A.I., Skirda, V.D., Fatkulin, N.F.: Self-diffusion in solutions and melts of polymers, p. 222. Publishing House of Kazan State University, Kazan (1987) (In Russian)
19. Chalykh, A.E., Zagaitov, A.L., Korotchenko, D.P.: Optical Diffusiometer, p. 34. IFKh RAN: Moscow, Russia (1996) (In Russian)
20. Malkin, A., Ascadsky, A., Kovriga, V., Chalykh, A.E.: Experimental Methods of Polymer Physics, vol. 520. MIR: Moscow, Russia (1983)
21. Zakirov, I.N., Irzhak, V.I., Lantsov, V.M., Rozenberg, B.A.: On the nature of large-scale mobility in dense network epoxide polymers. Vysokomol. Soedin. Ser. A **30**(5), 915–921 (1988)
22. Koike, T.: Melt viscosity at glass-transition temperature for some epoxide oligomers. J. Appl. Polym. Sci. **56**(9), 1183–1186 (1995). https://doi.org/10.1002/app.1995.070560919
23. Lantsov, V.M., Pakter, M.K., Abdrakhmanova, L.A., Zakirov, I.N., Paramonov, Y.M., Zaitsev, Y.S.: Study of molecular mobility of epoxy-amine polymers by the impulse NMR method. Vysokomol. Soedin., Ser. A **28**(5), 1047–1051 (1986)
24. Irzhak, V.I., Mezhikovskii, S.M.: Structural aspects of polymer network formation upon curing of oligomer systems. Russ. Chem. Rev. **78**(2), 165–194 (2009). https://doi.org/10.1070/RC2009v078n02ABEH003896
25. Lu, M., Kim, S.: Kinetics and thermal characterization of epoxy-amine systems. J. Appl. Polym. Sci. **71**(14), 2401–2408 (1999). https://doi.org/10.1002/(SICI)1097-4628(19990404)71:14%3c2401::AID-APP12%3e3.0.CO;2-C
26. Khozin, V.G.: Reinforcing Epoxy Resins, p. 446. House of Press, Kazan (2004). ISBN 5-94259-143-1 (In Russian)
27. Askadskii, A.A., Bartenev, G.M., Belyakov, A.P., Pastukhov, A.V.: Various forms of molecular mobility and relaxation transitions in epoxydian polymer. Vysokomolekulyarnye Soedineniya Seriya B. **30**(11), 868–873 (1998). (In Russian)
28. Chalykh, A.E., Zhavoronok, E.S., Kolesnikova, E.F., Kostina, Y.V., Bondarenko, G.N.: Kinetics of curing of diane and aliphatic epoxy oligomer blends: IR-spectroscopy study. Polym. Sci. Ser. B **53**(7–8), 466–475 (2011). https://doi.org/10.1134/S156009041108001X
29. Shmaliy, O.N., Diffusion in Epoxy Oligomers, p. 144. Ph.D. Thesis, Institute of Physical Chemistry Russian Academy of Sciences (IPC RAS), Moscow, Russia (1995)
30. Bartenev, G.M., Shut, N.I., Danilenko, G.D., Askadskii, A.A., Pastukhov, V.V.: Relaxation properties of a linear epoxy polymer. Vysokomolekulyarnye Soedineniya Seriya A Seriya B. **35**(9), A1498–A1506 (1993)
31. Skirda, V.D., Sevriugin, V.A., Maklakov, A.I.: Peculiarities of translational mobility of macromolecules in melts and solutions of polymers. Dokl. Akad. Nauk SSSR **269**(3), 638–640 (1983)
32. Tanner, J.E., Liu, K.J., Anderson, J.E.: Proton magnetic resonance self-diffusion studies of poly(ethylene oxide) and polydimethylsiloxane solution. Macromolecules **4**(5), 586–588 (1971). https://doi.org/10.1021/ma60023a014
33. Kumagai, J., Watanabe, H., Miyasaka, K., Hata, T.: Diffusion measurement of tritium labeled polystyrene in polymer bulk—effect of molecular-weight on diffusion-coefficient. J. Chem. Eng. Jpn. **12**(1), 1–4 (1979). https://doi.org/10.1252/jcej.12.1
34. de Gennes, P.-G.: Scaling Concepts in Polymer Physics, p. 324. Cornell University Press, London (1979)
35. Chalykh, A.E.: Diffusion in Polymer Systems, p. 312. Chemistry Publishing House, Moscow, Russia (1987) (In Russian)

36. Paolillo, S., Bose, R.K., Santana, M.H., Grande, A.M.: Intrinsic self-healing epoxies in polymer matrix composites (PMCs) for aerospace applications. Polymers **13**, 201 (2021). https://doi.org/10.3390/polym13020201
37. Peterson, A.M., Jensen, R.E., Palmese, G.R.: Room-temperature healing of a thermosetting polymer using the Diels-Alder reaction. Appl. Mater. Interf. **2**(4), 1141–1149 (2010). https://doi.org/10.1021/am9009378
38. Bai, N., Saito, K., Simon, G.P.: Synthesis of a diamine cross-linker containing Diels-Alder adducts to produce self-healing thermosetting epoxy polymer from a Widely used epoxy monomer. Polym. Chem. **4**, 724–730 (2013). https://doi.org/10.1039/c2py20611k
39. Billiet, S., Camp, V.W., Hillewaere, X., Rahier, H., Du Prez, F.E.: Development of optimized autonomous self-healing systems for epoxy materials based on maleimide chemistry. Polymer **53**(12), 2320–2326 (2012). https://doi.org/10.1016/j.polymer.2012.03.061
40. Wang, S., Urban, M.W.: Self-healing polymers. Nature Rev. Mater. **5**, 562–583 (2020). https://doi.org/10.1038/s41578-020-0202-4
41. Toohey, K.S., Hansen, C.J., Lewis, J.A., White, S.R., Sottos, N.R.: Delivery of two-part self-healing chemistry via microvascular networks. Adv. Func. Mat. **19**, 1399–1405 (2009). https://doi.org/10.1002/adfm.200801824
42. McIlroy, D.A., Blaiszik, B.J., Caruso, M.M., White, S.R., Moore, J.S., Sottos, N.R.: Microencapsulation of a reactive liquid-phase amine for self-healing epoxy composites. Macromolecules **43**, 1855–1859 (2010). https://doi.org/10.1021/ma902251n
43. Reddy, K.R., El-Zein, A., Airey, D.W., Alonso-Marroquin, F., Schubel, P., Manalo, A.: Self-healing polymers: synthesis methods and applications. Nano-Struct. Nano-Obj. **23** (2020). https://doi.org/10.1016/j.nanoso.2020.100500
44. Zhao, Y.H., Vuluga, D., Lecamp, L., Burel, F.: Photoinitiated thiol–epoxy addition for the preparation of photoinduced self-healing fatty coatings. RSC Adv. **6**, 32098–32105 (2016). https://doi.org/10.1039/c6ra03693g
45. Bellamy, L.: The Infra-red Spectra of Complex Molecules, p. 433. Springer, Dordrecht (1975). ISBN 978-0-412-13850-8
46. Nielsen, L.E.: Mechanical Properties of Polymers and Composites, vol. 2, p. 556. Marcel Dekker (1974). ISBN 978-0-8247-6208-7
47. D.R. Paul, C.B. Bucknall, Polymer Blends. John Wiley & Sons, Inc.: Hoboken, NJ, USA (2000)
48. Farooq, U., Teuwen, J., Dransfeld, C.: Toughening of epoxy systems with interpenetrating polymer network (IPN): a review. Polymers **12** (2020). https://doi.org/10.3390/polym12091908
49. Korokhin, R.A., Solodilov, V.I., Zvereva, U.G., Solomatin, D.V., Gorbatkina, Y.A., Shapagin, A.V., Lebedeva, O.V., Bamborin, M.Y.: Epoxy polymers modified with polyetherimide. Part II: Physicomechanical properties of modified epoxy oligomers and carbon fiber reinforced plastics based on them. Polym. Bull. **77**, 2039–2057 (2020). https://doi.org/10.1007/s00289-019-02841-9
50. Kishi, H., Tanaka, S., Nakashima, Y., Saruwatari, T.: Self-assembled three-dimensional structure of epoxy/polyethersulphone/silver adhesives with electrical conductivity. Polymer **82**, 93–99 (2016). https://doi.org/10.1016/j.polymer.2015.11.043
51. Chen, Z.G., Luo, J., Huang, Z., Cai, C.Q., Tusiime, R., Li, Z.Y., Wang, H.X., Cheng, C., Liu, Y., Sun Z.Y., et al.: Synergistic toughen epoxy resin by incorporation of polyetherimide and amino groups grafted MWCNTs. Compos. Commun. **21** (2020). https://doi.org/10.1016/j.coco.2020.100377
52. Tretyakov, I.V., Vyatkina, M.A., Cherevinskiy, A.P., Solodilov, V.I., Shapagin, A.V., Korokhin, R.A., Budylin, N.Y., Kireinov, A.V., Gorbatkina, Y.A.: Effect of polyethersulfone on the properties of epoxy resin and wound unidirectional glass fiber reinforced plastics based on it. Bull. Russ. Acad. Sci. Phys. **85**, 876–880 (2021). https://doi.org/10.3103/s1062873821080293
53. Sun, Z.Y., Xu, L., Chen, Z.G., Wang, Y.H., Tusiime, R., Cheng, C., Zhou, S., Liu, Y., Yu, M.H., Zhang, H.: Enhancing the mechanical and thermal properties of epoxy Resin via blending with thermoplastic polysulfone. Polymers **11** (2019). https://doi.org/10.3390/polym11030461

54. Korokhin, R.A., Solodilov, V.I., Gorbatkina, Y.A., Shapagin, A.V.: Rheological and physicomechenical properties of epoxy-polyetherimide compositions. Mech. Compos. Mater. **51**, 313–320 (2015). https://doi.org/10.1007/s11029-015-9502-y
55. Jiang, M.Q., Liu, Y., Cheng, C., Zhou, J.L., Liu, B.H., Yu, M.H., Zhang, H.: Enhanced mechanical and thermal properties of monocomponent high performance epoxy resin by blending with hydroxyl terminated polyethersulfone. Polym. Test. **69**, 302–309 (2018). https://doi.org/10.1016/j.polymertesting.2018.05.039
56. Solodilov, V.I., Korokhin, R.A., Gorbatkina, Y.A., Kuperman, A.M.: Comparison of fracture energies of epoxypolysulfone matrices and unidirectional composites based on them. Mech. Compos. Mater. **51**, 177–190 (2015). https://doi.org/10.1007/s11029-015-9488-5
57. Mimura, K., Ito, H., Fujioka, H.: Improvement of thermal and mechanical properties by control of morphologies in PES-modified epoxy resins. Polymer **41**, 4451–4459 (2000). https://doi.org/10.1016/s0032-3861(99)00700-4
58. Shapagin, A.V., Budylin, N.Y., Chalykh, A.E.: Regulation of a phase structure at the interface in epoxy-polysulfone systems. Russ. Chem. Bull. **67**, 2172–2177 (2018). https://doi.org/10.1007/s11172-018-2350-x
59. Won, J.S., Lee, J.E., Park, J.K., Lee, M.Y., Kang, S.H., Lee, S.G.: Cure behavior and toughness properties of polyethersulfone/multifunctional epoxy Resin blends. Polym. Korea **43**, 60–68 (2019). https://doi.org/10.7317/pk.2019.43.1.60
60. Brantseva, T.V., Solodilov, V.I., Antonov, S.V., Gorbunova, I.Y., Korokhin, R.A., Shapagin, A.V., Smirnova, N.M.: Epoxy modification with poly(vinyl acetate) and poly(vinyl butyral). I. Structure, thermal, and mechanical characteristics. J. Appl. Polym. Sci. **133** (2016). https://doi.org/10.1002/app.44081
61. Chistyakov, E.M., Terekhov, I.V., Shapagin, A.V., Filatov, S.N., Chuev, V.P.: Curing of epoxy Resin DER-331 by Hexakis(4-acetamidophenoxy)cyclotriphosphazene and properties of the prepared composition. Polymers **11**, 12 (2019). https://doi.org/10.3390/polym11071191
62. Rosetti, Y., Alcouffe, P., Pascault, J.P., Gerard, J.F., Lortie, F.: Polyether sulfone-based epoxy toughening: from micro- to nano-phase separation via PES end-chain modification and process engineering. Materials **11** (2018). https://doi.org/10.3390/ma11101960
63. Chalykh, A.E., Gerasimov, V.K., Bukhteev, A.E., Shapagin, A.V., Kudryakova, G.K., Brantseva, T.V., Gorbatkina, Y.A., Kerber, M.L.: Compatibility and phase structure evolution in polysulfone-curable epoxy oligomer blends. Polym. Sci. Ser. A **45**, 676–685 (2003)
64. Korokhin, R.A., Shapagin, A.V., Solodilov, V.I., Zvereva, U.G., Solomatin, D.V., Gorbatkina, Y.A.: Epoxy polymers modified with polyetherimide. Part I: rheological and thermomechanical characteristics. Polym. Bull. **78**, 1573–1584 (2021). https://doi.org/10.1007/s00289-020-03174-8
65. Shapagin, A.V., Budylin, N.Y., Chalykh, A.E., Solodilov, V.I., Korokhin, R.A., Poteryaev, A.A.: Phase equilibrium, morphology, and physico-mechanics in epoxy–thermoplastic mixtures with upper and lower critical solution temperatures. Polymers **13**, 35 (2020). https://doi.org/10.3390/polym13010035
66. Surendran, A., Joy, J., Parameswaranpillai, J., Anas, S., Thomas, S.: An overview of viscoelastic phase separation in epoxy based blends. Soft. Matter. **16**, 3363–3377 (2020). https://doi.org/10.1039/c9sm02361e
67. Zhang, Y.W., Shen, Y.C., Shi, K.X., Wang, T.W., Harkin-Jones, E.: Constructing a filler network for thermal conductivity enhancement in epoxy composites via reaction-induced phase separation. Compos. Part A Appl. Sci. Manuf. **110**, 62–69 (2018). https://doi.org/10.1016/j.compositesa.2018.04.009
68. Nikulova, U.V., Chalykh, A.E.: Phase Equilibrium and Interdiffusion in Poly(Vinyl Methyl Ether)-Water System. Polymers **12** (2020). https://doi.org/10.3390/polym12112445
69. Chalykh, A.E., Gerasimov, V.K., Mikhailov, Y.M.: Phase State Diagrams of Polymer Systems. Yanus-K: Moscow, Russia (1998) (In Russian)
70. Mandelkern, L.: Crystallization of Polimers. McGraw-Hill book company, New York-San-Franciscko-Toronto-London (1964)

Mechanism of Extrinsic and Intrinsic Self-healing in Polymer Systems

Sérgio Henrique Pezzin

Abstract Self-healing materials, which can increase the lifespan of various types of products, have been researched quite intensively in recent decades. In general, self-healing polymers and composites are classified based on their mechanisms of action. While extrinsic systems depend on an external healing agent, the process takes place through reversible bonds or supramolecular interactions in intrinsic systems. In this chapter, the main mechanisms of self-healing epoxy systems, involving extrinsic and intrinsic approaches, autonomous and non-autonomous, are presented and discussed. Since the development of the first extrinsic self-healing epoxy systems, based on microcapsules and vascular networks, which are still the most studied approaches for coatings and composites, many new possibilities have been researched, especially systems involving intrinsic mechanisms. Among them, mechanisms of dynamic covalent networks based on thermally activated reversible Diels–Alder reactions and disulfide bonds, and photoreversible cross-linking have been considered. Furthermore, new trends in self-healing processes concerning vitrimers, non-covalent supramolecular systems, shape memory-assisted self-healing, and bio-based epoxy materials are introduced, looking forward to a wider range of possible applications.

Keywords Epoxy · Self-healing · Mechanism · Extrinsic · Intrinsic · Microcapsules · Vitrimers · Shape memory · Dynamic bonds · Supramolecular

1 Introduction

Self-healing materials are, simply, materials that have the built-in ability to regenerate or ‘cure themselves’ autonomously, that is, without human intervention. Since the early 2000s, researchers in academia and industry have begun to use several innovative scientific techniques and ideas to create a variety of materials that self-heal

S. H. Pezzin (✉)
Center of Technological Sciences, Department of Chemistry, Santa Catarina State University (UDESC), Rua Paulo Malschitzki, 200 - Bairro Zona Industrial Norte, Joinville/SC 89219-710, Brazil
e-mail: sergio.pezzin@udesc.br

N. Hameed et al. (eds.), *Multifunctional Epoxy Resins*, Engineering Materials,
https://doi.org/10.1007/978-981-19-6038-3_4

damage, thus providing a means to significantly extend their service life, increase reliability, and reduce costs.

The great initial motivation for the development of these materials was that in applications with high mechanical demand, such as in aircraft, wind blades, cars, ships, etc., they are subjected, during their useful life, to mechanical and/or thermal fatigue, exposure to ultraviolet radiation, exposure to chemicals or a combination of these factors, leading to the formation of microcracks. These microcracks are difficult to visualize and repair and can propagate along with the material, leading to premature failure [1–5]. These materials are, therefore, especially important in case of internal matrix damage in composite materials, for example, in wind blades, which are difficult to detect, and/or in which it is impossible to carry out corrective maintenance *in loco* [6].

The inspiration for the design of these materials came from nature, a field of science called 'biomimetics' and which is currently undergoing rapid development. We all know that living things, like plants and animals, can seal and heal injuries to a certain extent. In general, there is first a self-sealing phase to avoid desiccation of the cellular tissue and the attack of pathogenic microorganisms, which is followed by a self-healing phase. These processes have been the basis for, bioinspired self-healing materials [7–10], including polymer composites [11–15]. This field is also related to other biomimetic materials, such as those with self-organization, self-lubrication, and self-cleaning capacity [16].

Following these motivations and inspirations, a variety of self-healing polymer materials have been investigated, including thermosets, such as those based on epoxy [1, 17–24] and vinyl-ester [25] matrices, thermoplastics [26–28], and elastomers [29–31].

In short, it is hoped that these materials can [32]:

- regenerate autonomously and multiple times;
- regenerate defects of any size;
- perform better or equal to traditional materials;
- present lower maintenance cost and lower cost compared to other high-performance materials.

1.1 Historical Background

Although cementitious materials with self-healing properties have been used since the ancient Romans [33] and academically studied for more than one century [34], autonomous self-healing polymer materials are a product of the twenty-first century.

Before going into autonomous self-healing materials, it is worth remembering that since the middle of the last century, several researchers had already developed and tested some methods to repair/heal polymer-based materials, including composites, but which still involved some degree of human intervention. For example, pouring a curing agent into the crack [35], injection of adhesive/resin through capillary tubes [36], immersion in solvents [37, 38], or heat and pressure welding [39]. The work

of researcher Carolyn Dry [36] stands out, including a 'recipe' for the development of future self-healing systems using hollow glass fibers containing the curing agent embedded in the polymer matrix, which would break by mechanical stress.

The first works involving autonomous repairing appeared in 2001. The cornerstone was laid by researchers from the University of Illinois at Urbana-Champaign (USA), who presented a self-healing polymer system consisting of an epoxy matrix containing a catalyst (Grubb's catalyst), to which microencapsulated dicyclopentadiene (DCPD), the healing agent, was added [1].

In general, 'first-generation' self-healing materials have a single chance of curing, the ability to repair only minor superficial scratches, or require heat to be repaired. Toohey et al. [40] prepared an epoxy material containing a microchannel framework containing dicyclopentadiene (DCPD) and Grubbs catalyst incorporated into the surface to address these problems. By this concept, the self-healing process can be repeated several times due to the possibility of replenishing the channels after use, but not *ad aeternum* since the polymer generated in previous cures would accumulate in the crack plane with time. It also did not fit into the more restricted concept of 'autonomous,' as it would require an external intervention to replenish the microchannel system.

From there to now, a myriad of self-healing systems based on thermoset and thermoplastic polymers has been developed [2, 11, 12, 15, 30, 41–47] for diverse types of applications in composite structural materials and coatings. The most recent approaches deal with materials that can self-heal indefinitely, for example, by shape memory effect [48–52], or by reversible cross-linking via intermolecular interactions (supramolecular chemistry) [53–56], and reversible chemical reactions [57–60].

To get an idea of the growing interest in the topic, Fig. 1 provides a profile of the number of publications in the period 2001 to 2021, and it can be noted that there is an almost exponential growth in scientific works in this area.

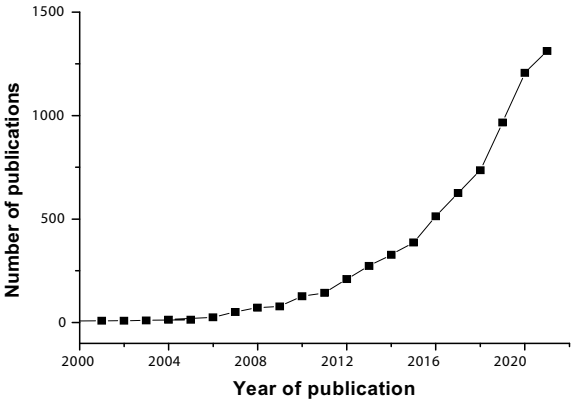

Fig. 1 Graph of the number of publications per year, from 2001 to 2021, according to a survey by "self-healing AND polymer*" with the 'web of sciences' (accessed in 15/03/2022)

1.2 Types of Self-healing Materials

Self-healing polymers generally follow a three-step process very similar to a biological response. The first response is the trigger, which occurs almost immediately after the damage occurs. The second is the transport (diffusion) of the healing agent to the affected area, which is usually also relatively quick. The third step is the physicochemical repair process, which may involve different mechanisms, such as polymerization, interchain interactions, reversible cross-linking, entanglement which will be discussed later.

Based on these different repair mechanisms, autonomous self-healing materials can be divided into three different groups: extrinsic, intrinsic, or combined [30, 47, 61–63].

Extrinsic systems are those that depend on an 'external' healing agent, normally released from microcapsules dispersed in the matrix or by vascular networks. In this process, self-healing is generally triggered by the displacement of a microcrack, and cross-linking begins at room temperature. The first generation of self-healing materials is based on these systems.

In intrinsic systems, the regeneration process takes place through the restoration of reversible bonds (covalent or ionic) or intermolecular or supramolecular interactions and/or through molecular interdiffusion processes [64, 65]. Recently, combined systems have been proposed, especially for applications in elastomers, which involve several types of intrinsic covalent (Diels–Alder, disulfide/diselenide bonds, transesterification, etc.) and non-covalent (hydrogen bonds, π-π interactions, ionic interactions, metallic coordination bonds, shape memory, etc.) processes [30, 66–68].

A new classification was proposed in 2020 [30], based on constructive criticism of the most used categories (extrinsic and intrinsic), considering the chronological order of the development of self-healing polymer materials. In this approach, the materials are classified into generations, being the 1st those based on microcapsules (extrinsic), the 2nd based on intrinsic approaches, the 3rd those presenting vascular systems (extrinsic), and the 4th those consisting of combined (essentially covalent/non-covalent intrinsic) systems.

When the material needs the application of an external stimulus such as heat and/or pressure [69, 70], light, or pH [71] for the repairing process to occur, the material is still considered self-healing but not autonomous [72–74].

2 Autonomous Self-healing Epoxy Systems: Extrinsic Approaches

In extrinsic systems, healing agents are added to the polymer matrix in microcapsules or vascular networks. In both cases, the autonomous healing process is initiated by fatigue or external damage, in the form of microcracks or fissures, which act as

starting mechanisms (triggers) for self-healing. A propagating microcrack breaks the microcapsules or capillaries embedded within the polymer matrix, releasing the healing agent, which by capillary action, is deposited in the plane of the microcrack [1, 75]. Polymerization is initiated when a healing agent encounters an initiator incorporated into the matrix (a catalyst, for instance), the resin's functional groups, or another reactive compound, previously added to the matrix or also released from microcapsules/capillaries, binding the crack faces [1, 4, 19, 41].

Epoxy resins are extensively employed as matrices in self-healing polymer materials [4, 44], as, in general, there is no need for external intervention other than microcracks since polymerization/cross-linking can occur at room temperature. Extrinsic self-healing epoxy materials can achieve healing efficiencies above 100%, even when damaged severely [76].

These systems can be separated into several groups. While microcapsule-based systems only release healing agents when they are ruptured, vascular materials contain the healing agent in hollow capillary channels, which can be uni-, bi-, or three-dimensionally interconnected. When one of these capillary channels is damaged, the network can be recharged by another channel that has not been damaged (in the autonomic approach) or by an external source (non-autonomous system) [77].

2.1 Systems Based on Microcapsules

The idea of using a microencapsulated healing agent in an epoxy matrix, aiming to restore physical properties after stress is applied to the material, has attracted the interest of many researchers and various industrial segments, such as aerospace, automotive and high-tech industries [4, 73, 78–80].

Healing agents and/or hardeners/catalysts are encapsulated to be protected from environmental and matrix influences so that they can remain inactive for a long period of time. Generally, healing agents are microencapsulated by emulsification. In this process, the monomers polymerize to form an envelope that surrounds the drops of the liquid healing agent in suspension or, in the case of hollow microcapsules, that enclose air bubbles in suspension [75, 78, 81–83].

The flowchart in Fig. 2 represents the stages of development to give materials the ability to self-heal by using microencapsulated agents.

To provide this functionality, the first step is to choose a healing agent that presents a suitable chemical repairing mechanism. Next, an appropriate shell material for the preparation of microcapsules containing the healing agent and/or the hardener and the encapsulation method is determined. In the latter step, the core properties, the matrix's processing capacity, and the crack response must be considered [74]. For instance, an increase in microcapsule or catalyst content can reduce the processability due to increased resin viscosity, and, thus, care must be taken with processing conditions to minimize microcapsule breakage during mixing and mold filling stages.

In self-healing systems that employ microencapsulated healing agents, at least one component must be flowable [43, 74]. These systems can also consist of an

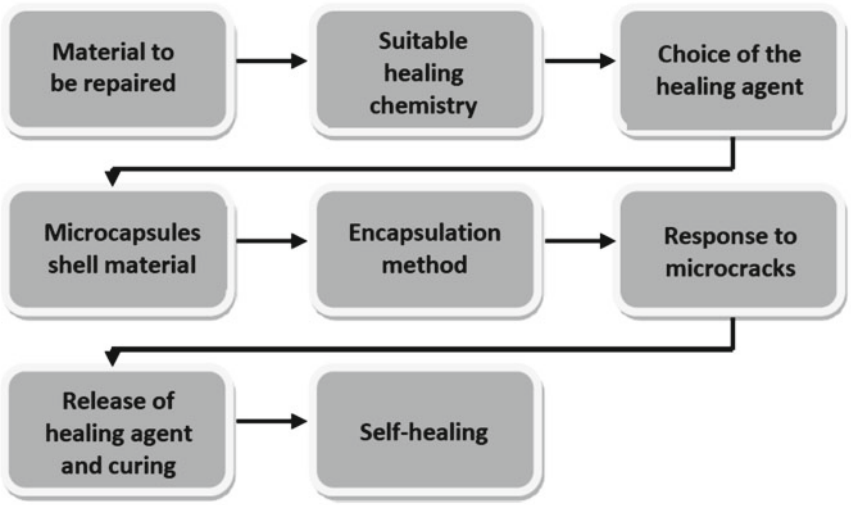

Fig. 2 Flowchart of development steps to provide self-healing capacity to polymer materials using microencapsulated curing agents

encapsulated component [1, 83, 84], two encapsulated components [17, 24, 25], or even a 'dual' system, where one component is a particle or droplets, and the other component is in the form of microcapsules [85]. Figure 3 represents the scheme of the healing mechanism of each of the systems described above.

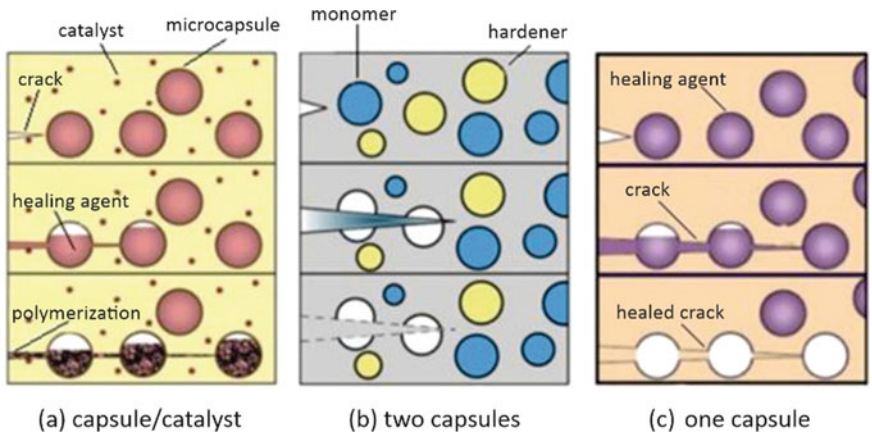

Fig. 3 Microcapsule-based self-healing approaches **a** a two-component system, where one component is a particle (catalyst), and the other is a capsule (reproduced with permission [1], copyright 2001, Springer Nature); **b** a two-component encapsulated system in which the monomer and healing agent are encapsulated (based on Jin [86]); **c** encapsulated single component system

Self-healing systems of one encapsulated healing agent generally consist of a single type of microcapsule [74], in which the release of the healing agent starts a reaction with adjacent functional groups of the matrix on the fractured surface. In a two-component system, the two components are encapsulated so that one capsule can contain the resin or monomer and the other the hardener. Soon after the microcapsules rupture, due to the propagation of microcracks in the matrix, the monomer is polymerized under the action of the surrounding hardener/catalyst. In two-component systems formed by particles/droplets and capsules, at least one component must be fluid to be released with the crack propagation and react with a neighboring component, such as a catalyst. That is, these systems are formed by a reactive component that must be encapsulated and particles or droplets in a separate phase of the matrix. The closure of the crack occurs through capillarity and polymerization, which is triggered by the contact with a catalyst [74].

As already pointed out, self-healing occurs when the microcapsule breaks due to the appearance of microcracks inevitably generated in polymer materials during their time of use or external damage [1, 4, 45, 75]. For this process to take place without manual intervention and at room temperature and for the healing agent to remain intact inside the microcapsule, a catalyst/initiator can also be encapsulated or dispersed in the polymer matrix [1, 2, 4, 25]. In each case, the microcapsule disruption mechanism at the crack points offers a specific autonomous repair control [75, 84]. There are many challenges in designing microcapsule-catalyst systems. Firstly, the reactivity of the catalyst needs to be preserved even after it is dispersed in the matrix or encapsulated. In addition, the healing agent must have an adequate viscosity to completely fill the microcrack before it is polymerized [18, 87].

The first studies on autonomic systems with microcapsules containing a healing agent have been reported by White and colleagues [1, 13, 18, 82]. They induced the polymerization of dicyclopentadiene (DCPD) in the presence of Grubbs catalyst (benzylidene-*bis*(tricyclohexylphosphine)dichlororuthenium) in an epoxy matrix. The healing agent, DCPD, was microencapsulated in poly(urea–formaldehyde) (PUF) by in situ polymerization in an emulsified system, forming a capsule that surrounds the liquid DCPD drops. The monomer itself is relatively unreactive, and polymerization does not occur within the microcapsule [88]. When a microcrack reaches the capsule containing DCPD and the catalyst, however, the monomer is liberated from the microcapsule and meets the bare catalyst, undergoing polymerization by ring-opening metathesis (ROMP). They found that the microcapsules effectively released the healing agent in the crack plane, inducing polymerization and damage repair. The self-healing efficiency of this system was 75% in terms of fracture toughness. These experiments paved the way for many other works using DCPD, aimed at improving the encapsulation technique and/or evaluating the effect of mechanical agitation speed, concentration, and type of surfactant [13, 25, 82, 89]. For example, Brown et al. [18, 82], varying the stirring speed from 200 to 2000 rpm, obtained capsule sizes from 10 to 1000 μm, while Blaiszik et al. [89] studied the reduction of the size of capsules to the nanoscale by modifying the agitation process with the joint use of sonication. The effects of the size and concentration of microcapsules on mechanical properties of epoxy matrices, such as fracture toughness and

self-healing efficiency, have also been evaluated [3, 25, 90, 91]. These studies defined the percentages and sizes of microcapsules with the best results on the self-healing efficiencies of different epoxy matrices. An interesting variation was proposed by Skipor et al. [92], in which the catalyst is fixed to the outside wall of microcapsules filled with the healing agent. But few experimental details and results of self-healing efficiency have been given in their patent.

Other self-healing epoxy systems using diverse encapsulated healing agents, such as the epoxy resin itself [19, 93], linseed oil [94, 95], tung oil [72], poly(dimethylsiloxane)s [24, 85], polyamines [17, 24, 96], and polyurethanes [97, 98], have also been studied for both structural and coating applications. In most of these cases, the use of catalysts is not mandatory, since the healing agents can react with residual amines and/or epoxy groups within the polymer matrix [17, 75, 99]. An interesting example is the use of encapsulated amines since, due to their reactivity and solubility in water, the preparation of capsules with PUF or polyurethane shells is tricky. Jin et al. [17] developed a method to encapsulate amines by vacuum infiltration into hollow PUF microcapsules prepared by interfacial polymerization using air/water emulsions. In their work, the best results in mechanical properties were obtained using 17.5% epoxy- and amine-filled microcapsules with an average diameter of 220 μm. Weihermann et al. [24] improved this process, introducing a self-healing epoxy system based on PUF microcapsules infiltrated with an amine-functionalized poly(dimethylsiloxane) (PDMS-a). The amine-functionalized poly(dimethylsiloxane), in contact with triethylenetatramine (TETA), was able to efficiently repair the cracks by the reaction of the amine groups with epoxy rings remaining in the matrix.

Another important consideration is the change in mechanical properties and processing characteristics of epoxy matrices caused by the addition of microencapsulated healing agents/catalysts, which will depend on the volumetric fraction of the microcapsules, and the extent of the matrix/microcapsule interfacial interaction [90, 100]. However, it has been shown that epoxy resin can be significantly toughened (up to 127%) with 15 wt% of microcapsules filled with DCPD [1] or 2.5 wt% with amino-functional polydimethylsiloxane [24], and by addition of Grubbs catalyst [18]. The concentration of microcapsules for maximum toughness is greatly dependent on the mean diameter of the microcapsules, with smaller diameters providing maximum toughness at lower concentrations, as evidenced by fractographic analysis [13, 18, 75].

X-ray micro-computed tomography (μCT) is a non-destructive technique that can be very useful to evaluate self-healing materials and mechanisms, making possible bulk visualization by 3D reconstruction [101, 102]. For instance, μCT was applied to monitor the rupture of microcapsules filled with healing agents in the fracture region [75, 103], enabling the quantification of the amount of released healing agents and detecting healed and non-healed areas. Tomography using synchrotron radiation [104] showed that the rate of absorption/reaction of healing agents after fracture depends on the diameter of the microcapsule. A delay is observed for larger microcapsules due to smaller surface/volume ratios. Recently, Caballero-Peñas and coworkers [105] showed that free OH groups are responsible for self-healing of

epoxy samples with different curing agents, after producing a superficial cut and heating the sample above its T_g. The authors suggested evaluating larger areas to confirm the healing mechanisms. It is also possible to follow the crack propagation as a mechanical test is performed, making is possible to obtain in situ information about how microcapsules are broken, how the healing agent fills the cracks and self-healing efficiency. μCT, in combination with electron microscopy, was also used in the study of self-healing mechanisms in epoxy systems using microencapsulated amine-functionalized polysiloxanes (PDMS-a) as healing agents [75]. When analyzing specimens after mechanical stress, it was possible to evaluate the distribution and stability of the microcapsules, as well as to recognize the trigger mechanism when a crack appears within the matrix, showing that PDMS-a was effective to heal microcracks even at room temperature. It was observed that most microcapsules with diameters >60 μm (shell thickness ca. 0.4 μm) are broken during dispersion into the epoxy matrix, in contrast to those with diameters <60 μm, which remain intact during the dispersion and curing of the resin. μCT and SEM images confirmed that the self-healing process occurs by a mechanism involving crack bowing and deflections, as shown in Fig. 4, indicating that the microcapsules are very well adhered to the polymer matrix. High fracture toughness values obtained using the same system [24] can thus be explained by this crack deflection mechanism.

The same epoxy/PDMS-a self-healing system, now in glass fiber-reinforced composites, has also been studied, under mechanical stress, using multi-contrast X-ray imaging with an inverted Hartmann mask [106]. Absorption and differential phase-contrast images revealed the distribution of glass microfibers, while scattering contrast imaging showed the changes in the inner structure of the polymer composites, indicating microfracture propagation and uniform microcapsule distribution.

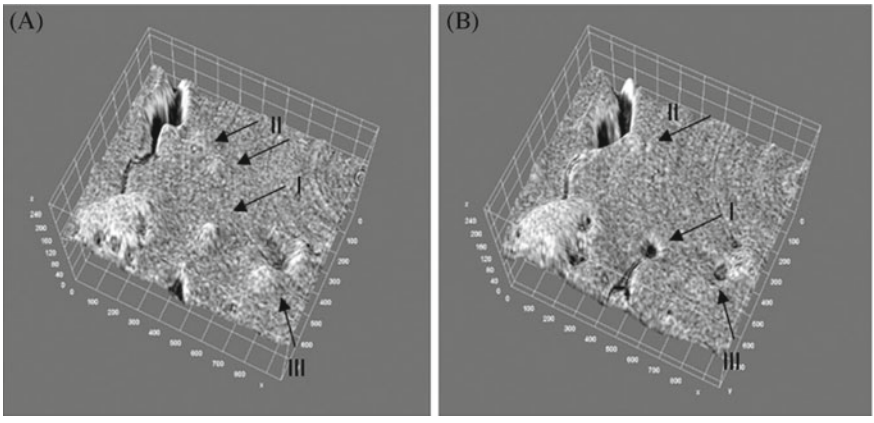

Fig. 4 **a** 3D plotting of a slice surface of an epoxy sample containing PUF microcapsules filled with PDMS-a. The light gray spots, pointed by arrows I, II, and III are microcapsules responsible for the release of the PDMS-a in the crack area; **b** 3D plotting showing cavities after the release of the healing agent (arrows II and III). Reused from [75] (Wiley-VCH GmbH, CC BY 4.0)

It was thus possible to track the self-healing triggering mechanism acting on the polymer composite under mechanical stress.

There are not many studies on systems using polymeric nanocapsules yet [42, 89, 107, 108]. A study by Blaiszik et al. [89] showed that PUF nanocapsules (diameters 220 ± 113 nm, with a mean wall thickness of 77 nm) containing DCPD, prepared by in situ encapsulation using ultrasound, were uniform and thermally stable up to 150 °C. The encapsulation efficiency in these capsules was almost 94%, with the great advantage of allowing a much better dispersion in the epoxy matrix (up to 2% volume fraction). The authors concluded that nanocapsules exhibit damage-responsiveness, which can be useful in several applications.

2.2 Systems Based on Vascular Networks

By this concept, healing agents can be delivered from an external source to damage points throughout a vascular network structure, and the process could be, in principle, repeated several times due to the replenishment capacity of the channels after a regeneration. In one of the first representative works using this approach, Toohey et al. [40] prepared an epoxy material containing an array of microchannels containing dicyclopentadiene (DCPD) with Grubbs' catalyst incorporated on the surface (similar to the microcapsules approach), demonstrating the partial recovery of toughness after a fracture. The strategy can be applied to vascular systems in one (1D), two (2D), or three dimensions (3D) [40, 77, 109]. Nevertheless, several issues are still challenging [77]. The first point is the limit on the number of times the material can be healed since the polymer formed in the plane of the crack of previous cures accumulates with time, obstructing any further flow of the healing agent. The second is the upscaling of the process, as currently, only the proximity of the network channels can be healed. Furthermore, as in systems based on microcapsules, care must be taken not to damage the matrix in the formation/integration of the channels, which could lead to a worsening of the mechanical properties of the material.

2.2.1 Hollow Tube Approach

The first works on vascular systems used capillaries, i.e., hollow fibers, usually glass, embedded in a polymer matrix [10, 36, 110–113]. Part of this capillary network is filled with monomer and part with a curing agent (hardener). When material damage occurs from regular use, the tubes also crack, and monomers and hardeners are released into the matrix microcracks, promoting their repair (Fig. 5) [10]. A patent related to this concept was granted in 2006 [114].

There are important things to consider when hollow tubes are introduced into a polymer system. The first consideration is that the channels created can compromise the load-bearing capacity of the material. For instance, self-healing materials that do not need to withstand much mechanical stress allow the addition of more

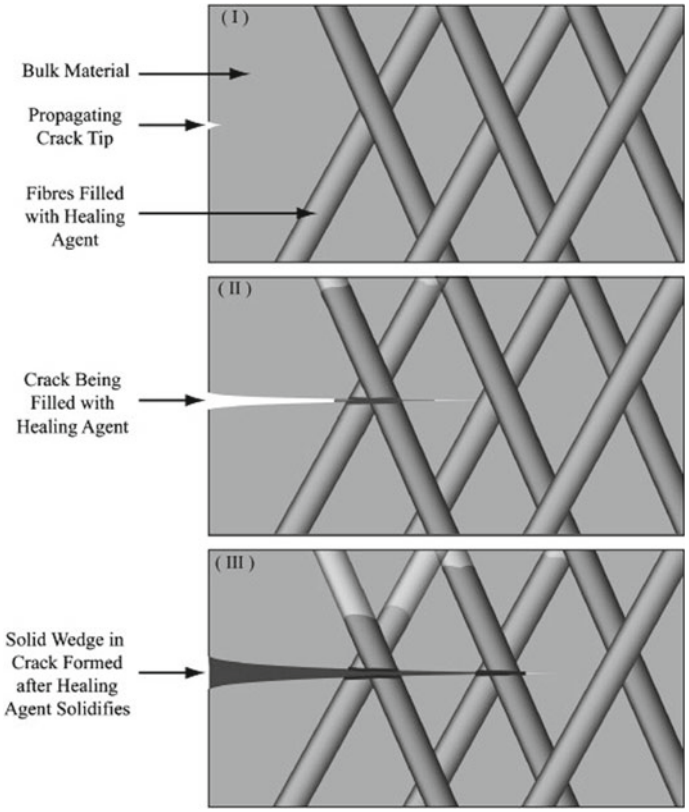

Fig. 5 Concept of self-healing mechanism in composites based on hollow fibers. Reproduced from [2] with permission from Elsevier. Copyright 2008

microchannels (hollow fibers) than structural materials designed to withstand heavy loads [109]. An interesting approach proposed for E-glass epoxy laminates is the use of sandwich structures with PVC tubes forming a vascular network housed in the core of laminate, which offers a potentially robust and replenishable system to deliver a healing agent from a remote reservoir to a region of damage [113]. Due to their high stiffness and self-healing efficiency, these sandwich structures are attractive for pressurized chambers.

It has been shown, however, that the introduction of mili- or micro-meter-sized hollow fibers into an epoxy matrix will detrimentally affect the mechanical properties due to stress concentrations. The use of carbon nanotubes (CNT) network, for instance, could avoid this problem. Sinha-Ray and coworkers [115] proposed a self-sustained Fickian diffusion method to fill CNT bores (50–100 nm) with DCPD and isophorone diisocyanate (IPDI), as healing agents, from benzene solutions. The authors also prepared core–shell polyacrylonitrile (PAN) nanofibers filled with the

same healing agents (DCPD and IPDI) by electrospinning techniques and characterized their release in an epoxy matrix. The encapsulation of the healing monomers was demonstrated by fiber crush tests, confirming the filling of CNTs with IPDI and PAN with DCPD and IPDI. Microscopy techniques were used to evaluate toughening mechanisms and validate proof-of-concept epoxy composites reinforced with self-healing core–shell nanofibers at the interfaces.

Nevertheless, due to the need for more efficient methods to fill and seal narrow hollow fibers, effective placement of hollow fibers in large-scale applications, etc., this approach, although conceptually interesting, is currently less studied.

2.2.2 Discrete Channels and Interconnected Networks

Most of the more recent research on vascular systems involves the creation of micro- or submicro-channels (vascules) within the polymer matrix. Currently, the methods commonly used for vascule fabrication are micromachining, fugitive scaffold and 'lost-wax' processes, and the vaporization of sacrificial components [77]. Two types of systems are possible, those with discrete channels and those with interconnected channels [109].

Discrete channels can be constructed independently and arrayed throughout the material. There are several key points to ponder when constructing microchannels within a material, like the channel diameter and orientation, the degree of branching, and the location of branch points. Another important factor to consider is that the closer the tubes are, the lower the resistance, but the more efficient the healing [10, 109]. Interconnected three-dimensional vascular networks are in principle more efficient than discrete channels, but more difficult and expensive to be produced [109].

Machining principles to create microscale grooves have been used as the basic way to create microchannels for self-healing applications. These techniques can produce 600–700 μm channels and work very well on two-dimensional planes, but when trying to create a 3D network, they are limited [109]. However, recent developments in additive manufacturing (AM) technologies allow the fabrication of more effective, bioinspired vascular designs (VDs) [77, 116].

The direct-write assembly (DWA) or direct ink writing (DIW) is a controlled extrusion technique to design interconnected three-dimensional networks using viscoelastic inks [40, 77, 109, 117]. It works by first depositing an organic fugitive ink to a defined pattern. The structure ('scaffold') is infiltrated with epoxy, which is cured, and then the scaffolds are removed by applying heating and vacuum, creating hollow channels, generally around 200 μm. The first studies used DCPD/Grubb's catalyst or a two-part epoxy-based healing chemistry [40, 117, 118], reaching from 7 to 16 successful healing cycles at 30 °C. Hansen et al. [119] introduced the concept of interpenetrating 3D networks, achieving 30 sequential healing cycles. In another work, three-dimensional micro-scaffolds were fabricated using a computer-controlled robot, with the deposition of ink-based filaments on an epoxy substrate [120]. Liquid 5-ethylidene-2-norbornene (5E2N/CNT) containing 0.5 wt% CNT, as

reinforcement, has been microinjected in the empty microfluidic networks inside an epoxy matrix with Grubb's catalyst nanoparticles. It was observed that the kinetics of the ROMP reaction of 5E2N was very effective over a relatively wide temperature range (from 15 to up to 45 °C). The results showed a significant increase in Young's modulus and hardness for CNT-loaded composites in comparison with the pure polymer.

Another method to create channels with diameters around 0,5 mm is the incorporation of PTFE-coated steel [121, 122], or solder [8] wires, silicone tubing [123], or polyamide strings [124] in carbon (or glass) fiber-reinforced epoxy laminates. After the laminate curing process, the wires/strings are pulled out of the matrix (or removed by heating and vacuum), leaving behind hollow channels (vascules). This kind of process is called 'lost-wax' [77]. In most cases, the healing agent is manually injected from an external source into the vascules, but Norris and colleagues [125] proposed an autonomous system with a low-pressure sensor connected to the vascules, which triggered a peristaltic pump that circulated the healing agent (a premixed low-viscosity epoxy resin). The fatigue behavior of such systems has been also studied [126]. However, a rapid loss in stiffness after 2500 cycles was reported, which was attributed to the low performance of the epoxy system (low-viscosity resin). A view of the integration of these vascular networks is shown in Fig. 6.

In the vaporization of sacrificial component (VaSC) approach, polylactide (PLA) filaments treated with tin oxalate, as a catalyst for thermal decomposition, are woven through layers of fiber-reinforced polymer laminates. After the laminate curing cycle, the composite is heated above 200 °C under a vacuum, leaving behind empty channels in the form of a 3D vascular network that can be filled with healing agents [77]. An advantage of this method is that the interference in the architecture of the composite is minimized, as the sacrificial PLA fibers replace part of the preform carbon (or glass) fibers. Tests using double cantilever beam (DCB) specimens of epoxy composites reinforced with E-glass woven considering two different arrangements, parallel and

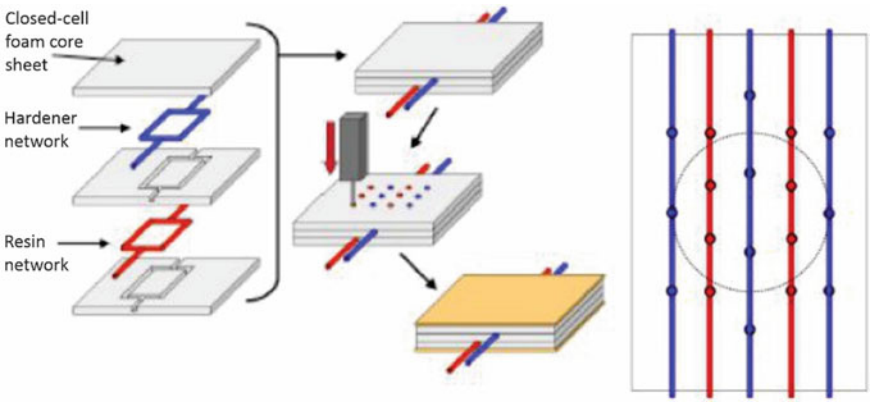

Fig. 6 Vascular network integration in composite sandwich panels (reproduced from [125] with permission from IOP Publishing, Ltd. Copyright 2012)

interpenetrating (herringbone), showed that the networks introduced via VaSC have little impact on the inherent fracture properties of the composite [127]. The dual-vascular channels filled with a two-part (resin/hardener) healing chemistry permitted the continuous delivery of the healing agents to crack planes when the samples were under load. Herringbone specimens achieved healing efficiencies above 100%, significantly higher than those reached with the parallel pattern, evidencing the importance of the vascular architecture on the healing performance. Further developments have been made by Gergely and coworkers [128], who tested VaSC with different dimensions, 0D (spheres), 1D (fibers), 2D (sheets), and 3D printed structures, and showed, by flow rate tests, that the fluid transport through these systems is viable. More recently, Cuvellier and collaborators [129] reported a study on the selection of healing agents for VaSC self-healing systems. After comparing different compositions, they found that the best healing performance is observed for TETA/trimethylolpropane triglycidyl ether (TMPTE). However, it is pointed out that an extensive swelling of the matrix with the healing agents may prevent its application in VaSC epoxy thermosets. Furthermore, the need for compatibility to promote adhesion, combined with time-consuming steps for fiber dissolution and infusion of the healing agents, make the upscaling of VaSC systems to an industrial level difficult.

3 Non-autonomous Self-healing Epoxy Systems

3.1 Thermally Induced Self-healing

It has been shown that thermosets can heal cracks or scratches via interdiffusion of dangling chains or chain slippage in the polymer network [2, 130, 131]. Due to molecular diffusion, when two parts of the same polymer are brought into contact, the interface between them gradually disappears above the glass transition temperature (T_g). This process increases the mechanical strength at the polymer–polymer interface and can heal also internal microcracks.

In one of the first reports on the healing of epoxy resin via thermally induced chain rearrangement [132], fractured resins based on bisphenol-A diglycidyl ether (DGEBA) containing methyl nadic anhydride (NMA) and benzyldimethylamine (BDMA), have been repeatedly shown to heal when heated above 150 °C. Very high healing efficiency across multiple fracture events has been verified both visually and by a double twist fracture test. The healing process only occurred when the system was heated above its T_g (120 °C) but, at higher temperatures, seemed to be independent of the healing temperature or the presence of unreacted monomer. The cure was attributed to interdiffusion/entanglement of the pendant chain ends, caused by micro-Brownian movement, with the local flow allowing a strong interfacial bond and restoration of the original surface contours. Kim and Wool [133] also presented a microscopic theory for the diffusion and randomization stages, proposing

that the recovery of mechanical strength during the healing process is related to chain interdiffusion and subsequent entanglement formation.

Amorphous and semi-crystalline thermoplastics can also be used for the toughening of thermoset resins, which can generate blends with different dispersed and continuous structures, just varying the amount of thermoplastic modifier (generally with less than 15% by mass). Thermoplastic additives allow the original polymer matrix to remain unaltered, while also providing a solidifiable crack filling capable of relinking fracture surfaces [2]. Among these are co-continuous morphologies composed of thermoplastic and thermoset phases, called semi-interpenetrating polymeric networks (semi-IPNs), which are the most suitable for toughening [134]. This thermoplastic phase, in any morphology, can work for heat-induced regeneration, but semi-IPN structures are more efficient than dispersed morphology [135–137].

This approach has been tested by Zako and Takano [138], who added up to 40 vol% of small thermoplastic epoxy particles (average diameter 105 μm) in a glass fiber-reinforced composite. When the composite is heated at 120 °C for 10 min, the particles melt, flow to microcracks or internal flaws and solidify, healing the material to 100% of its original stiffness, as verified by three-point tensile and bending tests. Samples fatigued under traction until stiffness decreased by 12.5% and then heated to trigger the flow, with subsequent solidification of the incorporated thermoplastic particles, showed almost total stiffness recovery. The proposed mechanism is shown in Fig. 7.

An alternative way of using this self-healing mechanism is the use of a blend of thermoplastic and thermoset polymers, in which the matrix can contain 10–30 wt% a thermoplastic polymer [139, 140]. In this case, several factors will affect the self-healing efficiency, such as the compatibility of the two polymers. The thermoplastic healing agent should preferably be miscible with the thermoset polymer but do not chemically react with it at room temperature. Another factor is that the $T_g s$ of thermoplastic and thermoset polymers must be similar. Thermoplastic should enter the viscous regime above room temperature but not at a temperature that can cause thermal degradation of the thermoset. Another factor is the molecular mass distribution of the thermoplastic. Low molecular mass polymers diffuse faster, resulting in faster healing, while high molecular mass polymers provide better mechanical properties. Lastly is the healing temperature. Self-healing occurs by diffusion; thus, temperature influences the speed and efficiency of healing [141].

An ingenious example of heat-triggered self-healing was reported by Luo and coworkers [142], who described a polymerization-induced phase separation (PIPS) process for the preparation of a material consisting of a cross-linked epoxy matrix and a co-continuous percolating polycaprolactone phase, responsible for the healing behavior. In the concept, the damaged epoxy matrix is thermally mended by molten polycaprolactone (PCL) that wets and fills the crack surfaces. The self-healing efficiency was confirmed by tensile tests, which presented a resemblance between the virgin and the thermally mended material.

Thermoplastic polymers have also been employed as curing agents for glass fiber-reinforced epoxy composites [141, 143]. Composites containing 7–10% of poly(bisphenol-A-*co*-epichlorohydrin) (PBE) tested in several impact cure cycles

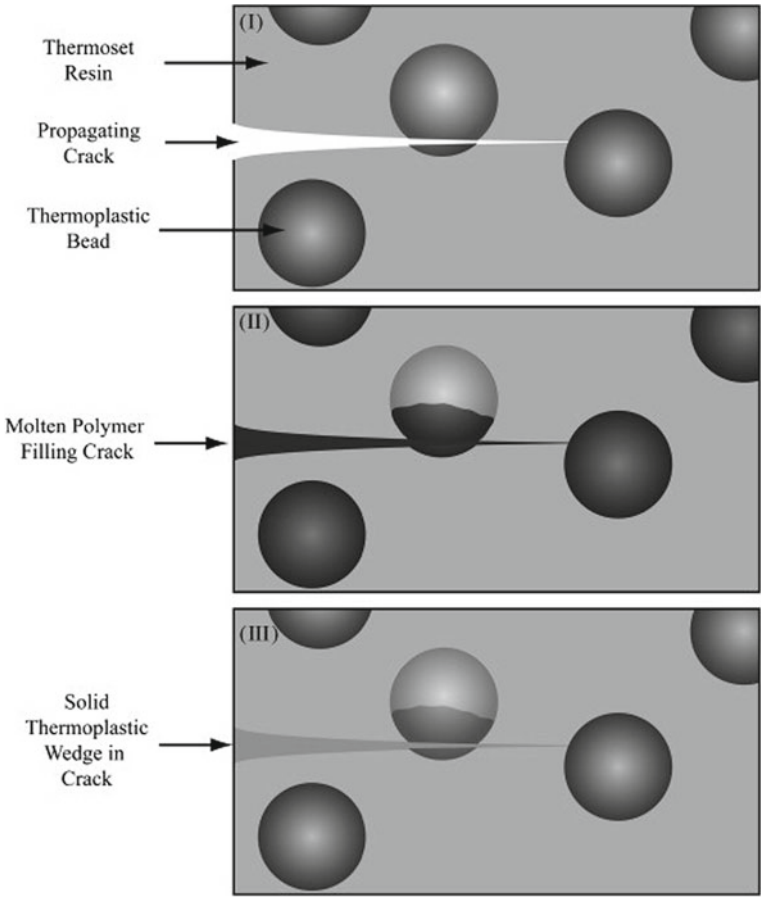

Fig. 7 Concept of healing mechanism in thermoplastic bead-based self-healing composites. Reproduced from [2] with permission from Elsevier. Copyright 2008

presented a cure efficiency of 30–50%. These values are lower than that reported in the first studies on this approach [138]. It must, however, be considered that the matrix resins and the test methods used to assess self-healing efficiency were different. Pingkarawat and coworkers [144, 145] reported the use of reactive thermoplastic additives, such as polyethylene-*co*-glycidyl methacrylate (EMAA) and polyethylene-*co*-glycidyl methacrylate (PEGMA), and two types of non-reactive additives, ethylene vinyl acetate (EVA) and acrylonitrile butadiene styrene (ABS), showing that even incompatible thermoplastic additives with high internal pressure and/or low viscosity can be also an effective crack healing agent for carbon/epoxy composites. The same group also proposed other thermally activated healing agents, such as tetra-glycidyl diamino diphenyl methane [146].

While the feasibility of this concept is proven in terms of stiffness recovery, potential problems related to the heating of thicker parts without causing excessive heat to the surface have yet to be assessed. The use of carbon nanotubes can help to solve this issue. When CNTs are incorporated into epoxy matrices, forming a percolating network, and a direct current is passed through the nanotubes, a significant change in the detection curve can indicate damage to the polymer, 'detecting' a crack [147]. This feature can also be used to create CNT networks that impart a self-healing function to the material. When dissolving a thermoplastic linear polymer within a thermoset epoxy matrix, forming a semi-interpenetrating network, the thermoplastic domains become movable at a certain temperature [148]. Carbon nanotubes can thus detect microcracks within the structure and be used as thermal conductors to heat the system, allowing linear polymer chains to diffuse and fill cracks in the epoxy matrix, healing the composite [143, 149].

3.2 Photoinduced Self-healing

The concept of photoinduced curing is potentially attractive because the reaction takes place at room temperature and is normally simple, fast and environmentally friendly.

The application of this approach for epoxy resins was proposed by Sriram [150] by using photoactivated catalysts for ROMP, with polymerization of norbornene (NBE) or DCPD, instead of the traditional Grubbs catalyst. The main motivation of the work was the use of a catalyst that can be easily synthesized in large quantities. Moreover, the photoactivated ring-opening metathesis polymerization reaction (PROMP) is extremely fast (<5 min), with minimal volume change. ^{1}H NMR analysis confirmed the occurrence of PROMP with DCPD and NBE at room temperature. However, no self-healing tests were reported.

Other works with photoactivated self-healing involving photoreversible cross-links will be discussed in the next section.

4 Intrinsic Self-healing Epoxy Systems

Intrinsic approaches consider that the system can self-heal inherently. However, most intrinsic systems require an energy supply, i.e., an external trigger, such as thermal, mechanical, electrical, or photo-stimuli, to repair microcracks efficiently on the atomic/molecular level. Nonetheless, it is important to note that they differ from non-autonomic approaches due to the reversible nature of intrinsic self-healing processes. There are two main kinds of intrinsic systems, those based on reversible covalent bonds and those supported by non-covalent supramolecular approaches.

4.1 Dynamic Covalent Networks (Reversible Covalent Bond Cleavage)

4.1.1 Reversible Reticulation Systems

This concept involves a class of cross-linked polymers capable of healing internal cracks through thermo- or photoreversible covalent bonds, being suitable for the development of self-healing epoxy resins used to make fiber-reinforced composites for structural applications. The use of reversible cross-links to cure epoxy systems eliminates the need to incorporate 'reservoirs' (hollow fibers or microcapsules) containing healing agents or catalysts. However, it is usually necessary to provide heat to trigger and/or support the healing process [151–154]. As the curing agent and heat source can be integrated into these materials, they are characterized as intrinsic systems [2].

Among the thermo-reversible healing polymers, the most studied systems are those based on Diels–Alder (DA) reaction and its retro-Diels–Alder (RDA) analog (Fig. 8). DA-based systems undergo a fully reversible cycloaddition, allowing multiple cycles of crack regeneration [12, 152]. In addition, there are still other advantages over extrinsic approaches, as it eliminates the need for additional reagents, such as catalysts or monomers, or interfacial treatment at the crack surface. In general, the monomer containing the functional groups, such as furan or maleimide, forms two C–C bonds to build the polymer network through DA reaction. When heated, at temperatures normally higher than 120 °C, or under mechanical stress, the polymer chain breaks down into its monomeric units by RDA reaction. The polymer is restored (healed), again by DA reaction, after cooling, or by any other conditions that were initially used to synthesize the polymer. Two types of DA reversible polymers have been proposed: (i) systems where pendant groups, such as furan or maleimide, cross-link through successive coupling reactions; (ii) systems in which multifunctional monomers link together [66].

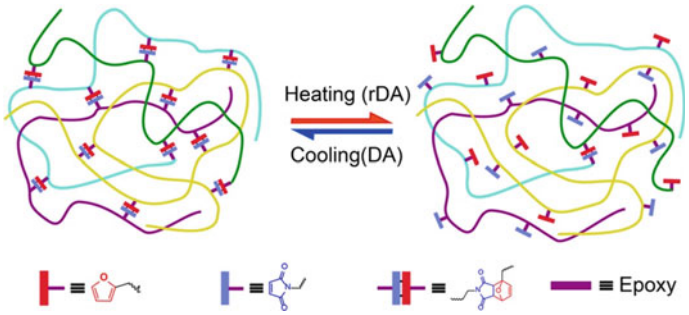

Fig. 8 Diels–Alder cross-linking agents and thermally reversible cross-linking mechanism (reproduced from [154] with permission from John Wiley and Sons. Copyright 2015)

The first works using this approach [151, 152] described the preparation of highly cross-linked and transparent materials, by DA cycloaddition of furan and maleimide (derived from DGEBA), with the thermal reversibility of the bonds due to retro-Diels–Alder reactions. The reversibility of the cross-linked structure was confirmed using solid-state ^{13}C-NMR by submitting the polymerized films to multiple heating and cooling cycles. The self-healing efficiency, quantified by fracture tests, was about 50% at 150 °C and 41% at 120 °C, but there was a drop in mechanical properties from the second to the third healing process [151]. Further improvements in the polymerization processes, for instance, the removal of reaction solvents, improved the healing efficiencies to about 80% [152]. This process has been patented [155], as well as its possible application to sports materials (thermally patchable golf balls) [156].

Looking for applications in the production of advanced composites, Liu and Hsieh [153] employed epoxy precursors to prepare multifunctional monomers containing furan and maleimide groups. These monomers present the desirable characteristics of conventional epoxy resins, such as chemical resistance, low melting point, and solubility in a range of organic solvents, allowing them to be processed similarly to commercial resins. The DA reaction regeneration mechanism has also been used to integrate conductive electromagnetic materials such as copper wires or coils into fiber-reinforced composites [157], enabling the healing of internal damage in composites through thermo-reversible covalent bonds under moderate heat application. The crack disappearance was visually observed after the samples had been heated above 80 °C for at least 6 h under a nitrogen atmosphere.

Peterson and coworkers proposed two new systems for reversible DA cross-linking in epoxy resins [158, 159]. The first one used a thermo-reversible cross-linked gel, obtained by mixing 1,10-(methylenedi-4,1-phenylene)bismaleimide to furfuryl amine and DGEBA oligomers- as a repairing agent for epoxy-amine resins. The DA healing mechanism involves liquefaction of the gel phase upon heating, which flows into the crack plane. After cooling, cross-linking is reformed, restoring the initial epoxy network structure [158]. Later, they proposed a DA system working at room temperature by the use of furan-functionalized epoxy resins with a mixture of *N,N*-dimethylformamide (DMF) to swell the epoxy network structure, and *N,N'*-(4,4'-methylenediphenyl)bismaleimide (BMI), as a DA reagent. This system enabled contact between crack surfaces, improving the strength of the repaired interface [159].

Thiol-based polymers present disulfide bonds that can be reversibly cross-linked through oxidation and reduction. Under the reducing condition, the disulfide bridges (SS) can break down and result in monomers. However, under the oxidizing condition, the thiols (SH) of each monomer form the disulfide bond, cross-linking the starting materials to reform the polymer. In one of the first works on this approach, Saegusa et al. showed a thiol-based reversible cross-linked polymer based on poly(*N*-acetylethyleneimine) [160]. Considering epoxy systems, Lei and coworkers [161] reported the curing reaction of polysulfide diglycidyl ether with diethylenetriamine using tri-*n*-buthylphosphine as a catalyst. Tensile tests showed that this epoxy cross-linked with disulfide bonds can self-heal at room temperature and without any manual intervention, but the low Tg (below room temperature) limits its applications. Other

recent papers describe different possibilities using disulfide bond exchange reactions [162–164], demonstrating new features, such as reprocessability, weldability, and potential use in structural composite applications.

The formation of disulfide bonds is one of the ways to produce epoxy vitrimers [164–166]. Vitrimers are a group of polymers based on adaptive dynamic covalent networks, which fill the gap between thermoplastics and thermosets. Dissociative and associative exchanges within these networks make it possible to obtain robust 'Recyclable, Repairable, and Reshapable' (3R) materials, which maintain their original structural properties and mechanical resistance [165, 167]. The bond exchanges in these cross-linked species as a response to externally applied stimuli, such as heat or stress, define the self-healing behavior of these materials (Fig. 9). Dissociative exchange, such as pericyclic reactions, nucleophilic transalkylation, and amine transamination, is the process by which cross-links are broken prior to recombination of the cross-linking species, thus recovering the cross-link density after the exchange, while associative exchange, such as transesterification and transamination, preserve the cross-links during the exchange by substitution reactions [168]. In addition to recycling, vitrimer materials, such as self-healing bio-epoxy [169], are very promising for medical and electronic applications [170, 171].

Photoreversible cross-linked epoxy resins containing photoactive anthracene moieties have been recently reported [172, 173]. Radl and coworkers [172] dissolved the photoactive agent in a low-viscosity monofunctional epoxy resin to obtain a photocured repairable epoxy material. The results showed that, after mechanical damage, the epoxy system under UV light (>300 nm) undergoes a photoreversible polymerization along the crack surface. Nonetheless, additional heating at 60 °C is required to induce the interdiffusion of polymer chains. A further development [173] employed two anthrylamines as crosslinkers, confirming that the healing effect is due to the photochemical reaction of the cleavage of anthracene dimers, which act as cross-linking agent, causing a transition from a rigid to a softer phase, and then to a flowable material that can fill the cracks before returning to the rigid phase.

4.2 Non-covalent Supramolecular Approaches

Self-assembly of supramolecular polymers allows the formation of new structural organizations through highly selective cooperative non-covalent interactions, such as hydrogen bonding, ionic/dipole interactions, metal coordination, and π–π stacking [174–176]. It has been shown that non-covalent cross-linked structures can be self-assembled to create supramolecular polymer networks (SPNs), which can respond to stimuli such as heat, light, pH, or electricity, i.e., be manipulated to obtain a wide variety of multifunctional materials with adequate mechanical properties [177, 178]. In other words, SPNs represent a promising approach for the development of a new generation of self-healing dynamic systems, which can allow the spontaneous formation of a three-dimensional network with fast and reversible responses to various environmental conditions.

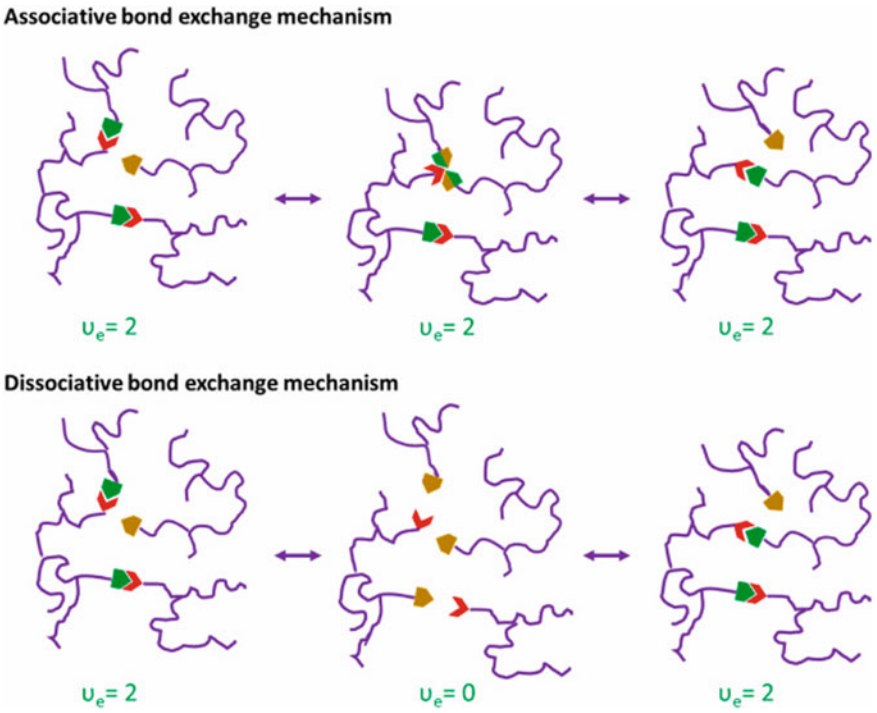

Fig. 9 Bond exchange mechanism of covalent adaptable networks, where υ_e is the cross-linking density. First is the associative bond exchange mechanism, where the overall cross-link density remains constant; i.e., cross-links are merely broken when new ones are created. Vitrimers might undergo associative or dissociative bond exchange mechanisms depending upon the covalent adaptable network present in the compound. Reproduced from [171] (Elsevier, CC-BY-NC-ND)

Various supramolecular epoxy systems have been reported in the literature [179–182]. Sordo and coworkers [179] described supramolecular epoxy-based rubbers incorporating a large number of physical cross-links through cooperative hydrogen bonds and chemical cross-links, looking for materials resistant to solvents and creep. Starting from a single reactive prepolymer, functionalized with hydrogen-bonding groups, a series of networks presenting different ratios of diepoxide and tetraepoxide were prepared (Fig. 10). The introduction of tetrafunctional epoxide, using 2-methylimidazole as the catalyst, gave rise to gelled materials with high rigidity and tensile strength and improved creep resistance. All materials presented self-healing, with 50–100% complete recovery in a day depending on tetraepoxide content.

Epoxy-based coatings with tailored hydrogen bonds have been prepared and studied by Villani and coworkers [180], who introduced physical cross-links (hydrogen bonds into an epoxy-amine network) by the incorporation of amide groups. These cross-links promoted enhanced temporary local network mobility and relaxation of the mechanical stresses, without significant changes in modulus and adhesion

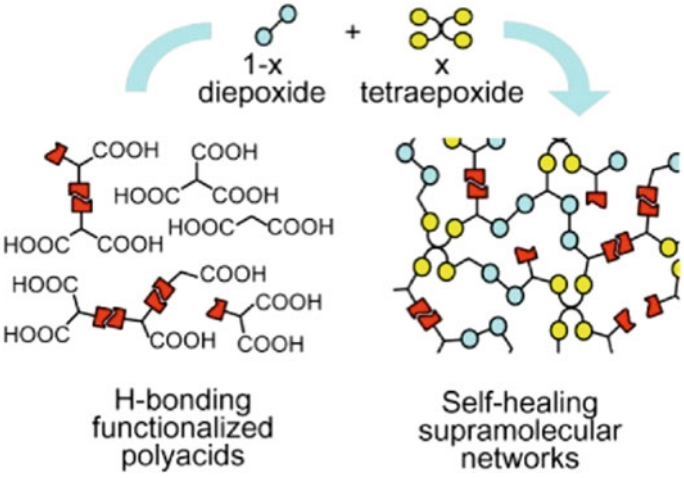

Fig. 10 Synthetic strategy used to generate insoluble hybrid networks containing a fixed amount of terminal H-bonding groups and a tunable number of cross-links. Step 1: partial amidation of poly(carboxylic acid)s with a fixed amount of an H-bonding molecule. Step 2: cross-linking with a variable amount of the difunctional DGEBA and tetrafunctional TGMDA epoxy resins. Reprinted (adapted) with permission from [Sordo, F., Mougnier, S.-J., Loureiro, N., Tournilhac, F., Michaud, V.: Design of self-healing supramolecular rubbers with a tunable number of chemical cross-links. Macromolecules 2015, 48, 4394]. Copyright 2015 American Chemical Society

behavior. The reversibility of hydrogen bonds also resulted in the efficient healing of superficial scratches with no detrimental effect on the adhesion properties.

Guadagno and coworkers [181] also developed structural self-healing resins based on dynamic hydrogen bonds supported by carbon nanotubes to enhance mechanical properties. A rubber-toughened epoxy matrix was filled with multi-wall carbon nanotubes (MWCNTs) covalently functionalized with barbiturate and thymine, which act as reversible healing agents due to simultaneous donor/acceptor character. Strong, attractive interactions between the rubber phase, finely dispersed in the matrix, and MWCNT walls have been formed due to reversible MWCNTs-bridges throughout the matrix. Healing efficiencies higher than 50% were reported for the epoxy resin loaded with 0.5 wt% MWCNTs functionalized with barbituric acid or thymine groups.

Shape memory polymers such as those described by Lendlein and Kelch [48] may also be considered for self-healing materials, the so-called shape memory-assisted self-healing (SMASH) [175]. This approach typically requires heating for healing to occur and is applicable to repairing superficial scratches, for example. Shape memory epoxy resin and its composites, including SMASH materials, have been recently reviewed by Luo and coworkers [183]. In one of the examples, self-healing coatings were prepared by inserting electrospinning thermoplastic poly(ε-caprolactone) (PCL) fibers into a shape memory epoxy matrix [184]. The self-healing of the coating after mechanical damage was triggered by heating, which promotes the

shape recovery of the matrix by approximating the crack surfaces, while the melting and subsequent flow of the PCL fibers were responsible to relink the crack.

The self-healing efficiency, at room temperature, of shape memory epoxy/graphene nanocomposites has been also studied [185]. The authors reported an improvement in the scratch resistance of the nanocomposite materials, which was attributed to the in-plane fracture resistance of the graphene sheets. It was concluded that the incorporation of graphene resulted in significant improvement in different properties compared to the pure shape memory epoxy matrix.

5 Conclusions

The state of the art on the extrinsic and intrinsic self-healing mechanisms for epoxy systems has been reviewed. New technologies involving dynamic bonds, supramolecular arrangements, and shape memory-assisted self-healing open a myriad of options in the development of epoxy materials for applications in medicine, electronics, and transportation (automotive, aeronautical, and naval industries). For instance, the reversible recovery characteristics of shape memory polymers have great potential in biomedical, driving sensing, and other fields, while multifunctional and high-performance integrated self-healing composite materials are promising in the aerospace field.

Although the interest in microcapsule-based systems, especially for coatings, and in vascular systems, with 3D architectures manufactured by VaSC, continues, there is a current trend toward the development of structures by 3D printing and recyclable epoxy vitrimers. The ability to control cross-link density and defects in epoxy networks will permit the achievement of materials with a better compromise between self-healing ability, mechanical properties, such as strength, toughness, creep resistance, and fatigue, and multifunctional features, such as recyclability, thermal and electrical transport, weldability, piezoelectricity, and tribological control. Self-healing nano-systems involving reactive nanoparticles (for covalent or non-covalent supramolecular dynamic systems) or the incorporation of nanocapsules/nanovascules, are going to be much enhanced and will probably guide many efforts of researchers in this field. Modeling using computer simulation is also an open field that can significantly assist in the creation of innovative multifunctional self-healing materials [186]. Intelligent design for material structure-performance-function integration and synergistic combinations brings big opportunities for new developments.

Nevertheless, a lot of work has yet to be done to produce cost-effective self-healing materials. In special, the development of commercially viable chemical systems/healing agents and testing protocols to better assess and understand the material properties over its lifetime (e.g., fatigue and post-reprocessing cycles).

Last but not least, in the search toward a more sustainable society, there is today a great interest in replacing, entirely or at least partially, epoxy polymers from petroleum products for bio-based resins. For instance, it was shown that shape

memory self-healing bio epoxy could also have degradable and recyclable properties [165, 168]. It must also be highlighted that the main purpose of self-healing materials is to effectively extend their lifetime, being an important way to reduce waste.

References

1. White, S.R., Sottos, N.R., Geubelle, P.H., Moore, J.S., Kessler, M.R., Sriram, S.R., Brown, E.N., Viswanathan, S.: Autonomic healing of polymer composites. Nature **409**, 794–797 (2001)
2. Wu, D.Y., Meure, S., Solomon, D.: Self-healing polymeric materials: a review of recent developments. Prog. Polym. Sci. **33**, 479–522 (2008)
3. Fainleib, A.M., Purikova, O.H.: Self-healing polymers: approaches of healing and their application. Polym. J. **41**, 4–18 (2019)
4. Zhang, F., Zhang, L., Yaseen, M., Huang, K.: A review on the self-healing ability of epoxy polymers. J. Appl. Polym. Sci. **138**, e50260 (2021)
5. Thakur, V.K., Kessler, M.R.: Self-healing polymer nanocomposite materials: a review. Polymer **69**, 369–383 (2015)
6. Kirkby, E.L., et al.: Performance of self-healing epoxy with microencapsulated healing agent and shape memory alloy wires. Polymer **50**, 5533–5538 (2009)
7. Trask, R.S., Williams, H.R., Bond, I.P.: Self-healing polymer composites: mimicking nature to enhance performance. Bioinspir. Biomim. **2**, 1–9 (2007)
8. Trask, R.S., Bond, I.P.: Bioinspired engineering study of Plantae vascules for self-healing composite structures. J. R. Soc. Interface **7**, 921–931 (2010)
9. Cremaldi, J.C., Bhushan, B.: Bioinspired self-healing materials: lessons from nature. Beilstein J. Nanotechnol. **9**, 907–935 (2018)
10. Pang, J.W.C., Bond, I.P.: A hollow fibre reinforced polymer composite encompassing self-healing and enhanced damage visibility. Compos. Sci. Technol. **65**, 1791–1799 (2005)
11. Wang, Y., Pham, D.T., Ji, C.: Self-healing composites: a review. Cogent Eng. **2**, 1075686 (2015)
12. Yuan, Y.C., Yin, T., Rong, M.Z., Zhang, M.Q.: Self healing in polymers and polymer composites. Concepts, realization and outlook: a review. eXPRESS Polym. Lett. **2**, 238–250 (2008)
13. Kessler, M.R., Sottos, N.R., White, M.R.: Self-healing structural composite materials. Compos. Part A, Appl. Sci. Manuf. **34**, 743–753 (2003)
14. Bond, I.P., Trask, R.S., Williams, H.R.: Self-healing fiber-reinforced polymer composites. MRS Bull. **33**, 770–774 (2008)
15. Kanu, N.J., Gupta, E., Vates, U.K., Singh, G.K.: Self-healing composites: a state-of-the-art review. Compos. A: Appl. Sci. Manuf. **121**, 474–486 (2019)
16. Nosonovsky, M., Rohatgi, P.: Biomimetics in Materials Science: Self-healing, Self-lubricating, and Self-cleaning Materials, vol. 152. Springer Series in Materials Science. Springer (2011)
17. Jin, H., Mangun, C.L., Stradley, D.S., Moore, J.S., Sottos, N.R., White, S.R.: Self-healing thermoset using encapsulated epoxy-amine healing chemistry. Polymer **53**, 581–587 (2012)
18. Brown, E.N., Sottos, N.R., White, S.R.: Fracture testing of a self-healing polymer composite. Exp. Mech. **42**, 372–379 (2002)
19. Safaei, F., Khorasani, S.N., Rahnama, H., Neisiany, R.E., Koochaki, M.S.: Single microcapsules containing epoxy healing agent used for development in the fabrication of cost efficient self-healing epoxy coating. Prog. Org. Coat. **114**, 40–46 (2018)
20. Guadagno, L., Longo, P., Raimondo, M., Naddeo, C., Mariconda, A., Vittoria, V., Iannuzzo, G., Russo, S.: Use of Hoveyda–Grubbs' second generation catalyst in self-healing epoxy mixtures. Compos. B. Eng. **41**, 296–301 (2011)

21. Jin, H., Miller, G.M., Pety, S.J., Griffin, A.S., Stradley, D.S., Roach, D., Sottos, N.R.: Fracture behavior of a self-healing, toughened epoxy adhesive. Int. J. Adhes. Adhes. **44**, 157–165 (2013)
22. Mcilroy, D.A., Blaiszik, B.J., Caruso, M.M., White, S.R., Moore, J.S., Sottos, N.R.: Microencapsulation of a reactive liquid-phase amine for self-healing epoxy composites. Macromolecules **43**, 1855–1859 (2010)
23. Caruso, M.M., Blaiszik, B.J., Jin, H., Schelkopf, S.R., Stradley, D.S., Sottos, N.R., White, S.R., Moore, J.S.: Robust, double-walled microcapsules for self-healing polymeric materials. Appl. Mater. Interfaces **2**, 1195–1199 (2010)
24. Weihermann, W.R.K., Meier, M.M., Pezzin, S.H.: Microencapsulated amino-functional polydimethylsiloxane as autonomous external self-healing agent for epoxy systems. J. Appl. Polym. Sci. **136**, 47627 (2019)
25. Cho, S.H., White, S.R., Braun, P.V.: Self-healing polymer coatings. Adv. Mater. **21**, 645–649 (2009)
26. Jackson, A.C., Bartelt, J.A., Braun, P.V.: Transparent self-healing polymers based on encapsulated plasticizers in a thermoplastic matrix. Adv. Funct. Mater. **21**, 4705–4711 (2011)
27. Celestine, A.-D.N., Sottos, N.R., White, S.R.: Autonomic healing of PMMA via microencapsulated solvent. Polymer **69**, 241–248 (2015)
28. Wang, H.P., Yuan, Y.C., Rong, M.Z., Zhang, M.Q.: Self-healing of thermoplastics via living polymerization. Macromolecules **43**, 595–598 (2010)
29. Chen, Y., Kushner, A.M., Williams, G.A., Guan, Z.: Multiphase design of autonomic self-healing thermoplastic elastomers. Nat. Chem. **4**, 467–472 (2012)
30. Utrera-Barrios, S., Verdejo, R., López-Manchado, M.A., Hernández Santana, M.: Evolution of self-healing elastomers, from extrinsic to combined intrinsic mechanisms: a review. Mater. Horiz. **7**, 2882–2902 (2020)
31. Yu, K., Xin, A., Feng, Z., Lee, K.H., Wang, Q.: Mechanics of self-healing thermoplastic elastomers. J. Mech. Phys. Solids **137**, 103831 (2020)
32. Zwaag, S.V.D.: An Introduction to Material Design Principles: Damage Prevention Versus Damage Management, pp. 2–19 (R. Hull, R. M. Osgood Jr., J. Parisi, & H. Warlimont, Orgs.). Springer (2007)
33. Jackson, M.D., et al.: Mechanical resilience and cementitious processes in Imperial Roman architectural mortar. Proc. Natl. Acad. Sci. U. S. A. **111**, 18484–18489 (2014)
34. De Rooij M., Van Tittelboom K., De Belie N., Schlangen E.: Self-Healing Phenomena in Cement-Based Materials. RILEM State-of-the-Art Reports, vol. 11. Springer Netherlands (2011)
35. Raghavan, J., Wool, R.: Interfaces in repair, recycling, joining and manufacturing of polymers and polymer composites. J. Appl. Polym. Sci. **71**, 775–785 (1999)
36. Dry, C.: Procedures developed for self-repair of polymer matrix composite materials. Compos. Struct. **35**, 263–264 (1996)
37. Wang, P.P., Lee, S., Harmon, J.P.: Ethanol-induced crack healing in poly(methyl methacrylate). J. Polym. Sci. B Polym. Phys. **32**, 1217–1227 (1994)
38. Lin, C.B., Lee, S.B., Liu, K.S.: Methanol-induced crack healing in poly(methyl methacrylate). Polym. Eng. Sci. **30**, 1399–1406 (1990)
39. Jud, K., Kausch, H.H., Williams, J.G.: Fracture mechanics studies of crack healing and welding of polymers. J. Mater. Sci. **16**, 204–210 (1981)
40. Toohey, K.S., et al.: Self-healing materials with microvascular networks. Nat. Mater. **6**, 581–585 (2007)
41. Xiao, D.S., Yuan, Y.C., Rong, M.Z.: Self-healing epoxy based on cationic chain polymerization. Polymer **50**, 2967–2975 (2009)
42. Samadzadeh, M., Hatami Boura, S., Peikari, M., Kasiriha, S.M., Ashrafi, A.: A review on self-healing coatings based on micro/nanocapsules. Prog. Org. Coat. **68**, 159–164 (2010)
43. Rule, J.D., Sottos, N.R., White, S.R.: Effect of microcapsule size on the performance of self-healing polymers. Polymer **48**, 3520–3529 (2007)

44. Urdl, K., Kandelbauer, A., Kern, W., Müller, U., Thebault, M., Zikulnig-Rusch, E.: Self-healing of densely crosslinked thermoset polymers—a critical review. Prog. Org. Coat. **104**, 232–249 (2017)
45. Yuan, L., Gu, A., Liang, G.: Preparation and properties of poly(urea–formaldehyde) microcapsules filled with epoxy resins. Mater. Chem. Phys. **110**, 417–425 (2008)
46. Yao, Y., Xiao, M., Liu, W.: A short review on self-healing thermoplastic polyurethanes. Macromol. Chem. Phys. **222**, 2100002 (2021)
47. Bekas, D.G., Tsirka, K., Baltzis, D., Paipetis, A.S.: Self-healing materials: a review of advances in materials, evaluation, characterization and monitoring techniques. Compos. B. Eng. **87**, 92–119 (2016)
48. Lendlein, A., Kelch, S.: Shape-memory polymers. Angew. Chem. Int. Ed. **41**, 2034–2057 (2002)
49. Wang, X., Zhao, J., Chen, M., Ma, L., Zhao, X., Dang, Z.M., et al.: Improved self-healing of polyethylene/carbon black nanocomposites by their shape memory effect. J. Phys. Chem. B **117**, 1467–1474 (2013)
50. Hornat, C.C., Urban, M.W.: Shape memory effects in self-healing polymers. Prog. Polym. Sci. **102**, 101208 (2020)
51. Habault, D., Zhang, H., Zhao, Y.: Light-triggered self-healing and shape-memory polymers. Chem. Soc. Rev. **42**, 7244–7256 (2013)
52. Kong, D., Li, J., Guo, A., Zhang, X., Xiao, X.: Self-healing high temperature shape memory polymer. Eur. Polym. J. **120**, 109279 (2019)
53. Burattini, S., Colquhoun, H.M., Greenland, B.W., Hayes, W.: A novel self-healing supramolecular polymer system. Faraday Discuss. **143**, 251–264 (2009)
54. Fox, J., Wie, J.J., Greenland, B.W., Burattini, S., Hayes, W., Colquhoun, H.M., et al.: Highstrength, healable, supramolecular polymer nanocomposites. J. Am. Chem. Soc. **134**, 5362–5368 (2012)
55. Coulibaly, S., Roulin, A., Balog, S., Biyani, M.V., Foster, E.J., Rowan, S.J., et al.: Reinforcement of optically healable supramolecular polymers with cellulose nanocrystals. Macromolecules **47**, 152–160 (2014)
56. van Gemert, G.M.L., Peeters, J.W., Söntjens, S.H.M., Janssen, H.M., Bosman, A.W.: Self-healing supramolecular polymers in action. Macromol. Chem. Phys. **213**, 234–242 (2012)
57. Kuhl, N., Bode, S., Hager, M.D., Schubert, U.S.: U.S. Schubert, Self-healing polymers based on reversible covalent bonds. In: Hager M., van der Zwaag S., Schubert U. (eds) Self-healing Materials. Advances in Polymer Science, vol 273. Springer, Cham (2015)
58. Scheltjens, G., Diaz, M.M., Brancart, J., Van Assche, G., Van Mele, B.: A self-healing polymer network based on reversible covalent bonding. React. Funct. Polym. **73**, 413–420 (2013)
59. Cho, S., Hwang, S.Y., Oh, D.X., Park, J.: Recent progress in self-healing polymers and hydrogels based on reversible dynamic B–O bonds: boronic/boronate esters, borax, and benzoxaborole. J. Mater. Chem. A **9**, 14630–14655 (2021)
60. Li, C.-H., Zuo, J.-L.: Self-healing polymers based on coordination bonds. Adv. Mater. **32**, 1903762 (2020)
61. Yang, Y., Urban, M.W.: Self-healing polymeric materials. Chem. Soc. Rev. **42**, 7446–7467 (2013)
62. Garcia, S.J.: Effect of polymer architecture on the intrinsic self-healing character of polymers. Eur. Polym. J. **53**, 118–125 (2014)
63. Hager, M.D., Zechel, S.: Chapter 3—Self-Healing Polymers: from General Basics to Mechanistic Aspects. In: Thomas, S., Surendran, A. (eds.) Self-Healing Polymer-Based Systems, Elsevier, pp. 75–94 (2020)
64. Deng, Y., et al.: Self-healing ability and application of impact hardening polymers. Polym. Test. **76**, 43–53 (2019)
65. Deng, Z., Hu, T., Lei, Q., He, J., Ma, P.X., Guo, B.: Stimuli-responsive conductive nanocomposite hydrogels with high stretchability, self-healing, adhesiveness, and 3D printability for human motion sensing. ACS Appl. Mater. Interfaces **11**, 6796–6808 (2019)
66. Bergman, S.D., Wudl, F.: Mendable polymers. J. Mater. Chem. **18**, 41–62 (2008)

67. Huang, X., Wang, X., Shi, C., Liu, Y., Wei, Y.: Research on synthesis and self-healing properties of interpenetrating network hydrogels based on reversible covalent and reversible non-covalent bonds. J. Polym. Res. **28**, 1 (2021)
68. Li, X., Yu, R., He, Y., Zhang, Y., Yang, X., Zhao, X., Huang, W.: Self-healing polyurethane elastomers based on a disulfide bond by digital light processing 3D printing. ACS Macro Lett. **8**, 1511–1516 (2019)
69. Li, Y., et al.: Novel polyurethane with high self-healing efficiency for functional energetic composites. Polym. Test. **76**, 82–89 (2019)
70. Yang, Y., et al.: Defect-targeted self-healing of multiscale damage in polymers. Nanoscale **12**, 3605–3613 (2020)
71. Mirmohseni, A., et al.: Self-healing waterborne polyurethane coating by pH-dependent triggered-release mechanism. J. Appl. Polym. Sci. **136**, 47082 (2019)
72. Li, H., et al.: Preparation and application of polysulfone microcapsules containing tung oil in self-healing and self-lubricating epoxy coating. Colloids Surf. A Physicochem. Eng. Asp. **518**, 181–187 (2017)
73. Tan, Y.J., Susanto, G.J., Ali, H.P.A., Tee, B.C.K.: Progress and roadmap for intelligent self-healing materials in autonomous robotics. Adv. Mater. **33**, 2002800 (2021)
74. Zhu, D.Y., Rong, M.Z., Zhang, M.Q.: Self-healing polymeric materials based on microencapsulated healing agents: from design to preparation. Prog. Polym. Sci. **49**, 176–215 (2014)
75. Da Costa, S.F., Zuber, M., Zakharova, M., Mikhaylov, A., Baumbach, T., Kunka, D., Pezzin, S.H.: Self-healing triggering mechanism in epoxy-based material containing microencapsulated amino-polysiloxane. Nano Select **3**, 577–593 (2022)
76. Romero-Sabat, G., Gago-Benedí, E., Rovira, J.J.R., González-Gálvez, D., Mateo, A., Medel, S., Chivite, A.T.: Development of a highly efficient extrinsic and autonomous self-healing polymeric system at low and ultra-low temperatures for high-performance applications. Compos. Part A Appl. Sci. Manuf. **145**, 106335 (2021)
77. I.P.S. Qamar, N.R. Sottos, R.S. Trask, Grand challenges in the design and manufacture of vascular self-healing. Multifunct. Mater. **3**, 013001 (2020)
78. Ullah, H., Azizli, K.A.M., Man, Z.B., Ismail, M.B.C., Khan, M.I.: The potential of microencapsulated self-healing materials for microcracks recovery in self-healing composite systems: a review. Polym. Rev. **56**, 429–485 (2016)
79. Das, R., Melchior, C., Karumbaiah, K.M.: 11—Self-healing composites for aerospace applications. In: Rana, S., Fangueiro, R. (eds.) Advanced Composite Materials for Aerospace Engineering, Woodhead Publishing, pp. 333–364 (2016)
80. Rahman, M.W., Shefa, N.R.: Minireview on self-healing polymers: versatility, application, and prospects. Adv. Polym. Technol. **2021**, 7848088 (2021)
81. Tiarks, F., Landfester, K., Antonietti, M.: Preparation of polymeric nanocapsules by miniemulsion polymerization. Langmuir **17**, 908–918 (2001)
82. Brown, E.N., et al.: In situ poly(urea-formaldehyde) microencapsulation of dicyclopentadiene. J. Microencapsul. **20**, 719–730 (2003)
83. Yuan, L., et al.: Preparation and characterization of poly(urea-formaldehyde) microcapsules filled with epoxy resins. Polymer **47**, 5338–5349 (2006)
84. Liu, X., Zhang, H., Wang, J., Wang, Z., Wang, S.: Preparation of epoxy microcapsule based self-healing coatings and their behavior. Surf Coat. Technol. **206**, 4976–4980 (2012)
85. Cho, S.H., et al.: Polydimethylsiloxane-based self-healing materials. Adv. Mater. **18**, 997–1000 (2006)
86. Jin, H.: Self-healing of High Temperature Cured Epoxy and Composites. PhD Thesis. University of Illinois at Urbana-Champaign, Illinois (2012)
87. Caruso, M.M., Delafuente, D.A., Ho, V., Sottos, N.R., Moore, J.S., White, S.R.: Solvent-promoted self-healing in epoxy materials. Macromolecules **40**, 8830–8832 (2007)
88. Knop, W.R., Meier, M.M., Pezzin, S.H.: Preparation and characterization of poly(urea-formaldehyde) microcapsules filled with dicyclopentadiene. Matéria (Rio J.) **19**, 266–273 (2014)

89. Blaiszik, B.J., Sottos, N.R., White, S.R.: Nanocapsules for self-healing materials. Compos. Sci. Technol. **68**, 978–986 (2008)
90. Brown, E.N., White, S.R., Sottos, N.R.: Microcapsule induced toughening in a self-healing polymer composite. J. Mater. Sci. **39**, 1703–1710 (2004)
91. Kessler, M.R., White, S.R.: Cure kinetics of the ring-opening metathesis polymerization of dicyclopentadiene. J. Polym. Sci. A: Polym. Chem. **40**, 2373–2383 (2002)
92. Skipor, A., Scheifer, S., Olson, B.: Self-healing Polymer Compositions (Motorola Inc. U) US: 2004007784-A1 (2004)
93. Liao, L., Zhang, W., Xin, Y., Wang, H.M., Zhao, Y., Li, W.: Preparation and characterization of microcapsule containing epoxy resin and its self-healing performance of anticorrosion covering material. Chin. Sci. Bull. **56**, 439–443 (2011)
94. Lang, S., Zhou, Q.: Synthesis and characterization of poly(urea-formaldehyde) microcapsules containing linseed oil for self-healing coating development. Prog. Org. Coat. **105**, 99–110 (2017)
95. Siva, T., Sathiyanarayanan, S.: Self healing coatings containing dual active agent loaded urea formaldehyde (UF) microcapsules. Prog. Org. Coat. **82**, 57–67 (2015)
96. Schlemper, D.M., Pezzin, S.H.: Self-healing epoxy coatings containing microcapsules filled with different amine compounds - a comparison study. Prog. Org. Coat. **156**, 106258 (2021)
97. Huang, M., Yang, J.: Facile microencapsulation of HDI for self-healing anticorrosion coatings. J. Mater. Chem. **21**, 11123–11130 (2011)
98. Henry, J.J.M.: Nano-based self-healing anti-corrosion coating. WO2012178193 (2012)
99. Mangun, C.L., Mader, A.C., Sottos, N.R., White, S.R.: Self-healing of a high temperature cured epoxy using poly(dimethylsiloxane) chemistry. Polymer **51**, 4063–4068 (2010)
100. El-Hadek, M.A., Tippur, H.V.: Simulation of porosity by microballoon dispersion in epoxy and urethane: mechanical measurements and models. J. Mater. Sci. **37**, 1649–1660 (2002)
101. Stappen, J.V., Bultreys, T., Gilabert, F.A., Hillewaere, X.K., Gómez, D.G., Tittelboomd, K.V., Dhaene, J., Belie, N.D., Paepegem, W.V., Prez, F.E.D., Cnudde, V.: The microstructure of capsule containing self-healing materials: a micro-computed tomography study. Mater. Charact. **119**, 99–109 (2016)
102. Mayo, C.S., Stevenson, A.W., Wilkins, S.W.: In-line phase-contrast x-ray imaging and tomography for materials science. Materials **5**, 937–965 (2012)
103. Mayo, C.S., Stevenson, A.W., Wilkins, S.W., Gao, D., Mookhoek, S., Meure, S., Hughes, T., Mardel, J.: Phase-contrast tomography for quantitative characterisation of self-healing polymers. Mater. Sci. Forum. **654**, 2322–2325 (2010)
104. Mookhoek, S.D., Mayo, S.C., Hughes, A.E., Furman, S.A., Fischer, H.R., van der Zwaag, S.: Applying SEM-based x-ray microtomography to observe self-healing in solvent encapsulated thermoplastic materials. Adv. Eng. Mater. **12**, 228–234 (2010)
105. Peñas-Caballero, M., Santana, M.H., Verdejo, R., Lopez-Manchado, M.A.: Measuring self-healing in epoxy matrices: The need for standard conditions. React. Funct. Polym. **161**, 104847 (2021)
106. Mikhaylov, A., Zakharova, M., Vlnieska, V., Khanda, A., Bremer, S., Zuber, M., Pezzin, S.H., Kunka, D.: Inverted Hartmann mask made by deep X-ray lithography for single-shot multi-contrast X-ray imaging with laboratory setup. Opt. Express **30**, 8494–8509 (2022)
107. Wei, H., Wang, Y., Guo, J., Shen, N.Z., Jiang, D., Zhang, X., Yan, X., Zhu, J., Wang, Q., Shao, L., Lin, H., Wei, S., Guo, Z.: Advanced micro/nanocapsules for self-healing smart anticorrosion coatings. J. Mater. Chem. A **3**, 469–480 (2015)
108. Bagale, U.D., Sonawane, S.H.: Synthesis of nanocapsules using safflower oil for self-healing material. Nanomater. Energy **8**, 42–50 (2019)
109. Olugebefola, S.C., Aragón, A.M., Hansen, C.J., Hamilton, A.R., Kozola, B.D., Wu, W., et al.: Polymer microvascular network composites. J. Compos. Mater. **44**, 2587–2603 (2010)
110. Motuku, M., Vaidya, U.K., Janowski, G.M.: Parametric studies on self-repairing approaches for resin infused composites subjected to low velocity impact. Smart Mater. Struct. **8**, 623–638 (1999)

111. Bleay, S.M., Loader, C.B., Hawyes, V.J., Humberstone, L., Curtis, P.T.: A smart repair system for polymer matrix composites. Compos. Part A Appl. Sci. Manuf. **32**, 1767–76 (2001)
112. Trask, R.S., Bond, I.P.: Biomimetic self-healing of advanced composite structures using hollow glass fibers. Smart Mater. Struct. **15**, 704–710 (2006)
113. Williams, H.R., Trask, R.S., Bond, I.P.: Self-healing composite sandwich structures. Smart Mater. Struct. **16**, 1198–1207 (2007)
114. Dry, C.M.: Self-repairing, reinforced matrix materials (Individual U). US:7022179-B1 (2006)
115. Sinha-Ray, S., Pelot, D.D., Zhou, Z.P., Rahman, A., Wu, X.F., Yarin, A.L.: Encapsulation of self-healing materials by coelectrospinning, emulsion electrospinning, solution blowing and intercalation. J. Mater. Chem. **22**, 9138–9146 (2012)
116. Almutairi, M.D., Aria, A.I., Thakur, V.K., Khan, M.A.: Self-healing mechanisms for 3D-printed polymeric structures: from lab to reality. Polymers **12**, 1534 (2020)
117. Therriault, D., Shepherd, R.F., White, S.R., Lewis, J.A.: Fugitive inks for direct-write assembly of three-dimensional microvascular networks. Adv. Mater. **17**, 395–399 (2005)
118. Toohey, K.S., Hansen, C.J., Lewis, J.A., White, S.R., Sottos, N.R.: Delivery of two-part self-healing chemistry via microvascular networks. Adv. Funct. Mater. **19**, 1399–1405 (2009)
119. Hansen, C.J., Wu, W., Toohey, K.S., Sottos, N.R., White, S.R., Lewis, J.A.: Self-healing materials with interpenetrating microvascular networks. Adv. Mater. **21**, 4143–4147 (2009)
120. Aissa, B., Haddad, E., Jamroz, W., Hassani, S., Farahani, R.D., Merle, P.G., et al.: Micromechanical characterization of single-walled carbon nanotube reinforced ethylidene norbornene nanocomposites for self-healing applications. Smart Mater. Struct. **21**, 105028 (2012)
121. Huang, C.Y., Trask, R.S., Bond, I.P.: Characterization and analysis of carbon fibre-reinforced polymer composite laminates with embedded circular vasculature. J. R. Soc. Interface **7**, 1229–1241 (2010)
122. Norris, C.J., Bond, I.P., Trask, R.S.: Interactions between propagating cracks and bioinspired self-healing vascules embedded in glass fibre reinforced composites. Compos. Sci. Technol. **71**, 847–853 (2011)
123. Kousourakis, A., Bannister, M.K., Mouritz, A.P.: Tensile and compressive properties of polymer laminates containing internal sensor cavities. Compos. Part A Appl. Sci. Manuf. **39**, 1394–1403 (2008)
124. Bekas, D.G., Baltzis, D., Paipetis, A.S.: Nano-reinforced polymeric healing agents for vascular self-repairing composites. Mater. Des. **116**, 538–544 (2017)
125. Norris, C.J., White, J.A.P., McCombe, G., Chatterjee, P., Bond, I.P., Trask, R.S.: Autonomous stimulus triggered self-healing in smart structural composites. Adv. Funct. Mater. **21**, 3624–3633 (2011)
126. Luterbacher, R., Trask, R.S., Bond, I.P.: Static and fatigue tensile properties of cross-ply laminates containing vascules for self-healing applications. Smart Mater. Struct. **25**, 015003 (2016)
127. Patrick, J.F., Hart, K.R., Krull, B.P., Diesendruck, C.E., Moore, J.S., White, S.R., Sottos, N.R.: Continuous self-healing life cycle in vascularized structural composites. Adv. Mater. **26**, 4302–4308 (2014)
128. Gergely, R.C.R., Pety, S.J., Krull, B.P., Patrick, J.F., Doan, T.Q., Coppola, A.M., Thakre, P.R., Sottos, N.R., Moore, J.S., White, S.R.: Multidimensional vascularized polymers using degradable sacrificial templates. Adv. Funct. Mater. **25**, 1043–1052 (2015)
129. Cuvellier, A., Torre-Muruzabal, A., Van Assche, G., De Clerck, K., Rahier, H.: Selection of healing agents for a vascular self-healing application. Polym. Test. **62**, 302–310 (2017)
130. Yamaguchi, M., Ono, S., Terano, M.: Self-repairing property of polymer network with dangling chains. Mater. Lett. **61**, 1396–1399 (2007)
131. Chian, W., Timm, D.C.: Chemical/mechanical analyses of anhydride-cured thermosetting epoxys: DGEBA/NMA/BDMA. Macromolecules **37**, 8098–8109 (2004)
132. Outwater, J.O., Gerry, D.J.: On the fracture energy, rehealing velocity and refracture energy of cast epoxy resin. J. Adhes. **1**, 290–298 (1969)
133. Kim, Y.H., Wool, R.P.: A theory of healing at a polymer–polymer interface. Macromolecules **16**, 1115–1120 (1983)

134. Pascault J.-P., Williams R.J.J.: Epoxy Polymers: New Materials and Innovations, pp. 1–12. Wiley-VCH, New Jersey (2010)
135. Fejos, M., Molnar, K., Karger-Kocsis, J.: Epoxy/polycaprolactone systems with triple-shape memory effect: electrospun nanoweb with and without graphene versus cocontinuous morphology. Materials **6**, 4489–4504 (2013)
136. Wei, H., Yao, Y., Liu, Y., Leng, J.: A dual-functional polymeric system combining shape memory with self-healing properties. Compos B. **83**, 7–13 (2015)
137. Yao, Y., Wang, J., Lu, H., Xu, B., Fu, Y., Liu, Y., Leng, J.: Thermosetting epoxy resin/thermoplastic system with combined shape memory and self-healing properties. Smart Mater. Struct. **25**, 015021 (2016)
138. Zako, M., Takano, N.: Intelligent material systems using epoxy particles to repair microcracks and delamination damage in GFRP. J. Intell. Mater. Syst. Struct. **10**, 836–841 (1999)
139. Jones, F., Hayes, S.A.: Self-healing composite material. University of Sheffeld G, WO:2005066244-A2 (2005)
140. Meure, S., Varley, R.J., Dong, Y.W., Mayo, S., Nairn, K., Furman, S.: Confirmation of the healing mechanism in a mendable EMAA-epoxy resin. Eur. Polym. J. **48**, 524–531 (2012)
141. Hayes, S.A., Jones, F.R., Marshiya, K., Zhang, W.: A self-healing thermosetting composite material. Compos. Part A Appl. Sci. Manuf. **38**, 1116–1120 (2007)
142. Luo, X., Ou, R., Eberly, D.E., Singhal, A., Viratyaporn, W., Mather, P.T.: A thermoplastic/thermoset blend exhibiting thermal mending and reversible adhesion. Appl. Mater. Interfaces **1**, 612–620 (2009)
143. Hayes, S.A., Zhang, W., Branthwaite, M., Jones, F.R.: Self-healing of damage in fibre-reinforced polymer–matrix composites. J. R. Soc. Interface **4**, 381–387 (2007)
144. Pingkarawat, K., Wang, C.H., Varley, R.J., Mouritz, A.P.: Self-healing of delamination cracks in mendable epoxy matrix laminates using poly[ethylene-co-(methacrylic acid)] thermoplastic. Compos. Part A Appl. Sci. Manuf. **43**, 1301–1307 (2012)
145. Pingkarawat, K., Bhat, T., Craze, D.A., Wang, C.H., Varley, R.J., Mouritz, A.P.: Healing of carbon fibre–epoxy composites using thermoplastic additives. Polym Chem **4**, 5007–5015 (2013)
146. Pingkarawat, K., Dell'Olio, C., Varley, R.J., Mouritz, A.P.: An efficient healing agent for high temperature epoxy composites based upon tetra-glycidyl diamino diphenyl methane. Compos. Part A-Appl. Sci. Manuf. **78**, 201–210 (2015)
147. Thostenson, E.T., Chou, T.W.: Carbon nanotube networks: sensing of distributed strain and damage for life prediction and self healing. Adv. Mater. **18**, 2837–2841 (2006)
148. Guo, S., Meshot, E.R., Kuykendall, T., et al.: Nanofluidic transport through isolated carbon nanotube channels: advances, controversies, and challenges. Adv. Mater. **27**, 5726–5737 (2015)
149. Kausar, A.: Self-healing polymer/carbon nanotube nanocomposite: a review. J. Plast. Film Sheeting **37**, 160–181 (2021)
150. Sriram, S.R.: Development of Self-healing Polymer Composites and Photoinduced Ring Opening Metathesis Polymerisation. PhD thesis, University of Illinois at Urbana-Champaign, Urbana, USA (2002)
151. Chen, X., Wudl, F., Mal, A.K., Shen, H., Nutt, S.R.: New thermally patchable highly cross-linked polymeric materials. Macromolecules **36**, 1802–1807 (2003)
152. Chen, X., Dam, M.A., Ono, K., Mal, A., Shen, H.B., Nutt, S.R., et al.: A thermally re-mendable cross-linked polymeric material. Science **295**, 1698–1702 (2002)
153. Liu, Y.L., Hsieh, C.Y.: Crosslinked epoxy materials exhibiting thermal remendablility and removal from multifunctional maleimide and furan compounds. J. Polym. Sci. Part A Polym. Chem. **44**, 905–913 (2006)
154. Kuang, X., Liu, G., Dong, X., Liu, J., Xu, D.: Wang, Facile fabrication of fast recyclable and multiple self-healing epoxy materials through Diels-Alder adduct cross-linker. J. Polym. Sci. Part A **53**, 2094–2103 (2015)
155. Wudl, F., Chen, X.: Thermally Re-mendable Cross-linked Polymers. University of California U, US:2004014933-A1 (2004)

156. Harris, K.M., Rajagopalan, M.: Self healing Polymers in Sports Equipment (Acushnet Company U) US:2003032758-A1 (2003)
157. Plaisted, T.A., Amirkhizi, A.V., Arbelaez, D., Nemat-Nasser, S.C., Nemat-Nasser, S.: Self-healing structural composites with electromagnetic functionality. Smart Struct. Mater. SPIE-5054, 372–381 (2003)
158. Peterson, A.M., Jensen, R.E., Palmese, G.R.: Reversibly cross-linked polymer gels as healing agents for epoxy− amine thermosets. ACS Appl. Mater. Interfaces **1**, 992–995 (2009)
159. Peterson, A.M., Jensen, R.E., Palmese, G.R.: Room-temperature healing of a thermosetting polymer using the Diels−Alder reaction. ACS Appl. Mater. Interfaces **2**, 1141–1149 (2010)
160. Saegusa, T., Sada, K., Naka, A., Nomura, R., Saegusa, T.: Synthesis and redox gelation of disulfide-modified polyoxazoline". Macromolecules **26**, 883–887 (1993)
161. Lei, Z.Q., Xiang, H.P., Yuan, Y.J., Rong, M.Z., Zhang, M.Q.: Room-temperature self-healable and remoldable cross-linked polymer based on the dynamic exchange of disulfide bonds. Chem. Mater. **26**, 2038–2046 (2014)
162. Memon, H., Wei, Y.: Welding and reprocessing of disulfide-containing thermoset epoxy resin exhibiting behavior reminiscent of a thermoplastic. J. Appl. Polym. Sci. **137**, 49541 (2020)
163. Fengtao, Z., Zijian, G., Wenyan, W., Xingfeng, L., Baoliang, Z., Hepeng, Z., Qiuyu, Z.: Preparation of self-healing, recyclable epoxy resins and low-electrical resistance composites based on double-disulfide bond exchange. Compos. Sci. Technol. **167**, 79–85 (2018)
164. Si, H., Zhou, L., Wu, Y., Song, L., Kang, M., Zhao, X., Chen, M.: Rapidly reprocessable, degradable epoxy vitrimer and recyclable carbon fiber reinforced thermoset composites relied on high contents of exchangeable aromatic disulfide crosslinks. Compos. Part B **199**, 108278 (2020)
165. Di Mauro, C., Malburet, S., Graillot, A., Mija, A.: Recyclable, repairable, and reshapable (3R) thermoset materials with shape memory properties from bio-based epoxidized vegetable oils. ACS Appl. Bio Mater. **3**, 8094–8104 (2020)
166. De Luzuriaga, A.R., Martin, R., Markaide, N., Rekondo, A., Cabanero, G., Rodriguez, J., Odriozola, I.: Epoxy resin with exchangeable disulfide crosslinks to obtain reprocessable, repairable and recyclable fiber-reinforced thermoset composites. Mater. Horiz. **3**, 241–247 (2016)
167. Denissen, W., Winne, J.M., Du Prez, F.E.: Vitrimers: permanent organic networks with glass-like fluidity. Chem. Sci. **7**, 30–38 (2016)
168. Scheutz, G.M., Lessard, J.J., Sims, M.B., Sumerlin, B.S.: Adaptable crosslinks in polymeric materials: resolving the intersection of thermoplastics and thermosets. J. Am. Chem. Soc. **141**, 16181–16196 (2019)
169. Liu, T., Hao, C., Zhang, S., Yang, X., Wang, L., Han, J., Li, Y., Xin, J., Zhang, J.: A self-healable high glass transition temperature bioepoxy material based on vitrimer chemistry. Macromolecules **51**, 5577–5585 (2018)
170. Memon, H., Liu, H., Rashid, M.A., Chen, L., Jiang, Q., Zhang, L., Wei, Y., Liu, W., Qiu, Y.: Vanillin-based epoxy vitrimer with high performance and closed-loop recyclability. Macromolecules **53**, 621–630 (2020)
171. Memon, H., Wei, Y., Zhu, C.: Recyclable and reformable epoxy resins based on dynamic covalent bonds—present, past, and future. Polym. Test. **105**, 107420 (2022)
172. Radl, S., Kreimer, M., Griesser, T., Oesterreicher, A., Moser, A., Kern, W., Schlögl, S.: New strategies towards reversible and mendable epoxy based materials employing [4πs + 4πs] photocycloaddition and thermal cycloreversion of pendant anthracene groups. Polymer **80**, 76–87 (2015)
173. Hughes, T., Simon, George P., Saito, K.: Light-healable epoxy polymer networks via anthracene dimer scission of diamine crosslinker. ACS Appl. Mater. Interfaces **11**, 19429–19443 (2019)
174. Cordier, P., Tournilhac, F., Soulié-Ziakovic, C., et al.: Self-healing and thermoreversible rubber from supramolecular assembly. Nature **451**, 977–980 (2008)
175. Yan, T., Schröter, K., Herbst, F., Binder, W.H., Thurn-Albrecht, T.: What controls the structure and the linear and nonlinear rheological properties of dense, dynamic supramolecular polymer networks? Macromolecules **50**, 2973–2985 (2017)

176. Campanella, A., Döhler, D., Binder, W.H.: Self-healing in supramolecular polymers. Macromol. Rapid Commun. **39**, 1700739 (2018)
177. Seiffert, S., Sprakel, J.: Physical chemistry of supramolecular polymer networks. Chem. Soc. Rev. **41**, 909–930 (2012)
178. Aida, T., Meijer, E.W., Stupp, S.I.: Functional supramolecular polymers. Science **335**, 813–817 (2012)
179. Sordo, F., Mougnier, S.-J., Loureiro, N., Tournilhac, F., Michaud, V.: Design of self-healing supramolecular rubbers with a tunable number of chemical cross-links. Macromolecules **48**, 4394 (2015)
180. Villani, M., Deshmukh, Y.S., Camlibel, C., Esteves, A.C.C., de With, G.: Superior relaxation of stresses and self-healing behavior of epoxy-amine coatings. RSC Adv. **6**, 245–259 (2016)
181. Guadagno, L., Vertuccio, L., Naddeo, C., Calabrese, E., Barra, G., Raimondo, M., Sorrentino, A., Binder, W.H., Michael, P., Rana, S.: Self-healing epoxy nanocomposites via reversible hydrogen bonding. Compos. Part B: Eng. **157**, 1–13 (2019)
182. Rodriguez, E.D., Luo, X., Mather, Patrick T.: Linear/network poly(ε-caprolactone) blends exhibiting shape memory assisted self-healing (SMASH). ACS Appl. Mater. Interfaces **3**, 152–161 (2011)
183. Luo, L., Zhang, F., Leng, J.: Shape memory epoxy resin and its composites: from materials to applications. AAAS Research **2022**, 9767830 (2022)
184. Luo, X., Mather, P.T.: Shape memory assisted self-healing coating. ACS Macro Lett. **2**, 152–156 (2013)
185. Xiao, X., Xie, T., Cheng, Y.-T.: Self-healable graphene polymer composites. J Mater Chem **20**, 3508–3514 (2010)
186. Zhang, M.Q., Rong, M.Z.: Theoretical consideration and modeling of self-healing polymers. J. Polym. Sci. B Polym. Phys. **50**, 229–241 (2012)

Synthetic Design of Self-Healing Epoxy Systems

Xiwei Xu, Jin Zhu, and Songqi Ma

Abstract Epoxy resins are widely used in our life due to their excellent thermal and mechanical properties, dimensional stability, and processability, but they are inevitably impacted by chemical/physical events, which leads to micro-cracks during use. Self-healable epoxy resins can repair the micro-cracks, greatly extending the life and safety of the resin. This chapter reviews the methods of achieving self-healable epoxy resins, including embedding hollow fibers (or microcapsules) filled with healing agents, thermoplastic additives, or dynamic bonds in the epoxy networks. The self-healing mechanisms, advantages, and disadvantages of each method are summarized. Finally, the conclusion and prospect of self-healing epoxy resins are highlighted.

Keywords Epoxy resins · Extrinsic self-healing · Intrinsic self-healing · Dynamic bonds

1 Introduction

Biological tissues can self-repair when damaged. As an example, most animal skins can completely self-repair within a few hours or days when damaged to protect other subcutaneous tissues from further harm. In contrast, traditional synthetic resins are challenging to achieve self-healing when damaged and may lose or weaken their special functions such as super hydrophobicity, anti-corrosion property, antibacterial activity, and conductivity.

Resins with self-healing properties can repair damage triggered by physical or chemical events in working conditions or specific environments (such as heating) at the molecular level. It is complicated and trivial to design resin structures similar to

X. Xu · J. Zhu · S. Ma (✉)
Key Laboratory of Bio-Based Polymeric Materials Technology and Application of Zhejiang Province, Laboratory of Polymers and Composites, Ningbo Institute of Materials Technology and Engineering, Chinese Academy of Sciences, Ningbo 315201, P. R. China
e-mail: msqhyd@126.com

X. Xu
University of Chinese Academy of Sciences, Beijing 100049, P. R. China

N. Hameed et al. (eds.), *Multifunctional Epoxy Resins*, Engineering Materials,
https://doi.org/10.1007/978-981-19-6038-3_5

living organism's self-healing and regeneration ability as a benchmark [1] because organisms possess exceptionally complex and highly synergistic cells. Cognizant of the broad application of resins, straightforward and efficient methods in imparting self-healing properties to resins received widespread attention. According to the self-healing mechanisms, we can simply divide the self-healing process into physical and chemical processes. The main physical self-healing processes include diffusion, [2] shape-memory effects, [3] the loading of superparamagnetic nanoparticles,[4] and phase-separated morphologies [5, 6]. At present, the design of self-healing systems by chemical processes including the covalent, [7–9] free-radical, [10, 11] or supramolecular [12–14] dynamic bonds have attracted significant attention from researchers.

Epoxy resin is a high-performance thermosetting resin obtained by reacting epoxide-containing monomers/oligomers with curing agents. It is often used to construct adhesives, coatings, and composites on account of its favorable mechanical performance, thermal properties, dimensional stability, and processability. However, during service, epoxy resin will inevitably be damaged by external factors, resulting in cracks at the macro or molecular scale, reducing the material's mechanical performance and even compromising its special functions, such as anti-fouling, hydrophobic, and antibacterial effects. On account of the highly and permanently cross-linked network structure of traditional epoxy resin, using physical processes (such as diffusion and shape-memory effects) alone could not achieve a satisfactory self-healing effect. Combining chemical processes with physical processes can lead to a superior self-healing effect. Through the works reported recently, the self-healing of epoxy resin can be achieved by adding hollow fiber [15–17], microcapsule[17–19], and thermoplastic additive [20] to the epoxy resin matrix, which is known as extrinsic self-healing. During the past two decades, intrinsic self-healing epoxy networks triggered by dynamic bonds have captured increasing attention. Especially since Leibler's pioneer report on vitrimers, [21] the application of dynamic chemistries in epoxy resins has been rapidly developed, and various dynamic bonds have been used to construct self-healing epoxy resins.

2 Extrinsic Self-Healing Epoxy Resins

2.1 Hollow Fiber

Most of the micro-cracks on the resins are generated when they receive an external impact. Therefore, adding appropriate hollow fibers to the epoxy resins can reduce the expansion of cracks in the resins when impacted by force. Meanwhile, adding a certain amount of self-healing agents (such as small-molecule monomer and initiator) to the hollow fibers can realize the self-repairing of cracks (Fig. 1). When cracks are generated in the epoxy resins from an external force, hollow fibers at the cracks will also be broken, and the healing agents stored in the hollow fibers will fill the

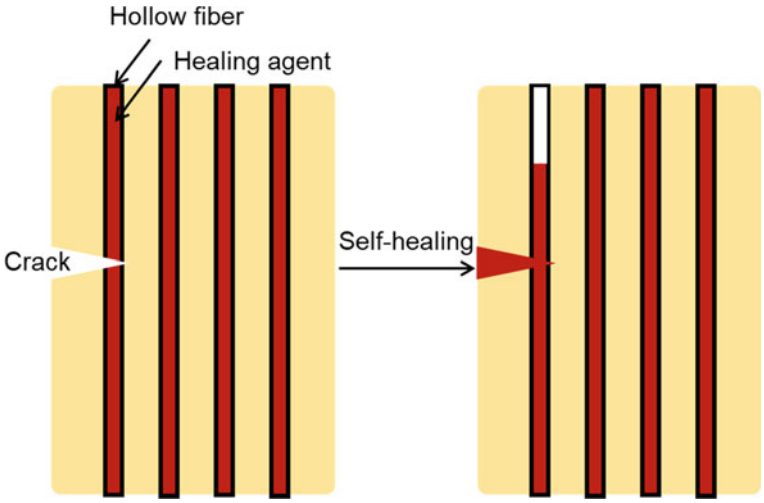

Fig. 1 Self-healable epoxy resins based on hollow fiber filled with healing agent

cracks and then quickly cure under the action of the initiator to regain the mechanical properties of the resin.

In 1996, Dry [22] developed an epoxy resin/hollow fiber composite that achieved self-healing of the internal cracks. The authors employed microscopy observation and mechanical properties analysis to characterize the self-repairing performance of the composite and found that the cracks can be controlled by hollow fiber, and the adhesive entered the crack and repaired it. In 2005, Pang and Bond [23] developed a bionic visualized seal-healing method, ultraviolet fluorescent dyes as well as the healing agent were filled into the hollow fiber, and the self-healing and impact damage was visualized through the exudation of the ultraviolet fluorescent dyes when the hollow fiber was broken. Bending tests showed that the damaged resin self-healed with high efficiency. Kling and Czigány [20] replaced the commonly used epoxy resin with unsaturated polyester resin as the healing agent to fill the hollow fiber, mainly because the curing of unsaturated polyester material was less susceptible to the mix than that of the commonly used healing agent (epoxy resin) in the reported literature. Curing of the unsaturated polyester led to a 20% increase in flexural properties.

2.2 Microcapsule

Up to now, the microcapsule is one of the largest reported self-healing approaches for epoxy resin [24]. Similar to the hollow fiber method, the healing agent (often small-molecule monomers) is encapsulated in microcapsules. The catalyst for curing is evenly distributed in the resin matrix. On account of its outstanding self-healing

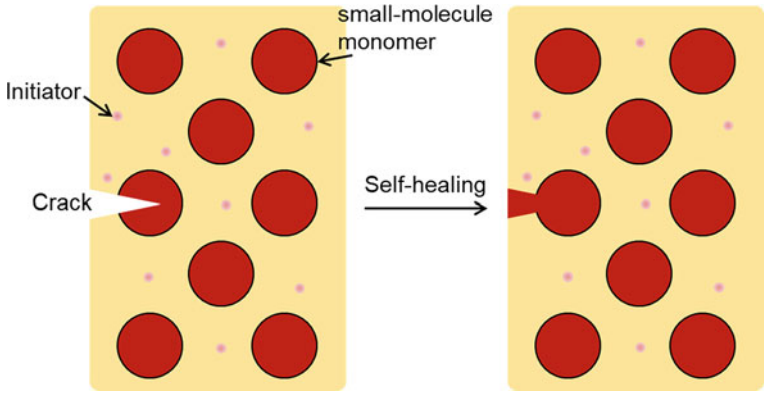

Fig. 2 Self-healable epoxy resins based on microcapsules filled with a healing agent

efficiency and no requirement of manual intervention, it is widely used in metal anti-corrosion coatings [25].

White et al. [26] innovatively developed a structural polymer material that can self-heal in a straight line without manual intervention by the microcapsule self-repairing method (Fig. 2). When a crack formed upon the damage, it would rupture the microcapsule. The self-healing agents released and interacted with the dispersed initiator (or catalyst) in the matrix, which realized polymerization and achieved a self-healing effect. According to the fracture toughness test, the willful recovery rate of the material on the fracture surface reaches 75%, which has a relatively high application value. In addition, the authors also expected their mechanism to be applied to other hard materials, including glass, ceramics, etc.

Anti-corrosion of metallic materials is of great significance both economically and ecologically [27, 28]. Anti-corrosion coatings can effectively block water and ions from corroding the metal substrates. Nevertheless, once the coating is damaged, water and ions can freely reach the metal substrate, causing rapid corrosion and eventually cracking of the coating. Adding corrosion inhibitors can improve the corrosion resistance of the coatings. However, such materials are now widely restricted by EU law because of ecological and toxicological concerns [29, 30]. Thus, it is significant to develop self-healable anti-corrosion coatings. Suryanarayana et al. [31] investigated the self-healing efficiency of epoxy coatings containing linseed oil-filled microcapsules and applied it to the anti-corrosion of metal materials. The authors prepared microcapsules in situ by urea–formaldehyde resin. The linseed oil in the microcapsules is released under the mechanical action to repair the cracks. Meanwhile, owing to the repair of the epoxy coating cracks, the metal protected by the anti-corrosion coating was re-protected.

2.3 Thermoplastic Additives

Adding thermoplastic resin or additives to the thermosetting resins is also a way to realize self-repairing for thermosetting resin/composite (Fig. 3). The above two methods (hollow fiber and microcapsule) cannot perform repeated self-repair after the resin achieves self-repair and are subject to certain restrictions in the application. In addition, the preparation process in the above two methods required the encapsulation of the healing agent, which is relatively complex and can often only be used in the preparation of composite materials. While thermoplastic particles only need to be added during the molding process of the thermosetting resin matrix, which is simpler and more efficient.

Zako and Takano [32] loaded thermoplastic particles at a volume ratio of 40% to the glass fiber/epoxy composite (GFRP) laminate. The three-point bending and tensile tests found that the addition of thermoplastic particles did not decrease mechanical properties, and since thermoplastic resins can melt at elevated temperatures, cracks in the matrix of the composite material can be self-healed. The service life of the composite material can be increased.

Meure et al. [33] developed a thermoplastic healing agent (polyethylene-co-methacrylic acid (EMAA) particles) for epoxy networks and proposed a related mechanism. Incorporating the thermoplastic additive improved the epoxy resin's breaking strength and achieved critical stress strength recovery up to 85%. They also revealed the self-healing mechanism: recovery of damaged resin's strength through the formation of a sticky EMAA layer between the EMAA particle and epoxy matrix, while swelling of the healing agent occurs during heating and forces it into the broken area of the epoxy matrix, facilitating its repair.

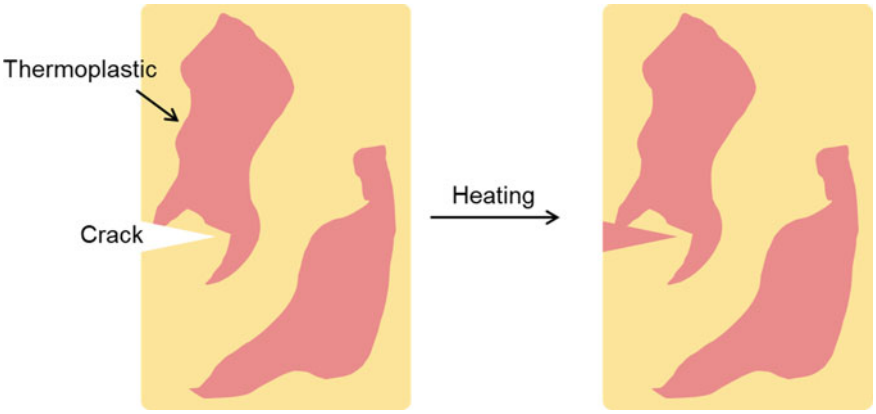

Fig. 3 Self-healable epoxy resins based on thermoplastic additives

3 Intrinsic Self-Healing Epoxy Resins

The damage to traditional epoxy resin often needs to be repaired by welding, gluing, and other methods. Adding hollow fiber or microcapsule filled with healing agents and thermoplastic resin can be an extension of this traditional repair method. During the past two decades, dynamic bonds-based self-healable epoxy resins have made great progress. Here is a theory about self-healing properties that are instructive for developing self-healable epoxy resins from dynamic bonds. From the point of thermodynamics, to realize the resin's self-repairing process, it is indispensable to satisfy the change of Gibbs free energy (ΔG ($=\Delta H - T\Delta S$) < 0) of the whole process. The above-mentioned self-repairing process mainly follows two processes: (1) breakage of the molecular chains at the rupture when a physical or chemical event damaged the material, and (2) thermal motion and diffusion of the molecular chains when the interface distance was appropriate, and under the premise that the two interfaces are fused by the exchange between the dynamic bonds on the molecular chain. In this process, due to the exchange reaction, the enthalpy value before and after the reaction was almost unchanged, so the ΔH in this process was almost zero. However, the change in the degree of the disorder before and after the reaction was significant. The increase in the degree of disorder leads to the migration of molecular chains on the fracture surface to the gap and eventually fused. Since ΔH can hardly change greatly, ΔG can be assumed as $(-T\Delta S)$. For the sake of increasing the driving force for self-repairing, it was a feasible idea to increase the amount of disorder. Reducing the number of atoms in repeating units between two dynamic bonds can increase the degree of disorder (ΔS) in the process of dynamic bond exchange and molecular chain migration, and there are some efficient approaches such as increasing the dynamic bond content and designing dynamic bonds on the main chain instead of side chains. In addition, as shown in Fig. 4, increasing the flexibility of the molecular chain of the polymer network is also beneficial to the increase of ΔS. The relationships between the length of the repeating unit of the molecular chain, the flexibility of the chain segment and the change of Gibbs free energy (ΔG) are shown in Fig. 4.

The above-mentioned methods for realizing the self-healing feature of epoxy resins are all by adding external healing agents. As a result, the currently commercial epoxy resin can be directly modified, the research is relatively mature, and they are widely used. However, these methods still have some difficult problems to solve. For example, the first two methods (hollow fiber and microcapsule) can only endow the self-healing property for one time. In addition, these two methods are suitable for composite materials. They are difficult to apply in pure resin materials such as coatings, adhesives. These two methods need to add hollow fibers or microcapsules. Adding thermoplastics to thermosetting epoxy resin seems to be a better method, which can achieve self-healing multiple times, and the preparation was relatively simple, but there are still several issues. As an example, to achieve a better self-healing effect, it is essential to add a large number of thermoplastic additives [32]. In addition, the loading of a large amount of thermoplastic resin inevitably reduces

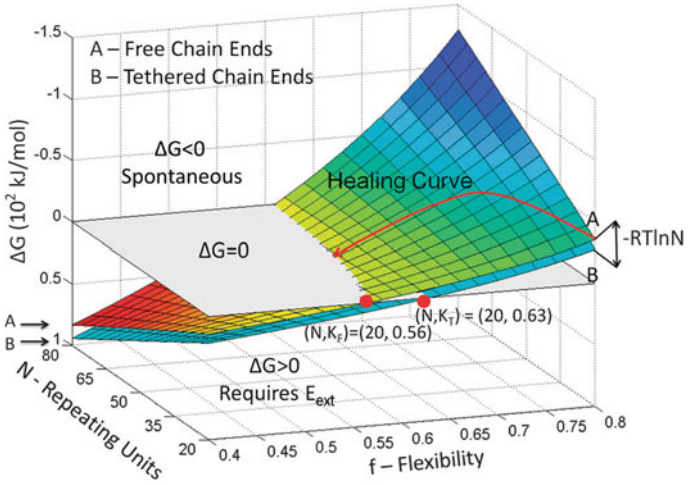

Fig. 4 Curves of ΔG versus segment number (N) in a polymeric chain and flexibility (f) for free (surface A) and tethered (surface B) chain ends *Reproduced with permission from* Yang and Urban [1]

the mechanical properties of the resin matrix. Meanwhile, this method requires the thermoplastic resins and epoxy resins with favorable compatibility, which reduces the selection range of thermoplastic resins, and after repairing, the crack is simply bonded by a thermoplastic resin with superior fluidity, which theoretically becomes a weak point. For instance, when it is used in a high-temperature environment, the thermoplastic resin tends to fail, leading to the crack breaking again.

In recent two decades, the self-healing of epoxy resins was realized by incorporating dynamic structures. The network rearrangement and the migration of molecular chains can be realized through the exchange of dynamic structures under certain conditions (such as heating, ultraviolet light), corresponding to the repairing of the resin. By introducing supramolecular chemistries such as hydrogen bonding, epoxy resin can obtain self-healing ability, while appropriate content of supramolecular bonds can enhance the mechanical performance of the epoxy resin [34, 35]. By introducing dynamic covalent bonds, self-healing can also be achieved for epoxy resins. Self-healing epoxy resins from dynamic covalent bonds have two catalogs: dissociative and associative. For the dissociative one, during the self-healing of the epoxy network or network rearrangement, dynamic covalent bonds are first dissociated, and then new dynamic covalent bonds are formed in another place. For the associative one, the cleaving and reformation of the dynamic covalent bonds occur simultaneously, and the resin's cross-link density is unchanged. Albeit there is a big difference between these two catalogs, they both can achieve effective self-healing for epoxy resins via the rational design of the molecular structure.

3.1 Supramolecular Dynamic Bonds

A hydrogen bond is a typical supramolecular dynamic bond in nature, so its strength is lower than most covalent bonds. Nevertheless, hydrogen bond-contained materials with high mechanical properties can still be designed and prepared. In recent years, urea isopyrimidone (UPy) captured great attention because it can form quadruple hydrogen bonding. Compared with ordinary hydrogen bonds, UPy-based quadruple hydrogen bonds have a stronger binding force, which is beneficial to enhancing the mechanical performance of materials. Thermosets that only use UPy-based hydrogen bonds as cross-linking points showed the same rheological characteristics as thermoplastic resins as a result of the de-bonding of hydrogen bonds at elevated temperatures [36] and possessed pretty good mechanical properties at room temperature (Fig. 5).

Zhang et al. [37] used UPy-modified bisphenol-A epoxy resin to prepare cross-linked supramolecular polymers through epoxy curing reaction and formation of hydrogen bonds between UPys (Fig. 6). This epoxy resin can be self-healed at the cut point after heating (90°C) for 2 h, and high self-repairing efficiency was reached (99%). At the same time, the epoxy resin had excellent mechanical properties (elongation at break was 247%, and tensile strength was 3.10 MPa). This resin was also applied to self-healable conductive composites. Sun et al. [35] applied the epoxy resin containing UPy to the reusable hot melt adhesive (Fig. 7). They grafted UPy to bisphenol-A epoxy resin by chemical modification and prepared reusable adhesive through epoxy curing and hydrogen bonding between UPys. The SEA had ultra-high bonding performance with a bonding strength of 10 MPa. Meanwhile, the SEA can also be reused by heating at 80°C for 5 min through the dynamic exchange of hydrogen bonds, and it can be reused six times with 80% maintained mechanical properties.

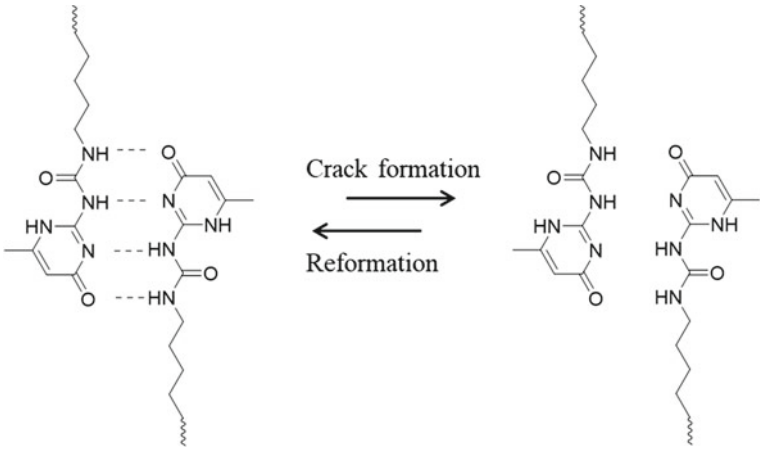

Fig. 5 Thermal dynamic exchange of urea isopyrimidone (UPy)

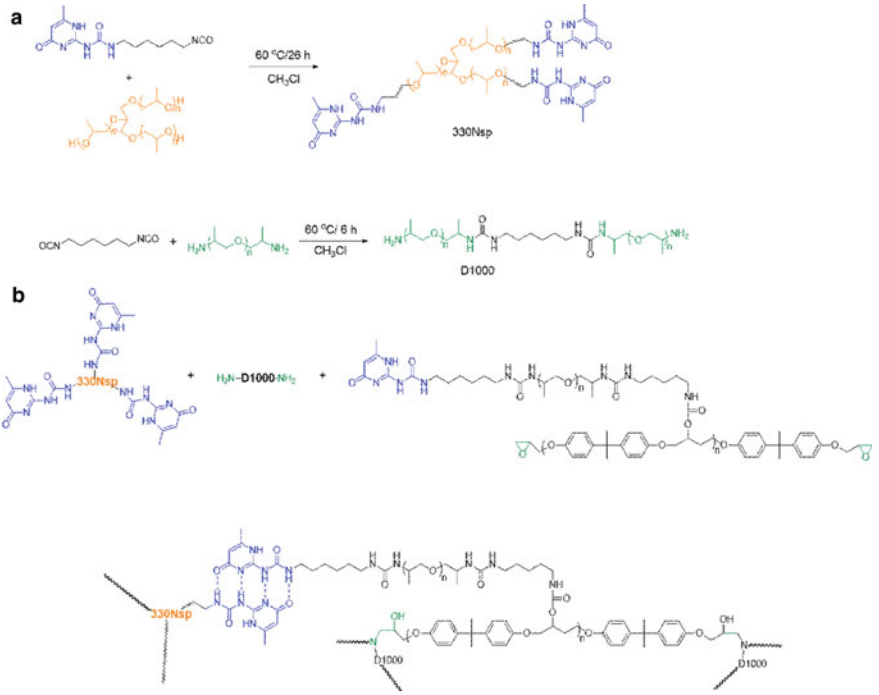

Fig. 6 Preparation of the UPy-based self-healing epoxy resin [37]

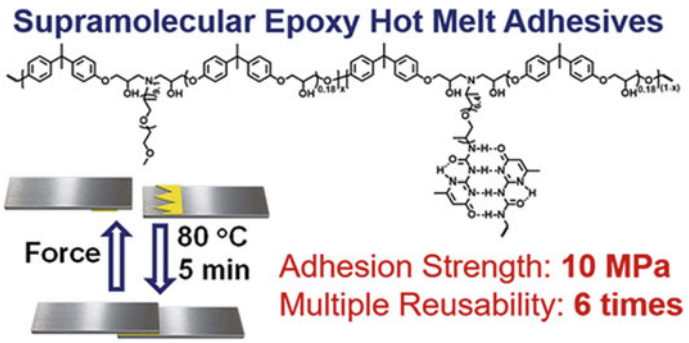

Fig. 7 Reusable hot melt adhesive based on supramolecular epoxy *Reproduced with permission from* Sun et al. [35]

UPy is suitable for preparing self-healing epoxy resins with high performance, but the chemical structure of UPy is still complex, and the synthesis route is cumbersome. In addition to the UPy-based hydrogen bonding, there are other common hydrogen bonds or supramolecular chemistries used in self-healing epoxy resins [38]. For instance, Kostopoulos et al. [39] introduced the hydrogen bond-based self-healing

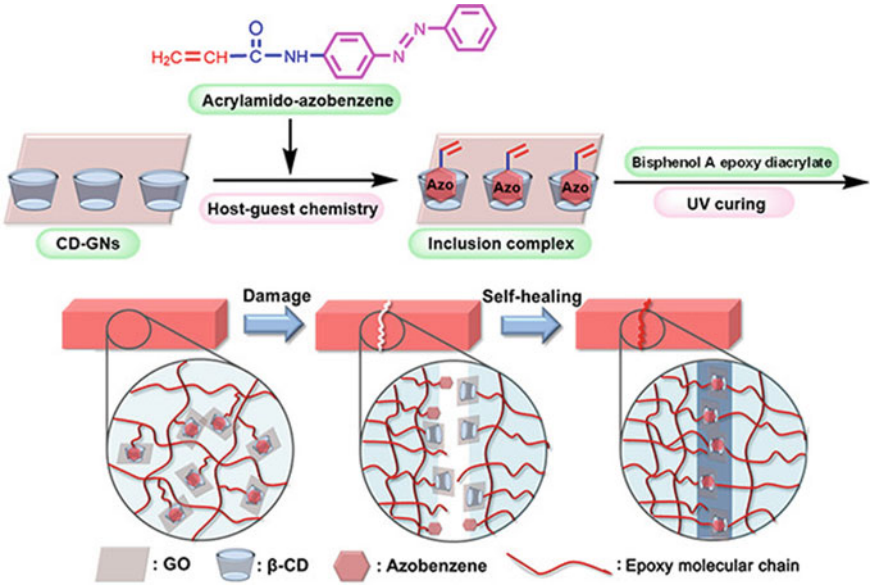

Fig. 8 The preparation process of the host–guest epoxy system and Schematic diagram of its self-healing process *Reproduced with permission from* Hu et al. [40]

epoxy resin into carbon fiber composites, and the self-healing performance was greatly improved after adding hydrogen-bonded supramolecular polymers. The host–guest system is a widely studied supramolecular chemistry. Hu et al. [40] introduced a host–guest system into an epoxy resin system, the obtained epoxy resin can achieve self-healing at 120°C with self-healing efficiency as high as 79.2%, but its synthetic method was relatively complicated (Fig. 8). For the sake of achieving epoxy resins combining excellent anti-corrosion performance and self-repairing performance, Boumezgane et al. [41] combined the advantages of supramolecular bonds (ionic dynamic bonds) and microcapsules (Fig. 9). The amino/carboxyl groups terminated PDMS was introduced into epoxy resin systems, and microcapsules were formed in situ. The surface damage of the resin released the functional PDMS oligomers to form supramolecular ionic networks, which endowed self-repairing capabilities and improved the anti-corrosion performance of the anti-corrosion coating on scratches.

3.2 Reversible Diels–Alder (DA) Addition

Diels–Alder (DA) adduct is generated by the cycloaddition of the conjugated diene system with the alkene or alkyne bond. Unlike the hydrogen bond mentioned above, the DA adduct was a kind of dynamic covalent structure, with larger bond energy than the hydrogen bond. Therefore, it is more suitable to prepare high-performance epoxy

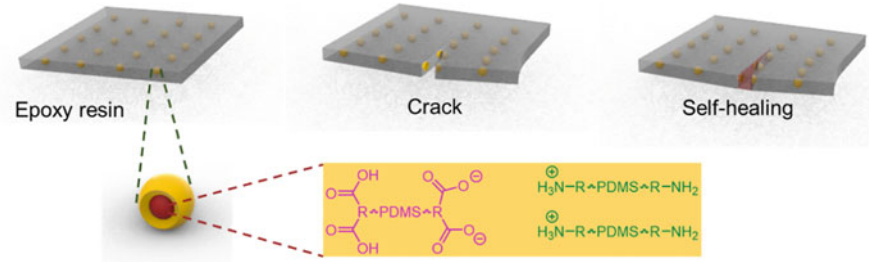

Fig. 9 Anti-corrosion epoxy resin based on ionic dynamic bond and microcapsules

resins. At high temperatures, the DA system dissociates to realize the easy migration of a part of the chain segments and further realize the self-healing of cracks. When the temperature drops, the decomposed conjugated diene system, and the alkene or alkyne bond undergo a cycloaddition reaction again to recover the resin's mechanical performance.

Chen et al. [7] first reported a cross-linked polymer that can be healed in a mild condition through disconnection and reconnection of DA adducts. The authors investigated the reversibility of Diels–Alder (DA) cross-linking by solid-state NMR, which demonstrated that DA adducts could decompose above 120°C and form at low temperatures. Further, they exposed the relationship between the rate of the formation of DA adduct and temperature. Taking advantage of this feature of DA adducts, Kuang et al. [42] prepared a DA adduct-containing diamine and further reacted with a commercial epoxy to produce an epoxy network with outstanding reprocessing and repeated self-healing. Cross-linked epoxy resins containing DA adducts can essentially behave like typical thermosets at room temperature, which cannot be dissolved in solvents. Nevertheless, it can be reprocessed quickly at high temperatures like thermoplastics. This is ascribed to the cleavage of the DA adduct at elevated temperature, which makes the resin reversibly switch between the cross-linked state and the linear structure.

Peterson et al. [43] developed a DA adduct-based reversibly cross-linked gel that can be utilized to repair epoxy resins. This gel can apply to the crack surface directly, and the resin's mechanical performance was recovered by 37%. Being heated, on account of the DA adduct's dissociation, the gel transformed into a fluid oligomer that diffused into the resin's crack, and the molecular chains of the oligomers also entangled with the chain segment on the crack surface. As the temperature dropped, the furan groups on the oligomers re-reacted with maleimide groups to rebuild a complete network structure (Fig. 10).

Since the DA addition reaction occurs on the crack surface, the healing effect between cracks is extremely sensitive to the distance between the crack surfaces. An effective way to reduce the crack distance is to expand and soften the material. Peterson et al. [44] invented a room temperature self-healing agent (a solution containing bismaleimide (BMI)) for DA adduct-containing thermosetting polymer. Solvent swelled and softened the crack surface, which led to the physical bonding of

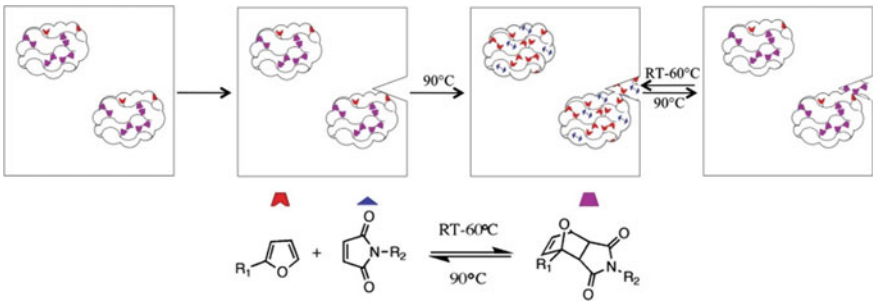

Fig. 10 DA adduct-based reversibly cross-linked gel as the secondary healing phase to repair epoxy networks *Reproduced with permission from* Peterson et al. [43]

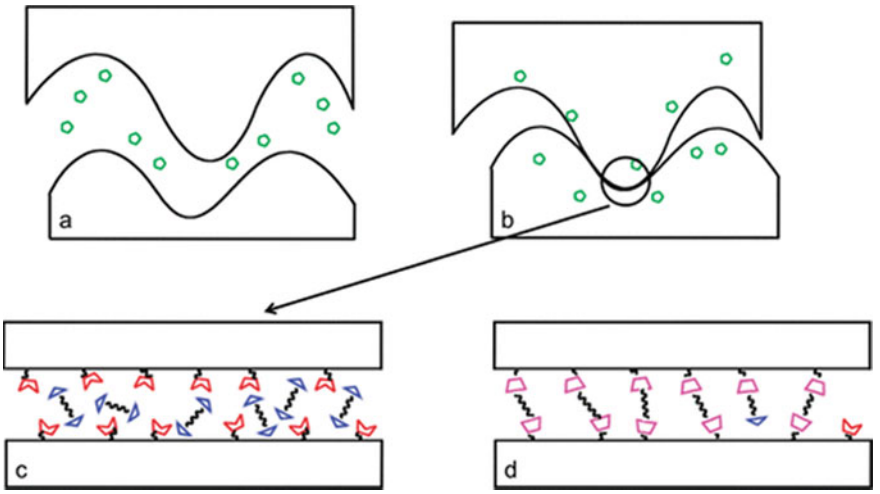

Fig. 11 Room temperature self-healing agent for DA adduct-containing thermosetting polymer. Green pentagon: solvent molecules, red notched trapezoid: furan, blue triangle: maleimide, and magenta trapezoid: DA adduct *Reproduced with permission from* Peterson et al. [44]

the cracks, and then chemical bonding from the DA addition reaction also occurred at room temperature as the crack width is less than the length of BMI (Fig. 11). The physical bonding contributed to 28.4% healing efficiency, and chemical bonding led to another 41.6% healing efficiency.

3.3 Disulfide Bond Exchange

In recent years, self-healable epoxy resins based on disulfide bonds have received extensive attention from researchers. Unlike DA addition, during the healing process,

the disulfide bond does not undergo significant dissociation at high temperatures. However, it undergoes a rapid exchange reaction, so the cross-link density of the material does not decrease significantly. Consequently, no annealing is necessary to realize self-healing for disulfide bond-based self-healing epoxy resins, while DA adduct-based ones often require a long time of annealing to achieve favorable recovery of mechanical properties.

Lei et al. [45] added tri-*n*-butylphosphine (TBP) into an epoxy resin containing disulfide bonds. TBP could catalyze the metathesis exchange of disulfide bonds at room temperature under alkaline conditions. Through this reaction, the cross-linked epoxy resin containing disulfide bonds can self-heal at room temperature (Fig. 12), which is demonstrated by the repeated recovery of tensile strength. In addition, this polymer can also realize the network rearrangement through the dynamic exchange of disulfide bonds, and the reprocessed resin maintains the original mechanical performance. Without a TBP catalyst or disulfide bond, the control group failed to achieve self-healing or reprocessing.

Memon and Wei [46] designed and synthesized an epoxy resin containing a disulfide bond. Through the curing reaction of this epoxy resin and methyl hexahydrophthalic anhydride, disulfide bonds were introduced into the epoxy network (Fig. 13). The obtained epoxy network possesses excellent thermal properties and mechanical performance. Via the reversible bonding of disulfide bonds, the resin can realize welding repair and remodeling processing. After reprocessing three times, the resin maintained mechanical performance well with a recovery of > 90%. This resin can also be degraded in a solution containing sulfhydryl groups to yield oligomers.

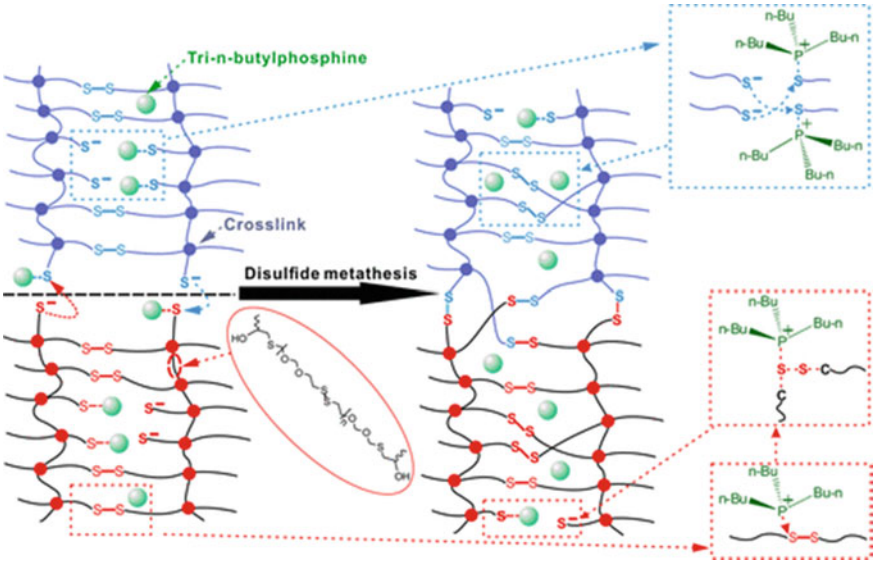

Fig. 12 Epoxy network containing disulfide bonds catalyzed by tri-n-butylphosphine *Reproduced with permission from* Lei et al. [45]

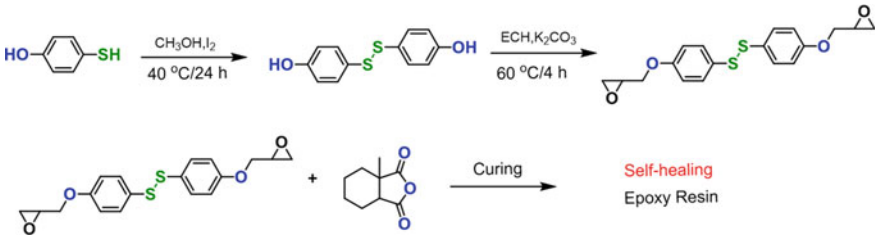

Fig. 13 Synthesis of epoxy monomer containing disulfide bond and its self-healing epoxy resin [46]

Si et al. [47] prepared an epoxy network from a diepoxy and a diamine containing aromatic disulfide bonds. High glass transition temperature (T_g, 147°C) and tensile strength (63.1 MPa) were achieved. Besides the benefit of the abundant disulfide bonds, the exchange efficiency of the network is greatly improved, enabling rapid relaxation without a catalyst. Carbon fiber composites (CFRP) based on this epoxy network could be easily degraded by small-molecule sulfhydryl compounds to obtain recycled carbon fibers, which can be reused to prepare CFRP with excellent mechanical properties.

3.4 Imine Exchange

Similar to the disulfide bond, the imine bond is also a dynamic bond with high exchange activity, which allows for rapid exchange without a catalyst via the metathesis reaction (Fig. 14) [48]. In addition, the raw materials are commonly available because they can be facilely prepared by the condensation reaction of the amino group with the aldehyde group. Lei et al. [48] first demonstrated that the self-healing of thermosets could be achieved via incorporating an imine bond.

For epoxy resins, imine bonds can be introduced into the chemical structures of epoxy monomer (Fig. 15a) or curing agents (Fig. 15b) or can be in-situ built during the formation of the cross-linked network. The introduction of imine bonds into

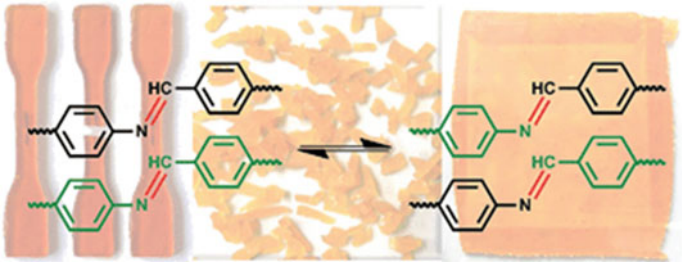

Fig. 14 Exchange mechanism of imine bond [48]

epoxy resins can provide self-healing performance without scarifying thermal and mechanical properties. In addition, imine bonds can also bring quite a few attractive features, such as antibacterial activity, [49, 50] anti-corrosion property, [51] and degradability [52, 53] etc. In 2019, Mo et al. [51] introduced the imine bond into the curing agent. The imine bond was incorporated into the epoxy network through the curing reaction of the curing agent and the epoxy monomer. The prepared epoxy resin can achieve self-healing within 1 h at 90°C, but with increasing cross-linking density of the network, the resin's healing process was hindered. Meanwhile, incorporating an imine bond also endows epoxy resin with excellent corrosion resistance. Similarly, Mai et al.[54] prepared a curing agent containing imine bonds through the reaction of vanillin with hexane-1,6-diamine and then used this curing agent to cure epoxy resins. The prepared epoxy resin can achieve self-healing within a few minutes at 90°C. The introduction of imine bonds into epoxy monomers was also a common method for preparing imine-based epoxy resins. Jiang et al. [55] prepared imine-containing epoxy monomers using 4-aminophenol and vanillin as raw materials. The cured epoxy resins can be self-healed within a few hours at 120°C and possess excellent mechanical properties, thermal stability, and solvent resistance.

To accelerate the dynamic exchange reaction and increase the self-healing efficiency, we designed an epoxy resin containing both imine bond and DA adduct [56]. The synergistic exchange effect accelerated the network rearrangement to realize the fast self-repairing and reprocessing of the epoxy resin. In addition, by adjusting the ratio of imine bond and DA adduct, the tensile strength of this material can be adjusted in the range of 10–90 MPa, which has the characteristics of a large adjustment range and good mechanical properties. Since the degree of reaction of DA adducts increases with annealing time, the authors investigated the effect of imine bonds on the formation of DA adducts and found that the formation rate of DA adducts increased when increasing imine bond content. At the same time, a series of

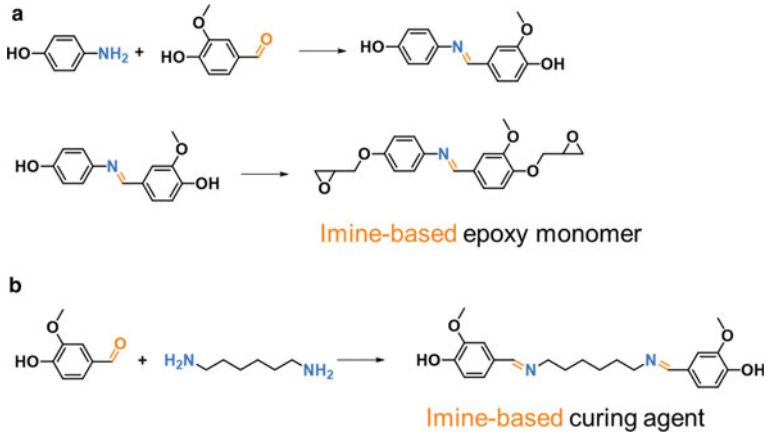

Fig. 15 Synthetic routes of imine-based epoxy monomer and curing agent

materials with various mechanical performances can be easily achieved by adjusting the annealing time.

3.5 Ester Bond Exchange

In addition to the above-mentioned dynamic bonds, the ester bond is also a commonly reported dynamic bond, which can be readily introduced into the cross-linked epoxy networks through the curing reaction of epoxy monomers or oligomers with acid anhydrides or carboxylic acids. However, compared with the dynamic bonds mentioned above, the exchange efficiency of ester bonds was relatively low. Therefore, to realize the self-repairing performance of epoxy resins, it is essential to adopt catalytic methods to accelerate the exchange of ester bonds. Liu et al. [57] prepared eugenol-based epoxy monomers and then used succinic anhydride as the curing agent to prepare a dynamic network based on an ester bond (Fig. 16). The self-healing was achieved by transesterification catalyzed by zinc acetylacetonate hydrate ($Zn(acac)_2$). However, limited by the efficiency of the transesterification, the crack required to be thermally treated for 1 h (190°C) to realize partial repair. Similarly, the authors further prepared a bio-based self-healable epoxy network with a bio-based triepoxy and 4-methylcyclohexane-1,2-dicarboxylic anhydride. Self-healing was achieved within several minutes at 220°C with the catalysis of Zn^{2+} [57]. Ding et al. [58] also introduced ester bond into epoxy resins via curing of epoxy monomers with glutaric anhydride. However, owing to the low ester exchange activity, the system required to be thermally treated for two hours (200°C) to realize self-healing. Besides, the above works realized the self-repairing performance of ester bond-based epoxy resins by introducing external catalysts. Therefore, the addition of catalysts would inevitably bring about issues such as toxicity and environmental protection. Thus, several auto-catalytic systems based on tertiary amine, [59, 60] excess hydroxyl group, [61] carboxyl group [62] etc., were developed. For instance, Liu et al. [61] reported a catalyst-free self-healable epoxy resin through hyperbranched epoxy oligomers. The excess hydroxyl groups in the system catalyzed the transesterification so that the resin could achieve partial self-healing within several hours at 150°C without additional catalyst.

4 Conclusion and Prospect

There are two catalogs of self-healable epoxy resins: extrinsic and intrinsic. Extrinsic self-healable epoxy resins were based on loading hollow fibers, microcapsules, or thermoplastic additives. The mechanisms for hollow fiber and microcapsule methods are the same. Both realize self-repairing by releasing a healing agent from the broken hollow fibers or microcapsules in the cracks. For these two methods, self-healing is independent of the properties of the epoxy resins. Those with high modulus and high

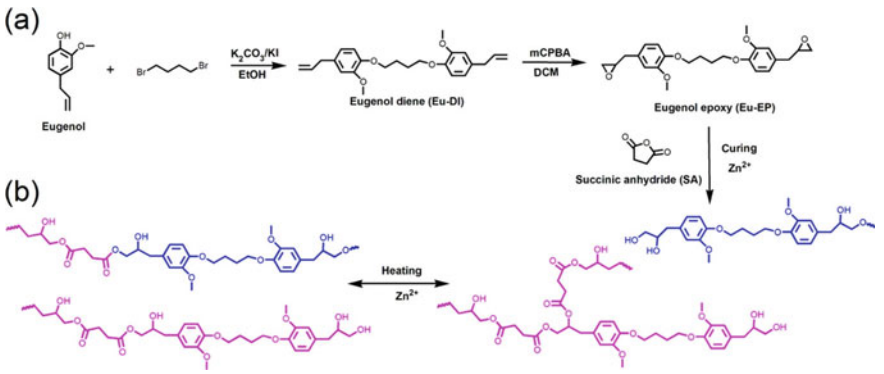

Fig. 16 **a** Synthesis and curing of eugenol-based epoxy monomer and **b** exchange mechanism of ester bonds in epoxy cross-linked networks [57]

T_g can also be self-healed. However, the preparation of hollow fibers and microcapsules filled with healing agents is not easy. Loading them also affects the epoxy system's viscosity and processability, and the cracks can be self-healed only once. For the method of using thermoplastic additives, the preparation process is simple, and the cracks can be self-healed multiple times. However, it requires high loading of thermoplastic additives and favorable compatibility of thermoplastic additives and epoxy resins, and the healed cracks re-break easily at elevated temperatures.

Recent two decades witnessed the rapid development of intrinsic self-healable epoxy resins from dynamic bonds: non-covalent (supramolecular) or covalent. For the supramolecular method, hydrogen bonds, ionic dynamic bonds, or host–guest systems were applied to realize the self-repairing of epoxy resins. For the method of using dynamic covalent bonds, Diels–Alder adduct, imine bond, disulfide bond, and ester bond were commonly used to produce self-healing epoxy resins, and diselenide bond, etc. were also exploited. For the intrinsic method, the epoxy resins can be theoretically self-healed many times. Diels–Alder adduct-based self-healing epoxy resins can repair the cracks easily at elevated temperature by virtue of the cleavage of Diels–Alder adduct and the reduction of the epoxy networks' cross-link density, but to achieve enough strength of the healed cracks required further annealing. Disulfide and imine bonds as the dynamic bonds based on associative mechanisms can also provide excellent self-healing properties to the epoxy resins. While the disulfide bond is flexible, as a result, the obtained epoxy resins often exhibited relatively lower T_g and modulus compared with traditional epoxy resins. Imine bond-based self-healing epoxy resins can possess high modulus and T_g, which is attributed to the rigidity of its excellent hydrogen bonding and conjugated ability with the benzene ring. At the same time, it is easy to be thermally aged during the thermal-triggered healing process. Ester bond-based self-healing epoxy resins have attracted significant attention, especially after the first report of vitrimers. However, their self-repairing efficiency is limited on account of the slow transesterification. For the intrinsic self-healable epoxy resins, the self-repairing is often triggered by other stimuli such as

heating, UV radiation, etc. As a result, most of them are not the real self-healable ones; and it is still a challenge to achieve outstanding self-healing for those with high modulus and T_g.

In the future, self-healing efficiency should be improved. For example, the synergistic effect of two or more dynamic bonds can be utilized to accelerate the dynamic exchange and self-healing. During the service, stability and durability of the epoxy resins are also exceedingly important, so the stability or aging resistance of dynamic bond-based self-healing epoxy resins should be focused on to realize a delicate balance between self-repairing efficiency and stability. Epoxy resins are mainly from nonrenewable fossil resources, so self-healing epoxy resins from renewable bioresources should also be investigated. Materials with multiple functions are the future trend, so other functions such as flame retardancy, anti-fouling, anti-corrosion, shape-memory, recyclability, should also be introduced into self-healing epoxy resins. Although applications of self-healing epoxy resins in composite materials, anti-corrosion coatings, etc., were reported, research on specific applications' overall properties is still limited.

Acknowledgements Authors thank financial support from National Natural Science Foundation of China (No. 52073296), Youth Innovation Promotion Association of Chinese Academy of Sciences (No. 2018335), and Zhejiang Ten Thousand Talent Program.

Conflicts of Interest There is no conflict of interest to be declared.

References

1. Yang, Y., Urban, M.W.: Self-healing polymeric materials. Chem. Soc. Rev. **42**(17), 7446–7467 (2013). https://doi.org/10.1039/C3CS60109A
2. Wool, R.P., O'Connor, K.M.: A theory crack healing in polymers. J. Appl. Phys. **52**(10), 5953–5963 (1981). https://doi.org/10.1063/1.328526
3. Nji, J., Li, G.: A biomimic shape memory polymer based self-healing particulate composite. Polymer **51**(25), 6021–6029 (2010). https://doi.org/10.1016/j.polymer.2010.10.021
4. Corten, C.C., Urban, M.W.: Repairing polymers using oscillating magnetic field. Adv. Mater. **21**(48), 5011–5015 (2009). https://doi.org/10.1002/adma.200901940
5. Chen, Y., Kushner, A.M., Williams, G.A., Guan, Z.: Multiphase design of autonomic self-healing thermoplastic elastomers. Nat. Chem. **4**(6), 467–472 (2012). https://doi.org/10.1038/nchem.1314
6. Yang, Y., Davydovich, D., Hornat, C.C., Liu, X., Urban, M.W.: Leaf-inspired self-healing polymers. Chem **4**(8), 1928–1936 (2018). https://doi.org/10.1016/j.chempr.2018.06.001
7. Chen, X., Matheus, A.D., Ono, K., Mal, A., Shen, H., Steven, R.N., et al.: A thermally remendable cross-linked polymeric material. Sci. **295**(5560), 1698–1702 (2002). https://doi.org/10.1126/science.1065879
8. Ying, H., Zhang, Y., Cheng, J.: Dynamic urea bond for the design of reversible and self-healing polymers. Nat. Commun. **5**(1), 3218 (2014). https://doi.org/10.1038/ncomms4218
9. Zhou, L., Dai, C., Fan, L., Jiang, Y., Liu, C., Zhou, Z., et al.: Injectable self-healing natural biopolymer-based hydrogel adhesive with thermoresponsive reversible adhesion for minimally invasive surgery. Adv. Func. Mater. **31**(14), 2007457 (2021). https://doi.org/10.1002/adfm.202007457

10. Ghosh, B., Marek, W.U.: Self-repairing oxetane-substituted chitosan polyurethane networks. Sci. **323**(5920), 1458–1460 (2009). https://doi.org/10.1126/science.1167391
11. Imato, K., Nishihara, M., Kanehara, T., Amamoto, Y., Takahara, A., Otsuka, H.: Self-healing of chemical gels cross-linked by diarylbibenzofuranone-based trigger-free dynamic covalent bonds at room temperature. Angew. Chem. Int. Ed. **51**(5), 1138–1142 (2012). https://doi.org/10.1002/anie.201104069
12. Yanagisawa, Y., Nan, Y., Okuro, K., Aida, T.: Mechanically robust, readily repairable polymers via tailored noncovalent cross-linking. Sci. **359**(6371), 72–76 (2018). https://doi.org/10.1126/science.aam7588
13. Fujisawa, Y., Asano, A., Itoh, Y., Aida, T.: Mechanically robust, self-healable polymers usable under high humidity: humidity-tolerant noncovalent cross-linking strategy. J. Am. Chem. Soc. **143**(37), 15279–15285 (2021). https://doi.org/10.1021/jacs.1c06494
14. Jeon, I., Cui, J., Illeperuma, W.R.K., Aizenberg, J., Vlassak, J.J.: Extremely stretchable and fast self-healing hydrogels. Adv. Mater. **28**(23), 4678–4683 (2016). https://doi.org/10.1002/adma.201600480
15. Rahmani, H., Najafi, S.H.M., Ashori, A.: Mechanical performance of epoxy/carbon fiber laminated composites. J. Reinf. Plast. Compos. **33**(8), 733–740 (2014). https://doi.org/10.1177/0731684413518255
16. Nademi, M., Mozaffari, A., Farrokhabadi, A.: A new self healing method in composite laminates using the hollow glass fiber. Key Eng. Mater. **471–472**, 548–551 (2011). https://doi.org/10.4028/www.scientific.net/KEM.471-472.548
17. Vijayan, P., AlMaadeed, M.A. 'Containers' for self-healing epoxy composites and coating: Trends and advances. Express Polym. Lett. **10**(6) (2016). https://doi.org/10.3144/expresspolymlett.2016.48
18. Madbouly, S.A., Xia, Y., Kessler, M.R.: Rheokinetics of ring-opening metathesis polymerization of bio-based castor oil thermoset. Macromol. **45**(19), 7729–7739 (2012). https://doi.org/10.1021/ma301458n
19. Sheng, X., Lee, J.K., Kessler, M.R.: Influence of cross-link density on the properties of ROMP thermosets. Polym. **50**(5), 1264–1269 (2009). https://doi.org/10.1016/j.polymer.2009.01.021
20. Kling, S., Czigány, T.: Damage detection and self-repair in hollow glass fiber fabric-reinforced epoxy composites via fiber filling. Compos. Sci. Technol. **99**, 82–88 (2014). https://doi.org/10.1016/j.compscitech.2014.05.020
21. Montarnal, D., Capelot, M., Tournilhac, F., Leibler, L.: Silica-like malleable materials from permanent organic networks. Sci. **334**(6058), 965–968 (2011). https://doi.org/10.1126/science.1212648
22. Dry, C.: Procedures developed for self-repair of polymer matrix composite materials. Compos. Struct. **35**(3), 263–269 (1996). https://doi.org/10.1016/0263-8223(96)00033-5
23. Pang, J.W.C., Bond, I.P.: A hollow fibre reinforced polymer composite encompassing self-healing and enhanced damage visibility. Compos. Sci. Technol. **65**(11), 1791–1799 (2005). https://doi.org/10.1016/j.compscitech.2005.03.008
24. Zhang, F., Zhang, L., Yaseen, M., Huang, K.: A review on the self-healing ability of epoxy polymers. J. Appl. Polym. Sci. **138**(16), 50260 (2021). https://doi.org/10.1002/app.50260
25. An, S., Lee, M.W., Yarin, A.L., Yoon, S.S.: A review on corrosion-protective extrinsic self-healing: Comparison of microcapsule-based systems and those based on core-shell vascular networks. Chem. Eng. J. **344**, 206–220 (2018). https://doi.org/10.1016/j.cej.2018.03.040
26. White, S.R., Sottos, N.R., Geubelle, P.H., Moore, J.S., Kessler, M.R., Sriram, S.R., et al.: Autonomic healing of polymer composites. Nat. **409**(6822), 794–797 (2001). https://doi.org/10.1038/35057232
27. Hughes, A.E., Cole, I.S., Muster, T.H., Varley, R.J.: Designing green, self-healing coatings for metal protection. NPG Asia Mater. **2**(4), 143–151 (2010). https://doi.org/10.1038/asiamat.2010.136
28. Osborne, J.H., Blohowiak, K.Y., Taylor, S.R., Hunter, C., Bierwagon, G., Carlson, B., et al.: Testing and evaluation of nonchromated coating systems for aerospace applications. Prog. Org. Coat. **41**(4), 217–225 (2001). https://doi.org/10.1016/S0300-9440(01)00132-1

29. Katz, S.A., Salem, H.: The toxicology of chromium with respect to its chemical speciation: A review. J. Appl. Toxicol. **13**(3), 217–224 (1993). https://doi.org/10.1002/jat.2550130314
30. Langård, S., Norseth, T.: A cohort study of bronchial carcinomas in workers producing chromate pigments. Br. J. Ind. Med. **32**(1), 62–65 (1975). https://doi.org/10.1136/oem.32.1.62
31. Suryanarayana, C., Rao, K.C., Kumar, D.: Preparation and characterization of microcapsules containing linseed oil and its use in self-healing coatings. Prog. Org. Coat. **63**(1), 72–78 (2008). https://doi.org/10.1016/j.porgcoat.2008.04.008
32. Zako, M., Takano, N.: Intelligent material systems using epoxy particles to repair microcracks and delamination damage in GFRP. J. Intell. Mater. Syst. Struct. **10**(10), 836–841 (1999). https://doi.org/10.1106/YEIH-QUDH-FC7W-4QFM
33. Meure, S., Wu, D.Y., Furman, S.: Polyethylene-co-methacrylic acid healing agents for mendable epoxy resins. Acta Mater. **57**(14), 4312–4320 (2009). https://doi.org/10.1016/j.actamat.2009.05.032
34. Zhang, P., Kan, L., Zhang, X., Li, R., Qiu, C., Ma, N., et al.: Supramolecularly toughened and elastic epoxy resins by grafting 2-ureido-4[1H]-pyrimidone moieties on the side chain. Eur. Polymer J. **116**, 126–133 (2019). https://doi.org/10.1016/j.eurpolymj.2019.04.001
35. Sun, P., Li, Y., Qin, B., Xu, J.-F., Zhang, X.: Super strong and multi-reusable supramolecular epoxy hot melt adhesives. ACS Mater. Lett. **3**(7), 1003–1009 (2021). https://doi.org/10.1021/acsmaterialslett.1c00277
36. Feldman, K.E., Kade, M.J., de Greef, T.F.A., Meijer, E.W., Kramer, E.J., Hawker, C.J.: Polymers with multiple hydrogen-bonded end groups and their blends. Macromol. **41**(13), 4694–4700 (2008). https://doi.org/10.1021/ma800375r
37. Zhang, P., Wei, Y., Li, R., Wan, Y., Zhang, X., Ouyang, X., et al.: Self-healable, highly stretchable modified epoxy resin materials by incorporation with quadruple hydrogen-bonded supramolecular polymers. Macromol. Mater. Eng. **306**(1), 2000501 (2021). https://doi.org/10.1002/mame.202000501
38. Wei, P., Yan, X., Huang, F.: Supramolecular polymers constructed by orthogonal self-assembly based on host–guest and metal–ligand interactions. Chem. Soc. Rev. **44**(3), 815–832 (2015). https://doi.org/10.1039/C4CS00327F
39. Kostopoulos, V., Kotrotsos, A., Tsantzalis, S., Tsokanas, P., Loutas, T., Bosman, A.W.: Toughening and healing of continuous fibre reinforced composites by supramolecular polymers. Compos. Sci. Technol. **128**, 84–93 (2016). https://doi.org/10.1016/j.compscitech.2016.03.021
40. Hu, Z., Zhang, D., Lu, F., Yuan, W., Xu, X., Zhang, Q., et al.: Multistimuli-responsive intrinsic self-healing epoxy resin constructed by host–guest interactions. Macromol. **51**(14), 5294–5303 (2018). https://doi.org/10.1021/acs.macromol.8b01124
41. Boumezgane, O., Suriano, R., Fedel, M., Tonelli, C., Deflorian, F., Turri, S.: Self-healing epoxy coatings with microencapsulated ionic PDMS oligomers for corrosion protection based on supramolecular acid-base interactions. Prog. Org. Coat. **162**, 106558 (2022). https://doi.org/10.1016/j.porgcoat.2021.106558
42. Kuang, X., Liu, G., Dong, X., Liu, X., Xu, J., Wang, D.: Facile fabrication of fast recyclable and multiple self-healing epoxy materials through Diels-Alder adduct cross-linker. J. Polym. Sci. Part A: Polym. Chem. **53**(18), 2094–2103 (2015). https://doi.org/10.1002/pola.27655
43. Peterson, A.M., Jensen, R.E., Palmese, G.R.: Reversibly cross-linked polymer gels as healing agents for epoxy−amine thermosets. ACS Appl. Mater. Interfaces **1**(5), 992–995 (2009). https://doi.org/10.1021/am900104w
44. Peterson, A.M., Jensen, R.E., Palmese, G.R.: Room-temperature healing of a thermosetting polymer using the Diels−alder reaction. ACS Appl. Mater. Interfaces **2**(4), 1141–1149 (2010). https://doi.org/10.1021/am9009378
45. Lei, Z.Q., Xiang, H.P., Yuan, Y.J., Rong, M.Z., Zhang, M.Q.: Room-temperature self-healable and remoldable cross-linked polymer based on the dynamic exchange of disulfide bonds. Chem. Mater. **26**(6), 2038–2046 (2014). https://doi.org/10.1021/cm4040616
46. Memon, H., Wei, Y.: Welding and reprocessing of disulfide-containing thermoset epoxy resin exhibiting behavior reminiscent of a thermoplastic. J. Appl. Polym. Sci. **137**(47), 49541 (2020). https://doi.org/10.1002/app.49541

47. Si, H., Zhou, L., Wu, Y., Song, L., Kang, M., Zhao, X., et al.: Rapidly reprocessable, degradable epoxy vitrimer and recyclable carbon fiber reinforced thermoset composites relied on high contents of exchangeable aromatic disulfide crosslinks. Compos. B Eng. **199**, 108278 (2020). https://doi.org/10.1016/j.compositesb.2020.108278
48. Lei, Z.Q., Xie, P., Rong, M.Z., Zhang, M.Q.: Catalyst-free dynamic exchange of aromatic Schiff base bonds and its application to self-healing and remolding of crosslinked polymers. J. Mater. Chem. A **3**(39), 19662–19668 (2015). https://doi.org/10.1039/C5TA05788D
49. Xu, X., Ma, S., Wu, J., Yang, J., Wang, B., Wang, S., et al.: High-performance, command-degradable, antibacterial Schiff base epoxy thermosets: synthesis and properties. J. Mater. Chem. A **7**(25), 15420–15431 (2019). https://doi.org/10.1039/C9TA05293C
50. Xu, X., Ma, S., Wang, S., Wu, J., Li, Q., Lu, N., et al.: Dihydrazone-based dynamic covalent epoxy networks with high creep resistance, controlled degradability, and intrinsic antibacterial properties from bioresources. J. Mater. Chem. A **8**(22), 11261–11274 (2020). https://doi.org/10.1039/D0TA01419B
51. Mo, R., Hu, J., Huang, H., Sheng, X., Zhang, X.: Tunable, self-healing and corrosion inhibiting dynamic epoxy–polyimine network built by post-crosslinking. J. Mater. Chem. A **7**(7), 3031–3038 (2019). https://doi.org/10.1039/C8TA11546J
52. Xu, X., Ma, S., Feng, H., Qiu, J., Wang, S., Yu, Z., et al.: Dissociate transfer exchange of tandem dynamic bonds endows covalent adaptable networks with fast reprocessability and high performance. Polym. Chem. **12**(36), 5217–5228 (2021). https://doi.org/10.1039/D1PY01045J
53. Wang, B., Ma, S., Yan, S., Zhu, J.: Readily recyclable carbon fiber reinforced composites based on degradable thermosets: A review. Green Chem. **21**(21), 5781–5796 (2019). https://doi.org/10.1039/C9GC01760G
54. Mai, V.-D., Shin, S.-R., Lee, D.-S., Kang, I.: Thermal healing, reshaping and ecofriendly recycling of epoxy resin crosslinked with Schiff base of vanillin and hexane-1, 6-diamine. Polym. **11**(2), 293 (2019). https://doi.org/10.3390/polym11020293
55. Jiang, H., Cheng, M., Ai, C., Meng, F., Mou, Y., Sun, S., et al.: Surface modified halloysite nanotube enhanced imine-based epoxy composites with high self-healing efficiency and excellent mechanical properties. Polym. Chem. **12**(37), 5342–5356 (2021). https://doi.org/10.1039/D1PY00715G
56. Xu, X., Ma, S., Wang, S., Wang, B., Feng, H., Li, P., et al.: Fast-reprocessing, postadjustable, self-healing covalent adaptable networks with Schiff base and Diels–alder adduct. Macromol. Rapid Commun. 2100777 (2022). https://doi.org/10.1002/marc.202100777
57. Liu, T., Hao, C., Wang, L., Li, Y., Liu, W., Xin, J., et al.: Eugenol-derived biobased epoxy: shape memory, repairing, and recyclability. Macromol. **50**(21), 8588–8597 (2017). https://doi.org/10.1021/acs.macromol.7b01889
58. Ding, Z., Yuan, L., Guan, Q., Gu, A., Liang, G.: A reconfiguring and self-healing thermoset epoxy/chain-extended bismaleimide resin system with thermally dynamic covalent bonds. Polymer **147**, 170–182 (2018). https://doi.org/10.1016/j.polymer.2018.06.008
59. Li, Y., Liu, T., Zhang, S., Shao, L., Fei, M., Yu, H., et al.: Catalyst-free vitrimer elastomer based on dimer acid: Robust mechanical performance, adaptivity and hydrothermal recyclability. Green Chem. (2020). https://doi.org/10.1039/c9gc04080c
60. Altuna, F.I., Hoppe, C.E., Williams, R.J.J.: Epoxy vitrimers with a covalently bonded tertiary amine as catalyst of the transesterification reaction. Eur. Polymer J. **113**, 297–304 (2019). https://doi.org/10.1016/j.eurpolymj.2019.01.045

61. Liu, T., Zhang, S., Hao, C., Verdi, C., Liu, W., Liu, H., et al.: Glycerol induced catalyst-free curing of epoxy and vitrimer preparation. Macromol. Rapid Commun. e1800889 (2019). https://doi.org/10.1002/marc.201800889
62. Liu, Y., Ma, S., Li, Q., Wang, S., Huang, K., Xu, X., et al.: Dynamic transfer auto-catalysis of epoxy vitrimers enabled by the carboxylic acid/epoxy ratio based on facilely synthesized trifunctional monoesterified cyclic anhydrides. Eur. Polymer J. **135**, 109881 (2020). https://doi.org/10.1016/j.eurpolymj.2020.109881

Self-healing Epoxy Resin with Multi-Stimuli-Responsive Behavior

P. Poornima Vijayan, Jesiya Susan George, and R. V. Revathy

Abstract Self-healing ability of epoxy have been aroused as a strategy to improve the performance of epoxy-based structures, coatings and adhesives. Though there are several reports on the development of self-healing epoxy, the sustained and controlled healing of epoxy matrix is critical for achieving desired performance. Hence, scientists paid much attention to designing self-healing systems that would trigger and act upon certain stimuli. The stimuli should be non-destructing and available in the user environment. Both intrinsic and extrinsic self-healing in epoxy systems have been tailored to respond to the external environment. Earlier, single stimuli responsive self-healing epoxy systems were introduced as smart materials with superior performance. Later on, dual-to multiple stimuli-responsive self-healing epoxy systems were developed. Moreover, other epoxy systems have been developed to sense different combinations of stimuli such as light, temperature, pH, moisture, and restore the original functionalities. As a budding research area, practicing more advanced designs on multi-stimuli self-healing would benefit future material developments.

Keywords Self-healing · Epoxy · Stimuli-responsive

1 Introduction

Epoxy resins are the widely studied thermoset, considering their high demand in the aerospace, construction and electronic industries [1]. Though epoxies are critical components in coatings, adhesives and structural composites, they are vulnerable to damage by external factors like mechanical impact, temperature and UV irradiation [2, 3]. These factors lead to the micro-cracks deep inside, which are tough to find and restore manually [4]. Fabrication of new materials that solves the weakness of existing

P. Poornima Vijayan (✉) · R. V. Revathy
Department of Chemistry, Sree Narayana College for Women (Affiliated to University of Kerala), Kollam, Kerala 691001, India
e-mail: poornimavijayan2007@gmail.com

J. S. George
School of Chemical Sciences, Mahatma Gandhi University, Kottayam, Kerala 686560, India

N. Hameed et al. (eds.), *Multifunctional Epoxy Resins*, Engineering Materials,
https://doi.org/10.1007/978-981-19-6038-3_6

materials is the symbol of ever-progressing society. The last two-decade witnessed a milestone in polymer science and technology, which is the development of intelligent polymers, also known as smart polymers, which possess active functionalities just like in natural material [5]. With the advancement in smart and intelligent polymer materials, epoxy thermosets have also been explored for the development of smart thermosets [6, 7].

Self-healing, a promising smart functionality for the sustainable future, has been successfully integrated into the epoxy matrix [8]. Nature's mechanism of wound healing has been mimicked by material scientists in self-healing epoxy systems. With the integration of self-healing functionality, the epoxy matrix would eliminate the limitation of its high brittleness, thereby improving its service time and reliability. Self-healing epoxies are considered the future of the automobile, construction, aviation, electronics, ships, boats etc., as coatings, adhesives and structural composites. The use of epoxy in those diverse environments prompts the researchers to design a suitable triggering mechanism to initiate self-healing. The stimuli for the autonomous healing process in epoxy have been varying depending on the type of self-healing system developed (i.e., extrinsic or intrinsic) [9]. While extrinsic self-healing is achieved by incorporating healing agent encapsulated micro-or nanocontainers into matrix material, intrinsic self-healing operates via. dynamic covalent bonds and noncovalent interactions [10].

A well-controlled healing process is indeed required irrespective of the healing mechanism. The self-healing performance of epoxy, which responds to multiple physiochemical stimuli, are highly desirable for those applications [11]. Hence, investigations on multi-stimuli-responsive self-healing epoxy for specific applications have improved the reliability and lifetime of epoxy structures.

The early research on self-healing was mainly devoted to single stimuli-responsive epoxies. However, the need for highly reliable epoxy structures, coatings and adhesives, lead to the discovery of synergetic multi-stimuli-response self-healing epoxy. Although several single-responsive epoxies have been well researched, epoxy responses to multiple stimuli are intriguing but challenging. Special care is required while designing multi-stimuli-responsiveness in self-healing epoxy. Developing new chemistries, controlled release mechanism, after all structure to function behavior is the key to successful multi-stimuli-responsive self-healing epoxy systems. The simple mechanism of action, fast response time, high sensitivity and multiple healing cycles are the major self-healing characteristics. The current chapter initially discusses epoxy systems self-heals upon single stimuli response. It follows the primary focus of this chapter, i.e., the importance of the multi-stimuli-responsive self-healing process, the mechanism of action in the various external environment and their performance.

2 Stimuli for Self-healing Performance in Epoxy

The simplest and straightforward healing strategy for an epoxy matrix is to use thermal stimuli where they can be heated above their T_g, at which the molecular chains freely move and rearranges. However, it would not be considered an 'autonomous' process, as there is a human intervention in heating. In a self-healing epoxy matrix based on thermo-reversible Diels–Alder dynamic chemical reaction, the mechanical strength and adhesive behavior of healed epoxy largely depends upon the temperature change [12]. As temperature varies, the cracks can be healed and the healed one showed higher flexural strength and adhesive performance than the unhealed sample. Compared with thermal stimulus, other stimuli like light, pH, moisture, etc. would be better considered as instantaneous triggering resources for self-healing epoxy.

As a potential stimulus for the healing of epoxy, light can be effectively applied to epoxy structures and coatings which are exposed to outdoor environment. Several reports show that light initiated self-healing of an epoxy matrix has been successfully applied to extend the service life of epoxy-based materials. The presence of the photothermal compound and suitable crosslink density of epoxy to favor thermally induced healing based on chain diffusion and entanglement is the key to achieving a good light-responsive self-healing epoxy. Chen et al. [13] developed an epoxy coating which self-heals upon light irradiation. The near-infrared (NIR) (808 nm) initiated healing has been designed using carbon black as a photothermal filler. Carbon black has excellent photothermal conversion efficiency toward NIR. The crosslink density and glass transition temperature (T_g) of epoxy matrix have been lower by replacing the diamine curing agent with monoamine. Enhanced chain mobility facilitated by the low crosslinking density and T_g of the epoxy matrix favors thermally induced healing even with a small amount of carbon black. NIR irradiation at 808 nm has found to help in healing the crack completely. Fang et al. [14] controlled the crosslink density of diglycidylether of bisphenol A (DGEBA) network by replacing *m*-xylylenediamine (MXDA) with 4-(heptadecafluorooctyl) aniline (HFOA). They used aniline black to transmit thermally induced healing into a sunlight responsive one.

Recently, the photothermal response of plasmonic titanium nitride nanoparticles (TiN NPs) has been successfully used in epoxy coating for self-healing corrosion protection [15]. In which epoxy matrix was reinforced with titanium nitride nanoparticles grafted to mesoporous SiO_2 core–shell nanocontainers loaded with benzotriazole (BTA) corrosion inhibitors. In the presence of NIR irradiation, the thermogenesis effect of TiN NPs promoted both the release of corrosion inhibitors from nanocontainers and the shape memory effect to heal the scratch on the coating. This dual-action suppresses the corrosion at the exposed metal surface. Polyaniline (PANI) nanofibers are another promising photothermal compound used to develop self-healing epoxy in polyaniline (PANI) nanofibers [16]. The temperature required for the photothermal conversion of PANI nanofibers found to be increased with the NIR irradiation (808 nm). The shape memory effect and self-healing performance were enhanced directly with the increase of PANI nanofibers content.

UV light harms the polymer coatings applied in transportation, oil, gas, construction and in agricultural industries resulting in their costly maintenance or renewal of the coating. In this case, the synthesis of self-healing epoxy coating in which UV light activates autonomous healing response to mechanical damage would be an intelligent approach. A notable application of UV light initiated self-healing is in spacecraft, which are subject to severe environmental factors, including UV light, thermal variations, and mechanical impact from space debris [17]. UV-responsive microcapsule embedded epoxy coating has been developed for in-orbit damage repairing. One such microcapsule were reported with UV-curable epoxy in the core and a novel UV-protecting shell wall of poly(urea–formaldehyde) embedded with carbon black particles [18]. As confirmed by Raman spectroscopy, the core material is released upon damage with scribe and cured after UV exposure. It was worth noting that the carbon black remained with the shell wall and did not get released into the scribe damage. About 65% degree of protection was achieved by using UV-blocking shell wall after UV exposure.

Another reported stimulus for self-healing is water. Water responsive self-healing epoxy coatings and composites offer a dynamic healing facility for structures exposed to water or moisture. In addition, to ensure the safety and long service life of submerged structures, their self-healing functionality should be active in aqueous environment. In such an attempt, Yuan et al. [19] developed a water-responsive self-healing system with reversible and permanent covalent networks inspired by sea cucumber. As shown in Fig. 1a, the rapidly and reversibly modulus shifting nature of sea cumber arises owing to the crosslinking as well as de-crosslinking collagen fibrils in a low-modulus matrix. Mimicking from this nature architecture, poly (propylene glycol) chains were crosslinked with dynamic covalent boroxine bonds and permanent epoxy bonds. This network is stiff and strong in the dry state, and upon contact with water, the boroxine bonds dissociate to form unbound boronic acid, thus breaking the dynamic network. In this state, the system acts like a soft rubber. Once water is removed, boronic acid can reverse back to boroxine and return to the matrix's original stiffness. The whole process is illustrated in Fig. 1b.

It is a challenge to establish an anticorrosion coating that self-heals intrinsically in water. Underwater intrinsic self-healing has been constructed via. host–guest chemistry involving β-cyclodextrin/graphene (CD/G) in an epoxy network [20]. The host β-cyclodextrin was attached to the graphene surface which act as the guest molecule in the epoxy chain (Fig. 2a). The self-healing behavior has been attributed to the action of CD/G as a noncovalent macro-crosslinker which provides the interaction sites for the epoxy matrix molecules. Figure 2b shows the self-healing process in graphene-epoxy nanocomposite with different content of CD/G nanosheets under immersion in water for 24 h. The graphene-epoxy nanocomposite with 1% CD-G nanosheets showed the best healing performance among all the samples.

Extrinsic self-healing can also be triggered by water. In epoxy coatings, cellulose nanofiber (CNF) could effectively assist the release of healing agents upon exposure to the electrolyte solution. An effective epoxy coating on the metal substrate has been developed for submerged application with cellulose nanofiber as a key component [21]. Epoxy monomer and amine curing agents were immobilized on the surface

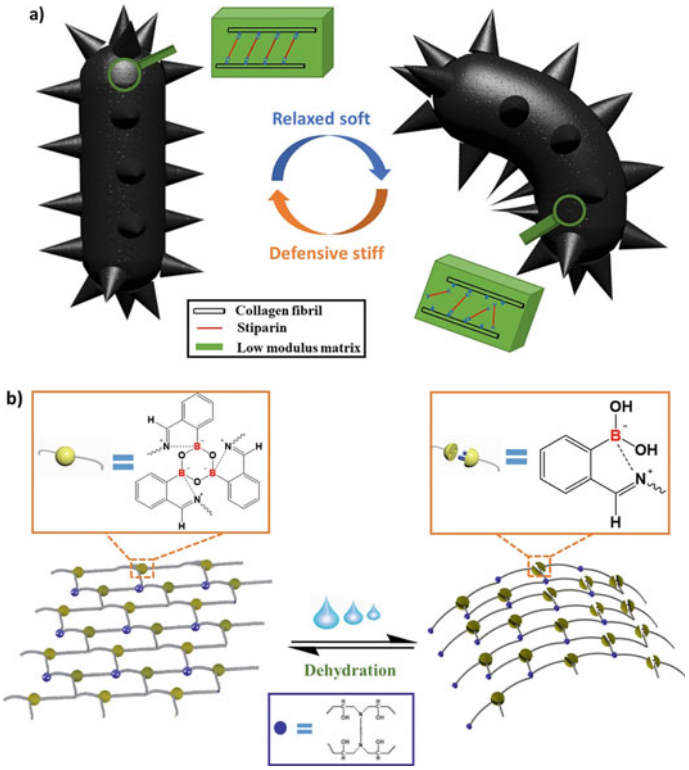

Fig. 1 **a** Schematic representation of the structure change and tunable property process, **b** Mechanism of water-triggered self-healing and property in epoxy-boroxine hybrid. The blue beads represent the permanent crosslinks of epoxy [19]

of cellulose nanofiber and incorporated into the epoxy coating. Once the coating is damaged while exposed to water, the cellulose nanofibers get deformed, releasing the physically adhered epoxy monomer into the damaged area. Thus, mobilized epoxy monomer readily reacts with-NH_2 group on the surface of amine immobilized CNF to form an epoxy crosslinked network to recover the scratch.

Self-healing has been developed as a solution for metal corrosion, which can sense even a micro-crack at the early stage, and thereby avoid economic losses and infrastructure failures at industries. The self-healing functionality has been successfully used as an alternative strategy for corrosion protection [22, 23]. The direct addition of corrosion inhibitors into epoxy coating adversely affects the coating integrity. The encapsulation of inhibitors inside suitable containers provides safe storage and controlled release into the matrix on-demand basis [24, 25]. Polymer capsules [26], inorganic mesoporous materials [27], nanotubes [22, 23] and layered hydroxides [28, 29] are commonly used for the safe encapsulation of corrosion inhibitors. The microcapsules and nanocontainers are encapsulated or immobilized with anticorrosive agents. Several findings reported self-healing anticorrosive coatings developed

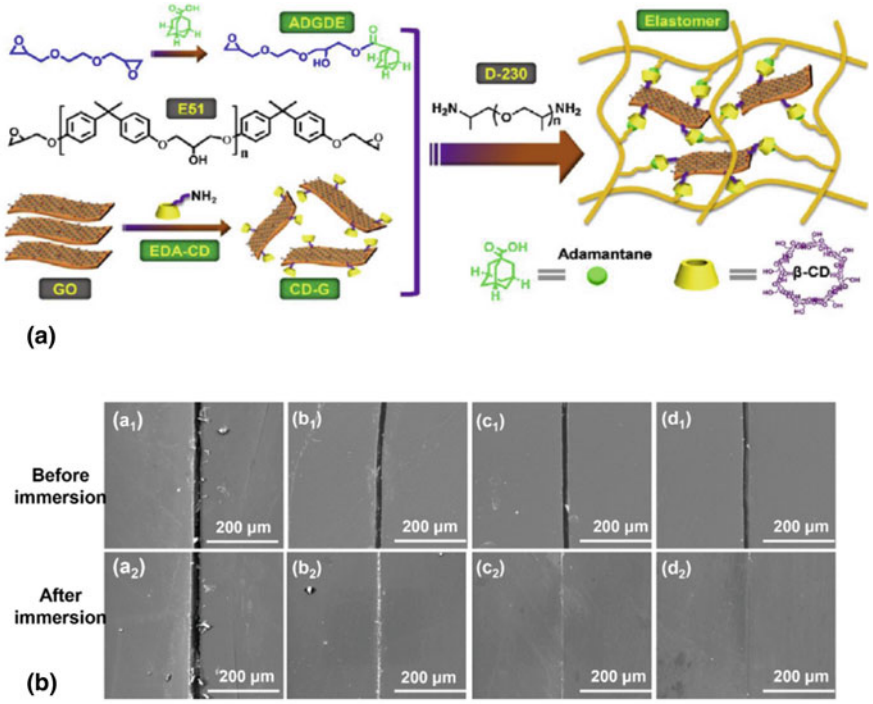

Fig. 2 **a** Pictorial representation of fabrication of graphene-epoxy nanocomposites, **b** Micrographs showing self-healing behaviors of different samples during 24 h immersion process: (a) pure epoxy; (b) neat elastomer; (c) CD-G0.5% and (d) CD-G1% coatings [20]

with corrosion inhibitors as healing agents [30]. A promising self-healing stimulus for anticorrosive epoxy coating is pH. To protect metal substrates from corrosion, self-healing coating doped with pH-sensitive nano-or micro-containers has been developed. Halloysite nanotubes [31], cellulose nanofibers [32], mesoporous nanomaterials [33], lignin microspheres [34], and core–shell nanofibers [35, 36] are extensively use for the encapsulation or immobilization of corrosion inhibitors. The loaded micro-or nano-containers were carefully designed to initiate the release of corrosion inhibitors upon pH change. For instance, carboxyl-functionalized mesoporous silica nanomaterials (MSNs-COOH) were used as pH sensitive nanocontainers and were loaded with benzotriazole (BTA) molecules [33]. BTA-loaded MSNs-COOH were wrapped with polyethylenimine (PEI) to get BTA@MSNs-COOH-PEI nanocontainers to release BTA with pH variation. Figure 3a shows the steps involved in fabricating BTA@MSNs-COOH-PEI nanocontainer and its action in the epoxy coating matrix. Self-healing coating fabricated via. the incorporation of BTA@MSNs-COOH-PEI in epoxy released BTA inhibitor upon localized corrosion. An accelerated release of BTA sustained at least 25 h has been overserved at alkaline pH. The mechanism of action of BTA@MSNs-COOH-PEI in epoxy coating is due to

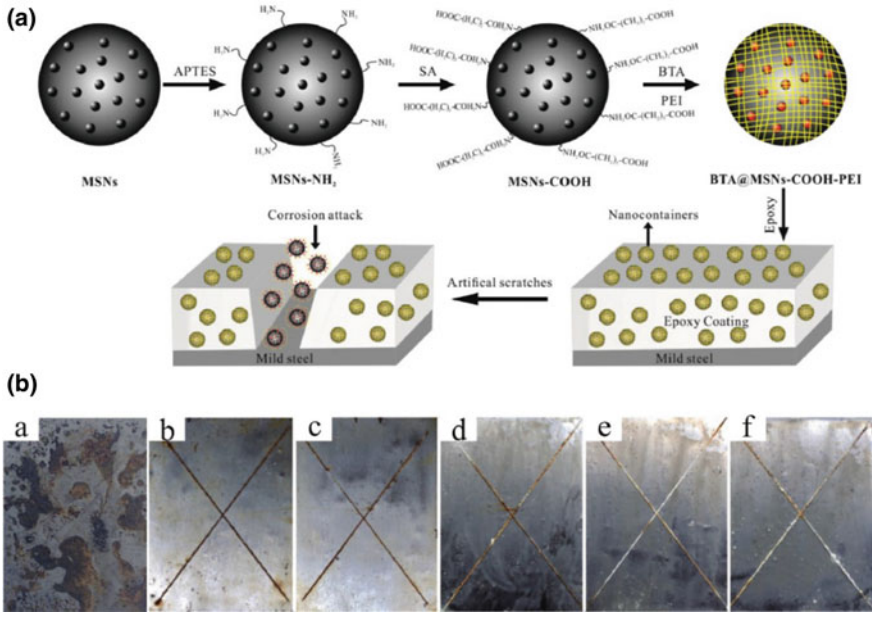

Fig. 3 **a** The schematic representation of fabrication processes of the smart coating containing BTA@MSNs-COOH-PEI and the release mechanism of BTA molecules upon corrosion and **b** Digital images of the uncoated and coated steel panels after 120 h exposure in the salt spray tester: (a) uncoated steel, (b) pure epoxy coating, epoxy coating with (c) 8 wt% MSNs-COOH-PEI, (d) 4 wt%, (e) 8 wt% and (f) 12 wt% BTA@MSNs-COOH-PEI [33]

the structure changes of PEI polymer with pH. The shrinkage and desorption of PEI chains from the nanocontainers with increase in pH cause the accelerated release of the BTA. The corrosion protection ability of BTA@MSNs-COOH-PEI in epoxy has been demonstrated by salt spray test, where steel panels coated with this self-healing coatings are almost devoid of corrosion attack after 120 h exposure (Fig. 3b).

Chitosan/poly (vinyl alcohol) core–shell nanofiber loaded with corrosion inhibitor system of oleic acid (OA) and 2-mercaptobenzimidazole (MBI) have been found effective in imparting pH-responsive self-healing property to epoxy coating over metal substrates [36]. The corrosion protection performance evaluated by electrochemical impedance spectroscopy (EIS) revealed high inhibition efficiency of 96.66 and 99.36% for OA/MBI after 10 and 20 days immersion in alkaline and acidic electrolyte, respectively. The high corrosion inhibition efficiency in the acidic condition is owing to the synergistic action of chitosan protonation and MBI corrosion inhibitor. Cellulose nanofiber facilitates controlled release of the corrosion inhibitor with pH change due to the − OH terminal on the molecular chain of cellulose nanofiber [32]. Figure 4b shows the micrographs of CNF with well-adhered corrosion inhibitors (oleic acid). An increase in local pH initiated the release of OA from CNF surface into the micro-crack. OA adsorbed onto the CNF at pH 11.4 was desorbed by a slight increase in the pH as OA could be desorbed at a pH higher than 12 (Fig. 4c).

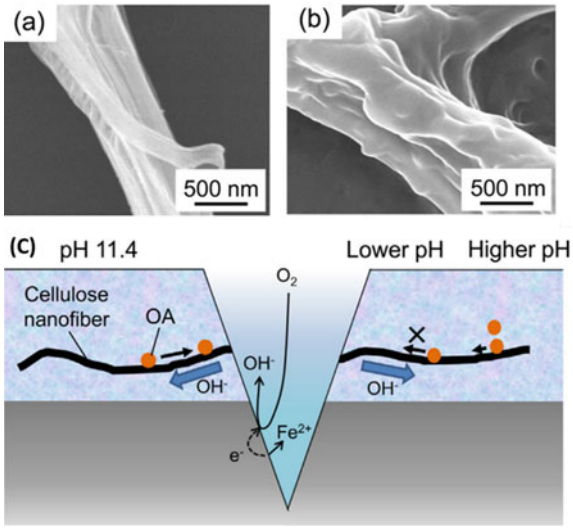

Fig. 4 SEM images of **a** cellulose nanofibers (CNF), **b** CNF mixed with oleic acid and **c** schematic representation of mechanism of self-healing in a CNF + OA coating [32]

3 Dual Responsive Self-healing Epoxy

A dual responsive self-healing healing system could sense and act upon two different stimuli, which would be beneficial for several applications concerning efficiency and repeatability of healing. Development of micro-crack followed by extensive corrosion in metal pipelines could be better sensed and healed by duel responsive self-healing epoxy coatings. To protect carbon steel against corrosion, a duel responsive self-healing epoxy coating has been developed with a photothermal and pH triggering mechanism [36]. In this case, microcapsules have been engineered to simultaneously load the healing agent/corrosion inhibitor and tailor stimuli-responsive components. Huang et al. [37] synthesized a sandwich-like microcapsules with reduced graphene oxide/mesoporous silica (rGO@MS) assembled with a pH-responsive poly(N,N-dimethylaminoethyl methacrylate) (PDMAEMA) layer. Such microcapsule has been loaded with benzotriazole (BTA) inhibitors. Under NIR irradiation, microcapsules effectively absorb the radiation and helps to increase the surface temperature of the coating and initiate shape memory and self-healing effect. Light triggered self-healing activity could be triggered and completed within 15 s of NIR irradiation. The effect of pH on BTA release was analyzed by the UV–Visible spectra of the dispersion of microcapsules under pH (3, 7 and 11) as shown in Fig. 5. They observed an increased release of BTA from the microcapsules in acidic condition than that in neutral and basic conditions, owing to the protonation effect of PDMAEMA under acidic condition and accelerate the release of BTA by opening several nanopores. Moreover, in a practical condition, anodic dissolution of the carbon steel leads to the formation of hydrated cations. The hydrolysis of the hydrated cations is always accompanied by acidification, which triggers the release of BTA and retards the corrosion process.

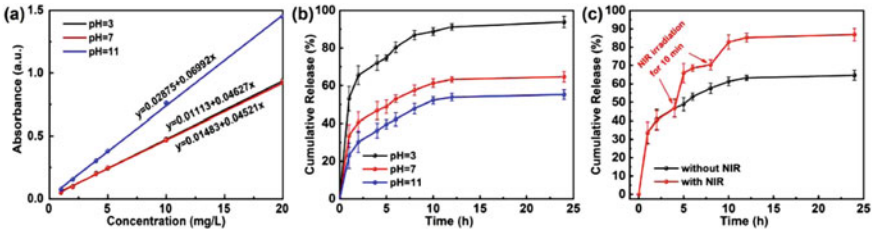

Fig. 5 UV–Visible absorption spectra **a** release of BTA at different pH conditions, **b** release of BTA from the microcapsules at different pH, **c** release of BTA in saline water with and without irradiation [36]

Similarly, a dual responsive anticorrosive epoxy coating which sense both pH and temperature variations, could achieved using naturally occurring halloysite (HNT) nanocontainers in epoxy coating [37]. With pH variations, benzotriazole (BTA) immobilized in HNT layer-by-layer (LBL) assembly had a controlled and sustained release upon damage of the coating surface. In addition, the system is responsive to temperature by the thermos-sensitivity of polyelectrolyte grafted around HNT.

In epoxy self-healing systems, polycaprolactone (PCL) microspheres could function as carriers of the corrosion inhibitor and seal the crack by melting microspheres [38]. Self-healing epoxy coating incorporated with corrosion inhibitor 8-hydroxyquinoline (8HQ) loaded PCL microspheres has been developed to protect the aluminum alloy. Upon damage, the 8HQ leached from the microspheres and suppressed corrosion. The crack was sealed upon heating by melting the inhibitor-loaded PCL microspheres.

In another study, epoxy cured with cashew nut shell liquid (CNSL) blended with polycaprolactone (PCL) showed dual–responsive shape memory and self-healing behaviors [39]. Such an epoxy/PCL blend system showed excellent shape memory response to thermal and chemical stimuli. After thermal treatment, the epoxy/20 wt % PCL blend showed self-healing ability with 93.70 % tensile strength recovery. The self-healing ability could be due to the melting of PCL followed by the volumetric thermal expansion to fill the damage [40].

Recently, Abrantes et al. [42] fabricated epoxy coatings that are sensitive to mechanical stress and pH variation. Dual stimuli-responsiveness has been achieved by adding microcapsules containing linseed oil as self-healing agent and BTA as a corrosion inhibitor. Stimuli-responsive mechanisms exhibited by the coatings are mechanical stimulus results in the release of linseed oil and pH variation responsible for the controlled release of benzotriazole helps achieve self-healing ability and inhibition of corrosion. Figure 6 illustrates the graphical representation of the dual responsive epoxy system. The mechanical stress creates scratches in the system, which is also responsible for releasing the linseed oil from the microcapsules. Thus, released linseed oil fills the cracks and heals (by film formation) the damage to the site. Further, corrosion protection was achieved by releasing BTA with the change in pH.

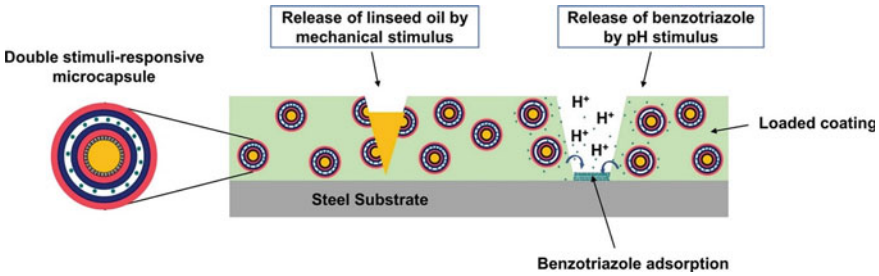

Fig. 6 Graphical representation of mechanism of self-healing in epoxy/linseed oil@BTA microcapsules [41]

These two effects can be triggered independently in the microcapsule incorporated epoxy system.

The coating which could sense both crack and pH variation has been developed for steel parts in acid/base transfer pipes or storage tanks [42]. Tetraphenylethylene (TPE) containing double-wall poly(urea–formaldehyde) (UF)/ polyurethane (PU) microcapsules dispersed in the thiol-epoxy thermoset coated over steel substrates self-reports the occurrence of crack. TPE shows aggregation induced emission (AIE), and the crack is detected by the fluorescence emission of released TPE. The pH variation could be detected by adding thymol blue to the matrix. Such dual stimuli-responsive coatings are extremely beneficial, since they are able to detect the leakage at tank part and the crack formation at coating materials (Fig. 7). In further advancement, such self-reporting systems could be upgraded with the encapsulation of healing agents in capsules and fluorescence materials as multi-walled microcapsule or dual capsule systems.

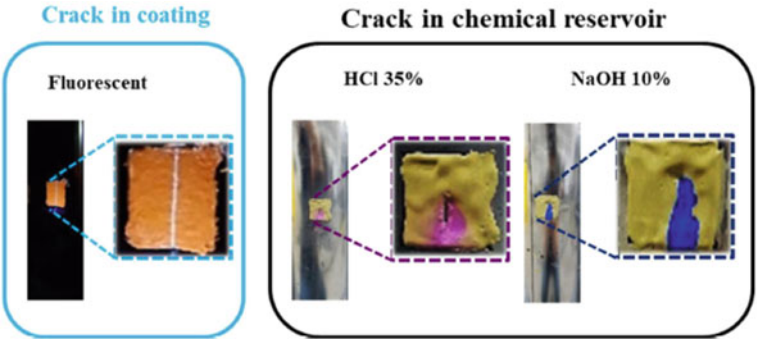

Fig. 7 Application of the self-reporting thiol-epoxy thermoset coatings to the laboratory scale chemical reservoirs: actual crack test [42]

4 Multi-Stimuli-Responsive Self-healing Epoxy

Very recently, research on multi-responsive self-healing epoxy systems is getting much interest in scientific research [43]. The development of multi-stimuli-responsive self-healing epoxy systems for high-end applications is really exciting but challenging one. Combining multiple stimuli-responses into a single polymer matrix is really a difficult task. The self-healing process assisted by multi-stimuli occurs within only a few minutes or even seconds. Those systems can respond to stimuli to deal with various environmental changes. Multi-stimuli-responsive systems are fabricated for the selective release of self-healing agents in an efficient way such that it can respond to external stimuli very rapidly and effectively along with a sudden feedback rate [43].

The latest developments in multi-responsive epoxy-based self-healing systems are discussed here. Hu et al. [44] examined the self-healing action of epoxy systems via graphene-assisted host−guest chemistry. β-cyclodextrin anchored-graphene sheets (host) on acrylamidoazobenzene (guest) (CD-GNs/AAAB) act as macro-crosslinker and photothermal agents to trigger the self-healing action in the system. The cleaved bonds are recombined by including CD-GNs on AAAB in epoxy systems by the crosslinked anchoring effects of graphene. They observed an increased healing efficiency with the amount of CD-GNs/AAAB. As shown in Fig. 8, an external damage can break the link between the host and guest (CD-GNs and AAAB), irradiating the broken samples with UV light (366 nm) to disconnect the connection between host and guest, further improves the self-healing efficiency. Self-healing was triggered by either heating at 120 °C in dark or photothermally using a NIR laser.

Very recently, Sun et al. [45] reported a triple-response self-healing epoxy system. The response to three different stimuli was achieved by incorporating core–shell structured material $Fe_3O_4@SiO_2$ and $TiO_2@SiO_2$, in which PU oligomers are embedded in the core. The core of the nanostructures which selectively triggered by the moisture/UV in the external environment. Under an external magnetic field, $Fe_3O_4@SiO_2$ drive the microcapsules toward the direction of the magnetic field.

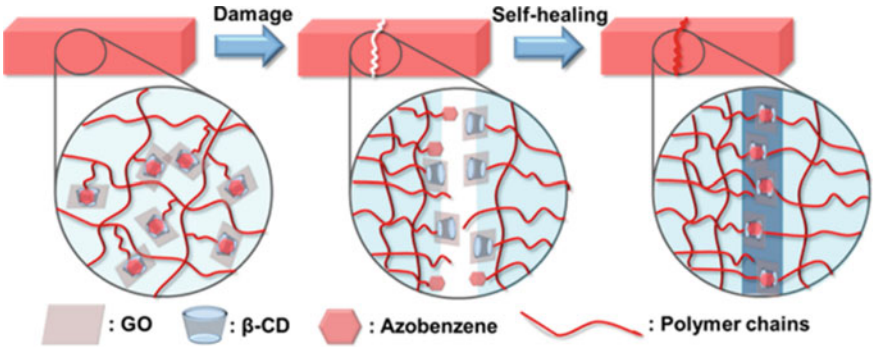

Fig. 8 Mechanism of self-healing in epoxy/CD-GNs/AAAB systems [43]

TiO_2@SiO_2 nanostructure can absorb external UV light. The mechanism of healing exhibited by this system is fascinating, the photo initiator in the healing agent gets excited and results in the formation of an active free radical, initiates the polymerization and heals the crack formed. Water triggered curing in the same achieved by releasing healing agent (from microcapsule). Water is reacted with the isocyanate group of the PU acrylate oligomer (healing agent) to form an acidic amine group. This acidic amine is further dissociated and results in the formation of an amine. In another advancement, epoxy vitrimers were successfully explored for developing multi-responsive self-healing materials. Introduction of aniline trimer (ACAT, an oligoaniline) [45] and Fe_3O_4 nanoparticles [46], in to epoxy vitrimers were noticed for their multi-responsive functions.

5 Conclusion and Future Perspective

The versatility offered by the multi responsive self-healing system would satisfy the demanding requirements for practical applications of modern society. Considering the future demands for industrial application, the research in this area would explore more and more simple designs and chemistries in achieving multi-stimuli-responsive self-healing epoxy systems for advanced applications. Hybrid structures involving graphene oxide, mesoporous and tubular inorganic materials, nanocellulose, etc. are the potential components in multi-stimuli-responsive self-healing epoxies. The associated functionalities like reprocessing, recycling and self-welding would be better practiced in self-healable epoxy materials as a sustainable approach. Designing and fabricating a multi-stimuli-responsive epoxy-based self-healing system is a facile approach to overcoming the existing challenges of epoxy-based products. Multiple triggered self-healing systems will improve the working efficiency during service time.

References

1. Karak, N.: Overview of epoxies and their thermosets. In: Sustainable epoxy thermosets and nanocomposites, vol. 1385, pp. 1–36. American Chemical Society (2021)
2. Goodman, S.H.: 6-Epoxy resins. In: Goodman, S.H. (ed.) Handbook of thermoset plastics, second edition, pp. 193–268. William Andrew Publishing (1998). https://doi.org/10.1016/B978-081551421-3.50009-6
3. Gibson, G.: Chapter 27-Epoxy resins. In: Gilbert, M. (ed.) Brydson's plastics materials, eighth edition, pp. 773–797. Butterworth-Heinemann (2017). https://doi.org/10.1016/B978-0-323-35824-8.00027-X
4. Yuan, C., Zhang, M.Q., Rong, M.Z.: Application of alkoxyamine in self-healing of epoxy. J. Mater. Chem. A **2**, 6558–6566 (2014)
5. Tan, L., Davis, A.C., Cappelleri, D.J.: Smart polymers for microscale machines. Adv. Funct. Mater. **31**, 2007125 (2021)

6. Nagappan, S., Moorthy, M.S., Rao, K.M., Ha, C.-S.: Stimuli-responsive smart polymeric coatings: an overview. In: Hosseini, M., Makhlouf, A.S.H. (eds.) Industrial applications for intelligent polymers and coatings, pp. 27–49. Springer International Publishing, (2016). https://doi.org/10.1007/978-3-319-26893-4_2
7. Vertuccio, L., et al.: Smart coatings of epoxy based CNTs designed to meet practical expectations in aeronautics. Compos. B Eng. **147**, 42–46 (2018)
8. Hager, M.D., Greil, P., Leyens, C., van der Zwaag, S., Schubert, U.S.: Self-healing materials. Adv. Mater. **22**, 5424–5430 (2010)
9. Zhang, F., Zhang, L., Yaseen, M., Huang, K.: A review on the self-healing ability of epoxy polymers. J. Appl. Polym. Sci. **138**, 50260 (2021)
10. Williams, K.A., Dreyer, D.R., Bielawski, C.W.: The underlying chemistry of self-healing materials. MRS Bull. **33**, 759–765 (2008)
11. Fu, X., et al.: Stimuli-responsive self-healing anticorrosion coatings: from single triggering behavior to synergetic multiple protections. Mater. Today Chem. **22**, 100575 (2021)
12. Zhang, Y., et al.: Thermo-adjusted self-healing epoxy resins based on Diels-Alder dynamic chemical reaction. Polym. Eng. Sci. **61**, 2257–2266 (2021)
13. Chen, J., Fang, L., Xu, Z., Lu, C.: Self-healing epoxy coatings curing with varied ratios of diamine and monoamine triggered via near-infrared light. Prog. Org. Coat. **101**, 543–552 (2016)
14. Fang, L., et al.: Self-healing epoxy coatings via focused sunlight based on photothermal effect. Macromol. Mater. Eng. **302**, 1700059 (2017)
15. Ma, L., et al.: Dual-action self-healing protective coatings with photothermal responsive corrosion inhibitor nanocontainers. Chem. Eng. J. **404**, 127118 (2021)
16. Dong, Y., Geng, C., Liu, C., Gao, J., Zhou, Q.: Near-infrared light photothermally induced shape memory and self-healing effects of epoxy resin coating with polyaniline nanofibers. Synth. Met. **266**, 116417 (2020)
17. Zhu, Y., Cao, K., Chen, M., Wu, L.: Synthesis of UV-responsive self-healing microcapsules and their potential application in aerospace coatings. ACS Appl. Mater. Interfaces **11**, 33314–33322 (2019)
18. Odarczenko, M., et al.: Sunlight-activated self-healing polymer coatings. Adv. Eng. Mater. **22**, 1901223 (2020)
19. Yuan, D., et al.: Biomimetic water-responsive self-healing epoxy with tunable properties. ACS Appl. Mater. Interfaces **11**, 17853–17862 (2019)
20. Liu, C., et al.: Synthesis of graphene-epoxy nanocomposites with the capability to self-heal underwater for materials protection. Compos. Commun. **15**, 155–161 (2019)
21. Vijayan, P.P., Tanvir, A., El-Gawady, Y. H., Al-Maadeed, M.: Cellulose nanofibers to assist the release of healing agents in epoxy coatings. Prog. Org. Coat. **112**, 127–132 (2017)
22. Vijayan, P.P., Al-Maadeed, M.A.S.A.: TiO2 nanotubes and mesoporous silica as containers in self-healing epoxy coatings. Sci. Rep. **6**, 38812 (2016)
23. Vijayan, P.P., Hany El-Gawady, Y.M., Al-Maadeed, M.A.S.A.: Halloysite nanotube as multifunctional component in epoxy protective coating. Ind. Eng. Chem. Res. **55**, 11186–11192 (2016)
24. EBSCOhost | 114268242 | 'Containers' for self-healing epoxy composites and coating: Trends and advances. https://web.p.ebscohost.com/abstract?direct=true&profile=ehost&scope=site&authtype=crawler&jrnl=1788618X&AN=114268242&h=9GuxrK0rvD%2f5Ekb1bdeuFyXvuLwnqqR2yhGnBgzMJza4Bv5o1ubDzaEyXw5ilJ2m%2fzT%2bzD%2fIZO8FQKDdikA9fw%3d%3d&crl=c&resultNs=AdminWebAuth&resultLocal=ErrCrlNotAuth&crlhashurl=login.aspx%3fdirect%3dtrue%26profile%3dehost%26scope%3dsite%26authtype%3dcrawler%26jrnl%3d1788618X%26AN%3d114268242
25. Zheludkevich, M.L., Tedim, J., Ferreira, M.G.S.: "Smart" coatings for active corrosion protection based on multi-functional micro and nanocontainers. Electrochim. Acta **82**, 314–323 (2012)
26. Matsuda, T., Jadhav, N., Kashi, K.B., Jensen, M., Gelling, V.J.: Release behavior of pH sensitive microcapsules containing corrosion inhibitor. Prog. Org. Coat. **132**, 9–14 (2019)

27. Vijayan, P.P., Al-Maadeed, M.A.S.A.: Inorganic porous materials based epoxy self-healing coatings. In: EEPP2129, vol. 2016. Hamad Bin Khalifa University Press (HBKU Press) (2016)
28. Zheludkevich, M.L., et al.: Active protection coatings with layered double hydroxide nanocontainers of corrosion inhibitor. Corros. Sci. **52**, 602–611 (2010)
29. Carneiro, J., et al.: Polyelectrolyte-modified layered double hydroxide nanocontainers as vehicles for combined inhibitors. RSC Adv. **5**, 39916–39929 (2015)
30. Odarczenko, M., et al.: Self-protecting epoxy coatings with anticorrosion microcapsules. ACS Omega **3**, 14157–14164 (2018)
31. He, Y., Xu, W., Tang, R., Zhang, C., Yang, Q.: pH-responsive nanovalves based on encapsulated halloysite for the controlled release of a corrosion inhibitor in epoxy coating. RSC Adv. **5**, 90609–90620 (2015)
32. Yabuki, A., Shiraiwa, T., Fathona, I.W.: pH-controlled self-healing polymer coatings with cellulose nanofibers providing an effective release of corrosion inhibitor. Corros. Sci. **103**, 117–123 (2016)
33. Wen, J., et al.: Polyethylenimine wrapped mesoporous silica loaded benzotriazole with high pH-sensitivity for assembling self-healing anti-corrosive coatings. Mater. Chem. Phys. **253**, 123425 (2020)
34. Tan, Z., et al.: pH-responsive self-healing anticorrosion coating based on a lignin microsphere encapsulating inhibitor. Ind. Eng. Chem. Res. **59**, 2657–2666 (2020)
35. Ji, X., et al.: Developing wide pH-responsive, self-healing, and anti-corrosion epoxy composite coatings based on encapsulating oleic acid/2-mercaptobenzimidazole corrosion inhibitors in chitosan/poly(vinyl alcohol) core-shell nanofibers. Prog. Org. Coat. **161**, 106454 (2021)
36. Wang, Q., et al.: Self-healing coatings containing core-shell nanofibers with pH-responsive performance. ACS Appl. Mater. Interfaces **13**, 3139–3152 (2021)
37. Huang, Y., et al.: Photothermal and pH dual-responsive self-healing coating for smart corrosion protection. J. Mater. Sci. Technol. **107**, 34–42 (2022)
38. Liu, Y. et al.: A novel dual-responsive halloysite nano-container for anti-corrosion coatings. Anti-Corros. Methods Mater. ahead-of-print (2022)
39. Huang, Y., et al.: Triple-action self-healing protective coatings based on shape memory polymers containing dual-function microspheres. ACS Appl. Mater. Interfaces **10**, 23369–23379 (2018)
40. Lorwanishpaisarn, N., et al.: Dual-responsive shape memory and self-healing ability of a novel copolymer from epoxy/cashew nut shell liquid and polycaprolactone. Polym. Testing **81**, 106159 (2020)
41. Luo, X., et al.: A thermoplastic/thermoset blend exhibiting thermal mending and reversible adhesion. ACS Appl. Mater. Interfaces **1**, 612–620 (2009)
42. Abrantes, D., et al.: Smart coating based on double stimuli-responsive microcapsules containing linseed oil and benzotriazole for active corrosion protection. Corros.Sci. **130**, 56–63 (2018)
43. Lee, T.H., et al.: Dual stimuli responsive self-reporting material for chemical reservoir coating. Appl. Surf. Sci. **434**, 1327–1335 (2018)
44. Hu, Z., et al.: Multistimuli-responsive intrinsic self-healing epoxy resin constructed by Host−Guest interactions. Macromolecules **51**, 5294–5303 (2018)
45. Sun, P., et al.: A novel UV, moisture and magnetic field triple-response smart insulating material achieving highly targeted self-healing based on nano-functionalized microcapsules. Nanoscale **14**, 2199–2209 (2022)
46. Chen, Q., et al.: Multi-stimuli responsive and multi-functional oligoaniline-modified vitrimers. Chem. Sci. **8**, 724–733 (2016)
47. Chen, M., et al.: Multi-functional epoxy vitrimers: controllable dynamic properties, multiple-stimuli response, crack-healing and fracture-welding. Compos. Sci. Technol. **221**, 109364 (2022)

Bio-Derived Self-healing Epoxy Resins

Nataša Z. Tomić and Mohamed Nasr Saleh

Abstract This chapter discusses different bio-renewable sources for epoxy resins and adhesives. The objective is to shed some light on the potential of using bio-renewable resources to replace the toxic epoxy components while not compromising their high-performance characteristics. Such bio-renewable alternatives can be obtained from but are not limited to vegetable oils, lignin, isosorbide, natural phenols, and tannic acid (TA). For each of these alternatives, their self-healing mechanisms capabilities are detailed. Moreover, the synthesis of natural phenols and TA is provided, highlighting the effect of their structure on the mechanical properties and the healing efficiency. Thanks to their superior thermal and mechanical properties, some of these "green" solutions demonstrated a high potential for industrial applications.

Keywords Bio-based resins · Self-healing · Vitrimers · Epoxy resins

1 Introduction

Thanks to the outstanding mechanical properties, chemical resistance, thermal stability, minimal shrinkage, and great adhesion to many substrates, epoxy resins, are widely used in a variety of applications, including adhesives [1–4], coatings [5], and composites [6, 7]. One of the important facts is that almost 90% of used epoxy resins consist of the bisphenol-A (BPA) building component [8–10]. Nevertheless, BPA is derived from nonrenewable fuel sources, and it is designated as an endocrine-disrupting compound that cannot be used in food-related products, or devices where the leached BPA can affect human health [11]. Considering the possible harmful

N. Z. Tomić (✉)
Technology Innovation Institute, Self-healing Materials Group, Advanced Materials Research Center, Masdar City, Abu Dhabi, United Arab Emirates
e-mail: natasa.tomic@tii.ae

M. N. Saleh
Technology Innovation Institute, Advanced Materials Research Center, High Temperature Thermoplastic Composites Group, Masdar City, Abu Dhabi, United Arab Emirates
e-mail: mohamed.saleh@tii.ae

N. Hameed et al. (eds.), *Multifunctional Epoxy Resins*, Engineering Materials,
https://doi.org/10.1007/978-981-19-6038-3_7

impacts on health and energy concerns, caused by nonrenewable fossil feedstock, the inevitable goal is to resort to renewable resources for creating bio-based epoxy resins without compromising the performance offered by the petroleum-based equivalents.

For decades, vegetable oils have been recognized as one of the most significant renewable options due to their availability, low cost, and long-term viability [12, 13]. Moreover, they represent an excellent foundation for different pathways to produce bio-based monomers and polymers because of their particular triglyceride structure and three flexible nonpolar chains of fatty acids. These chains have 8–24 carbon segments and up to seven unsaturated bonds [14]. Therefore, epoxidation of unsaturated bonds of vegetable oils, which were cured with various cross-linkers (e.g., amines, anhydrides, bisphenols, acids, etc.), produced multipurpose epoxy resins based on vegetable oils [15–17]. The functional vegetable oil-based epoxy resins might successfully mitigate the drawbacks associated with the over-reliance on petroleum-based monomers. However, in terms of properties, like mechanical characteristics and glass transition temperature (T_g), epoxy resins derived from vegetable oils could not compete with fossil-based epoxy resins available in the market [18]. The soft, branched, and flexible architecture of triglyceride chains, as well as the low cross-link density, would undoubtedly lead to low mechanical characteristics and thermal stability of epoxy resins [19]. Furthermore, epoxy resins are thermosets with permanent cross-links, which are making their degradation and recycling more challenging, resulting in significant environmental and societal implications. Compared to thermosets, thermoplastics with no or low branching can be recycled since they can be reprocessed by melting. As a result, developing high-strength vegetable oil-based epoxy resins while having the benefits of both thermosets and thermoplastics is a challenge that has attracted much attention and opened the horizon for other bio-based resources to be utilized.

Vitrimers are a recent family of polymers that may rearrange their polymer network by induced dynamic covalent bond exchange processes, giving them reshaping and reprocessing capabilities [20, 21]. Therefore, they have become especially appealing because of their potential shape memory, self healing, and reprocessing capabilities [22, 23]. At low temperatures, they act like conventional thermoset polymers, but at high temperatures, their network structure changes [24]. These properties, which complement restructuring or reprocessing efficiency with dimensional stability, create more opportunities for epoxy resins [25]. The earliest known vitrimer systems were epoxy/acid or epoxy/anhydride polyester-based resins, which have been extensively investigated [20, 26]. Transesterification reactions appeared to be a promising reaction mechanism for vitrimers. Some "green" alternatives with numerous epoxy functionality have been explored in the production of "green" vitrimers based on this process. A bio-based vitrimer with shape memory, mending capabilities, and possible adhesive uses, has been created by curing sebacic acid epoxy with ozonized Kraft lignin [21]. Another bio-based vitrimer, obtained by curing bio-based triepoxy (TEP) with anhydride monomer, possessed mechanical properties similar to the cured reference BPA epoxy resin [27]. The ability to make bio-based vitrimers from biomass feedstock has been demonstrated by the synthesis of the aforementioned vitrimers. As a result, vitrimer research has

gained momentum, and the creation of ecologically safe and sustainable vitrimers has become an appealing alternative. Thus, this chapter is structured in a way to highlight the possible routes to use vitrimers to produce self-healing bio-based epoxy resins from (i) vegetable oils, (ii) lignin, (iii) isosorbide, and (iv) natural phenols. Nevertheless, the last section is dedicated to a relatively new trend in creating self-healing epoxy resins, not as part of the group of vitrimers, by replacing the BPA epoxy component from another bio source which is tannic acid in this case.

2 Bio-Renewable Sources for Epoxy Components

2.1 Vegetable Oils

In order to improve the drawbacks of poor mechanical properties of resins based on vegetable oils, the addition of a stiff benzene ring to the networks was successfully used [28, 29]. Covalent adaptable networks (CANs) have been proposed as a way to add healing and re-processability into cross-linked polymers. The use of dynamic covalent bonds can enable the rearrangement of a polymer network resulting in functional smart materials with intrinsic stability. Independent or activated-healing ability, reversible malleability, and force imaging capacity are all characteristics of these materials [30–35]. Moreover, to increase the molecular mobility of recyclable thermosets, dynamic covalent linkages have also been used. Boronic ester transesterifications [29], Diels–Alder reactions [36], Schiff-based [37] or disulfide exchange [38], and other methods have been established to add dynamic covalent bonding process to epoxy vitrimers. Recently, the only vitrimers that could be successfully healed and reprocessed at mild temperatures were soft vitrimers with limited mechanical properties (tensile strength lower than 10 MPa). The constraints for high mechanical properties, self-healing, and processability of epoxy resins are complex and require additional research.

Tricyclic dioxaborolane was used as a hardener to synthesize epoxy vitrimers based on vegetable oils with triple exchange cross-linkers of carboxylate ester linkage, disulfide bridge, and dioxaborolane [39]. The efficiency of boronic ester introduction in polymer network could provide the elastomer with outstanding self-healing and re-processing properties via dioxaborolane metathesis of boronic ester. Those properties can be triggered at room temperature and average humidity, while the degree of rearrangement can be varied on several orders of magnitude, from passive to exceedingly rapid [31]. Free sulfur alcohol arched in polymers may create reversible S–S bridges that would split under specific conditions or instantaneously, which was proven to be an effective approach as well for the production of multi-functional polymers. The advantage of conventional thermosets with plasticity was also demonstrated by thermally induced carboxylate transesterification. The strategically integrated three dynamic cross-linkers in the network can speed polymer chain

stress relaxation and should make vitrimers bendable at more mild temperatures in a shorter time.

2.1.1 Self-healing Mechanism

Boronic ester, carboxylic ester, and S–S bonds are examples of common segments found in vitrimer chemistry formulation to gain dynamic covalent bonding and a variety of functions. Polymers with numerous dynamic covalent bonds may be unstable and thus divide into many tiny pieces. A technique for creating a highly cross-linked polymer was developed, which was created by "thiol-epoxy" click chemistry involving multi-branched epoxy monomers and reactive disulfide nucleophiles capable of forming a variety of dynamic covalent connections [39]. Vegetable oil is an effective multi-branched monomer due to its unique triglyceride structure represents ideal flexible building blocks (see Scheme 1). The primary disadvantage of polymers derived from vegetable oils is their poor mechanical characteristics. Incorporating rigid building blocks, such as aromatic structures, is an effective way to enhance the mechanical characteristics of such polymers. Therefore, Scheme 1 shows a highly cross-linked polymer network synthesized from various epoxidized vegetable oils [39] and cured with 2, 2´-(1, 4-phenylene)-bis [4-mercaptan-1, 3, 2-dioxaborolane] (BDB) at 160°C in the presence of 4-dimethylaminopyridine (DMAP). Dynamic bonds of this system can be a subject of transesterification reactions, disulfide, and dioxoborolane metathesis at room temperature.

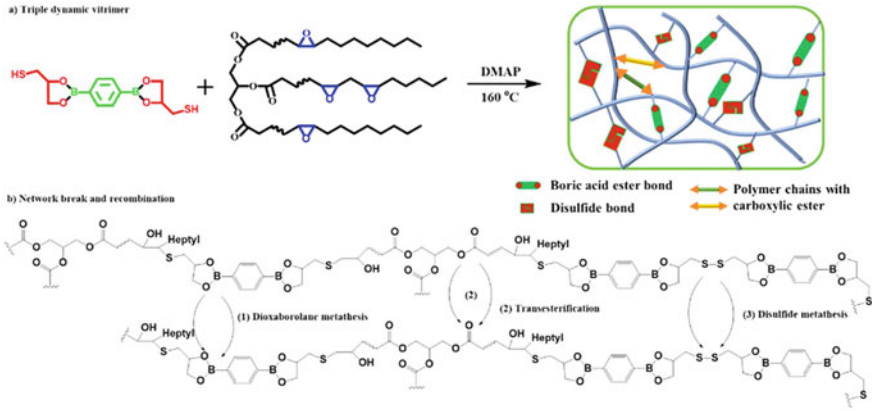

Scheme 1 Chemical structure and healing mechanism of bio-based epoxy resin from epoxidized soybean oil (Republished with permission of the Royal Society of Chemistry, from [39]; permission conveyed through Copyright Clearance Center, Inc.)

2.1.2 The Influence of Vegetable Oils' Structure on Resin Properties

Several epoxidized vegetable oils with varying epoxy-equivalent weight (EEW) values were used in to achieve different cross-linking densities of bio-based epoxy resins, including epoxidized linseed oil (ELO), epoxidized rubber seed oil (ERSO), epoxidized soybean oil (ESO), and epoxidized olive oil (EOO) [39]. BELO, BERSO, BESO, and BEOO were the names given to the developed epoxy resins. Under ideal conditions, a variety of bio-based epoxy resins were produced through thermally induced thiol-epoxy click chemistry too. DSC results of the studied epoxy resins showed enhanced T_g when the EEW of the epoxy resin increased [39]. Changing the EEW can alter the mechanical characteristics of the epoxy resins. Increasing epoxy contents often leads to higher cross-linking densities and stiffer BDB concentrations (assuming the molar ratios of BDB and ESO remain same), which improves the tensile strength and Young's modulus while lowering elongation at break [31]. Notably, the epoxy resins' mechanical performance was significantly dependent on humidity and heat treatment [39]. The mechanical characteristics of epoxy resins are considerably reduced by increasing humidity, particularly for materials with a low EEW (few cross-linking sites), such as BEOO and BERSO. The elongation at break of these epoxy resins, on the other hand, was significantly enhanced following the same treatment. Since there are fewer cross-linking sites in BEOO and BERSO, the cross-linking density is reduced, resulting in poor surface compactness. Water molecules can easily penetrate the core of the cross-linking networks, in addition to the hydrophilic hydroxyl groups. Water breaks the equilibrium of the dynamic reversible chemical bonds, causing the boronic ester groups to split into free boronic acid and diol groups, causing the breakdown of the polymer network [31]. At the same time, the plasticizing effect of water molecules play a vital role in shifting from rigid plastics to flexible elastomers [40]. BESO and BELO (high EEW) had mechanical characteristics, and were less susceptible to humidity, which may be associated to higher cross-linking density limiting the water molecule diffusion.

2.1.3 The Influence of Temperature Treatment on Healing Efficiency

Figure 1 shows the dependence of the healing efficiency on various thermal treatments for 24 h and humidity of 70%. An increase of the temperature of the thermal treatment caused the epoxy resins' tensile strength and young's modulus to improve considerably. The increase of temperature from 30 to 60°C and 90°C, improved the tensile strength of BERSO by 203 and 258%, respectively, coupled with 426 and 768% increase in young's modulus. The reason behind it is that the mobility of the polymer chain is increased at high temperatures, which speeds up the metathesis process between the boronic acid and the diol groups, improving a cross-link density of the epoxy resins. Stimulated with temperature, the free boronic acid and the diol groups which did not engage in the curing reactions could react again [41]. Furthermore, the rearrangement of the disulfide connections caused by temperature stimulation may encourage additional reactions and result in a better organized polymer

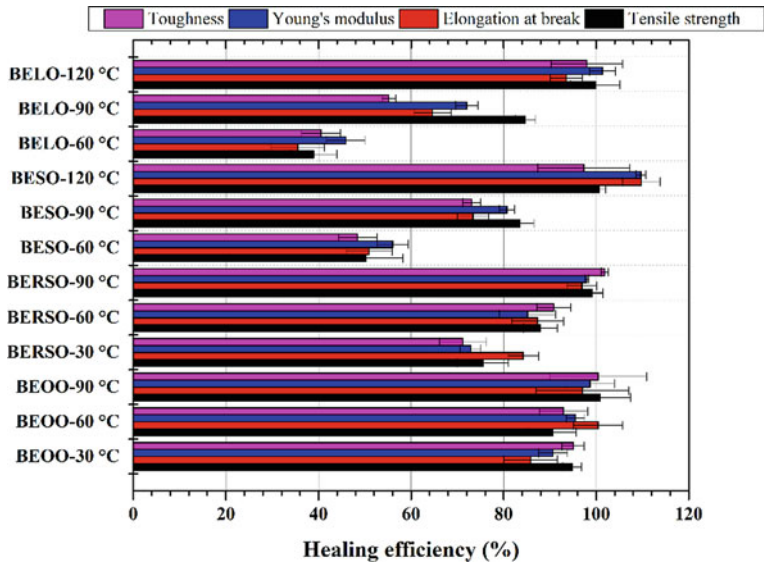

Fig. 1 Healing efficiency after healing at different temperatures for 24 h with a humidity of 70% (produced according to the results from the literature [39])

structure, improving the mechanical characteristics [42, 43]. When the temperature was raised to 120°C, the mechanical characteristics of the epoxy resins remained relatively unchanged, indicating that the reaction between the reactive centers had nearly completed at 90°C [39].

2.2 Lignin

Many plants contain lignin, which is the second most prevalent natural polymer. The utilization of lignin in obtaining thermosets like phenol–formaldehyde and epoxy resins has received a lot of attention lately [44, 45]. However, because of its bulky and aromatic structure, lignin is frequently incompatible with other components, restricting its use [46, 47]. As a result, chemical lignin modification is required for its uses.

Ozonation is used as a green approach to treat the product in the pulping process and to split part of the aromatic rings in the lignin structure. During this treatment, carboxylic acid groups are introduced, improving the solubility of the degraded lignin [48–50]. On the other hand, lignin after the ozone treatment has carboxylic acid groups, which can be employed as a hardener for epoxy resins [51].

2.2.1 Self-healing Mechanism

A completely bio-based vitrimer with a high lignin content was recently demonstrated [21]. Bond-exchangeable cross-linked networks are formed by curing ozone-treated Kraft lignin (Oz-L) with sebacic acid derived epoxy (Se-EP) in the presence of zinc catalyst ($Zn(acac)_2$). At high temperatures, the vitrimer based on lignin has outstanding shape memory and mending capabilities [21]. The typical production techniques for monomer compounds and bio-based vitrimers are depicted in Scheme 2.

The lignin structure was altered by ozone oxidation in two ways: (1) a portion of the benzene rings was cleaved, reducing the rigidity of the lignin, and (2) additional carboxylic acid groups were added [48]. Oz-L had reduced thermal stability than Kraft lignin because of the lowering of the amount of thermally stable aromatic rings, which was reflected in the temperature drop for a 5 wt % loss (T_{d5}) [21]. The decrease of the aromatic rings and the rise of carboxylic acid functionalities caused by ozone treatment increased the solubility in polar solutions.

Oz-L can be employed as a hardener for epoxy resins since it contains reactive carboxylic acid (–COOH) and hydroxyl groups (–OH). Sebacic acid, produced from castor oil, was converted to a diglycidyl ester (Se-EP), then reacted with Oz-L. A modest quantity of ethanol was added to help the two reagents and Zn-based catalyst mix well. The mixture was cured in a hot press after removing ethanol [21]. The curing process and transesterification following curing are depicted in Scheme 2. The carboxylic acid and phenolic OH groups on Oz-L interacted with the epoxy groups to create ester bonds in the presence of Zn^{2+} catalyst, and the resultant oxygen anions tended to grab the active hydrogen atoms to form hydroxyl groups. The stoichiometry ratio (R) is dependent on the ratio of epoxy to the sum of the phenolic OH and carboxyl groups because both of them (–OH and–COOH) can react with epoxy groups [22]. Therefore, different curing systems were produced by changing the (R). Guaiacol and adipic acids were employed to react with Se-EP to differentiate the relative reactivity of phenolic OH and carboxylic acid groups in Oz-L. Guaiacol contains a single phenolic hydroxyl group, whereas adipic acid has two carboxylic acid groups. DSC was employed to study the reactions between model compounds. Results showed that the carboxylic acid groups had better reactivity than the phenolic groups. Thus, the mixture was treated at 150°C for 1 h and 190°C for 2 h to complete curing and maximize ester linkage formation [21].

2.2.2 Self-healing Capability

The ability of Oz-L-based epoxy to heal was examined by observing the change in surface artificial defect size at 190°C. With a pressure of ~ 0.14 MPa, the damaged specimens were put in a press. Figure 2 suggests that the widths of the scratches in all samples were reduced by more than 70% in approximately 5 min. The effective transesterification reactions (TERs) produced a thermal-responsive shape change attributed to the shrinking of the gap. According to the findings of this investigation,

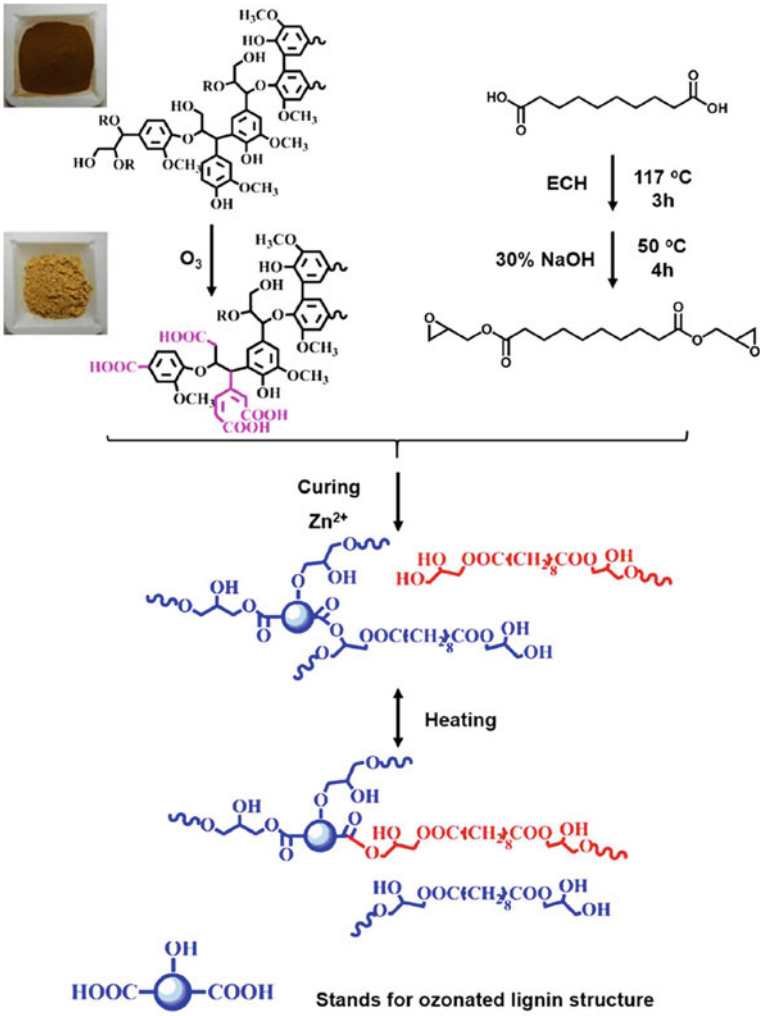

Scheme 2 Schematic representation of lignin modification and production of Se-EP/Oz-L vitrimer (Republished with permission of the Royal Society of Chemistry, from [21]; permission conveyed through Copyright Clearance Center, Inc.)

the Se-EP/Oz-L vitrimer with Zn catalyst might be utilized as temperature-triggered self-healing adhesives [21].

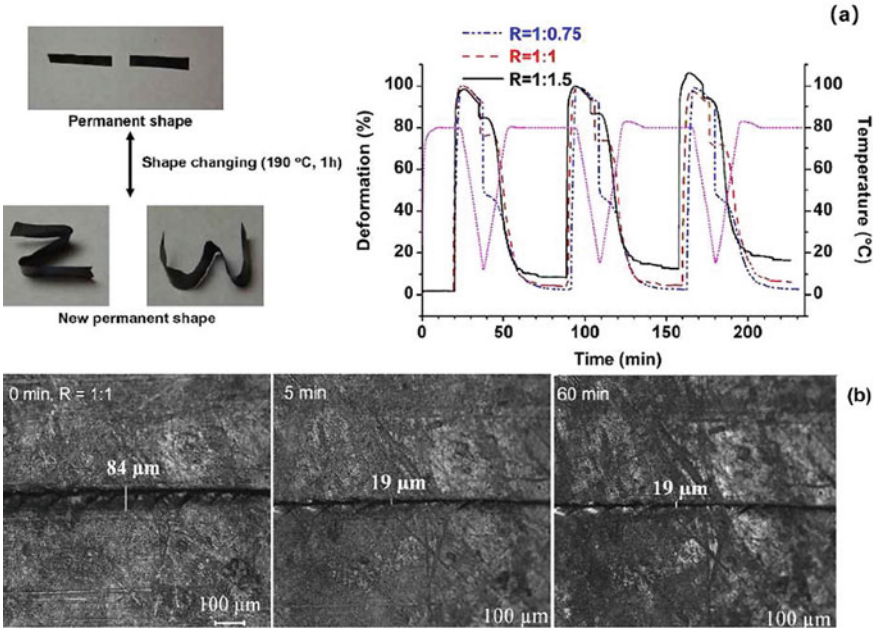

Fig. 2 **a** Shape memory capability (R = 1:1), and consecutive memory cycles for different compositions **b** thermally-induced self-healing of Se-EP/Oz-L with R = 1:1 (Republished with permission of the Royal Society of Chemistry, from [21]; permission conveyed through Copyright Clearance Center, Inc.)

2.3 Isosorbide

The economic and environmental challenges linked with standard thermosets have prompted research toward the creation of recyclable and re-processable thermosets, as well as the synthesis of bio-based polymers. An isosorbide-derived epoxy (ISEPO) and aromatic diamines with disulfide linkages (4,4´-disulfanediyldianiline (MDS)) were used to create a bio-based vitrimer (MDS-EPO) (see Fig. 3) [52]. Isosorbide was chosen as a natural building block because of its plentiful resources from maize and its high stiffness and thermal stability, which has been utilized to make renewable polymers with high glass transition temperatures (T_g) [53, 54]. Isosorbide's relatively strong thermal stability contributed to the improved re-processability of epoxy vitrimers on higher temperatures. In the meantime, the dynamic reactions of the disulfide linkages are governed by many processes that vary depending on the reaction circumstances. External stresses caused the disulfide connections to break mechanically, generating thiol radicals that could quickly exchange with other disulfide linkages, leading to the repairing or recycling of epoxy thermosets [55–57].

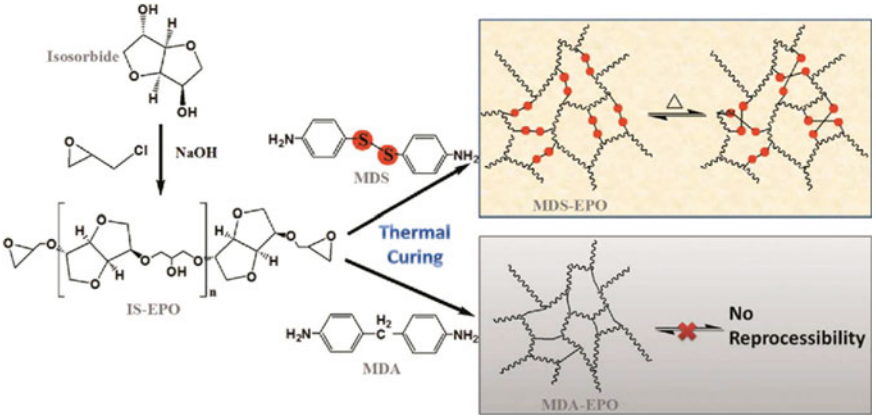

Fig. 3 The synthesis of isosorbide-derived epoxy (IS-EPO) (Republished with permission of John Wiley & Sons-Books, from [52]; permission conveyed through Copyright Clearance Center, Inc.)

2.3.1 Self-healing Capability

Traditional epoxy resins were unable to regain their integrity after being damaged. The use of dynamic bonds in polymer networks provides a satisfactory answer to this problem no matter the failure mechanism. When MDS-EPO was damaged, in the form of a scratch or fracture, all that was required was thermal treatment of the scratched sample to cause matrix relaxation and the dynamic bonds processes to recover disulfide bonds and heal the crack. For instance, Fig. 4 shows created crack on MDS-EPO, which starts to self-heal at 100°C, and the crack completely disappears after 60 min [52]. Thanks to the vitrimer-like behavior of MDS-EPO, it was also possible to repair the catastrophic damage, i.e., to make an integrated sample out of all broken pieces. To show this, scientists crushed the MDS-EPO into a fine powder before processing it in a hot press at 100°C for 60 min [52]. Following that, the sample's structure was restored with the formation of a clear and homogenous thin layer. On the contrary, when the MDA-EPO powder was treated using the same process, the sample was just physically attached, and it lacked any mechanical properties. This comparison proved the re-processibility of MDS-EPO thanks to the viscoelastic flow generated by the disulfide exchange.

Ma et al. [52] performed the grinding/hot pressing cycles three times to investigate the influence of consecutive treatments on the tensile characteristics of MDS-EPO. The mechanical characteristics of MDS-EPO after one reprocessing cycle were similar to those of starting specimens. For instance, the recovery rate of the average Young's modulus (E), tensile strength (σ_b), and elongation at break (ε_b) were 103.5 $\pm$ 4.5, 82.6 $\pm$ 9.6, and 80.0 $\pm$ 11.7%, respectively [52]. The recovery rate of E was maintained over 80.0% after second and third cycle, whereas the recovery rate of σ_b and ε_b was reduced. Obtained results can be related to the oxidation of sulfur radicals at elevated temperatures, resulting in the loss of the disulfide bonds, or to the

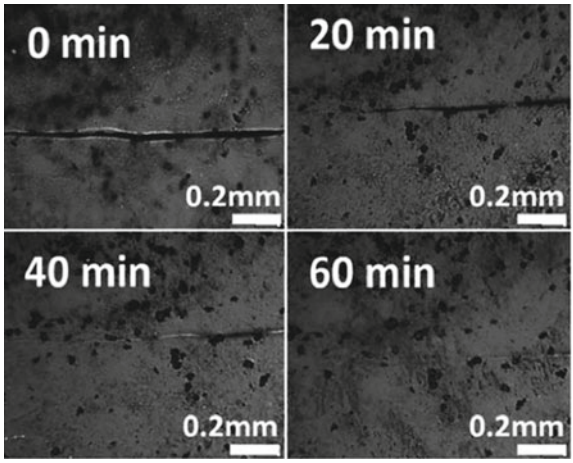

Fig. 4 Optical microscopic photographs of fractured MDS-EPO after treatment at 100°C for different treatment times (Republished with permission of John Wiley & Sons-Books, from [52]; permission conveyed through Copyright Clearance Center, Inc.)

cleavage of C–C backbone as a result of frequent and full milling of materials into powders [58, 59]. The mechanical characteristics of vitrimers were also reported to deteriorate in other systems [58, 60].

The research of isosorbide-derived epoxy is designed to give one more alternative solution epoxy resin tailoring from both economic and environmental perspectives.

2.4 Natural Phenols

One of the primary hurdles is the preparation of high T_g epoxy-based vitrimers [61]. To fulfill the requests of application at high environmental temperatures, especially for aerospace applications, T_g values of such epoxy materials should be greater than 100°C [62]. Nevertheless, as shown in Table 1, the majority of reported epoxy vitrimers have low glass transition temperatures (less than 100°C), limiting their uses. The low T_g obtained can be attributed to at least two factors. On the one side, epoxy vitrimers are intentionally not completely cross-linked using a quantity much lower than the required stoichiometric quantity of anhydride or carboxylic acid cross-linker in the system. The cross-linking density of the cured polymer is limited by the need to reserve a sufficient quantity of available hydroxyl groups to react in transesterification, which is done by reducing the quantity of the cross-linker [22]. On the other side, to obtain acceptable molecular mobility at increased temperatures, existing epoxy vitrimers' cross-linked structures are usually made of flexible epoxy component or cross-linker, resulting in reduced T_g's of the final thermoset. Generally, stiff segments and higher values of cross-linking density restrict the polymer chain mobility, compromising reparability and re-processability [63].

The backbone stiffness and the cross-linking density of a thermosetting polymer's cross-linked network are both important factors affecting its T_g. Bisphenol-A epoxies

Table 1 T_g values of some epoxy vitrimers [27]

Vitrimer starting materials	Self-healing mechanism	Healing temperature (°C)	T_g (°C)	Ref
Epoxidized soybean oil, citric acid	Transesterification	> 150	0–30	Altuna et al. [64]
1,4-bis(2-(prop-2-yn-1-yloxy)ethoxy)benzene, 4,4-bis(azidomethyl)-1,1-biphenyl, 1,6-dibromohexane	Transalkylation	> 130	90–100	Tang et al. [65]
α-azide-ω-alkyne, 1,6-dibromohexane	Transalkylation	> 130	− 39–3	Obadia et al. [60]
Dimer and trimer acids, BPA epoxy	Transesterification	> 130	0–20	Montarnal et al. [20]
Glutaric anhydride, BPA epoxy	Transesterification	> 130	60–80	Montarnal et al. [20]
Bis(cyclic carbonate), tris(2-aminoethyl)amine	Transcarbamoylation	> 150	50–55	Fortman et al. [66]
Diphenyl epoxy, sebacic acid	Transesterification	> 160	55	Pei et al. [23]
Amines and acetoamide monomers	Transamination	> 100	100–110	Denissed et al. [67]
Isosorbide epoxy and 4,4′-disulfanediyldianiline	Disulfide exchange	> 130	40.6	Ma et al. [52]

are the most common epoxy resins, accounting for more than 90% of the overall epoxy market. Values of T_g up to 150°C can be achieved with a completely cured BPA epoxy. Multifunctional epoxy resins (functionality ≥ 3) are frequently utilized as matrices in composites to attain greater T_g for applications such as aerospace equipment. After curing with aromatic amines, N,N,N′,N′-tetraglycidyl-4,4′-diaminodiphenylmethane (TGDDM), a tetrafunctional epoxy, can reach a T_g higher than 200°C [68, 69].

2.4.1 Synthesis of Bio-Based Triepoxy (TEP)

Using sustainable feedstocks such as vanillin and guaiacol (derived from lignin), a bio-based triepoxy (TEP) vitrimer was developed and produced [27]. As indicated in Scheme 3a, TEP was obtained using easy two-stage technique. In the first stage, the triphenol chemical was created. Guaiacol's ortho and para-positions are both reactive [70, 71]. The para-substitution product is the major product due to steric hindrance in ortho-substitution. The triphenol produced in the first stage was epoxidized in the second stage to yield TEP. The reaction utilized an excess of epichlorohydrin (10 times more compared to the hydroxyl groups) as both a reagent and a solvent, as in a conventional industrial approach. TEP was a pale-yellow powder, whereas triphenol appeared to be a red solid. It is generally known that phenol groups are susceptible to oxidation, leading to the formation of quinone groups and a red appearance. The coloring of triphenol became substantially lighter after the phenolic OH groups were changed to glycidyl ether groups.

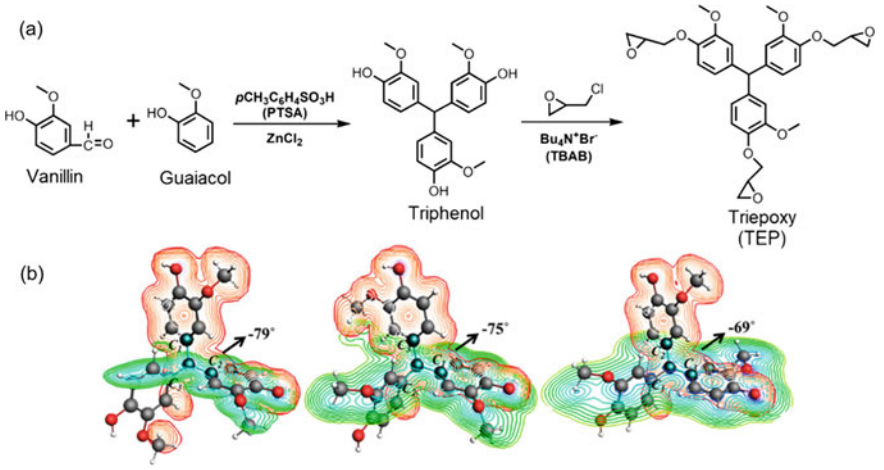

Scheme 3 **a** Triepoxy (TEP) synthetic route using vanillin and guaiacol as biomass resources; **b** Molecular Simulation of Triphenol (dihedral angles of triphenylmethane are determined and annotated) (Reprinted (adapted) with permission from [27]. Copyright (2018) American Chemical Society)

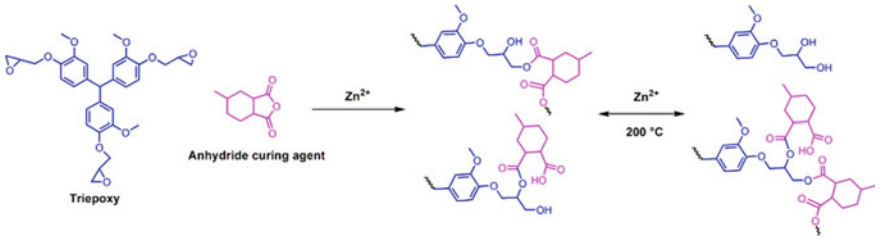

Scheme 4 TEP and anhydride curing reaction and illustration of dynamic transesterification reactions (TERs) in a cross-linked network structure (Reprinted (adapted) with permission from [27]. Copyright (2018) American Chemical Society)

TEP's molecular modeling (Scheme 3b) further indicates that the three stiff benzene rings are noncoplanar, and the three epoxy groups are spaced far enough apart to prevent undesirable cyclization side reactions. Consequently, the epoxy groups in TEP efficiently engaged in the curing processes, resulting in a faster cross-linking reaction and higher cross-linking density and T_g.

2.4.2 Curing of TEP with Anhydride

At varying stoichiometric ratios (R = epoxy/anhydride) and amounts of catalyst, TEP and anhydride (4-methylcyclohexane-1,2-dicarboxylic anhydride, MHHPA) were reacted [27]. MHHPA has a solid molecular structure and is a low-viscosity liquid. MHHPA was used as a cross-linker to ensure the formulation's processability and a high T_g. At increased temperatures, $Zn(acac)_2$–H_2O catalyzed the cross-linking as well as subsequent transesterification in the produced cured product. $Zn(acac)_2$–H_2O is a solid powder that does not dissolve well in an epoxy/anhydride combination below 100°C. Before adding the catalyst, the epoxy/anhydride mixture was warmed to 130–140°C to ensure proper mixing. The anhydride ring is opened and activated by the catalyst during the curing process, and the produced carboxylate anions combine with epoxy groups to form ester linkages and release oxygen anions, which then reacts with the anhydride or epoxy (Scheme 4). The cured TEP showed a high T_g (187°C), and mechanical properties equivalent to the cured BPA-based epoxide [27].

2.4.3 Self-healing Capability of Bio-Based TEP

The existence of thermally induced transesterification processes is expected according to the results of the stress relaxation measurements. These reactions cause the cross-linked network to reorganize, giving the material self-healing capability. The specimens were damaged in a form of a scratch and then put in a press to evaluate the reparability/self-healing [27]. The self-healing was done at 220°C for

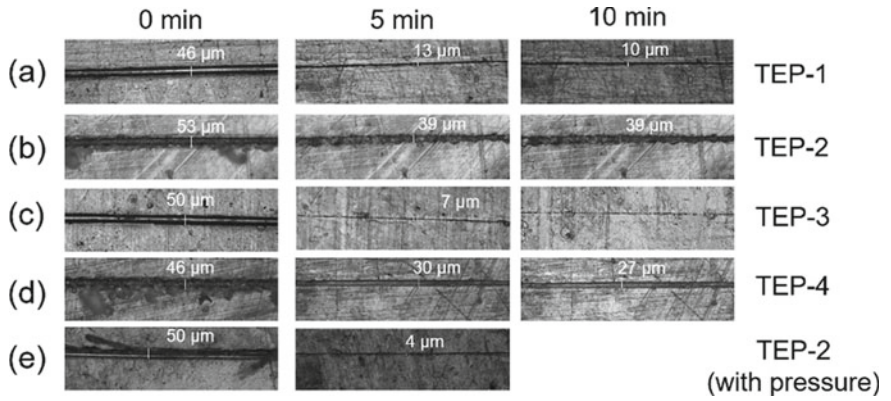

Fig. 5 Thermally healed **a** TEP-1, **b** TEP-2, **c** TEP-3, and **d** TEP-4 samples by clipping the samples between two metal plates and heating in a convection oven. **e** TEP-2 thermal repair using a hot press and mild pressing. The width of the crack as a function of healing time was measured at the same spot for each sample in all measurements. Thermal deterioration cannot be prevented since the mending is high (220°C). If the repairing period is too lengthy (>10 min), thermal degradation will occur. (Reprinted (adapted) with permission from [27]. Copyright (2018) American Chemical Society)

various durations. The change of the surface scratches was monitored using an optical microscope (see Fig. 5).

The size of the scratch on the cured TEP having R = 1/1 (TEP-1) shrunk by nearly 70% in only 5 min, as illustrated in Fig. 5a, demonstrating their exceptional reparability. The reparability was improved when the amount of the catalyst (TEP-3) was increased. The cured TEP with R = 1/0.5 (TEP-2), on the other hand, demonstrated unfavorable reparability. At the 5th minute, the crack's size had shrunk by just 27%, and at the 30th minute, it had shrunk by 38% [27]. External tension is usually required to gain material mobility when repairing the vitrimer. When exposed to the same force, the material with a greater modulus deforms less than the material with a lower modulus. TEP-2 with the scratched surface was put under pressure at 220°C to validate the theoretical mechanism. Figure 5e shows that the crack width reduced by nearly 90% in only 5 min, which is substantially quicker than the results shown in Fig. 5b.

This relatively good reparability is most likely due to (1) the adequate quantities of hydroxyl groups and ester linkages accessible for transesterification, (2) the low rubbery modulus promoting facile reshaping, and (3) the noncoplanar structure of TEP, giving higher free volume in the cured polymer and enabling higher polymer chain mobility at the self-healing temperature. This research presents the first high-T_g bio-based epoxy material with exceptional self-healing capacity, as well as a straightforward process for making high-T_g repairable epoxy materials.

Recently, a novel eugenol-derived epoxy (Eu-EP) was obtained, and vitrimers were created by curing Eu-EP with succinic anhydride (SA) at different amounts (1:0.5, 1:0.75, and 1:1) in the presence of Zn-based catalysts [22]. The vitrimer,

produced with a 1:0.5 stoichiometric ratio, displayed a quick transesterification at a high temperatures, outstanding repairability, shape altering, and recycling capabilities similar to those described elsewhere [72, 73]. Even though vitrimers with epoxy/anhydride ratios of 1:0.75 and 1:1 had substantially lower transesterification degree than the vitrimer with an epoxy/anhydride ratio of 1:0.5 and could not be recycled, they demonstrated significant repairability and shape altering characteristics. Nonetheless, ethanol dissolved these two components efficiently at a low temperature (180°C). The degrading reaction was carried out without introducing an extra catalyst because vitrimers already included an efficient catalyst ($Zn(acac)_2$). After 3 h of exposure at 190°C, the degraded polymers were transformed back into vitrimers. This significant discovery suggests that cured epoxy/anhydride material with a wide range of their proportions (from 1:0.5 to 1:1) may be recycled and exhibit repairability and shape altering capabilities [22].

Eu-EP was obtained in two stages, as illustrated in Scheme 5a. The first stage was the Williamson ether synthesis with 1,4-dibromobutane to make a eugenol-derived diene (Eu-DI). The epoxidation of Eu-DI was used to make Eu-EP in the second step. The epoxidation reagent was *m*-chloroperoxybenzoic acid (*m*CPBA), which was used at room temperature in CH_2Cl_2. Eu-EP and succinic anhydride (SA) reacted at various stoichiometric ratios (R = epoxy/anhydride).

Scheme 6 shows the possible curing reaction mechanism of Eu-EP and SA catalyzed by $Zn(acac)_2$. The anhydride ring is first opened and activated by $Zn(acac)_2$, and the generated carboxylate anions combine with the epoxy groups to create ester bonds and release oxygen anions, which then react with the anhydride or epoxy. The hydroxyl anions may also bind active hydrogen to produce hydroxyl groups [74–76]. Since the boiling point of acetylacetone produced by $Zn(acac)_2$ is substantially lower than the post-curing temperature, it evaporates through the cross-linking. In the meantime, new ligands interact with the Zn^{2+} ions (i.e., carboxyl or hydroxyl group) [73, 77].

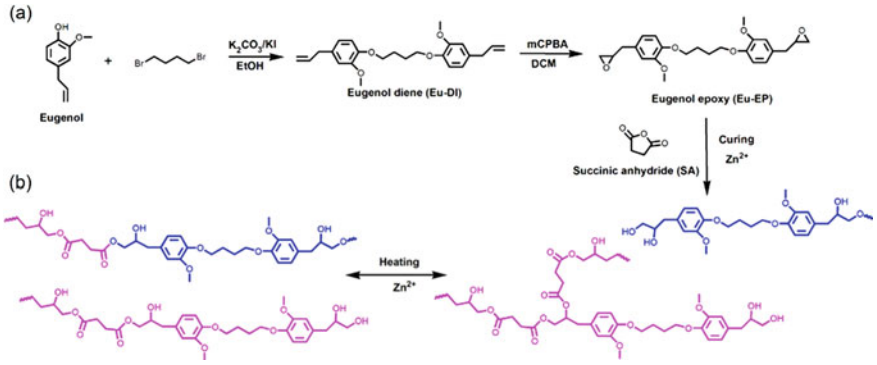

Scheme 5 **a** Synthesis of Eugenol Epoxy (Eu-EP); **b** Curing Reaction of Eu-EP and SA in the Presence of Zinc Catalyst and Illustration of Heat-Induced Transesterification Reactions (TERs) (Reprinted (adapted) with permission from [22]. Copyright (2018) American Chemical Society)

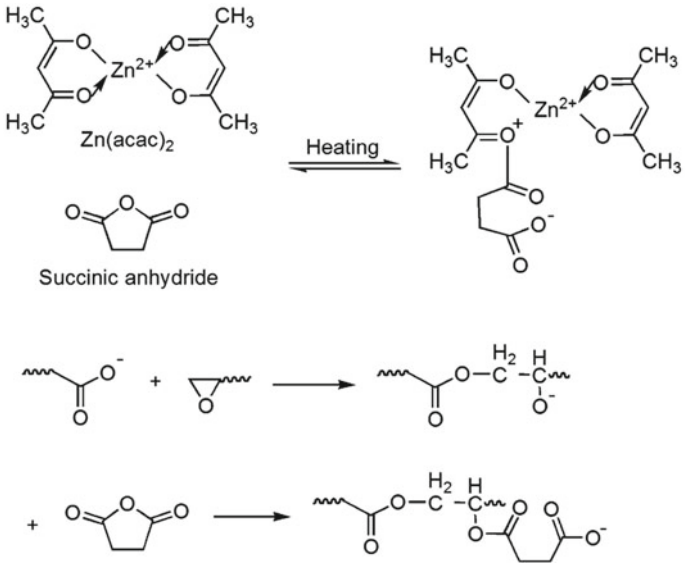

Scheme 6 Possible curing mechanism of eugenol-based epoxy and SA in the presence of $Zn(acac)_2$ catalyst (Reprinted (adapted) with permission from [22]. Copyright (2018) American Chemical Society)

2.4.4 Self-healing Capability

The transition of vitrimer polymers from thermosets to thermoplastics at elevated temperatures was governed by the stress relaxation caused by the transesterification reactions (TER). This transition is of tremendous interest since it gives the materials multifunctional features, including shape change, repair, and recycling. The shape-changing characteristics of Eu-EP/SA flat films with varied ratios (R = 1:0.5, 1:0.75, and 1:1) were investigated by wrapping them in Al foil, and the forms of specimens were pushed to adopt the shape of "W-S-U" [22]. The specimens were left to cool down to room temperature after processing in a convection oven at 200°C for 1 h. All Eu-EP/SAs specimens effectively transformed their forms to "W-S-U" after this treatment. The newly developed shape, "W-S-U," remained constant throughout an extensive temperature range (25–100°C), showing that the specimens conformed to given novel forms. The form modification is flexible, and the procedure can be repeated. This reversibility is due to the triggered dynamic bond reactions causing the cross-linked polymer network to reorganize. The specimen film can adapt to a new shape if it is attached to the required shape at elevated temperature minimum for 1 h. Even though the relaxations of Eu-EP/SAs with R = 1:0.75 and 1:1 were substantially slower than those of Eu-EP/SAs with R = 1:0.5, they nevertheless had significant shape-changing characteristics.

Figure 6 demonstrates the high self-healing capability of Eu-EP/SA films to repair after the cutting process. Furthermore, all Eu-EP/SA specimens were scratched to

fracture the surface and then put between two metal plates to analyze the healing characteristics (Fig. 7) [22]. The healing process was carried out in a convection oven at 190°C. The fractures progressively vanished as a function of time under heating, as illustrated in Fig. 7, exhibiting outstanding healing characteristics. In just 10 min, the fracture widths of all Eu-EP/SAs shrank by more than half. The crack widths of Eu-EP/SAs with R = 1:0.5 and 1:1 reduced by more than 90% in 1 h. Eu-EP/SA with R = 1:0.75 did not repair as well as the other two Eu-EP/SAs due to its delayed stress relaxation rate, but its healing capability was still satisfactory. The aforementioned Eu-EP/SA repairs were completed without applying pressure. Under pressure, the healing process might be enhanced (Fig. 7). A home iron with a working temperature of 60 to 240°C, which includes the temperature range of the TER reactions, can also be used to simplify the healing process [22].

Although catalyzed dynamic TER in epoxy-anhydride vitrimers has been achieved and described [20], the majority of research has been on epoxy anhydride systems with a stoichiometric ratio of 1:0.5 (0.5 anhydrides to 1 epoxy group). The shape altering and healing of Eu-EP/SAs can also be achieved through a higher variety of epoxy anhydride ratios (from 1:0.5 to 1:1) [22]. This represents a significant result,

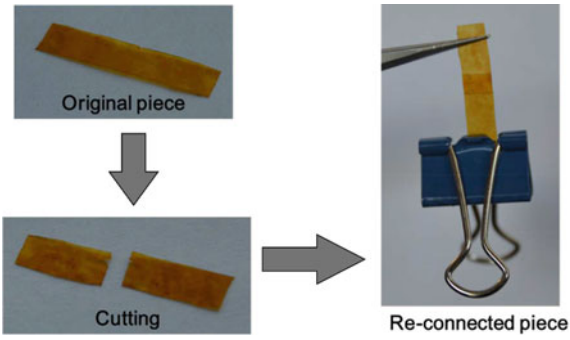

Fig. 6 Cutting and repairing of the cut cured Eu-EP/SA having R = 1/0.5 (molar ratio of epoxy/anhydride = 1/0.5) (Reprinted (adapted) with permission from [22]. Copyright (2018) American Chemical Society)

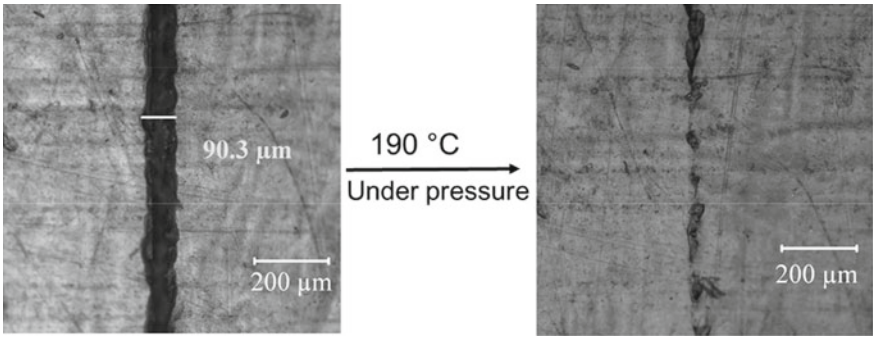

Fig. 7 Self-healing behavior of Eu-EP/SA specimen having R = 1/0.5 (molar ration of epoxy/anhydride = 1/0.5) under external stimuli (force) at 190°C for 10 min (Reprinted (adapted) with permission from [22]. Copyright (2018) American Chemical Society)

and the formulation technique might be applied to other epoxy-anhydride polymeric systems with dynamic bond exchange.

2.5 Tannic Acid (TA)

The repair procedure is primarily challenging for adhesively bonded joints. Although adhesive bonding improves the load transfer and structural performance, adhesives have traditionally been used only in secondary structures [78]. The main issues were fatigue and durability of the bonded joints throughout their structural lifespan [79], as well as the difficulties of evaluating a bond line after construction and during operation [80]. Such challenges could be overcome with the introduction of self-healing adhesives featuring a long lifetime and cheaper maintenance expenses. Only a few investigations have been done on self-healing epoxy adhesives used for the bonding of structural elements like aluminum (Al) and steel [81–84]. Adhesive bonds are designed to work under shear, in which tractions are applied parallel to the adhesive's cross-section [85] Shear testing is used to determine the maximum stress that a bonded component can bear once it has been correctly constructed. Thanks to its production simplicity, cost-effectiveness, and practicality, single-lap joint (SLJ) shear testing is widely used in the aerospace and automotive sectors [86, 87]. Even though the self-healing capability of the bulk polymer has been appropriately established, there are minimal studies on the self-healing potential of the interfacial properties of such polymeric adhesives when used for joining/bonding different adherends. Therefore, it is crucial to analyze the joints formed by these materials to understand how they may be utilized as adhesives. N. Tomić et al. [83] presented a novel repair approach for adhesively bonded joints utilizing tannic acid's intrinsic healing capabilities (TA). The efficiency of healing was calculated based on the maximum load recovery following a complete disbond/failure after the SLJ test. Digital image correlation (DIC) and acoustic emission (AE) are two more approaches used to investigate the self-healing phenomena of TA-based epoxy adhesives. Demonstrating the outstanding bio-based adhesives' healing efficiency bonding lightweight structures should increase the level of confidence in using them in structural bonding.

2.5.1 Synthesis of Epoxy Components from TA

In the first route, the TA was modified in the reaction with epichlorohydrin (EPH) to introduce epoxy functionality. Adhesive A obtained in this manner is shown in Fig. 8 with the appearance of the resulting product, which was a highly viscous brownish oil.

In the second route, the TA was modified by reacting with $POCl_3$ and glycidol to introduce reactive epoxy groups. The entire synthesis is available in [3]. Adhesive B, synthesized in this manner, is shown in Fig. 8 characterized with a highly viscous light brownish oil. The measured epoxy equivalent weight (EEW) was 170 g/mol, which

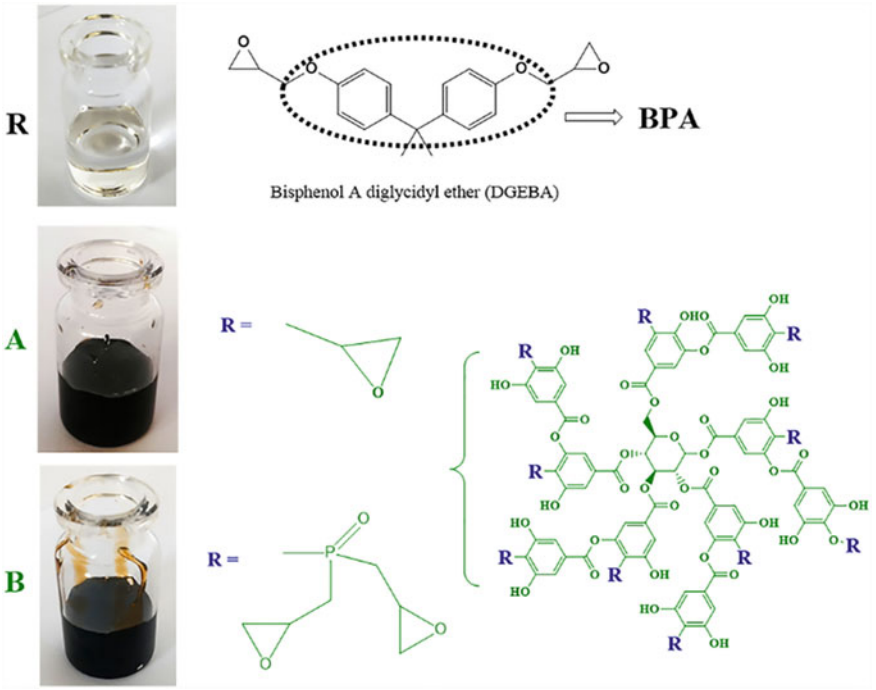

Fig. 8 Schematic representation of the TA modified adhesives R, A and B (*Reproduced from* [83] with the CC BY license (https://creativecommons.org/licenses/by/4.0/)

introduced 10 epoxy groups per TA molecule. The investigation of the chemical structure was reported in an earlier publication [3].

2.5.2 Characterization of Self-healing Epoxy Based on TA

The experimental approach was thoroughly designed to address all the critical components and meet the study's research objectives [83]. DSC analysis was the first step in determining: i) whether the synthesized adhesives have residual chemical activity, indicating possible self-healing capability, and if yes, ii) what the healing process parameters should be, i.e., temperature and duration. Later, FTIR was carried out, which revealed the structural changes that occurred after the self-healing process. Moreover, DMA analysis was crucial in determining the influence of these changes, as discovered by the FTIR analysis, on the mechanical properties of the bulk material. Even with reports gathered through the presented rigorous approach, there is still a knowledge gap as these methodologies cannot capture changes at the bonded-joint level, which was the subject of two recent studies [83, 84]. As a result, it was critical to test the self-healing concept, using several popular interface characterization techniques, such as single-lap joint (SLJ) and mode I double cantilever beam (DCB)

testing. Furthermore, in-situ monitoring methods such as DIC and AE were utilized to validate and identify any differences between the virgin and healed specimens during both SLJ and DCB tests.

2.5.3 Self-healing Mechanism

Figure 9 represents potential self-healing mechanisms using adhesives R, A, and B at high temperatures. Apart from the epoxy groups' homopolymerization of DGEBA component (adhesive R), the reactions between phenolic groups of TA core and epoxy groups were possible (adhesives A and B) [88]. In adhesive A, the remaining phenolic groups of TA and the hydroxyl groups of DGEBA are accessible, but in adhesive B, the glycidyl phosphate functional groups sterically hinder access to the phenolic groups, as illustrated in Fig. 9. Except for the steric barrier, the mobility of the bulky modified TA molecules is substantially reduced in the cured adhesive B as opposed to A, causing self-healing to be much more challenging.

According to DSC results [83], the self-healing procedure for eco-epoxy adhesives was established to be maintaining 180°C and two bars of pressure (one from the vacuum and one of pressure) in a Scholtz Autoclave for 2 h. The temperature rate was + 3°C/min, and the cooling rate was –3°C/min.

The consequence of the self-healing process of adhesive A was a structural change of the bulk material, in the form of a reduction of hydroxyl groups amount and an increase of the amount of the C–O bonds, which was confirmed by the FTIR analysis [83]. These results proved that the phenolic group participated and busted the self-healing process. The yellowing phenomenon noticed for adhesive R associated with carbonyl group formation was not present in the case of adhesive A and B, indicating their improved thermo-oxidative resistance and thermal stability [5, 83, 84, 89].

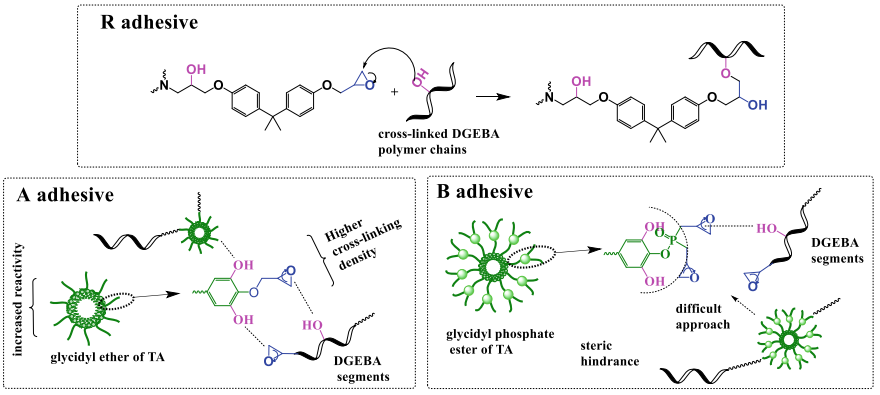

Fig. 9 Hypotheses of self-healing mechanisms for R, A, and B adhesives at high temperatures (*Reproduced from* [83] with the CC BY license (https://creativecommons.org/licenses/by/4.0/)

2.5.4 Mechanical Characterization of Self-Healed Adhesively Bonded Joint

Figure 10 demonstrates a typical SLJ specimen of each adhesive type (A, B, and R) along with the AE data. These results can be divided into two segments: a linear part up to 4 kN and 0.8 mm and a nonlinear section, mainly for adhesive B and R specimens. Nevertheless, as shown in Fig. 10 with the horizontal dotted line, this nonlinear behavior might be linked to probable slippage at the gripping area beyond that load level. This slippage theory could be proven with the AE RMS data response (see Fig. 10a). The RMS of the AE signals in specified time intervals is estimated to determine the severity of the AE activity. As can be seen, specific AE signals (RMS < 5 V) exist from the start of the test until 0.6 mm displacement, which can be linked to micro-damage creation in the adhesive or elastic deformation of the adhesive and adherends. Beyond the 0.6 mm displacement, a dramatic increase in the RMS value of the signals is observed. This sudden rise in the RMS in the case of adhesive A relates to the adhesive's macroscopic damage leading to the specimen's eventual collapse. For adhesives R and B, however, the immediate rise trend was followed by a low-level steady RMS trend associated with specimen slippage. As a result of the specimen slippage for these two adhesives, the initial macroscopic damage could not progress throughout the joint. The RMS value rose again at the end of the test due to the joint's failure. The AE early-stage signals' energy was insignificant compared to the AE signals that originated before the specimens' eventual failure, as shown by the cumulative AE energy curves, which were compatible with the RMS curves. The brittle fracture nature of the adhesives was indicated by the definite rising trend in the cumulative energy curves closer to the ultimate fracture.

Only adhesive A specimens were bonded again after the healing process. Both adhesive R and B specimens were easily opened while handling, right before testing.

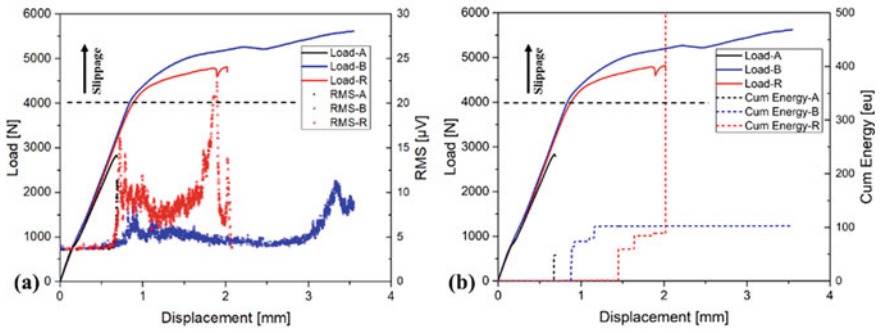

Fig. 10 Virgin representative macroscopic load–displacement curves with AE features a) root mean square (RMS) and b) Cumulative energy (*Reproduced from* [83] with the CC BY license (https://creativecommons.org/licenses/by/4.0/)

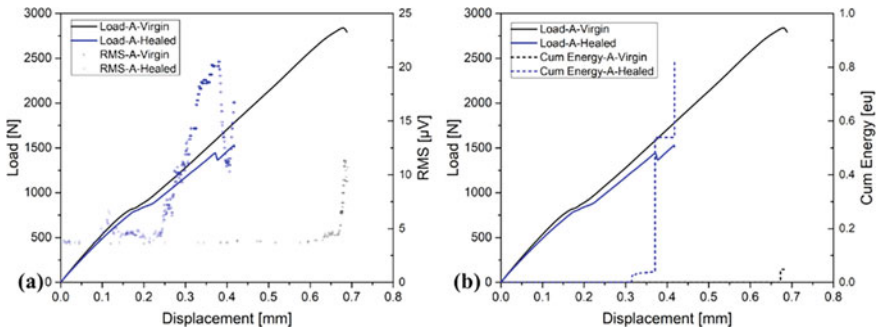

Fig. 11 Virgin versus healed representative macroscopic load–displacement curves with AE features **a** RMS and **b** Cum. Energy (*Reproduced from* [83] with the CC BY license (https://creativecommons.org/licenses/by/4.0/)

Even though minor mechanical connections occurred for R and B adhesive specimens, they were insufficient to keep the specimens intact. The macroscopic load–displacement responses of the virgin and healed adhesives were compared. Adhesive A specimen (see Fig. 11) revealed that healing was quite successful, with just a < 10% reduction in stiffness and 50% in the ultimate load. In other words, from the stiffness and ultimate load perspective, the healing efficiency, measured as the healed normalized by the virgin instance, was 90 and 50%, respectively [83].

Another noteworthy finding was the difference in the slope between the virgin and healed specimens at 0.2 mm. As previously mentioned and reported by Hodgkinson et al. [90], this might be because of the specimen's adjustment in the grips while testing. The same observation was captured in the virgin specimens' testing, regardless of the adhesive type, indicating that it is not a material attribute. The healed specimen's RMS and cumulative AE curves vary from the virgin specimen's. The repaired specimen has more AE events than the unhealed specimen, indicating that the mechanical linkages created during the healing process are weaker. As a result, the damage is more progressive than in the virgin example, which has far fewer AE signals and is mostly localized closer to the end of the test.

Figure 12a shows the macroscopic response for DCB specimens of the three adhesive types in their virgin state. A linear elastic area defines the load–displacement response at the beginning of the loading, independent of the adhesive type, in which the applied load is proportional to the displacement (Δ) by the stiffness of the aluminum cantilever arm. The crack started propagating from the initial crack length of a_0 to the crack length of a once the crack-tip opening displacement reached a critical value. The force was then released, allowing these specimens to be used again for the self-healing experiment. When comparing the load–displacement curves of the virgin specimens, it was clear that adhesive B had the maximum load, followed by adhesives R and A. Adhesives B, R, and A had average G_{IC} values of 52.04, 39.40, and 22.65 J/m^2, respectively. As shown, adhesive B had a fracture toughness that was more than double that of adhesive A. The enhanced adherence and cohesiveness of adhesive B was attributed to the addition of glycidyl phosphate ester of

TA [91], which contributed to a better hydrogen bonding with the adherend. Furthermore, adhesive B's modified tannic acid can be used as a phosphatizing agent to increase the adherence of adhesives, coatings, or paint [92]. The phosphatizing agent must complete two tasks in order to achieve this goal: first, diffuse to the metal contact and acquire excellent adhesion, and second, interact with the bulk polymer. These processes are only achievable for virgin samples since liquid adhesive B might diffuse/penetrate, but not for the softened adhesive B during the self-healing process at temperatures above T_g. This effect can boost the adhesion and cohesion strength of virgin samples, leading to a greater G_{IC} for adhesive B compared to adhesive A. Adhesive A having a lower G_{IC} than adhesive R is caused by its weaker structure, which was expected to improve during the self-healing process compared to the other two adhesives.

The healed DCB specimens were exposed to mode I fracture testing after being cured in the autoclave, using identical conditions as the virgin testing. Figure 12b–d shows the load–displacement response of each type of the healed specimens compared to its virgin counterpart. It was observed that only adhesive A's load curve

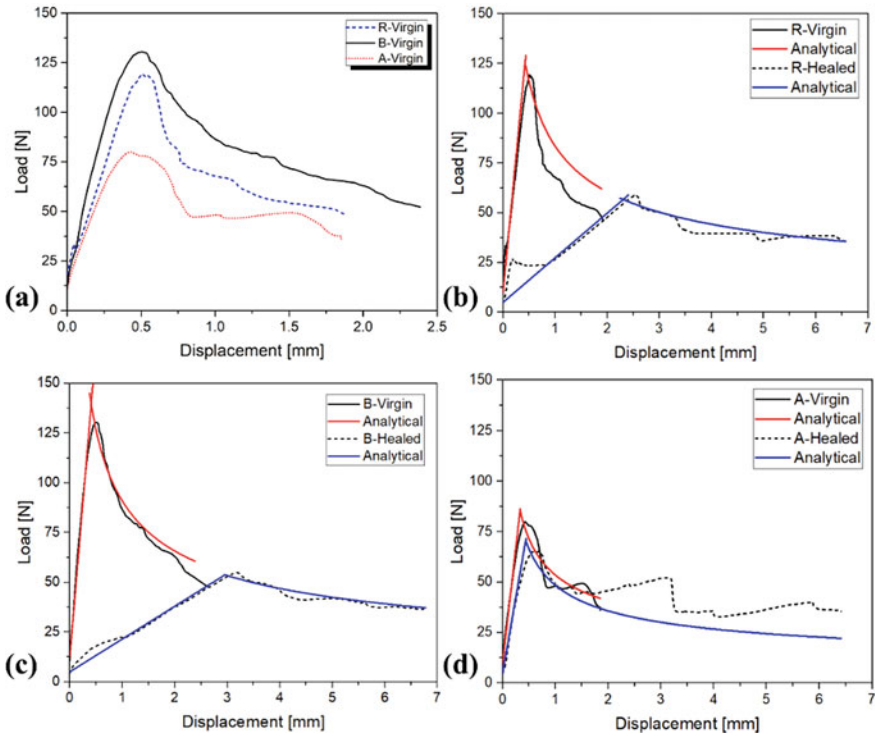

Fig. 12 DCB Mode I load–displacement curve of a) virgin specimens, virgin vs. healed adhesive b) R, c) B, and d) A (*Reproduced from* [84] with the CC BY license (https://creativecommons.org/licenses/by/4.0/)

followed the same trend as its virgin condition, indicating its self-healing potential. For both the virgin and healed adhesives, the stiffness of the linear-elastic section for adhesive A specimen was about the same value (see Fig. 12d). This revealed that the "after-healing" initial crack length was nearly identical to the virgin case's initial crack length (a_0). The behavior of the other adhesives (R and B) was much different. A considerable reduction in stiffness was detected in both cases, indicating that the "after-healing" initial crack length differed from the virgin case's initial crack length. Through the healing process, weak mechanical connections were established because of the applied pressure and temperature, leading to an increase in the load as a function of the applied displacement of up to 20 N. From that point on, the load was again linked to the applied displacement via the cantilever beam's stiffness, but with a greater crack length this time (a). This was verified by the analytical load–displacement curves of the simple beam theory (SBT) for the virgin and healed examples, indicated in red and blue, respectively (see Fig. 12b–d). The SBT linear connection between the applied displacement and the measured load as a function of the adherends' mechanical and geometrical properties was used to predict the linear section of the curves. The propagation curves were produced by matching the energy release rate with the average G_{IC} value of adhesives R, B, and A.

The energy calculated as the area under the load–displacement curve was used to develop a quantitative index to compare the healing capabilities of each adhesive type (see Fig. 13). In that sense, the healing index was defined as the ratio of energy dissipated by the healed specimens to reach the crack length at which the virgin test was stopped (a_v), denoted by E_H, to the energy dissipated by the virgin specimen testing to extend the crack from the initial crack length ($a_{0\text{-}v}$) to the final crack length (a_v), denoted by E_V (*Healing index* $= E_H/E_V$). If no healing occurred, the healed specimen's loading curve should identically match the virgin case's unloading curve, resulting in a healing index of zero. Based on the reasoning above, the healing index for adhesives R, B, and A was determined to be 8.9, 3.0, and 82.5%, respectively. As a result, while adhesive A did not have the highest fracture toughness in its virgin form compared to R and B adhesives, it did have the best healing capabilities.

Figure 14 depicts the distribution of the AE signals amplitude generated during modeI testing of the virgin and healed DCB specimens. Significant AE occurrences began right after the onset of the test, as seen in Fig. 14a, c, and e, in the case of virgin specimens, as shown by the red circle on the x-axis. Few AE occurrences with displacements smaller than the specified displacement might be attributed to the creation of distributed micro-cracks around existing manufacturing flaws within the adhesive layer, which could be neglected since they do not lead to major fracture/failure. AE activity remained high till the end of testing of the virgin specimens. In the case of the healed specimens, the AE events of the adhesive A specimen began at almost the same displacement as they did in its virgin stage (see Fig. 14b). This suggested that the recovered connections had high strength and nearly experienced the same load as the virgin condition, however in the case of adhesives R and B, the AE events of the healed specimens began sooner than the virgin state, indicating that these adhesives formed weak connections (see Fig. 14d and f). The loading phase of the healed R and B specimens could be categorized into three segments, from

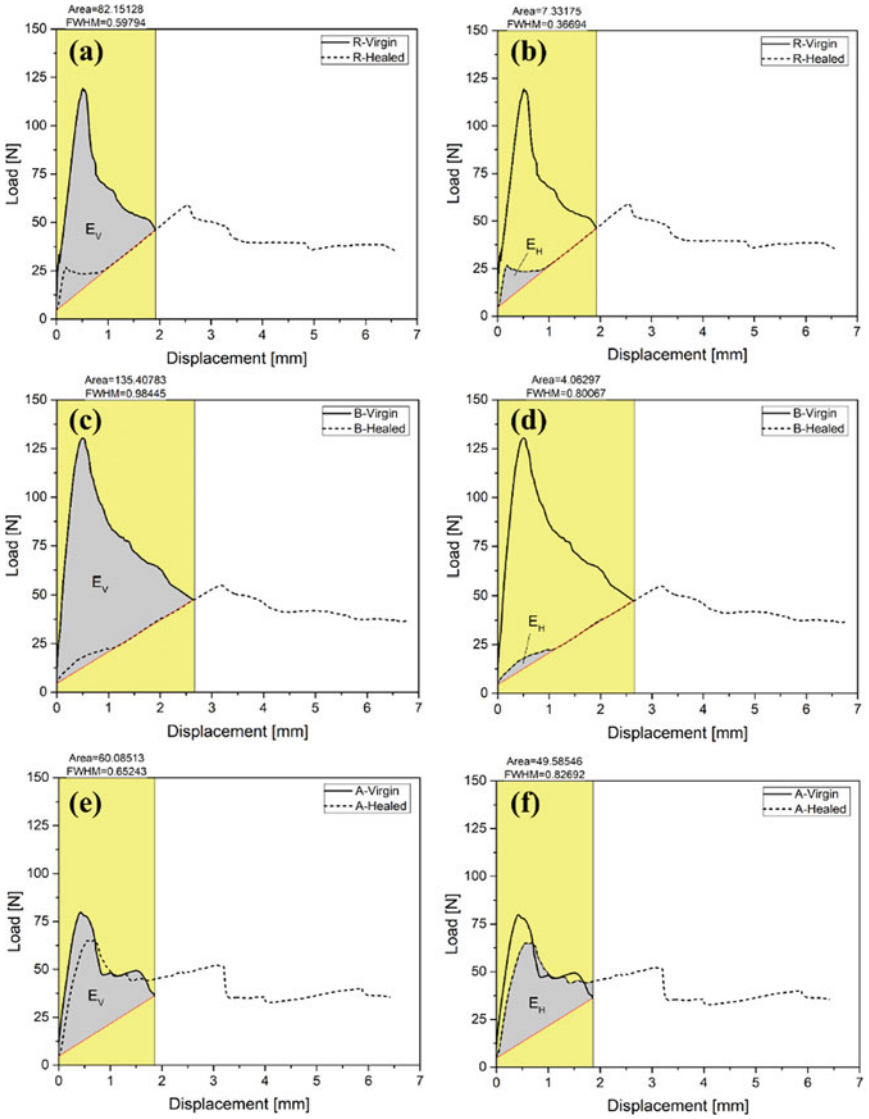

Fig. 13 The determination of the dissipated energy for the virgin and healed DCB specimens; **a** adhesive R-virgin, **b** adhesive R-healed, **c** adhesive B-virgin, **d** adhesive B-healed, **e** adhesive A-virgin, and **f** adhesive A-healed (*Reproduced from* [84] with the CC BY license (https://creativecommons.org/licenses/by/4.0/)

the AE perspective: Region I, in which weak connections created during the healing process could carry minor forces (up to 20 N) before breaking. There was no additional fracture propagation in Region II, and the aluminum cantilever beam arms were only deformed elastically. There was very little AE activity in this area. Region III, in which the new fracture propagates beyond a_v in the healed specimen, resulting in many additional AE events. However, no indication of Region II in the loading process in the case of adhesive A was observed. The breakdown of the high-strength bonds produced during the healing process was represented by Region I, which was followed by Region III, which was associated with the creation and expansion of the new fracture surface beyond a_v in the healed specimen. The proposed AE segments were compatible with the AE trends for crack propagation in adhesively bonded joints described in the literature [93].

3 Summary

- Vegetable oils can provide flexibility to self-healing bio-based epoxy resin owing to their long flexible fatty acid structure, but on the other hand, they decrease their mechanical properties. One of the possible ways to improve these mechanical properties is to incorporate rigid segments such as aromatic rings, increase the epoxy equivalent weight (EEW) values, or increase the temperature of the healing process. Healing efficiencies of more than 100% can be achieved at temperatures up to 120°C for 24 h.
- Lignin can be utilized as a curing agent of epoxy resins after ozonization treatment and introducing carboxylic acid groups by cleavage of benzene rings during this treatment. Fast self-healing capability was observed when the width of the surface scratch was reduced by 70% in ~ 5 min. Reversible transesterification reactions enabled effective shape memory properties of lignin-based self-healing epoxy resins.
- The high stiffness and thermal stability of isosorbide were employed to produce self-healing bio-based epoxy resins with high glass transition temperatures (T_g). An isosorbide-derived epoxy, cured with 4,4´-disulfanediyldianiline, completely healed the scratch after 60 min at 100°C. This capability demonstrated the potential of healing the catastrophic damages with full recovery of mechanical properties of a material. Furthermore, multiple recoveries were investigated, and the healing efficiency based on mechanical properties was 80% after the second and third cycles of re-processing.
- The highest T_g of 187°C was achieved using bio-based triphenyl epoxy (TEP) while maintaining strength and modulus equivalent to the cured bisphenol-A epoxy. The self-healing of such materials was done at 220°C, and under external pressure, the crack width was reduced by nearly 90% in just 5 min.
- Another epoxy resin from natural phenols, eugenol-derived epoxy cured with succinic anhydride (SA), was healed under pressure and 190°C. In that case, the crack shrunk more than 90% in 1 h.

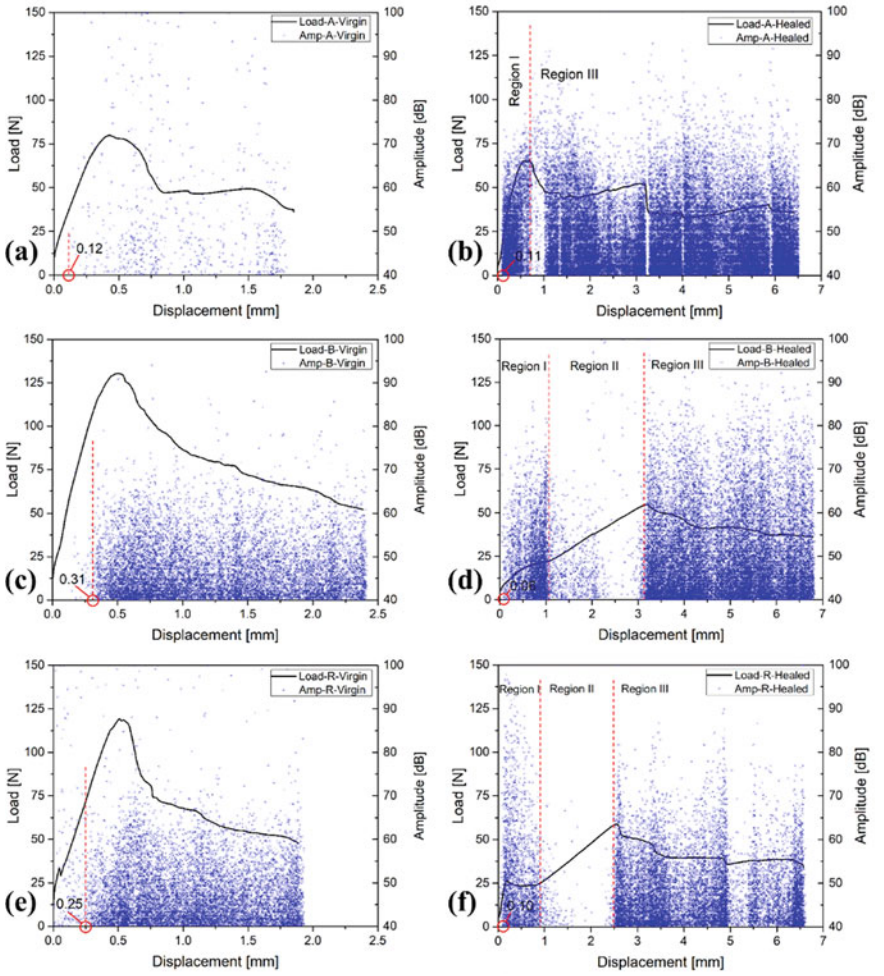

Fig. 14 A comparison of the macroscopic load–displacement response and the AE signals' amplitude distribution captured during the DCB tests: **a** adhesive A-virgin, **b** adhesive A-healed, **c** adhesive B-virgin, **d** adhesive B-healed, **e** adhesive R-virgin and **f** adhesive R-healed (*Reproduced from* [84] with the CC BY license (https://creativecommons.org/licenses/by/4.0/)

- Most of the presented results showed bio-based epoxy materials designed in the form of vitrimers except a couple of relatively novel research studies that showed the intrinsic self-healing behavior of tannic acid (TA), which was used to repair the adhesively bonded joints of lightweight structures (aluminum, Al). TA was modified to introduce epoxy groups, and the design of its structure played a major role in determining the self-healing capability. A smaller molecule of modified TA was able to diffuse to the interface and recover the adhesion forces. The healing efficiency of completely fractured single-lap joint (SLJ) samples from a stiffness

point of view was 90%. Besides, the healing efficiency of the double cantilever beam (DCB) samples was 82.5%.

References

1. Khelifa, F., Habibi, Y., Bonnaud, L., Dubois, P.: Epoxy monomers cured by high cellulosic nanocrystal loading. ACS Appl. Mater. Interfaces. **8**, 10535–10544 (2016). https://doi.org/10.1021/acsami.6b02013
2. Han, X., Wang, T., Owuor, P.S., Hwang, S.H., Wang, C., Sha, J., Shen, L., Yoon, J., Wang, W., Salvatierra, R.V., Ajayan, P.M., Shahsavari, R., Lou, J., Zhao, Y., Tour, J.M.: Ultra-stiff graphene foams as three-dimensional conductive fillers for epoxy resin. ACS Nano **12**, 11219–11228 (2018). https://doi.org/10.1021/acsnano.8b05822
3. Tomić, N.Z., Saleh, M.N., Teixeira de Freitas, S., Živković, A., Vuksanović, M., Poulis, J.A., Marinković, A.: Enhanced interface adhesion by novel eco-epoxy adhesives based on the modified tannic acid on al and cfrp adherends. Polym. Basel **12**, 1541 (2020). https://doi.org/10.3390/polym12071541
4. Saleh, M.N., Saeedifar, M., Zarouchas, D., de Freitas, S.T.: Stress analysis of double-lap bi-material joints bonded with thick adhesive. Int. J. Adhes. Adhes. 102480 (2019). https://doi.org/10.1016/J.IJADHADH.2019.102480
5. Živković, A., Tomić, N., Vuksanović, M., Marinković, A.: Synthesis and characterization of epoxy resin coating with improved fire resistance by the addition of modified tannic acid. In: Proc. 8th Int. Conf. Renew. Electr. Power Sources, SMEITS, pp. 35–42, (2020). https://doi.org/10.24094/mkoiee.020.8.1.35
6. Hamdy, L.B., Wakeham, R.J., Taddei, M., Barron, A.R., Andreoli, E.: Epoxy cross-linked polyamine CO_2 sorbents enhanced via hydrophobic functionalization. Chem. Mater. **31**, 4673–4684 (2019). https://doi.org/10.1021/acs.chemmater.9b00574
7. Saeedifar, M., Saleh, M.N., De Freitas, S.T., Zarouchas, D.: Damage characterization of adhesively-bonded Bi-material joints using acoustic emission. Compos. Part B Eng. **176**, 107356 (2019). https://doi.org/10.1016/j.compositesb.2019.107356
8. Auvergne, R., Caillol, S., David, G., Boutevin, B., Pascault, J.-P.: Biobased thermosetting epoxy: present and future. Chem. Rev. **114**, 1082–1115 (2014). https://doi.org/10.1021/cr3001274
9. Raquez, J.-M., Deléglise, M., Lacrampe, M.-F., Krawczak, P.: Thermosetting (bio)materials derived from renewable resources: a critical review. Prog. Polym. Sci. **35**, 487–509 (2010). https://doi.org/10.1016/j.progpolymsci.2010.01.001
10. Wang, S., Ma, S., Li, Q., Xu, X., Wang, B., Yuan, W., Zhou, S., You, S., Zhu, J.: Facile in situ preparation of high-performance epoxy vitrimer from renewable resources and its application in nondestructive recyclable carbon fiber composite. Green Chem. **21**, 1484–1497 (2019). https://doi.org/10.1039/C8GC03477J
11. Decostanzi, M., Auvergne, R., Boutevin, B., Caillol, S.: Biobased phenol and furan derivative coupling for the synthesis of functional monomers. Green Chem. **21**, 724–747 (2019). https://doi.org/10.1039/C8GC03541E
12. Liu, L., Lu, J., Zhang, Y., Liang, H., Liang, D., Jiang, J., Lu, Q., Quirino, R.L., Zhang, C.: Thermosetting polyurethanes prepared with the aid of a fully bio-based emulsifier with high bio-content, high solid content, and superior mechanical properties. Green Chem. **21**, 526–537 (2019). https://doi.org/10.1039/C8GC03560A
13. Lligadas, G., Ronda, J.C., Galià, M., Cádiz, V.: Renewable polymeric materials from vegetable oils: a perspective. Mater. Today. **16**, 337–343 (2013). https://doi.org/10.1016/j.mattod.2013.08.016

14. Zhang, C., Garrison, T.F., Madbouly, S.A., Kessler, M.R.: Recent advances in vegetable oil-based polymers and their composites. Prog. Polym. Sci. **71**, 91–143 (2017). https://doi.org/10.1016/j.progpolymsci.2016.12.009
15. Altuna, F.I., Ruseckaite, R.A., Stefani, P.M.: Biobased thermosetting epoxy foams: mechanical and thermal characterization. ACS Sustain. Chem. Eng. **3**, 1406–1411 (2015). https://doi.org/10.1021/acssuschemeng.5b00114
16. Pawar, M., Kadam, A., Yemul, O., Thamke, V., Kodam, K.: Biodegradable bioepoxy resins based on epoxidized natural oil (cottonseed & algae) cured with citric and tartaric acids through solution polymerization: a renewable approach. Ind. Crops Prod. **89**, 434–447 (2016). https://doi.org/10.1016/j.indcrop.2016.05.025
17. Xiao, L., Huang, J., Wang, Y., Chen, J., Liu, Z., Nie, X.: Tung oil-based modifier toughening epoxy resin by sacrificial bonds. ACS Sustain. Chem. Eng. **7**, 17344–17353 (2019). https://doi.org/10.1021/acssuschemeng.9b04284
18. Tran, T.-N., Di Mauro, C., Graillot, A., Mija, A.: Chemical reactivity and the influence of initiators on the epoxidized vegetable oil/dicarboxylic acid system. Macromolecules **53**, 2526–2538 (2020). https://doi.org/10.1021/acs.macromol.9b02700
19. Hernandez, E.D., Bassett, A.W., Sadler, J.M., La Scala, J.J., Stanzione, J.F.: Synthesis and characterization of bio-based epoxy resins derived from vanillyl alcohol. ACS Sustain. Chem. Eng. **4**, 4328–4339 (2016). https://doi.org/10.1021/acssuschemeng.6b00835
20. Montarnal, D., Capelot, M., Tournilhac, F., Leibler, L.: Silica-like malleable materials from permanent organic networks. Sci. **334**, 965–968 (2011). https://doi.org/10.1126/science.1212648
21. Zhang, S., Liu, T., Hao, C., Wang, L., Han, J., Liu, H., Zhang, J.: Preparation of a lignin-based vitrimer material and its potential use for recoverable adhesives. Green Chem. **20**, 2995–3000 (2018). https://doi.org/10.1039/C8GC01299G
22. Liu, T., Hao, C., Wang, L., Li, Y., Liu, W., Xin, J., Zhang, J.: Eugenol-derived biobased epoxy: shape memory, repairing, and recyclability. Macromolecules **50**, 8588–8597 (2017). https://doi.org/10.1021/acs.macromol.7b01889
23. Pei, Z., Yang, Y., Chen, Q., Terentjev, E.M., Wei, Y., Ji, Y.: Mouldable liquid-crystalline elastomer actuators with exchangeable covalent bonds. Nat. Mater. **13**, 36–41 (2014). https://doi.org/10.1038/nmat3812
24. Dhers, S., Vantomme, G., Avérous, L.: A fully bio-based polyimine vitrimer derived from fructose. Green Chem. **21**, 1596–1601 (2019). https://doi.org/10.1039/C9GC00540D
25. Chen, M., Zhou, L., Wu, Y., Zhao, X., Zhang, Y.: Rapid stress relaxation and moderate temperature of malleability enabled by the synergy of disulfide metathesis and carboxylate transesterification in epoxy vitrimers. ACS Macro Lett. **8**, 255–260 (2019). https://doi.org/10.1021/acsmacrolett.9b00015
26. Denissen, W., Winne, J.M., Du Prez, F.E.: Vitrimers: permanent organic networks with glass-like fluidity. Chem. Sci. **7**, 30–38 (2016). https://doi.org/10.1039/C5SC02223A
27. Liu, T., Hao, C., Zhang, S., Yang, X., Wang, L., Han, J., Li, Y., Xin, J., Zhang, J.: A self-healable high glass transition temperature bioepoxy material based on vitrimer chemistry. Macromolecules **51**, 5577–5585 (2018). https://doi.org/10.1021/acs.macromol.8b01010
28. Liang, H., Li, Y., Huang, S., Huang, K., Zeng, X., Dong, Q., Liu, C., Feng, P., Zhang, C.: Tailoring the performance of vegetable oil-based waterborne polyurethanes through incorporation of rigid cyclic rings into soft polymer networks. ACS Sustain. Chem. Eng. **8**, 914–925 (2020). https://doi.org/10.1021/acssuschemeng.9b05477
29. Zhang, C., Liang, H., Liang, D., Lin, Z., Chen, Q., Feng, P., Wang, Q.: Renewable castor-oil-based waterborne polyurethane networks: simultaneously showing high strength, self-healing, processability and tunable multishape memory. Angew. Chemie Int. Ed. **60**, 4289–4299 (2021). https://doi.org/10.1002/anie.202014299
30. Taylor, D.L., In Het Panhuis, M.: Self-healing hydrogels. Adv. Mater. **28,** 9060–9093 (2016). https://doi.org/10.1002/adma.201601613
31. Chen, Y., Tang, Z., Zhang, X., Liu, Y., Wu, S., Guo, B.: Covalently cross-linked elastomers with self-healing and malleable abilities enabled by boronic ester bonds. ACS Appl. Mater. Interfaces. **10**, 24224–24231 (2018). https://doi.org/10.1021/acsami.8b09863

32. Pettignano, A., Grijalvo, S., Häring, M., Eritja, R., Tanchoux, N., Quignard, F., Díaz, D.D.: Boronic acid-modified alginate enables direct formation of injectable, self-healing and multistimuli-responsive hydrogels. Chem. Commun. **53**, 3350–3353 (2017). https://doi.org/10.1039/C7CC00765E
33. Cao, Y., Morrissey, T.G., Acome, E., Allec, S.I., Wong, B.M., Keplinger, C., Wang, C., Transparent, A.: Self-healing, highly stretchable ionic conductor. Adv. Mater. **29**, 1605099 (2017). https://doi.org/10.1002/adma.201605099
34. Du, R., Xu, Z., Zhu, C., Jiang, Y., Yan, H., Wu, H., Vardoulis, O., Cai, Y., Zhu, X., Bao, Z., Zhang, Q., Jia, X.: A highly stretchable and self-healing supramolecular elastomer based on sliding crosslinks and hydrogen bonds. Adv. Funct. Mater. **30**, 1907139 (2020). https://doi.org/10.1002/adfm.201907139
35. Cao, S., Tong, X., Dai, K., Xu, Q.: A super-stretchable and tough functionalized boron nitride/PEDOT:PSS/poly(N-isopropylacrylamide) hydrogel with self-healing, adhesion, conductive and photothermal activity. J. Mater. Chem. A. **7**, 8204–8209 (2019). https://doi.org/10.1039/C9TA00618D
36. Schäfer, S., Kickelbick, G.: Double Reversible networks: improvement of self-healing in hybrid materials via combination of Diels-alder cross-linking and hydrogen bonds. Macromolecules **51**, 6099–6110 (2018). https://doi.org/10.1021/acs.macromol.8b00601
37. Lei, Z.Q., Xie, P., Rong, M.Z., Zhang, M.Q.: Catalyst-free dynamic exchange of aromatic Schiff base bonds and its application to self-healing and remolding of crosslinked polymers. J. Mater. Chem. A. **3**, 19662–19668 (2015). https://doi.org/10.1039/C5TA05788D
38. Rekondo, A., Martin, R., Ruiz de Luzuriaga, A., Cabañero, G., Grande, H.J., Odriozola, I.: Catalyst-free room-temperature self-healing elastomers based on aromatic disulfide metathesis. Mater. Horiz. **1**, 237–240 (2014). https://doi.org/10.1039/C3MH00061C
39. Zhang, C., Wang, X., Liang, D., Deng, H., Lin, Z., Feng, P., Wang, Q.: Rapid self-healing, multiple recyclability and mechanically robust plant oil-based epoxy resins enabled by incorporating tri-dynamic covalent bonding. J. Mater. Chem. A. **9**, 18431–18439 (2021). https://doi.org/10.1039/D1TA04593H
40. Liu, L., Liang, H., Zhang, J., Zhang, P., Xu, Q., Lu, Q., Zhang, C.: Poly(vinyl alcohol)/Chitosan composites: Physically transient materials for sustainable and transient bioelectronics. J. Clean. Prod. **195**, 786–795 (2018). https://doi.org/10.1016/j.jclepro.2018.05.216
41. Cromwell, O.R., Chung, J., Guan, Z.: Malleable and self-healing covalent polymer networks through tunable dynamic boronic ester bonds. J. Am. Chem. Soc. **137**, 6492–6495 (2015). https://doi.org/10.1021/jacs.5b03551
42. Canadell, J., Goossens, H., Klumperman, B.: Self-healing materials based on disulfide links. Macromolecules **44**, 2536–2541 (2011). https://doi.org/10.1021/ma2001492
43. Ruiz de Luzuriaga, A., Martin, R., Markaide, N., Rekondo, A., Cabañero, G., Rodríguez, J., Odriozola, I.: Epoxy resin with exchangeable disulfide crosslinks to obtain reprocessable, repairable and recyclable fiber-reinforced thermoset composites. Mater. Horizons. **3**, 241–247 (2016). https://doi.org/10.1039/C6MH00029K
44. Xin, J., Li, M., Li, R., Wolcott, M.P., Zhang, J.: Green epoxy resin system based on lignin and Tung oil and its application in epoxy asphalt. ACS Sustain. Chem. Eng. **4**, 2754–2761 (2016). https://doi.org/10.1021/acssuschemeng.6b00256
45. Zhang, W., Ma, Y., Wang, C., Li, S., Zhang, M., Chu, F.: Preparation and properties of lignin–phenol–formaldehyde resins based on different biorefinery residues of agricultural biomass. Ind. Crops Prod. **43**, 326–333 (2013). https://doi.org/10.1016/j.indcrop.2012.07.037
46. Saito, T., Brown, R.H., Hunt, M.A., Pickel, D.L., Pickel, J.M., Messman, J.M., Baker, F.S., Keller, M., Naskar, A.K.: Turning renewable resources into value-added polymer: development of lignin-based thermoplastic. Green Chem. **14**, 3295 (2012). https://doi.org/10.1039/c2gc35933b
47. Qin, J., Woloctt, M., Zhang, J.: Use of Polycarboxylic acid derived from partially depolymerized lignin as a curing agent for epoxy application. ACS Sustain. Chem. Eng. **2**, 188–193 (2014). https://doi.org/10.1021/sc400227v

48. Ma, R., Xu, Y., Zhang, X.: Catalytic Oxidation of Biorefinery Lignin to Value-added Chemicals to Support Sustainable Biofuel Production. Chemsuschem **8**, 24–51 (2015). https://doi.org/10.1002/cssc.201402503
49. Rounsaville, J., Rice, R.G.: Evolution of ozone for the bleaching of paper pulps. Ozone Sci. Eng. **18**, 549–566 (1996). https://doi.org/10.1080/01919512.1997.10382863
50. Lachenal, D., Fernandes, J.C., Froment, P.: Behavior of residual lignin in kraft pulp during bleaching. J. Pulp Pap. Sci. **21**, J173 (2015)
51. Koike, T.: Progress in development of epoxy resin systems based on wood biomass in Japan. Polym. Eng. Sci. **52**, 701–717 (2012). https://doi.org/10.1002/pen.23119
52. Ma, Z., Wang, Y., Zhu, J., Yu, J., Hu, Z.: Bio-based epoxy vitrimers: reprocessibility, controllable shape memory, and degradability. J. Polym. Sci. Part A Polym. Chem. **55**, 1790–1799 (2017). https://doi.org/10.1002/pola.28544
53. Fenouillot, F., Rousseau, A., Colomines, G., Saint-Loup, R., Pascault, J.-P.: Polymers from renewable 1,4:3,6-dianhydrohexitols (isosorbide, isomannide and isoidide): a review. Prog. Polym. Sci. **35**, 578–622 (2010). https://doi.org/10.1016/j.progpolymsci.2009.10.001
54. Duan, R.-T., He, Q.-X., Dong, X., Li, D.-F., Wang, X.-L., Wang, Y.-Z.: Renewable sugar-based diols with different rigid structure: comparable investigation on improving poly(butylene succinate) performance. ACS Sustain. Chem. Eng. **4**, 350–362 (2016). https://doi.org/10.1021/acssuschemeng.5b01335
55. Martin, R., Rekondo, A., Ruiz de Luzuriaga, A., Cabañero, G., Grande, H.J., Odriozola, I.: The processability of a poly(urea-urethane) elastomer reversibly crosslinked with aromatic disulfide bridges. J. Mater. Chem. A. **2**, 5710 (2014). https://doi.org/10.1039/c3ta14927g
56. Yang, W.J., Tao, X., Zhao, T., Weng, L., Kang, E.-T., Wang, L.: Antifouling and antibacterial hydrogel coatings with self-healing properties based on a dynamic disulfide exchange reaction. Polym. Chem. **6**, 7027–7035 (2015). https://doi.org/10.1039/C5PY00936G
57. Black, S.P., Sanders, J.K.M., Stefankiewicz, A.R.: Disulfide exchange: exposing supramolecular reactivity through dynamic covalent chemistry. Chem. Soc. Rev. **43**, 1861–1872 (2014). https://doi.org/10.1039/C3CS60326A
58. Xiang, H.P., Qian, H.J., Lu, Z.Y., Rong, M.Z., Zhang, M.Q.: Crack healing and reclaiming of vulcanized rubber by triggering the rearrangement of inherent sulfur crosslinked networks. Green Chem. **17**, 4315–4325 (2015). https://doi.org/10.1039/C5GC00754B
59. Imbernon, L., Oikonomou, E.K., Norvez, S., Leibler, L.: Chemically crosslinked yet reprocessable epoxidized natural rubber via thermo-activated disulfide rearrangements. Polym. Chem. **6**, 4271–4278 (2015). https://doi.org/10.1039/C5PY00459D
60. Obadia, M.M., Mudraboyina, B.P., Serghei, A., Montarnal, D., Drockenmuller, E.: Reprocessing and recycling of highly cross-linked ion-conducting networks through transalkylation exchanges of C-N bonds. J. Am. Chem. Soc. **137**, 6078–6083 (2015). https://doi.org/10.1021/jacs.5b02653
61. Yang, Y., Urban, M.W.: Self-healing polymeric materials. Chem. Soc. Rev. **42**, 7446 (2013). https://doi.org/10.1039/c3cs60109a
62. Liu, T., Zhang, L., Chen, R., Wang, L., Han, B., Meng, Y., Li, X.: Nitrogen-free tetrafunctional epoxy and its DDS-cured high-performance matrix for aerospace applications. Ind. Eng. Chem. Res. **56**, 7708–7719 (2017). https://doi.org/10.1021/acs.iecr.7b00096
63. Liu, W., Schmidt, D.F., Reynaud, E.: Catalyst selection, creep, and stress relaxation in high-performance epoxy vitrimers. Ind. Eng. Chem. Res. **56**, 2667–2672 (2017). https://doi.org/10.1021/acs.iecr.6b03829
64. Altuna, F.I., Pettarin, V., Williams, R.J.J.: Self-healable polymer networks based on the cross-linking of epoxidised soybean oil by an aqueous citric acid solution. Green Chem. **15**, 3360 (2013). https://doi.org/10.1039/c3gc41384e
65. Tang, J., Wan, L., Zhou, Y., Pan, H., Huang, F.: Strong and efficient self-healing adhesives based on dynamic quaternization cross-links. J. Mater. Chem. A. **5**, 21169–21177 (2017). https://doi.org/10.1039/C7TA06650C
66. Fortman, D.J., Brutman, J.P., Cramer, C.J., Hillmyer, M.A., Dichtel, W.R.: Mechanically activated, catalyst-free polyhydroxyurethane vitrimers. J. Am. Chem. Soc. **137**, 14019–14022 (2015). https://doi.org/10.1021/jacs.5b08084

67. Denissen, W., De Baere, I., Van Paepegem, W., Leibler, L., Winne, J., Du Prez, F.E.: Vinylogous Urea Vitrimers and Their Application in Fiber Reinforced Composites. Macromolecules **51**, 2054–2064 (2018). https://doi.org/10.1021/acs.macromol.7b02407
68. Kandola, B.K., Biswas, B., Price, D., Horrocks, A.R.: Studies on the effect of different levels of toughener and flame retardants on thermal stability of epoxy resin. Polym. Degrad. Stab. **95**, 144–152 (2010). https://doi.org/10.1016/j.polymdegradstab.2009.11.040
69. Galpaya, D., Wang, M., George, G., Motta, N., Waclawik, E., Yan, C.: Preparation of graphene oxide/epoxy nanocomposites with significantly improved mechanical properties. J. Appl. Phys. **116**, 053518 (2014). https://doi.org/10.1063/1.4892089
70. Liu, T., Geng, X., Nie, Y., Chen, R., Meng, Y., Li, X.: Hyperbranched polyethers with tunable glass transition temperature: controlled synthesis and mixing rules. RSC Adv. **4**, 30250–30258 (2014). https://doi.org/10.1039/C4RA04077E
71. Liu, T., Miao, X., Geng, X., Xing, A., Zhang, L., Meng, Y., Li, X.: Control-synthesized multilayer hyperbranched–hyperbranched polyethers with a tunable molecular weight and an invariant degree of branching. New J. Chem. **40**, 3432–3439 (2016). https://doi.org/10.1039/C5NJ02895G
72. Capelot, M., Montarnal, D., Tournilhac, F., Leibler, L.: Metal-catalyzed transesterification for healing and assembling of thermosets. J. Am. Chem. Soc. **134**, 7664–7667 (2012). https://doi.org/10.1021/ja302894k
73. Chabert, E., Vial, J., Cauchois, J.-P., Mihaluta, M., Tournilhac, F.: Multiple welding of long fiber epoxy vitrimer composites. Soft Matter **12**, 4838–4845 (2016). https://doi.org/10.1039/C6SM00257A
74. Kumar, V.: Role of accelerator in curing of epoxy-anhydride pressure impregnant. IEEE Trans. Dielectr. Electr. Insul. **19**, 968–972 (2012). https://doi.org/10.1109/TDEI.2012.6215101
75. Li, Y., Rios, O., Keum, J.K., Chen, J., Kessler, M.R.: Photoresponsive liquid crystalline epoxy networks with shape memory behavior and dynamic ester bonds. ACS Appl. Mater. Interfaces. **8**, 15750–15757 (2016). https://doi.org/10.1021/acsami.6b04374
76. Lu, X., Guo, S., Tong, X., Xia, H., Zhao, Y.: Tunable photocontrolled motions using stored strain energy in malleable azobenzene liquid crystalline polymer actuators. Adv. Mater. **29**, 1606467 (2017). https://doi.org/10.1002/adma.201606467
77. Hamerton, I.: Metals and coordination compounds as modifiers for epoxy resins. Coord. Chem. Rev. **224**, 67–85 (2002). https://doi.org/10.1016/S0010-8545(01)00393-9
78. Budzik, M.K., Wolfahrt, M., Reis, P., Kozłowski, M., Sena-Cruz, J., Papadakis, L., Nasr Saleh, M., Machalicka, K.V., Teixeira de Freitas, S., Vassilopoulos, A.P.: Testing mechanical performance of adhesively bonded composite joints in engineering applications: an overview. J. Adhes. 1–77 (2021). https://doi.org/10.1080/00218464.2021.1953479
79. Jethwa, J.K., Kinloch, A.J.: The fatigue and durability behaviour of automotive adhesives. Part I: Fracture mechanics tests. J. Adhes. **61**, 71–95 (1997). https://doi.org/10.1080/00218469708010517
80. Hart-Smith, L.J.: A peel-type durability test coupon to assess interfaces in bonded, co-bonded, and co-cured composite structures. Int. J. Adhes. Adhes. **19**, 181–191 (1999). https://doi.org/10.1016/S0143-7496(98)00033-5
81. Ghazali, H., Ye, L., Zhang, M.-Q.: Lap shear strength and healing capability of self-healing adhesive containing epoxy/mercaptan microcapsules. In: AIP Conference Proceedings **1713**, 140004 (2016). https://doi.org/10.1063/1.4942339
82. Jin, H., Miller, G.M., Pety, S.J., Griffin, A.S., Stradley, D.S., Roach, D., Sottos, N.R., White, S.R.: Fracture behavior of a self-healing, toughened epoxy adhesive. Int. J. Adhes. Adhes. **44**, 157–165 (2013). https://doi.org/10.1016/j.ijadhadh.2013.02.015
83. Tomić, N.Z., Saleh, M.N., Saeedifar, M., Marinković, A., Teixeira de Freitas, S.: Self-healing capability of novel eco-epoxy adhesives based on the modified tannic acid on Al adherends tested in a single lap joint. Int. J. Adhes. Adhes. 103013 (2021). https://doi.org/10.1016/j.ijadhadh.2021.103013
84. Tomić, N.Z., Saeedifar, M., Saleh, M.N., Marinković, A., Zarouchas, D., Teixeira de Freitas, S.: Synthesis and characterization of novel eco-epoxy adhesives based on the modified tannic

acid for self-healing joints. Polym. Test. **106**, 107444 (2022). https://doi.org/10.1016/j.polymertesting.2021.107444
85. Pocius, A.V.: Introduction. In: Adhesion and adhesives technology, pp. 1–15. Carl Hanser Verlag GmbH & Co. KG, München, (2012). https://doi.org/10.3139/9783446431775.001
86. Naito, K., Onta, M., Kogo, Y.: The effect of adhesive thickness on tensile and shear strength of polyimide adhesive. Int. J. Adhes. Adhes. **36**, 77–85 (2012). https://doi.org/10.1016/j.ijadhadh.2012.03.007
87. Grant, L.D.R., Adams, R.D., da Silva, L.F.M.: Experimental and numerical analysis of single-lap joints for the automotive industry. Int. J. Adhes. Adhes. **29**, 405–413 (2009). https://doi.org/10.1016/j.ijadhadh.2008.09.001
88. Doszlop, S., Vargha, V., Horkay, F.: Reactions of epoxy with other functional groups and the arising sec-hydroxyl groups. Period. Polytech. Chem. Eng. **22**, 253–275 (1978)
89. Kim, Y.-O., Cho, J., Yeo, H., Lee, B.W., Moon, B.J., Ha, Y.-M., Jo, Y.R., Jung, Y.C.: Flame retardant epoxy derived from tannic acid as biobased hardener. ACS Sustain. Chem. Eng. **7**, 3858–3865 (2019). https://doi.org/10.1021/acssuschemeng.8b04851
90. Hodgkinson, J.M.: Testing the strength and stiffness of polymer matrix composites. In: Robinson, P., Greenhalgh, E., Pinho, S. (eds.) Failure mechanisms in polymer matrix composites,1st edition, pp. 129–182. Woodhead Publishing (2012). https://www.elsevier.com/books/failure-mechanisms-in-polymer-matrix-composites/robinson/978-1-84569-750-1
91. Saleh, M.N., Tomić, N.Z., Marinković, A., Teixeira de Freitas, S.: The effect of modified tannic acid (TA) eco-epoxy adhesives on mode I fracture toughness of bonded joints. Polym. Test. **96**, 107122 (2021). https://doi.org/10.1016/j.polymertesting.2021.107122
92. Mequanint, K., Sanderson, R., Pasch, H.: Adhesion properties of phosphate-and siloxane-containing polyurethane dispersions to steel: an analysis of the metal-coating interface. J. Appl. Polym. Sci. **88**, 900–907 (2003). https://doi.org/10.1002/app.11680
93. Teixeira de Freitas, S., Zarouchas, D., Poulis, J.A.: The use of acoustic emission and composite peel tests to detect weak adhesion in composite structures. J. Adhes. **94**, 743–766 (2018). https://doi.org/10.1080/00218464.2017.1396975

Modeling and Simulation of Vitrimers

Alessandro Perego, Harsh Pandya, and Fardin Khabaz

Abstract The healing response in self-healing materials is regulated by the rates of three distinct stages: actuation, transport, and repair. The healing efficiency is dictated by delicately balancing the rate of damage versus the rate of healing. The material damage rate is determined by the frequency of strain rate, loading, and stress amplitude. However, by changing the reaction kinetics through temperature or concentration the healing rate can be designed to specific damage modes. Vitrimers are a particular subcategory of intrinsic self-healing materials that flow at temperatures higher than the topology freezing temperature and show thermoset-like behavior at low temperatures. Vitrimer chemistry is an excellent way to combine the favorable mechanical properties of covalently crosslinked thermosets with full recyclability and create intrinsic self-healing materials without needing a healing agent. Recently, several theoretical frameworks, coarse-grained particle dynamics simulations, and finite element analysis (FEA) have been used to probe the thermodynamics, dynamics, rheology, and mechanics of these transient networks. Particle-based dynamic simulations have successfully produced key features of vitrimers, rubbery plateau, and terminal modulus behaviors. On a continuum level, constitutive equations have been developed to study the effect of the kinetics of the bond exchange on the macroscopic material response. In this chapter, the recent advances in the modeling aspect of vitrimers ranging from particles-based simulation techniques to FEA are reviewed.

Keywords Vitrimers · Thermoset · Rheology · Mechanics · Molecular simulations · Finite element analysis

A. Perego · H. Pandya · F. Khabaz (✉)
School of Polymer Science and Polymer Engineering, The University of Akron, Akron, OH 44325, USA
e-mail: fkhabaz@uakron.edu

F. Khabaz
Department of Chemical, Biomolecular, and Corrosion Engineering, The University of Akron, Akron, OH 44325, USA

N. Hameed et al. (eds.), *Multifunctional Epoxy Resins*, Engineering Materials,
https://doi.org/10.1007/978-981-19-6038-3_8

1 Introduction

The aim of self-healing process is to achieve equilibrium in the material by carefully adjusting the rate of healing and the rate of damage [1]. Self-healing materials are usually classified into three main categories: *capsule based*, *vascular*, and *intrinsic* [2]. This classification is based on the mechanism used to isolate the healing functionality of the material. According to the type of sequestration used, it is possible to control how many times the material can be healed, the damaged volume available for healing, and the kinetics of the recovery rate.

Capsule-based self-healing materials sequester the healing agent in discrete capsules. When the induced damage ruptures these capsules, the release and reaction of the healing agent initiate the self-healing process [3]. In *vascular self-healing* materials, the self-healing materials are stored in capillaries. These networks may be interconnected in one, two, or three dimensions until damage triggers the self-healing process [3]. After the rupture of the capillaries and subsequent release of the healing agent, the material can be replenished with the healing agent, thus allowing for multiple local healing events to occur.

There is no healing agent in *intrinsic* self-healing materials, but they possess self-healing functionalities directly embedded in their chemical structure. These functionalities are usually initiated by damage or an external stimulus. For polymeric materials, this self-healing process can be achieved by phenomena such as reversible polymerization, hydrogen bonding, ionic interactions, and reversible bond exchange reactions [3]. Each of these reactions is reversible, and thus, multiple healing events can occur for intrinsic self-healing materials [1].

Generally, polymers are divided into thermoplastics, in which polymer chains are not chemically attached, and thermosets, in which chains are permanently crosslinked [4–9]. Thermoplastic materials show flow behavior similar to a viscoelastic liquid when heated [8, 10, 11] that allowing these materials to be re-processable [12]. However, the molecular topology changes directly result in weak solvent resistance and poor mechanical properties [5, 13]. The diffusion of polymer chains in thermoset materials is suppressed since the network is crosslinked [14], thus making the thermosets suitable for applications that require strong mechanical properties such as coatings, electronics, and structural applications [12, 15]. However, as thermosets present a theoretically infinite rubbery plateau when heated above the glass transition temperature (T_g) due to the connectivity of the network; thus these materials cannot be reprocessed after they are crosslinked [16]. Considering the latter limitation, i.e., difficulty in reprocessing thermosets, these materials provide a significant challenge for recycling polymers (see Fig. 1) [16–18].

Several attempts have been made to implement non-covalent bonds as crosslinkers in thermoset, including hydrogen bonds [19, 20], π–π stacking [21], and metal–ligand bonds. However, due to the weaker energy of the non-covalent bond interactions [22], these materials show poor mechanical properties compared to commercially available thermosets. A more promising approach introduces dynamic covalent bonding into thermosetting materials, creating what is commonly known

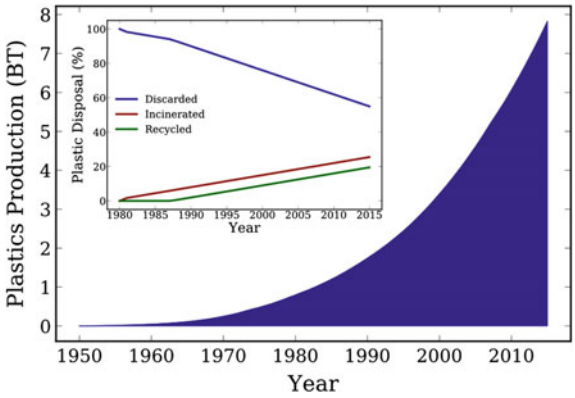

Fig. 1 Cumulative global plastic production from 1950 to 2015. Inset: Global plastic waste disposal from 1980 to 2015. As it emerges from the data, as of 2015, only, ~ 19% of the total plastic produced is recycled successfully [18]. The data in the figure are obtained from Geyer, Jambeck, Lavender Law; Production, use, and the fate of all plastics ever made; Sci. Adv.; 2017; American Association for the Advancement of Science

as covalent adaptive networks (CANs) [4–6, 23]. Depending on the chemistry of the bond exchange mechanism, CANs can be further classified as either *associative* or *dissociative* [24, 25]. *Associative* CANs rely on associative exchange mechanisms in which the original crosslink is only broken when a new covalent bond to another position has been formed [4–6, 25–28]. As a result, upon heating, there is no depolymerization and the crosslink density of these networks also remains constant [29, 30]. Despite displaying promising rheological properties, the timescale associated with the bond exchange reaction of these systems remains restricted due to the radical nature of the catalyst used [25].

In 2011, Leibler and coworkers [27] proposed a unique approach to *associative* CANs by adding a suitable transesterification catalyst to an epoxy/acid or epoxy/anhydride polyester-based network. These materials are named vitrimers, and they show a gradual decrease in the viscosity of the system upon heating following an Arrhenius law with an activation energy of ~ 80 k J/mol K, similar to inorganic materials such as silica [4, 31, 32]. This characteristic viscosity behavior enables vitrimers to be processed in wide temperature ranges without any potential loss in network integrity [6]. Also, unlike *dissociative* CANs, vitrimers show solvent resistance [25]. Additionally, rheology and birefringence experiments show that these networks can rapidly relax stress and display great malleability [5, 27, 33, 34], weldability [25, 26], and shape memory [35–37]. Leibler and coworkers proposed a new class chemical route using the metathesis of dioxaborolanes to create vitrimers using polymethyl methacrylate, polystyrene, and high-density polyethylene as backbone chains of the network. These vitrimers can be processed several times via extrusion or injection molding [6]. Hence, there is a possibility for repair assembly and alloying incompatible polymers, and most importantly, providing new routes for recycling thermosetting plastics.

Two transition temperatures describe the thermodynamics and kinetics of vitrimers [6, 28, 38–40]: (1) the glass transition temperature, T_g, which is common in amorphous polymeric materials [11] and (2) the topology freezing temperature, T_v, which shows the transition from viscoelastic solid to viscous liquid behavior and often appears at a temperature above the T_g. At this temperature, the timescale of the topological change becomes slow upon cooling, and the network rearrangement becomes sluggish. In experiments, this transition is selected at a temperature where the value of shear viscosity reaches 10^{12} Pa·s [4, 11, 41]. Different factors, such as the chemistry of the monomer and crosslinker, number density of crosslinker, loading of catalyst, quenching rate, and the density of exchangeable bonds, dictate the viscoelastic properties of vitrimers [4]. Ideally, these materials should be designed such that they behave like a thermoset network in practical applications and flow like a viscous liquid during processing at high temperatures without loss of network integrity. It has been suggested that it might be possible to determine the T_v from volumetric data similar to the glass transition, but as of now, due to the instrument limitations, the detection of T_v from direct experimental measurements is a challenging task [5].

Atomistically detailed molecular dynamics (MD) simulations have been successfully used to study the bonds exchange reactions at the interface during stretching and welding processes in polymeric materials. However, the high computational cost of all-atom simulations poses a serious limitation on the choice of the system size and on the time scale accessible, making it challenging to capture the complex dynamics of *associative* CANs such as vitrimers accurately. A possible way to extend the molecular modeling time scale and bridge it with experimental procedures is to apply coarse-graining. This technique allows representing a system by a reduced (in comparison with an all-atoms simulation) number of degrees of freedom. The simulation of a coarse-grained (CG) system is less computationally expensive than the same system in all-atom representations due to reduced degrees of freedom and elimination of the fine interaction details. This results in an increase of orders of magnitude in the simulated time and length scales. In the case of vitrimers, there is an urgent need to predict their viscoelastic properties and dynamics in a relevant timescale to experiments [28].

Continuum models also show quantitative agreement between the stress–strain behavior and stress relaxation modulus and experimental results [42]. Recently, a patchy particle model implementing a three-body potential similar to the Stillinger–Weber force field was proposed to investigate the dynamics of the vitrimers [40]. This model was used to study the phase separation [40], self and collective dynamics of the vitrimer system formed using the patchy colloidal particles [40, 43–46]. A recent study [47] on aging dissociating polymers based on a coarse-grained bead-spring method and Langevin dynamics concluded that the aging is due to the dissociation of small clusters of sticky monomers and transformation of the small clusters to a large one. In our recent study [48, 49], we have combined molecular dynamics (MD) and Monte Carlo (MC) simulations to predict the dynamics and rheology of a model vitrimer and compared its properties with a permanently crosslinked one. Our

results show that a simple bond exchange protocol accompanied with an appropriate coarse-graining level generates the essential characteristics of vitrimers.

In this chapter, we review the available simulation methods and summarize the results on the mechanical and rheological properties of these novel polymeric systems. We close this chapter with a summary of the models and an outlook on the computational techniques.

2 Simulation and Modeling Techniques and Theoretical Frameworks

2.1 Particle-Based Models

Generally, in these types of simulations, a collection of a few atoms is considered one particle, or bead, with an appropriate nonbonded and bonded energy that governs the force field between all the beads in the system tuned to capture roughly the effect of polymer chemistry. The trajectories of particles are predicted using appropriate equations of motion, and using the principles of statistical mechanics, the properties of the system are predicted as a function of the simulation time.

2.1.1 Patchy Particles and Three-Body Potential

Using a coarse-grained model, Smallenburg et al. [50] studied the phase behavior of vitrimers in a solvent phase. The study used event-driven molecular dynamic simulations (EDMD) and Wertheim's theory for free energy calculations for simulating vitrimers [51]. The model system presented a mixture of two types of patchy particles, namely particles A and B with $f_A = 4$ and $f_B = 2$, where f denotes the number of attractive patches on the particle surface arranged in tetrahedral and polar geometries, respectively. The particles were designed based on the Kern-Frenkel model [52]. The size of the patches was defined based on their opening angle θ_m with $\cos\theta_m = 0.8$. The patches can only be involved in one bond at a time, and that is, multiple bonding partners are available. This type of associative bond exchange in the system satisfies the requirement for a vitrimer network. The interactions in the model system were considered as a combination of the repulsive potential between beads of diameter σ with a mass of m and attractive interaction between the surface particle patches. The bonding between patches could not exceed the maximum bond length of 1.2σ with the condition that the vector linking the centers of any two particles passes through at least one patch on each particle. The rate of bond switching was controlled according to the system by varying the temperature and/or the catalyst load. Using the autocorrelation of the off-diagonal elements of the stress tensor, the dimensionless shear viscosity $\eta\beta\sigma^3 / \tau$, where $\beta = 1 / k_B T$, with k_B is the Boltzmann constant, and τ is

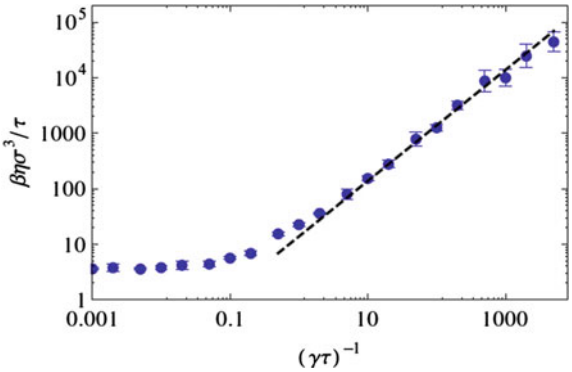

Fig. 2 Dimensionless shear viscosity $\beta\eta\sigma^3/\tau$ as a function of the average time interval between bond switching events. The dashed line indicates an Arrhenius fit (slope = 1). The viscosities were calculated at the composition of $x = 0.25$ (where x is the ratio of the number of patches of A to the total number of patches (A + B)), and number density of $\rho\sigma^3 = 0.35$, where σ is the diameter of the particle, well away from the area where phase separation occurs. τ is the units of time and is defined as $\tau \equiv \sqrt{\beta m\sigma^2}$, where m is the mass of particle and $\beta = 1/k_BT$, with k_B is the Boltzmann constant. The figure is obtained from Smallenburg, Leibler, Sciortino; Patchy Particle Model for Vitrimers; Phys. Rev. Lett.; 2013; American Physical Society

the units of time and is defined as $\tau \equiv \sqrt{\beta m\sigma^2}$, was obtained at different average times between bond switching events, as seen in Fig. 2 (note that the frequency of the bond exchange γ scales with $\exp(-\varepsilon_a/k_BT)$, where ε_a is the activation energy). At small time intervals, when bond switching occurs fast, the viscosity of the system is constant, while at $(\gamma\tau)^{-1} \gg 1$, a linear relationship with $(\gamma\tau)^{-1}$ is seen for the viscosity, and consequently, an Arrhenius-like behavior of the viscosity is observed.

Another type of coarse-grained simulation for polymers often is performed using the bead-spring model [53], where beads interact using a Weeks-Chandler-Anderson (WCA) potential [54]. The monomer bond exchange was implemented using the WCA potential for nonbonded particles, the harmonic potential for bonded particles, and a three-body potential based on the Stillinger–Weber potential. The dynamics of the transient networks are predicted as a function of time. A similar method incorporating a three-body potential based on the Stillinger–Weber potential [55] was proposed to study the self and collective dynamics of vitrimers [46]. These two types of dynamics were quantified using the intermediate scattering functions (ISFs), and a two-step relaxation was observed for the self and collective part of the ISF.

Eight-arm star-shaped polymers with carboxyl and hydroxyl end groups, respectively, were simulated using the latter method [56]. The underlying idea behind the three-body potential is based on the addition of a repulsive potential based on interactions three-body interactions between *i-j* and *i-k* particles. It also involves a parameter λ used to interpolate between a bong swapping and permanently connected systems. When the value of $\lambda >> 1$, a system with an infinitely long bond lifetime is simulated. When $\lambda = 1$, the additional potential energy gain associated with the

formation of the double bond is compensated by the value of the three-body potential. The systems were divided into a defect free mixture (DFM), which was a mixture of star polymers with either only groups A or B as the end groups, and a defect allowing mixture (DAM), which consisted of star polymers with seven arms ending with group A and one with group B. After forming bonds in the DAM, the A-type ends were free to initiate bond swapping. Both systems were equilibrated in periodic cubic boxes with a packing fraction of 0.3. For the stress relaxation calculations, the Green–Kubo method [57] was used in a constant number of particles, volume, and temperature (NVT) ensemble to calculate the stress $\sigma(t)$ autocorrelation function.

In Fig. 3a and b, the stress relaxation of DFM and DAM systems as a function of the time at different energy barrier values is plotted. For times shorter than that elastic plateau timescale, the chain motion dominates stress relaxation. When the energy barrier of the bond swap is high, the topology of the network remains unchanged, and the elastic plateau extends beyond the time scale for simulation. However, for the case with no energy barrier, which enables bond swapping, there is a second relaxation observed, as shown in Fig. 3. This is a characteristic feature of transient networks such as vitrimers. The stress relaxation time in this scenario was about 20 μs. In the case of DAM, the solid plateau is achieved by the fixed network, while the transient networks result in stress relaxation over shorter timescales. The stress relaxation was 10 times faster with the stress relaxation time of 2 μs which essentially shows the DAM networks behave like a viscous liquid. In the inset of Fig. 3b, the comparison between the stress relaxation modulus in these two networks is presented, and as seen, the improved stress relaxation is a result of the defects when the number of the bond swaps was the same for both. It was indicated that a defect loop was formed every time an intra-star bond was experiencing stress which led to dissipation, and given that the swap rates were the same for both networks, it was concluded that the defect loops acted like highways for stress relaxation. It was further hypothesized that these loop defects could be used to speed up the stress relaxation process, enhance properties of self-healing, and make the material more malleable and recyclable.

2.1.2 Hybrid Molecular Dynamics–Monte Carlo Technique

Recently, we proposed a hybrid molecular dynamics–Monte Carlo (MD–MC) method to describe the dynamics and linear rheology of vitrimers at different temperatures [49, 58]. Pant and Theodorou devised an algorithm based on the connectivity-altering atomistic Monte Carlo (MC) approach to accelerate the equilibrium of condensed phases of long-chain systems with a range of chain architectures [58, 59]. Following their work, similar MD–MC algorithms have been implemented to examine materials with reversible bonds, such as thermoreversible gels, supramolecular polymer, and telechelic polymers [47, 60–62]. Based on those methods, it is proposed an adaptation of the MD–MC algorithm that can be used for reproducing the bond exchange reactions in associative CANs, specifically in vitrimers.

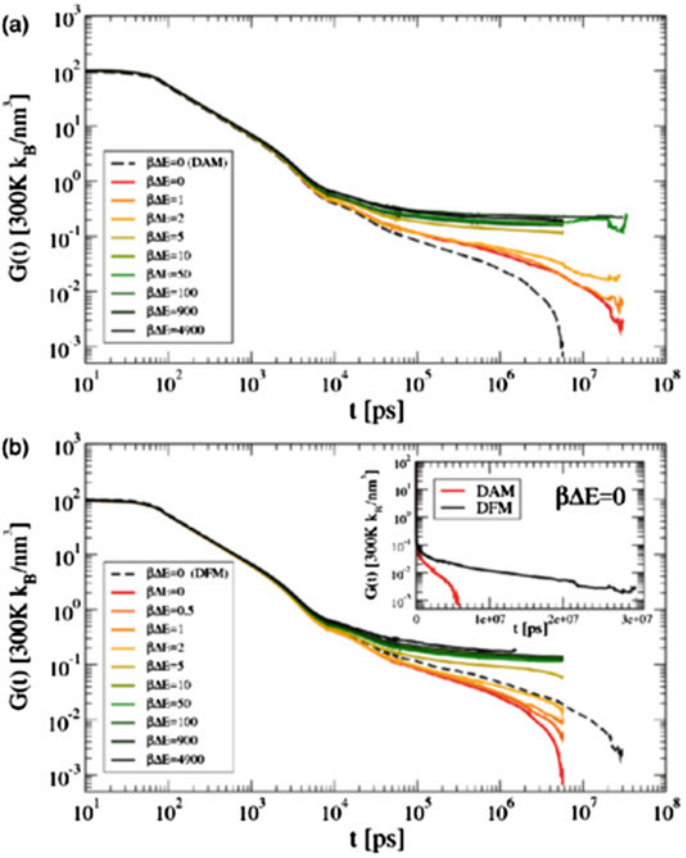

Fig. 3 **a** Stress relaxation for DFM for a range of energy barrier values. **b** Comparison between the DAM and DFM stress relaxation values. The figure is obtained from Ciarella, Sciortino, Ellenbroek; Dynamics of Vitrimers: Defects as a Highway to Stress Relaxation; Phys. Rev. Lett.; 2018; American Physical Society

To explain how the algorithm works, let us suppose we have a system consisting of a few polymers chains such as the one depicted in Fig. 4. These polymers are made of n monomers units, but only one terminal monomer can react to form additional bonds with other chains. At $t = t_0$, two polymer chains are covalently bonded with each other. At every user-defined time step, each reactive monomer is sampled to find a possible new monomer for the bond exchange. Assuming that (i, j) and (k,l) are two exchangeable bonds pairs, for a monomer found at a distance r defined by the user, the energy change $\Delta\tilde{U}_{\text{Exchange}}$:

$$\Delta\tilde{U}_{\text{Exchange}} = \alpha\Big(\tilde{U}_{\text{New}}(i,l) + \tilde{U}_{\text{New}}(j,k) - \tilde{U}_{\text{Old}}(i,j) - \tilde{U}_{\text{Old}}(k,l)\Big), \qquad (1)$$

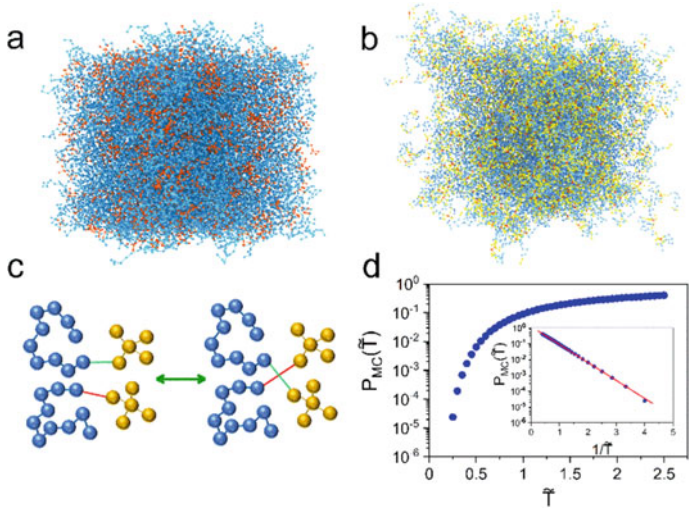

Fig. 4 Mixture of 10-mer chains (blue) with crosslinkers (orange) before **a** and after **b** crosslinking the network (yellow correspond to the reacted beads). **c** Bond exchange reaction schematic. Red and green colors are used to represent the exchangeable bonds. **d** Probability of an exchange reaction $P_{\mathrm{MC}}\left(\tilde{T}\right)$ as a function of temperature $\tilde{T}$ in vitrimers. The red line in the inset shows the exponential fit to the data. The figure is obtained from Perego, Khabaz; Volumetric and Rheological Properties of Vitrimers: A Hybrid Molecular Dynamics and Monte Carlo Simulation Study; Macromolecules; 2020; American Chemical Society

can be computed. If $\Delta\tilde{U}_{\mathrm{Exchange}} \leq 0$, the new configuration will be accepted, and if $\Delta\tilde{U}_{\mathrm{Exchange}} > 0$, the move is accepted based on the Boltzmann acceptance criterion [63, 64]. The α parameter is a dimensionless factor that is introduced to mimic the effect of a bond exchange reaction assisted by a catalyst. The polymer network is simulated using the well-established CG framework introduced by Kramer and Grest, in which the polymer chains are modeled as spherical beads connected by springs [53]. Within an atomistic model, each bead corresponds to multiple monomer units. All units are normalized in terms of reduced Lennard–Jones (LJ) parameters: length $= \sigma$, energy $= \epsilon$, and time $= (m\sigma^2/\epsilon)^{1/2}$ with the bead mass of m. The nonbonded interaction is calculated using a shifted and truncated Lennard–Jones (LJ) potential defined as:

$$\tilde{U}_{\mathrm{LJ}}(\tilde{r}) = \begin{cases} 4\left[\left(\frac{1}{\tilde{r}}\right)^{12} - \left(\frac{1}{\tilde{r}}\right)^{6} - \left(\frac{1}{\tilde{r}_c}\right)^{12} + \left(\frac{1}{\tilde{r}_c}\right)^{6}\right] & \text{for } \tilde{r}_c \leq 2.5 \\ 0 & \text{for } \tilde{r}_c > 2.5 \end{cases}, \tag{2}$$

where r represents the distance between two beads and r_c represents the cut-off distance. Throughout the simulation, the chain structure is maintained numerically such that the nearest-neighbor beads along the chain are permanently bonded. These permanent bonds are anharmonic, finitely extensible, nonlinear, and described by an

elastic (FENE) potential:

$$\tilde{U}_{\text{Bond}}(\tilde{r}) = -\frac{K}{2}\tilde{r}_0^2 \ln\left[1 - \left(\frac{\tilde{r}}{\tilde{r}_0}\right)^2\right], \tag{3}$$

An appropriate choice of parameter consists of setting $R_{\max} = 1.5\sigma$, and k $= 30\epsilon/\sigma$ as it avoids the possibility of chains passing through one another [64–66].

The initial crosslink network is constructed using a tetrafunctional crosslinker consisting of five beads with the four end beads being reactive and a linear molecule with two reactive terminal beads. Reactions are only allowed between the reactive beads. The simulated annealing polymerization technique [67, 68] is used to connect the tetrafunctional molecules with the linear ones and build the final crosslinked structure. In Fig. 4a–c, the simulation box before and after reaction and the schematics of the monomer and crosslinker are shown, respectively. The relaxation and quenching simulations from a high temperature of 2.0 to 0.1 were performed in an isothermal–isobaric ensemble with a pressure of zero. The probability of the bond exchange between the crosslinker junctions $P_{\text{MC}}\left(\tilde{T}\right)$ is determined and plotted in Fig. 4d at each temperature. As seen in the figure, $P_{\text{MC}}\left(\tilde{T}\right)$ follows an Arrhenius-like temperature dependence.

The volumetric properties of the model thermoset and vitrimer networks were quantified by determining the specific volume, coefficient of thermal expansion, and glass transition temperature. In Fig. 5a, the specific volume of the model systems is plotted as a function of temperature. Both thermoset and vitrimer systems show similar $\tilde{T}_g$ values, which are expected since the bond exchanges become relevant only at high temperatures (see Fig. 4d for the probability of the bond exchange). At temperatures higher than $\tilde{T}_g$, the specific volume of vitrimer becomes larger than that of thermoset that is more visible in the dimensionless excess volume $\tilde{V}^E = \left(\tilde{V}_{\text{vitrimer}} - \tilde{V}_{\text{thermoset}}\right) \Big/ \tilde{V}_{\text{thermoset}}$ in the inset of Fig. 5a. We plot the coefficient of thermal expansion $\tilde{\alpha} \cdot \left(\tilde{\alpha} = \left(\partial V \Big/ \partial T\right)_p \Big/ V\right)$ in Fig. 5b for these two systems. Both thermoset and vitrimer networks show a discontinuous behavior for $\tilde{\alpha}$ at $\tilde{T}_g$. At $\tilde{T} > \tilde{T}_g$ the thermoset shows a constant value of $\tilde{\alpha}$; on the other hand, a local minimum point at $\tilde{T} \simeq 0.87$ for the values of $\tilde{\alpha}$ is seen in the model vitrimer.

The dynamics of the crosslinkers in the model systems were determined by calculating the mean squared displacement (MSD) $\left\langle \Delta\tilde{r}^2(\tilde{t}) \right\rangle$ at different temperatures. As seen in Fig. 6a, at temperatures below the glass transition temperature, both systems show similar mobility. As the temperature steadily increases and exceeds the $\tilde{T}_g$, the vitrimer shows higher mobility. At higher temperatures (see Fig. 6c and d), the crosslinkers show a nearly diffusive behavior, while the motion of the crosslinker in the thermoset network is impeded due to the existence of permanent bonds.

Using the hybrid MD–MC method [58], the rheology of the networks can also be determined. We refer readers to our study on the volumetric, dynamics, and rheology of the vitrimers for detailed discussion. Here, we focus on the primary outcomes of

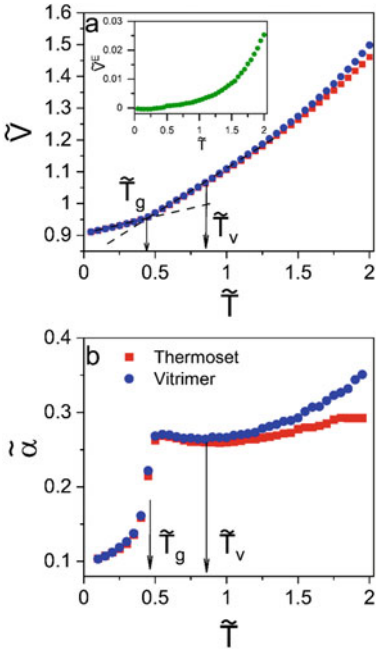

Fig. 5 **a** The specific volume $\tilde{V}$ and **b** thermal expansion coefficient $\tilde{\alpha}$ as a function of reduced temperature $\tilde{T}$ for both thermoset and vitrimer. Inset in **a:** The rescaled excess volume $\tilde{V}^E = \left(\tilde{V}_{\text{vitrimer}} - \tilde{V}_{\text{thermoset}}\right) \Big/ \tilde{V}_{\text{thermoset}}$ as a function of the temperature. At every temperature, the uncertainty for each data point is about 0.1% of the magnitude of the specific volume (smaller than symbol size). The intersection of the fitted lines (dashed lines in **a**) in the rubbery and glassy regions corresponds to the glass transition temperature $\tilde{T}_g$ of the system. The figure is obtained from Perego, Khabaz; Volumetric and Rheological Properties of Vitrimers: A Hybrid Molecular Dynamics and Monte Carlo Simulation Study; Macromolecules; 2020; American Chemical Society

the rheological simulations that are (1) applicability of the time–temperature superposition (TTS) principle to extend the simulation timescale and (2) Arrhenius-like temperature dependence of the viscosity of vitrimer. The linear viscoelastic moduli of the thermoset and vitrimer were determined using the NEMD method [69] by incorporating the SLLOD equations of motion [70] at different frequencies and temperatures. The TTS principle is used to collapse data onto master curves at a reference temperature of $\tilde{T}_0 = 0.6$. In Fig. 7a, the elastic modulus of the thermoset network is plotted against the oscillation frequency. The thermoset network exhibits a rubbery modulus at low frequencies and a glassy response after a Rouse-like transition regime. The vitrimer model essentially behaves the same way as the thermoset at intermediate and high frequencies, given that the deformation rate is larger than the bond exchange rate, as seen in Fig. 7b. On the other hand, at lower frequencies, the elastic modulus of the vitrimer appears to show a liquid-like behavior (or so-called terminal regime). The latter observation is due to the fast timescale of the bond exchange in that deformation regime, which corresponds to long times. Both

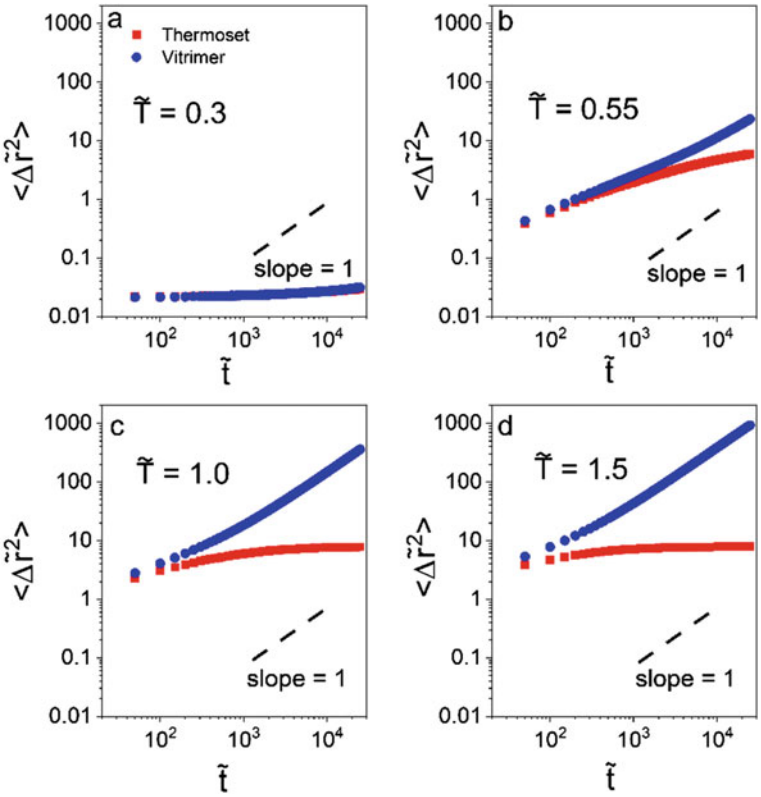

Fig. 6 Mean-squared displacement (MSD) $\left\langle \Delta\tilde{r}^2(\tilde{t}) \right\rangle$ of the crosslinking beads (reactive beads that can participate in the exchangeable reaction) in thermoset and vitrimer at **a** $\tilde{T} = 0.3$, **b** $\tilde{T} = 0.55$, **c** $\tilde{T} = 1.0$, and **d** $\tilde{T} = 1.5$. The diffusive motion is shown by the dashed line, which has a slope of unity on the log–log scale. The figure is obtained from Perego, Khabaz; Volumetric and Rheological Properties of Vitrimers: A Hybrid Molecular Dynamics and Monte Carlo Simulation Study; Macromolecules; 2020; American Chemical Society

viscous moduli of thermoset and vitrimer show the same behavior (see Fig. 7c and d). We expect to observe the difference in the viscous moduli at lower frequencies which are not accessible in the current simulations. Note that the shift factors used to collapse rheological data follow Williams-Landel-Ferry (WLF) equation for the thermoset network, while this temperature dependence for the vitrimer model becomes more complex (see Fig. 8). The temperature dependence of the shift factor follows a combination of the WLF equation at low temperatures and Arrhenius behavior at high temperatures in model vitrimer. The intersecting temperature between these two regimes corresponds to a temperature of 0.85, which is very close to the temperature that coefficient of thermal expansion shows a local minimum. In addition, the zero-shear viscosity of the vitrimer model shows an Arrhenius-like form which validates the model consistency with the temperature dependence of shift factors.

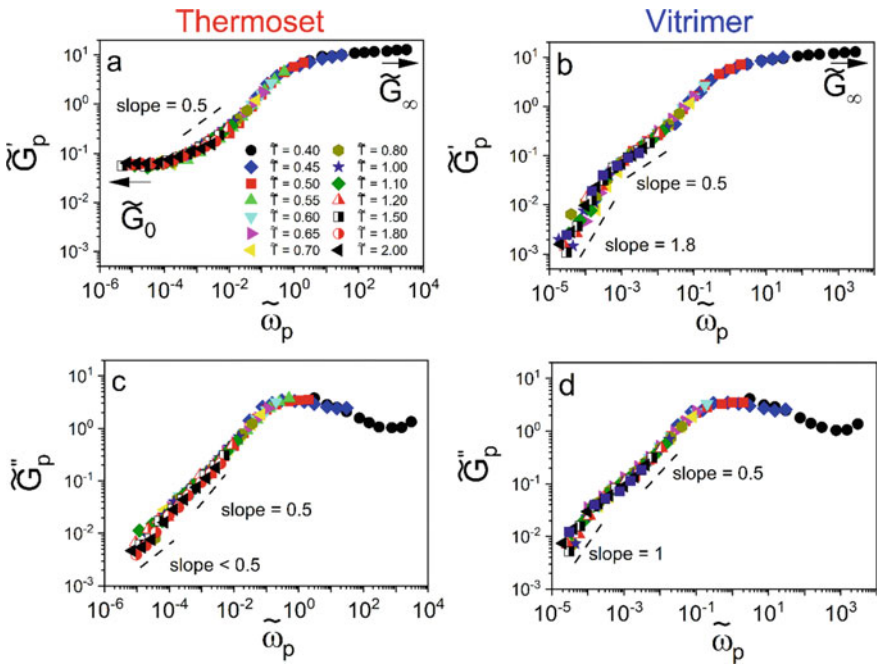

Fig. 7 Universal curves of rescaled **a–b** elastic $\tilde{G}'_p$ and **c–d** loss $\tilde{G}''_p$ moduli as a function of the reduced frequency $\tilde{\omega}_p$ in the model thermoset (left panel) and vitrimer (right panel). The reference temperature in both sets of master curves is $\tilde{T}_0 = 0.6$. The figure is obtained from Perego, Khabaz; Volumetric and Rheological Properties of Vitrimers: A Hybrid Molecular Dynamics and Monte Carlo Simulation Study; Macromolecules; 2020; American Chemical Society

The nonlinear mechanics of vitrimers have also been studied using the hybrid MD–MC method [49] when the exchange reaction rate was adjusted by introducing a constant parameter α in the MC step to adjust the downhill moves energy barrier. The model system was constructed using a tetrafunctional crosslinker and 5-mer monomer chain. The mobility of the vitrimer network showed an inverse relationship with the α value, *i.e.*, smaller values of α led to more frequent bond exchanges in the system, and crosslinker particles could move large distances. Using the NEMD technique, the stress–strain curves of the vitrimer models with different exchange rates under uniaxial deformation were determined at three different temperatures (Fig. 9a–f). Note that the stress–strain curves are plotted until the failure point. When the temperature is below the $\tilde{T}_g$, the thermoset and vitrimer networks with varying values of α show similar behavior at low strain values. On the other hand, when the strain becomes larger, and the response of the networks to the strain becomes nonlinear, vitrimers with slower bond exchanges show a closer stress–strain behavior to the thermoset one. At higher temperatures, we also see the same behavior with a difference that the magnitude of the stress decreases at the failure point. In all cases,

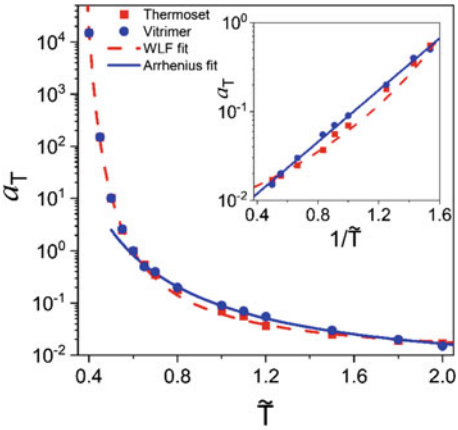

Fig. 8 Horizontal shift factors a_T used in collapsing the moduli data in Fig. 7 for the thermoset and vitrimer as a function of the temperature. Inset: Arrhenius plot of the shift factors obtained at $T > T_v$. The WLF and Arrhenius fit to the data are shown by blue and dashed red lines, respectively. The figure is obtained from Perego, Khabaz; Volumetric and Rheological Properties of Vitrimers: A Hybrid Molecular Dynamics and Monte Carlo Simulation Study; Macromolecules; 2020; American Chemical Society

vitrimers outperform thermoset networks in the failure strain. This strain increases by decreasing the value α.

2.2 Continuum Models

2.2.1 Constitutive Equations

On a continuum level, most of the current models are built on the approach pioneered by Terentjev and coworkers, where they developed a set of microscopic constitutive equations to describe transient polymer networks (such as vitrimers and other self-healing materials) undergoing small deformations in stress relaxation, creep, and uniaxial deformation experiments [71, 72]. In their approach, the energy of the system is described by treating the polymers as Gaussian chains (*i.e.*, Neo-Hookean model) [73]. Here, we briefly review the main features of the constitutive equations, and the reader is referred to ref. [73–75] for detailed derivations.

Breaking and Reforming of Cross-links: Microscopically, the rate of crosslinks breakage can be described using the local force acting on the chain. Assuming a potential energy well with a characteristic energy barrier, in which the crosslink is held, one can derive an equation for a total number of crosslinked chains at a given time $N_c(t)$:

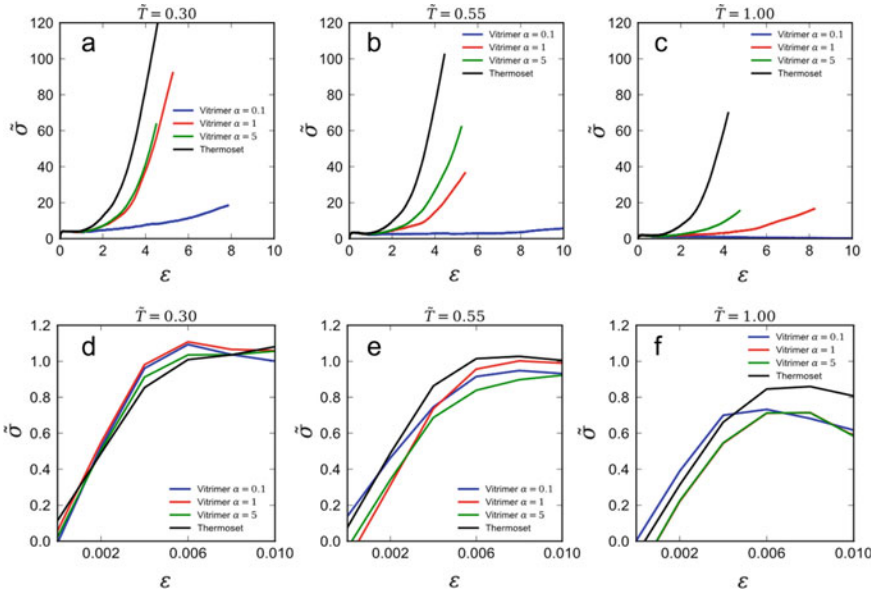

Fig. 9 Stress-strain curves at different temperatures of the simulated thermoset and vitrimer system for various values of α. **d–f** are zoomed-in graphs of **a–c,** respectively, used to show the initial linear response of the four networks. The strain rate used for all the simulations was $\tilde{\dot{\varepsilon}} = 10^{-1}$. The figure is obtained from Perego, Khabaz; Effect of bond exchange rate on dynamics and mechanics of vitrimers; J. Poly. Sci.; 2021; Wiley

$$N_c(t) = N_c(0)\exp\left(-\int_0^t \beta(t';0)dt'\right) + \int_0^t N_b(t')\exp\left(-\int_{t'}^t \beta(t'';t')dt''\right)\rho dt', \tag{4}$$

where β is the equilibrium Kramers rate [74], ρ the effective rate or re-crosslinking, and $N_b(t)$ is the number of un-cross linked chains at a given time. The first term of Eq. (1) indicates the crosslinked chains from $t\prime = 0$ as a function of time. The re-crosslinking of the chains, from the original chains and other chains broken at different times during the same period, is represented by the second term. As $N_b(t) = N_{\text{tot}} - N_c(t)$, Eq. (4) can be seen as an integral equation that helps to determine $N_c(t)$ at a particular dynamic deformation state.

Macroscopic Elastic Energy: The structure of the deformation energy can be characterized macroscopically by adopting Gaussian chains approximation (e.g., using rubber elasticity theory) [75]. For a permanently crosslinked rubbery network, the system's energy density while being deformed is described as:

$$F_{\text{rub}}(t;0) = \frac{1}{2}G\big(\text{tr}\big[\mathbf{E}^{T}(t;0)\mathbf{E}(t;0)\big] - 3\big), \tag{5}$$

where G represents the shear modulus and $\mathbf{E}(t;0)$ is the affine deformation tensor at time t to $t = 0$, which is the reference state.

However, for a transient network undergoing deformation, there are numerous contributions to the average elastic-free energy due to the dynamics of the crosslinks. Thus, the elastic free energy density $F(t;t_0)$ with regards to the reference state t_0 is determined by the deformation tensor $\mathbf{E}(t;t_0)$ defined as:

$$\mathbf{E}(t;t_0) = \mathbf{E}(t;0)\cdot\mathbf{E}^{-1}(t_0;0), \tag{6}$$

The energy density can then be written as:

$$\begin{aligned} F_{\text{tr.}n.}(t) \; &= \exp\left(-\int_0^t \beta(t';0)dt'\right) F_{\text{rub}}(t;0) \\ &+ \int_0^t \rho\frac{N_b(t')}{N_c(0)}\exp\left(-\int_{t\prime}^t \beta\big(t'',t\prime\big)dt''\right) F_{\text{rub}}(t;t\prime)dt', \end{aligned} \tag{7}$$

The second term is computed using the dynamically changing strain tensor defined in Eq. (6) is used to calculate the neo-Hookean free energy density.

Contrary to a permanent rubbery network where the reference state is at $t = 0$, in a transient network, the reference can only be locally specified for different chains, depending on their time of crosslinking. Tracking the real-reference state thus becomes a difficult task, and it is appropriate to describe an effective shear modulus G^* as the following ratio:

$$G^*(t) = \frac{2F_{\text{tr.}n}(t)}{\text{tr}\big[\mathbf{E}^{\text{T}}(t;0)\cdot\mathbf{E}(t_0;0)\big] - 3} \tag{8}$$

Elastic Stress Tensor: In transient networks, the stress is defined by both the elastic and viscous stresses ($\boldsymbol{\sigma}^{\text{ela}}+\boldsymbol{\sigma}^{\text{vis}}$). As the origins of $\boldsymbol{\sigma}^{\text{vis}}$ are very complex (*e.g.,* dangling chains, nonaffine movement of crosslinks and the dynamics of entanglements), it is convenient to express this term as:

$$\boldsymbol{\sigma}^{\text{vis}} = \boldsymbol{\eta}(\dot{\gamma})\cdot\dot{\gamma}, \tag{9}$$

with the viscosity tensor $\boldsymbol{\eta}$ defined as a function of the strain rate tensor $\dot{\gamma}$.

To account for the material incompressibility, it is possible to work with the Gibbs free energy of the system as:

$$g(t) = F_{tr.n.}(t) - p\cdot\det\mathbf{E}. \tag{10}$$

By defining the elastic stress, σ_{ij}^{ela}, as a function of $g(t)$ (*e.g.*, $\sigma_{ij}^{ela}(t) = \frac{\sigma g(t)}{\delta E_{ij}(t;0)}$), the expression for the stress tensor can be obtained:

$$\begin{aligned}\sigma_{ij}^{ela}(t) &= \exp\left(-\int_0^t \beta(t\prime;0)dt\prime\right) G E_{ij}(t;0) \\ &+ \int_0^t \int \rho \frac{N_b(t\prime)}{N_c(0)} \exp\left(-\int_{t\prime}^t \beta(t\prime\prime,t\prime)dt\prime\prime\right) G E_{jk}(t;t\prime) E_{jk}^{-1}(t\prime;0)dt\prime \\ &- p \cdot \det \mathbf{E} \cdot E_{ji}^{-1}. \end{aligned} \tag{11}$$

Equation (11) provides the constitutive equation of the model and can be used to study how a transient network responds to an imposed uniaxial stretch. Figure 10a shows a schematic of a polymer sheet undergoing uniaxial stretching**.** By defining the length (L), width (W), and thickness (T) elongation ratios as λ_L, λ_W, and λ_T, respectively, the deformation can be described using the following relationships: $L = \lambda_L L_0$, $W = \lambda_W W_0$, and $T = \lambda_T H_T$. Due to the incompressibility of the system, one can write $\lambda_L = \lambda$ making λ_W together with λ_T equal to $1/\sqrt{\lambda}$.

The deformation tensor at a time t for a particular crosslink formed a time $t\prime$ can be obtained through Eq. (6):

$$\mathbf{E}(t;t\prime) = \frac{\lambda(t)}{\lambda(t\prime)} \mathbf{e}_L \mathbf{e}_L + \sqrt{\frac{\lambda(t\prime)}{\lambda(t)}} (\mathbf{e}_W \mathbf{e}_W + \mathbf{e}_T \mathbf{e}_T), \tag{12}$$

with $\mathbf{e}_L$, $\mathbf{e}_W$, and $\mathbf{e}_T$ as the unit vectors in three orthogonal directions. The average end-to-end distance $\langle r \rangle$ (Fig. 9b) that indicates the deformation occurring at a time t with respect to a reference time τ can then be calculated using:

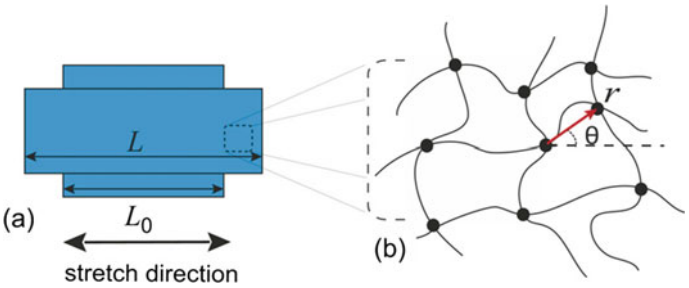

Fig. 10 **a** Illustration of a polymeric sheet undergoing uniaxial stretched deformation. **b** schematic of a sample of polymer chains in the network undergoing the same deformation, with r as the end-to-end distance and θ as the angle between the end-to-end vector and the stretch direction. The figure is obtained from Meng, Pritchard, Terentjev; Stress Relaxation, Dynamics, and Plasticity of Transient Polymer Networks; Macromolecules; 2016; American Chemical Society

$$\langle r_{t;\tau} \rangle = r_0 \int_0^{\pi/2} d\theta \sin\theta \sqrt{\left(\frac{\lambda(t)}{\lambda(\tau)}\right)^2 \cos^2\theta + \left(\frac{\lambda(\tau)}{\lambda(t)}\right)^2 \sin^2\theta}, \tag{13}$$

with $r_0 \sim \sqrt{N_s} b$ being the network mesh size in its reference state. The transient network's elastic free energy can be expressed as:

$$\begin{aligned} F_{\text{tr.n.}}(t) &= \exp\left(-\int_0^t \beta(t';0)dt'\right) F_{\text{rub}}(t;0) \\ &+ \int_0^t \rho \frac{N_b(t')}{N_c(0)} \exp\left(-\int_{t'}^t \beta(t'',t')dt''\right) F_{\text{rub}}(t;t')dt'. \end{aligned} \tag{14}$$

Similarly, using Eq. (8) and dividing both the terms of Eq. (14) by the characteristic new-Hookean strain, we can obtain the effective shear modulus:

$$\begin{aligned} G^*(t) &= G \exp\left(-\int_0^t \beta(t';0)dt'\right) \\ &+ G \int_0^t \rho \frac{N_b(t')}{N_0} \exp\left(-\int_{t'}^t \beta(t'';t')dt''\right) \\ &\times \left(\frac{\lambda(t)^2/\lambda(t\prime)^2 + 2\lambda(t')/\lambda(t) - 3}{\lambda(t)^2 + 2/\lambda(t) - 3}\right) dt'. \end{aligned} \tag{15}$$

Using Eq. (11)**,** it is possible to calculate the transverse diagonal components of the stress, thus obtaining:

$$\begin{aligned} \sigma_L(\lambda,t) &= G \exp\left(-\int_0^t \beta(t\prime;0)dt\prime\right)\left(\lambda(t) - \frac{1}{\lambda(t)^2}\right) \\ &+ G \int_0^t \frac{N_b(t\prime)}{N_0} \rho \exp\left(-\int_{t'}^t \beta(t\prime\prime;t\prime)dt\prime\prime\right)\left(\frac{\lambda(t)}{\lambda(t\prime)^2} - \frac{\lambda(t\prime)}{\lambda(t)^2}\right) dt\prime. \end{aligned} \tag{16}$$

Thus, to calculate this dynamic stress under uniaxial deformation, one must first solve Eq. (4) to determine $N_b(t)$ and subsequently compute the time-integrals of Eq. (16).

Stress-relaxation: The simplest way to test model accuracy is to compute the stress relaxation behavior of the transient network when a uniaxial stepwise deformation λ is applied at $t = 0$. In this scenario, $\lambda(t) = \lambda(t\prime)$ makes the second term of Eq. (15) equal to zero. The tensile stress can be easily computed along the stretching direction

from Eq. (16), thus obtaining:

$$\sigma_L = Ge^{\beta(\lambda)t}\left(\lambda - \frac{1}{\lambda^2}\right). \tag{17}$$

Equation (17) shows how the stress relaxes following a stretched exponential form with the characteristic relaxation time defined as $\tau = 1/\beta(\lambda)$ [76, 77]. Using Eq. (13) to calculate the average end-to-end chain length, we can write the explicit form of $\beta(\lambda)$ as:

$$\begin{aligned}\beta(\lambda) &= \omega_0 \exp\left(\kappa r_o \int_0^{\pi/2} \sin\theta\sqrt{(1/\lambda)}\sin\right) \exp(-W_b/k_bT) \\ &= c_0(\lambda)\exp(-W_b/k_bT),\end{aligned} \tag{18}$$

with

$$c_0(\lambda) = \omega_0 \exp\left[\frac{3}{2\sqrt{N_s}\lambda}\left(\lambda^{3/2} + \frac{\operatorname{arcsinh}\left(\sqrt{\left(\lambda^3-1\right)}\right)}{\sqrt{\left(\lambda^3-1\right)}}\right)\right] \tag{19}$$

Equation (19) indicates that $c_0(\lambda)$ increases monotonically with the stretching ratio λ. At lower limits (small strain) $c_0 \approx \omega_0 \exp\left(3/\sqrt{(N_s)}\right)$ while at upper limit (high strain) $c_0 \approx \omega_0 \exp\left(3\lambda/2\sqrt{(N_s)}\right)$. The theoretical normalized shear modulus $G(t)/G_{max}$ (Fig. 11)of two vitrimer systems shows an excellent agreement with the experimental data obtained by Montarnal et al. [5] and rom Hillmyer et al. [33].

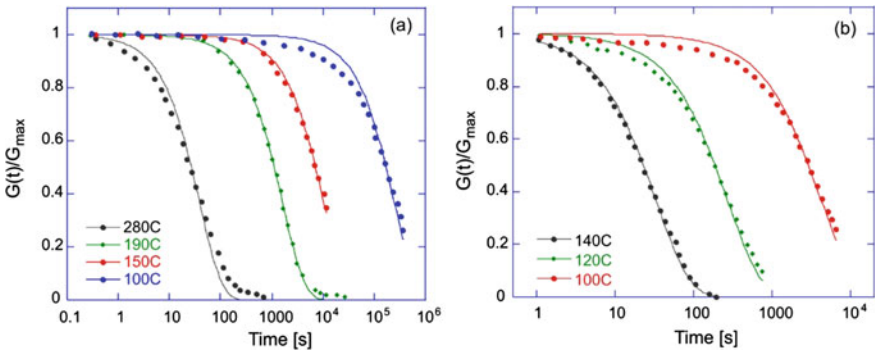

Fig. 11 Normalized shear modulus $G(t)/G_{max}$ as a function of relaxation time at different temperatures. The solid lines are the predicted values from the model, and the markers are the experimental data from **a** Montarnal et al. [5] (epoxy vitrimer) and **b** from Hillmyer et al. [33] (polylactide vitrimer). The figure is obtained from Meng, Pritchard, Terentjev; Stress Relaxation, Dynamics, and Plasticity of Transient Polymer Networks; Macromolecules; 2016; American Chemical Society

The takeaway message is that stress relaxation in transient networks decays in a stretched exponential manner. In contrast to ordinary rubbers which relax under stress, this behavior, due to the permanent nature of the crosslinks, displays a long-time power-law/logarithmic tail.

The authors further demonstrate the accuracy of the proposed model by performing a strain-ramp simulation on the system. The results show remarkable agreement with the experimental values obtained for various vitrimer systems. The proposed theoretical framework highlighted that the material response is strongly influenced by the crosslinker exchange kinetics. However, the model was built using several approximations. For example, the nonaffine displacement of the system is not considered in the development of the theory. This is particularly crucial when the entangled chain mobility is significant. Additionally, the neo-Hookean model is only valid for deformation below 100% strain. When dealing with larger deformations, different elastic models should be implemented. Despite these limitations, the proposed model provided an excellent picture of the dynamics and relaxation in vitrimers and laid the foundation for developing subsequent continuum models for transient networks.

2.2.2 FEA Implementation

Continuing within the scope of continuum mechanics, Qi and coworkers developed a model which successfully accounts for the coupling between the macroscopic and microscopic properties of the network (*e.g.* bond exchange reactions) [77]. Their basic approach was built based on the idea developed by Tobolsky et al. [77, 79] in which, during the loading history, the polymer network is broken down into two groups of chains, each one reforming at a different period.

The model requires the following fields variables to be solved for: temperature T, the chain composition as a function of time $C_{OR}(t)$ and $\Delta(\tau, t)$, the Lagrangian multiplier p (used to reinforce isothermal incompressibility), as well as the displacement vector $\mathbf{u} \equiv \mathbf{x} - \mathbf{X}$ which describes the deformed position. These five coupled equations that connect these five variables are as follows:

1. Energy balance:

$$\left[\gamma + \frac{\mathrm{S{:}F}}{3}\left(\alpha_{\mathrm{v}} + \frac{\mathrm{d}\alpha_{\mathrm{v}}}{\mathrm{dT}}T\right)\right]\dot{\mathrm{T}} = \left(1 - \frac{\alpha_{\mathrm{v}}\mathrm{T}}{3}\right)\mathrm{S}{:}\,\dot{\mathrm{F}} - \nabla_{\mathrm{x}} \cdot \mathrm{Q} + \Psi - \frac{\alpha_{\mathrm{v}}\mathrm{T}}{3}\,\dot{\mathrm{S}}\,{:}\mathrm{F}, \tag{20}$$

where γ is the specific heat per unit volume, S is the first Piola–Kirchhoff (nominal), stress tensor, F is the deformation gradient, α_v is the thermal expansion coefficient, T is the temperature, Q is the heat flux vector, and Ψ is the rate of eternal heat supply per unit volume. The dot on top of the variables denotes the material time derivative. The x in the subscript of the gradient operator denoted the gradient being taken with respect to the reference configuration.

2. Linear momentum balance

$$\nabla_x \cdot \mathrm{S}^{\mathrm{T}} + \mathrm{b} = 0, \tag{21}$$

where b is the body force vector per unit volume.

3. Incompressibility constraint

$$\det(\boldsymbol{F}_t) = J_t = \left(F_{\mathrm{t}}^a\right)^3 = \exp\left(\int_{T_0}^{T} \alpha_v\left(\tilde{T}\right) d\tilde{T}\right), \tag{22}$$

where F_t^a is the thermal component of F at the deformation time t.

4. Constitutive equation for the normal stress tensor

$$\begin{aligned} \mathrm{S} \; &= -\frac{p}{F_t^a}\left(\mathrm{F}_t^e\right)^{-T} \\ &+ \frac{C_{\mathrm{OR}}}{F_t^a C_0}\Omega(I(t))\mathrm{F}_t^e \\ &+ \int_0^t \left[\frac{\Delta(\tau,t)}{F_t^a C_0}\Omega(H(\tau,t))\mathrm{F}_t^e\left(\mathrm{F}_\tau^e\right)^{-1}\left(\mathrm{F}_\tau^e\right)^{-T}\right] d\tau, \end{aligned} \tag{23}$$

where:

$$\Omega(y) \equiv \frac{C_0 RT\sqrt{N}}{\sqrt{3y}} L^{-1}\left(\sqrt{\frac{y}{3N}}\right), \tag{24}$$

and

$$I(t) \equiv tr\left(\mathrm{F}_t^e\left(\mathrm{F}_t^e\right)^T\right), \;\; H(t,\tau) \equiv tr\left(\mathrm{F}_t^e\left(\mathrm{F}_t^e\right)^{-1}\left(\mathrm{F}_t^e\left(\mathrm{F}_\tau^e\right)^{-1}\right)^T\right), \tag{25}$$

Here, F_t^e is the mechanical component of F at the deformation time t; C_0 is the original (before deformation) molar density of all the polymer chains; N is a material parameter that indicates the length of the chain between crosslinkers. L^{-1} is the inverse Langevin function.

5. Kinetic equations for heat flux and exchange reaction rate

$$\mathrm{Q} = -K_t \det(\mathrm{F})(\mathrm{F}^T\mathrm{F})^{-1}\nabla_x T, \tag{25}$$

$$rdtd\mathrm{v} = -\dot{C}_{\mathrm{OR}} dtdV \Rightarrow \dot{C}_{\mathrm{OR}} = -Jr = -k\exp\left(-\frac{E_a}{RT}\right)C_{\mathrm{OR}}, \tag{26}$$

$$\frac{\partial \Delta(\tau,t)}{\partial t} = -k\exp\left(-\frac{E_a}{RT}\right)\Delta(\tau,t),\ (\tau \le t). \tag{27}$$

Here, K_t is the thermal conductivity; k is a kinetic coefficient (always positive), and E_a is the activation energy of the bond exchange reaction. Initials and boundaries conditions (B.C.) are also necessary to solve these field equations.

The model includes six materials parameters: γ (specific heat), K_b (thermal conductivity), C_0 (original chain density), N (Arruda-Boyce chain segment number), E_a (activation energy), and k (bond exchange rate coefficient). Considering isothermal conditions, one can disregard the thermal parameters γ and K_t from the model, while all other parameters are accessible through stress-relaxation experiments.

To validate the model, it is important to consider the case of the uniaxial extension during an isothermal process. Due to isothermal conditions and using the initial B.C., Eq. (26) can be solved for the evolution of the chain composition, to obtain:

$$C_{\mathrm{OR}} = C_0\exp\left(-k\exp\left(-\frac{E_a}{RT}\right)t\right), \tag{28}$$

Likewise, Eq. (29) is solved to yield:

$$\Delta(\tau,t) = k\exp\left(-\frac{E_a}{RT}\right)C_0\exp\left(-k\exp\left(-\frac{E_a}{RT}\right)(t-\tau)\right),\ (\tau \le t). \tag{29}$$

The associative nature of the bond exchange in transient networks enables the total chain density of the system to be calculated by adding the original with the reformed chains together (at any time t the total chain density is equal to C_0). Additionally, by considering isothermal conditions $F^a = 1 \rightarrow \mathbf{F}^e = \mathbf{F}$. The unit vector $\mathbf{e}_1$ denotes the direction of stretching for the sample. λ, $\lambda^{1/2}$, and $\lambda^{1/2}$ are the three principal stresses. To obtain S_{11} (tensile stress along $\mathbf{e}_1$), it is useful to introduce first the following notation:

$$\lambda_t \equiv \lambda(t) \text{ and } \lambda_\tau \equiv \lambda(\tau). \tag{30}$$

We can then write Eq. (25) as:

$$I(t) = \lambda_t^2 + 2/\lambda_t,\ \text{and } H(\tau,t) = (\lambda_t/\lambda_\tau)^2 + 2\lambda_\tau/\lambda_t. \tag{31}$$

Finally, substituting Eq. (30) and Eq. (31) into Eq. (23), we obtain:

$$S_{11}(t) = \frac{C_{OR}(t)}{C_0}\Omega(I(t))\left(\lambda_t - \frac{1}{\lambda_t^2}\right) + \int_0^t \left[\frac{\Delta(\tau,t)}{C_0}\Omega(H(\tau,t))\left(\frac{\lambda_t}{\lambda_\tau^2} - \frac{\lambda_\tau}{\lambda_t^2}\right)\right]d\tau. \tag{32}$$

S_{11} represents the applied tensile force per unit cross-sectional area A_0 of the undeformed stress (nominal tensile stress), and it can be used to study the material response for various deformation cases (such as stress relaxation, tensile tests, and creep).

Stress Relaxation

During a stress relaxation experiment, at $t = 0^+$, a constant stretch ratio λ_C is applied. Therefore, $\lambda_t = \lambda_\tau = \lambda_C$ transforming the tensile stress S_{11} in:

$$S_{11}(t) = \left(\lambda_C - \lambda_C^{-2}\right)\Omega\left(\lambda_C^2 + 2/\lambda_C\right)\exp\left(-k\exp\left(-\frac{E_a}{RT}\right)t\right) \tag{33}$$

As seen in the theory developed by Meng et al. [71], the stress decays exponentially with time (e.g., $\frac{S_{11}(t)}{S_{11}(t=0^+)} = \exp\left(-\frac{t}{t_r}\right)$) where $t_R = \frac{1}{k}\exp\left(\frac{E_a}{RT}\right)$ is the characteristic relaxation time. Equation (33) it is also consistent with the observations of Leibler and coworkers, where they illustrate how the kinetics of bond exchange reaction influences t_R [78].

Figure 12a shows the agreement between the tensile stress values calculated by solving Eq. (33) and the experimental data obtained using an epoxy-acid vitrimer network catalyzed with 5 mol% zinc acetate [5]. Solving for the relaxation time t_R and plotting as a function of inverse temperature (Fig. 12b) allows calculating the activation energy of the system. The model predicts a value of $E_a = 81.1$ kJ mol^{-1} which is in agreement with the value of 80 kJ mol^{-1} reported in Montarnal et al. [5].

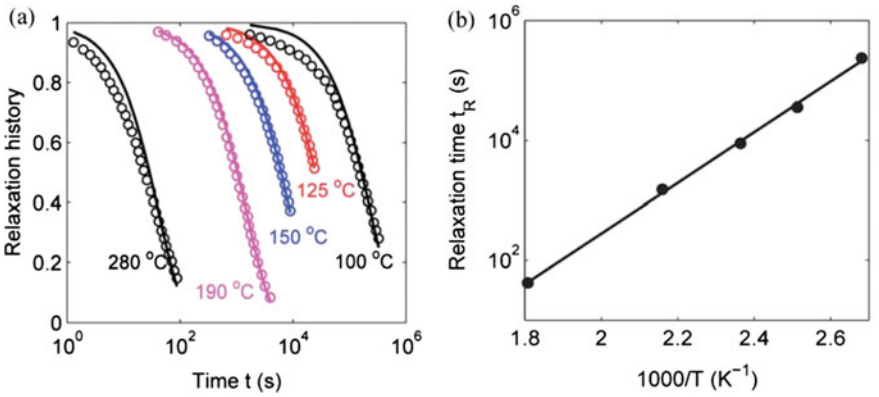

Fig. 12 **a** Stress relaxation curves at different temperatures. The solid lines are the values predicted by the model, while the symbols are the experimental data extracted from Montarnal et al. [5] **b** Relaxation time t_R as a function of inverse temperature. The solid line is the fit according to the model, and the symbols are the values obtained from the fitting of the experimental data [5]. The figure is obtained from Long, Qi, Dunn; Modeling the mechanics of covalently adaptable polymer networks with temperature-dependent bond exchange reactions; Soft Matter; 2013; Royal Society of Chemistry

FEM implementation–Modeling thermoforming processes: The notable feature of this model is that it can be implemented into three-dimensional finite element code (*e.g.,* ABAQUS [80]) using a user material subroutine (UMAT). One of the technologically remarkable properties of vitrimers is their ability to be easily reshaped through thermoforming processes. Thus, the capability to model these types of deformation events is essential from a processing perspective. The following three steps are typical in the thermoforming process:

1. The material undergoes a prescribed deformation at a low temperature (*e.g.*, 25°C).
2. The prescribed deformation is maintained, while the sample is heated over a time period. During this step, the network topology of vitrimers is re-arranged because of the activation of the bond exchange reactions.
3. The sample is cooled, and the applied deformation is released. As the vitrimer undergoes stress relaxation during Step 2, the original shape of the sample will not recover.

Twisting a strip: This simulation is inspired by the experiment used by Montarnal et al. [5] to illustrate the stress relaxation event in vitrimers. A twist angle of 5π is applied to a sample with dimensions $12 \times 1 \times 0.1$ cm. Figure 13 shows results obtained at $T = 523$ K using two processing times ($t_a = 10$ and $t_a = 100$ s). During the stress relaxation (Step 2), the extent of stress relaxation depends substantially on t_a consequently affecting the final shape of the material. At $t_a = 10$ s, as only a modest amount of stress is relaxed, the sample virtually returns to its original shape. In contrast, at $t_a = 100$ s, more stress is relaxed producing the shape memory in the material. These observations are also consistent with the experiments of Montarnal et al. [5] Generally, upon increasing temperature, less processing time is necessary to increase the rate of stress relaxation. To explore this effect more quantitatively, a fixity parameter can be introduced as the ratio of the deformation obtained after thermoforming and the given initially prescribed deformation (for more details, see Long et al. [42]).

Although this model shows remarkable agreement with stress-relaxation experiments, it still lacks the ability to capture some important features observed in vitrimers. For example, the model shows a shortcoming to describe the network's hysteresis accurately and creep compliance behavior. Furthermore, this continuum model does not account for heat conduction and thermal expansions events observed during thermo-mechanical tests. This is particularly crucial if local heat is used to process the material [77].

To account for some of the shortcomings of the model presented by Qi and coworkers, such as the inability to study surface welding on the material, a more robust multiscale modeling framework was developed in 2016 by Yu et al. [81]. In this theoretical model, the dependency of interfacial kinetics of vitrimers was studied under various mechanical and thermal fields. Their approach was firstly to model the kinetics of the bond exchange reaction at the macromolecular scale. This model was used to capture the effect of bond exchange on the evolution of the chain density at the interface.

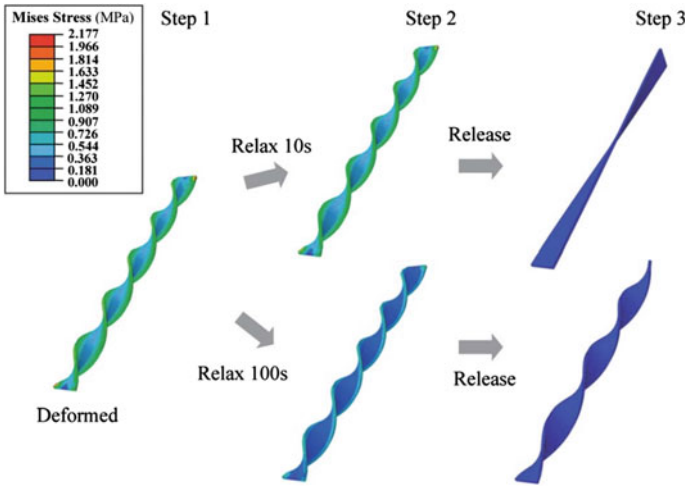

Fig. 13 FEM simulation of the thermoforming process in vitrimer network. The temperature used is 523 K. Two processing times are shown: 10 and 100 s. The figure is obtained from Long, Qi, Dunn; Modeling the mechanics of covalently adaptable polymer networks with temperature-dependent bond exchange reactions; Soft Matter; 2013; Royal Society of Chemistry

In later studies, a cohesive zone approach was incorporated with the model to predict the behavior of epoxy vitrimers undergoing interfacial welding and failure. Using this multiscale model, the chain density and fracture energy of the material can be obtained and later be used as input parameters for the FEM simulations. The proposed multiscale model can also be used to analyze more complex welding problems like polymer reprocessing with irregular shape and particle size [82].

2.2.3 Outlook

Although the mentioned models successfully account for the kinetics of the bonds exchange reactions of vitrimers, they all still rely on elastic models on the continuum level such as neo-Hookean and Arruda–Boyce. Consequently, they cannot provide a direct comparison between the macroscopic mechanics of the network and the single-chain physics of the polymer. As a result, using those models to describe more complex molecular phenomena like entanglement and chain diffusion becomes fundamentally challenging. In addition, both models require a large number of materials parameters and variables to be successfully implemented computationally. To address these limitations, Vernerey et al. [83] introduced a statistically based continuum theory for transient networks polymers. In their framework, the polymer physical state is characterized by a statistical distribution of the length and direction of the end-to-end chains. Both macroscopic deformations and molecular-level events can be used to alter this distribution. Using a so-called distribution tensor, it is possible to relate the chain distribution to stress, strain, and entropy of the network.

This model provides an extension of the classic rubber elasticity theory. It is usable in the range of inelastic deformation, and it can be extended to account for large-chain deformations.

3 Conclusions

Vitrimers provide a practical route for synthesizing intrinsic self-healing materials and reprocessing thermosets. Particle-based simulations techniques mainly utilize patchy particles [50], three-body potential [80], and hybrid MD–MC methods to describe the bond swap between the crosslinkers. The patchy particles model successfully predicts the Arrhenius-like behavior zero shear viscosity of vitrimers that has been observed in experiments. Using the three-body potential for bond swapping, it was shown that the stress relaxation modulus of transient networks exhibits a secondary relaxation due to the change in the network topology [46]. Recently [48], we employed a hybrid MD–MC technique to simulate and predict the dynamics of a model vitrimer and evaluate its thermodynamics and rheological properties. Our simulations showed that the topology freezing temperature, which marks the transition from the rubbery to the viscoelastic fluid regime in vitrimers, can be detected from volumetric and rheological data. The onset of the network rearrangement was related to the lifetime of the exchangeable bonds, which determines the rheology of the network. The current simulation frameworks [48, 49, 56, 80] provide an excellent opportunity to study the linear and nonlinear rheology and mechanics of vitrimers with different topologies. One can adjust the bond exchange rate and control the competition between self-healing ability in the rubber and the damage caused by external stimuli and design the final rubber product with superior mechanical strength, re-processability, and self-healing property.

On a continuum level, different network models have been developed to study transient polymer networks such as vitrimers undergoing small to large deformations. By treating the polymer chains as neo-Hookian chains and starting from the classic theory of rubber elasticity, it is possible to derive constitutive equations that accurately predict the stress relaxation behavior of these networks [71]. Consistent with experimental observations [5], these models show that stress relaxation in vitrimers decays in a stretched exponential manner contrary to the long-time power-law/logarithmic tail observed in permanently crosslinked networks [4]. Additionally, energy balances can be incorporated to account for the coupling between the macroscopic thermo-mechanics and microscopic bond exchange reactions of vitrimers [77]. Continuum models can also be implemented in commercially available FEA software to simulate processes such as thermoforming and polymer welding [77].

Considering the current developments in the field of vitrimers, it is of interest to investigate the rheology and mechanics of vitrimers as a function of network topology, the energy barrier of the bond exchange and chemistry of the network, and identify the underlying mechanism of macroscopic flow behavior, fracture,

and fatigue at different service conditions in these networks, which combines recyclability and self-healing ability with maximum solvent resistance.

References

1. Blaiszik, B.J., Kramer, S.L., Olugebefola, S.C., Moore, J.S., Sottos, N.R., White, S.R.: Self-healing polymers and composites. Annu. Rev. Mater. Res. **40**, 179–211 (2010)
2. Wool, R.P.: Self-healing materials: a review. Soft Matter **4**(3), 400–418 (2008)
3. Ghosh, S.K.: Self-healing materials: fundamentals, design strategies, and applications. Wiley Online Library (2009)
4. Cordier, P., Tournilhac, F., Soulié-Ziakovic, C., Leibler, L.: Self-healing and thermoreversible rubber from supramolecular assembly. Nat. **451**(7181), 977–980 (2008)
5. Montarnal, D., Capelot, M., Tournilhac, F., Leibler, L.: Silica-like malleable materials from permanent organic networks. Sci. **334**(6058), 965–968 (2011)
6. Röttger, M., Domenech, T., van der Weegen, R., Breuillac, A., Nicolaÿ, R., Leibler, L.: High-performance vitrimers from commodity thermoplastics through dioxaborolane metathesis. Sci. **356**(6333), 62–65 (2017). https://doi.org/10.1126/science.aah5281
7. Poliskie, M.: Solar module packaging: polymeric requirements and selection. CRC Press(2016)
8. Rubinstein, M., Colby, R.H.: Polymer physics, vol. 23. Oxford University Press, New York (2003)
9. Tabor, D., Tabor, D.: Gases, liquids and solids: and other states of matter. Cambridge University Press (1991)
10. Ferry, J.D.: Viscoelastic properties of polymers. Wiley (1980)
11. Angell, C.A.: Formation of glasses from liquids and biopolymers. Sci. **267**(5206), 1924–1935 (1995). https://doi.org/10.1126/science.267.5206.1924
12. Biron, M.: Thermoplastics and thermoplastic composites. William Andrew (2018)
13. Van Zee, N.J., Nicolaÿ, R.: Vitrimers: permanently crosslinked polymers with dynamic network topology. Prog. Polym. Sci. 101233 (2020)
14. Dodiuk, H., Goodman, S.H.: Handbook of thermoset plastics. William Andrew (2013)
15. Kutz, M.: Applied plastics engineering handbook: processing, materials, and applications. William Andrew(2016)
16. Ibarra, R.M.: Recycling of thermosets and their composites. In: Thermosets, pp. 639–666. Elsevier (2018)
17. Pickering, S.J.: Recycling technologies for thermoset composite materials—current status. Compos. A **37**(8), 1206–1215 (2006)
18. Geyer, R., Jambeck, J.R., Law, K.L.: Production, use, and fate of all plastics ever made. Sci. Adv. **3**(7), e1700782 (2017)
19. Bowman, C.N., Kloxin, C.J.: Covalent adaptable networks: reversible bond structures incorporated in polymer networks. Angew. Chem. Int. Ed. **51**(18), 4272–4274 (2012)
20. Herbst, F., Döhler, D., Michael, P., Binder, W.H.: Self-healing polymers via supramolecular forces. Macromol. Rapid Commun. **34**(3), 203–220 (2013)
21. Thakur, V.K., Kessler, M.R.: Self-healing polymer nanocomposite materials: a review. Polym. **69**, 369–383 (2015)
22. Higaki, Y., Otsuka, H., Takahara, A.: A thermodynamic polymer crosslinking system based on radically exchangeable covalent bonds. Macromolecules **39**(6), 2121–2125 (2006)
23. Drozdov, A., Christiansen, Jd.: Thermo-mechanical behavior of elastomers with dynamic covalent bonds. Int. J. Eng. Sci. 147, 103200 (2020)
24. Krishnakumar, B., Sanka, R.P., Binder, W.H., Parthasarthy, V., Rana, S., Karak, N.: Vitrimers: associative dynamic covalent adaptive networks in thermoset polymers. Chem. Eng. J. **385**, 123820 (2020)

25. Denissen, W., Winne, J.M., Du Prez, F.E.: Vitrimers: permanent organic networks with glass-like fluidity. Chem. Sci. **7**(1), 30–38 (2016)
26. Capelot, M., Montarnal, D., Tournilhac, F., Leibler, L.: Metal-catalyzed transesterification for healing and assembling of thermosets. J. Am. Chem. Soc. **134**(18), 7664–7667 (2012). https://doi.org/10.1021/ja302894k
27. Denissen, W., Rivero, G., Nicolaÿ, R., Leibler, L., Winne, J.M., Du Prez, F.E.: Vinylogous urethane vitrimers. Adv. Funct. Mater. **25**(16), 2451–2457 (2015)
28. Winne, J.M., Leibler, L., Du Prez, F.E.: Dynamic covalent chemistry in polymer networks: a mechanistic perspective. Polym. Chem. **10**(45), 6091–6108 (2019)
29. Scott, T.F., Schneider, A.D., Cook, W.D., Bowman, C.N.: Photoinduced plasticity in crosslinked polymers. Sci. **308**(5728), 1615–1617 (2005)
30. Amamoto, Y., Kamada, J., Otsuka, H., Takahara, A., Matyjaszewski, K.: Repeatable photoinduced self-healing of covalently crosslinked polymers through reshuffling of trithiocarbonate units. Angew. Chem. Int. Ed. **50**(7), 1660–1663 (2011)
31. Dahlke, J., Zechel, S., Hager, M.D., Schubert, U.S.: How to design a self-healing polymer: general concepts of dynamic covalent bonds and their application for intrinsic healable materials. Adv. Mater. Interfaces **5**(17), 1800051 (2018)
32. Montarnal, D., Tournilhac, F., Hidalgo, M., Leibler, L.: Epoxy-based networks combining chemical and supramolecular hydrogen-bonding crosslinks. J. Polym. Sci. Part A Polym. Chem. **48**(5), 1133–1141 (2010)
33. Brutman, J.P., Delgado, P.A., Hillmyer, M.A.: Polylactide vitrimers. ACS Macro Lett. **3**(7), 607–610 (2014)
34. Fortman, D.J., Brutman, J.P., Cramer, C.J., Hillmyer, M.A., Dichtel, W.R.: Mechanically activated, catalyst-free polyhydroxyurethane vitrimers. J. Am. Chem. Soc. **137**(44), 14019–14022 (2015). https://doi.org/10.1021/jacs.5b08084
35. Yang, Y., Pei, Z., Li, Z., Wei, Y., Ji, Y.: Making and remaking dynamic 3D structures by shining light on flat liquid crystalline vitrimer films without a mold. J. Am. Chem. Soc. **138**(7), 2118–2121 (2016). https://doi.org/10.1021/jacs.5b12531
36. Pei, Z., Yang, Y., Chen, Q., Wei, Y., Ji, Y.: Regional Shape Control of Strategically Assembled Multishape Memory Vitrimers. Adv. Mater. **28**(1), 156–160 (2016). https://doi.org/10.1002/adma.201503789
37. Zheng, N., Fang, Z., Zou, W., Zhao, Q., Xie, T.: Thermoset shape-memory polyurethane with intrinsic plasticity enabled by transcarbamoylation. Angew. Chem. Int. Ed. **55**(38), 11421–11425 (2016)
38. Capelot, M., Unterlass, M.M., Tournilhac, F., Leibler, L.: Catalytic control of the vitrimer glass transition. ACS Macro Lett. **1**(7), 789–792 (2012)
39. Ricarte, R.G., Tournilhac, F., Cloître, M., Leibler, L.: Linear viscoelasticity and flow of self-assembled vitrimers: the case of a polyethylene/dioxaborolane system. Macromolecules **53**(5), 1852–1866 (2020)
40. Smallenburg, F., Leibler, L., Sciortino, F.: Patchy particle model for vitrimers. Phys. Rev. Lett. **111**(18), 188002 (2013)
41. Dyre, J.C.: Colloquium: the glass transition and elastic models of glass-forming liquids. Rev. Mod. Phys. **78**(3), 953–972 (2006). https://doi.org/10.1103/RevModPhys.78.953
42. Long, R., Qi, H.J., Dunn, M.L.: Modeling the mechanics of covalently adaptable polymer networks with temperature-dependent bond exchange reactions. Soft Matter **9**(15), 4083–4096 (2013)
43. Ciarella, S., Ellenbroek, W.G.: Swap-driven self-adhesion and healing of vitrimers. Coat. **9**(2), 114 (2019)
44. Ciarella, S., Biezemans, R.A., Janssen, L.M.: Understanding, predicting, and tuning the fragility of vitrimeric polymers. Proc. Natl. Acad. Sci. **116**(50), 25013–25022 (2019)
45. Wertheim, M.: Thermodynamic perturbation theory of polymerization. J. Chem. Phys. **87**(12), 7323–7331 (1987)
46. Rovigatti, L., Nava, G., Bellini, T., Sciortino, F.: Self-dynamics and collective swap-driven dynamics in a particle model for vitrimers. Macromolecules **51**(3), 1232–1241 (2018)

47. Singh, K., Rabin, Y.: Aging of thermoreversible gel of associating polymers. Macromolecules **53**(10), 3883–3890 (2020). https://doi.org/10.1021/acs.macromol.0c00258
48. Perego, A., Khabaz, F.: Volumetric and rheological properties of vitrimers: a hybrid molecular dynamics and Monte Carlo simulation study. Macromolecules **53**(19), 8406–8416 (2020). https://doi.org/10.1021/acs.macromol.0c01423
49. Perego, A., Khabaz, F.: Effect of bond exchange rate on dynamics and mechanics of vitrimers. J. Polym. Sci. **59**(21), 2590–2602 (2021)
50. Smallenburg, F., Leibler, L., Sciortino, F.: Patchy particle model for vitrimers. Phys. Rev. Lett. **111**, 1–5 (2013). https://doi.org/10.1103/PhysRevLett.111.188002
51. Wertheim, M.: Fluids with highly directional attractive forces. I. Statistical thermodynamics. J. Stat. Phys. **35**(1), 19–34 (1984)
52. Kern, N., Frenkel, D.: Fluid–fluid coexistence in colloidal systems with short-ranged strongly directional attraction. J. Chem. Phys. **118**(21), 9882–9889 (2003)
53. Kremer, K., Grest, G.S.: Dynamics of entangled linear polymer melts: A molecular-dynamics simulation. J. Chem. Phys. **92**(8), 5057–5086 (1990)
54. Weeks, J.D., Chandler, D., Andersen, H.C.: Role of repulsive forces in determining the equilibrium structure of simple liquids. J. Chem. Phys. **54**(12), 5237–5247 (1971)
55. Stillinger, F.H., Weber, T.A.: Computer simulation of local order in condensed phases of silicon. Phys. Rev. B **31**(8), 5262 (1985)
56. Ciarella, S., Sciortino, F., Ellenbroek, W.G.: Dynamics of vitrimers: defects as a highway to stress relaxation. Phys. Rev. Lett. **121**(5) (2018). https://doi.org/10.1103/physrevlett.121.058003
57. Kubo, R.: Statistical-mechanical theory of irreversible processes. I. General theory and simple applications to magnetic and conduction problems. J. Phys. Soc. Jpn. **12**(6), 570–586 (1957)
58. Pant, P.K., Theodorou, D.N.: Variable connectivity method for the atomistic Monte Carlo simulation of polydisperse polymer melts. Macromolecules **28**(21), 7224–7234 (1995)
59. Karayiannis, N.C., Mavrantzas, V.G., Theodorou, D.N.: A novel Monte Carlo scheme for the rapid equilibration of atomistic model polymer systems of precisely defined molecular architecture. Phys. Rev. Lett. **88**(10), 105503 (2002)
60. Sides, S.W., Grest, G.S., Stevens, M.J., Plimpton, S.J.: Effect of end-tethered polymers on surface adhesion of glassy polymers. J. Polym. Sci. Part B Polym. Phys. **42**(2), 199–208 (2004)
61. Hoy, R.S., Fredrickson, G.H.: Thermoreversible associating polymer networks. I. Interplay of thermodynamics, chemical kinetics, and polymer physics. J. Chem. Phys. **131**(22), 224902 (2009)
62. Stukalin, E.B., Cai, L.-H., Kumar, N.A., Leibler, L., Rubinstein, M.: Self-healing of unentangled polymer networks with reversible bonds. Macromolecules **46**(18), 7525–7541 (2013)
63. Frenkel, D., Smit, B.: Understanding molecular simulation: from algorithms to applications, vol. 1. Elsevier (2001)
64. Wilson, M., Rabinovitch, A., Baljon, A.R.C.: Computational study of the structure and rheological properties of self-associating polymer networks. Macromolecules **48**(17), 6313–6320 (2015). https://doi.org/10.1021/acs.macromol.5b00885
65. Simmons, D.S., Douglas, J.F.: Nature and interrelations of fast dynamic properties in a coarse-grained glass-forming polymer melt. Soft Matter **7**(22), 11010–11020 (2011)
66. Ma, C., Ji, T., Robertson, C.G., Rajeshbabu, R., Zhu, J., Dong, Y.: Effect of filler–polymer interface on elastic properties of polymer nanocomposites: a molecular dynamics study. Tire Sci. Technol. **45**(3), 227–241 (2017)
67. Khare, R., Paulaitis, M.E., Lustig, S.R.: Generation of glass structures for molecular simulations of polymers containing large monomer units: Application to polystyrene. Macromolecules **26**(26), 7203–7209 (1993)
68. Khabaz, F., Mani, S., Khare, R.: Molecular origins of dynamic coupling between water and hydrated polyacrylate gels. Macromolecules **49**(19), 7551–7562 (2016)
69. Todd, B.D., Daivis, P.J.: Nonequilibrium molecular dynamics: theory, algorithms and applications. Cambridge University Press (2017)

70. Edwards, B., Baig, C., Keffer, D.: A validation of the p-SLLOD equations of motion for homogeneous steady-state flows. J. Chem. Phys. **124**(19), 194104 (2006)
71. Meng, F., Pritchard, R.H., Terentjev, E.M.: Stress relaxation, dynamics, and plasticity of transient polymer networks. Macromolecules **49**(7), 2843–2852 (2016)
72. Meng, F., Saed, M.O., Terentjev, E.M.: Elasticity and relaxation in full and partial vitrimer networks. Macromolecules **52**, 7423–7429 (2019)
73. Treloar, L.R.G.: The physics of rubber elasticity (1975).
74. Kramers, H.A.: Brownian motion in a field of force and the diffusion model of chemical reactions. Phys. **7**(4), 284–304 (1940)
75. Doi, M.: Soft matter physics. Oxford University Press (2013)
76. Yu, K., Taynton, P., Zhang, W., Dunn, M.L., Qi, H.J.: Influence of stoichiometry on the glass transition and bond exchange reactions in epoxy thermoset polymers. RSC Adv. **4**(89), 48682–48690 (2014)
77. Green, M.S., Tobolsky, A.V.: A new approach to the theory of relaxing polymeric media. J. Chem. Phys. **14**(2), 80–92 (1946)
78. Smith, M.: ABAQUS/Standard User's Manual. Version **6**, 9 (2009)
79. Tobolsky, A.V.: Stress relaxation studies of the viscoelastic properties of polymers. J. Appl. Phys. **27**(7), 673–685 (1956). https://doi.org/10.1063/1.1722465
80. Sciortino, F.: Three-body potential for simulating bond swaps in molecular dynamics. Eur. Phys. J. E **40**, 3–6 (2017). https://doi.org/10.1140/epje/i2017-11496-5
81. Yu, K., Shi, Q., Li, H., Jabour, J., Yang, H., Dunn, M.L., Wang, T., Qi, H.J.: Interfacial welding of dynamic covalent network polymers. J. Mech. Phys. Solids **94**, 1–17 (2016). https://doi.org/10.1016/j.jmps.2016.03.009
82. Yu, K., Shi, Q., Wang, T., Dunn, M.L., Jerry Qi, H.: A computational model for surface welding in covalent adaptable networks using finite-element analysis. J. Appl. Mech. **83**(9), 091002 (2016). https://doi.org/10.1115/1.4033682
83. Vernerey, F.J., Long, R., Brighenti, R.: A statistically-based continuum theory for polymers with transient networks. J. Mech. Phys. Solids **107**, 1–20 (2017)

Modeling of Crack Self-Healing in Thermally Remendable Fiber-Reinforced Composites

Peyman Shabani and Mahmood M. Shokrieh

Abstract For incorporating thermally reversible covalent bonds into polymers, Diels–Alder (DA) cycloaddition reaction has been widely used. The thermally reversible DA reaction is a [4 + 2] cycloaddition between an electron-poor dienophile and an electron-rich diene. Furan and maleimide are the most popular pair that has been used as diene and dienophile. These healing agents can be embedded into fiber-reinforced composites. Matrix cracking is a type of damage that usually initiates during the manufacturing process or in the early service life. By giving composites the self-healing capability, these cracks can be healed before resulting in a catastrophic type of damage. In the current research, 4,4'-bismaleimidodiphenylmethane (BMI) and furfuryl glycidyl ether (FGE) were utilized along with an epoxy-based polymer as the resin system in the fabrication of glass fiber-reinforced composites. The synthesized polymer and its composites were thermally and mechanically characterized. After analyzing the kinetics of the DA reaction in the synthesized polymer, a model was proposed based on a shear-lag analysis and the classical lamination theory to predict the recovered stiffness of laminated composites as a function of healing temperature and time. Finally, the model was validated by conducting experiments on cross-ply laminates with a $[90_3/0/90_3]$ stacking sequence.

Keywords Self-healing composites · Diels–Alder reaction · Matrix cracking · Self-healing kinetics · Conversion degree

1 Introduction

In the last decades, polymeric composites have been one of the dominant emerging materials. Their number and volume of applications have grown steadily, and they are conquering new markets every year. However, despite their wide usage, polymeric composites are susceptible to micro-cracks initiation during fabrication and in the

P. Shabani · M. M. Shokrieh (✉)
Composite Research Laboratory, Center of Excellence in Experimental Solid Mechanics and Dynamics, School of Mechanical Engineering, Iran University of Science and Technology, 16846-13114 Tehran, Iran
e-mail: Shokrieh@iust.ac.ir

N. Hameed et al. (eds.), *Multifunctional Epoxy Resins*, Engineering Materials,
https://doi.org/10.1007/978-981-19-6038-3_9

early service life due to thermal and mechanical mismatches of their constituents. The growth and coalescence of these micro-cracks can result in a catastrophic failure. In pursuance of finding a way to heal these premature matrix cracks, many research works have been done. Employing self-healing agents in polymers was one of the techniques that have been considered by many researchers [1–13]. The self-healing mechanisms are categorized under intrinsic and extrinsic mechanisms. In the extrinsic mechanism, the recovery happens via deploying healing agents in the polymer matrix. This embedding can be in the form of microcapsules [14–18], hollow-fibers [19, 20], or microvascular networks [21–24]. In the intrinsic self-healing mechanisms [25–31], the macromolecules of the polymer act as self-healing agents, and the polymer can be healed itself.

To give intrinsic self-healing properties to polymers, non-covalent bonds [32–34] or thermally reversible covalent bonds based on acylhydrazones [35], disulfides [36–38], or the DA cycloaddition [39–41] can be incorporated into the polymer. It has been reported that using reversible covalent bonds would increase the strength of the material compared with using noncovalent bonds [42], which is important in several industrial applications.

In this chapter, after reviewing the Diels–Alder (DA) self-healing mechanism, a new self-healing polymer is introduced. The kinetics of the cross-link formation during the self-healing process is analyzed quantitatively to find the influence of the cross-links' conversion degree on the mechanical properties. The glass-fiber-reinforced composites made by utilizing this self-healing polymer are mechanically characterized, and their healing efficiency has been obtained. Afterward, for estimating the residual flexural stiffness of damaged laminates, a model is proposed combining classical lamination theory and a shear-lag model. Finally, the model is extended to predict the recovered flexural stiffness of the healed laminate considering the temperature and time at which the healing process has been carried out.

2 Diels–Alder Reaction

The self-healing mechanism in intrinsic DA-based self-healing polymers operates based on a thermally reversible reaction that happens between a diene and a dienophile to form a cyclohexene ring as shown in Fig. 1. Unlike conventional thermoset polymers, DA-based self-healing polymers can separate into their original groups under certain thermal conditions through a reaction called retro-DA reaction.

2.1 Furan and Maleimide Self-Healing Systems

Furan (F) and maleimide (M) have been employed as diene and dienophile in many DA-based self-healing systems [42–44]. 3M4F was one of the self-healing systems was proposed by Chen et al. [41]. The high melting point of maleimide was one of the

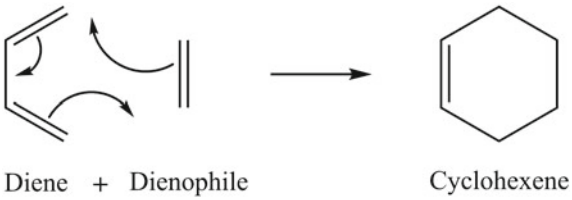

Fig. 1 Schematic of a cycloaddition reaction

drawbacks of this self-healing system which makes it challenging to dissolve it in the furan compound. Chen et al. [40] solved the problem by using 1,8-bis(maleimido)-1-ethylpropane (2MEP) and 1,8-bis(maleimido)-3,6-dioxaoctane (2ME) which have lower melting points to produce 2MEP4F and 2ME4F polymers. A lower melting point was observed for 2ME4F (160 °C) compared to 2MEP4F (180 °C). However, 2ME4F showed slightly higher mechanical properties compared to 2MEP4F. Overall, 2MEP4F was suggested as the optimized combination.

Tian et al. [45] introduced a thermally reversible polymer using bismaleimide, hexahydro-4-methylphthalicanhydride (MHHPA), and N,N-diglycidyl-furfurylamine (DGFA). The mechanical properties of the resulting polymer were similar to traditional epoxy resins. A healing efficiency of 66% was obtained for this polymer. In a subsequent study, the blend of furfuryl glycidyl ether (FGE) and DGFA was utilized to achieve a higher healing efficiency [46]. By adding more FGE, a 15% enhancement in healing efficiency was achieved due to a higher amount of DA bonds. However, this enhancement was at the expense of lower tensile strength. The retro-DA reaction for this polymer was completed after 20 min at 140 °C. For the DA reaction, the specimens were heated at 80 °C for 72 h.

The time required for DA and retro-DA reactions to proceed was studied in more detail by Zhang et al. [47]. Fourier transform infrared spectroscopy (FTIR) test results were employed to monitor the progress of DA and retro-DA reactions. It was observed that the DA reaction proceed by keeping the specimen at 50 °C for 2 h. However, the retro-DA reaction was completed by keeping the specimen for only 5 min at 150 °C. To find if the polymer is able to restore its mechanical properties after multiple healing, the specimens were damaged and healed seven times. It was reported that the specimens were able to regain their strength completely even after seven damaging and healing cycles. Yoshie et al. [48] prepared a thermally reversible polymer based on furfuryl-telechelic poly(ethylene adipate) ($PEAF_2$) and tris-maleimide (M_3). By heating the material for 15 h at 60 °C, the crosslinks were formed and the retro-DA happened at 145 °C within 120 min. The self-healing property of $PEAF_2M_3$ was assessed by joining two pieces of a specimen after the cut. It was observed that 68% of the tensile strength was recovered. Postiglione et al. [49] used bismaleimide and difunctional and trifunctional furanized monomers to synthesize a self-healing polymer. With dynamic mechanical analysis (DMA), differential scanning calorimetry (DSC), and FTIR tests the reversibility of the polymer was examined. The DA and retro-DA reactions occurred at 50 °C and 120 °C, respectively. To reduce the brittleness of the polymer, 10% benzyl alcohol was added to

the polymer as a plasticizer. It was observed that this polymer can heal scratches up to 95%. However, only 48% of the tensile strength was recovered. Another self-healing system was designed by Liu et al. [50] based on trifunctional furan (TF) and trifunctional maleimide (TMI). The specimens were first split into two pieces by a knife. Then, the broken parts were heated up to 120 °C for 20 min and, subsequently, at 50 °C for 24 h for activating retro-DA and DA reactions, respectively. The reversibility was investigated by FTIR and DSC tests, and the self-healing process was assessed by scanning electron microscopy (SEM). A full recovery of properties was reported for this polymer. The same authors also introduced another self-healing polymer based on maleimide- and furan-containing polyamides (PA-MI and PA-F) [51]. The resulting polymer showed higher glass transition temperature, superior mechanical properties, and higher toughness. However, the healing efficiency of this polymer was not as good as TMI/TF polymer and it was observed that after 3 h heating of specimens at 120 °C and keeping them at 50 °C for 5 days, the specimens were able to partially heal the damaged surface.

Plaisted et al. [52] employed double cleavage drilled compression (DCDC) test method to investigate the self-healing behavior of 2MEP4F polymer. A full recovery was reported for these specimens. Subsequently, by considering an autocatalytic conversion model the rate of the DA reaction was estimated at different temperatures for 2MEP4F [53]. A similar self-healing polymer containing 4FS (4F with an ester group) and diphenyl bismaleimide (DPBM) was synthesized by Weizman et al. [54]. Using the DSC results, the DA and retro-DA temperatures were obtained equal to 79 °C and 110 °C.

A self-healing functional copolymer was synthesized by Wouters et al. [55] using butyl methacrylate (BMA) and furfuryl methacrylate (FMA) along with various bismaleimide components. After blending furan with bismaleimides, it was mixed with commercial amines, e.g., Jeffamine D-230, D-400, and Euredur 76. The self-healing property of this material was tested by making polymer films out of this material and it was stated that this material can be used in self-healing coating. A similar polymer, containing 1,1'-(methylenedi-4,1-phenylene)bismaleimide (DPBM) and FGE-functionalized Jeffamine D-400 was designed by Scheltjens et al. [56]. It was observed that scratches on the coated specimens were healed completely after heating the specimen at 130 °C for 2 min. In another article by the same authors, it was observed that by replacing aliphatic amines with aromatic amines, the self-healing temperature increased. Later, many researchers tried to fine-tune the properties of the coating by using different amines [57–60].

There are a limited number of studies in which it has been tried to deploy intrinsic self-healing systems in fiber-reinforced composites [31, 61–65] to add self-healing properties to them. Park et al. [61, 62] used 2MEP4F as the matrix in composite specimens. By conducting three-point bending tests, the healing efficiency of this remendable composite was investigated. To examine the effect of heating time on the healing efficiency, samples were kept at 110 °C for one to three hours, and it was concluded that by increasing the heating time, and it was concluded that higher healing efficiencies can be achieved by increasing the heating time. However, no attempt was made to quantitatively correlate the cracks' density reduction to

recovered mechanical properties. To make a correlation between the recovered flexural modulus and the temperature corresponding to the DA reaction, a model was proposed by Nielsen et al. [53, 66]. They used 2MEP4FS polymer in the fabrication of cross-ply composite samples with $[90/0]_s$ layup configuration for the dynamic mechanical analysis (DMA). However, the role of time in the healing process was ignored in this model.

Overall, it can be stated that the furan/maleimide system is a prime example of DA covalent bonds that has been employed by many research groups, and the applicability of using this polymer in fiber-reinforced composites has been partially investigated. However, there is a lack of quantitative study on DA cross-links formation during the self-healing process. In the following sections, the kinetics of the self-healing procedure will be analyzed quantitatively and the healing conversion degree will be obtained as a function of time and temperature. Afterward, this polymer will be used in the fabrication of glass-fiber-reinforced composite specimens and the healing efficiency at different conversion degrees will be obtained. Finally, a model will be put forward to predict the modulus degradation in cracked cross-ply laminate and subsequently the recovered modulus in the healed laminate.

3 Material Preparation and Characterization

3.1 Self-Healing Polymer Synthesis

The healing agents that were employed in the current research were 4,4'-bismaleimidodiphenylmethane (BMI), furfuryl glycidyl ether (FGE), and hexahydro-4-methylphthalicanhydride (MHHPA). First, FGE, MHHPA, and BMI were blended with an FGE/MHHPA/BMI molar ratio of 1:0.85:0.5 and mixed for 10 min at 75 °C. The mixing temperature was chosen considering the DSC results of the healing agents (FGE and BMI). Based on DSC results, the DA reaction proceeds at the maximum rate when heating at 75 °C. Therefore, to let the DA cycloaddition proceeds as much as possible before the solidification of the polymer, the healing temperature was set to 75 °C. The cured polymer consists of thermally reversible bonds as a result of the DA reaction between maleimide and furan moieties (Fig. 2) and irreversible bonds caused by the reaction between the epoxide group of FGE and MHHPA. As illustrated in Fig. 3, MHHPA accompanied by the epoxide group of FGE would create the chains of the polymer. Also, for the establishment of cross-links, two FGE monomers are required for each BMI. Thus, the molar ratio of 1:0.5 was chosen for FGE/BMI. The reason for selecting a non-stoichiometric ratio for FGE/MHHPA was to prolong the curing process and let the DA cycloaddition proceeds as far as possible.

Increasing the molar ratio of FGE can result in a higher DA bonds density in the synthesized polymer that can lead to a higher self-healing efficiency. However, using more FGE would deteriorate the mechanical performance of the polymer considering that each FGE molecule has only one epoxide moieties that can contribute to the

Fig. 2 DA and retro-DA reactions between maleimide (M) and furan (F). Reprinted with permission from [31]

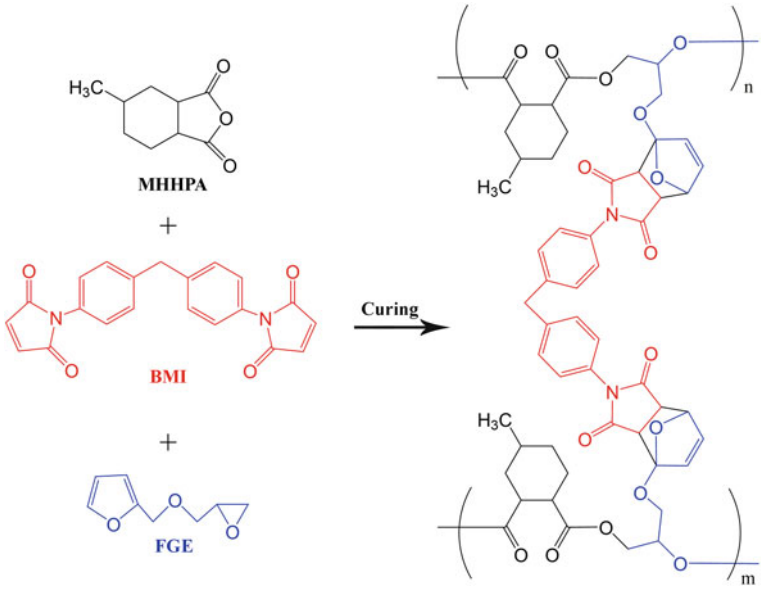

Fig. 3 (Left) Monomers utilized in the self-healing polymer; (Right) The cured polymer. Reprinted with permission from [31]

creation of epoxy bonds in the cured polymer. To balance the properties of the self-healing polymer, the synthesized polymer was mixed with a commercial hot-curing resin. Mixing self-healing agents with commercial epoxy resins might decrease the healing efficiency, but it will enhance the mechanical performance. Considering the complementary properties of the synthesized polymer and the epoxy resin, a hot-curing epoxy resin (Araldite LY-556/HY-917) with a similar curing temperature as the synthesized polymer was added to the mixture (mass ratio of 1:1) to reach a balanced performance. Then, the mixture was cured for 4 h at 75 °C and post-cured for 8 h at 115 °C. The post-curing temperature was selected according to the epoxy resin's datasheet. Due to the proximity of the post-curing and retro-DA temperatures, the specimens were kept for another 4 h at 75 °C to ensure that the DA bonds are re-established.

3.2 Thermal Characterization

3.2.1 Differential Scanning Calorimetry

The behavior of the materials through a heating process can be studied via differential scanning calorimetry (DSC). Considering the exothermic and endothermic nature of the DA and retro-DA reactions, the DSC results of the self-healing agents can be used to analyze the behavior of the self-healing polymer and find the span of temperatures in which DA and retro-DA reactions take place. The DSC tests were conducted on the mixture of FGE and BMI that are taking part in the DA reaction using the Mettler Toledo DSC 1 instrument. DSC tests were performed at two different heating rates for subsequent analysis of the DA reaction and for developing a quantitative kinetic model.

For selecting suitable heating rates to perform DSC tests, it should be bear in mind that at higher heating rates the sample cannot completely absorb the heat because of the thermal lag effect. Hence, the then temperature shown on the monitor will be higher than the sample's temperature. On the other hand, by using a lower heating rate, the effect of thermal lag decreases [67]. However, the heat flux signals will also become weaker which can cause a reduction in sensitivity. In the ASTM E2890 standard [68], it has been suggested that the heating rate should be selected in a way that the maximum heat flow remains lower than 8 mW. Based on these discussions, heating rates of 5 °C/min and 3 °C/min were selected. The DA reaction can be identified in Fig. 4a by the exothermic peak that was captured between 30 and 95 °C with the maximum peak at 74 °C. The maximum peak indicates the temperature at which the DA cycloaddition proceeds at the maximum speed. The broad exothermic peak was followed by an endothermic peak which denotes the material melting. Considering the DSC results, 23.65 kJ/mol was exposed during the DA reaction, which was much lower than the value that can be obtained from bond energies, i.e., 156 kJ/mol per DA reaction product. Poor mixing of FGE and BMI and the consumed energy for melting the BMI powder were the causes of this discrepancy. Furthermore, because of the dynamic scanning of samples, some potential DA reactants may not be given enough time to participate in the DA cycloaddition.

In Fig. 4b, the DSC test result of the cured polymer is shown. The first glass transition observed at 53 °C was attributed to the epoxide moieties movement [40], and the other glass transition, which was followed by an endothermic peak owing to the retro-DA reaction, occurred at 95 °C. In the healing process, the temperature of 120 °C was selected as the retro-DA temperature.

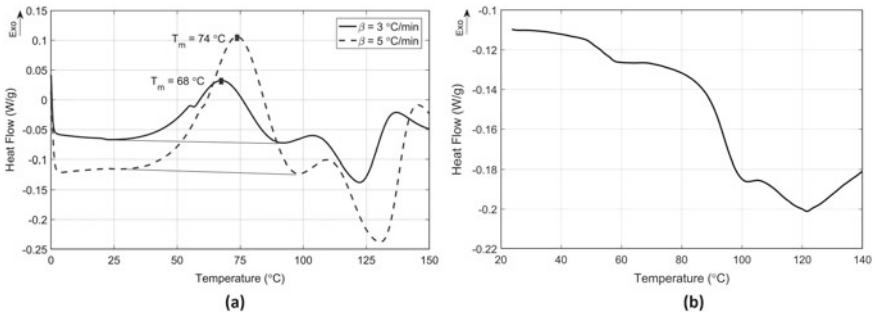

Fig. 4 **a** DSC results of FGE and BMI mixture, **b** DSC results of the cured polymer (test was performed at 5 °C/min heating rate)

3.3 Mechanical Characterization

3.3.1 Neat Self-Healing Polymer

Since the Diels–Alder based self-healing polymers are brittle compared with commercial epoxy resins, in almost all of the publications on the healing efficiency of DA-based polymers either double cleavage drilled compression (DCDC) [45, 46] or bending tests (three-point bending [47, 63, 65, 69] or four-point bending [61, 62]) have been employed. In the current study, by mixing a hot-curing epoxy resin with the healing agents the brittleness of the polymer was controlled. However, still it was more brittle than commercial epoxy resins. Therefore, the bending test method was selected to examine the healing efficiency. Between three-point and four-point bending tests, the three-point bending was chosen to ensure that all samples would break into two pieces and to eliminate the influence of shape and number of fractures on the healing efficiency. Following recommendations of ASTM D790 standard [70], nine specimens were fabricated with the dimensions that are summarized in Table 1. All three-point bending tests were perfomed by using the Santam STM-150 testing machine. The fixtures are shown in Fig. 5a and b, and some of the failed specimens are shown in Fig. 5c. The results of the initial characterization tests are summarized in Table 2. The data acquisition was done according to procedure-A of ASTM D790 [70] that applies to specimens with small deflections.

Five compression specimens were fabricated considering the ASTM D695 standard [71] to find the compressive modulus and strength of the neat polymer. The fixture is shown in Fig. 5b. No barreling or side-slip buckling was observed during the test, and the results showed a small scatter. In Table 2, the results are reported.

The analytical method introduced by Mujika et al. [72] was employed to find the tensile modulus of linear-elastic transversely-isotropic materials by having its compressive and flexural moduli. In this method, by using classical beam theory, the relation shown in Eq. (1) was established between the tensile, compressive, and flexural moduli. Since the synthesized polymer meets the mentioned assumptions,

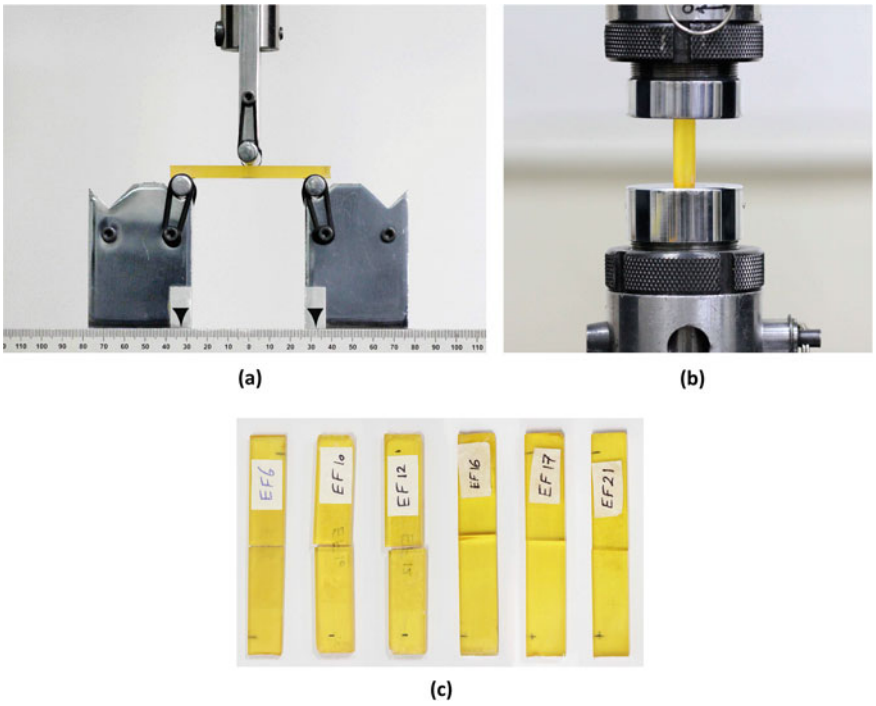

Fig. 5 **a** The three-point bending fixture, **b** The compression fixture test, **c** Failed specimens after the three-point bending test

this method can be applied to this material:

$$E_F = \frac{4}{\left(1 + \sqrt{\frac{E_T}{E_C}}\right)^2} E_T \tag{1}$$

where E_F, E_C, and E_T are flexural, compressive, and tensile moduli, respectively. The tensile modulus of the polymer was obtained equal to 4.04 GPa, using Eq. (1).

3.3.2 Self-Healing Fiber-Reinforced Composites

Using the synthesized self-healing polymer, three-point bending fiber-reinforced composite standard specimens [70] were fabricated. A unidirectional E-glass (Interglas 92145) fiber with an areal density of 220 g/m^2 was utilized for manufacturing fiber-reinforced composite specimens. The hand-layup method was used for the fabrication of specimens as shown in Fig. 6. The curing procedure of the laminates was the same as neat polymer specimens. All specimens were made with $[90_3/0/90_3]$ stacking sequence. The high number of 90° to 0° plies maximized the influence

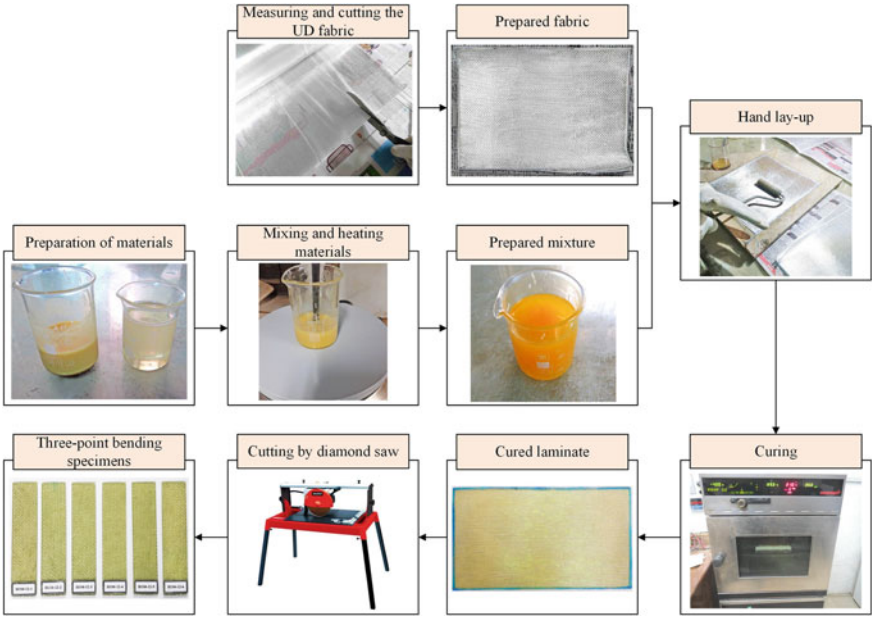

Fig. 6 Process of making three-point bending composite specimens. Reprinted with permission from [65]

Table 1 Three-point bending and compression test specimens' dimensions

Three-point bending test specimens	
Thickness (mm)	5
Length (mm)	80
Width (mm)	13
Support span (mm)	65
Compression test specimens	
Diameter (mm)	11.2
Length (mm)	33

Table 2 The mechanical properties of the synthesized self-healing polymer

	Flexural modulus E_F (GPa)	Compressive modulus E_C (GPa)	Flexural strength X_F (MPa)	Compressive strength X_C (MPa)
Value	3.48	3.03	27.75	89.10
Standard deviation	0.18	0.07	6.75	8.27

Table 3 The three-point bending composite specimens' dimensions

Thickness (mm)	Width (mm)	Length (mm)	Support span (mm)
1.7	19.8	87.5	64

Table 4 Mechanical properties of the self-healing composite and its constituents. f and m subscripts represent fiber and matrix

Property	E_f (GPa)	E_m (GPa)	V_f	ρ_f (g/m^2)	ρ_m (g/cm^3)	Ply thickness† (mm)
Value	69‡	4.04	0.56	220	1.18	0.243
Property	E_1 (GPa)	E_2 (GPa)	G_{12} (GPa)	G_{23} (GPa)	ν_{12}	ν_{23}
Value	40.42*	8.54*	4.28‡	2.63*	0.27*	0.62*

* Calculated with micromechanical relations [73]
‡ Taken from the reference [74] in which the same fiber has been used
† The thickness of a single ply

of transverse matrix cracks on the flexural behavior. In this way, it was easier to distinguish the effect of crack density on the flexural modulus and, subsequently, the effect of the self-healing process on the recovered flexural modulus. All tests were performed according to ASTM D790 standard recommendations [70] using the Santam STM-150 testing machine. The dimensions of the specimens are shown in Table 3.

For finding the mechanical properties of the unidirectional composites of the E-glass and the synthesized polymer, the micromechanical relations were used [73]. The required properties for the current analysis are reported in Table 4.

4 Self-Healing Kinetic Analysis

Due to the dependency of the mechanical properties of thermoset polymers on their cross-linking density, for predicting the recovered mechanical properties after the healing process, it is critical to know the number of reconnected cross-links at the given healing time and temperature. Despite its key role, little quantitative analysis has been done to correlate the cross-links' conversion degree to the self-healing conditions. In this section, the kinetics of DA reaction is investigated quantitatively and a model is developed to calculate the degree of conversion of reversible cross-links by having the healing time and temperature.

To correlate the cross-links' conversion degree to time and temperature, first, a conversion model should be selected. Many models have been introduced so far, and some of them have become standards, e.g., Daniel [75], Ozawa [76], and Kissinger [68] models. With these methods, we can predict the progression of a reaction by having DSC test results. Each method has reaction order and temperature limitations and can only be applied to certain DSC curve shapes. These limitations are mentioned

in Table 5 for three standardized methods. For the synthesized self-healing polymer, regarding the DSC results and the Diels–Alder cycloaddition order of reaction, the Kissinger method was selected for analyzing the kinetic of the current polymer.

The cross-linking level describes by the degree of conversion (α). $\alpha = 1$ represents the completely cured polymer in which the level of cross-links is maximum. According to ASTM E2041 standard [75], α can be stated as Eq. (2):

$$\alpha = \frac{H_T - H_R}{H_T} \tag{2}$$

where H_T and H_R are the amounts of total and residual exposed energies during the polymerization process as illustrated in Fig. 7.

Table 5 Limitations of reaction progression methods

Method	Standard code	Limitations		
		Temperature span (°C)	Reaction order	Notes
Flynn–Wall–Ozawa	ASTM E698 [76]	–	–	– Not applicable to reactions including a phase change
Daniel	ASTM E2041 [75]	−100 to 600	≤ 2	– No shift in the baseline – Only applicable to smooth exothermic curves – Not applicable to an accelerated reaction
Kissinger	ASTM E2890 [68]	27 to 627	0.5 to 4	

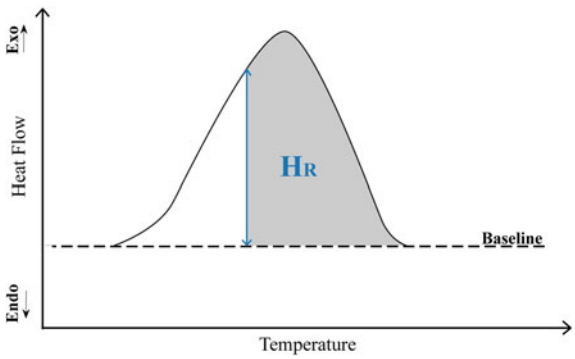

Fig. 7 Schematic of the DSC result of an exothermic reaction. Reprinted with permission from [31]

The rate of conversion degree can be stated as Eq. (3):

$$\frac{d\alpha}{dt} = K(T)F(\alpha) \tag{3}$$

where $F(\alpha)$ is the conversion function and $K(T)$ represents the constant of the conversion rate which is a function of temperature. The conversion function is connected to the shape of the conversion rate $(d\alpha/dt)$ versus conversion degree (α). Many functions have been suggested for the conversion function. Each of them can be used in a certain kinetic condition. The most popular conversion functions are summarized in Table 6. An autocatalytic or an *n*th order conversion function can describe most of the reactions. In an *n*th order reaction, the conversion degree rate decreases following a power law equation (Eq. (4)) as the reactants are consumed. However, in an autocatalytic reaction, the product of the reaction catalyzes the reaction resulting in an initial increase in the reaction rate following a decline as a result of the consumption of the reactants. The autocatalytic conversion function has the form of Eq. (5).

$$F(\alpha) = (1-\alpha)^n \tag{4}$$

$$F(\alpha) = (1-\alpha)^n \alpha^m \tag{5}$$

In Eq. (5), n and m are the order of reactions. Although at low conversion degrees the shapes of these functions are different, they both converge to the same value as the conversion degree increases. To model the DA cycloaddition reaction, both autocatalytic and *n*th order functions were employed, and based on the DSC results, it was observed that the autocatalytic model is more suitable.

For $K(T)$, the Arrhenius equation can be stated as Eq. (6):

Table 6 A summary of conversion functions

Reaction type	Equation type	Symbol	Conversion function $f(\alpha)$
Formal	*n*th-order	Fn	$(1-\alpha)^n$
Diffusion	One dimensional	D1	$1/2\alpha$
	Two dimensional	D2	$-[\ln(1-\alpha)]^{-1}$
	Three dimensional–Jander equation	D3	$\frac{3}{2}\frac{(1-\alpha)^{2/3}}{1-(1-\alpha)^{1/3}}$
	Three dimensional–Ginstling-Brounstein equation	D4	$\frac{3}{2}\frac{(1-\alpha)^{1/3}}{1-(1-\alpha)^{1/3}}$
	Three dimensional–Carter equation	D5	$\frac{3}{2}\frac{(1+(z-1)\alpha)^{1/3}(1-\alpha)^{1/3}}{(1+(z-1)\alpha)^{1/3}-(1-\alpha)^{1/3}}$
Nucleation	Avrami-Tompkin equation	An	$n(1-\alpha)[-\ln(1-\alpha)]^{\frac{n-1}{n}}$
Autocatalytic	Prout-Tompkin equation	B1	$\alpha^m(1-\alpha)^n$

$$K(T) = Ze^{\frac{-E_a}{RT}} \tag{6}$$

where R and E_a are the gas constant and the activation energy, respectively. By substituting Eq. (6) and (5) into Eq. (3), the differential equation shown in Eq. (7) can be obtained.

$$\frac{d\alpha}{dt} = \left(Ze^{\frac{-E_a}{RT}}\right)\left((1-\alpha)^n \alpha^m\right) \tag{7}$$

To be able to solve this differential equation, n, m, E_a, and Z should be obtained from DSC results. E_a and Z can be found by having two DSC results that are obtained at different heating rates. First, the time derivative of the conversion rate should be found as shown in Eq. (8):

$$\frac{\left(\frac{d\alpha}{dt}\right)}{dt} = \frac{dK(T)}{dt}F(\alpha) + K(T)\frac{dF(\alpha)}{dt} \tag{8}$$

As the temperature increases, the conversion rate goes up and reaches a peak, which is corresponding to the temperature at which the DA cycloaddition proceeds at the maximum speed. At this point, the derivative of $F(\alpha)$ with respect to time is equal to zero. Therefore, at the peak we have:

$$\ln\left[\beta/T_m^2\right] = \ln[ZR/E] - E/RT_m \tag{9}$$

where T_m is the temperature at the peak and β is the heating rate. It should be noted that T_m in Eq. (9) should be absolute temperature. Considering Eq. (9) as a line equation, the slope is E/R, and the intercept is $\ln[ZR/E]$. Therefore, by having at least two DSC curves with different heating rates, E_a and Z can be determined. The diagram of $\ln\left[\beta/T_m^2\right]$ versus $1/T_m$ is shown in Fig. 8(a). With respect to this diagram, E_a and Z were found equal to 75.19 J/mol and 1.332×10^9 1/s.

Considering Eq. (2), the rate of conversion gives Eq. (10):

$$\frac{d\alpha}{dt} = \frac{-dH_R/dt}{H_T} \tag{10}$$

where the rate of the heat flow $(-dH_R/dt)$ was obtained from the DSC curve. For analyzing the conversion degree, a proper curve was fitted to the DSC results. For this purpose, the function shown in (6) was suggested.

$$\begin{aligned} q = {} & 0.1542 \times \mathrm{Sin}(0.0461 \times T - 1.726) \\ & + 0.0154 \times \mathrm{Sin}(0.2324 \times T - 3.629) \\ & + 0.0588 \times \mathrm{Sin}(0.1413 \times T - 2.476) \\ & + 0.0026 \times \mathrm{Sin}(0.3890 \times T - 7.824) \end{aligned} \tag{11}$$

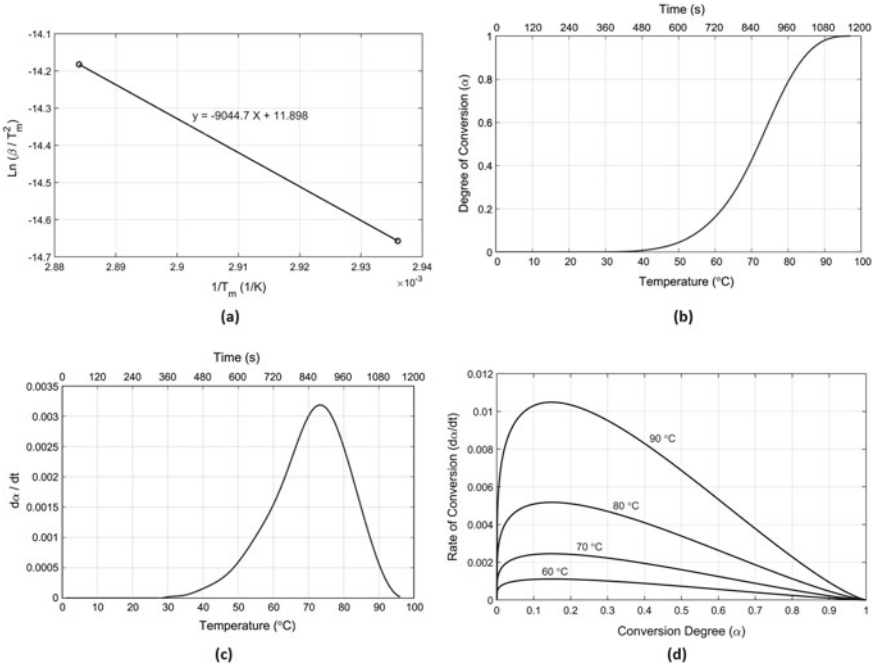

Fig. 8 **a** The Kissinger plot. **b** The degree of conversion versus temperature and time. **c** The conversion degree rate versus temperature and time. **d** The conversion rate of the DA reaction versus conversion degree at different temperatures

Using Eq. (2) and Eq. (10), the conversion degree and the rate of conversion can be plotted as can be seen in Fig. 8b and c. Since the heating rate was constant during DSC tests, the conversion curve has an identical shape in terms of temperature or time. For finding n and m parameters, the time derivative of the conversion was obtained. The graph of $d\alpha/dt$ against α is illustrated in Fig. 8d. Since by changing the conversion degree, the temperature would change, the $K(T)$ would get different values. Hence, the rate of conversion $d\alpha/dt$ was divided by *K(T)* as shown in Eq. (12). Then, by fitting an autocatalytic function to these curves, n and m were attained equal to 1.32 and 0.23.

$$\frac{\frac{d\alpha}{dt}}{K(T)} = (1-\alpha)^n \alpha^m \tag{12}$$

By substituting the obtained values for *n*, *m*, E_a, and *Z*, Eq. (7) can be rewritten as shown in Eq. (13). This differential equation was solved at different temperatures using MATLAB. The results are reported in Fig. 9.

$$\frac{d\alpha}{dt} = \left(1.332 \times 10^9 e^{\frac{-75197}{RT}}\right)\left((1-\alpha)^{1.32}\alpha^{0.23}\right) \tag{13}$$

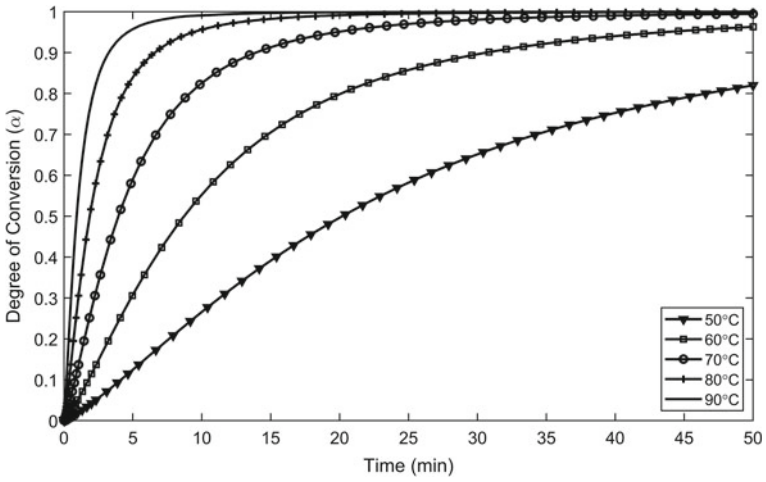

Fig. 9 Conversion degree curves at different healing temperatures

5 Healing Efficiency

5.1 Self-Healing Polymer

5.1.1 Flexural Properties Recovery

Cracked specimens should be sequentially heated for a certain time at retro-DA and DA corresponding temperatures to activate the self-healing mechanism. By heating at retro-DA temperature, the chains of the polymer would gain mobility to transfer to the damaged regions and fill the gaps. However, the amount of these movements is not that much to change the specimens' shape. The subsequent DA reaction would re-establish the cross-links. Therefore, considering the retro-DA and DA temperatures that were obtained from DSC tests, the failed specimens were kept for 30 min at 120 °C to let the retro-DA cycloreversion proceed. For the DA reaction, a temperature should first be selected. This temperature can be between 30 and 95 °C according to the DSC result of the healing agents shown in Fig. 4a. It has been reported by Nielsen et al. [53, 66] that to have an accurate prediction, the selected temperature should be near the peak temperature at which the DA cycloaddition proceeds at the highest speed. For this reason, the temperature of 75 °C, which corresponds to the peak of DA cycloaddition, was chosen. The times required for achieving different conversion degrees were chosen considering the diagram presented in Fig. 9. For achieving conversion degrees of 60%, 80%, and 100%, the temperature was kept at 75 °C for 4, 6, and 40 min, respectively, to let the DA cycloaddition reaction proceed. Since the specimens were broken into two pieces after the three-point bending test, before starting the healing process, the failed surfaces should meet each other. For

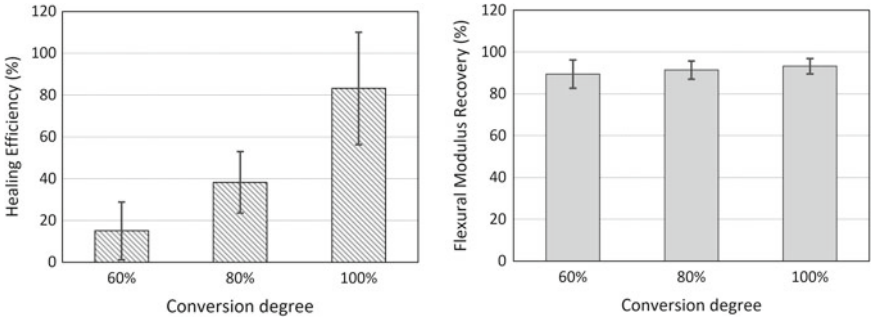

Fig. 10 Healing efficiencies and flexural modulus recoveries at different degrees of conversion

this purpose, a fixture was made to apply equal pressure to both ends of the specimens while the healing process was on run.

By dividing the recovered flexural strength ($X_{F.healed}$) by the initial flexural strength (X_F), the healing efficiency parameter can be stated as Eq. (14).

$$\eta = \frac{X_{F.healed}}{X_F} \tag{14}$$

To obtain the healing efficiency at different conversion degrees, three conversion degrees of 60%, 80%, and 100% were selected, and at each conversion degree, three specimens were tested. As shown in Fig. 10, the healing efficiency at conversion degrees of 60%, 80%, and 100% was 15%, 38%, and 83%, respectively. A relatively high scattering was witnessed for the healing efficiencies due to different fracture surface shapes. Contrary to the flexural strengths, there was a small deviation in recovered flexural moduli at various degrees of conversion. The flexural moduli regained by 89%, 91%, and 93% after healing up to 60%, 80%, and 100% degrees of conversion.

The weakest covalent bonds in the synthesized polymer are the DA bonds [40]. Therefore, as a crack propagates, the breakage of these bonds is more probable that the other irreversible bonds of the polymer (Fig. 11). This issue can enhance the healing efficiency since the DA bonds, which are healable, are highly influential on the recovered strength because they are constructing the cross-links of the thermoset polymer. After the healing process, only the thermally reversible bonds would have the chance to be re-established. When subjecting the specimens to the bending test again, only these newly re-established bonds would carry the load in the healed area. Hence, the recovered strengths are only associated with these thermally reversible bonds.

In Fig. 12, the optical microscopic images of the damaged and healed samples are presented at conversion degrees of 60%, 80%, and 100%. In these images, the darker regions show the damaged area. It was observed that more healing agents had the chance to reconnect the cross-links by increasing the healing time. The smaller dark areas in the completely healed specimen are the evidence for this claim. Microscopic

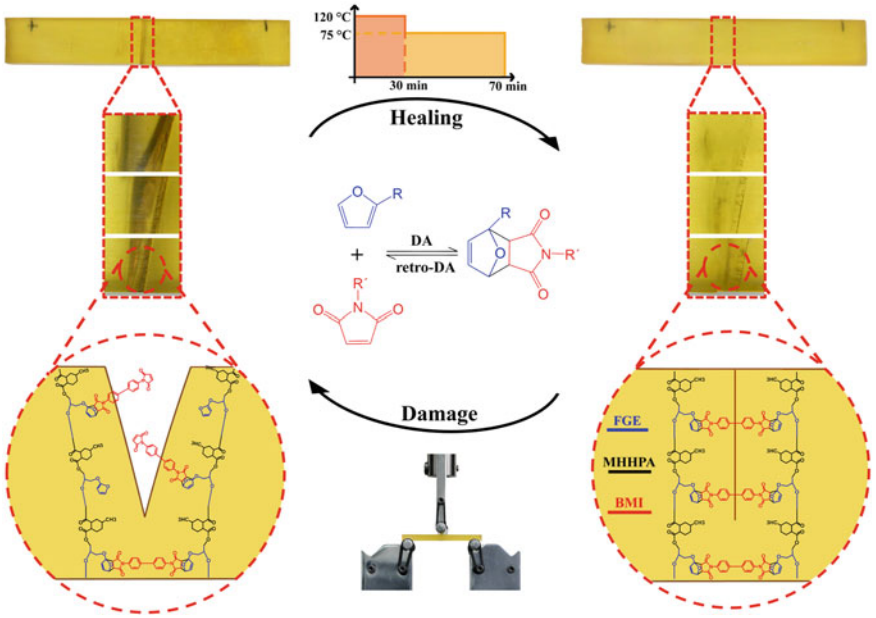

Fig. 11 Schematic of the polymer network of damaged and healed specimens after healing

images also showed that the healed specimens were split from the same region at which the intact specimens failed. Only in the fully healed specimens, a slight change in the breakage shape was witnessed.

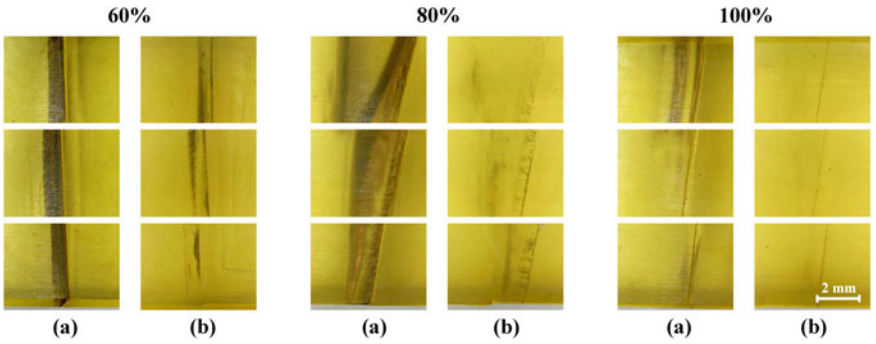

Fig. 12 Optical microscopy images of three specimens healed up to 60%, 80%, and 100%. **a** before healing, **b** after healing (each column represents different regions of a crack). Reprinted with permission from [31]

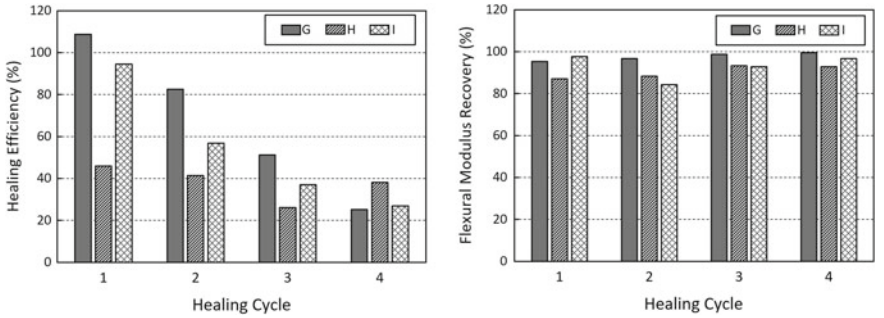

Fig. 13 Healing efficiency and flexural modulus recovery after multiple healing (G, H, and I are specimen codes)

5.1.2 Multiple Healing of Self-Healing Polymer

One of the benefits of intrinsic self-healing polymers is their potential to restore their mechanical properties after multiple damaging and healing cycles. However, a reduction in healing efficiency has been reported after each healing cycle [77]. To obtain the recovered stiffness and strength of the synthesized polymer after multiple healing, three of the samples were damaged and fully healed four times. The results for the healing efficiency and recovered modulus are presented in Fig. 13. It was observed that the specimens were able to regain most of their modulus completely even after the fourth healing cycle. However, the healing efficiency declined after each healing cycle. This reduction was due to the DA cycloaddition between adjacent maleimide and furan moieties that were on the same side of the failed specimen. This reaction made some of the DA reactants incapable of re-establishing cross-links across the damaged surface [78]. Another reason for this observation was the diffusion of BMI molecules farther away from the cracked surfaces [79].

After each damaging and healing cycle, optical microscopic images of the damaged area were taken and it was witnessed that for all specimens, the failure happened at the healed region with some slight changes in the shape of the crack. This happening was owing to the small defects that remained in the specimen after the healing process. These defects acted as initiators of crack during the bending test [80]. The optical microscopic images of a specimen's cracked region after each damaging and healing cycle are illustrated in Fig. 14.

5.2 Self-Healing Fiber-Reinforced Composite

5.2.1 Inducing Initial Matrix Cracks

To induce initial damage to the three-point bending specimens for further healing efficiency analysis, specimens were initially damaged by being subjected to the

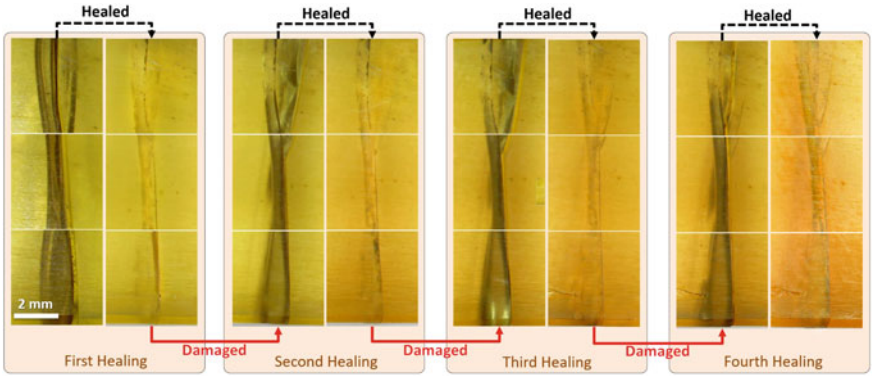

Fig. 14 Optical microscope images of a three-point bending specimen after each damaging and healing cycle

tensile stress. First, the tensile strength of the specimens was found by performing three tensile tests. During the initial tensile tests, the crack density was measured by online optical microscopy. It was observed that crack appearance starts at the stress level of 10%. Then, the crack density increased by stress level up to the stress level of 70%. After this point, which is called characteristic damage state (CDS), the crack density remained constant until the final failure of the specimen. Overall, 31 three-point bending specimens were fabricated. Three specimens were employed for finding the flexural strength and modulus. For finding the residual flexural strength of specimens versus crack density, 16 specimens were used. These specimens were exposed to tensile tests up to different load levels from 10 to 70% and their crack densities were measured after the tensile tests. The rest of the specimens were utilized for the healing efficiency analysis. This group of specimens was damaged under tensile loading until CDS and then healed up to different degrees of conversion.

One series of the images that were taken during the tensile test are presented in Fig. 15. These nine images were taken with constant extension intervals from the extension of 0.10 mm to 1.30 mm that were correlated to 13% and 68% stress levels. The initiation of cracks can be seen in the first image (Fig. 15a). By comparing the last three images (Fig. 15g–i) it can be stated that the specimen is reaching its CDS and the change in crack density is negligible.

5.2.2 Flexural Properties Recovery

The procedure followed for healing the composite specimens was similar to what is mentioned for the neat polymer specimens. The damaged specimens were kept at 120 °C and 75 °C, which are the temperatures corresponding to retro-DA and DA reactions, for a particular time until reaching the desired degree of conversion. To find the influence of the degree of conversion on the healing efficiency, nine composite specimens were damaged up to CDS under tensile loading. Then, these

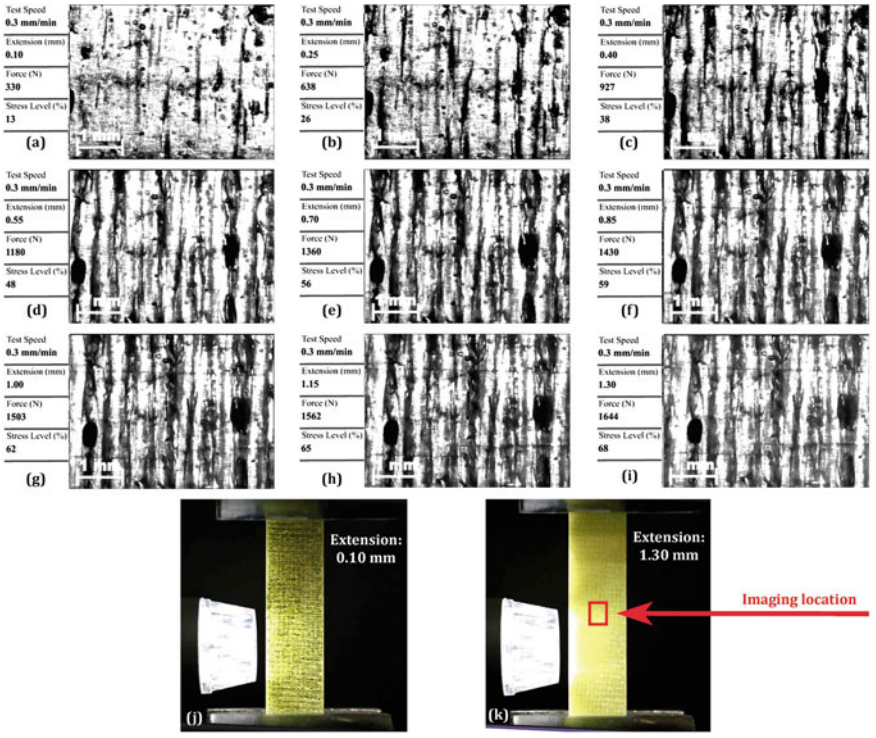

Fig. 15 **a–i** Optical microscopic images of a specimen at different extensions, **j** a specimen at the extension of 0.10 mm, **k** the same specimen at the extension of 1.30 mm. Reprinted with permission from [65]

specimens were healed up to 60%, 80%, and 100%. The required time for reaching each of these conversion degrees was selected similar to the neat polymer specimens based on the conversion degree diagram illustrated in Fig. 9. Similar to polymeric specimens, three-point bending tests were used to find the flexural properties recovery of the composite specimens. As illustrated in Fig. 16, after the complete healing of specimens, both strength and modulus were completely recovered.

5.2.3 Multiple Healing of Self-Healing Composites

Similar to the procedure mentioned for the neat polymer, the composite specimens were damaged up to CDS and healed four times. The results are shown in Fig. 17. In specimen B, the occurrence of fiber breakage after the second healing cycle was the reason for the considerably decreased in healing efficiency after the second healing cycle. The increase that can be seen in the healing efficiency of specimens B and C after the second cycle of healing was attributed to the better wetting of fibers. Since the polymer's viscosity was relatively high, the penetration of resin into fiber

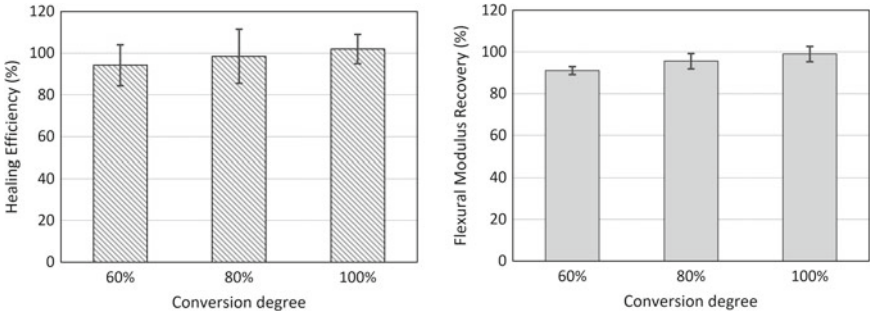

Fig. 16 Healing efficiencies and flexural modulus recoveries

filaments was slow. Hence, when heating at retro-DA temperature, the wetting of fibers would improve which can enhance the healing efficiency. Overall, it can be interpreted from the results that if the only mode of damage was the matrix cracking in the failed specimen, the flexural strength can be fully restored. The reason supporting this statement is that the weakest covalent bonds in the synthesized polymer are the DA bonds [40]. Hence, during the crack growth, it is more likely that the crack propagates by breaking the bonds of DA adducts, which are thermally reversible and can fully regain their strength after healing. The percentage of recovered flexural modulus is also presented in Fig. 17. As can be seen, the level of recovery was constant after each healing cycle, and the specimens were able to recover more than 90% of their flexural modulus.

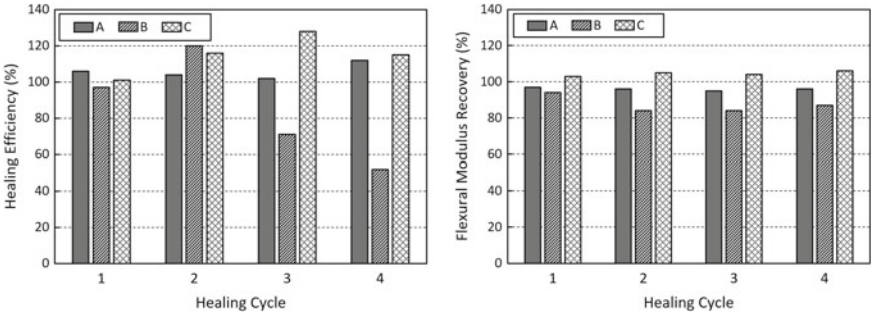

Fig. 17 Healing efficiency and flexural modulus recovery after multiple healing of composite specimens. (A, B, and C are the specimen codes)

6 Modeling of Crack Self-Healing

6.1 Introduction

Despite a large number of papers on the prediction of the transverse cracking effects on the mechanical behavior of cross-ply laminates subjected to tensile loading, the number of studies focusing on stiffness reduction under flexural loading is very limited. Adumitroaie and Barbero [81–83] introduced a model based on the crack opening displacement (COD) technique, for correlating the residual stiffness to the crack density. Their model could estimate the flexural stiffness of thin cross-ply laminates with satisfactory accuracy. However, the predictions deviate from the experimental results as the number of 90° plies increased as a result of matrix crack-induced delamination in thicker laminates, which was overlooked in their model. Another model based on the COD technique to predict the residual flexural stiffness was proposed by Adolfsson et al. [84, 85]. This model was verified by conducting experiments on quasi-isotropic and cross-ply laminates. The analytical results showed a higher stiffness compared with experimental results at low crack densities.

The existing models for predicting the behavior of self-healing composite laminates are limited to continuum damage models. The continuum damage mechanics (CDM) framework was extended by Barbero et al. [86] to continuum damage healing mechanics (CDHM). In the CDHM, only the physical meaning of the damage and healing procedures would be considered. Thus, it can be used for analyzing all self-healing mechanisms. Barbero et al. [86] identified and verified the damage portion of their model in the same article. Subsequently, the healing portion of the model was developed [87]. Later, Voyadjis et al. [88, 89] formulated the CDHM model. The major limitation of the CDHM method is the large number of required material parameters. In the following section, a model was proposed for correlating the flexural stiffness of cross-ply composite laminates to the crack density. In this model, a suitable shear-lag model was used for estimating the residual modulus of the cracked plies, and the classical lamination theory (CLT) was employed to determine the residual stiffness of the laminate.

6.2 Crack Formation Analysis

6.2.1 Shear-Lag Analysis

For explaining the stress transfer between fiber and matrix in discontinuous fiber composites, the shear-lag model was developed by Cox [90]. This model was later modified to predict the strain corresponding to the initiation of multiple matrix cracking [91]. Garrett et al. [92, 93] implemented a similar method to analyze the transverse matrix cracking. Subsequently, the Garrett model was modified by Manders et al. [94] to consider the effect of adjacent cracks. Steif [95] introduced

another shear-lag model to take into account the progressive shear at 90° plies. Contrary to the Garrett et al. [92, 93] model, variable displacement was considered through the thickness of 90° plies which led to a model with a similar form to the Garrett et al. [92, 93] model. Afterward, by using a shear-lag method similar to the Garett model, Ogin et al. [96, 97] obtained the stiffness reduction in a cross-ply laminate subjected to static and fatigue loadings.

In a cross-ply composite laminate, before the occurrence of transverse cracks in the 90° plies, the applied load is shared between 0 and 90° plies. After the transverse cracking occurrence, the stress will be released from the crack planes in the 90° plies. At these regions, all the applied load will be carried by 0° plies after the occurrence of damage. By moving away from the cracked regions, some part of the load would transfer to the 90° plies again through the shear transfer mechanism. Using the shear-lag analysis we can find the axial stress variation in a cracked 90° ply. With respect to Fig. 18, the shear stress at the 0°/90° interface can be stated as Eq. (15):

$$\tau = G_{23}^{90}\left(\frac{u_{90} - u_0}{t_{90}}\right) \tag{15}$$

where u_{90} and u_0 are displacements in the x-direction for 90° and 0° plies, and G_{23}^{90} is the transverse shear modulus of 90° plies. 0 and 90 superscripts or subscripts representing 0° and 90° plies in this chapter. Numerical subscripts denote the material principal coordinates, which 1, 2, and 3 are corresponding to the fiber, perpendicular to the fiber, and out-of-plane directions. Additionally, alphabetical subscripts are used for the global coordinates. The x and z directions are indicated in Fig. 18, and y is perpendicular to the page.

The forces equilibrium in the x-direction can be stated as Eq. (16) for an element in the 90° plies.

$$\frac{d\sigma_x^{90}}{dx} = G_{23}^{90}\left(\frac{u_{90} - u_0}{t_{90}^2}\right) \tag{16}$$

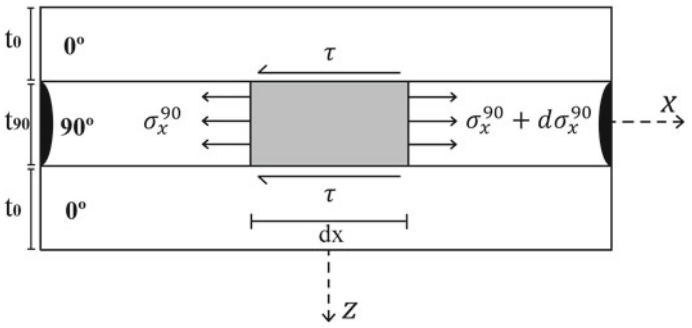

Fig. 18 Stresses acting on the 90° plies between two transverse cracks. Black regions in the 90° ply represent crack surfaces. Reprinted with permission from [65]

The axial stresses in the 90° and 0° plies have the following relation with the total applied axial stress (σ_x^T):

$$(1+\lambda)\sigma_x^T = \lambda\sigma_x^0 + \sigma_x^{90} \tag{17}$$

where $\lambda = t_0/t_{90}$. The relation between stress and strain in 0° and 90° plies can be established as Eq. (18), in which i can be either 0 or 90, and E_x^i is the tensile modulus in the x-direction.

$$\sigma_x^i = E_x^i \varepsilon_x^i, \varepsilon_x^i = \frac{du_i}{dx} \tag{18}$$

By finding the derivative of Eq. (16) with respect to x and by utilizing Eqs. (17) and (18), the differential equation of the axial stress in 90° plies is found as Eq. (19):

$$\frac{d^2\sigma_x^{90}}{dx^2} - \frac{\beta^2}{t_{90}^2}\sigma_x^{90} = -\frac{\beta^2}{t_{90}^2}\frac{E_x^{90}}{E_x^T}\sigma_x^T \tag{19}$$

where E_x^T denotes the tensile modulus of the whole laminate in the x-direction, and β^2 will be specified as Eq. (15).

$$\beta^2 = \gamma G_{23}^{90}\left[\frac{1}{E_x^{90}} + \frac{1}{\lambda E_x^0}\right] \tag{20}$$

Based on the Garrett model [92, 93], the coefficient γ is equal to 1, and by considering the Ogin et al. [96, 97] model, γ would be equal to 3. For the current analysis, both of these values are taken into account for γ. Using Eq. (20), the cracked ply residual stiffness will be obtained as shown in Eq. (21) [98]. In this equation, $E_{x,0}$ and E_x are the initial and the residual stiffnesses of the ply in the x-direction, and ρ represents the crack density. Crack density is the number of cracks per mm length. In the current study, it has been assumed that transverse cracks are evenly spaced along the specimen's length.

$$\frac{E_x}{E_{x,0}} = \left[1 + \frac{E_x^{90}}{\lambda E_x^0}\frac{tanh(2\beta\rho)}{2\beta\rho}\right]^{-1} \tag{21}$$

Many shear-lag models have been proposed so far. The major shear-lag models for analyzing cracked cross-ply laminates are summarized in Table 7. Although more complicated models have a higher number of adjustable parameters, their accuracy is not necessarily higher. Because the inaccuracy of the shear-lag models is inherited from the one-dimensional stress field that is used for deriving the equations. It should be bear in mind that although some models are claimed to be two-dimensional, they are basically similar to one-dimensional models with slight modifications to the Poisson's ratio, and these two-dimensional models also suffer from deficiencies mentioned for the shear-lag models.

Table 7 A summary of major shear-lag models for cross-ply laminates

References	Model dimension	Shear Lag parameter (β^2)	Notes
Garret and Bailey [93]	One-dimensional	$G_{23}^{90}\left[\frac{1}{E_x^{90}}+\frac{1}{\lambda E_x^0}\right]$	
Laws and Dvorak [99]	One-dimensional	$Kt_{90}\left[\frac{1}{E_x^{90}}+\frac{1}{\lambda E_x^0}\right]$	K is a curve-fitting constant
Ogin et al. [96, 97]	One-dimensional	$3G_{23}^{90}\left[\frac{1}{E_x^{90}}+\frac{1}{\lambda E_x^0}\right]$	
Highsmith and Reifsnider [100]	One-dimensional	$G_{23}^{90}\frac{t_{90}}{t_s}\left[\frac{1}{E_x^{90}}+\frac{1}{\lambda E_x^0}\right]$	t_s: resin-rich region thickness†
Fukunaga et al. [101]	One-dimensional	$G_{23}^{90}\frac{t_{90}}{t_s}\left[\frac{1}{Q_{22}}+\frac{1}{\lambda Q_{11}}\right]$	Q_{ij}: stiffness matrix coefficients
Lim and Hong [102]	One-dimensional	$G_{23}^{90}\frac{t_{90}}{t_s}\left[\frac{1}{Q_{22}}+\frac{1}{\lambda Q_{11}}\right]$	Q_{ij}: stiffness matrix coefficients
Lee and Daniel [103, 104]	One-dimensional	$\frac{3G_{xz}^{90}}{1+\lambda\frac{G_{xz}^{90}}{G_{xz}^0}}\left[\frac{1}{E_x^{90}}+\frac{1}{\lambda E_x^0}\right]$	
Nuismer and Tan [105, 106]	Two-dimensional	$\frac{\frac{1}{Q_{xx}^{90}}+\frac{1}{\lambda Q_{xx}^0}}{\frac{1}{3Q_{xz}^{90}}+\frac{\lambda}{3Q_{xz}^0}}$	Q_{ij}: stiffness matrix coefficients
Flaggs [107]	Two-dimensional	$\frac{2\left[\frac{1}{\lambda Q_{xx}^0}+\frac{Q_{yy}^{90}-Q_{xy}^{90}Q_{xy}^0/Q_{xx}^0}{Q_{xx}^{90}Q_{yy}^{90}-\left(Q_{xy}^{90}\right)^2}\right]}{\left[\frac{1}{k^2}-\frac{1}{2}\right]\frac{1}{G_{xz}^{90}}+\frac{\lambda}{2G_{xz}^0}}$	k: transverse shear correction factor Q_{ij}: stiffness matrix coefficients

† It has been assumed that the shear deformation is limited to a thin resin-rich region near the neighboring plies interfaces

6.2.2 The Residual Flexural Stiffness of the Cracked Specimens

The stress–strain relation in a symmetric cross-ply laminate can be stated as Eq. (17):

$$\begin{Bmatrix} N_1 \\ N_2 \\ N_6 \\ M_1 \\ M_2 \\ M_6 \end{Bmatrix} = \begin{bmatrix} A_{11} & A_{12} & 0 & 0 & 0 & 0 \\ A_{21} & A_{22} & 0 & 0 & 0 & 0 \\ 0 & 0 & A_{66} & 0 & 0 & 0 \\ 0 & 0 & 0 & D_{11} & D_{12} & 0 \\ 0 & 0 & 0 & D_{21} & D_{22} & 0 \\ 0 & 0 & 0 & 0 & 0 & D_{66} \end{bmatrix} \begin{Bmatrix} \varepsilon_1 \\ \varepsilon_2 \\ \varepsilon_6 \\ k_1 \\ k_2 \\ k_6 \end{Bmatrix} \tag{22}$$

where A_{ij} and D_{ij} $(i, j = 1,2,6)$ are the in-plane and flexural moduli of the laminate, M_i and N_i $(i = 1, 2, 6)$ are in-plane moments and forces per unit length, and k_j and ε_j $(j = 1, 2, 6)$ are curvatures and strains of the mid-plane of the laminate. The moment–curvature relation for a laminate subjected to pure bending can be written

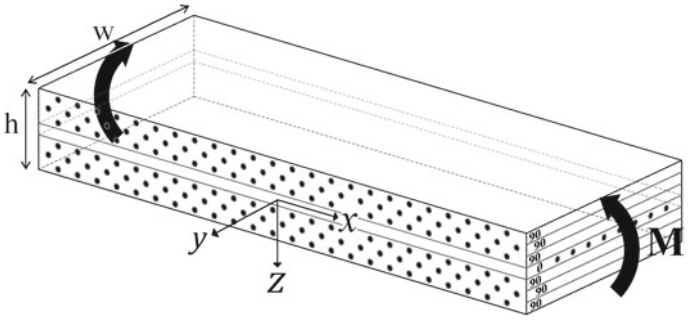

Fig. 19 Schematic of a cross-ply laminate with the stacking sequence of $[90_3/0/90_3]$ subjected to bending. Reprinted with permission from [65]

as Eq. (23):

$$\frac{M_1}{k_1} = D_{11} = \frac{wh^3}{12} E_F \tag{23}$$

In Eq. (23), h, w and E_F are total thickness, width, and flexural stiffness of the laminate, respectively. To determine the flexural stiffness (E_F), first D_{11} should be obtained by using CLT. For a $[90_3/0/90_3]$ laminate (Fig. 19) with a ply thickness of $t = 0.243$ mm, D_{11} is calculated as shown in Eq. (24):

$$D_{11} = \frac{12E_1 + 4089E_2}{10000} \tag{24}$$

where E_1 is the elastic modulus of a unidirectional ply in the fiber direction and E_2 is the elastic modulus perpendicular to the fiber direction. The flexural modulus of the laminate can be calculated by substituting Eq. (24) into Eq. (23). In Eq. (25) h is the laminate total thickness.

$$E_F = \frac{12}{h^3}\left[\frac{12E_1 + 4089E_2}{10000}\right] \tag{25}$$

The modulus of the intact laminate in the loading direction can be stated as Eq. (26) according to the rule-of-mixture. It has been reported [108] that the modulus obtained using this equation would differ up to 5% from the CLT solution.

$$E_{x,0} = \frac{\lambda E_1 + E_2}{\lambda + 1} \tag{26}$$

Using Eq. (26), the total stiffness of the cracked laminate will be found as shown in Eq. (27). In Eq. (27), E_2^* indicates the cracked ply residual modulus.

$$E_x = \frac{\lambda E_1 + E_2^*}{\lambda + 1} \tag{27}$$

Substitution Eq. (26) and (27) into Eq. (21), which is deduced from the shear-lag analysis, the cracked ply residual modulus (E_2^*) can be calculated as shown in Eq. (28).

$$E_2^* = \frac{\left[1 - \frac{tanh(2\beta\rho)}{2\beta\rho}\right] E_2}{1 + \left[\frac{tanh(2\beta\rho)}{2\beta\rho}\right] \frac{E_2}{\lambda E_1}} \tag{28}$$

During the bending test, as the load increases, the 90° plies that are placed below the neutral axis would experience matrix cracking. These cracks would reduce the stiffness of the 90° plies that are under the neutral axis and consequently the position of the neutral axis would change. This issue is schematically shown in Fig. 20. By using the moment equilibrium equations, the neutral axis movement (δ_{NA}) can be calculated. As long as the neutral axis movement is smaller than half of a ply thickness, the Eq. (29) is valid for the current layup configuration.

$$\delta_{NA} = \frac{6t\left(E_2 - E_2^*\right)}{3E_2 + E_1 + 3E_2^*} \tag{29}$$

In Eq. (29), t is the ply thickness. By substituting the characteristics of the current laminate with the layup configuration of $[90_3/0/90_3]$ and considering the limiting case of $E_2^* = 0$, which is the worst scenario, the neutral axis movement would be smaller than half of a ply thickness.

To predict the cross-ply laminates' flexural stiffness by having the crack density, a computer code was written in the MATLAB framework. The procedure for finding the flexural stiffness is presented in the flowchart shown in Fig. 21. This code gradually increases the crack density, and by taking into account the reduced modulus of cracked plies $\left(E_2^*\right)$, the neutral axis movement (δ_{NA}) and crack closure effect, it calculates the residual flexural stiffness for the given layup configuration. This procedure continues until reaching the crack saturation condition (CDS).

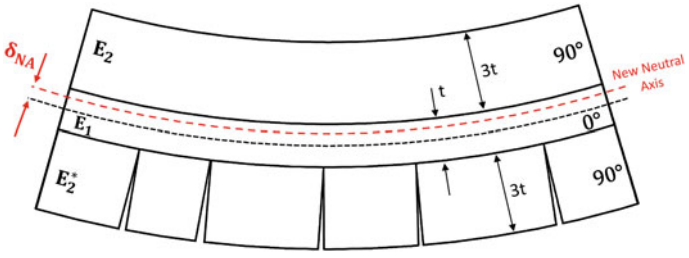

Fig. 20 Schematic of the neutral axis movement after damage occurrence

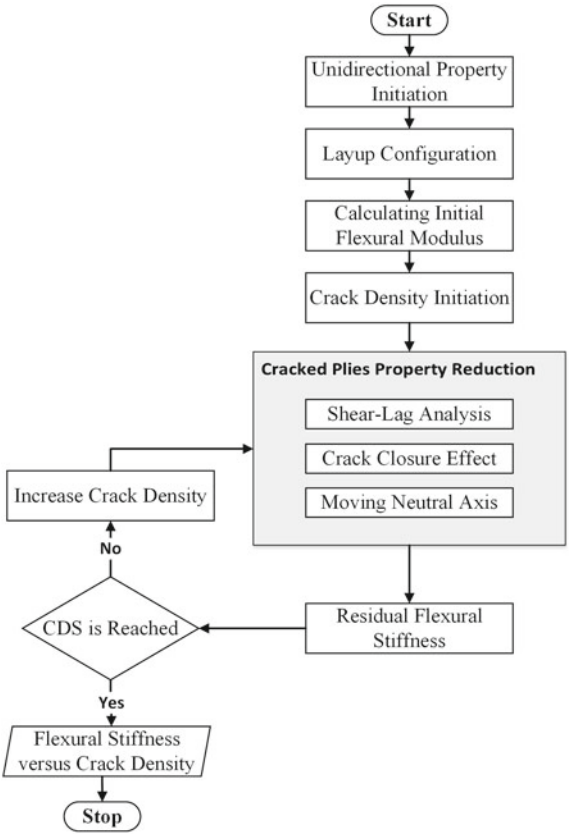

Fig. 21 Flowchart of residual flexural stiffness prediction in a cracked cross-ply laminate. Reprinted with permission from [65]

Using the developed code, the residual flexural stiffness of a laminate with the stacking sequence of $[90_3/0/90_3]$ was predicted. In this analysis, the shear-lag models of Garrett et al. [92, 93] and Ogin et al. [96, 97] were taken into account. In these two models, the coefficient γ in Eq. (20) was equal to 1 and 3, respectively. The prediction of other shear-lag models would place between these two [98]. In Fig. 22, the analytical results were compared with experimental results that were obtained from 16 specimens that were damaged by subjecting them to tensile loading until 10% to 70% of their tensile strength. The flexural moduli of these damaged specimens were obtained by performing standard three-point bending tests [39]. For the fabricated self-healing polymer, the Ogin model gives a better estimation. As pointed out in the shear-lag section, the inaccuracy of the shear-lag models is because of the one-dimensional stress field assumption. This problem exists even in those models that are claimed to be two-dimensional. The second shortcoming of the shear-lag analysis lies in another assumption that says intra-laminar cracks would remain far apart. Based on this assumption the mutual interactions of neighboring cracks are overlooked which is not a valid assumption, especially at higher crack densities. It should be

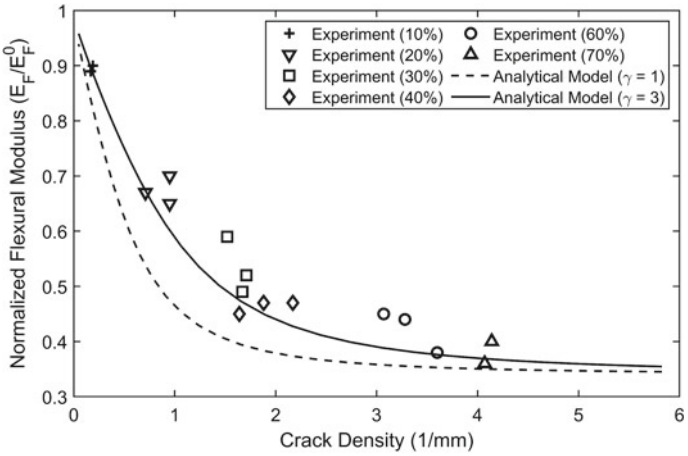

Fig. 22 Comparison between analytical and experimental results of the residual flexural modulus of cracked laminates with a $[90_3/0/90_3]$ stacking sequence. E_F^0 is the laminates' initial flexural modulus

noted that the occurrence of delamination cannot be considered as a source of error because considering the microscopic images the only observable damage type was matrix cracking.

6.3 Crack Self-Healing Modeling

During the self-healing process, two happenings contribute to flexural modulus recovery. First, the decrease in crack density due to the transfer of healing agents to the damaged regions and filling the cracks. Second, the increase in matrix modulus due to DA reaction and re-establishment of cross-links. These two events are illustrated in Fig. 23 for the current material and stacking sequence. After the healing process, the crack density would reduce. However, some cracks may remain in the healed specimen. This issue necessitates finding crack density at different conversion degrees. In Fig. 23, the curves are showing the correlation between flexural modulus and crack density for composite specimens with different fiber-to-matrix modulus ratios (E_f/E_m). For the current self-healing composite material, since the modulus of the matrix would change during the healing process, the flexural modulus will not follow any of these lines. But, it changes the curve after the healing process as schematically shown in Fig. 23 (from points A to B). Therefore, to be able to estimate the recovered flexural modulus, the crack density and matrix modulus should first be correlated to conversion degree.

For correlating the crack density to the degree of conversion, the saturated crack densities of the nine specimens were measured at CDS. In the same way, the crack densities were measured after the healing process until conversion degrees of 60%,

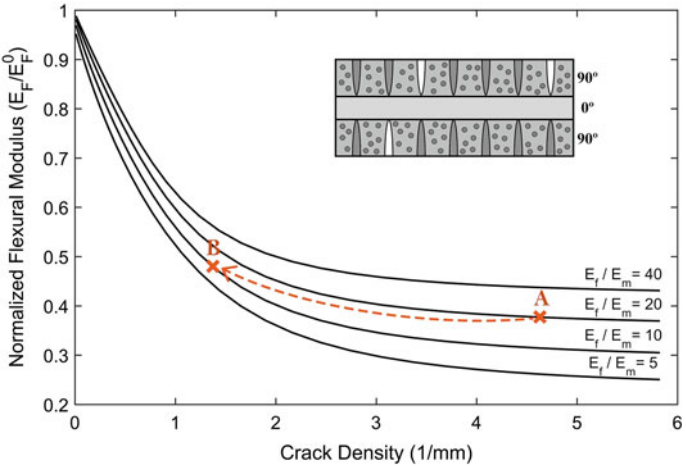

Fig. 23 Analytical results of the residual flexural modulus versus crack density with various fiber-to-matrix moduli, and a schematic of a cracked cross-ply laminate after the healing process. Reprinted with permission from [65]

80, and 100%. For measuring the crack densities, optical microscopic images were taken from 10 different regions along the length of specimens, and the average of the crack densities was taken into account. In Fig. 24, one series of these images are displayed. These images are taken from one region in the intact specimen, after tensile loading, and after the healing process. Brighter areas in Fig. 24b to c represent the cracks. It was observed that most of the cracks were healed after the healing process. However, a few cracks remained in the specimen. One of the healed cracks and one of the remained cracks are specified in Fig. 24c and d.

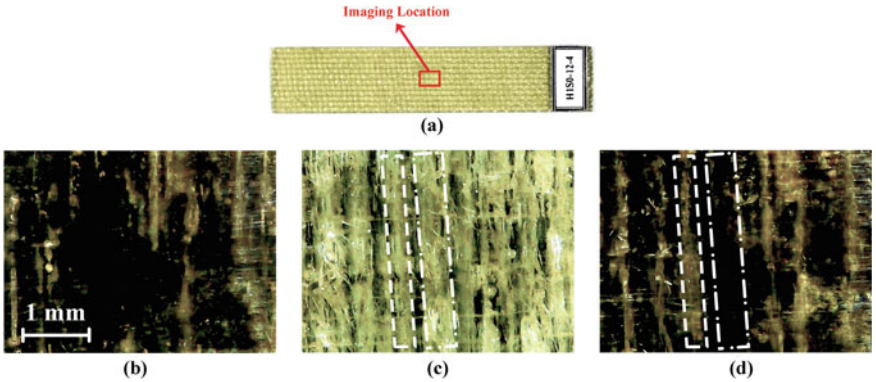

Fig. 24 **a** A three-point bending composite specimen, **b** an optical microscopic image of the intact specimen, **c** after tensile loading up to CDS (Two transverse cracks are indicated inside the boxes), **d** after the healing process (the remaining parts of the same cracks are indicated inside the boxes)

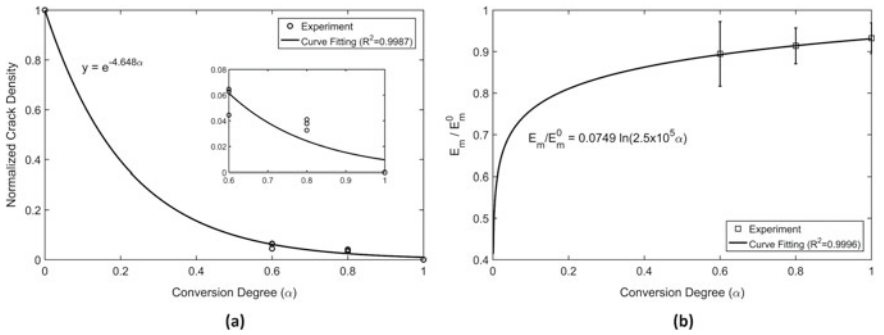

Fig. 25 **a** Normalized crack density versus conversion degree, and the magnified values (inset). **b** The normalized modulus recovery versus the conversion degree

The measured crack densities are illustrated in Fig. 25a. As expected, the crack density reduced by the conversion degree, and in the conversion decree of 1, almost all cracks were disappeared. To be able to implement these results in a computer code, the results were normalized and an exponential curve was fitted to the results. The crack densities were normalized by the saturated crack density. Since only the thermally reversible bonds would re-establish after the healing procedure, the healed specimens will not regain their initial modulus. Thus, it is required to obtain the recovered modulus of the neat polymer after the healing process. To this end, the recovered moduli of the healed polymers were obtained at 60%, 80%, and 100% of conversion degrees. The results are provided in Fig. 25b. In this figure, E_m and E_m^0 are the recovered and initial moduli of the neat polymer. By considering the value of zero for a broken specimen, a logarithmic curve was fitted to the results. This logarithmic function was also employed in the code for flexural modulus recovery predictions.

A MATLAB code was developed to correlate the flexural modulus recovery to the conversion degree by having the crack density reduction and the change in modulus as a function of conversion degree. The predictions of the code for the cross-ply laminate that was used in this study are shown in Fig. 26. To verify the predictions, the experimental results that were previously obtained at conversion degrees of 0.6, 0.8, and 1 are plotted on the diagram. By comparing the results, it can be stated that the model can predict the recovered flexural modulus with high accuracy. Using Fig. 9 along with this diagram, it is possible to correlate the recovered flexural modulus to the healing time and temperature.

7 Conclusion

Although many intrinsic self-healing polymers have been introduced recently, the number of quantitative investigations in the field is very limited and most of the studies

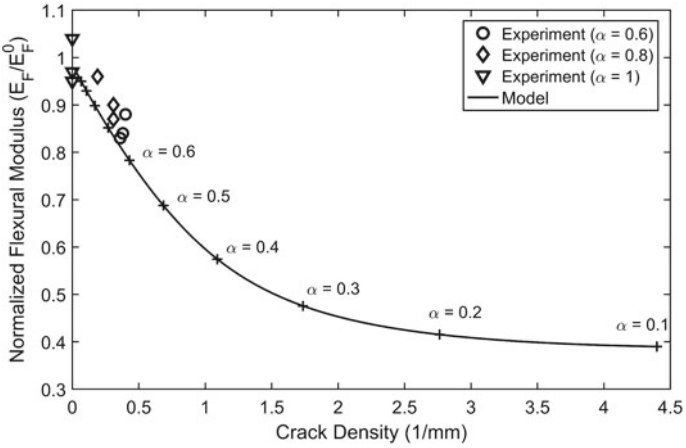

Fig. 26 Comparison between predicted and experimental flexural stiffness recovery after the healing process up to different degrees of conversion for a laminate with a stacking sequence of $[90_3/0/90_3]$

are solely experimental. The limited knowledge on the behavior of self-healing materials has hindered extending their usage from laboratories to practical applications. One of the areas that require more exploration is the influence of conversion degree on the healing efficiency. In some applications, due to technical limitations, it might not be possible to increase the temperature of the composite structure to the temperature at which the Diels–Alder (DA) reaction proceeds at the highest speed, or there might be a time limitation. Therefore, the material may not be healed completely. To address this issue, a model was developed to predict the cross-links' conversion degree as a function of temperature and time, and to correlate the healing efficiency to conversion degree. The model was applied to a new self-healing system containing maleimide and furan groups as healing agents. The three-point bending test method was selected for investigating the healing efficiency of the self-healing polymer, and the healing efficiencies were obtained at conversion degrees of 60%, 80%, and 100%. In the neat polymer specimens, the flexural strength recovered 15%, 38%, and 83% of its initial value, and the flexural modulus was restored 89%, 91%, and 93% of its initial value after healing up to conversion degrees of 60%, 80%, and 100%.

Using the synthesized self-healing polymer, cross-ply glass fiber-reinforced composites were fabricated. After inducing cracks in the bending specimens until reaching CDS, the specimens were divided into three groups and healed up to conversion degrees of 60%, 80%, and 100%, and it was observed that the specimens restored 94%, 97%, and 99% of their initial flexural strength and 91%, 95% and 99% of their initial flexural modulus, respectively. Afterward, a model was proposed using the shear-lag method and CLT to estimate the residual flexural stiffness of cross-ply laminates at different crack densities. The validity of the model was approved by performing a series of three-point bending tests. Then, the model was further developed to estimate the recovered flexural stiffness after the healing process up to the

desired conversion degree. The accuracy of the self-healing portion of the model was also confirmed by experimental results.

The multiple healing capability of both neat polymer and composite specimens were examined by damaging and healing the specimens four times. The composite specimens recovered their mechanical properties completely. However, in the neat polymer specimens, the healing efficiency degraded cycle-by-cycle due to DA reaction between healing agents on the same side of the damaged surfaces instead of cross-linking across the damaged surfaces.

References

1. Blaiszik, B.J., Kramer, S.L.B., Olugebefola, S.C., Moore, J.S., Sottos, N.R., White, S.R.: Self-healing polymers and composites. Annu. Rev. Mater. Res. **40**, 179–211 (2010)
2. Wu, D.Y., Meure, S., Solomon, D.: Self-healing polymeric materials: a review of recent developments. Prog. Polym. Sci. **33**, 479–522 (2008)
3. Liu, Y.-L., Chuo, T.-W.: Self-healing polymers based on thermally reversible Diels–Alder chemistry. Polym. Chem. **4**, 2194–2205 (2013)
4. Herbst, F., Döhler, D., Michael, P., Binder, W.H.: Self-healing polymers via supramolecular forces. Macromol. Rapid. Commun. **34**, 203–220 (2013)
5. Yuan, Y.C., Yin, T., Rong, M.Z., Zhang, M.Q.: Self healing in polymers and polymer composites. Concepts, realization and outlook: a review. Express. Polym. Lett. **2**, 238–250 (2008)
6. Bekas, D.G., Tsirka, K., Baltzis, D., Paipetis, A.S.: Self-healing materials: a review of advances in materials, evaluation, characterization and monitoring techniques. Compos. Part B Eng. **87**, 92–119 (2016)
7. Trask, R.S., Williams, H.R., Bond, I.P.: Self-healing polymer composites: mimicking nature to enhance performance. Bioinspir. Biomim. **2**, P1 (2007)
8. Wang, S., Urban, M.W.: Self-healing polymers. Nat. Rev. Mater. **5**, 562–583 (2020)
9. Zhang, P., Li, G.: Advances in healing-on-demand polymers and polymer composites. Prog. Polym. Sci. **57**, 32–63 (2016)
10. Hia, I.L., Vahedi, V., Pasbakhsh, P.: Self-healing polymer composites: prospects, challenges, and applications. Polym. Rev. **56**, 225–261 (2016)
11. Scheiner, M., Dickens, T.J., Okoli, O.: Progress towards self-healing polymers for composite structural applications. Polymer (Guildf) **83**, 260–282 (2016)
12. Kanu, N.J., Gupta, E., Vates, U.K., Singh, G.K.: Self-healing composites: a state-of-the-art review. Compos. Part A Appl. Sci. Manuf. **121**, 474–486 (2019)
13. Cohades, A., Branfoot, C., Rae, S., Bond, I., Michaud, V.: Progress in self-healing fiber-reinforced polymer composites. Adv. Mater. Interfaces **5**, 1800177 (2018)
14. Ilyaei, S., Sourki, R., Akbari, Y.H.A.: Capsule-based healing systems in composite materials: a review. Crit. Rev. Solid State Mater. Sci. **46**, 491–531 (2021)
15. Santos, A.N.B., dos Santos, D.J., Carastan, D.J.: Microencapsulation of reactive isocyanates for application in self-healing materials: a review. J. Microencapsul. **38**, 338–356 (2021)
16. Feng, J., Ming, Y., Zhang, Y., Guo, H., Huang, K., Hu, J., et al.: Progress of research on encapsuled isocyanate self-healing polymeric materials. Chem. Ind. Eng. Prog. **35**, 175–181 (2016)
17. Ullah, H., Azizli, M.K.A., Man, Z.B., Ismail, M.B.C., Khan, M.I.: The potential of microencapsulated self-healing materials for microcracks recovery in self-healing composite systems: a review. Polym. Rev. **56**, 429–485 (2016)

18. Zhu, D.Y., Rong, M.Z., Zhang, M.Q.: Self-healing polymeric materials based on microencapsulated healing agents: from design to preparation. Prog. Polym. Sci. **49**, 175–220 (2015)
19. Trask, R.S., Bond, I.P.: Biomimetic self-healing of advanced composite structures using hollow glass fibres. Smart. Mater. Struct. **15**, 704 (2006)
20. Pang, J.W.C., Bond, I.P.: A hollow fibre reinforced polymer composite encompassing self-healing and enhanced damage visibility. Compos. Sci. Technol. **65**, 1791–1799 (2005)
21. Toohey, K.S., Sottos, N.R., White, S.R.: Characterization of microvascular-based self-healing coatings. Exp. Mech. **49**, 707–717 (2009)
22. Toohey, K.S., Hansen, C.J., Lewis, J.A., White, S.R., Sottos, N.R.: Delivery of two-part self-healing chemistry via microvascular networks. Adv. Funct. Mater. **19**, 1399–1405 (2009)
23. Toohey, K.S., Sottos, N.R., Lewis, J.A., Moore, J.S., White, S.R.: Self-healing materials with microvascular networks. Nat. Mater. **6**, 581–585 (2007)
24. Saeed, M.-U., Chen, Z., Li, B.: Manufacturing strategies for microvascular polymeric composites: a review. Compos. Part A Appl. Sci. Manuf. **78**, 327–340 (2015)
25. Paolillo, S., Bose, R.K., Santana, M.H., Grande, A.M.: Intrinsic self-healing epoxies in polymer matrix composites (PMCs) for aerospace applications. Polymers (Basel) **13**, 201 (2021)
26. Utrera-Barrios, S., Verdejo, R., López-Manchado, M.A., Santana, M.H.: Evolution of self-healing elastomers, from extrinsic to combined intrinsic mechanisms: a review. Mater. Horizons. **7**, 2882–902 (2020)
27. Wang, Z., Lu, X., Sun, S., Yu, C., Xia, H.: Preparation, characterization and properties of intrinsic self-healing elastomers. J. Mater. Chem. B **7**, 4876–4926 (2019)
28. Zhong, N., Post, W.: Self-repair of structural and functional composites with intrinsically self-healing polymer matrices: a review. Compos. Part A Appl. Sci. Manuf. **69**, 226–239 (2015)
29. Zhang, M.Q., Rong, M.Z.: Intrinsic self-healing of covalent polymers through bond reconnection towards strength restoration. Polym. Chem. **4**, 4878–4884 (2013)
30. Garcia, S.J.: Effect of polymer architecture on the intrinsic self-healing character of polymers. Eur. Polym. J. **53**, 118–125 (2014)
31. Shabani, P., Shokrieh, M.M., Zibaei, I.: Effect of the conversion degree and multiple healing on the healing efficiency of a thermally reversible self-healing polymer. Polym. Adv. Technol. **30**, 2906–2917 (2019). https://doi.org/10.1002/pat.4723
32. Cordier, P., Tournilhac, F., Soulié-Ziakovic, C., Leibler, L.: Self-healing and thermoreversible rubber from supramolecular assembly. Nature **451**, 977–980 (2008)
33. Kalista, S.J., Ward, T.C.: Thermal characteristics of the self-healing response in poly (ethylene-co-methacrylic acid) copolymers. JR. Soc. Interface **4**(13), 405–411; Kalista, S.J.: Self-healing of poly (ethylene-co-methacrylic acid) copolymers following projectile puncture. Mech. Adv. Mater. Struct. **14**, 391–7 (2007)
34. Varley, R.J., Shen, S., van der Zwaag, S.: The effect of cluster plasticisation on the self healing behaviour of ionomers. Polymer (Guildf) **51**, 679–686 (2010)
35. Deng, G., Tang, C., Li, F., Jiang, H., Chen, Y.: Covalent cross-linked polymer gels with reversible sol−gel transition and self-healing properties. Macromolecules **43**, 1191–1194 (2010)
36. Amamoto, Y., Otsuka, H., Takahara, A., Matyjaszewski, K.: Self-healing of covalently cross-linked polymers by reshuffling thiuram disulfide moieties in air under visible light. Adv. Mater. **24**, 3975–3980 (2012)
37. Canadell, J., Goossens, H., Klumperman, B.: Self-healing materials based on disulfide links. Macromolecules **44**, 2536–2541 (2011)
38. Lafont, U., Van Zeijl, H., Van Der Zwaag, S.: Influence of cross-linkers on the cohesive and adhesive self-healing ability of polysulfide-based thermosets. ACS Appl. Mater. Interfaces **4**, 6280–6288 (2012)
39. Kötteritzsch, J., Stumpf, S., Hoeppener, S., Vitz, J., Hager, M.D., Schubert, U.S.: One-component intrinsic self-healing coatings based on reversible crosslinking by Diels–Alder cycloadditions. Macromol. Chem. Phys. **214**, 1636–1649 (2013)

40. Chen, X., Wudl, F., Mal, A.K., Shen, H., Nutt, S.R.: New thermally remendable highly cross-linked polymeric materials. Macromolecules **36**, 1802–1807 (2003)
41. Chen, X., Dam, M.A., Ono, K., Mal, A., Shen, H., Nutt, S.R. et al.: A thermally re-mendable cross-linked polymeric material. Science (80-) **295**, 1698–702 (2002)
42. Kuhl, N., Bode, S., Hager, M.D., Schubert, U.S.: Self-healing polymers based on reversible covalent bonds. Self-Healing Mater. 1–58 (2015)
43. Zhang, M.Q., Rong, M.Z.: Self-healing Polymers and Polymer Composites. Wiley (2011)
44. Diaz, M.M., Van Assche, G., Maurer, F.H.J., Van Mele, B.: Thermophysical characterization of a reversible dynamic polymer network based on kinetics and equilibrium of an amorphous furan-maleimide Diels–Alder cycloaddition. Polymer (Guildf) **120**, 176–188 (2017)
45. Tian, Q., Rong, M.Z., Zhang, M.Q., Yuan, Y.C.: Optimization of thermal remendability of epoxy via blending. Polymer (Guildf) **51**, 1779–1785 (2010)
46. Tian, Q., Rong, M.Z., Zhang, M.Q., Yuan, Y.C.: Synthesis and characterization of epoxy with improved thermal remendability based on Diels–Alder reaction. Polym. Int. **59**, 1339–1345 (2010)
47. Zhang, Y., Broekhuis, A.A., Picchioni, F.: Thermally self-healing polymeric materials: the next step to recycling thermoset polymers? Macromolecules **42**, 1906–1912 (2009)
48. Yoshie, N., Watanabe, M., Araki, H., Ishida, K.: Thermo-responsive mending of polymers crosslinked by thermally reversible covalent bond: polymers from bisfuranic terminated poly (ethylene adipate) and tris-maleimide. Polym. Degrad. Stab. **95**, 826–829 (2010)
49. Postiglione, G., Turri, S., Levi, M.: Effect of the plasticizer on the self-healing properties of a polymer coating based on the thermoreversible Diels–Alder reaction. Prog. Org. Coat. **78**, 526–531 (2015)
50. Liu, Y., Hsieh, C.: Crosslinked epoxy materials exhibiting thermal remendablility and removability from multifunctional maleimide and furan compounds. J. Polym. Sci. Part A Polym. Chem. **44**, 905–913 (2006)
51. Liu, Y., Chen, Y.: Thermally reversible cross-linked polyamides with high toughness and self-repairing ability from maleimide-and furan-functionalized aromatic polyamides. Macromol. Chem. Phys. **208**, 224–232 (2007)
52. Plaisted, T.A., Nemat-Nasser, S.: Quantitative evaluation of fracture, healing and re-healing of a reversibly cross-linked polymer. Acta. Mater. **55**, 5684–5696 (2007)
53. Nielsen, C., Weizman, H., Nemat-Nasser, S.: Thermally reversible cross-links in a healable polymer: estimating the quantity, rate of formation, and effect on viscosity. Polymer (Guildf) **55**, 632–641 (2014)
54. Weizman, H., Nielsen, C., Weizman, O.S., Nemat-Nasser, S.: Synthesis of a self-healing polymer based on reversible Diels–Alder reaction: an advanced undergraduate laboratory at the interface of organic chemistry and materials science. J. Chem. Educ. **88**, 1137–1140 (2011)
55. Wouters, M., Craenmehr, E., Tempelaars, K., Fischer, H., Stroeks, N., van Zanten, J.: Preparation and properties of a novel remendable coating concept. Prog. Org. Coat. **64**, 156–162 (2009)
56. Scheltjens, G., Brancart, J., De Graeve, I., Van Mele, B., Terryn, H., Van Assche, G.: Self-healing property characterization of reversible thermoset coatings. J. Therm. Anal. Calorim. **105**, 805–809 (2011)
57. Peterson, A.M., Jensen, R.E., Palmese, G.R.: Reversibly cross-linked polymer gels as healing agents for epoxy−amine thermosets. ACS Appl. Mater. Interfaces **1**, 992–995 (2009)
58. Bai, N., Simon, G.P., Saito, K.: Investigation of the thermal self-healing mechanism in a cross-linked epoxy system. RSC Adv. **3**, 20699–20707 (2013)
59. Bai, N., Saito, K., Simon, G.P.: Synthesis of a diamine cross-linker containing Diels–Alder adducts to produce self-healing thermosetting epoxy polymer from a widely used epoxy monomer. Polym. Chem. **4**, 724–730 (2013)
60. Scheltjens, G., Diaz, M.M., Brancart, J., Van Assche, G., Van Mele, B.: A self-healing polymer network based on reversible covalent bonding. React. Funct. Polym. **73**, 413–420 (2013)
61. Park, J.S., Kim, H.S., Hahn, H.T.: Healing behavior of a matrix crack on a carbon fiber/mendomer composite. Compos. Sci. Technol. **69**, 1082–1087 (2009)

62. Park, J.S., Darlington, T., Starr, A.F., Takahashi, K., Riendeau, J., Hahn, H.T.: Multiple healing effect of thermally activated self-healing composites based on Diels–Alder reaction. Compos. Sci. Technol. **70**, 2154–2159 (2010)
63. Kotrotsos, A., Tsokanas, P., Tsantzalis, S., Kostopoulos, V.: Healing of carbon fiber reinforced plastics by Diels–Alder based polymers: effects of healing agent concentration and curing cycle. J. Appl. Polym. Sci. **136**, 47478 (2019)
64. Saeedi, A., Shokrieh, M.M.: A novel self-healing composite made of thermally reversible polymer and shape memory alloy reinforcement. J. Intell. Mater. Syst. Struct. **30**, 1585–1593 (2019)
65. Shabani, P., Shokrieh, M.M., Saeedi, A.: A novel model to simulate the formation and healing of cracks in self-healing cross-ply composites under flexural loading. Compos. Struct. 235 (2020)
66. Nielsen, C., Nemat-Nasser, S.: Crack healing in cross-ply composites observed by dynamic mechanical analysis. J. Mech. Phys. Solids **76**, 193–207 (2015)
67. Höhne, G.W.H., Hemminger, W.F., Flammersheim. H.-J.: DSC Curves and Further Evaluations. Differential Scanning Calorimetry, pp. 115–46. Springer (2003)
68. ASTM E2890-12, Standard Test Method for Kinetic Parameters for Thermally Unstable Materials by Differential Scanning Calorimetry Using the Kissinger Method. ASTM Int. (2012).
69. Murphy, E.B., Bolanos, E., Schaffner-Hamann, C., Wudl, F., Nutt, S.R., Auad, M.L.: Synthesis and characterization of a single-component thermally remendable polymer network: staudinger and stille revisited. Macromolecules **41**, 5203–5209 (2008)
70. ASTM D790-15, Standard Test Methods for Flexural Properties of Unreinforced and Reinforced Plastics and Electrical Insulating Materials. ASTM Int. (2015)
71. ASTM D695-15, Standard Test Method for Compressive Properties of Rigid Plastics. ASTM Int. (2015)
72. Mujika, F., Carbajal, N., Arrese, A., Mondragon, I.: Determination of tensile and compressive moduli by flexural tests. Polym. Test. **25**, 766–771 (2006)
73. Clyne, T.W., Hull, D.: An Introduction to Composite Materials. Cambridge University Press (2019)
74. Shokrieh, M.M., Salamat-Talab, M., Heidari-Rarani, M.: Effect of interface fiber angle on the R-curve behavior of E-glass/epoxy DCB specimens. Theor. Appl. Fract. Mech. **86**, 153–160 (2016)
75. ASTM E2041-13, Standard Test Method for Estimating Kinetic Parameters by Differential Scanning Calorimeter Using the Borchardt and Daniels Method. ASTM Int. (2013)
76. ASTM E698-16, Standard Test Method for Kinetic Parameters for Thermally Unstable Materials Using Differential Scanning Calorimetry and the Flynn/Wall/Ozawa Method. ASTM Int. (2016)
77. Amendola, V., Meneghetti, M.: Self-healing at the nanoscale. Nanoscale **1**, 74–88 (2009)
78. Diaz, M.M., Brancart, J., Van Assche, G., Van Mele, B.: Room-temperature versus heating-mediated healing of a Diels–Alder crosslinked polymer network. Polymer (Guildf) **153**, 453–463 (2018)
79. Peterson, A.M., Jensen, R.E., Palmese, G.R.: Room-temperature healing of a thermosetting polymer using the Diels−Alder reaction. ACS Appl. Mater. Interfaces **2**, 1141–1149 (2010)
80. Dello Iacono, S., Martone, A., Pastore, A., Filippone, G., Acierno, D., Zarrelli, M., et al.: Thermally activated multiple self-healing Diels–Alder epoxy system. Polym. Eng. Sci. **57**, 674–679 (2017)
81. Barbero, E.J., Barbero, J.C.: Analytical solution for bending of laminated composites with matrix cracks. Compos. Struct. **135**, 140–155 (2016)
82. Adumitroaie, A., Barbero, E.J., Schagerl, M.: Matrix cracking in non-symmetric laminates under combined membrane and flexural loading. Int. J. Mater. Mech. Manuf. **4**, 223–231 (2016)
83. Adumitroaie, A., Barbero, E.J.: Intralaminar damage model for laminates subjected to membrane and flexural deformations. Mech. Adv. Mater. Struct. **22**, 705–716 (2015)

84. Adolfsson, E., Gudmundson, P.: Thermoelastic properties in combined bending and extension of thin composite laminates with transverse matrix cracks. Int. J. Solids Struct. **34**, 2035–2060 (1997)
85. Adolfsson, E., Gudmundson, P.: Matrix crack initiation and progression in compositelaminatessubjected to bending and extension. Int. J. Solids Struct. **36**, 3131–3169 (1999)
86. Barbero, E.J., Greco, F., Lonetti, P.: Continuum damage-healing mechanics with application to self-healing composites. Int. J. Damage Mech. **14**, 51–81 (2005)
87. Barbero, E.J., Ford, K.J., Mayugo, J.A.: Modeling self-healing of fiber-reinforced polymer–matrix composites with distributed damage. Self-Healing Mater. (2009)
88. Voyiadjis, G.Z., Shojaei, A., Li, G.: A thermodynamic consistent damage and healing model for self healing materials. Int. J. Plast. **27**, 1025–1044 (2011)
89. Voyiadjis, G.Z., Shojaei, A., Li, G., Kattan, P.I.: A theory of anisotropic healing and damage mechanics of materials. Proc. R Soc. A Math. Phys. Eng. Sci. **468**, 163–183 (2012)
90. Cox, H.L.: The elasticity and strength of paper and other fibrous materials. Br. J. Appl. Phys. **3**, 72 (1952)
91. Aveston, J., Kelly, A.: Theory of multiple fracture of fibrous composites. J. Mater. Sci. **8**, 352–362 (1973)
92. Parvizi, A., Garrett, K.W., Bailey, J.E.: Constrained cracking in glass fibre-reinforced epoxy cross-ply laminates. J. Mater. Sci. **13**, 195–201 (1978)
93. Garrett, K.W., Bailey, J.E.: Multiple transverse fracture in 90 cross-ply laminates of a glass fibre-reinforced polyester. J. Mater. Sci. **12**, 157–168 (1977)
94. Manders, P.W., Chou, T.-W., Jones, F.R., Rock, J.W.: Statistical analysis of multiple fracture in 0/90/0 glass fibre/epoxy resin laminates. J. Mater. Sci. **18**, 2876–2889 (1983)
95. Steif, P.S.: Parabolic shear-lag analyses of a [0/90] s laminate. Transverse Ply Crack Growth Assoc Stiffness Reduct Dur Fatigue a Simple Crossply Laminate, pp. 40–1 (1984)
96. Ogin, S.L., Smith, P.A., Beaumont, P.W.R.: A stress intensity factor approach to the fatigue growth of transverse ply cracks. Compos. Sci. Technol. **24**, 47–59 (1985)
97. Ogin, S.L., Smith, P.A., Beaumont, P.W.R.: Matrix cracking and stiffness reduction during the fatigue of a (0/90) s GFRP laminate. Compos. Sci. Technol. **22**, 23–31 (1985)
98. Talreja, R., Singh, C.V.: Damage and Failure of Composite Materials. Cambridge University Press (2012)
99. Laws, N., Dvorak, G.J.: Progressive transverse cracking in composite laminates. J. Compos. Mater. **22**, 900–916 (1988)
100. Highsmith, A.L., Reifsnider, K.L.: Stiffness-reduction Mechanisms in Composite Laminates. Damage Composites Material basic Mechanics Accumulation, Toler. Charact., ASTM International (1982)
101. Fukunaga, H., Chou, T.-W., Peters, P.W.M., Schulte, K.: Probabilistic failure strength analyses of graphite/epoxy cross-ply laminates. J. Compos. Mater. **18**, 339–356 (1984)
102. Lim, S.G., Hong, C.S.: Prediction of transverse cracking and stiffness reduction in cross-ply laminated composites. J. Compos. Mater. **23**, 695–713 (1989)
103. Lee, J.-W., Daniel, I.M.: Progressive transverse cracking of crossply composite laminates. J. Compos. Mater. **24**, 1225–1243 (1990)
104. Lee, J.-W., Daniel, I.M., Yaniv, G.: Fatigue Life Prediction of Cross-ply Composite Laminates. Composite Materials Fatigue Fracture Second Vol., ASTM International (1989)
105. Tan, S.C., Nuismer, R.J.: A theory for progressive matrix cracking in composite laminates. J. Compos. Mater. **23**, 1029–1047 (1989)
106. Nuismer, R.J., Tan, S.C.: Constitutive relations of a cracked composite lamina. J. Compos. Mater. **22**, 306–321 (1988)
107. Flaggs, D.L.: Prediction of tensile matrix failure in composite laminates. J. Compos. Mater. **19**, 29–50 (1985)
108. Boniface, L., Ogin, S.L., Smith, P.A.: Strain energy release rates and the fatigue growth of matrix cracks in model arrays in composite laminates. Proc. R Soc. London Ser. A Math. Phys. Sci. **432**, 427–444 (1991)

Fundamentals of Thermal Conductivity in the Epoxy Polymer Network

Lalson Daniel Mathews and Nishar Hameed

Abstract In metals, the heat is carried predominantly by electrons. However, it is observed in polymers that the thermal conductivity is driven by lattice vibrations known as phonons. The thermal conductivity through an epoxy polymer is controlled by the state, structure, and orientation of the polymer chain network. Basic understanding of the thermal conductivity of epoxy resins is explained through Debye's theory and Fourier's law. The theories of correlation between thermal conductivity and thermal diffusivity, explanation of phonon transport in a 2D epoxy network, and electronic contribution of thermal conductivity in undoped polymers lay foundation to the topic of thermal conductivity in epoxy resins. The heat transfer through the epoxy resin is controlled by incorporating high thermal conductivity fillers to form composites, or, by the intrinsic modification of the epoxy nanostructure for improved crystallinity. The thermal degradation of epoxy polymer is proportionally dependant on the thermal conductivity. This chapter covers the basic theories of thermal conductivity, methods to improve thermal conductivity, factors influencing thermal conductivity, and effect of thermal conductivity in the thermal degradation of epoxy resins.

Keywords Epoxy resins · Thermal conductivity · Thermal diffusivity · Phonon transport · Lattice vibration

1 Introduction

Often, materials are designed so that they spread heat very effectively for applications such as heat exchangers and microelectronics. Conversely, thermal insulators are designed for applications such as building insulation materials and space shuttle tiles. In such applications, low or no thermal conductivity is preferred. High temperature generated at the integrated circuits and electron flow regions of electronic devices require high thermal conductivity materials to carry the heat away. Heat generated

L. D. Mathews · N. Hameed (✉)
School of Engineering, Swinburne University of Technology, Hawthorn, VIC 3122, Australia
e-mail: nisharhameed@swin.edu.au

N. Hameed et al. (eds.), *Multifunctional Epoxy Resins*, Engineering Materials,
https://doi.org/10.1007/978-981-19-6038-3_10

from the integrated circuits, especially those demanding ultra-fast processing requirements, has become a performance decelerator for micro-electronics. Miniaturisation of electronic devices further enhances the heat production due to the increased resistance causing fire hazard. Materials with high thermal conductivity and low electrical conductivity are suitable to carry the heat away from the electronics [1]. It has been proven that proper thermal management of the electronic devices will effectively improve its reliability and service life [2].

Epoxy resins are the commonly used electronic packaging material due to their excellent chemical resistance, mechanical, and fatigue properties [3], where excellent thermal conductivity is indispensable [4, 5]. However, the thermal conductivity coefficient (λ) of epoxy resin is very low at ~ 0.2 W m^{-1} K^{-1} [6] due to the amorphous state of the molecular chain. The heat management applications of thermally conductive epoxy resins are not constrained within the electronic industry. In a recent research, ultra-high thermal conductivity of epoxy composites using multi-dimensional fillers composed of micro- and nano-silver particles further treated with trace amount of MXene increased the thermal conductivity of epoxy resin to 72.7 W m^{-1} K^{-1} [7]. The improved fire retardancy of thermally conductive epoxy resins extends its potential application in building, construction, automotive, and aerospace.

A proper understanding of the theories of thermal conductivity in epoxy matrices, factors affecting thermal conductivity, and technique to improve thermal conductivity, and thermal degradation of epoxy resins is explained in this chapter.

1.1 Thermal Conductivity in Epoxy Resins

Thermal conductivity of polymers depends primarily on its morphology [8, 9]. Polymers exist in crystalline, semi-crystalline, amorphous, solid, melt, and glassy states [10]. Hence, thermal conduction through polymers cannot be expressed in one mechanism. Thermal conductivity is higher in crystalline polymers and lower in amorphous polymers. The thermal conductivity of epoxy resins—for that being an amorphous polymer—is relatively lower than crystalline polymers due to the lack of crystallinity in epoxy matrix. Scattering of the propagation of thermal energy caused by voids, entanglements, chain ends, and impurities reduces thermal conductivity in epoxy polymers [11, 12].

In a perfect crystal, the surface atoms exposed to thermal energy gain vibrational energy and propagate thermal energy through the sample by transferring the vibrational energy to the adjacent atom. The vibration is in the wave form and is called phonon. The enthalpy or energy of that system can be linked to the total amount of thermal motion and interaction on a microscopic level [13]. It is important to understand the significance of thermodynamics of polymers where heat capacity is brought into account. Heat capacity for any polymer is a heat dependant quantity. Heat capacity is defined as the heat required to change its temperature by one degree. For an accurate useful quantity, specific heat capacity at constant pressure (C_P) is defined as the amount of heat required to increase the temperature of a material of

unit mass by 1 K or 1 °C at constant pressure. This is presented by Eq. (1)

$$C_P = \Delta Q / m \Delta T \tag{1}$$

where ΔQ is the heat required in Jules, m is the mass of the sample, and ΔT is the increase in temperature in K or °C. Heat capacity of a polymer is usually measured using differential scanning calorimetry or adiabatic calorimetry [10].

Heat capacity of a solid is largely contributed from atomic and molecular vibrations. This is presented by equation (2) below [14].

$$C_V = k \frac{\int_0^\infty \left(\frac{hv}{kT}\right)^2 e^{-\frac{hv}{kT}} g(v) dv}{\left(1 - e^{-\frac{hv}{kT}}\right)^2} \tag{2}$$

where k is Boltzmann's constant, h is Planck's constant, v is the frequency of oscillation, T is temperature, and $g(v)$ represents the vibrational density of states.

Majority of the basic theories of the thermal conductivity of epoxy resins is based on the heat capacity of the system.

2 Basic Theories of Thermal Conductivity in Epoxy Networks

The difference between temperature and heat is often misconceived. Temperature is the measure of the vibration of microscopic particles in a system that generates thermal energy. Heat is the transfer of thermal energy (vibration energy) from one part of the body to the other or to the adjacent body because of difference in temperature. In solids, heat transfer can occur through thermal conduction, convection, or radiation [1]. Thermal conductivity is the relationship between heat flux and thermal gradient. The mechanism of thermal conductivity is different for crystalline and amorphous solids. In a steady state system, the amount of heat conducted per unit time—heat flux—is proportional to the product of temperature gradient, area of the material, and thermal conductivity.

In the microscopic level of a solid, the atoms arranged in a regular structure, called lattice, will be on constant vibration about the equilibrium position when it is above the absolute zero temperature. The vibration increases proportionally with temperature. A quantum of vibrational energy associated with a particular normal mode is known as a phonon. In conjunction with this, there are free electrons which are travelling in random direction through solid. Heat transfer can occur through any of these interactions, such as lattice vibrations (phonons), electron–electron interaction, or electron lattice interaction.

The main contributing component of thermal conductivity in polymers is phonons. Phonon contribution for the thermal conductivity is high in polymers with strongly

bonded linearly arranged polymer chains. Electronic contribution for the thermal conductivity of a polymer is negligibly low.

2.1 Phonon Contribution of Thermal Conductivity in Epoxy Resins

Thermal conductivity is predominantly caused by phonon transport in polymers. Study of phonons is an important part of thermal conductivity research especially in condensed matter physics. Rate of heat transfer in polymers depends on three factors, area, length, and temperature difference at either end of the conductor. Fourier's law of heat conduction connects the relationship between these three variables.

2.1.1 Debye's Theory

The history of the concept of thermal conductivity and heat capacity in classical and quantum mechanics interestingly advances with filling the gaps. In 1907, Einstein proposed a model of a crystalline solid that contains large number of independent three-dimensional quantum harmonic oscillators. Einstein solid model can accurately predict heat capacity at high temperatures but failed to explain specific heat at lower temperature because all oscillations have one common frequency and specific heat value at lower temperature fast approaches to zero. In 1912, Peter Debye developed a model that treats atomic lattice vibration as particle in a box which treats the solid as individual, non-interacting quantum harmonic oscillators. Debye modelled the vibrations as the normal mode vibrations of a continuous elastic body [12]. Debye model accurately predicts low temperature dependence of heat capacity and is given by the equation

$$k(T) = \frac{1}{3} \sum_{j} \int C_j(\omega) v_j l_{j(\omega)} d\omega \tag{3}$$

where $C_j(\omega)$ is the specific heat of phonons with branch index j and frequency ω, v_j is the group velocity of the phonons, and $l_{j(\omega)}$ is the mean free path.

The simplified Debye's equation will be $\lambda = \frac{1}{3} c_v u l$ where λ is the thermal conductivity, c_v is the volumetric heat capacity, u is the velocity, and l is the mean free path of phonon [15].

A phonon is the normal mode energy quantum of vibration lattice energy and is analogous to photon. The quantisation of energy becomes important when a polymer reaches characteristic Debye temperature. The normal vibrations with certain frequency, direction of the wave vector, and polarization are excited with possible oscillations [16].

2.1.2 Fourier's Law of Heat Conduction

The area of conductor (A) is directly proportional to the rate of heat transfer (Q). This is because more electrons and atoms can participate in heat transfer. The length of conductor (L) is inversely proportional to the rate of heat transfer due to the higher chance of collision. The temperature difference (ΔT) between the objects is directly proportional the rate of heat transfer. A higher temperature difference results in vigorous heat transfer compared to a lower temperature difference. This relationship is plotted in (4).

$$Q \propto A(T_2 - T_1)/L \tag{4}$$

This proportionality relationship is converted into an equation by introducing a constant called the coefficient of thermal conductivity (K). The unit of K is watts per metre kelvin (W/mK).

$$Q = -K\,A(T_2 - T_1)/L$$

or it can also be represented as

$$Q = -K\,A\frac{\Delta T}{\Delta x}$$

This relationship is known as Fourier's law of heat conduction. The negative value is a correction factor for the direction of the heat flow; T_1 and T_2 are the temperatures at the colder and hotter regions of the conductor, respectively, and Δx is the thickness of the specimen.

2.2 *Electronic Contribution of Thermal Conductivity in Epoxy Resins*

Thermal conductivity of solids (K), especially metals, are well described by the movement of free electrons (K_e). Metals have the benefits of crystalline structure and delocalised free electrons to participate in thermal conductivity. In metals, atoms are bonded by metallic bonding where electrons are not bound to a particular atom. The electron sea model of metallic bonding describes this criterion clearly. These free delocalised charge carriers participate in the heat flow. Simultaneously, the lattice vibration—phonons—(K_p) contributes to the thermal conductivity as an independent entity. The overall thermal conductivity of metals, in general, solids consist of electronic contribution and phonon contribution [17, 18].

$$K = K_e + K_p$$

In metals, the phonon contribution to the thermal conductivity is negligibly low, i.e.,

$$K \approx K_e$$

However, in polymers, thermal conductivity caused by movement of electrons is insignificant due to the absence of free electrons except for doped polymers that contains polarons and free charge carriers [19]. The electronic contribution for thermal conductivity is significant compared to undoped polymers. Polaronic conduction through polymers is equated to electronic conduction through metals, and hence, the Wiedemann–Franz law for thermal conductivity in metals is applicable to polymers [20]. In 1853, Wiedemann and Franz reported that thermal conductivity of metals at room temperature is proportional to electrical conductivity [21, 22]. The law is represented by equation $Ke = \left(\frac{kb}{e}\right)^2 L\sigma T$, where kb is the Boltzmann constant, e is the elemental charge, and L is the Lorenz factor. The validity of Wiedemann and Franz has been in question due to the lack of theoretical understanding and challenges in thermal conductivity measurements of conducting polymers [23]. In general, a good electronic conductor is a good heat conductor.

2.3 Thermal Conductivity and Thermal Diffusivity

Thermal diffusivity is the measure of the rate of heat transfer to achieve equilibrium. It is the heat conducted away from the material to the heat stored in the material [24]. In a homogenous body, thermal conductivity λ and thermal diffusivity a are interrelated by specific density ρ and specific heat capacity C_P as per the equation below. Thermal diffusivity is the measure of rate of heat transfer to achieve equilibrium [25].

$$\lambda = aC_P\rho \tag{5}$$

Thermal diffusivity in epoxy polymers is measured by transient methods related to laser flash analysis [26]. The specimen is heated by the laser flash, and the diffused heat from the specimen is measured by infrared radiation sensor. The instrument set-up is illustrated in [27] (Fig. 1).

Assuming there is no heat loss, the normalised temperature increase on the bottom side is given by the equation below.

$$V = 1 + 2\sum_{n=1}^{\infty}(-1)^n \exp\left(-n^2\right)\omega$$

where $\omega = \pi^2\alpha t/L^2$, $V = T/T_{\mathrm{m}}$ which is the dimensionless temperature increase of the rear face, T, instantaneous temperature increase of the rear face of the specimen; $T_{\mathrm{m}} = Q/\rho c_{\mathrm{p}}L$ which is the maximum temperature increase of the rear face, Q, input

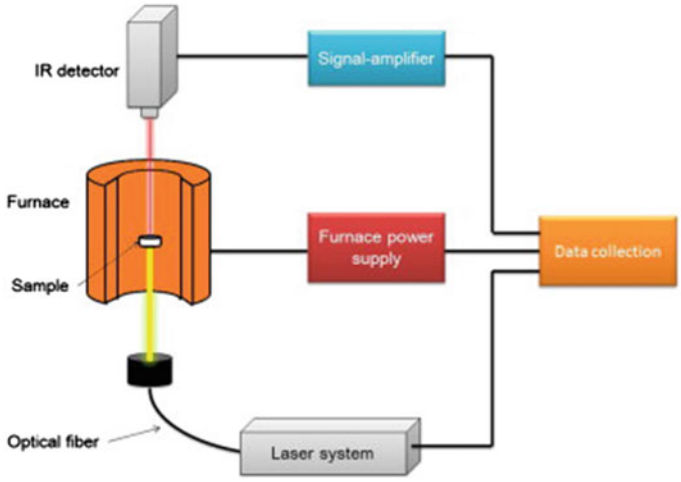

Fig. 1 Laser flash analysis instrument schematic diagram [27]. (Reproduced with permission from Elsevier Ltd.)

energy on the front face; ρ, density; c_p, specific heat; L, specimen length; t, time; and α, thermal diffusivity [28].

2.4 Phonon Mean Path

A fundamental understanding of thermal transport in 2D materials and its epoxy composites is obtained by analysing the phonon mean free path (MFP). Phonon mean free path is the average travelling distance between two consecutive phonon scattering events [29]. The phonon MFP is affected by scattering of phonon by an impurity, phonon–phonon scattering, and/or phonon boundary scattering. The effective mean free path $\left(l_{eff}\right)$ of phonon scattering can be expressed as

$$\frac{1}{l_{eff}} = \frac{1}{l_{p-p}} + \frac{1}{l_{p-b}}$$

where l is the phonon mean free path, and the subscripts $p - p$ and $p - b$ are the phonon–phonon and phonon-boundary scattering [30]. Dynamic scattering is caused by the inharmonic vibration of the molecules and static scattering is caused by defects [31].

In epoxy composites, phonon scattering at the boundaries is explained based on kinetic theory of phonon transport. According to the kinetic theory of phonon transport, thermal conductivity K is given by

$$K \sim \sum_i C_i v_i l_i$$

where C_i is the specific heat, v_i is the group velocity, and l_i is the mean free path of the phonon in mode i with angular frequency ω.

Therefore, the effective mean free path l_{eff} is determined as [32]

$$l_{eff} = \sum_i C_i v_i$$

3 Methods to Improve Thermal Conductivity in Epoxy Resins

Formulating epoxy composites with highly thermally conductive metallic or inorganic materials is a modest method to improve thermal conductivity of epoxy resins. The intrinsic thermal conductivity of the filler contributes to the enhanced thermal conductivity of the epoxy composite with that filler. Unfortunately, adding high content of the fillers in most cases destroys the flexibility, failure strength, and processability of the epoxy resin mainly due to high interfacial thermal resistance [33, 34]. Moreover, despite the highest loading levels, the thermal conductivity of the composites will never reach the individual thermal conductivity of the filler. Another commonly used method to improve thermal conductivity of epoxy resin is the molecular re-designing of epoxy matrix to synthesise intrinsically modified thermally conductive epoxy resins. Introducing liquid crystal units to the molecular structure is a widely used idea [35, 36]. This places molecular chain orientation in order, for a continuous heat transfer through the matrix [37].

3.1 By Forming Epoxy Composites

Generating effective three-dimensional thermal conduction pathways in epoxy matrix gives rises to increased thermal conductivity of epoxy resins. Various types of thermally conductive nano-fillers such as graphene, graphite, boron nitride, carbon nanotubes, metal powder, aluminium nitride, ceramic particles, cellulose nanofiber [38–46], and filler combinations [40, 47, 48] were studied in this region with significant thermal conductivity improvements. Figure 2 illustrates the synergistic effect of multi-particle composite system of epoxy matrix where micro-silver, nano-silver, MXene, and graphene work together to create a bridging effect that creates a continuous path for heat transfer between particles [7].

The high intrinsic thermal conductivity of the fillers enhances the overall thermal conductivity of the epoxy matrix by forming a continuous three-dimensional thermal

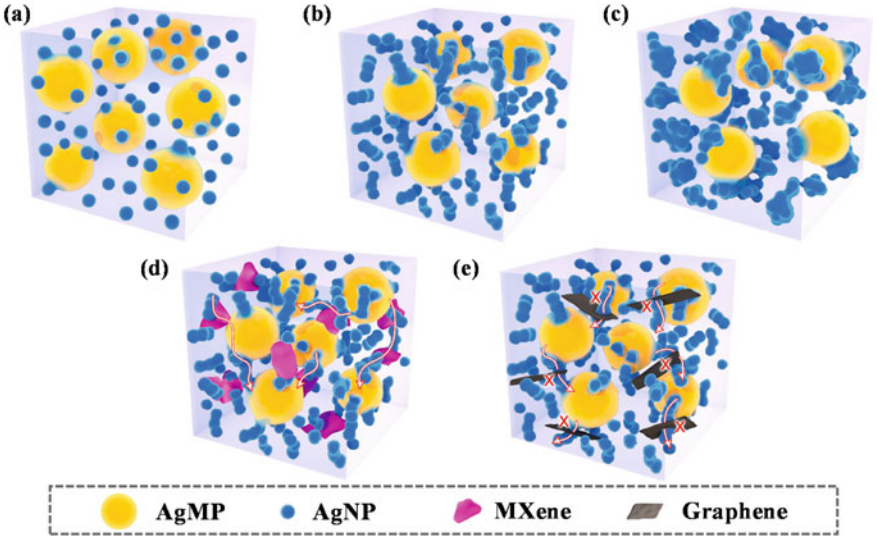

Fig. 2 Schematic figure of microstructural characteristics of composites. **a–c** The Ag/epoxy composites with an increment of AgNP. **d** The MXene/AgMP/AgNP composite. **e** The graphene/AgMP/AgNP composites [7]. (Reproduced with permission from Elsevier Ltd.)

pathway for heat transfer. In polymer composites, the thermal conductivity is determined by the thermal conductivity of the filler matrix [49, 50].

Interfacial thermal resistance is one important drawback of epoxy composites where phonon scattering causing rapid accumulation of heat inside the composite, reducing its stability [51, 52]. Similarly, excessive addition of fillers will not adequately improve the overall thermal conductivity of the composite over a certain point and large quantity of fillers will deteriorate the mechanical properties of the composite [53].

The filler aspect ratio, dimensions, and surface are important parameters that affect the resultant composite. Filler alignment and direction in the epoxy matrix also affect the overall thermal conductivity of the composite. Transfer of thermal conductivity at the filler-matrix is the biggest challenge that needs resolution to achieve superior thermal conductivity in polymer composites [54].

The thermal conductivity of a composite is explained by several models and equations. Maxwell model explains the composites with spherical filler and low volume fraction. Rayleigh model includes analytical expression for thermal conductivity of continuous matrix reinforced with parallel cylindrical fibres arranged in uniaxial simple cubic array. Hasselman–Johnson model states that the effective thermal conductivity of a composite depends not only on filler volume but particle size as well. The bruggeman theory gives formula for multicomponent systems in addition to the two components system.

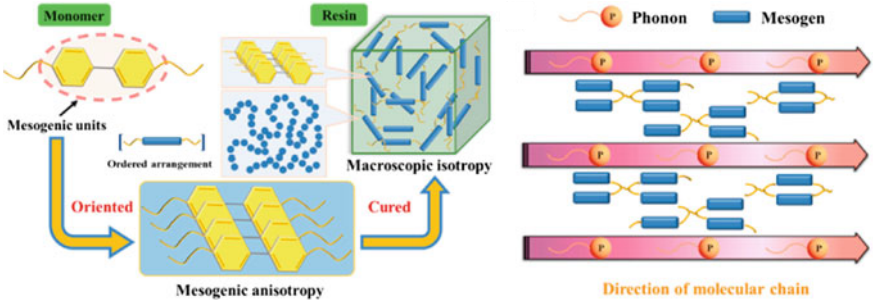

Fig. 3 Schematic diagram phase arrangement and heat flow transfer in liquid crystal epoxy [59]. (Reproduced with permission from Elsevier Ltd.)

3.2 By Intrinsic Modification of Thermal Conductivity in Epoxy

Designing and modification of the epoxy molecular chain structure and orientation, to introduce crystalline characteristics to the naturally amorphous epoxy matrix, has widely become a popular topic in recent years. This method successfully eliminates many issues caused by the filler enhanced thermal conductivity of epoxy composites.

Liquid crystal epoxy resins are an important thermosetting polymer in this category. They are formed by curing liquid crystal epoxy monomers containing rigid rod-shaped mesogens, special flexible segments, and epoxy end groups [36, 55]. A highly ordered mesogen structure shows high thermal conductivity [56]. The liquid crystal epoxy resins form partial crystal-like structure so that the heat flow is conducted along the molecular chain direction which inhibits the scattering of phonons. The thermal conductivity of the liquid crystal epoxy resins can be further improved by preparing its composites by the addition of fillers [35, 57]. The highly aligned microstructure in the liquid crystal gives the composite high thermal conductivity [58]. Figure 3 is a schematic representation of phase arrangement and heat flow transfer in liquid crystal epoxy.

4 Factors Influencing Thermal Conductivity of Epoxy Polymers

4.1 Radius of Gyration—Amorphous State

The amorphous structure intensifies the phonon scattering resulting in lower thermal conductivity of epoxy resins [15]. The ratio of the thickness dz to the radius of gyration R_g of a polymer film is known as the chain coefficient indicator dz/R_g.

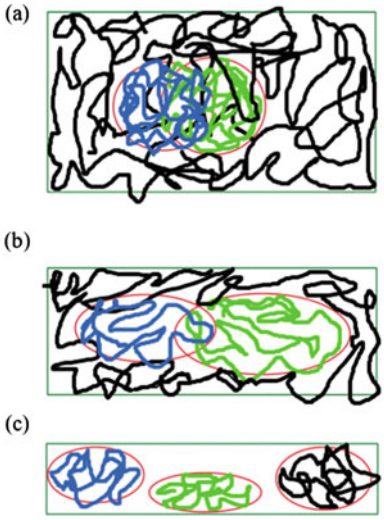

Fig. 4 Schematics of the chain structure as *dz*/*Rg* decreases. **a** Large *dz*/*Rg*, polymer chains entangle with each other; **b** Middle *dz*/*Rg*, polymer chains have less overlap; and **c** Small *dz*/*Rg*, polymer chains are isolated (limiting case) [60]. (Reproduced with permission from AIP publishing)

Thermal conductivity increases linearly with chain coefficient indicator for amorphous polymer films. Larger radius of gyration improves the thermal conductivity of amorphous polymer films by providing more space for heat transfer. Strongly confined and less entangled polymer chains in amorphous polymers will increase the thermal conductivity (Fig. 4) [60, 61].

4.2 High-Order Structure—Crystalline State

Phonon scattering caused by microscopic anisotropy reduces the thermal conductivity in epoxy polymers. In an anisotropic cross-linked polymer, thermal conductivity will also be anisotropic. Thermal conductivity values through the molecular chain direction could be higher than those of perpendicular direction [62]. The macroscopic isotropy can be achieved by the use of liquid crystal epoxy resins (LCEs) by disordering the domains of the crystal-like structure that is linked with the internal amorphous structure through covalent bond. This high order structure will suppress phonon scattering and enable the resin with high thermal conductivity. High density of covalent bonds and packaging of mesogenic groups lead to high thermal conductivity [63]. The covalent network of mesogenic epoxy can trap thermally conductive phase change material, polyethylene glycol, to achieve a homogenous solid state [64]. Formation of spherulites on the mesogenic resins enhances thermal conductivity by suppressing phonon scattering. Adjusting the initial curing temperature will have effect on the formation of larger spherulite structures further enhancing the thermal conductivity [15, 65, 66]. The spontaneous orientation of LCEs can be achieved by designing the molecules of LCE bringing diglycidyl moieties at the side position of the molecule to maintain the orientation after thermal curing [67].

4.3 Polymer Chain Orientation

The random chain orientation in amorphous epoxy polymers reduces the phonon mean path causing phonon scattering [68]. The orientation of epoxy molecular micro-chain in an ordered structure maximises the thermal conductivity path. Polymer chain can be oriented by applying external forces such as electrical, magnetic, or mechanical at low viscosity states [69, 70].

In epoxy composites, the thermal conductivity along the filler orientation increases the thermal conductivity of the composite [71]. However, the interfacial thermal resistance between the filler and the polymer matrix remains large. The interfacial thermal resistance (R_{int}) is defined as the ratio of temperature discontinuity ΔT occurring at the interface to the heat rate Q per unit area A flowing across the interface between two phases in contact [72, 73] and is given by the equation

$$R_{int} = \frac{\Delta T}{Q/A}$$

In epoxy composites, interfacial thermal resistance is caused by the lack of continuous thermal conductive paths between the polymer matrix and fillers [74]. Poor interfacial adhesion creates voids between the filler and epoxy matrix [75], whereas improved interfacial affinity between the filler and epoxy matrix decreases the resistance and reduces the number of voids in the composite [76] resulting in high thermal conductivity. The interfacial compatibility between filler and epoxy matrix requires effective methods that ensures a strong interfacial bonding [77]. The polymer–filler interfacial adhesion can be improved by modification [78] or functionalisation of the filler to generate or enhance van der Waals interaction or hydrogen bonding between the binder and the filler [79]. Functionalisation of the fillers will increase the thermal conductivity of the composite by reducing interfacial thermal resistance even though the intrinsic thermal conductivity of the filler itself is negatively affected by the functionalisation. Uniform dispersion and close contact of the fillers reduces the interfacial thermal resistance and provide a continuous thermal pathway. Unfortunately, some of the modification methods such as strong acid etching or high temperature ablation will destroy the crystal structure of the filler resulting in reduced thermal conductivity [80].

5 Thermal Degradation and Thermal Conductivity of Epoxy Polymer

Thermal degradation of a polymer is influenced by heat and may undergo either chain end degradation mechanism or random degradation mechanism. The chain end degradation mechanism results in generating monomers of the original polymer, whereas the random degradation mechanism results in producing smaller polymer

with a lower molecular weight. Thermal degradation mainly depends on the stability of carbon–carbon bond, substituent atoms on the carbon, presence of aromatic ring or oxygen in the polymer backchain, and formation of free radicals by breaking of the substituent groups on a polymer chain. A polymer with highly stable carbon–carbon bonds with high dissociation energy will have high thermal stability. When hydrogen atoms in a polymer chain is replaced with highly electronegative atoms such as fluorine, the polymer becomes thermally stable. Presence of aromatic rings increases the thermal stability of a polymer, whereas presence of oxygen decreases the thermal stability of a polymer. Thermal degradation or thermal stability of a polymer depends on the heat conducting properties of the polymer. As a matter of fact, thermal stability of a polymer increases proportionally with thermal conductivity.

The concept of reactive block copolymers where reactive groups are incorporated to promote covalent linkage with epoxy network in the resulting blend improves the thermal stability of the epoxy thermoset [81]. The ordered connections with covalent bond encourage efficient phonon transport [82]. The thermoset epoxy polymers when cross linked with ionic liquid system can also deliver flexible thermal behaviour. The material becomes soft and flexible when heated up to a certain temperature without thermal degradation [83].

6 Conclusion

The basic theories of thermal conductivity of epoxy resins have historically been revised to accommodate previously unidentified challenges. Based on those theories, several techniques have been evolved to improve the thermal conductivity of epoxy resins. Composites of epoxy resins prepared by inserting highly thermally conductive nanoparticles has gained popularity in research and application due to the variety of nanomaterials incorporated in the epoxy matrix resulting excellent improvement in thermal conductivity. Molecular chain modification and the use of mesogens such as liquid crystal epoxy significantly added crystallinity to the naturally amorphous epoxy structure. This change in the molecular chain significantly enhanced the heat transfer through the epoxy chain due to the reduced phonon scattering.

To expand the field of application for thermally conductive epoxy resins, the current state of molecular level nano-engineering should be expanded to address issues such as interfacial thermal resistance, deteriorated mechanical properties, failure strength, and processability. It is evident that the interfacial thermal resistance causes lack of continuous path for heat transport. Addressing these issues with the help of machine learning and numerical simulations will fast track the process when ultra-high thermal conductivity is targeted for epoxy resins. Thermal conductivity fostering fire retardancy of epoxy resins is identified as an appropriate characteristic improvement in fire retardant epoxy applications. Heat carried away from the surface of an epoxy coating is deemed ideal for fire retardant structural coating applications. Considering the definite application environment, the thermal conductivity of epoxy resins shall be a major research topic for years ahead.

Acknowledgements The authors acknowledge the Faculty of Science, Engineering and Technology (FSET) of Swinburne University of Technology Melbourne for the financial support provided to the first author, having been awarded a masters by research studentship; and research grants from the Australian Research Council for the ARC DECRA (DE170101249).

References

1. Li, J., et al.: New underfill material based on copper nanoparticles coated with silica for high thermally conductive and electrically insulating epoxy composites. J. Mater. Sci. **54**(8), 6258–6271 (2019)
2. Li, Z., et al., Effect of hexagonal-boron nitride/epoxy and BNNS/epoxy composite materials on the reliability of flip chip. J. Electronic Packaging. **144**(3) (2021)
3. Chen, H., et al.: Thermal conductivity of polymer-based composites: fundamentals and applications. Prog. Polym. Sci. **59**, 41–85 (2016)
4. Ammous, A., et al.: Developing an equivalent thermal model for discrete semiconductor packages. Int. J. Therm. Sci. **42**(5), 533–539 (2003)
5. Lu, T.: Thermal management of high power electronics with phase change cooling. Int. J. Heat Mass Transf. **43**(13), 2245–2256 (2000)
6. Guo, Y., et al.: Factors affecting thermal conductivities of the polymers and polymer composites: a review. Compos. Sci. Technol. **193**, 108134 (2020)
7. Wang, D., et al.: Achieving ultrahigh thermal conductivity in Ag/MXene/epoxy nanocomposites via filler-filler interface engineering. Compos. Sci. Technol. **213**, 108953 (2021)
8. Zhang, T., Wu, X., Luo, T.: Polymer nanofibers with outstanding thermal conductivity and thermal stability: fundamental linkage between molecular characteristics and macroscopic thermal properties. J. Phys. Chem. C **118**(36), 21148–21159 (2014)
9. Zhang, T., Luo, T.: Morphology-influenced thermal conductivity of polyethylene single chains and crystalline fibers. J. Appl. Phys. **112**(9), 094304 (2012)
10. Wen, J.: Heat capacities of polymers. In: Physical Properties of Polymers Handbook, pp. 145–154. Springer (2007)
11. Shen, S., et al.: Polyethylene nanofibres with very high thermal conductivities. Nat. Nanotechnol. **5**(4), 251–255 (2010)
12. Xu, X., et al.: Thermal conductivity of polymers and their nanocomposites. Adv. Mater. **30**(17), 1705544 (2018)
13. Wunderlich, B.: Heat capacity of polymers. Handb. Therm. Anal. Calorim. **3**, 1–47 (2002)
14. Schliesser, J.M., Woodfield, B.F.: Development of a Debye heat capacity model for vibrational modes with a gap in the density of states. J. Phys.: Condens. Matter. **27**(28), 285402–285402 (2015)
15. Akatsuka, M., Takezawa, Y.: Study of high thermal conductive epoxy resins containing controlled high-order structures. J. Appl. Polym. Sci. **89**(9), 2464–2467 (2003)
16. Zorin, V.A., Baurova, N.I., Kosenko, E.A.: Analysis of the influence of quantum-mechanical processes on the possibilities of determining the low degree of curing a binder when molding products from polymer composite materials. Polym. Sci., Ser. D **11**(3), 334–338 (2018)
17. Uher, C., Thermal conductivity of metals. In: Tritt, T.M. (ed.) Thermal Conductivity: Theory, Properties, and Applications, pp. 21–91. Springer US, Boston, MA (2004)
18. Ho, C.Y., Powell, R.W., Liley, P.E.: Thermal conductivity of the elements: a comprehensive review (1974)
19. Heeger, A.J.: Semiconducting and metallic polymers: the fourth generation of polymeric materials (Nobel lecture). Angew. Chem. Int. Ed. **40**(14), 2591–2611 (2001)
20. Goel, M., Thelakkat, M.: Polymer thermoelectrics: opportunities and challenges. Macromolecules **53**(10), 3632–3642 (2020)

21. Kumar, G.S., Prasad, G., Pohl, R.O.: Experimental determinations of the Lorenz number. J. Mater. Sci. **28**(16), 4261–4272 (1993)
22. Wiedemann, G., Franz, R.: Relative conductivity of solids. Ann. Phys. Chemie. **89**, 497–531 (1853)
23. Weathers, A., et al.: Significant electronic thermal transport in the conducting polymer poly(3,4-ethylenedioxythiophene). Adv. Mater. **27**(12), 2101–2106 (2015)
24. Lokanathan, M., et al.: Review of nanocomposite dielectric materials with high thermal conductivity. Proc. IEEE **109**(8), 1364–1397 (2021)
25. Weidenfeller, B., Höfer, M., Schilling, F.R.: Thermal conductivity, thermal diffusivity, and specific heat capacity of particle filled polypropylene. Compos. A Appl. Sci. Manuf. **35**(4), 423–429 (2004)
26. Parker, W., et al.: Flash method of determining thermal diffusivity, heat capacity, and thermal conductivity. J. Appl. Phys. **32**(9), 1679–1684 (1961)
27. Wu, Y., Yu, Z.: Thermal conductivity of in situ epoxy composites filled with ZrB2 particles. Compos. Sci. Technol. **107**, 61–66 (2015)
28. Nunes dos Santos, W., Mummery, P., Wallwork, A.: Thermal diffusivity of polymers by the laser flash technique. Polym. Test. **24**(5), 628–634 (2005)
29. Zeng, L., et al.: Measuring phonon mean free path distributions by probing quasiballistic phonon transport in grating nanostructures. Sci. Rep. **5**(1), 17131 (2015)
30. Chen, J., Li, L.: Thermal conductivity of graphene oxide: a molecular dynamics study. JETP Lett. **112**(2), 117–121 (2020)
31. Li, M., et al.: Nonperturbative quantum nature of the dislocation–phonon interaction. Nano Lett. **17**(3), 1587–1594 (2017)
32. Lin, S., Buehler, M.J.: Thermal transport in monolayer graphene oxide: atomistic insights into phonon engineering through surface chemistry. Carbon **77**, 351–359 (2014)
33. Liu, J., et al.: High thermal conductive epoxy based composites fabricated by multi-material direct ink writing. Compos. A Appl. Sci. Manuf. **129**, 105684 (2020)
34. Ruan, K., et al.: Interfacial thermal resistance in thermally conductive polymer composites: a review. Compos. Commun. **22**, 100518 (2020)
35. Tanaka, S., et al.: Formation of liquid crystalline order and its effect on thermal conductivity of AlN/liquid crystalline epoxy composite. Polym.-Plast. Technol. Eng. **57**(4), 269–275 (2018)
36. Ruan, K., et al.: Liquid crystal epoxy resins with high intrinsic thermal conductivities and their composites: a mini-review. Mater. Today Phys. **20**, 100456 (2021)
37. Zhong, X., et al.: Discotic liquid crystal epoxy resins integrating intrinsic high thermal conductivity and intrinsic flame retardancy. Macromol. Rapid Commun. **43**(1), 2100580 (2022)
38. Xu, Y., Chung, D.D.L., Mroz, C.: Thermally conducting aluminum nitride polymer-matrix composites. Compos.—Part A: Appl. Sci. Manufact. **32**(12), 1749–1757 (2001)
39. Wong, C.P., Bollampally, R.S.: Thermal conductivity, elastic modulus, and coefficient of thermal expansion of polymer composites filled with ceramic particles for electronic packaging. J. Appl. Polym. Sci. **74**(14), 3396–3403 (1999)
40. Yang, X., et al.: Synchronously improved electromagnetic interference shielding and thermal conductivity for epoxy nanocomposites by constructing 3D copper nanowires/thermally annealed graphene aerogel framework. Compos. Part A: Appl. Sci. Manuf. **128** (2020)
41. Thostenson, E.T., Chou, T.W.: Processing-structure-multi-functional property relationship in carbon nanotube/epoxy composites. Carbon **44**(14), 3022–3029 (2006)
42. Hu, J., et al.: Polymer composite with improved thermal conductivity by constructing a hierarchically ordered three-dimensional interconnected network of BN. ACS Appl. Mater. Interfaces. **9**(15), 13544–13553 (2017)
43. Zeng, X., et al.: Ice-templated assembly strategy to construct 3D boron nitride nanosheet networks in polymer composites for thermal conductivity improvement. Small **11**(46), 6205–6213 (2015)
44. Mamunya, Y.P., et al.: Electrical and thermal conductivity of polymers filled with metal powders. Eur. Polymer J. **38**(9), 1887–1897 (2002)

45. Chen, J., et al., Cellulose nanofiber supported 3D interconnected BN nanosheets for epoxy nanocomposites with ultrahigh thermal management capability. Adv. Funct Mater. **27**(5) (2017)
46. Biercuk, M.J., et al.: Carbon nanotube composites for thermal management. Appl. Phys. Lett. **80**(15), 2767–2769 (2002)
47. Im, H., Kim, J.: Thermal conductivity of a graphene oxide-carbon nanotube hybrid/epoxy composite. Carbon **50**(15), 5429–5440 (2012)
48. Yu, A., et al.: Enhanced thermal conductivity in a hybrid graphite nanoplatelet— arbon nanotube filler for epoxy composites. Adv. Mater. **20**(24), 4740–4744 (2008)
49. Meng, L., Fu, C., Lu, Q.: Advanced technology for functionalization of carbon nanotubes. Prog. Nat. Sci. **19**(7), 801–810 (2009)
50. Wang, Z., et al., Thermal conductivity improvement of epoxy composite filled with expanded graphite. Ceram. Int. **41**(10, Part A), 13541–13546 (2015)
51. Feng, C.-P., et al.: Recent advances in polymer-based thermal interface materials for thermal management: a mini-review. Compos. Commun. **22**, 100528 (2020)
52. Gu, J., Ruan, K.: Breaking through bottlenecks for thermally conductive polymer composites: a perspective for intrinsic thermal conductivity, interfacial thermal resistance and theoretics. Nano-Micro Lett. **13**(1), 1–9 (2021)
53. Song, P., et al.: Lightweight, flexible cellulose-derived carbon aerogel@ reduced graphene oxide/PDMS composites with outstanding EMI shielding performances and excellent thermal conductivities. Nano-micro Lett. **13**(1), 1–17 (2021)
54. Burger, N., et al.: Review of thermal conductivity in composites: mechanisms, parameters and theory. Prog. Polym. Sci. **61**, 1–28 (2016)
55. Barclay, G., et al.: Liquid crystalline epoxy thermosets based on dihydroxymethylstilbene: synthesis and characterization. J. Polym. Sci., Part A: Polym. Chem. **30**(9), 1831–1843 (1992)
56. Giang, T., Kim, J.: Effect of backbone moiety in diglycidylether-terminated liquid crystalline epoxy on thermal conductivity of epoxy/alumina composite. J. Ind. Eng. Chem. **30**, 77–84 (2015)
57. Lu, Y., et al.: Thermal and phase transformation behavior of epoxy-functional graphene oxide/liquid crystalline epoxy composite. Polym. Compos. **39**(S3), E1391–E1397 (2018)
58. Giang, T., Kim, J.: Effect of liquid-crystalline epoxy backbone structure on thermal conductivity of epoxy–alumina composites. J. Electron. Mater. **46**(1), 627–636 (2017)
59. Yang, X., et al.: High-efficiency improvement of thermal conductivities for epoxy composites from synthesized liquid crystal epoxy followed by doping BN fillers. Compos. B Eng. **185**, 107784 (2020)
60. Ma, H., Tian, Z.: Effects of polymer chain confinement on thermal conductivity of ultrathin amorphous polystyrene films. Appl. Phys. Lett. **107**(7), 073111 (2015)
61. Zhang, T., Luo, T.: Role of chain morphology and stiffness in thermal conductivity of amorphous polymers. J. Phys. Chem. B **120**(4), 803–812 (2016)
62. Hammerschmidt, A., Geibel, K., Strohmer, F.: In situ photopolymerized, oriented liquid-crystalline diacrylates with high thermal conductivities. Adv. Mater. **5**(2), 107–109 (1993)
63. Tang, N., et al.: Highly anisotropic thermal conductivity of mesogenic epoxy resin film through orientation control. J. Appl. Polym. Sci. **138**(47), 51396 (2021)
64. Luo, F., et al.: Highly thermally conductive phase change composites for thermal energy storage featuring shape memory. Compos. A Appl. Sci. Manuf. **129**, 105706 (2020)
65. Song, S.-H., Katagi, H., Takezawa, Y.: Study on high thermal conductivity of mesogenic epoxy resin with spherulite structure. Polymer **53**(20), 4489–4492 (2012)
66. Jeong, I., et al.: Liquid crystalline epoxy resin with improved thermal conductivity by intermolecular dipole–dipole interactions. J. Polym. Sci., Part A: Polym. Chem. **57**(6), 708–715 (2019)
67. Kim, Y., et al.: Highly thermal conductive resins formed from wide-temperature-range eutectic mixtures of liquid crystalline epoxies bearing diglycidyl moieties at the side positions. Polym. Chem. **8**(18), 2806–2814 (2017)
68. Anderson, D.: Thermal conductivity of polymers. Chem. Rev. **66**(6), 677–690 (1966)

69. Koerner, H., Ober, C.K., Xu, H.: Probing electric field response of LC thermosets via time-resolved X-ray and dielectric spectroscopy. Polymer **52**(10), 2206–2213 (2011)
70. Kang, D.-G., et al.: Heat transfer organic materials: robust polymer films with the outstanding thermal conductivity fabricated by the photopolymerization of uniaxially oriented reactive discogens. ACS Appl. Mater. Interfaces. **8**(44), 30492–30501 (2016)
71. Guo, H., et al.: Highly thermally conductive 3d printed graphene filled polymer composites for scalable thermal management applications. ACS Nano **15**(4), 6917–6928 (2021)
72. Swartz, E.T., Pohl, R.O.: Thermal boundary resistance. Rev. Mod. Phys. **61**(3), 605 (1989)
73. Karol, P., Tomasz, S.W.: A review of models for effective thermal conductivity of composite materials. J. Power Technol. **95**(1), 14 (2015)
74. Pan, D., et al.: Ice template method assists in obtaining carbonized cellulose/boron nitride aerogel with 3D spatial network structure to enhance the thermal conductivity and flame retardancy of epoxy-based composites. Adv. Compos. Hybrid Mater. **5**(1), 58–70 (2022)
75. Lee, S., Kim, J.: Diglycidyl ether of bisphenol—a functionalized graphene/copper foam composite with enhanced thermal conductivity and effective electromagnetic interference shielding. Synth. Met. **284**, 116989 (2022)
76. Wan, Y.-J., et al.: Grafting of epoxy chains onto graphene oxide for epoxy composites with improved mechanical and thermal properties. Carbon **69**, 467–480 (2014)
77. Yang, X., et al.: Synchronously improved electromagnetic interference shielding and thermal conductivity for epoxy nanocomposites by constructing 3D copper nanowires/thermally annealed graphene aerogel framework. Compos. A Appl. Sci. Manuf. **128**, 105670 (2020)
78. Han, Z., Fina, A.: Thermal conductivity of carbon nanotubes and their polymer nanocomposites: a review. 36: 914 Prog. Polym. Sci. (2011)
79. Xiao, H., et al.: Highly thermally conductive, superior flexible and surface metallisable boron nitride paper fabricated by a facile and scalable approach. Compos. Commun. **23**, 100584 (2021)
80. Huang, X., et al.: Thermal conductivity of graphene-based polymer nanocomposites. Mater. Sci. Eng. R. Rep. **142**, 100577 (2020)
81. Wu, S., et al.: A new route to nanostructured thermosets with block ionomer complexes. Soft Matter **8**(3), 688–698 (2011)
82. An, D., et al.: Flexible thermal interfacial materials with covalent bond connections for improving high thermal conductivity. Chem. Eng. J. **383**, 123151 (2020)
83. Hameed, N., et al.: Ductile thermoset polymers via controlling network flexibility. Chem. Commun. **51**(48), 9903–9906 (2015)

Modeling, Simulation, and Machine Learning in Thermally Conductive Epoxy Materials

Md Rahinul Hasan Mazumder, Premika Govindaraj, Lalson D. Mathews, Nisa Salim, Dennis Antiohos, and Nishar Hameed

Abstract In this chapter, modeling, simulation, and machine learning methodologies are discussed to design and predict the thermal conductivity of epoxy materials. Although epoxy has some excellent properties such as chemical resistance, high tensile, compression, and bending strengths, they have relatively low thermal conductivity (<0.1 W/m K). Therefore, it is ideal for designing epoxy-based composites with higher thermal conductivity for heat dissipation (TC) (1–10 W/m K). Here, recent progress in the field of modeling, simulation, and machine learning is explained, describing methods of predicting the TC of epoxy materials based on different factors. Several classical theoretical models are discussed here based on their applications on the TC of epoxy-based composites. Some examples of simulation studies of the micro- and macro-scale level on the TC of epoxy-based materials are elaborated to show how these studies can be carried out to predict the TC. Finally, an overview of two different ML techniques (transfer learning and deep learning) for predicting the TC of epoxy materials is explained.

1 Introduction

Due to the increased demand for high-speed processors with improved efficiency in the last several years, the electronic industry is leaning toward manufacturing miniaturized and integrated devices to meet the requirements. However, it poses severe problems due to the heat accumulation in the denser assemblies of electronic devices, which might degrade their performance or might cause premature failure [1]. To overcome this challenge, thermal management materials of superior thermal conductivity (TC) and low coefficient of thermal expansion (CTE) can dissipate the heat quickly and relieve the thermal stress in these devices. Epoxies are widely used for electronic packaging due to their lightweight, excellent adhesive strength, long service life, ease of manufacturability, and excellent moisture/corrosion resistance [2, 3]. Although pure epoxy possesses a low CTE of 50–90 $\times$ 10^{-6} K^{-1} [4], its TC

M. R. H. Mazumder · P. Govindaraj · L. D. Mathews · N. Salim · D. Antiohos · N. Hameed (✉)
School of Engineering, Swinburne University of Technology, Hawthorn, VIC 3122, Australia
e-mail: nisharhameed@swin.edu.au

N. Hameed et al. (eds.), *Multifunctional Epoxy Resins*, Engineering Materials,
https://doi.org/10.1007/978-981-19-6038-3_11

is relatively low (~0.2 Wm^{-1} K^{-1}) [5] to be used as thermal management materials. Therefore, research has been conducted in the past years on incorporating high thermal conductive fillers into the epoxy matrix to prepare epoxy-based materials or composites with superior thermal conductivity. The traditional thermally conductive epoxy-based materials are prepared by the addition of one or several kinds of fillers such as graphene [6], boron nitride [7], aluminum nitride [8], silicon carbide [9], and zinc oxide [10].

The TC is one of the most important intrinsic material properties to design materials for thermal management applications. The TC of epoxy-based materials is influenced by several factors: bulk TC of the epoxy matrix, intrinsic TC of the fillers, fabrication methods, interfacial thermal resistance, filler morphology, filler loading level, and filler functionalization [11]. Due to the dependence of TC of epoxy materials on several factors, there a large combination of possible variables to design a thermally conductive material with the best property. Therefore, to reduce the number of possible experiments, modeling and simulation could be implemented to find the best candidate materials, saving time and resources. Furthermore, modeling and simulation can be used to study qualitatively or quantitatively the effect of various parameters on the TC of the materials. Also, in the case of 2D materials with atomic-scale thickness, measuring the TC experimentally can be a daunting task and does not always produce the best result [12]. Modeling and simulation approaches are needed in this scenario to verify and validate the experimental characterization of the TC of 2D materials.

Another method to provide a promising solution for fast and accurate prediction of physical properties including TC is machine learning (ML). ML can precisely portray the relationship between structure and properties including interactions which are nonlinear and complex. Different physical laws govern the structure and properties which does not provide a universal relationship in traditional theory or experimental works. As ML uses data mining, it can build a proper relationship without considering the laws or principles [13]. Several studies have been carried out in recent years in applying ML techniques to discover materials with desirable thermal properties. These studies considered either the atomic/molecular scope or the macroscopic physical properties [14, 15].

Figure 1 shows the different approaches to science that have progressed over time. For several hundred years, the processing and designing of materials have been carried out by experimental observation from empirical knowledge. During the twentieth century, the theoretical modeling was achieved from the extracted experimental results. With the advent of supercomputers, the theories are implemented in the simulation of complex phenomena (e.g., thermal transport phenomenon), leading to accurate predictions of the properties of materials. However, some of these scientific events are too complicated to explicitly explain with the theory. The emergence groundbreaking ML methods to teach computers the concept of those phenomena using big data sparked the "fourth paradigm of science" for materials discovery [14].

This chapter will systematically present approaches to modeling, simulation, and ML related to TC of epoxy materials. The first section will provide the fundamental theories of thermal transport in amorphous polymers such as epoxy. In the second

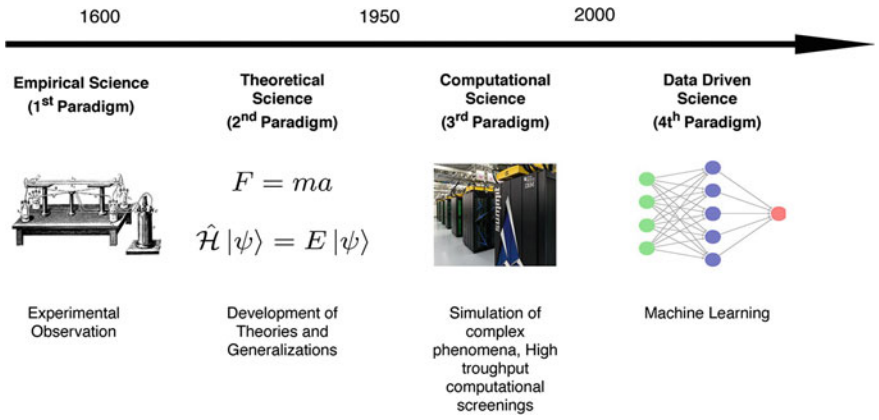

Fig. 1 Different scientific approaches over the last four hundred years. The supercomputer image was taken from Oak ridge national laboratory [14]

section, different theoretical modeling for determining TC of epoxy composites is discussed, considering several factors such as the interaction of fillers, interfacial thermal resistance, and filler geometry. Some simulation techniques for determining the TC of epoxy materials are presented with the examples drawn from the previous simulation studies conducted on epoxy materials. Finally, ML methods for predicting the TC of epoxy materials are explained in detail with two different approaches.

2 Theories of Thermal Conduction in Epoxy Polymers

Thermal conduction is the principal mechanism of heat transfer in a solid material. The characteristics of thermal conduction can be expressed by the TC and specific heat capacity. The TC of solid material is expressed via Fourier's law:

$$j_q = -\kappa \nabla T \tag{1}$$

where j_q is the heat flux (W/m^2), κ is the value of TC, and ∇T is the temperature gradient (K/m). The negative sign indicates that thermal transfer occurs down the temperature gradient. Another equation to describe the thermal conduction is the diffusive heat flow equation which is shown as

$$C\frac{\delta T}{\delta t} - \nabla(\kappa \nabla T) = \frac{\delta q_v}{\delta t} \tag{2}$$

where C is the volumetric heat capacity (J/Km^3), and q_v is the volumetric heat flow. These two equations are the central pillar for thermal conductivity modeling by providing an analytical or numerical solution with relevant initial and boundary

conditions. However, to understand the underlying relationship between the thermal conduction and structure or bonding, the microscopic level of the material needs to be considered.

Thermal conduction occurs via heat carriers such as phonons and electrons at the microscopic level. Phonons are the main contributors of vibrational energy for thermal transport, and the resulting TC, κ of a bulk material can be expressed by the Debye approximation:

$$\kappa(T) = \frac{1}{3}\sum_{j} C_j(\omega) v_j l_j(\omega) d\omega \tag{3}$$

where C_j is the phonon specific heat with branch index j and phonon frequency ω, v_j is the phonon group velocity, l_j is the phonon mean free path (MFP), and T is the temperature of the bulk material [16]. However, Debye's model assumes that the vibrations are harmonic with the distribution of frequencies and high-frequency cutoff ω, just like in a pure crystalline material. The TC increases with T^2 at low temperature caused by increased specific heat, whereas at high temperature, the TC decreases linearly with T due to the Umklapp scattering of phonons.

On the other hand, epoxy polymers are amorphous or semi-crystalline materials that deviate from Debye's high-temperature model. At high temperatures, the TC of epoxy polymers reaches a plateau as κ increases up to a saturation point resulting from the localization of the excited phonons. This might be because the polymer materials consist of non-homogenous bonding with stiff-force constant involving the covalent bonding within the polymer backbone, and side groups coexist with softer non-bonded interactions between the chains [17–19]. Also, these non-bonded interactions are nonlinear with localized an harmonic vibrations like the "fracton hopping" model, which contributes to thermal transport [20]. Therefore, the basic thermal transport for amorphous polymers is best described by the "minimum thermal conductivity model (MTMC)" which states that the amorphous limit can be derived from Debye's model as discussed above, assuming that the lifetime of vibration is half of the period of vibrations. Considering the contribution of individual vibrations, minimum thermal conductivity, κ_{min} can be expressed by two measured variables (the atomic density and average sound velocity) as shown below:

$$\kappa_{\min} = \left(\frac{\pi}{6}\right)^{1/3} \kappa_B n^{2/3} \sum_{j}^{3} V_j \left(\frac{T}{\theta_j}\right)^2 \int_0^{\theta_j/T} \frac{x^3 e^x}{(e^x - 1)^2} dx \tag{4}$$

where κ_B is the Boltzmann constant, n is the atomic density, $V_1 = V_l$ and $V_{2,3} = V_t$ are the longitudinal and transverse speed of sound, respectively, $\theta_j = V_j(\hbar/\kappa_B)(6\pi^2 n)^{1/3}$ is the Debye cutoff temperature, and $\hbar$ is the reduced Planck constant [21]. For amorphous polymers at or above room temperature, where all vibrational modes are assumed to be thermally excited, the minimum thermal conductivity can be given

by $\kappa_{min} = 0.40\ \kappa_B n^{2/3}(V_l + 2V_t)$. This is usually observed in polymers with long straight sections in longitudinal directions due to the drawing process.

3 Modeling of Thermal Conductivity of Epoxy Composites

Modeling of the TC of polymer is generally developed for their composite materials due to the low TC of the polymers. Classical theoretical modeling of TC for composites mainly falls into two types: "effective medium approximations" and "micromechanics method". In this section, several classical models of these categories for the TC of polymer composites are explained, considering the conditions in which models can be used. The application of these models on the TC of epoxy composites is also discussed to validate the accuracy of the models in specific conditions.

3.1 Rule of Mixtures and Equivalent Inclusion Models

Rule of mixtures models can calculate the TC of the composites as a function of its volume fraction and the individual components' properties. The parallel model (also known as the linear mixing rule) calculates the upper bound of the TC. In contrast, the series model (also known as the inverse mixing rule) calculates the lower bound of the TC of the composites. Most experimental results fall within these two limits in which the accuracy of the series model is greater. Assuming each component contributes independently to the overall TC of the composites and the two components are in perfect contact with each other, the series and parallel models are shown by

$$\begin{aligned} \kappa_c^{-1} &= V_f \kappa_f^{-1} + \left(1 - V_f\right)\kappa_m^{-1} \quad \text{(Series)} \\ \kappa_c &= V_f \kappa_f + \left(1 - V_f\right)\kappa_m \qquad \text{(Parallel)} \end{aligned} \tag{5}$$

where κ_c is the TC of the composites, κ_f and κ_m are the TCs of the filler and polymer matrix, respectively, and V_f is the volume fraction of the filler [22].

To understand the mechanism involved, Gozny et al. fitted three separate theoretical models (series model, parallel model, and equivalent inclusion model) to calculate the TC of epoxy composites consisting of amino-functionalized multiwalled carbon nanotubes (MWCNT) as fillers. The correlation of the experimentally obtained TC values for MWCNT(–NH_2)/epoxy composites with theoretical models is shown in Fig. 2. For the series model, they assumed that the composite was homogeneous with the fillers isolated in the matrix, which leads to TC values of the lower bound. The parallel model assumes that an internal network of conduction pathways is formed, with the fillers and matrix considered as separate phases without any interactions. This provides an overestimation of the TC values of the composites with an upper bound [23]. A third model, known as the equivalent inclusion model, which

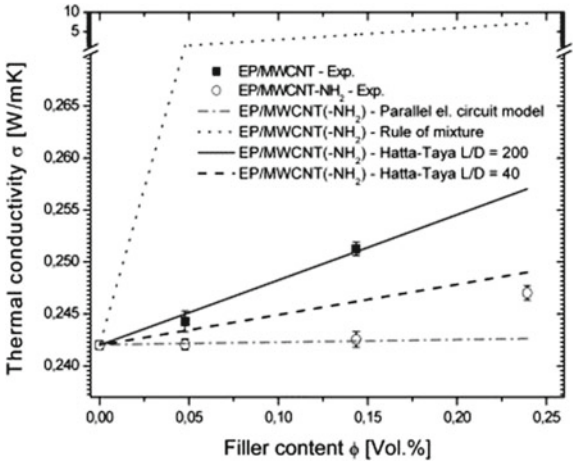

Fig. 2 Comparison of the TC values obtained experimentally for MWCNT(–NH_2)/epoxy composites with rule of mixtures and equivalent inclusion models [23]

was developed by Hatta et al. [24] based on the previous works from Eshelby [25], was chosen to overcome the limitations of the rule of mixtures models.

The equivalent inclusion model considers the aspect ratio of the fillers, especially in a random orientation. The derived equations for the calculation of TC of 3D random short fiber-reinforced composites are shown below:

$$\frac{\kappa_c}{\kappa_m} = 1 + V_f \frac{\left[\left(\kappa_f - \kappa_m\right)(2S_{33} + S_{11}) + 3\kappa_m\right]}{J} \tag{6}$$

$$J = 3\frac{\left(1 - V_f\right)\left(\kappa_f - \kappa_m\right)S_{11}S_{33} + \kappa_m\left[3(S_{11} + S_{33}) - V_f(2S_{11} + S_{33})\right]}{\left(\kappa_f - \kappa_m\right)} \tag{7}$$

$$S_{11} = \frac{1/D}{2[(l/D)^2 - l]^{3/2}}\left\{\left(\frac{l}{D}\right)\left[\left(\frac{l}{D}\right)^2 - l\right]^{1/2} - \cosh^{-1}\left(\frac{l}{D}\right)\right\} \tag{8}$$

$$S_{33} = 1 - 2S_{11} \tag{9}$$

where l is the length of the filler and D is the diameter of the filler. From Fig. 2, it can be concluded that the obtained values from the equivalent inclusion model are in good agreement for high aspect ratio fillers with the experimental data for MWCNT/epoxy composites compared to the rule of mixtures models. However, for low aspect ratio fillers, a significant difference is observed between the experimental and fitted values, which might be due to the agglomeration of CNTs, their waviness, and the shortening of fibers during processing. In the case of amino-functionalized MWCNTs, the experimental results tend to follow the equivalent inclusion model at high filler loadings because of the increased percolation threshold due to the functionalization process [23].

3.2 Maxwell–Garnett (MG) Model

The Maxwell–Garnett (MG) model is one of the earliest models for predicting the TC of composites derived from the early works of Maxwell's utilization of potential theory [26]. MG models assume that the spherical fillers are isolated within the matrix, and there is no interaction among them. At low filler loading, the theoretical values from the MG model follow a linear relationship for the TC of the composites. For a composite with no interaction between homogeneous spherical fillers randomly distributed in a homogeneous matrix, the TC is calculated by [27]:

$$\kappa_c = \kappa_m \left(1 + 3V_f \frac{\kappa_f - \kappa_m}{2\kappa_m + \kappa_f - V_f\left(\kappa_f - \kappa_m\right)} \right) \tag{10}$$

Nayak and coworkers are used two theoretical models (rule of mixtures model and Maxwell model) and a numerical analysis model (FEM model) to compare the experimental values for TC of pine wood dust particles-reinforced epoxy composites with the predicted values. According to the Maxwell model, the fillers were spherical and dispersed, whereas the matrix was in a continuous phase. Among the two theoretical models, they found out that the deviation of the theoretical results from the experimental results is 2–44% and 4–28% for the rule of mixtures model and Maxwell model, respectively. Furthermore, they concluded from their findings that the Maxwell model overestimates the TC values, and the rule of mixtures model underestimates the TC values with respect to the experimental ones. From Fig. 3 and the results obtained, it can be stated that the Maxwell model has greater accuracy than the rule of mixtures model for a particulate filler epoxy composite. However, the Maxwell model's accuracy is lower than the FEM model because it fails to take into account the interaction of fillers at high filler loading, and all fillers are not uniformly spherical [28].

3.3 Lewis-Nielsen Model

Unlike the MG model, the Lewis-Nielsen model considers the geometry and orientation of the fillers. It also considers that a thermally conductive pathway can be formed with a specific shape and size distribution of fillers at low filler loading. This model is shown as follows:

$$\kappa_c = \frac{1 + ABV_f}{1 - B\psi V_f} \tag{11}$$

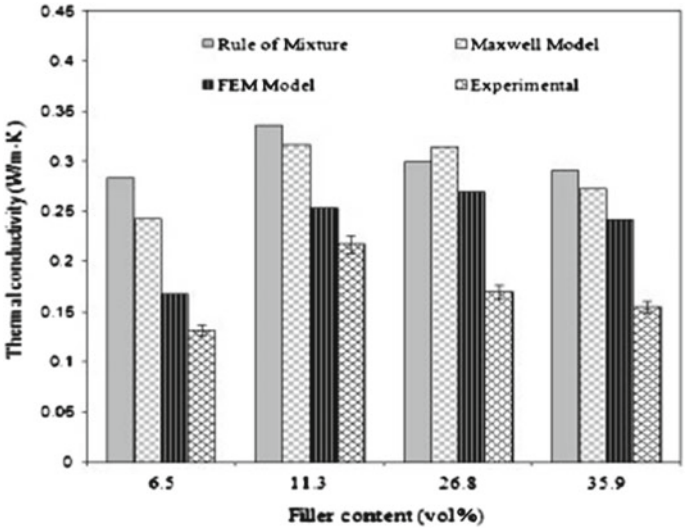

Fig. 3 Comparison of TC values obtained from the maxwell model with the other models [28]

where $B = \frac{\frac{\kappa_f}{\kappa_m} - 1}{\frac{\kappa_f}{\kappa_m} + A}$ and $\psi = 1 + \left(\frac{1-\psi_m}{\psi_m^2}\right) f$. A is a generalized Einstein coefficient that depends upon the filler geometry and orientation, and ψ_m is the maximum packing fraction [29].

Wang and Qiu investigated the effect of TC enhancement with incorporating CNT in glass fiber/epoxy composites through the experimental procedure and theoretical modeling with the Lewis-Nielsen model. They determined that the Lewis-Nielsen model underestimated the experimental TC values, as shown in Fig. 4. This might be because the model is invalid for fillers with a high aspect ratio, or it might have ignored entirely the orientation effect of the fillers during the processing of the composites [30].

3.4 Agari Model

Agari model is based on the generalization of the rule of mixtures models and considers the formation of thermal conduction chain by the interaction of fillers fraction, geometry, and the interaction between them. Therefore, the model can accurately predict the TC of composites for high filler loading [31]. Agari derived the following equation for determining TC:

$$\log \kappa_c = V_f C_2 \log \kappa_f + \left(1 - V_f\right) \log(C_1 \kappa_m) \tag{12}$$

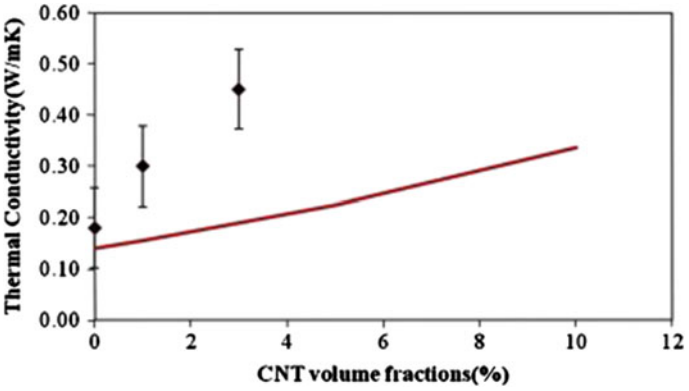

Fig. 4 Comparison of the TC values of epoxy-CNT composites for experimental results and results obtained from the Lewis-Nielsen model (square marks: experimental results, solid line: theoretical predictions) [30]

where C_1 is the correlation of the effect of the fillers on the crystallinity and crystal size of the polymer matrix, which directly influences κ_m, and C_2 is a factor of ease in forming conducting chains of fillers and falls between 0 and 1. The value of C_2 approaches 1 when particles can more easily form conductive chains, thus contributing to a greater effect to change the overall κ_c [32].

Wang and co-researchers analyzed the TC of the Si/epoxy composites by comparing the experimental data and the theoretical data from the Agari model to observe whether the model provides an accurate prediction of the TC of the composites. They reported that the predicted TC values of the composites are close to the experimental values at lower filler loading, as shown in Fig. 5. Although the model deviates at high filler loading, it should not be considered invalid because the error might be due to the poor filler dispersion and the presence of voids in the composites during the processing of the composites. Agari model does not consider these processing variables that might arise and only consider the intrinsic variables [33].

3.5 Bruggeman Model

The Bruggeman model considers the formation of the thermal conduction pathway due to the direct contact between the fillers. At high filler content, the distance between the fillers is small, and the fillers interact with each other. This model is an expansion of the Maxwell model as it also regards the fillers to be spherical. The Bruggeman model is defined by the following equation for a binary composite [34]:

$$1 - V_f = \frac{\kappa_f - \kappa_c}{\kappa_m - \kappa_c}\left(\frac{\kappa_m}{\kappa_c}\right)^{1/3} \tag{13}$$

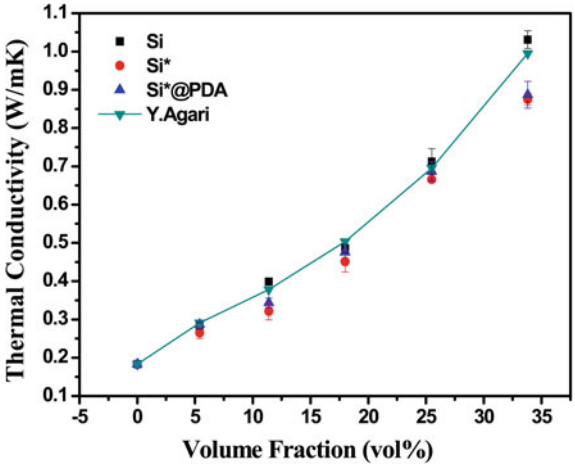

Fig. 5 Comparison of the experimental and the Agari model values of the TC of the three composites with different filler volume fractions [33]

Lee and coworkers fitted several models, including the Bruggeman model, to compare how the models predict the experimental data for TC values of aluminum nitride (AlN) filled epoxy composites, as shown in Fig. 6. Bruggeman's model provides a more accurate and consistent result at a high filler fraction than the Maxwell model as it considers the interaction among fillers. However, the Agari model matched better than the Bruggeman model as it considers the aforementioned factors, C_1 and C_2, which affect the TC of the composites, unlike in the Bruggeman model, where all fillers are assumed to be spherical [35].

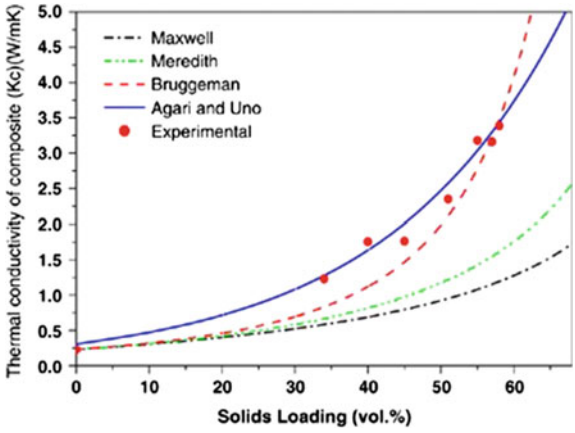

Fig. 6 Comparisons of the measured TC of aluminum nitride-filled epoxy composite with the calculated TC by various theoretical models, including the Bruggeman model [35]

3.6 Deng-Zheng Micromechanical Model

Deng-Zheng micromechanical model does not have the limitations that other models face and thus fit perfectly for composites with low filler loading. Besides considering the effect of anisotropy, aspect ratio, and rough surfaces of the fillers, it also considers the "interfacial thermal resistance (ITR)" between the fillers or matrix and filler. The equation shows Deng-Zheng model for a 2D shaped filler-reinforced composites [36]:

$$\frac{\kappa_c}{\kappa_m} = \left[\frac{1}{3}\frac{\eta}{\left(\frac{\kappa_m}{\eta\kappa_{ce}+H(\eta p)}\right)}\right]V_f + 1 \tag{14}$$

where κ_{ce} is the equivalent axial TC of the fillers as shown by the equation:

$$\kappa_{ce} = \frac{\kappa_f}{\left(1+\frac{2R_k\kappa_f}{L}\right)} \tag{15}$$

Here, R_k represents the Kapitza resistance, and L is the average largest lateral length of folded 2D fillers. The quantity $H(\eta p)$ can be shown by

$$H(\eta p) = \frac{1}{\left((\eta p)^2-1\right)}\left[\frac{\eta p}{\sqrt{\left((\eta p)^2-1\right)}}\ln\left((\eta p)+\sqrt{\left((\eta p)^2-1\right)}\right)-1\right] \tag{16}$$

where $p = S_A/S_L$ is the aspect ratio, $\eta = \frac{S_A^e}{S_A}$ is the folding degree, and S_A^e is the equivalent average area of flat surface of the 2D fillers.

In Fig. 7, it is shown that the theoretical values from the Deng-Zheng model fitted perfectly with the experimental values in a straight line for epoxy composites consisting of 2D exfoliated graphene (EG) nanosheets. From the figure, the intercept and slope are calculated and found to be 1 and 172.28, respectively. The slope can also be expressed as

$$\frac{\kappa_c}{\kappa_m} = \left[\frac{1}{3}\frac{\eta}{\left(\frac{\kappa_m}{\eta\kappa_{ce}+H(\eta p)}\right)}\right] \tag{17}$$

Putting the calculated value of the slope in the above equation, the folding degree η is calculated and found to be $\eta = 0.84$, which indicates that the fillers are not fully extended in the epoxy matrix. Therefore, Deng-Zheng's micromechanical model also provides information on the influence of the filler's microstructure in the matrix [37].

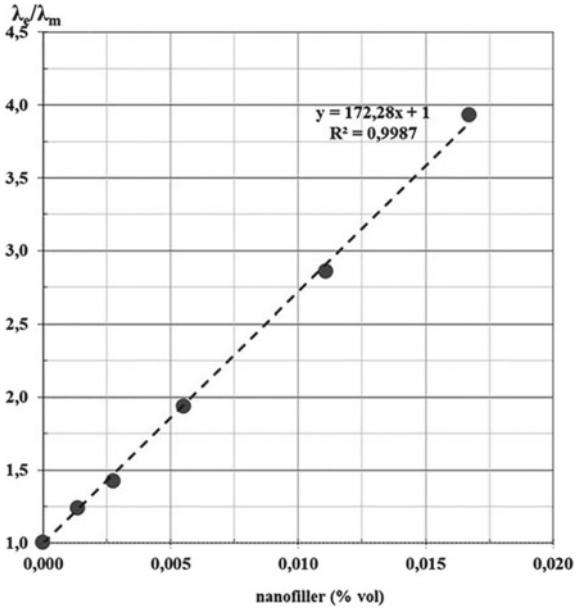

Fig. 7 Experimental values (dot) and Deng-Zheng micromechanical model derived values for effective TC λ_e/λ_m of 2D EG-epoxy nanocomposites [37]

4 Simulation of Thermal Conductivity of Epoxy Materials

4.1 Molecular Dynamics Simulation

Molecular dynamics (MD) simulation is a statistical mechanics-based tool where Newton's law of motion, $F = ma$, is combined for a collection of particles relative to time. Using Newton's law, MD can determine the microstructure and interactions between the particles considering the particles' physical movements in a short period. In MD simulation, a force-field file is used as input to describe the physical parameters of the particles such as the atomic mass, bond angle, and bond length. The size of the MD system is typically between 10 A and 100 nm; the number of atoms in the system is from several thousand to millions, and the simulation period is between 100 ns and microseconds [38]. MD simulations mainly fall into two categories: non-equilibrium MD (NEMD) and equilibrium MD (EMD).

The most straightforward approach for determining the TC of epoxy materials with MD simulations is the non-equilibrium molecular dynamics (NEMD) method. This method considers the arbitrary shapes and structures of the composites without any assumptions or simplifications and can describe in detail the vibrational motion of phonons. The temperature gradient is calculated by implementing heat source and sink, in which the temperatures are kept constant and then removed at a steady rate. However, it requires a large amount of computation power and time, and it also ignores the size effect of highly aligned polymer chains when the phonon mean free

path is longer than the length of aligned chains. To overcome this problem, equilibrium MD (EMD) based on Green–Kubo formalism is usually carried out. This method does not use any kind of heat source and sink and use periodic boundary conditions. Therefore, phonon scattering does not occur, and size effects are negligible. A smaller system size can be used as there is no need to establish the temperature gradient. Although the simulation time is longer, a single process can determine the whole TC tensor, which is applicable for anisotropic materials [39].

Before simulating epoxy materials, its model structures need to be generated with force acting between its atoms. Two types of molecular modeling are carried out to generate the epoxy structures: united-atom (UA) models and coarse-grained (CG) models. UA model combines a group of carbon and other heavy atoms into one particle, excluding the hydrogen atoms, and evaluates the dynamics and interaction between the particles based on united-atom force fields. As a result, it ignores most of the non-bonded interactions present in the epoxy materials. CG model treats small groups of atoms into a single particle or bead, considering all kinds of interactions and bonding energy present in the epoxy materials [38]. The non-bonded interactions are determined by pair potentials such as Lennard–Jones (LJ) potential to describe the "hard-core repulsion", "van der Waals attraction" or "Coulomb interactions". The bonded energies include the energy for "bond stretching", "angle bending", "torsion", "inversion", and the cross term of these functions.

4.1.1 NEMD Simulation of TC of Epoxy Materials

Several studies have been carried out in recent years on NEMD simulation of TC of epoxy-based materials. Wang et al. examined the effect of incorporating functionalized graphene (FG) in epoxy resin by NEMD. At first, the equilibrated molecular structure of FG/epoxy composites is constructed by the atomistic modeling of FG and epoxy with the implementation of NVE and NPT ensemble in the MD simulation. The term "NPT ensemble" indicates that the number of atoms (N), pressure (P), and temperature (T) is kept constant during the simulation. "NVE ensemble" indicates that the number of atoms (N), volume (V), and energy (E) remains constant during the simulation. The simulation cell consists of the FG positioned in the center of the box in the XY plane direction with the epoxy chains distributed evenly on both sides of the FG, as shown in Fig. 8a. A temperature gradient is created by applying heat energy to the right side of the cell (heat source) and removing the same amount of energy from the left side (heat sink) at a constant rate. The TC of the epoxy nanocomposites is then calculated by Fourier's law, as shown in Eq. (1). Another simulation cell is constructed to determine the TC of the nanocomposites by considering the "interfacial thermal conductance (ITC)" at the FG/epoxy interfaces. In this cell, the FG and the epoxy chains are oriented perpendicularly to the XY plane so that heat flux can pass through FG/epoxy interfaces, as shown in Fig. 8b. From the NEMD simulation, the ITC was calculated as shown by

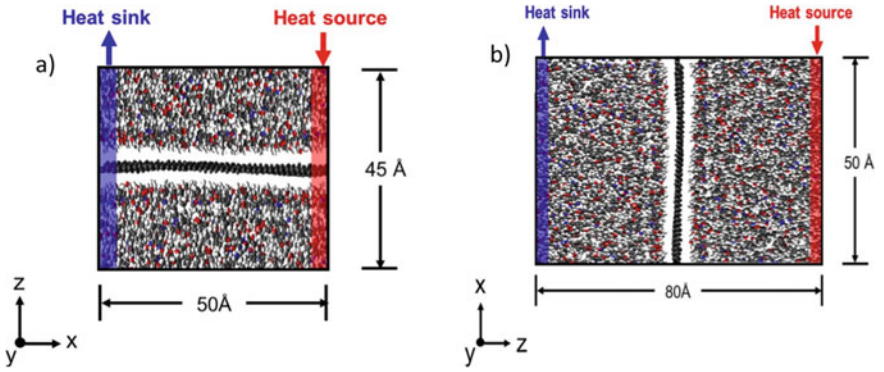

Fig. 8 NEMD simulation for **a** in-plane TC of graphene/epoxy composite and **b** ITC of graphene/epoxy interface [40]

$$H = \frac{q}{\Delta t.A.\Delta T} \tag{18}$$

where H is the ITC, A is the cross-sectional area through which the heat flux passes, and q is the supplied or removed heat energy in the nanocomposite model in each step of the NVE ensemble. ΔT is determined as the average of half of the temperature difference of the epoxy located at each side of the interface of the segmented cell regions [40].

4.1.2 EMD Simulation of TC of Epoxy Materials

EMD is the most efficient way to estimate the anisotropic TC of epoxy materials at various temperatures compared to the NEMD techniques, where a single scalar quantity of TC is measured. The first step in the EMD technique is to construct the atomic modeling of epoxy polymers with sufficient cross-linking units so that their properties are portrayed properly. "Dendrimer growth approach" is the most popular method to build epoxy networks. In this technique, a single monomer of epoxy resin is modeled first, followed by cross-linking a second layer of monomers around it. The third layer of monomers is cross-linked to the second layer, and in this way, layers of monomers are added to the core structure that grows at each pass to build cubic unit cells [41]. After constructing the dendrimer structure, the TC is estimated using the "Green–Kubo expression", which relates the TC tensor to the integral over time t of the heat flux autocorrelation function as follows:

$$\kappa = \frac{V}{3\kappa_B T^2} \int_0^\infty J(0).J(t)dt \tag{19}$$

where V is the volume of the unit cell, κ_B is the Boltzmann's constant, T is the temperature, J is the atomistic heat flux vector, and the angular brackets denote the ensemble average, heat current autocorrelation factor, $HCACF = J(0)\,.\,J(t)$ [42]. J is defined as

$$J = \sum_i e_i v_i + \frac{1}{2}\sum_{i<j}\left(f_{ij}\left(v_i + v_j\right)\right)x_{ij} \tag{20}$$

Liu et al. carried out an equilibrium MD study on the thermal and rheological properties of boron nitride nanosheets (BNNSs) filled epoxy composites. The models of neat epoxy resin and BNNS/epoxy composites were constructed using the Materials Studio 8.0 software, as shown in Fig. 9. Different force fields were used to characterize the interactions present in the model structure. CVFF potential is used for interactions between the epoxy resin and curing agent. Tersoff potential was applied to define the bonding within BNNS, and Lennard–Jones (LJ) potential was used for the interactions between epoxy and BNNS. Then, based on the "Green–Kubo theory", EMD simulation was carried out to determine the TC of the BNNS/epoxy composites. The calculations were carried out by using the large-scale atomic/molecular massively parallel simulator (LAMMPS) package. The energy of the constructed epoxy composites system was minimized by applying the conjugate-gradient algorithm. NVT and NPT ensembles were carried out using a Nose–Hoover thermostat and barostat to accurately construct the model with the actual density. Finally, the calculations for the TC of the composites were obtained by carrying out a dynamic equilibrium for the whole model at 300 K in the atmosphere with the periodic boundary conditions applied in three directions [43].

Figure 10 shows the TC of epoxy and epoxy/BNNS composites at 300 K with the change of correlation time. The heat current autocorrelation function calculates the TC with a correlation time of 50 ps and then integrated within the correlation time interval using Eq. (20). Ten independent calculations were performed for each system to calculate its TC by averaging the TC values of the ten systems in the last 5 ps. In the figure, the thin gray line represents TC of each system, and the blue line is the average.

4.2 Finite Element Modeling

Finite element modeling (FEM) is a powerful numerical simulation technique to solve many engineering problems at the macroscopic level involving stress analysis, heat transfer, fluid flow, etc. Software packages such as ANSYS, ABAQUS, and COMSOL Multiphysics are general-purpose finite element modeling packages for solving wide variety of engineering problems numerically. A physical problem usually occurs in a continuum of matter (solid, liquid, or gas) with several field variables which vary from point to point in a domain resulting in an infinite number

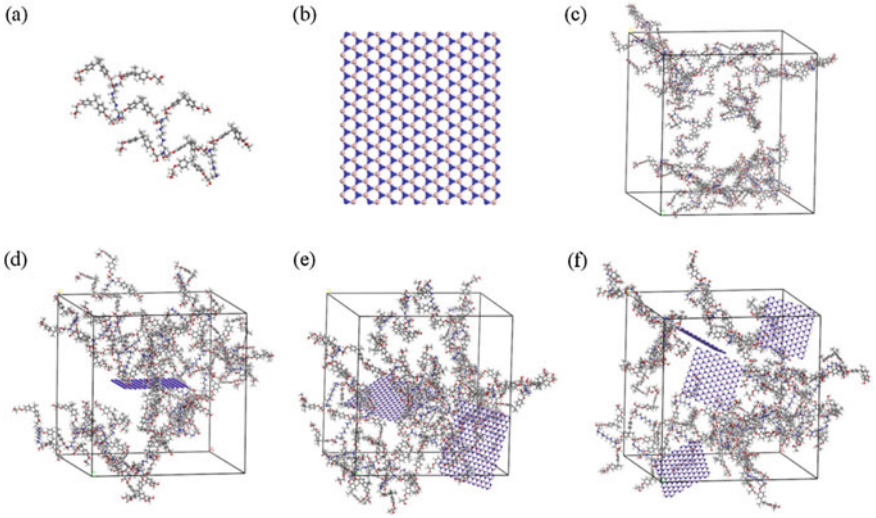

Fig. 9 Different types of models constructed using materials studio: **a** epoxy monomer, **b** boron nitride nanosheet (BNNS), **c** neat epoxy **d–f** 10 wt.%, 2 × 10 wt.%, 4 × 5 wt.% BNNS/epoxy composites, respectively [43]

of solutions. FEM helps to provide a finite number of solutions by segmenting the domains into elements consisting of nodes located at element boundaries. These nodes reduce the physical problem by solving the variables at its locations, and the solution of these nodes can be extrapolated further from its neighboring nodes to the whole domain [25].

FEM can be used to validate and verify the values obtained from numerical simulation by comparing them with the values obtained from experimental methods or theoretical models. Recent FEM studies on determining the TC of epoxy materials mainly focused on the epoxy-based composites due to their macroscopic structure. Sharma et al. carried out FEM analysis along with experimental investigation and theoretical models to compare the TC of unfilled and marble dust-filled needle punched nanowoven jute-epoxy composites (NNPJEC).

They used ANSYS to determine the TC of the composite for different filler concentrations. A three-dimensional model of the composites was constructed in the first step by the design modeler in the ANSYS Workbench as shown in Fig. 11. 100 × 100 × 100 μm cube is modeled and then segmented into alternate layers of 5 epoxy (in vol.%) and 4 jute as the reinforcing material. The marble dust particles were constructed as spherical shaped and randomly distributed in the layers of epoxy. In the next steps, the mesh parameters and boundary conditions are defined.

The geometrical model is meshed in program-controlled, linear element mode with an element size of 0.0001 mm, as shown in Fig. 12. For the boundary conditions, the temperature (T1) at nodes of face ABCD was set as 20 °C and nodes of face EFGH was set as 100 °C. The heat flow was applied in the X direction with all other sides

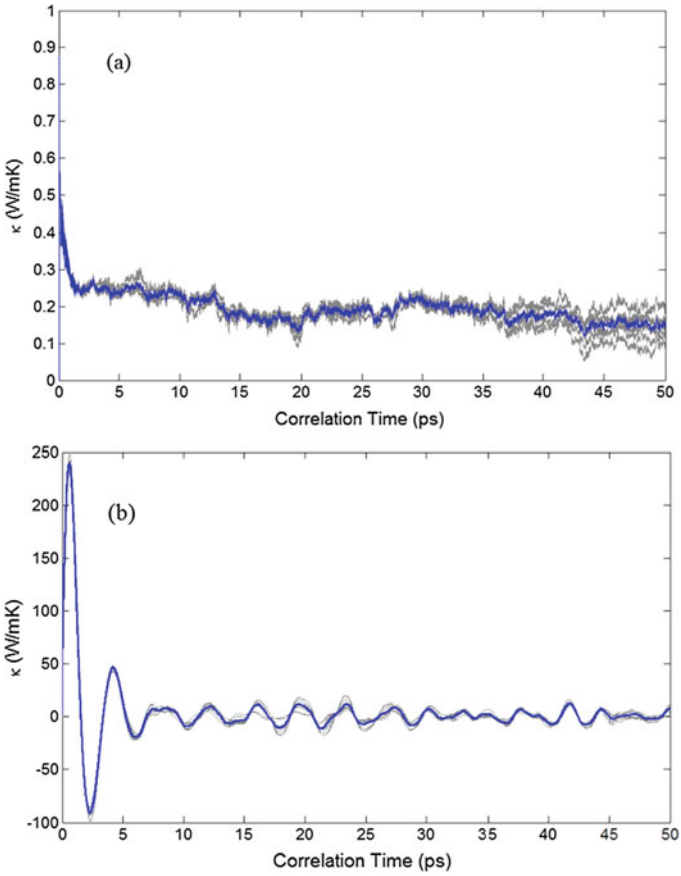

Fig. 10 TC vs correlation time of **a** neat epoxy and **b** 10 wt.% BNNS/epoxy at 300 K [43]

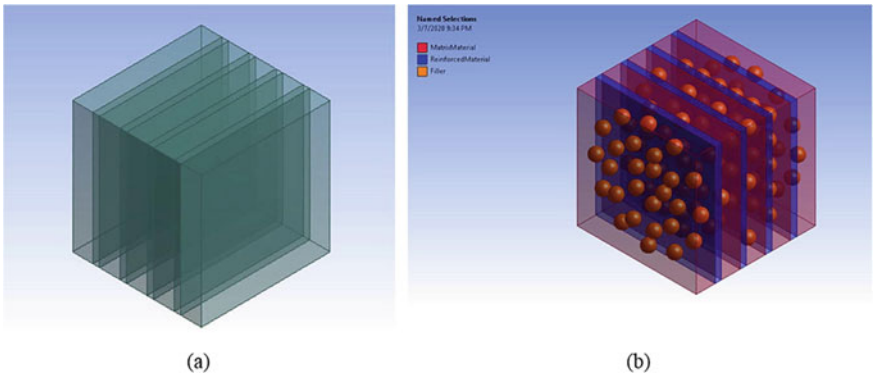

Fig. 11 3D geometry model for **a** unfilled and **b** MD filled NNPJEC [44]

completely insulated, as shown in Fig. 13. The numerical solution is performed using Eq. (1). The temperature distribution obtained from the simulation is shown in Fig. 14 [44].

The underlying mechanism of heat transfer in epoxy-based composites can also be understood by the FEM simulation technique. Xu and coworkers are used another simulation package for FEM called COMSOL Multiphysics 5.4 to study the heat transport and enhancement mechanism for randomly distributed BN/epoxy and 3D-BN/epoxy composites. They constructed three models of pure epoxy, randomly distributed BN (20 vol%)/epoxy, and 3D-BN (20 vol%)/epoxy with the boundary conditions defined. The temperature at the bottom is fixed at 120 °C, while the other sides are perfectly insulated with an initial temperature of 20 °C. Transient-state finite element methodology was implemented with a total time length of 0.02 s and step length of 0.002 s.

The temperature distribution and heat flux arrow of the three different models are shown in Fig. 15. The heat transfers occur evenly throughout the body of pure epoxy

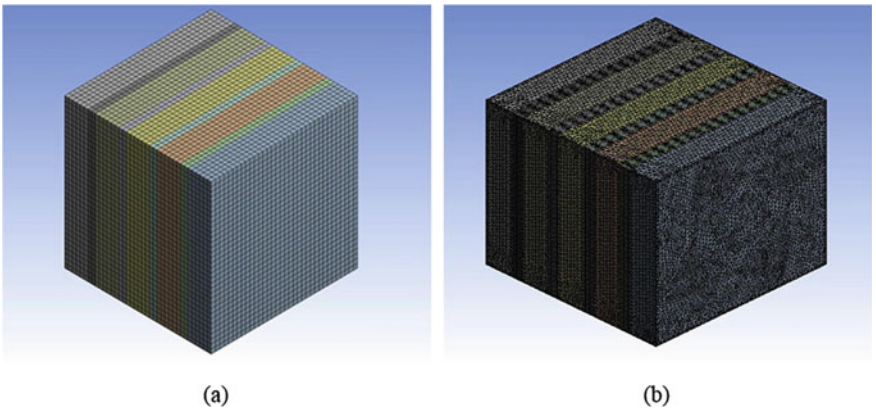

Fig. 12 Meshing for **a** unfilled and **b** MD filled NNPJEC [41]

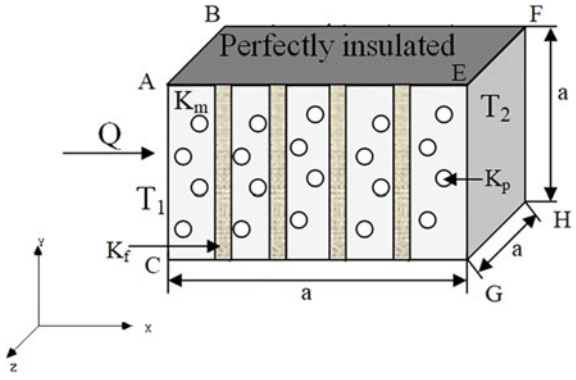

Fig. 13 Boundary conditions for the developed model [44]

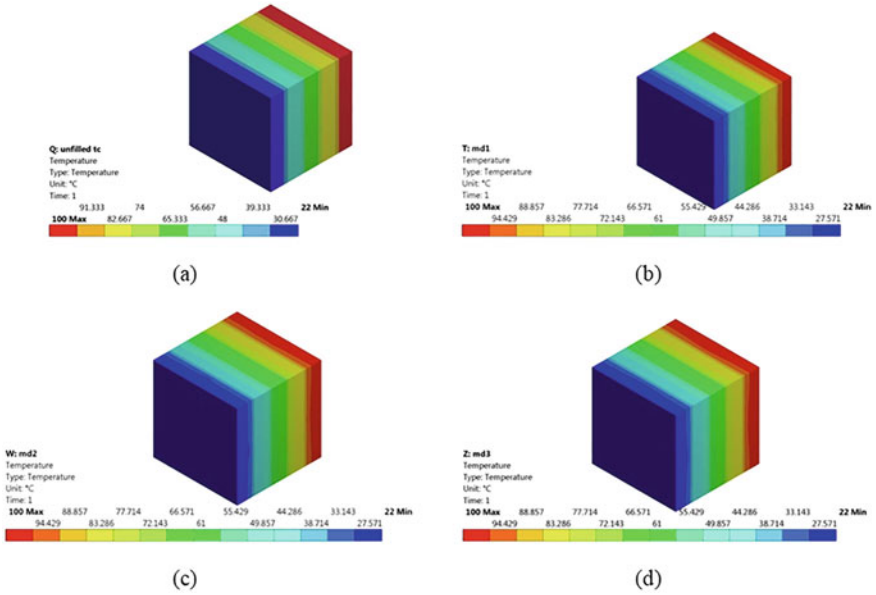

Fig. 14 Temperature distribution profile for **a** unfilled NNPJEC and **b**, **c**, and **d** 8, 16, and 24 wt.% MD filled NNPJEC [44]

and randomly distributed BN/epoxy. The average top surface temperatures of these models remain constant throughout the whole process. This is due to insufficient thermal conduction pathway and the epoxy matrix's low TC. On the other hand, the heat transfers faster, with the average top surface temperatures and bottom surface temperatures becoming almost equal. The 3D-BN provides selective and efficient thermal conduction pathways due to BN arrangement along the heat flow direction [45].

5 Machine Learning (ML) for the Thermal Conductivity of Epoxy-Based Materials

In the past few years, machine learning (ML) techniques have piqued interest in various research fields due to their excellent ability to extract useful information. ML methods can play a significant role in the design of novel materials or in predicting the physical properties of an unknown material. However, in polymer science, ML-based methods have not been widely implemented because there are not enough datasets due to the experiments being labor-intensive and expensive to construct. Furthermore, the datasets obtained from the previous literature sources are usually noisy and inconsistent because of several experimental factors such as process conditions, origin and purity of used chemicals, and environmental conditions. As a result, a

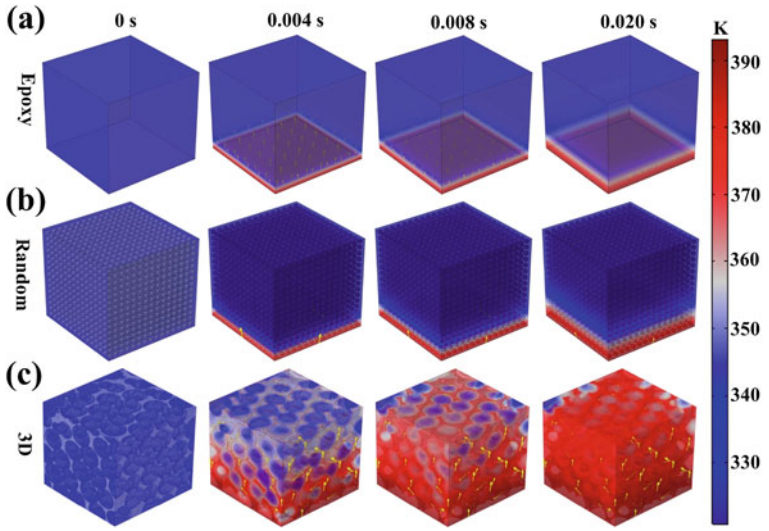

Fig. 15 Process of heat transfer displayed by finite element simulation. Temperature distribution and heat flow arrows of **a** pure epoxy resin, **b** randomly distributed BN/epoxy composite with 20 vol% BN, **c** 3D-BN/epoxy composite with 20 vol% BN [45]

vast and comprehensible source of information on polymer properties are not easily obtainable, and the datasets are scattered [46, 47]. Moreover, for polymeric materials like epoxy, it is difficult to construct an ML model to create a link between its structure and TC. This is due to the shortage of common public databases including TC of epoxy materials. Additionally, developing an extensive database by molecular dynamics for polymers that occupy an ample chemical space is seriously limited by its longer computation time. As a second rank tensor, the obtained TC values also depend on the factors such as polymer processing operations which are not recorded in the database [48].

Few workflows have been conducted in the past to predict polymers' TC by ML methods to overcome the issue of limited data. Here, two approaches will be discussed to predict the TC of epoxy or epoxy composites materials. The first approach combines experimental techniques with active learning and Bayesian optimization to model and maximize the κ from various epoxy materials. This approach also helps to find out the best condition for achieving the target TC from a limited dataset without requiring any data from the previous literature through designing controlled experiments [49]. In the second approach, several ML algorithms, including "convolution neural network (CNN)", are employed to train models that can predict the effective TC of epoxy-based composites. The datasets contain composites structures that are created from a "quartet structure generation set (QSGS)", and numerical methods are applied, such as the lattice Boltzmann method (LBM), to calculate the effective TC [50]. Before discussing these approaches, an overview of the methodology of the ML framework is explained.

5.1 ML Methodology Framework

ML techniques generally fall into three main categories: supervised learning, unsupervised learning, and reinforcement learning. Most of the techniques used for predicting TC utilize the supervised ML strategies. Supervised learning uses the training dataset that contains a labeled set of input and output pairs for N number of samples. The goal of the supervised learning method is to evaluate a prediction y for the corresponding input x with low bias and low variance error [51]. The overall process of developing ML models consists of four steps, as shown in Fig. 16. The first step is collecting enough data from experiments, trusted numerical simulations, or other reliable sources. The second step is choosing proper features (e.g., molecular structure, physical properties, and/or chemical properties of the material) on the subject as input parameters. This is followed by capturing the effect of each parameter on the output, which leads to model training. In the last step, the final model should be evaluated by another portion of the dataset known as the testing dataset [52].

Data collection should be done so that a suitable and reliable dataset is prepared after understanding the problem and thermal transport mechanism in the material. The main objective during this process is to ensure that the training dataset represents the complete diversity of reality as much as possible. Due to the development of materials informatics in the past several years, many research groups have contributed to building databases to collect material properties for both experimental and theoretical values. These commonly used databases are Materials Project Database, Citrine Informatics, Wolfram Data Repository, Polyinfo, Cambridge Structural Database, Nanomine, and Atomwork.

Feature generation or engineering is carried out by setting up features from the training dataset that can represent both the materials in the training dataset and the new dataset. The quality of feature selection seriously influences the accuracy of the ML models. For predicting the TC of epoxy-based materials, the features might include molecular weight, specific heat capacity, density, coefficient of thermal expansion, curing temperature, curing reagent, thermal stability, etc.

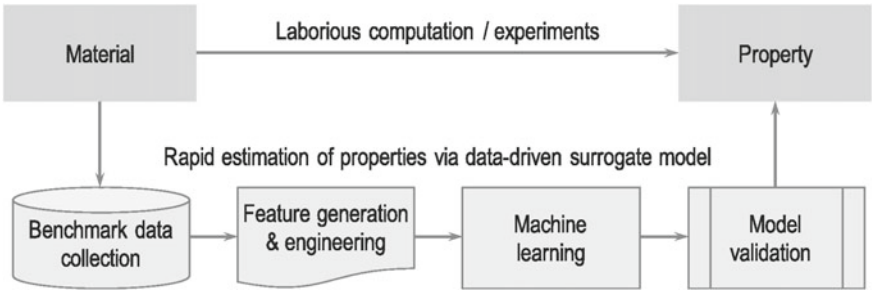

Fig. 16 Workflow for constructing a ML model for predicting TC [53]

After choosing the dataset and its features, the ML model is trained to draw a relationship between features (input data) and the TC (output data) through the ML algorithm. The complete set of data is divided into 3 sub-groups for training, validation, and testing purposes. The training data are used in the learning process by the ML algorithm to provide the ML models parameters. The validation data can optimize the hyperparameters in ML models for the best performance. To evaluate the predictive performance of the ML algorithms, three statistical performance measures are widely used: "linear correlation coefficient (R)", "mean absolute error (MAE)", and "root mean square error (RMSE)". If the obtained ML model shows low accuracy to predict the TC of the testing dataset for a particular ML algorithm, the previous steps are reiterated by increasing the samples of the training dataset or choosing a different ML algorithm until the ML model shows better accuracy with the performance metrics.

5.2 Prediction and Optimization of TC of Epoxy Materials from Small Dataset Through Transfer Learning

The barrier of the limited dataset in the field of polymer science can be tackled by a two-stage data-driven approach called transfer learning. Transfer learning involves active learning and Bayesian optimization to take relevant segments of a pre-trained ML model and applying it to a new and similar problem. The objective of the first stage, active learning, is to develop a model to find epoxy materials for a specific range of high TC. Bayesian optimization is carried out in the next stage to search for epoxy materials with extremely high TC after screening the experimental conditions. It is a sample-efficient optimization method that does not require many samples to obtain good results and suitable for tasks that requires function which are extremely expensive to evaluate. The schematic for this ML-guided process including different steps is shown in Fig. 17.

At first, the data are collected from the public database such as Polyinfo and QM9 for the forward prediction step. The data for TC values had only a few instances which provide a poor accuracy for the model obtained through direct learning as shown in Fig. 19d. Therefore, an indirect approach is preferred by mapping structures of epoxy materials to proxy properties which include glass transition temperature T_g, melt temperature T_m, density ρ, and heat capacity C_v. Molecular fingerprint (ECFP) can be selected as the molecular feature to represent the chemical structure of the epoxy monomer. A linear regression model is trained on a random selection of 80% of the instances of the given data for T_g and T_m. As shown in Fig. 18c–d, the modes gave decent predictions for glass transition temperature and melt temperature. Similarly, 1000 pre-trained models were constructed by using a different portion of the dataset to refine the weight parameters for the small dataset on TC values. The best transferable model to predict TC was identified from the 1000 pre-trained models that predicted the highest generalization capability on the five validation sets,

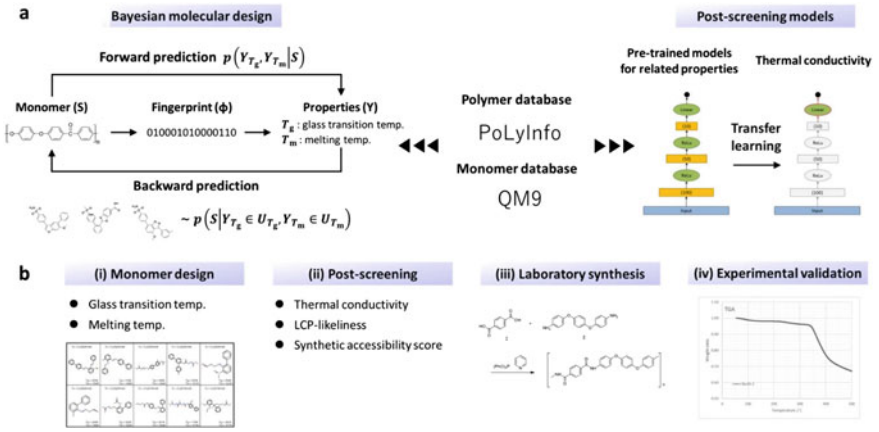

Fig. 17 Different steps for the prediction of TC of polymers from small datasets through transfer learning. **a** Forward prediction derives a model that describes polymeric properties (e.g., glass transition temperature (T_g) and melting temperature (T_m)) as a function of chemical structures in the constitutional repeat units. The forward model trained on the dataset from PoLyInfo was inverted to obtain a backward model, which was conditioned by desired property regions (U_{Tg} and U_{Tm}). The backward model produced a library of hypothetical chemical structures that exhibit the desired properties. In addition, a prediction model of TC was developed, which was utilized in the post-screening of the produced library. Here, an ML framework called transfer learning was used to overcome the issue of limited data on TC: prediction models of proxy properties were pre-trained on the given large datasets from PoLyInfo and QM9, and then, the pre-trained models were fine-tuned using the limited data on the target property. The transferred model is not directly used for the molecular design calculation because its generalization capability would likely be restricted by the design space spanned by the few training polymers. **b** Analytic workflow consisting of four internal steps toward materials discovery [54]

each randomly constructed from 20% of the data. In this way, "transfer learning" is constructed to correlate TC to the molecular structure [48, 54].

However, the model is unreliable since the test dataset only has a few data points for TC. Therefore, the properties T_g and T_m are considered as design targets, whereas the transferred model is used to screen promising candidates with a high TC. Figure 18c shows the excellent accuracy of transfer learning for predicting TC. The next stage involves backward propagation for the generation of the structure of the chosen candidates. A molecular library composed of different epoxy materials is generated using the Bayesian molecular design method which requires fewer training data values. In the molecule generation process, 1000 candidates are generated based on factors such as synthetic accessibility (SA), ease of processing, validity of chemical bond, and liquid-crystalline polymers (LCPs) likeness. At the final stage, three chemical structures are selected from these 1000 candidates based on three main criteria: TC, LCPs likeness, and SA score. Finally, the monomer of these three candidates is carried out for experiments to obtain the values of the thermophysical properties for validation [48, 54].

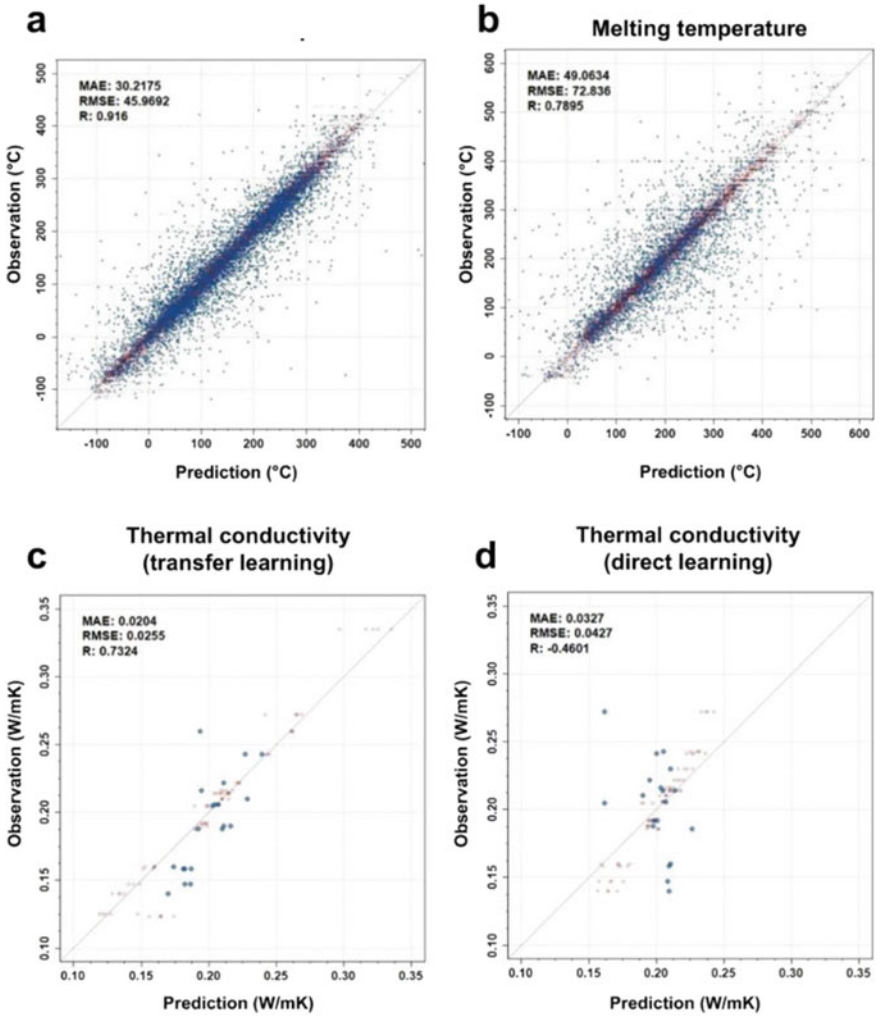

Fig. 18 Performance of forward prediction models. **a**–**b** Five-fold cross-validation of trained linear models for glass transition temperature (T_g) and melting temperature (T_m). All predicted values in the five validation sets are plotted against observed values, denoted by blue dots (red for the training). The mean absolute error (MAE), root mean square error (RMSE), and correlation coefficient (R) are shown in each plot. **c**–**d** Validation results for the prediction model on TC exhibited the best transferability (MAE = 0.0204 W/mK) out of 1000 pre-trained models on T_m. The prediction results of the best-transferred model and a random forest model trained directly using the 28 data points for TC (MAE = 0.0327 W/mK) are shown in **c**, **d**, respectively [54]

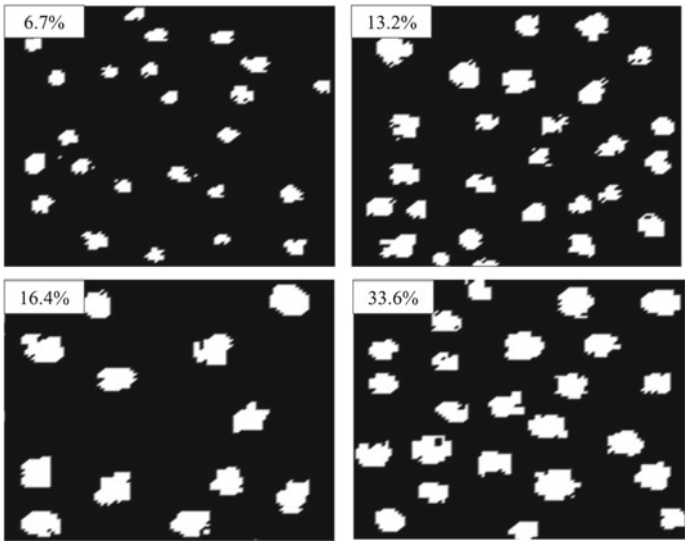

Fig. 19 Structure of composites for different volume fractions of inclusions [50]

5.3 Predicting the TC of Epoxy Composites Using Deep Learning (DL) Methods

A specialized branch of ML is the deep learning (DL) which can analyze unstructured data and automated identification of features by extracting high-level features from raw input data. The use of convolution neural network (CNN) in deep learning (DL) methods of ML has been developing fast in recent years and is a handy tool for image detection. Like face recognition, CNN can also be applied to record the feature of the composites' microstructure. The extracted structural features can be used to find out the relationship between these structures and the property of the compos. CNN can provide a rapid prediction of a composite without solving tedious simulation processes or carrying out experiments.

For analyzing the heat transfer phenomenon and predicting the TC of epoxy composites, a database with different composite material structures must be constructed. The structures can be created by the quartet structure generation set (QSGS) package, and lattice Boltzmann method (LBM) is applied to calculate its effective TC. The calculated TC values obtained from LBM by solving Boltzmann transport equation (BTE) are later used in the training dataset. This method is chosen because the dataset collected from QSGS and LBM is easily obtainable. Also, the results calculated from LBM have greater accuracy as the energy from BTE follows the heat diffusion laws in macroscale composite systems. The CNN model is then applied to train the dataset to predict the effective TC of composite materials.

A large number (about 1500) of structures are generated using QSGS with different volume loading of inclusions ranging from 2 to 30%, and each volume fraction has

about 100 data. Figure 19 shows some examples of the generated structure using QSGS. The extensive training data reduce over-fitting of data and provide a model with higher accuracy. The ratio of the TC of matrix material κ_1 and the TC of inclusion κ_2 is fixed at a specific value (1:10) as the objective of CNN is to represent the structural features. The dataset is then divided randomly into training data and testing data. For a dataset containing 1500 structures, 1400 structures consist of training and validation data, whereas the rest of the structures are used for testing the dataset.

Several CNNs with various generated structures have been previously constructed for image recognition such as LeNet-5, AlexNet, and ResNet. Wei et al. used the LeNet-5 CNN model to predict the effective TC of composites based on their training data [50]. The architecture of this CNN model as shown in Fig. 21 is discussed here to show how the CNN model works in predicting the TC of composites from its structure. The CNN involves an input layer (i.e., the structure), an output layer (i.e., the effective TC), and multiple hidden layers. The input layer is an image of the structure with a particular pixel size (in this case 100 × 112 with approx. 10_4 parameters). CNN reduces the number of parameters from the input to establish the mapping from the structure to the effective TC. The CNN can reduce the image to a few parameters in a one-dimensional vector using different kinds of functional layers without altering the key features of the structure, as shown in Fig. 20. Here, 96 feature maps with sizes of 54 × 48 pixels containing 96 different features were obtained using the kernels of 7 × 7 pixels in the first layer. The size of feature map was further reduced to 27 × 24 pixels using the corresponding kernels of 3 × 3 pixels in Pool-1. Using three convolution and pooling layers, the output features were converted to a one-dimensional feature vector by the fully connected layer FC-1 which in turn was processed by the fully connected layer FC-2. The feature vector is finally transformed into effective TC as the output which can be used to construct the regression model to predict the TC.

An activation function (e.g., sigmoid function) is added after each output layer to increase the nonlinearity of the network. A convolution neural kernel matrix is

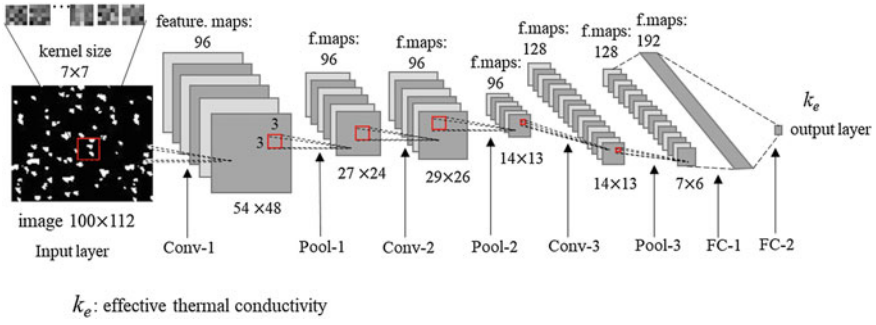

Fig. 20 Architecture of the convolution neural network LeNet-5. The size of kernels and the number of feature maps are indicated, and they can be adjusted according to specific needs [50]

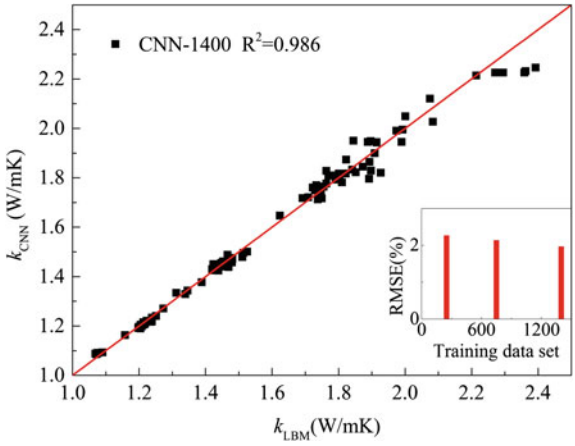

Fig. 21 Relationship between the TC predicted using CNN model and the LBM model. The CNN model is trained with 1400 datasets. The inset is the histogram of the RMSEs of the CNN models with different training datasets (1400, 750, 250) [50]

used for the mapping of the image of the structure to generate feature maps. The kernel parameters are first initialized by the "Gaussian initialization method" before extracting the features. Euclidean loss as the loss function is utilized for the parameters to be optimized to obtain the optimal regression model. Euclidean loss calculates the square sum of the difference between the two inputs among which one is the normalized target value, and the other is a predictive value as shown below:

$$\frac{1}{2N}\sum_{i=1}^{N}\left\|y_i - y_i'\right\|^2 \tag{21}$$

During the training of the neural network, the weighted parameters of the function are constantly updated according to the algorithm during each iteration to minimize the loss. After training the network, optimal parameters in the layers of the regression model are obtained which can best fit the target effective TC to the structure. From the trained CNN model, effective TC of testing data is predicted. With a testing dataset size of 100, the predicted effective TC values from the CNN model are compared with the TC values calculated by LBM. As shown in Fig. 21, the predicted results fit well with the calculated values by LBM which indicates a greater accuracy of the CNN model. It also shows that the root means square error (RMSE) decreases slightly with the number of training datasets. The RMSE is calculated by the following equation:

$$\mathrm{RMSE} = \sqrt{\frac{1}{n}\sum_{i}^{n}\left(\frac{\kappa_{LBM-i} - \kappa_{CNN}}{\kappa_{LBM-i}}\right)^2} \tag{22}$$

where κ_{LBM} and κ_{CNN} are the calculated results from LBM and predicted results from the CNN model, respectively.

6 Conclusions and Future Outlook

Epoxy-based materials are widely used for thermal management applications due to their electrically insulating nature and low coefficient of thermal expansion. Highly thermally conductive fillers are usually incorporated into the epoxy matrix to develop epoxy-based materials with high thermal conductivity. Modeling and simulation are required to reduce the number of potential experiments, develop new design criteria for the selection of matrix and fillers, and understand the heat transfer mechanism for existing materials.

Over the years, various theoretical and analytical models have been developed for the prediction and description of thermal conductivity in polymer composites. These models take into consideration several assumptions such as particle size and size distribution, filler volume fraction, shape, topology, spatial distribution, and so on. For instance, the Maxwell model considers diluting dispersion of spherical particles embedded in a continuous matrix ignoring the interactions between fillers. The Bruggeman model considers filler interaction and therefore, is more accurate for high filler volume fractions. Although these models are successful in describing experimental results, the accuracy largely depends on the introduction of fitting parameters (e.g., interfacial or Kapitza resistance).

To understand the phenomenon of heat transport at the molecular level within the matrix and/or fillers through various interfaces, classical molecular dynamics (MD) simulation can be carried out. It combines the computational efficiency and the relative accuracy of the description of atomic structure, chemistry, polymer chain conformation, and bonding to determine the TC. It also considers the interfacial thermal resistance when fillers are added into the polymer matrix and accurately describes the inter-atomic forces present within the polymer matrix or fillers. Numerical simulation methods in the form of finite element modeling are another simulation technique to predict the TC of epoxy composites considering the details of materials distribution. Finite element modeling calculates the TC of the material by directly solving the heat diffusion equation through partial differential equations methods. Unlike the numerical models, it can clearly portray the heat conduction mechanism that occurs throughout the material.

ML techniques are widely used in this era of the rapid growth of technology in different fields. The development of new materials synthesis technology and the fast-growing demand for the rapid and accurate prediction of physical properties require new computational approaches like ML methods. ML methods can correlate many variables to predict the TC of an epoxy material. Also, it can be used to design a new epoxy material with the desired TC value. Here, two studies are discussed to predict the TC of epoxy materials. The first study used transfer learning to estimate its TC with limited dataset while the other study implemented DL methods to predict the TC from the microstructure of epoxy composites. However, the ML methods are relatively new and developing in the field of polymer science, and more work is needed to be done in future related to TC of epoxy materials to reach its full potential.

Acknowledgements Author MRM would like to acknowledge the top up scholarship from Australian Carbon Innovation. Author PG would also like to acknowledge the Swinburne University Postgraduate Research Awards research grant and thank AINSE Limited for providing financial assistance (PGRA—ALNSTU12654). NH would like to thank the Australian Research Council for the ARC DECRA (DE170101249) research grant.

References

1. He, Z., Yan, Y., Zhang, Z.: Thermal management and temperature uniformity enhancement of electronic devices by micro heat sinks: a review. Energy **216**, 119223 (2021). https://doi.org/10.1016/j.energy.2020.119223
2. Wong, J.F., Hassan, A., Chan, J.X., Kabeb, S.M.: Plastics in corrosion resistant applications. Reference Module in Materials Science and Materials Engineering, Elsevier. (2020). https://doi.org/10.1016/B978-0-12-820352-1.00072-9
3. Hameed, N., Salim, N.V., Walsh, T.R., Wiggins, J.S., Ajayan, P.M., Fox, B.L.: Ductile thermoset polymers via controlling network flexibility. Chem. Commun. **51**, 9903–9906 (2015). https://doi.org/10.1039/C4CC10192H
4. Kim, W., Bae, J.-W., Choi, I.-D., Kim, Y.-S.: Thermally conductive EMC (epoxy molding compound) for microelectronic encapsulation. Polym. Eng. Sci. **39**, 756–766 (1999). https://doi.org/10.1002/pen.11464
5. Shimamura, A., Hotta, Y., Hyuga, H., Hotta, M., Hirao, K.: Improving the thermal conductivity of epoxy composites using a combustion-synthesized aggregated β-Si_3N_4 filler with randomly oriented grains. Sci. Rep. **10**, 14926 (2020). https://doi.org/10.1038/s41598-020-71745-w
6. Zhu, D., Qi, Y., Yu, W., Chen, L., Wang, M., Xie, H.: Enhanced thermal conductivity for graphene nanoplatelets/epoxy resin composites. J. Therm. Sci. Eng. Appl. 10 (2017). https://doi.org/10.1115/1.4036796
7. Zhang, Y., Gao, W., Li, Y., Zhao, D., Yin, H.: Hybrid fillers of hexagonal and cubic boron nitride in epoxy composites for thermal management applications. RSC Adv. **9**, 7388–7399 (2019). https://doi.org/10.1039/C9RA00282K
8. Wei, Z., Xie, W., Ge, B., Zhang, Z., Yang, W., Xia, H., et al.: Enhanced thermal conductivity of epoxy composites by constructing aluminum nitride honeycomb reinforcements. Compos. Sci. Technol. **199**, 108304 (2020). https://doi.org/10.1016/j.compscitech.2020.108304
9. Shen, D., Zhan, Z., Liu, Z., Cao, Y., Zhou, L., Liu, Y., et al.: Enhanced thermal conductivity of epoxy composites filled with silicon carbide nanowires. Sci. Rep. **7**, 2606 (2017). https://doi.org/10.1038/s41598-017-02929-0
10. Baghdadi, Y.N., Youssef, L., Bouhadir, K., Harb, M., Mustapha, S., Patra, D., et al.: The effects of modified zinc oxide nanoparticles on the mechanical/thermal properties of epoxy resin. J. Appl. Polym. Sci. **137**, 49330 (2020). https://doi.org/10.1002/app.49330
11. Guo, Y., Ruan, K., Shi, X., Yang, X., Gu, J.: Factors affecting thermal conductivities of the polymers and polymer composites: a review. Compos. Sci. Technol. **193**, 108134 (2020). https://doi.org/10.1016/j.compscitech.2020.108134
12. Sadeghi, M.M., Pettes, M.T., Shi, L.: Thermal transport in graphene. Solid State Commun. **152**, 1321–1330 (2012). https://doi.org/10.1016/j.ssc.2012.04.022
13. Wan, X., Feng, W., Wang, Y., Wang, H., Zhang, X., Deng, C., et al.: Materials discovery and properties prediction in thermal transport via materials informatics: a mini review. Nano Lett. **19**, 3387–3395 (2019). https://doi.org/10.1021/acs.nanolett.8b05196
14. Jablonka, K.M., Ongari, D., Moosavi, S.M., Smit, B.: Big-data science in porous materials: materials genomics and machine learning. Chem. Rev. **120**, 8066–8129 (2020). https://doi.org/10.1021/acs.chemrev.0c00004

15. Doblies, A., Boll, B., Fiedler, B.: Prediction of thermal exposure and mechanical behavior of epoxy resin using artificial neural networks and fourier transform infrared spectroscopy. Polymers (Basel) **11**, E363 (2019). https://doi.org/10.3390/polym11020363
16. Xu, X., Chen, J., Zhou, J., Li, B.: Thermal conductivity of polymers and their nanocomposites. Adv. Mater. **30**, 1705544 (2018). https://doi.org/10.1002/adma.201705544
17. Hsieh, W.-P., Losego, M.D., Braun, P.V., Shenogin, S., Keblinski, P., Cahill, D.G.: Testing the minimum thermal conductivity model for amorphous polymers using high pressure. Phys. Rev. B **83**, 174205 (2011). https://doi.org/10.1103/PhysRevB.83.174205
18. Wu, S., Peng, S., Hameed, N., Guo, Q., Mai, Y.-W.: A new route to nanostructured thermosets with block ionomer complexes. Soft Matter **8**, 688–698 (2011). https://doi.org/10.1039/C1SM06244A
19. Salim, N.V., Hameed, N., Fox, B.L., Hanley, T.L.: Novel approach to trigger nanostructures in thermosets using competitive hydrogen-bonding-induced phase separation (CHIPS). Macromolecules **48**, 8337–8345 (2015). https://doi.org/10.1021/acs.macromol.5b00687
20. Alexander, S., Entin-Wohlman, O., Orbach, R.: Phonon-fracton anharmonic interactions: the thermal conductivity of amorphous materials. Phys. Rev. B **34**, 2726–2734 (1986). https://doi.org/10.1103/PhysRevB.34.2726
21. Xie, X., Yang, K., Li, D., Tsai, T.-H., Shin, J., Braun, P.V., et al.: High and low thermal conductivity of amorphous macromolecules. Phys. Rev. B **95**, 035406 (2017). https://doi.org/10.1103/PhysRevB.95.035406
22. Ginzburg, V.V., Yang, J.: Modeling the thermal conductivity of polymer-inorganic nanocomposites. In: Ginzburg, V.V., Hall, L.M. (eds). Theory and Modeling of Polymer Nanocomposites, pp. 235–57. Cham: Springer International Publishing (2021). https://doi.org/10.1007/978-3-030-60443-1_9
23. Gojny, F.H., Wichmann, M.H.G., Fiedler, B., Kinloch, I.A., Bauhofer, W., Windle, A.H., et al.: Evaluation and identification of electrical and thermal conduction mechanisms in carbon nanotube/epoxy composites. Polymer **47**, 2036–2045 (2006). https://doi.org/10.1016/j.polymer.2006.01.029
24. Hatta, H., Taya, M., Kulacki, F.A., Harder, J.F.: Thermal diffusivities of composites with various types of filler. J. Compos. Mater. **26**, 612–625 (1992). https://doi.org/10.1177/002199839202600501
25. Eshelby, J.D., Peierls, R.E.: The determination of the elastic field of an ellipsoidal inclusion, and related problems. Proc. R. Soc. Lond. A **241**, 376–396 (1957). https://doi.org/10.1098/rspa.1957.0133
26. Maxwell, J.C.: A treatise on electricity and magnetism. Clarendon Press (1873)
27. Lin, W.: Modeling of thermal conductivity of polymer nanocomposites. Modeling and Prediction of Polymer Nanocomposite Properties, pp. 169–200. Wiley Ltd; n.d. https://doi.org/10.1002/9783527644346.ch8
28. Nayak, R., Tarkes, D.P., Satapathy, A.: A computational and experimental investigation on thermal conductivity of particle reinforced epoxy composites. Comput. Mater. Sci. **48**, 576–581 (2010). https://doi.org/10.1016/j.commatsci.2010.02.025
29. Yang, X., Liang, C., Ma, T., Guo, Y., Kong, J., Gu, J., et al.: A review on thermally conductive polymeric composites: classification, measurement, model and equations, mechanism and fabrication methods. Adv. Compos. Hybrid. Mater. **1**, 207–230 (2018). https://doi.org/10.1007/s42114-018-0031-8
30. Wang, S., Qiu, J.: Enhancing thermal conductivity of glass fiber/polymer composites through carbon nanotubes incorporation. Compos. B Eng. **41**, 533–536 (2010). https://doi.org/10.1016/j.compositesb.2010.07.002
31. Zhang, H., Zhang, X., Fang, Z., Huang, Y., Xu, H., Liu, Y., et al.: Recent advances in preparation, mechanisms, and applications of thermally conductive polymer composites: a review. J. Compos. Sci. **4**, 180 (2020). https://doi.org/10.3390/jcs4040180
32. Agari, Y., Uno, T.: Estimation on thermal conductivities of filled polymers. J. Appl. Polym. Sci. **32**, 5705–5712 (1986). https://doi.org/10.1002/app.1986.070320702

33. Wang, Z., Cheng, Y., Yang, M., Huang, J., Cao, D., Chen, S., et al.: Dielectric properties and thermal conductivity of epoxy composites using core/shell structured Si/SiO_2/Polydopamine. Compos. B Eng. **140**, 83–90 (2018). https://doi.org/10.1016/j.compositesb.2017.12.004
34. Bruggeman, D.A.G.: The calculation of various physical constants of heterogeneous substances. I. The dielectric constants and conductivities of mixtures composed of isotropic substances. Ann. Phys. **416**, 636–791 (1935)
35. Lee, E.-S., Lee, S.-M., Shanefield, D.J., Cannon, W.R.: Enhanced thermal conductivity of polymer matrix composite via high solids loading of aluminum nitride in epoxy resin. J. Am. Ceram. Soc. **91**, 1169–1174 (2008). https://doi.org/10.1111/j.1551-2916.2008.02247.x
36. Deng, F., Zheng, Q.-S., Wang, L.-F., Nan, C.-W.: Effects of anisotropy, aspect ratio, and nonstraightness of carbon nanotubes on thermal conductivity of carbon nanotube composites. Appl. Phys. Lett. **90**, 021914 (2007). https://doi.org/10.1063/1.2430914
37. Romano, V., Naddeo, C., Vertuccio, L., Lafdi, K., Guadagno, L.: Experimental evaluation and modeling of thermal conductivity of tetrafunctional epoxy resin containing different carbon nanostructures. Polym. Eng. Sci. **57**, 779–786 (2017). https://doi.org/10.1002/pen.24629
38. Zhao, J., Wu, L., Zhan, C., Shao, Q., Guo, Z., Zhang, L.: Overview of polymer nanocomposites: computer simulation understanding of physical properties. Polymer **133**, 272–287 (2017). https://doi.org/10.1016/j.polymer.2017.10.035
39. Keblinski, P.: Modeling of heat transport in polymers and their nanocomposites. In: Andreoni, W., Yip, S. (eds.) Handbook of Materials Modeling: Applications: Current and Emerging Materials, pp. 975–97. Cham: Springer International Publishing (2020). https://doi.org/10.1007/978-3-319-44680-6_31
40. Wang, T.-Y., Tsai, J.-L.: Investigating thermal conductivities of functionalized graphene and graphene/epoxy nanocomposites. Comput. Mater. Sci. **122**, 272–280 (2016). https://doi.org/10.1016/j.commatsci.2016.05.039
41. Kumar, A., Sundararaghavan, V., Browning, A.: Study of temperature dependence of thermal conductivity in cross-linked epoxies using molecular dynamics simulations with long range interactions. Model. Simul. Mater. Sci. Eng. 22 (2014). https://doi.org/10.1088/0965-0393/22/2/025013
42. Kubo, R.: Statistical-mechanical theory of irreversible processes. I. General theory and simple applications to magnetic and conduction problems. J. Phys. Soc. Jpn. **12**, 570–86 (1957). https://doi.org/10.1143/JPSJ.12.570
43. Liu, Z., Li, J., Zhou, C., Zhu, W.: A molecular dynamics study on thermal and rheological properties of BNNS-epoxy nanocomposites. Int. J. Heat Mass. Transf. **126**, 353–362 (2018)
44. Sharma, A., Choudhary, M., Agarwal, P., Kumar Patnaik, T., Kumar Biswas, S., Patnaik, A.: Experimental and numerical investigation of thermal conductivity of marble dust filled needle punched nonwoven jute-epoxy hybrid composite. Mater. Today: Proc. **38**, 248–252 (2021). https://doi.org/10.1016/j.matpr.2020.07.097
45. Xu, X., Hu, R., Chen, M., Dong, J., Xiao, B., Wang, Q., et al.: 3D boron nitride foam filled epoxy composites with significantly enhanced thermal conductivity by a facial and scalable approach. Chem. Eng. J. **397**, 125447 (2020). https://doi.org/10.1016/j.cej.2020.125447
46. Butler, K.T., Davies, D.W., Cartwright, H., Isayev, O., Walsh, A.: Machine learning for molecular and materials science. Nature **559**, 547–555 (2018). https://doi.org/10.1038/s41586-018-0337-2
47. Jha, A., Chandrasekaran, A., Kim, C., Ramprasad, R.: Impact of dataset uncertainties on machine learning model predictions: the example of polymer glass transition temperatures. Modell. Simul. Mater. Sci. Eng. **27**, 024002 (2019). https://doi.org/10.1088/1361-651X/aaf8ca
48. Chen, G., Shen, Z., Iyer, A., Ghumman, U.F., Tang, S., Bi, J., et al.: Machine-learning-assisted De novo design of organic molecules and polymers: opportunities and challenges. Polymers **12**, 163 (2020). https://doi.org/10.3390/polym12010163
49. Pruksawan, S., Lambard, G., Samitsu, S., Sodeyama, K., Naito, M.: Prediction and optimization of epoxy adhesive strength from a small dataset through active learning. Sci. Technol. Adv. Mater. **20**, 1010–1021 (2019). https://doi.org/10.1080/14686996.2019.1673670

50. Wei, H., Zhao, S., Rong, Q., Bao, H.: Predicting the effective thermal conductivities of composite materials and porous media by machine learning methods. Int. J. Heat Mass Transf. **127**, 908–916 (2018). https://doi.org/10.1016/j.ijheatmasstransfer.2018.08.082
51. Ouyang, Y., Yu, C., Yan, G., Chen, J.: Machine learning approach for the prediction and optimization of thermal transport properties. Front. Phys. **16**, 43200 (2021). https://doi.org/10.1007/s11467-020-1041-x
52. Kwon, B., Ejaz, F., Hwang, L.K.: Machine learning for heat transfer correlations. Int. Commun. Heat Mass. Transfer. **116**, 104694 (2020). https://doi.org/10.1016/j.icheatmasstransfer.2020.104694
53. Chen, L., Tran, H., Batra, R., Kim, C., Ramprasad, R.: Machine learning models for the lattice thermal conductivity prediction of inorganic materials. Comput. Mater. Sci. **170**, 109155 (2019). https://doi.org/10.1016/j.commatsci.2019.109155
54. Wu, S., Kondo, Y., Kakimoto, M., Yang, B., Yamada, H., Kuwajima, I., et al.: Machine-learning-assisted discovery of polymers with high thermal conductivity using a molecular design algorithm. Npj. Comput. Mater. **5**, 1–11 (2019). https://doi.org/10.1038/s41524-019-0203-2

Fundamentals of Electrical Conductivity in Polymers

Xoan F. Sánchez-Romate

Abstract The fundamentals of electrical conductivity in polymers have been explored, more specifically, in conductive nanofilled-based polymers. First, the determination of the percolation threshold was investigated as it constitutes a crucial parameter to enable electrical networks throughout the polymer media. Furthermore, the electrical transport mechanisms of electrically conductive polymers were identified. Particularly, intrinsic conductivity of nanofiller, contact, and tunneling resistance was identified as the main transport mechanisms, being very affected by the nature of the insulating media as well as the geometry and interactions of the nanofillers. Furthermore, the electromechanical properties of conductive polymers have been also explored, where the tunneling transport mechanisms play a very prevalent role, leading to very high electrical sensitivities to mechanical strain. Temperature dependance of the electrical conductivity has been also investigated, and electro-thermal capabilities of electrically conductive polymers were determined, highlighting the high correlation between the electrical conductivity and the heating efficiency by Joule's effect. Finally, some interesting applications of electrically conductive polymers were discussed where the development of strain and damage sensors and electrothermal heaters for de-icing and self-healable systems were identified among the most interesting ones.

Keywords Electrical properties · Polymers · Percolation threshold · Nanocomposites · Joule's effect · Electromechanical properties

1 Introduction

Nowadays, there is an increasing interest in polymer science. The reason lies in the fact that polymers usually present many interesting properties such as inherent corrosion resistance, lightness, and a good balance of mechanical properties, especially

X. F. Sánchez-Romate (✉)
Materials Science and Engineering Area, Escuela Superior de Ciencias Experimentales Y Tecnología, University Rey Juan Carlos, C/Tulipán S/N, 28933 Mostoles, Spain
e-mail: xoan.fernandez.sanchezromate@urjc.es

N. Hameed et al. (eds.), *Multifunctional Epoxy Resins*, Engineering Materials,
https://doi.org/10.1007/978-981-19-6038-3_12

in thermosets. This combination of properties makes polymers very useful in a wide range of applications.

Among the different properties of polymers, the electrical ones are quite interesting. In this regard, polymers are insulating by nature. In fact, the measurement of their dielectric constant has been subject of a deep investigation since the first studies reported by Senturia and Shepperd in 1986 [1] where they investigated the dielectric analysis during thermosetting curing.

In general, the main transport mechanism in polymer matrices is the ionic conductivity, and the electrical properties are significantly influenced by the ionic mobility during the curing process, as it is affected by the time, temperature, and frequency of the measurements. Regarding to this, Johari [2] studied the effect of these parameters on the electrical conductivity of epoxy resins, correlating the changes in some physical features such as viscosity during curing with the diffusion coefficient or impurity ions, which affected the electrical properties of the resin.

It has been pointed out that the electrical properties of conventional polymers have been widely studied. However, their insulating nature limits their applications in multiple fields. In this context, in the last decades, there have been an extensively development of electrically conductive polymers, as they can open a wide range of novel functionalities over the traditional polymers. These conductive polymers are based on the addition of conductive nanofillers inside the insulating media to create electrical networks. The understanding of the main mechanisms of electrical conductivity of this type of polymers is, thus, crucial for a proper development of novel functionalities.

Therefore, this chapter will be focused on the electrical properties of electrically conductive polymers. First, the main electrical transport mechanisms will be discussed, by exploring the effect of the insulating media as well as the conductive nanofillers. In addition, theoretical models will be explored to better understand the correlations between the different parameters on the electrical properties of conductive polymers. Furthermore, the complex analysis under AC electric field will be also explored, as it will give further information about the role of the insulating media and the interactions with the conductive elements. The temperature dependance of the electrical conductivity will be also investigated, as it will have a significant effect on the main transport mechanisms in both the insulating media (as it will affect the ionic mobility) and the conductive one. Moreover, electro-thermal capabilities of electrically conductive polymers will be discussed, by correlating the electrical properties of conductive polymers with their resistive heating capabilities.

Finally, a summary of some interesting applications of electrically conductive polymers will be listed, from strain sensors for wearable and structural devices to electro-thermal heaters for de-icing and self-healing applications.

2 Electrical Transport of Electrically Conductive Resins

As commented before, conventional polymers are insulating by nature. This is a limitation for a great number of applications requiring a certain level of electrical conductivity.

In this regard, the addition of conductive nanoparticles is a solution to achieve electrically conductive resins. The principle is based on the fact that their inclusion induces the creation of electrical pathways inside the material. These electrical pathways, once above a certain threshold, promote the creation of a continuous electrical network, and thus, the electrical conductivity may increase several orders of magnitude, leading from an insulating to an electrically conductive material.

2.1 Conductive Fillers

Therefore, electrically conductive resins consist of a non-conductive polymer matrix and conductive fillers. The conductive fillers include metal fillers, carbon-based fillers, ceramic fillers, and metal-coated fillers [3]:

- *Metal fillers*: Metal fillers comprise metal particles with diameters below 20 μm. They can be classified into silver (Ag), gold (Au), nickel (Ni), and copper (Cu), and they are now widely used at nanoscale (that is, with average size of around 10^{-9} nm) due to their exceptional properties at this scale. Silver particles present unique electrical and thermal properties and are usually used in the form of flakes with loadings between 15 and 30 wt.%. [4]. Gold particles are commonly used in electronics due to their good electrical conductivity and corrosion and oxidation resistance. Nickel particles are usually used in a spherical form. They possess higher electrical resistivity than silver ones, although a good oxidation and corrosion resistance. Finally, copper particles present excellent electrical properties although the oxidation of the particles may be a problem.
- *Carbon-based fillers*: Carbon-based nanofillers are usually divided accordingly to their geometry into 0D, 1D, and 2D nanoparticles. 0D nanoparticles are those that do not present any characteristic dimension outside the nanometer scale. Here, carbon black and fullerenes are among the most used nanofillers. 1D nanoparticles are those that present one characteristic dimension outside the nanometer scale (the length) and the other two in the range of nanometers (the diameter). Single-walled or multi-walled carbon nanotubes (SWCNTs, MWCNTs) and carbon nanofibers (CNFs) are the most used. The first one presents superior mechanical and electrical properties, whereas the second ones are much more cost-efficient [5]. Finally, 2D nanoparticles are those that present two characteristic dimensions outside the nanoscale (diameter) and the other one at nanoscale level (thickness). Graphene and graphene nanoplatelets (GNPs) are the most common nanoparticles used as it present outstanding in-plane electrical and thermal conductivity.

- *Ceramic fillers*: Ceramic fillers usually present semiconductive characteristics. In this regard, BaFe, BN, TiB2, TiN, and SiC are among the most common fillers for polymer matrices. However, in most cases, due to their semiconductive characteristics, they are used as secondary fillers for enhancing electrical and thermal conductivity [6].
- *Metal-coated fillers*: Metal-coated fillers can be categorized into two wide types involving metal core and non-metal core particles. The non-metal core materials include carbon-based fillers, glass, or polymers coated with silver, gold, nickel, aluminum, or chromium. They promote an enhancement on the electrical conductivity but also on the resistance to oxidation or to moisture, which is a relevant problem in several resins, such as epoxy polymers.

Apart from metallic, carbon-based, ceramic or metal-coated fillers, there are also a wide investigation in the use of conductive polymers as fillers to enhance the electrical properties of resins. These conductive polymers are organic materials which possess electro-conductivity due to their unique structure. Here, polypyrrole (PPy) and polyaniline (PANI) are among the most extensively studied inherently conductive polymers.

Table 1 summarizes some of the most relevant results concerning electrical conductivity of different nanocomposites depending on the type of conductive filler.

Once described the most typical fillers used to enhance the electrical conductivity of polymer matrices, it is important to defined and explore a critical parameter; the percolation threshold, as it plays a dominant role in the electrical transport of nanoparticle-based polymers.

2.2 Percolation Threshold

The percolation threshold is defined as the critical volume fraction of nano or microparticles where the polymer system becomes electrically conductive, that is, where the electrical pathways are created throughout the material.

The determination of the percolation threshold is a key factor to understand the electrical properties of nanoparticle-based polymer systems. In this regard, there are a great number of parameters that affect the determination of the percolation threshold.

On the one hand, the geometry of the nanoparticles plays a very prevalent role. It is well known that the percolation threshold is inversely proportional to the aspect ratio of the nanoparticles, defined as the ratio between the maximum and the minimum characteristic dimensions. Therefore, the higher the aspect ratio of the nanoparticles is the lower the critical volume fraction needed to create the electrical pathways throughout the material.

Apart from the aspect ratio of the nanoparticles, the intrinsic 0D, 1D, or 2D nature of the nanoparticles also have a very dominant role in the determination of the percolation threshold. More specifically, it has been proved that 2D nanoparticles present values of percolation threshold significantly higher than 1D ones.

Table 1 Summary of maximum electrical conductivity and volume fraction needed for different nanofilled-based polymer composites (some data was extracted from [3])

Main filler	Additional filler	Treatment	Volume fraction (wt.%)	σ_{max} (S/m)	References
Silver nanoparticles	–	Silane-based coupling agent	5	3.99×10^{-2}	[7]
MWCNTs	–	Mixed curing agent-assisted layer-by-layer method	15	12	[8]
MWCNTs	–	Three-roll milling	0.3	0.1	[9]
SWCNT	–	Purified	0.005	2×10^{-2}	[10]
CNF	Magnetite nanoparticles	Coating by magnetite, weak magnetic field alignment	0.2	1×10^{-9}	
GNPs	–	Ultrasonication	8	1	[11]
Graphene	–	PSS (noncovalent functionalization)	1.2	1×10^{-2}	[12]
BaFe	PANI	–	–	6.1×10^{-4}	[13]
Graphene	Gold	Gold functionalization	1	1×10^{-4}	[14]
GO	Polypyrrole (PPy)	PPy coating	0.5	6.5×10^{-5}	[15]

For example, graphene-based nanocomposites usually present values of percolation threshold around 1 to 10 wt.% [16], whereas the percolation threshold of carbon nanotube-based nanocomposites is usually below 0.1 wt.% [9]. On the other hand, nanocomposites based in 0D particles such as fullerene and carbon black present values of percolation threshold usually above 10 wt.% due to their low aspect ratio in comparison with 1D and 2D nanoparticles [17]. The reason lies in the fact that 1D particles present a very high aspect ratio in comparison with 0D and 2D nanoparticles, and thus, it is easier to create efficient electrical pathways inside the material even at low nanofiller contents.

Another important parameter affecting the determination of the percolation threshold is the waviness of the nanoparticles. The waviness ratio is defined as the effective length of the nanoparticle (i.e., the nanotube) divided by its actual length, as shown in the schematics of Fig. 1. Here, the higher the waviness ratio is the higher the percolation threshold will be, as the effective aspect ratio is reduced, and thus, the electrical transport mechanisms are less efficient. In this context, some studies demonstrated that the percolation threshold of, for example, functionalized nanoparticles are quite above than the percolation threshold of non-functionalized ones [18].

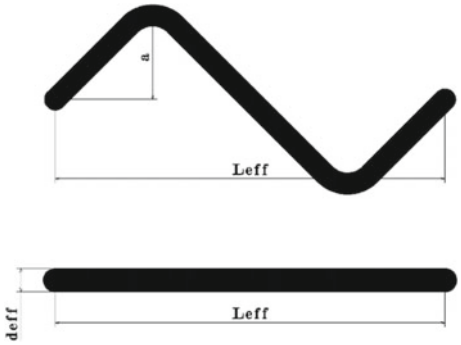

Fig. 1 Schematics of a CNT where the upper one denotes the real wavy CNT and the lower one the equivalent one. Here, the waviness ratio is defined as the amplitude, a, of the wavy CNT divided by L_{eff} (reproduced with permission from [18])

This is explained by their higher waviness ratio due to the lateral distortions induced by the functional groups [19].

The geometry of the nanofillers, thus, plays a very prevalent role. However, not only the geometry influences the percolation threshold, but also the dispersion state of the nanofillers, that is, their distribution within the polymer.

First, it is important to briefly describe the most common methods for dispersion of nanoparticles in polymer matrices. The aim of these methods is to achieve a homogeneous distribution of the nanoparticles as well as avoiding the presence of larger aggregates. In this regard, some methods are based in the prevalent action of shear forces to induce the disaggregation of larger agglomerates. More specifically, three-roll milling and toroidal stirring are among the most used dispersion techniques.

Three-roll milling consists in a progressive reduction of the gap between three rolls that are rotating at different speeds. Here, the higher the rotating speed or the lower the gap between adjacent rolls is the higher the shear forces induced in the mixture. Moreover, the resin also plays a very prevalent role as the shear forces involved are proportional to the viscosity of the mixture. Therefore, resins with higher viscosity will induce more prevalent shear forces during the dispersion process making it more efficient.

On the other hand, toroidal stirring consists in the induction of a toroidal 3D flow on the mixture that promotes a high homogenization of the nanoparticles as well as a good disaggregation of larger agglomerates. The principle for this disaggregation is the same than in case of three-roll milling, that is, the action of the shear forces induced by the blade. Here, the rotating speed of the blades, as well as the distance between the blades and the walls of the container, is the most important parameters that affect the effectiveness of the dispersion procedure. More specifically, the lower the gap between the blades and the walls or the higher the rotating speed is the higher the shear forces induced during the dispersion.

Apart from the dispersion procedures based on the action of shear forces, there are other techniques used to achieve a proper dispersion of the nanoparticles. For example, ultrasonication is one of the most common dispersion techniques for nanoparticles in low-viscosity resins. It is based on the emission of ultrasonic pulses that induces the breakage of larger agglomerates by the action of cavitation forces

in the fluid media. Here, the most important parameters of the dispersion procedure are the sonication time and the viscosity of the mixture. As expected, the increasing sonication time promotes a larger breakage of aggregates, whereas the viscosity acts in the opposite way as the higher the viscosity of the mixture, the lower the cavitation forces induced and thus, the lower the effectiveness of the ultrasonication process. In this regard, it is very common to use solvents during the dispersion process to reduce the viscosity of the mixture. These solvents are removed after the dispersion is achieved to avoid the formation of voids and generalized porosity in the final nanocomposite.

Therefore, once explained the most common techniques for the dispersion of nanoparticles in polymer systems, it is important to explore how the dispersion state affects the electrical properties of the final nanocomposite.

In this regard, there are several studies that investigate the correlations between the dispersion state and the electrical network created. More specifically, Li et al. [20] proposed a simple analytical model correlating some geometry factors and the dispersion state with the percolation threshold, P_c, of the system for CNT-doped nanocomposites:

$$P_c = \frac{\xi \varepsilon \pi}{6} + \frac{(1-\varepsilon)27\pi d^2}{4l^2} \tag{1}$$

where ξ is the proportion of the CNTs that are in form of aggregates, ε is the entanglement degree of the CNTs inside an agglomerate, and d and l are the average diameter and length of the CNTs, respectively.

Therefore, a high value of ξ would imply that most of CNTs are aggregated, that is, the dispersion state is not very good. On the other hand, a high value of ε would imply that the degree of entanglement of the CNTs inside the aggregates would be very high. A high value of aggregation parameters would lead, thus, to an increase of the percolation threshold, making the electrical network much less efficient.

As a general fact, therefore, it can be observed that the higher the aggregation of the nanoparticles is the higher the percolation threshold will be. This can be easily explained because well-dispersed nanoparticles promote the creation of more efficient electrical networks inside the material, as the distribution of these electrical pathways is much more homogeneous, as it can be observed in the schematics of Fig. 2.

Furthermore, by using this analytical model, it is possible to better understand the effect of the mentioned dispersion procedures on the percolation threshold by analyzing the dispersion achieved and the possible geometric modifications during the dispersion.

More specifically, it can be observed that ultrasonication is the most efficient technique in terms of disaggregation of larger aggregates, as the cavitation forces are, generally, very aggressive. However, it also induces a much more prevalent breakage of the nanoparticles themselves, leading to a reduction of their effective aspect ratio. In case of three-roll milling or mechanical stirring, the aggregation parameters are significantly higher, whereas the breakage of the nanoparticles is much less prevalent.

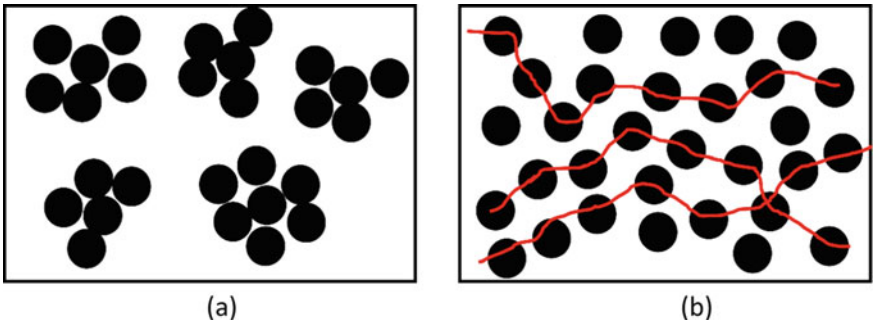

Fig. 2 Schematics of nanoparticle distribution for **a** an aggregated dispersion and **b** well-dispersed nanoparticles, where the red lines denote the main electrical pathways

2.3 Electrical Conductivity

Once understood how the electrical pathways are created and the importance of a proper determination of the percolation threshold; it is time to evaluate how these parameters affect the electrical properties of the nanocomposites. In this regard, the calculation of the electrical conductivity is a subject of huge interest.

2.3.1 Scaling Rule Model

As commented before, the percolation threshold is a critical parameter to determine the electrical properties of the final nanocomposites. Some analytical models for calculating the electrical conductivity are based in a scaling rule as follows:

$$\sigma_c = \sigma_0 \cdot (\phi - \phi_c)^t \tag{2}$$

where σ_0 is an invariable factor that depends on the aspect ratio of the nanoparticles, φ and φ_c are the volume fraction of the nanofiller and the percolation threshold, respectively, and t is an experimental fitting exponent which usually ranges from 1.3 to 2.

This model offers an initial evaluation of the electrical properties of the nanocomposite as a function of nanofiller content. However, it usually does not fit very well the experimental measurements, especially in nanofiller contents around the percolation threshold, where the changes in the electrical conductivity are very prevalent due to the changes in the main electrical transport mechanisms that occurs at these contents.

In these models, the percolation threshold is usually taken as a fixed parameter that is constant for each system. However, it significantly depends on the current dispersion state of the nanofillers inside the material. In fact, it has been proved that, during curing, the percolation threshold of the system changes, as the dispersion state

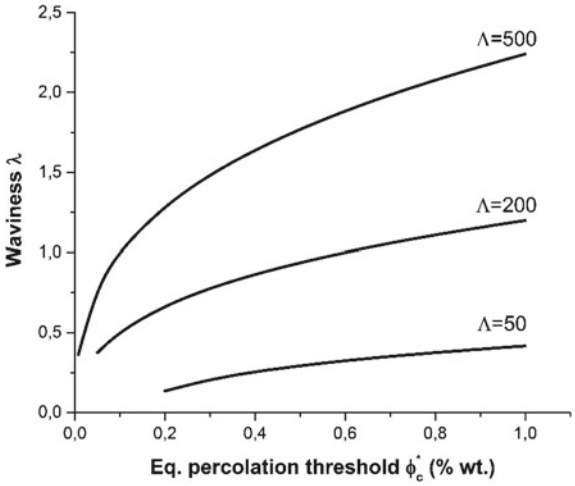

Fig. 3 Equivalent percolation threshold as a function of the waviness ratio, λ, and the aspect ratio, Λ, of the carbon nanofillers (reproduced with permission from [18])

of the nanofillers also changes because of a reaggregation before the gelation occurs [21].

Therefore, an equivalent percolation threshold was defined by Sánchez-Romate et al. [18]. This novel approach supposes that the percolation threshold is not a fixed parameter that depends on a fixed geometry and dispersion state, unique for each system, but a variable parameter that changes with the actual nanofiller content as it affects the interactions and distribution of the nanofillers. In other words, for a better understanding, this novel approach assumes that the percolation threshold depends on the actual dispersion state of the nanoparticles. It means that, for example, the percolation threshold increases with nanofiller content, as the aggregation of the nanoparticles is much more prevalent, and thus, the electrical pathways are much less efficient, accordingly to the model presented in Eq. (1).

This novel analytical method also takes geometry parameters such as the waviness or the aspect ratio of the nanoparticles, into account for the determination of the equivalent percolation threshold, as shown in the graph of Fig. 3. Here, it can be observed that the higher the waviness ratio of the nanofillers, the higher the percolation threshold, as the entanglement of the nanoparticles is much more prevalent, and thus, the electrical pathways created are less efficient.

Although the scaling law can offer an initial approximation, it does not really reflect the main electrical transport mechanisms governing nanofilled conductive polymers. In this regard, it is important to deeply explore these mechanisms to better understand the electrical properties of these systems.

2.3.2 Electrical Transport Mechanisms

In general, there are three main electrical transport mechanisms governing the nanofilled conductive polymers: the intrinsic electrical conductivity of the nanofillers,

the contact resistance between adjacent nanofillers, and the tunneling resistance between neighboring nanofillers that are not in direct contact.

The first mechanism only depends on the electrical properties of the nanofiller, and thus, it is out of scope of this chapter. However, the contact and the tunneling resistance between nanoparticles are very affected by the insulating media, that is, the polymer matrix, so it will be explored in the present throughout the chapter.

In this regard, it is important to define the tunneling effect. It is correlated with the probability of hoping conduction between two conductive particles that are separated by a thin insulating media. As a general fact, the higher the transmission probability, the lower the electrical resistance associated to this tunneling effect.

There are a lot of research exploring the tunneling effect in nanocomposites. More specifically, the electrical resistance associated to tunneling effect, R_{tunnel}, can be calculated from the following formula:

$$R_{\text{tunnel}} = \frac{h^2 t}{Ae^2\sqrt{2m\varphi}} exp\left(\frac{4\pi t}{h}\sqrt{2m\varphi}\right) \tag{3}$$

where m and e are the mass and charge of an electron, t *is* the interparticle distance, also called, tunneling distance, A is the cross-section area throughout the electron transmission may occur, also called tunneling area, and ϕ is the height barrier of the insulating media, which mainly depends on the nature of the polymer matrix.

Therefore, there are several parameters that govern the tunneling transport mechanism. More specifically, considering the mass and charge of the electron as invariable parameters, it is important to deeply study the effect of the others, that is, the tunneling distance, the tunneling area, and the height barrier of the polymer matrix.

Determination of Tunneling Distance

The tunneling distance, as mentioned earlier, is determined from the interparticle distance between adjacent and neighboring nanoparticles. Therefore, it heavily depends on the distribution of the nanoparticles inside the polymer media. Generally, the interparticle distance decreases by increasing the nanofiller content. More specifically, some studies propose a correlation between the interparticle distance and the volume fraction of the nanofillers as follows [22]:

$$t = t_c\left(\frac{\phi_c}{\phi}\right)^{\alpha} \tag{4}$$

where t and t_c are the tunneling distance at a determined volume fraction of nanoparticles, φ, and at percolation threshold, φ_c, defined as a fixed interparticle distance of 1.4 nm, respectively, and α is an experimental exponent which depends on the maximum compaction of the nanofillers.

Therefore, by increasing the volume fraction of the nanofiller, the tunneling distance between neighboring nanoparticles will be decrease, and thus, the electrical resistance associated to tunneling resistance will be also decreased.

However, the expression set in Eq. (4) is quite simple and does not take aggregation parameters into account. In this regard, there are several models that also study the influence of the nanofiller aggregation in the tunneling distance between nanoparticles. It can be considered that the interparticle distance inside an aggregate is the minimum distance between nanoparticles, set as 0.34 nm for nanofillers that are in direct contact. Outside the aggregates, the interparticle distance is significantly higher. Therefore, the mean interparticle distance does not only depend on the volume fraction of the nanofiller but also on the dispersion state.

Effect of Tunneling Area

The determination of the tunneling area throughout the tunneling transport may occur is also a very crucial factor to determine the electrical properties of the nanocomposites. This tunneling area mainly depends on the geometry of the nanofillers and the type of contact between adjacent and neighboring nanoparticles.

In this regard, several studies have explored the influence of the tunneling area and type of contact in the electrical properties of nanocomposites. For example, Kuronuma et al. [23] proposed an analytical model for the determination of tunneling resistance in CNT-doped polymers. They supposed that the contact between nanotubes may occur in-plane or out-of-plane. In the first case, the tunneling area, A_I, can be estimated as follows:

$$A_I = \frac{\pi d^2}{4} \tag{5}$$

where d is the outer diameter of the nanotube.

In case of out-of-plane contacts, the tunneling area, A_{II}, can be estimated by using the following formula:

$$A_{II} = d^2 \tag{6}$$

In both cases, the differences between the tunneling area for in-plane and out-of-plane contacts are quite slight. However, in case of 2D nanoparticles, the differences may be much more prevalent.

In this context, some studies have proposed different approximations of the tunneling area for [24] in-plane and out-of-plane contact in case of 2D nanoparticles, as observed in the schematics of Fig. 4. Here, the tunneling area for in-plane contacts may be estimated as follows:

$$A_{II} = l \cdot t \tag{7}$$

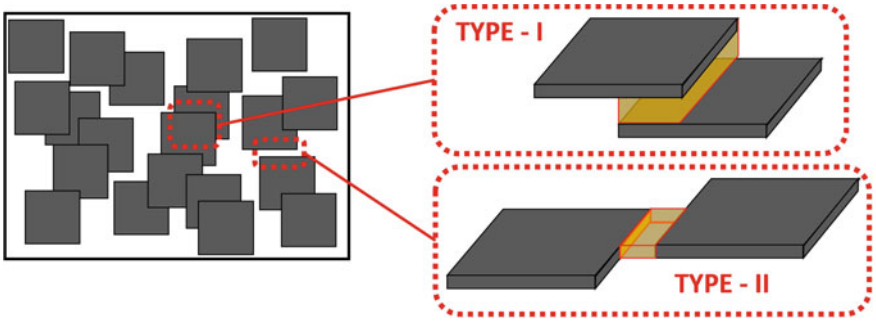

Fig. 4 Schematics of in-plane and out-of-plane contacts in a GNP network (reproduced with permission from [24])

where l and t are the average length (diameter) and the average thickness of the nanoplatelet, respectively.

However, in case of out-of-plane contacts, the estimation is quite more complicated than for nanotubes. A first simple approximation may suppose the tunneling area as a mean value of the total diameter of the nanoplatelet, by using the following expression:

$$A_I = \frac{l^2}{2} \tag{8}$$

Therefore, since $l \gg t$, the out-of-plane and in-plane tunneling areas are significantly different. For this reason, thus, the prevalence of in-plane or out-of-plane mechanisms will play a relevant role in the estimation of the electrical properties of the nanocomposite.

Effect of the Height Barrier

The height barrier of the polymer matrix, as commented, is the other parameter that plays an important role on the electrical transport mechanisms in nanocomposites, especially, at lower nanofiller loadings, since the tunneling mechanisms are most predominant in these cases. For example, the typical values of height barrier for epoxy resins usually range from 0.5 to 2.5 eV [25]. Therefore, depending on the estimated value of the height barrier, the electrical conductivity will change. More specifically, as observed in the graphs of Fig. 5, the electrical conductivity decreases with increasing height barrier from 0.5 to 2.5 eV in several orders of magnitude, accordingly to the expression of Eq. (3). These differences in the electrical conductivity are more prevalent at lower nanofiller contents, as commented before, due to a much more prevalent role of the insulating media in the electrical transport properties of the nanocomposite.

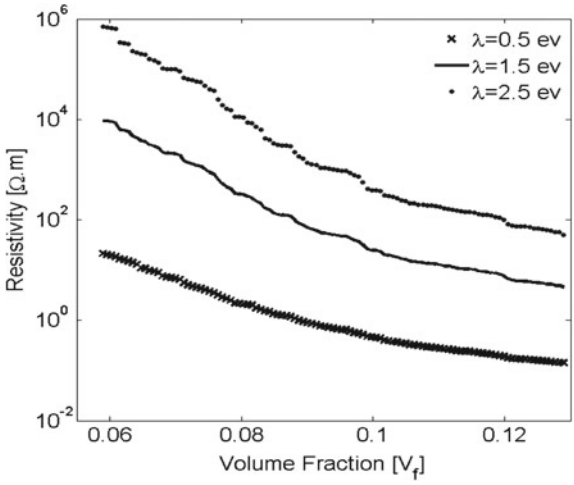

Fig. 5 Electrical resistivity as a function of height barrier of an epoxy matrix and volume fraction of the nanofiller (reproduced from [25] under Creative Commons CC-BY license)

2.3.3 Analytical Models for Electrical Conductivity Estimation

Therefore, once estimated the main transport mechanisms and how they are affected by the geometry, dispersion state and type of contact of the nanofillers, as well as by the height barrier of the insulating media, it is time to explore how it is reflected in, for example, the determination the electrical conductivity of polymer nanocomposites.

In this regard, Sánchez-Romate et al. [9] proposed a very simple analytical model for the calculation of the electrical conductivity of nanofilled polymer matrices that is reflected in the schematics of Fig. 6. It is based on a block model which assumes that the material may be divided in three main regions: one, which is dominated by the larger aggregates, where the main conduction mechanisms are governed by the intrinsic electrical conductivity of the nanofillers and the contact resistance between adjacent nanoparticles. The second region, also called the well-dispersed area, is given by these regions where the nanoparticles are not in contact but the interparticle distance is low enough to guarantee the conduction mechanisms by tunneling effect. Therefore, here, the main transport mechanism is given by the tunneling resistance. Finally, the third region, also called non-percolated area, is given by the zones of the material where there are not enough nanoparticles to guarantee a proper electrical network and thus, can be considered as an insulating region.

By dividing the material in these three main blocks, the electrical conductivity can be estimated as follows:

$$\frac{1}{R} = \xi_a \cdot \frac{1}{R_a} + \xi_d \cdot \frac{1}{R_d} + \underbrace{\xi_{non} \cdot \frac{1}{R_\infty}}_{\sim 0} \rightarrow R = \frac{R_a R_d}{(\xi_d R_a + \xi_a R_d)} \tag{9}$$

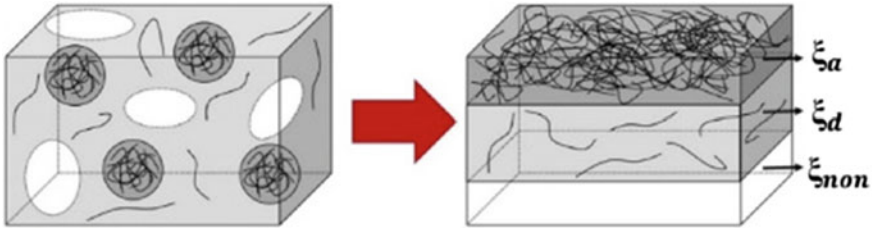

Fig. 6 Schematic of the proposed model in [9] showing (left) the real dispersion state and (right) the equivalent block disposition (reproduced with permission from [9])

where R is the equivalent electrical resistance of the element, and ξ_a, ξ_d, and ξ_{non} are the volume fractions of the agglomerated, well-dispersed, and non-percolated regions.

Therefore, by using this simple analytical model, it is possible to determine the correlation between the dispersion state and the electrical conductivity of the nanocomposite by taking the transport phenomena previously described. In this context, an aggregation parameter is defined as the ratio between the fraction of aggregated areas and the well-dispersed ones; $\varphi = \xi_a/\xi_d$.

Here, it can be observed that the electrical conductivity decreases by increasing the aggregation ratio. This is explained because the presence of larger agglomerates affects the creation of efficient electrical networks, as previously described. More specifically, by increasing the fraction of aggregated areas, also increases the fraction of non-percolated regions as the nanoparticles are much more entangled and thus occupy a lower volume fraction. As the correlation between the interparticle distance and the tunneling resistance follows a linear-exponential law, this would explain the lower efficiency of the electrical networks in this case.

Another important parameter that must be considered also in the estimation of the electrical conductivity of nanomposites is the orientation of the nanofillers. There are many of studies exploring the influence of this parameter in the creation of the electrical networks inside the material [26, 27]. It was found that electrical conductivity increases with CNT alignment due to the creation of more percolating networks [28]. Therefore, the possible alignment of the nanofillers, especially in case of 1D nanoparticles, is also an important factor to consider in order to determine the electrical properties of the nanocomposite.

2.4 Electromechanical Properties

The electrical conductivity does not only depend on the dispersion state, polymer nature or nanofiller type, but also is conditioned by the mechanical constraints of the material.

More specifically, the electrical properties of nanofilled resins change with mechanical strain. The reason lies in the fact that, the application of an external strain field promotes the deformation of the electrical network, leading to changes in the interparticle distance and/or in the type of contact between adjacent nanoparticles.

Moreover, most of nanofillers are piezoresistive. It means that their electrical conductivity changes with the applied strain. Therefore, even the intrinsic electrical resistance of the conductive nanofillers may vary with the application of an external strain field.

In this regard, it can be assumed, that at low strain levels, the deformation of the nanofillers can be negligible, as the Young's modulus of the nanofillers is usually several orders of magnitude above the Young's modulus of the polymer matrix. Therefore, the variations of the electrical conductivity due to the piezoresistive response of the nanofillers can be neglected and, for this reason, the changes in the electrical conductivity when applying a strain field will be due to the changes in the electrical resistance by tunneling effect, as the interparticle distance changes.

Concerning Eq. (3), it can be elucidated that the tunneling resistance increases in a linear-exponential fashion with applied strain as the correlation between the tunneling distance, and the applied strain can be approximated by the following expression:

$$t = t_0 \cdot (1 + \varepsilon) \tag{10}$$

where t_0 denotes the initial tunneling distance at zero strain conditions.

Regarding the electromechanical properties, it is important to study a key parameter, the gauge factor. It is defined as the ratio between the change of the normalized resistance $\Delta R/R_0$ and the applied strain, ε. The gauge factor denotes the electrical sensitivity of the system under an applied strain. Therefore, the higher the gauge factor is the higher the sensitivity of the system will be.

In this context, as it can be observed in the graph of Fig. 7, the changes of the normalized resistance are more prevalent when increasing the tunneling distance, due to the linear-exponential correlation between the tunneling distance and the tunneling resistance. Therefore, it implies that the lower the nanofiller content, the higher the gauge factor that can be achieved as the interparticle distance will increase. More specifically, the nearer the nanofiller content to the percolation threshold of the system is the more electromechanical sensitive the system will be.

As commented before, the electromechanical response is also affected by the dispersion state of the nanofillers, their geometry and the type of contacts between adjacent and neighboring nanoparticles.

More specifically, the dispersion state has been found to be a critical factor that governs the electromechanical properties of nanocomposites. Furthermore, as explored in [9], the fraction of aggregated, well-dispersed, and non-percolated areas plays a dominant role in the gauge factor of the system.

As a general fact, the gauge factor was supposed to be higher near the percolation threshold, due to a higher interparticle distance. However, this statement is only true if the nanoparticles are homogenously dispersed within the polymer matrix. More

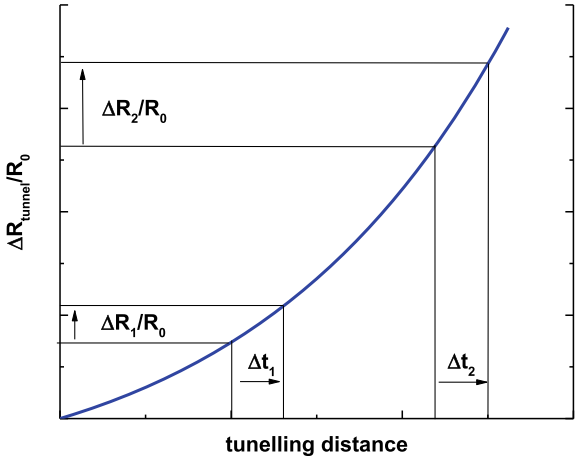

Fig. 7 Variation of the electrical resistance as a function of tunneling distance by using the expression from Eq. (3), where a linear-exponential correlation is observed

specifically, even a low nanofiller contents, if the aggregation ratio is very high, this will imply that the most prevalent conductive pathways take place throughout the aggregates. As commented before, the main conduction mechanisms inside larger aggregates are the intrinsic conductivity of the nanofiller itself. Therefore, the change of the electrical resistance with applied strain will not be as high as throughout the well-dispersed areas, where the interparticle distance is considerably higher.

On the opposite side, if the aggregation ratio is very low, this will imply that the most prevalent conduction mechanisms take place in the well-dispersed areas, that is, they will be governed by the tunneling effect. Therefore, the gauge factor will be increased.

In this regard, Fig. 8 shows the value of the gauge factor estimated by the model in [9] as a function of the mean interparticle distance and the aggregation ratio. It can be observed that the higher the aggregation ratio is the lower the value of interparticle distance where the maximum gauge factor is achieved. This can be explained because, at a very high fraction of aggregates, the main electrical mechanisms take place through the aggregates. It means that, if the interparticle distance in the well-dispersed regions is very high, these well-dispersed areas will not participate in the most prevalent electrical transport mechanisms, as the electrical resistance of these regions will be much higher than the electrical resistance of the aggregates. The opposite effect happens with a very low aggregation ratio, where the most prevalent electrical transport mechanisms take place through the well-dispersed regions, and thus, the gauge factor increases with interparticle distance.

Apart from the dispersion state, the type of contact between neighboring nanoparticles also plays a very prevalent role. Here, as commented before, in case of 1D nanoparticles such as nanotubes or nanowires, the slight differences between the tunneling area in in-plane and out-of-plane contacts are reflected in slight variations of the electromechanical behavior. However, in case of 2D nanoparticles, the

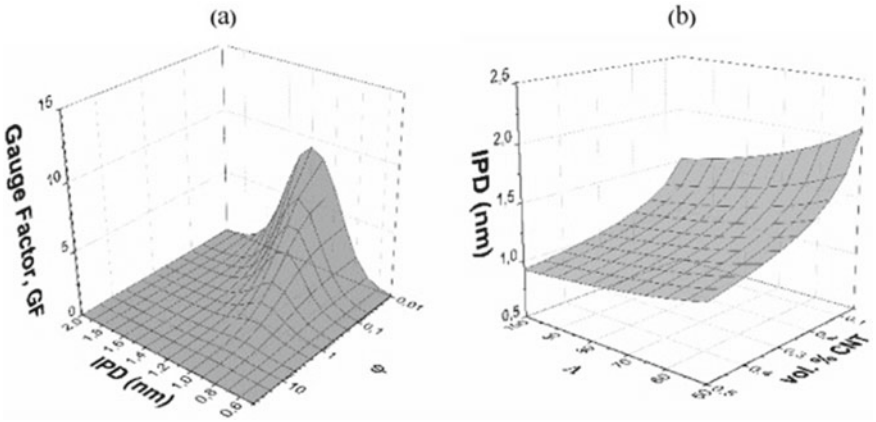

Fig. 8 **a** Effect of the aggregate ratio and interparticle distance (IPD) on the gauge factor (GF) and **b** effect of the aspect ratio and CNT content on the mean IPD (reproduced with permission from [9])

prevalence of in-plane or out-of-plane mechanisms will play a dominant role in the electromechanical response of the material.

In this context, Fig. 9 shows the electromechanical response under tensile conditions as a function of the fraction of in-plane and out-of-plane mechanisms. It can be observed that, by increasing the fraction of in-plane contacts, the sensitivity increases, whereas at very low fractions of in-plane mechanisms (under 0.1), the gauge factor is very low, even negative, due to the prevalence of Poisson effect.

Furthermore, the electromechanical response under compressive strain is quite more difficult to understand. Here, there are many mechanisms that take part. On the one side, the effect of the compressive strain itself that promotes a reduction in the interparticle distance between neighboring nanoparticles. On the other hand, the presence of local buckling mechanisms that may be reflected in the creation of microcavities [29], acting as disruptions in the electrical network.

The in-plane/out-of-plane models have been proved to be also an effective way to understand the electromechanical behavior under compressive strain. In fact, Fig. 10a summarizes the effect of in-plane/out-of-plane contact proportion on the electromechanical behavior of a GNP-epoxy nanocomposite under compressive strain. Here, it can be elucidated that the higher the in-plane proportion is the higher the electrical resistance decrease with applied strain will be. In this regard, this model has been proved to fit very well the experimental results obtained for compressive tests in GNP-epoxy nanocomposites (Fig. 10b). It can be observed that, at low strain levels, the electrical resistance decreases due to the decrease in the tunneling distance of in-plane contacts. However, at high strain levels, an increase of the electrical resistance is observed. This is explained by the presence of local buckling mechanisms as well as due to the prevalence of out-of-plane contacts, acting in an opposite way because of the Poisson effect. Therefore, as a general fact, the in-plane mechanisms dominate

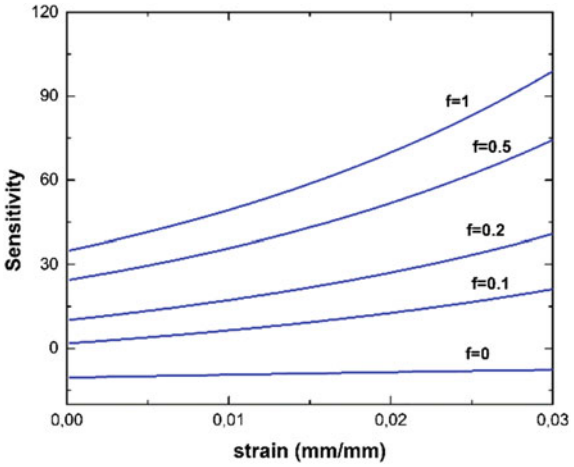

Fig. 9 Sensitivity estimated from the in-plane/out-of-plane contact model in [24] as a function of the applied strain, where f denotes the fraction of in-plane contacts in the network ($f = 1$ denotes a 100% proportion of in-plane contacts, whereas $f = 0$ denotes a 100% proportion of out-of-plane contacts) (reproduced with permission from [24])

the electromechanical response at low strains, whereas the out-of-plane mechanisms rule the electromechanical response at high strains.

The 1D or 2D nature of the nanoparticles also plays a prevalent role in the electromechanical capabilities of the nanocomposites. It can be observed that 2D nanoparticle-based composites usually present much higher gauge factor values than 1D nanoparticle-based ones. This can be easily explained accordingly to the expression in Eq. (3) by using the tunneling areas estimated from Eqs. (5–8). In case of 2D nanoparticles, the tunneling areas in both in-plane and out-of-plane contacts are generally much higher than in 1D nanoparticles, as $l \cdot t \gg d^2$. Therefore, the maximum interparticle distance between neighboring nanoparticles can be increased for 2D nanoparticles, and thus, the sensitivity increases due to the linear-exponential dependency with the tunneling distance. In fact, several studies have reported gauge factors of around 1–10 for nanotubes [31, 32], whereas it can be above 10–50 in case of nanoplatelets at low strain levels [16, 33].

Furthermore, the electromechanical response of 2D nanoparticle-based composites is usually much more exponential than in case of 1D nanoparticle-based ones, for the same reasons that those described before. In addition, the electromechanical response of hybrid 1D–2D nanoparticle-based composites has been also studied [34], to better understand the possible interactions in a hybrid network. Here, it can be noticed that the higher the ratio 2D to 1D nanoparticles is the higher the exponential behavior of the electrical response as a function of the applied strain will be, (Figs. 11a and b) as the number of electrical pathways through the 2D nanoparticle networks is increased, as observed in the schematics of Fig. 11c. Therefore, the

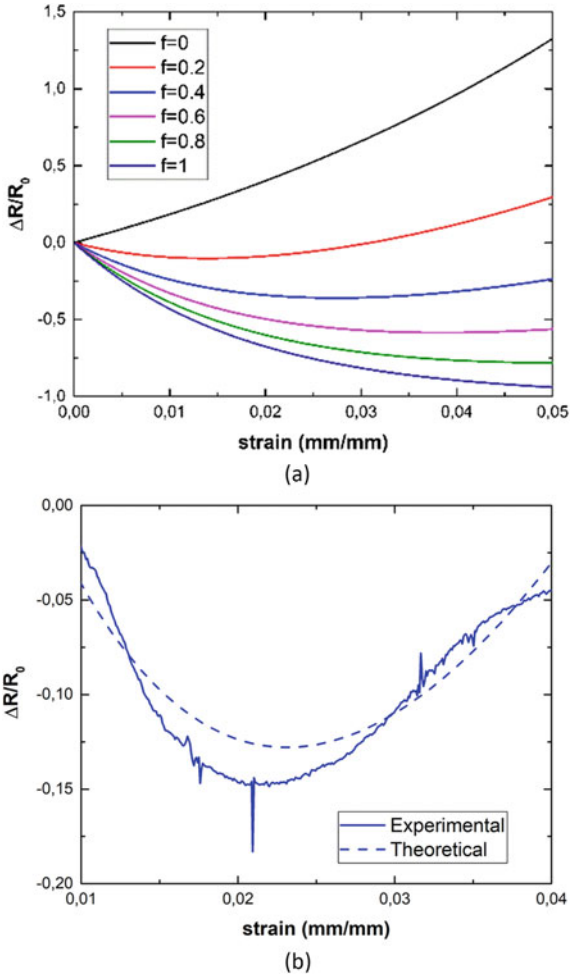

Fig. 10 Electromechanical behavior under compressive conditions showing **a** the influence of the f parameter (that is, the fraction of in-plane contacts) and **b** the theoretical to experimental comparison for a GNP-epoxy compressive test (reproduced with permission from [30])

selection of the type of nanoparticle is a very crucial factor for the development of electromechanical sensitive materials.

2.5 AC Electrical Analysis

Apart from the DC electrical conductivity, the nanocomposites also show complex, frequency-dependent electrical properties. In this regard, there are some investigations dealing with alternating current (AC) properties of nanofilled polymer matrices.

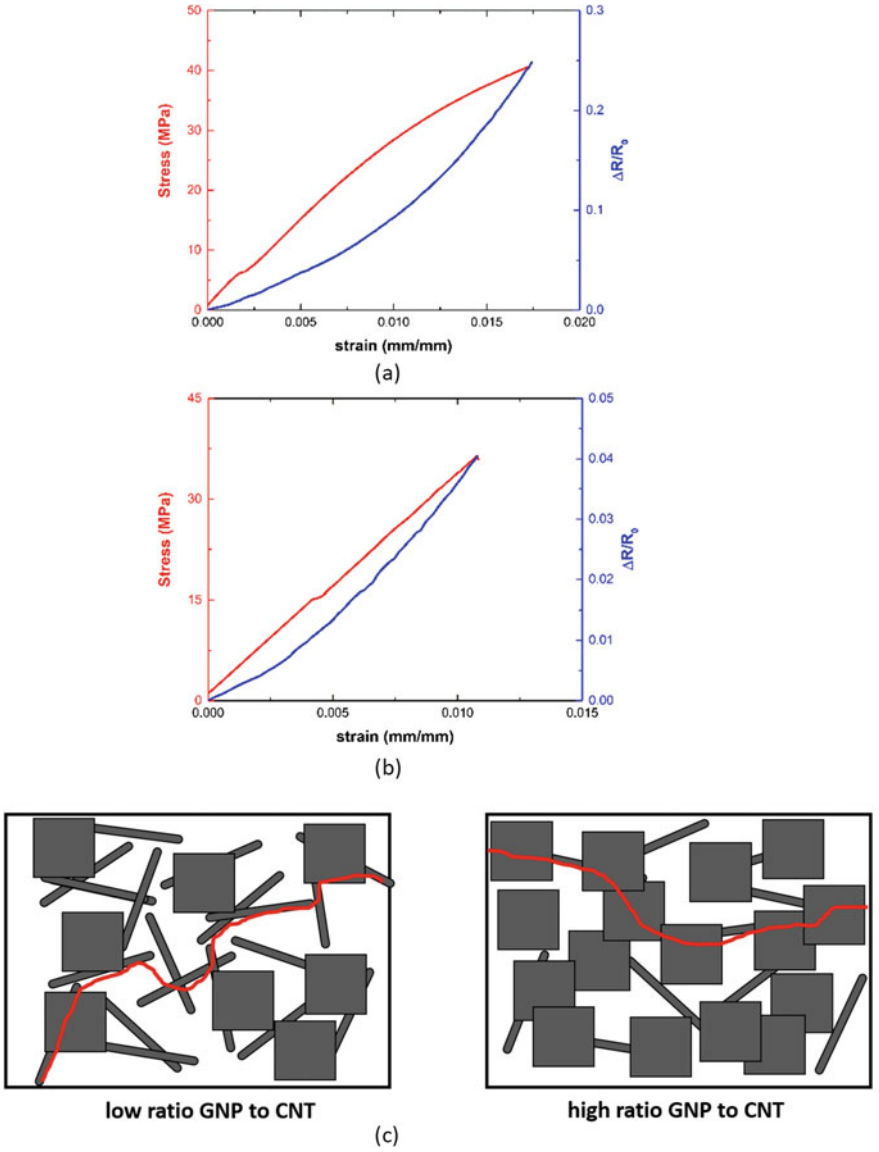

Fig. 11 Electromechanical behavior of **a** 5 wt.% GNP–0.2 wt.% CNT, **b** 5 wt.% GNP-0.1 wt.% CNT, and **c** schematics of electrical transport in a hybrid GNP-CNT network where the red line denotes the preferential electrical pathways (reproduced from [34] under Creative Commons CC-BY license)

As a general fact, the knowledge of the AC properties would allow to better understand the possible interactions among nanofillers and the particular effect of the insulating media on the electrical properties of the nanocomposites.

Figure 12 shows the typical Niqvist plot of the complex impedance as a function of AC frequency for an epoxy/CNF system. Here, it can be observed that both the real and imaginary parts of the complex impedance increase with decreasing the nanofiller content, in a similar way than in case of DC conductivity. More specifically, the electrical network can be modeled by a series–parallel circuit composed by an RC element, which corresponds to the tunneling effect occurring between adjacent nanoparticles and an LRC element, corresponding to the intrinsic and contact resistance between nanoparticles, as observed in the schematics of Fig. 13. Therefore, by adjusting the RC and LRC parameters, it is possible to quantify the effect of the intrinsic, contact, and tunneling mechanisms in the electrical properties of the nanocomposite. For example, a high RC/LRC ratio will be reflected in a high prevalence of the tunneling mechanisms inside the electrical network, typically for nanocomposites filled with low nanoparticle contents. However, a low RC/LRC ratio would denote a high prevalence of intrinsic and contact transport mechanisms, typically for nanocomposites filled with high nanoparticle contents.

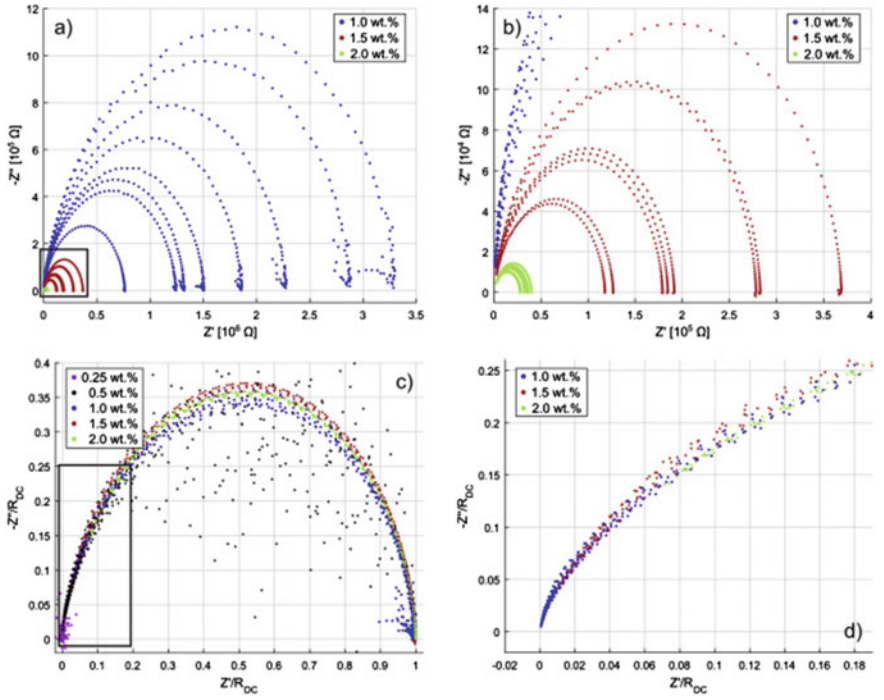

Fig. 12 **a** EIS data for 1.0, 1.5, and 2.0 wt% CNFs, **b** close up of boxed region from **a** showing 1.5 and 2.0 wt% more clearly, **c** EIS data for all weight fractions normalized by DC resistance, R_{DC}, and **d** close up of boxed region from **c** (reproduced with permission from [35])

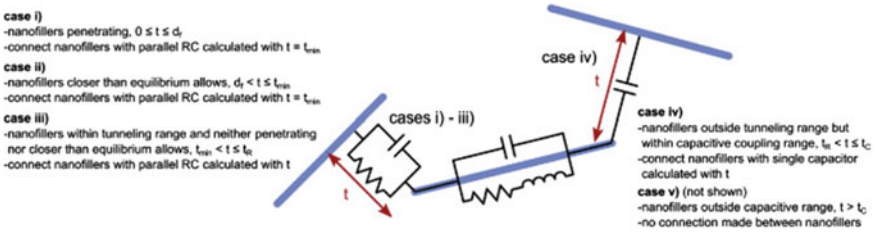

Fig. 13 Schematic of nanofiller and nanofiller-to-nanofiller junction. For cases **i–iii**, CNFs are proximate enough to enable inter-nanofiller electron tunneling. For case **iv**, it is assumed that the CNFs are too distant to participate in electron tunneling but near enough to enable inter-nanofiller capacitive coupling. Lastly, the intrinsic AC properties of the CNFs are modeled as a capacitor in parallel with a series resistor-inductor combination (reproduced with permission from [35])

The capacitance terms associated to tunneling effect can be explained by the formation of micro-capacitors between nanofillers due to the presence of a thin insulating layer between the conductive nanoparticles and can be modeled as follows:

$$C_j = \frac{\alpha \varepsilon_0 \varepsilon_r}{t} \tag{11}$$

where α is a scaling factor, ε_0 and ε_r are the permittivity of free space and the relative permittivity of epoxy, respectively, A *is* the overlapping area between nanofillers, which can be considered as the tunneling area, and t is the length of the thin layer, which can be considered as the tunneling distance.

On the other hand, the capacitance and inductance terms of the nanofillers, C_f and L_f, can be estimated from the following formulas:

$$C_f = \delta l C_q; \quad L_f = \zeta l L_k \tag{12}$$

where δ and ζ are two scaling factors, l is the length of the nanofiller; and C_q and L_k are the typical capacitance and inductance terms of the nanofillers that may be determined from the literature. For example, in case of CNTs, they have been estimated as $C_q = 100$ aF/μm and $L_k = 10$ nH/μm [36].

In addition, the effect of an applied strain on the complex impedance analysis is shown in the graphs of Fig. 14 for a GNP-PDMS system. Here, it can be observed that, at large deformations, there is an increase of both the real and the imaginary parts of the complex impedance. This is explained by the effect of out-of-plane contacts that, as explained before, play a relevant role at very high strains. As out-of-plane contacts promote an increase of the electrical resistance due to tunneling effect due to the separation of the nanofillers, it will be reflected in an increase of the capacitance term corresponding to the insulating media.

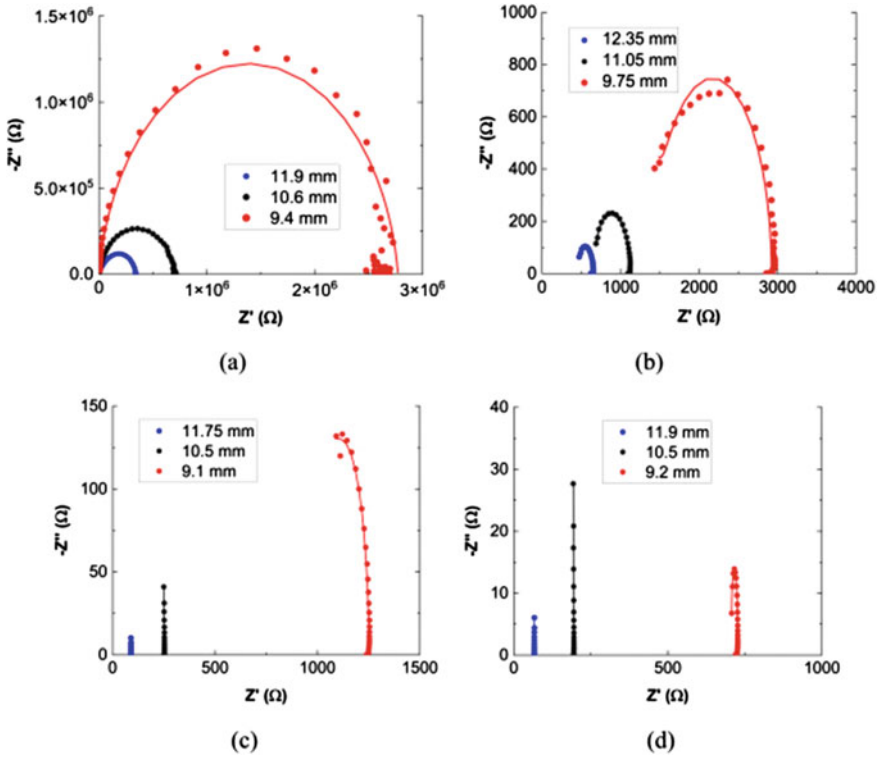

Fig. 14 EIS curves as a function of the compressive deformation for **a** 4, **b**, 6, **c** 8, and **d** 10 wt% GNP samples where the dots denote the experimental measurements and the solid lines the fitted data using the equivalent circuit (reproduced with permission from [37])

2.6 Temperature Dependance of Electrical Conductivity

The electrical conductivity does not only depend on the type and distribution of nanofillers inside the polymer matrix, but also on other factors such as the temperature. In fact, the effect of the temperature on the electrical conductivity of nanofilled polymers is quite complex to understand.

More specifically, the electrical properties as a function of the temperature highly depend on the nanofiller concentration. As explained before, for nanofiller contents below the percolation threshold, the insulating media dominates the electrical properties of the whole material as not enough electrical pathways are formed. On the other hand, for nanofiller contents above, the percolation threshold, the intrinsic, contact, and tunneling transport between adjacent and neighboring nanoparticles are the most dominating mechanisms governing the electrical properties of the nanocomposites.

Therefore, the temperature dependency of the electrical conductivity will be different depending on the nanofiller content, that is, if it is below or above percolation threshold.

In particular, the temperature effect on the tunneling conductivity can be approximated by the following formula [38]:

$$\sigma \sim \exp\left(-\frac{T_1}{T+T_0}\right) \tag{13}$$

Being

$$T_1 = \frac{wA\varepsilon_0^2}{8\pi k_B}; \quad T_0 = \frac{2T_1}{\pi \chi w} \tag{14}$$

where $\chi = \sqrt{\frac{2mV_0}{h^2}}$ and $\varepsilon_0 = \frac{4V_0}{ew}$, with e and m being the electron charge and mass, respectively, V_0 is the potential barrier height, w *is* the gap width, k_B is the Boltzmann constant, and A is the area of the nanoparticles.

Apart from the tunneling effect, which dominates when the nanofiller content is above the percolation threshold, there are other electrical transport mechanisms that governs the electrical properties of the polymer matrix.

On the one hand, the polymer matrix can be approximated filled with granular conductive materials, with a nanometer size, dispersed in the dielectric matrix. These granules can be formed by incomplete chemical reactions or by thermal variations during the curing process, resulting in trapped ions [39]. In this case, the electrical conductivity as a function of temperature can be estimated by applying the following expression:

$$\sigma \sim \sigma_0 + \ln\left[\frac{gE_c}{\max(T,\Gamma)}\right] + \sqrt{\frac{k_B T}{\Gamma}} \tag{15}$$

where σ_0 is related to the diffusion of the electrons from grain to grain, g is the dimensionless conductance ($g \gg 1$ in the strong coupling regime), E_c is the single-grain Coulomb charging energy, and Γ is a characteristic energy related to the tunneling conductance and the mean energy-level spacing.

Finally, the ionic conductivity is a very relevant electrical transport mechanisms inside the polymer matrix when below the grass transition temperature and is correlated to the presence of small concentrations of impurity molecules [40]. It can be given by the following formula:

$$\sigma \sim \sum_i \frac{A_i}{T} \exp\left(\frac{-Ea_i}{k_B T}\right) \tag{16}$$

where the sum runs for the different ionic species present in the system, Ea_i is the activation energy for a specific ionic species, and A_i is a constant associated with the electronic charge and the separation between neighboring potential walls for a characteristic ionic species.

Therefore, the electrical conductivity as a function of temperature can be calculated by taking all these effects into account, leading to the following formulas depending on the nanofiller content, that is, if the nanofiller content is below or above the percolation threshold:

$$\sigma \sim \sum_i \frac{A_i}{T}\exp\left(\frac{-Ea_i}{k_B T}\right) + \ln\left[\frac{gE_c}{\max(T,\Gamma)}\right] + \sqrt{\frac{k_B T}{\Gamma}} \quad \text{for } \phi < \phi_c \tag{17}$$

$$\sigma \sim \exp\left(-\frac{T_1}{T+T_0}\right) + \sum_i \frac{A_i}{T}\exp\left(\frac{-Ea_i}{k_B T}\right) + \ln\left[\frac{gE_c}{\max(T,\Gamma)}\right] + \sqrt{\frac{k_B T}{\Gamma}} \quad \text{for } \phi > \phi_c$$

These expressions, thus, allow to better understand the effect of the temperature on the electrical conductivity of a nanofilled polymer matrix. As a general fact, the ionic conductivity will increase with increasing the temperature and thus, at contents below the percolation threshold, the electrical conductivity will increase with temperature, as it is the main electrical transport mechanism.

However, at nanofiller contents above percolation threshold, tunneling transport mechanisms will play a very prevalent role in the electrical properties. Here, it is important to point out that, at nanofiller contents slightly above percolation threshold, tunneling resistance will be the most relevant electrical transport mechanism, whereas at nanofiller contents significantly above percolation threshold, the contact resistance will be the governing transport mechanism [41]. The tunneling resistance is reduced with temperature increase [42] as it depends on thermal fluctuations. However, the contact resistance has an opposite behavior with temperature since an increase in the temperature will enhance the kinetic energy of the carriers, and thus, contact resistance will increase due to scattering effects. For these reasons, the electrical conductivity of highly filled polymer composites usually decreases with temperature, as contact resistance is the most relevant transport mechanism. The effect of the temperature on the electrical conductivity as a function of nanofiller content is also described in the graph of Fig. 15.

2.7 Electro-Thermal Properties

The presence of electrically conductive nanofillers can offer a wide range of novel properties to the polymer matrix, as commented before. Here, the capability of heating by Joule's effect is one of the most interesting.

Joule's heating effect refers to the temperature increase in a conductive material due to the current flowing throughout it. More specifically, electrically conductive polymer matrices based on the addition of conductive nanofillers are susceptible to temperature increase when an electric field is applied. At atomic level, Joule's heating

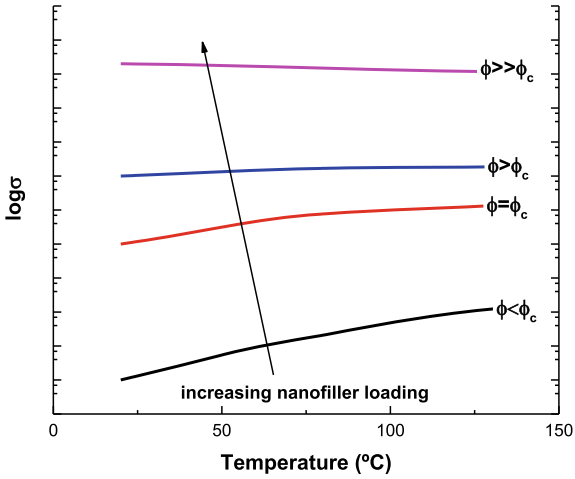

Fig. 15 Temperature dependance of the electrical conductivity of a nanofilled resin a function of the nanofiller loading showing the three typical behaviors: below percolation threshold; around or slightly above the percolation threshold and highly above the percolation threshold of the system

is a result of the movement of electrons that collides with atoms in a conductor. Therefore, impulses are transferred to the atoms, increasing their kinetic energy in form of heating.

As a general fact, the heating originated due to the applied voltage can be estimated by the well-known Joule's formula:

$$Q = I^2 Rt \tag{18}$$

where Q is the heating flow, I and R are the current flow and the electrical resistance of the material, respectively, and t is the time the electrical field is applied.

Therefore, there is a direct correlation between the Joule's heating capabilities and the electrical conductivity of the nanocomposites. Here, the presence of local aggregates of nanoparticles, defects, disruptions of the electrical network, etc., thus, will have a very significant impact on the Joule's heating capabilities of the material.

There are three main regimes when analyzing the heating by Joule's effect: the heating regime, which occurs in the first stages when applying the electric field; the maximum temperature regime, which occurs when the temperature is stabilized; and the cooling regime, which takes places once the electric field is not longer applied. The temperature can be estimated for each region by following these expressions [43, 44]:

$$\text{Heating regime} : T_t = (T_{\max} - T_0)\left(1 - e^{-\frac{t}{\tau_h}}\right) + T_0 \tag{19}$$

$$\text{Maximum temperature regime} : h_{r+c} = \frac{I_c V_0}{T_m - T_0} \tag{20}$$

$$\text{Cooling regime} : T_t = (T_{\max} - T_0)\left(e^{-\frac{t}{\tau_c}}\right) + T_0 \tag{21}$$

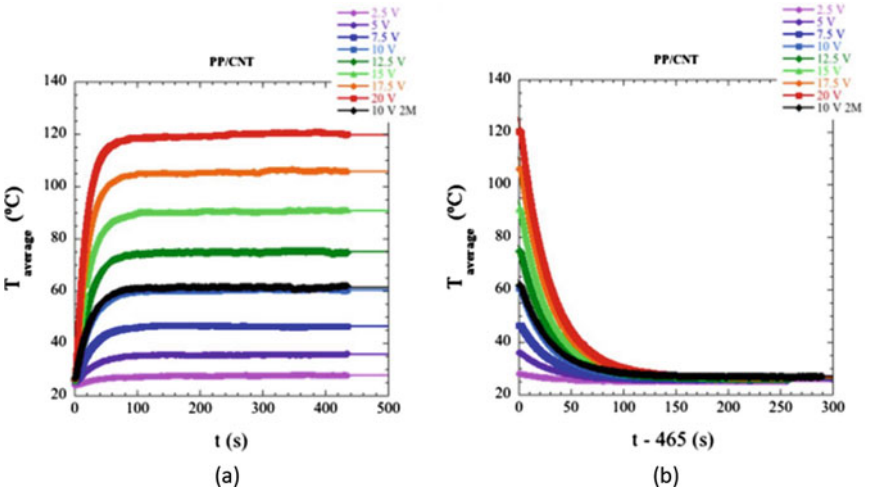

Fig. 16 **a** Heating and **b** cooling curves of PP/CNT nanocomposites as a function of applied voltage where the solid lines denote the theoretical fitting using expressions from Eqs. (19–21) (reproduced from [45] under creative commons CC-BY license)

where t is the time, $T_{\max}$ is the maximum temperature that can be reached, T_0 is the initial temperature, T_t is the temperature at each time or transient temperature, τ_h and τ_c are characteristic times, during heating and cooling, respectively, h_{r+c} is the heat transferred by radiation and convection, and I_c and V_0 are the current and applied voltage, respectively. A typical heating–cooling cycle is showed in the graphs of Fig. 16.

There are a lot of studies dealing with Joule's heating capabilities of nanofilled polymer composites for a multiple range of applications. Here, it is very common to plot the maximum temperature reached as a function of applied voltage. Usually, the correlation between the maximum temperature reached and the applied voltage follows a square law, due to the dependance between the heating flow and the current passing through the material, expressed in Eq. (18). However, this expression only fits in case of ohmic materials, that is, those who present a linear variation of the current flow with applied voltage. In case of materials with a very semiconductive behavior, where the hopping conduction is the main transport mechanisms, the correlation between the applied voltage and the current passing through the materials follows an exponential law [46], which is typical for low-filled polymer composites, where the intrinsic and contact transport mechanisms are not so prevalent:

$$I = GV\exp(kV) \tag{22}$$

where G is the conductance at 0 V, and k is a fitting parameter indicating the exponential ratio between current and voltage. Here, a higher value of this parameter would denote a higher exponential correlation between I and V.

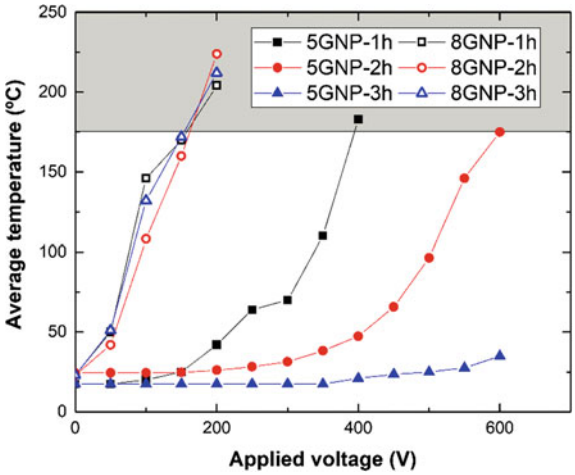

Fig. 17 Average temperature reached as a function of the applied voltage for a GNP-epoxy nanocomposites at different GNP contents and sonication time, where the gray-colored area indicates the degradation zone of the epoxy resin (reproduced from [11] under creative commons CC-BY license)

Therefore, in this case, the electrical conductivity at low voltage levels is much lower than at high voltage levels, and thus, the maximum temperature reached at high voltage levels would be much higher than expected by Joule's law.

On the other hand, in case of high-filled resins, the main transport mechanisms are due to intrinsic and contact effects between adjacent nanoparticles. Here, the I–V curve follows a linear fashion, and thus, they present an ohmic behavior. However, in this case, it has been elucidated that the electrical conductivity slightly decreases with temperature, so the maximum temperature reached as a function of voltage is lower than expected from the square law of Eq. (18). In this regard, Fig. 17 shows an example of temperature-voltage curves for Joule's heating test where the samples with the highest heating capabilities show a more linear response than those with the lowest heating response.

3 Applications of Electrically Conductive Polymers

Once understood the main electrical properties of conductive polymer matrices, it is important to explore the possible applications of this type of materials. In this regard, electrically conductive polymers open a wide range of applications in comparison with conventional polymers. Among these applications, their use as sensors, heaters, de-icing or self-healable systems is gaining a great deal of attention in the last decades.

3.1 Polymer-Based Strain and Damage Sensors

The use of nanofilled conductive polymers as strain and damage sensors is based on their electromechanical properties, which have been discussed previously.

Here, the main advantage of this type of sensors over the conventional metallic gauges is their high sensitivity. Whereas the gauge factor at low strains can reach 10–50 for GNP-based nanocomposites, in case of conventional metallic gauges is around 2–3. Therefore, the nanofilled resins can be used for the detection of very small strains.

In this regard, strain sensors may be divided in two broad groups: those for wearable devices, which require a huge flexibility and thus, very high failure strain; and those for structural applications, which require a high stiffness and strength.

3.1.1 Wearable Flexible Sensors

Most of thermosetting polymers are brittle, with high stiffness and very low failure strain. However, there are flexible thermosets, by working with systems with very low glass transition temperature. For example, one of the most used epoxy system for with high flexibility is based in poly(ethylene glycol) diglycidyl ether (PEGDGE) monomer, which presents a very low glass transition temperature (below room temperature), very high failure strain (up to 50%) and low stiffness; the ideal conditions for wearable devices.

Figure 18 shows an example of a CNT-PEGDGE system for the detection of small and large human movements. It can be observed that the high sensitivity of the system, due to the inherent piezoresistive behavior of the CNTs and the tunneling effect through the epoxy media, promotes a high motion detection.

Moreover, there are many research on wearable sensors based in nanofilled elastomers, such as polydimethylsiloxane (PDMS). Here, the electromechanical mechanisms are very similar to those commented before, but the elastomeric nature of the resin makes them highly applicable as wearable flexible devices.

Apart from the sensitivity for detection of large and small strain, the long-term stability is a crucial factor, as these sensors will be used in continuous cycling load conditions. In this context, it is important to study the electromechanical response when applying cycling load conditions. From Fig. 19, it can be observed that there is an initial decay of the electrical resistance. This can be associated to two effects: on the one hand, the inherent viscoelastic behavior of the elastomeric matrix, which promotes a delay between the electrical and the mechanical response and the possible irreversibility of the nanofiller network during the first stages of cycling load.

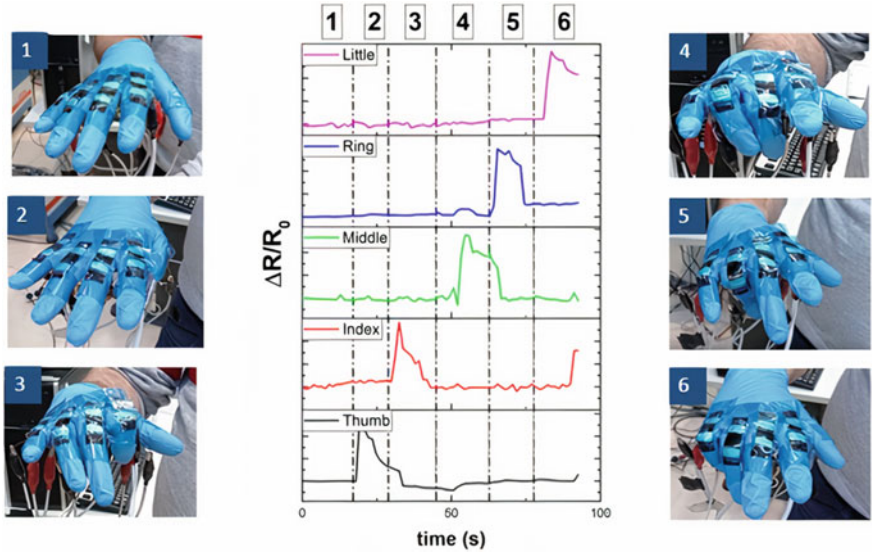

Fig. 18 Electromechanical measurements of finger motion monitoring in the case of fingers closing-opening for a CNT-PEGDGE wearable sensor (reproduced from [47] under creative commons CC-BY license)

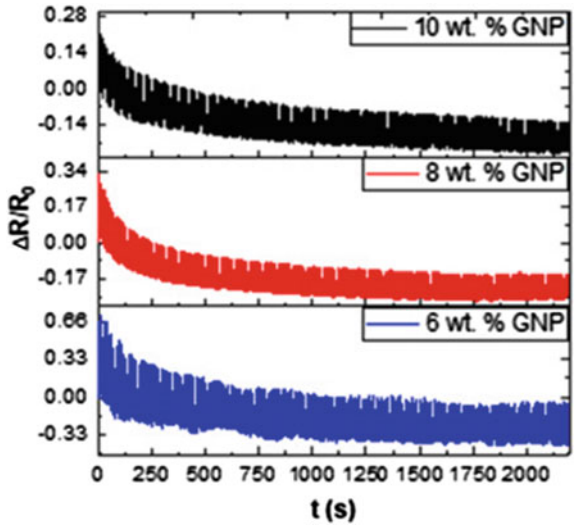

Fig. 19 Typical electromechanical response under cycling load in tensile conditions for a GNP-PDMS wearable system (reproduced with permission from [37])

3.1.2 Structural Electrically Conductive Polymers

The employment of structural conductive polymers for strain sensing and damage detection follows two main paths: their use as sensing coatings and their use as structural matrices in fiber-based multiscale composites.

In the first case, the development of electrically conductive polymers allows the creation of multifunctional smart coatings. In fact, there are many studies exploring their damage and strain sensing capabilities of nanofilled-based polymer coatings. It has been observed that, through electrical impedance tomography (EIT) techniques, which consists in the interpolation of electrical measurements through an electrode network, it is impossible to obtain an accurate mapping of the electrical conductivity of the material, making possible the identification of superficial defects [48].

In the second case, the use of nanofilled resins as matrices of fiber-based multiscale composites has been attracted the interest of many researchers. Here, it is possible to identify, not only the strain field throughout the material but also the presence of a wide range of defects such as matrix cracking, interfacial cracking or even, fiber breakage, as it induces a change in the surrounding strain field [49, 50]. In this regard, Fig. 20 shows an example of a multiscale CNT-GFRP composite under bending conditions. Here, it can be observed that it is possible to detect and locate the damage during the test, as the whole material acts as a sensor. This fact, in combination with their high sensitivity, makes nanofilled multiscale composites very promising materials for structural health monitoring (SHM) applications. The use of EIT techniques, as well as in case of polymer coatings, also offers a rapid mapping of defects in multiscale glass fiber composites [51, 52].

3.2 Applications as Electro-Thermal Heaters, De-Icing Devices, and Self-Healable Systems

The electro-thermal capabilities of nanofilled resins open a way for a wide range of applications including electro-thermal heaters for de-icing or self-healable devices.

Their capability as electro-thermal heaters is based on the extremely high efficiency of Joule's heating. More specifically, the heating rates that can be achieved are much superior to those achieved by other conventional heating (i.e., conventional oven or UV). Furthermore, the heating rate is increased with applied voltage, as the kinetic energy of the nanofillers is increased. In this regard, heating rates ranging from 0.18 to 2.89 °C/s for applied voltages ranging from 25 to 100 V, respectively, have been reported for CNT reinforced epoxy resins [54].

In this regard, these exceptional electro-thermal capabilities can be used for a wide range of applications. For example, there are many research taking advantage of Joule's heating capabilities for out-of-autoclave curing [55, 56]. Here, their fast heating rate in combination with a good nanofiller distribution is the crucial factors to ensure an homogeneous curing of the polymer matrix.

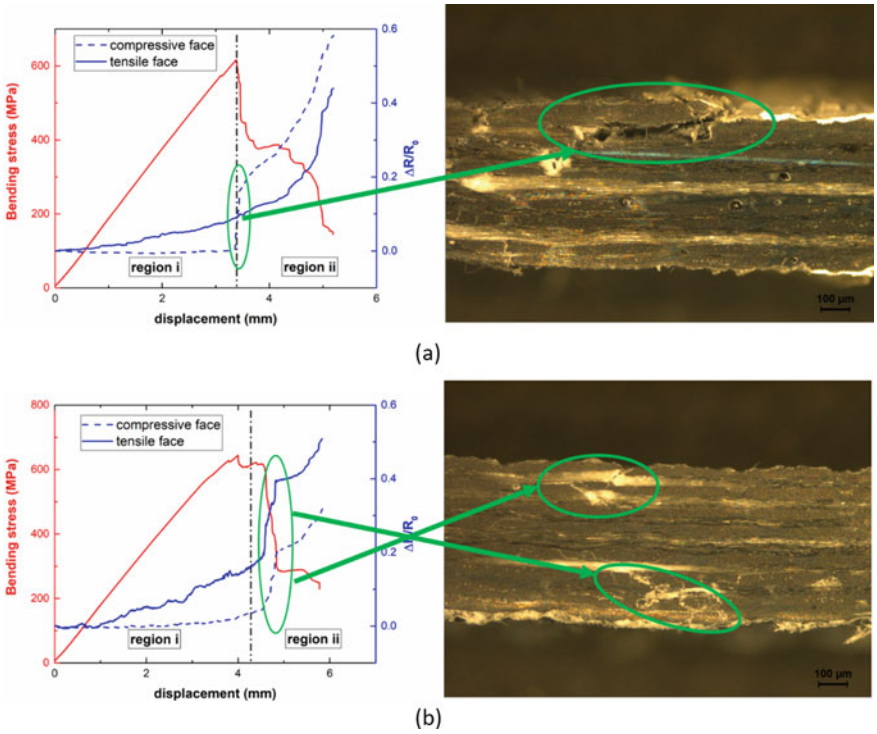

Fig. 20 Electromechanical response of glass fiber multiscale composites based on polycraplactone-epoxy blends filled with CNTs showing **a** a prevalent compressive failure and **b** mixed tensile-compressive failure, where the micrographs on the lefts denote the transversal sections (reproduced from [53] under creative commons CC-BY license)

Apart from curing by Joule's effect, this type of materials is commonly used for de-icing applications [57]. Here, when the ice is formed over the material surface, the application of an external voltage promotes an adequate surface heating, leading to the ice-melting. As observed in the graphs of Fig. 21, the de-icing capabilities of GNP-polymer composites are quite good, promoting an adequate, and fast ice-melting. Furthermore, most of the nanofillers enhance the hydrophobicity of the polymer matrix, avoiding the ice formation, as the wettability of water drops over these surfaces are quite poor.

Finally, another interesting application of the electro-thermal capabilities of nanofilled thermosetting resins is correlated to the development of self-healable systems. In this regard, self-healing refers to the capability of a material to restore their initial state after a damage takes place. Here, this self-healing capability can be achieved by an intrinsic or extrinsic stimulus. The external stimulus is usually based on healing processes that occurs by thermal activation. Therefore, heating by Joule's effect can be used to activate this external stimulus and promote the healing process inside the material.

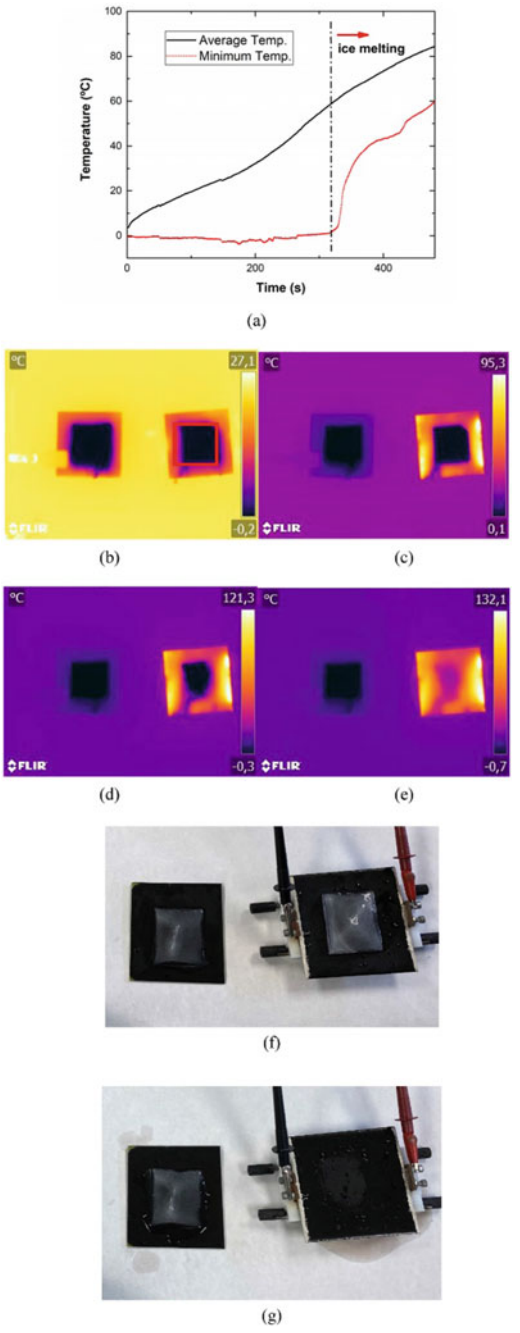

Fig. 21 **a** Temperature profile during de-icing tests of a GNP-epoxy coating, IR images at **b** initial state and after **c** 2 min, **d** 4 min, and **e** 6 min of voltage application and photographs showing **f** the initial state and **g** complete de-icing after Joule's heating test where the left specimen corresponds to the reference coating and the right one to the Joule's heated (reproduced from [60] under creative commons CC-BY license)

The self-healing process under Joule's heating is now gaining a great deal of attention. For example, some self-healable systems are comprised by blends of thermoplastic particles, such as polycaprolactone (PCL) and epoxy resins. Here, if the temperature reached is above the melting point of PCL, this thermoplastic phase may flow, filling a crack. The efficiency of self-healing process has proved to be very high, over 70% [58], indicating that the healing activation by Joule's heating is quite promising and avoids the use of conventional heating sources that are usually much less autonomous. Another example of self-healable systems activated by thermal stimulus is based on the presence of reversible bonds, such as Diels–Alder (DA) and retro-Diels–Alder (rDA) reactions. Here, the activation by Joule's effect has shown healing efficiencies of above 90% [59], proving the high potential of electro-thermal process for this type of self-healable systems.

4 Conclusions

Throughout this chapter, the electrical properties of polymers have been discussed. More specifically, the main transport mechanisms involving electrically conductive polymer composites have been discussed.

It has been observed that there are a wide range of conductive micro and nanofillers that can be incorporated to polymer resins: metal, carbon-based, ceramic, and metal-coated fillers. Here, the percolation threshold, that is, the critical volume fraction where the electrical pathways are created, promoting an electrically conductive network, is a critical parameter. It depends on the aspect ratio of the nanofillers, their dispersion state, and the possible interactions among them.

Furthermore, the main transport mechanisms were identified as intrinsic electrical conductivity of nanofillers, contact, and tunneling resistance between adjacent and neighboring nanoparticles. The first one depends on the nanofiller nature, whereas the contact and tunneling ones are influenced by the nanofiller, the insulating media, and the interactions nanofiller-polymer. More specifically, the interparticle distance, the tunneling area, and the height barrier of the insulating media were identified as the main parameters governing tunneling transport.

In addition, the linear-exponential correlation of tunneling resistance with interparticle distance makes nanofilled-based resins very susceptible to electrical changes with applied strain. Here, the sensitivity achieved in these systems is quite above that found in conventional strain gauges, making them very promising for strain sensing and damage detection devices.

Moreover, the electro-thermal properties of the nanofilled resins make them very susceptible to heating by Joule's effect, that is, by the application of an external electrical field. This interesting property can be used to develop thermo-electrical heaters, de-icing systems or to stimulate thermal activation of self-healing processes.

Therefore, it can be concluded that a good understanding of electrical properties of polymers is a key factor to take advantage of their multiple functionalities.

References

1. Senturia, S.D., Sheppard, N.F.: Dielectric analysis of thermoset cure. In: Epoxy Resins and Composites IV, pp. 1–47. Springer (1986)
2. Pitt, C., Barth, B., Godard, B.: Electrical properties of epoxy resins. IRE Trans. Compon. Parts. **4**, 110–113 (1957)
3. Aradhana, R., Mohanty, S., Nayak, S.K.: A review on epoxy-based electrically conductive adhesives. Int. J. Adhes. Adhes. **99**, 102596 (2020)
4. Yim, B., Kwon, Y., Oh, S.H., Kim, J., Shin, Y., Lee, S.H., Kim, J.: Characteristics of solderable electrically conductive adhesives (ECAs) for electronic packaging. Microelectron. Reliab. **52**, 1165–1173 (2012)
5. Ardanuy, M., Rodríguez-Perez, M.A., Algaba, I.: Electrical conductivity and mechanical properties of vapor-grown carbon nanofibers/trifunctional epoxy composites prepared by direct mixing. Compos. B Eng. **42**, 675–681 (2011)
6. Zhao, J., Hu, J., Jiao, D., Tosto, S.: Application of face centred cubic TiB powder as conductive filler for electrically conductive adhesives. Trans. Nonferrous Metals Soc. China. **24**, 1773–1778 (2014)
7. Tee, D.I., Mariatti, M., Azizan, A., See, C.H., Chong, K.F.: Effect of silane-based coupling agent on the properties of silver nanoparticles filled epoxy composites. Compos. Sci. Technol. **67**, 2584–2591 (2007)
8. Feng, Q., Yang, J., Fu, S., Mai, Y.: Synthesis of carbon nanotube/epoxy composite films with a high nanotube loading by a mixed-curing-agent assisted layer-by-layer method and their electrical conductivity. Carbon **48**, 2057–2062 (2010)
9. Sánchez-Romate, X.F., Artigas, J., Jiménez-Suárez, A., Sánchez, M., Güemes, A., Ureña, A.: Critical parameters of carbon nanotube reinforced composites for structural health monitoring applications: empirical results versus theoretical predictions. Compos. Sci. Technol. **171**, 44–53 (2019)
10. Bryning, M.B., Islam, M.F., Kikkawa, J.M., Yodh, A.G.: Very low conductivity threshold in bulk isotropic single-walled carbon nanotube–epoxy composites. Adv. Mater. **17**, 1186–1191 (2005)
11. Sánchez-Romate, X.F., Sans, A., Jiménez-Suárez, A., Campo, M., Ureña, A., Prolongo, S.G.: Highly multifunctional GNP/epoxy nanocomposites: from strain-sensing to joule heating applications. Nanomaterials. **10**, 2431 (2020)
12. Li, Y., Kanaji, N., Wang, X., Sato, T., Nakanishi, M., Kim, M., Michalski, J., Nelson, A.J., Farid, M., Basma, H., Patil, A., Toews, M.L., Liu, X., Rennard, S.I.: Prostaglandin E2 switches from a stimulator to an inhibitor of cell migration after epithelial-to-mesenchymal transition. Prostaglandins Other Lipid Mediat. **116–117**, 1–9 (2015)
13. Saad, G.R., Ezz, A.A., Ahmed, H.A.: Cure kinetics, thermal stability, and dielectric properties of epoxy/barium ferrite/polyaniline composites. Thermochim. Acta **599**, 84–94 (2015)
14. Martin-Gallego, M., López-Manchado, M.A., Calza, P., Roppolo, I., Sangermano, M.: Gold-functionalized graphene as conductive filler in UV-curable epoxy resin. J. Mater. Sci. **50**, 605–610 (2015)
15. Krushnamurty, K., Rini, M., Srikanth, I., Ghosal, P., Das, A.P., Deepa, M., Subrahmanyam, C.: Conducting polymer coated graphene oxide reinforced C–epoxy composites for enhanced electrical conduction. Compos. A Appl. Sci. Manuf. **80**, 237–243 (2016)
16. Moriche, R., Sanchez, M., Jimenez-Suarez, A., Prolongo, S.G., Urena, A.: Strain monitoring mechanisms of sensors based on the addition of graphene nanoplatelets into an epoxy matrix. Compos. Sci. Technol. **123**, 65–70 (2016)
17. Wu, K.H., Ting, T.H., Wang, G.P., Ho, W.D., Shih, C.C.: Effect of carbon black content on electrical and microwave absorbing properties of polyaniline/carbon black nanocomposites. Polym. Degrad. Stab. **93**, 483–488 (2008)
18. Sánchez-Romate, X.F., Jiménez-Suárez, A., Sánchez, M., Güemes, A., Ureña, A.: Novel approach to percolation threshold on electrical conductivity of carbon nanotube reinforced nanocomposites. Rsc Adv. **6**, 43418–43428 (2016)

19. Milowska, K., Birowska, M., Majewski, J.A.: Mechanical and electrical properties of carbon nanotubes and graphene layers functionalized with amines. Diam. Relat. Mater. **23**, 167–171 (2012)
20. Li, J., Ma, P.C., Chow, W.S., To, C.K., Tang, B.Z., Kim, J.: Correlations between percolation threshold, dispersion state, and aspect ratio of carbon nanotubes. Adv. Func. Mater. **17**, 3207–3215 (2007)
21. Kovacs, J.Z., Velagala, B.S., Schulte, K., Bauhofer, W.: Two percolation thresholds in carbon nanotube epoxy composites. Compos. Sci. Technol. **67**, 922–928 (2007)
22. Takeda, T., Shindo, Y., Kuronuma, Y., Narita, F.: Modeling and characterization of the electrical conductivity of carbon nanotube-based polymer composites. Polymer **52**, 3852–3856 (2011)
23. Kuronuma, Y., Takeda, T., Shindo, Y., Narita, F., Wei, Z.: Electrical resistance-based strain sensing in carbon nanotube/polymer composites under tension: analytical modeling and experiments. Compos. Sci. Technol. **72**, 1678–1682 (2012)
24. Sánchez, M., Moriche, R., Sánchez-Romate, X.F., Prolongo, S.G., Rams, J., Ureña, A.: Effect of graphene nanoplatelets thickness on strain sensitivity of nanocomposites: a deeper theoretical to experimental analysis. Compos. Sci. Technol. **181**, 107697 (2019)
25. Oskouyi, A.B., Sundararaj, U., Mertiny, P.: Tunneling conductivity and piezoresistivity of composites containing randomly dispersed conductive nano-platelets. Materials. **7**, 2501–2521 (2014)
26. Bao, W.S., Meguid, S.A., Zhu, Z.H., Meguid, M.J.: Modeling electrical conductivities of nanocomposites with aligned carbon nanotubes. Nanotechnology **22**, 485704 (2011)
27. Bao, W.S., Meguid, S.A., Zhu, Z.H., Pan, Y., Weng, G.J.: A novel approach to predict the electrical conductivity of multifunctional nanocomposites. Mech. Mater. **46**, 129–138 (2012)
28. Jangam, S., Raja, S., Maheswar Gowd, B.U.: Influence of multiwall carbon nanotube alignment on vibration damping of nanocomposites. J. Reinf. Plast. Compos. **35**, 617–627 (2016)
29. Moriche, R., Jiménez-Suárez, A., Sánchez, M., Prolongo, S.G., Ureña, A.: Sensitivity, influence of the strain rate and reversibility of GNPs based multiscale composite materials for high sensitive strain sensors. Compos. Sci. Technol
30. Sánchez-Romate, X.F., Moriche, R., Jiménez-Suárez, A., Sánchez, M., Prolongo, S.G., Ureña, A.: Sensitive response of GNP/epoxy coatings as strain sensors: analysis of tensile-compressive and reversible cyclic behavior. Smart Mater. Struct. **29**, 065012 (2020)
31. Zhai, T., Li, D., Fei, G., Xia, H.: Piezoresistive and compression resistance relaxation behavior of water blown carbon nanotube/polyurethane composite foam. Compos. A Appl. Sci. Manuf. **72**, 108–114 (2015)
32. Wichmann, M.H.G., Buschhorn, S.T., Boeger, L., Adelung, R., Schulte, K.: Direction sensitive bending sensors based on multi-wall carbon nanotube/epoxy nanocomposites. Nanotechnology **19**, 475503 (2008)
33. Moriche, R., Sanchez, M., Prolongo, S.G., Jimenez-Suarez, A., Urena, A.: Reversible phenomena and failure localization in self-monitoring GNP/epoxy nanocomposites. Compos. Struct. **136**, 101–105 (2016)
34. Sánchez-Romate, X.F., Jiménez-Suárez, A., Campo, M., Ureña, A., Prolongo, S.G.: Electrical properties and strain sensing mechanisms in hybrid graphene nanoplatelet/carbon nanotube nanocomposites. Sensors. **21**, 5530 (2021)
35. Tallman, T.N., Hassan, H.: A network-centric perspective on the microscale mechanisms of complex impedance in carbon nanofiber-modified epoxy. Compos. Sci. Technol. **181**, 107669 (2019)
36. Burke, P.J.: An RF circuit model for carbon nanotubes. IEEE Trans. Nanotechnol. **2**, 55–58 (2003)
37. Bosque, A.D., Sánchez-Romate, X.F., Sánchez, M., Ureña, A.: Ultrasensitive and highly stretchable sensors for human motion monitoring made of graphene reinforced polydimethylsiloxane: electromechanical and complex impedance sensing performance. Carbon. **192**, 234–248 (2022)
38. Cardoso, P., Silva, J., Agostinho Moreira, J., Klosterman, D., van Hattum, F.W.J., Simoes, R., Lanceros-Mendez, S.: Temperature dependence of the electrical conductivity of vapor grown

carbon nanofiber/epoxy composites with different filler dispersion levels. Phys. Lett. A. **376**, 3290–3294 (2012)
39. Beloborodov, I.S., Lopatin, A.V., Vinokur, V.M., Efetov, K.B.: Granular electronic systems. Rev. Mod. Phys. **79**, 469 (2007)
40. Bower, D.I.: No title. An Introduction to Polymer Physics (2003)
41. Jović, N., Dudić, D., Montone, A., Antisari, M.V., Mitrić, M., Djoković, V.: Temperature dependence of the electrical conductivity of epoxy/expanded graphite nanosheet composites. Scr. Mater. **58**, 846–849 (2008)
42. Weng, W., Chen, G., Wu, D.: Transport properties of electrically conducting nylon 6/foliated graphite nanocomposites. Polymer **46**, 6250–6257 (2005)
43. Kim, B., Park, S., Bandaru, P.R.: Anomalous decrease of the specific heat capacity at the electrical and thermal conductivity percolation threshold in nanocomposites. Appl. Phys. Lett. **105**, 253108 (2014)
44. Jeong, Y.G., An, J.: UV-cured epoxy/graphene nanocomposite films: preparation, structure and electric heating performance. Polym. Int. **63**, 1895–1901 (2014)
45. Sangroniz, L., Sangroniz, A., Fernández, M., Etxeberria, A., Müller, A.J., Santamaria, A.: Elaboration and characterization of conductive polymer nanocomposites with potential use as electrically driven membranes. Polymers **11**, 1180 (2019)
46. Pelech, I., Kaczmarek, A., Pelech, R.: Current-voltage characteristics of the composites based on epoxy resin and carbon nanotubes. J. Nanomaterials 405345 (2015)
47. del Bosque, A., Sánchez-Romate, X.F., Sánchez, M., Ureña, A.: Flexible wearable sensors based in carbon nanotubes reinforced poly (ethylene glycol) diglycidyl ether (PEGDGE): analysis of strain sensitivity and proof of concept. Chemosensors. **9**, 158 (2021)
48. Sánchez-Romate, XF., Moriche, R., Jiménez-Suárez, A., Sánchez, M., Prolongo, S.G., Güemes, A., Ureña, A.: Highly sensitive strain gauges with carbon nanotubes: from bulk nanocomposites to multifunctional coatings for damage sensing. Appl. Surf. Sci. **424**, 213–221 (2017)
49. Thostenson, E.T., Chou, T.: Carbon nanotube networks: sensing of distributed strain and damage for life prediction and self healing. Adv. Mater. **18**, 2837–+ (2006)
50. Gao, L., Chou, T., Thostenson, E.T., Zhang, Z., Coulaud, M.: In situ sensing of impact damage in epoxy/glass fiber composites using percolating carbon nanotube networks. Carbon **49**, 3382–3385 (2011)
51. Tallman, T.N., Gungor, S., Wang, K.W., Bakis, C.E.: Damage detection and conductivity evolution in carbon nanofiber epoxy via electrical impedance tomography. Smart Mater. Struct. **23**, 045034 (2014)
52. Tallman, T.N., Gungor, S., Wang, K.W., Bakis, C.E.: Damage detection via electrical impedance tomography in glass fiber/epoxy laminates with carbon black filler. Struct. Health Monit. **14**, 100–109 (2015)
53. Sánchez-Romate, X.F., Alvarado, A., Jiménez-Suárez, A., Prolongo, S.G.: Carbon nanotube reinforced poly (ε-caprolactone)/epoxy blends for superior mechanical and self-sensing performance in multiscale glass fiber composites. Polymers. **13**, 3159 (2021)
54. Donati, G., De Nicola, A., Munaò, G., Byshkin, M., Vertuccio, L., Guadagno, L., Le Goff, R., Milano, G.: Simulation of self-heating process on the nanoscale: a multiscale approach for molecular models of nanocomposite materials. Nanoscale Adv. **2**, 3164–3180 (2020)
55. Xia, T., Zeng, D., Li, Z., Young, R.J., Vallés, C., Kinloch, I.A.: Electrically conductive GNP/epoxy composites for out-of-autoclave thermoset curing through Joule heating. Compos. Sci. Technol. **164**, 304–312 (2018)
56. Sung, P., Chang, S.: The adhesive bonding with buckypaper–carbon nanotube/epoxy composite adhesives cured by Joule heating. Carbon **91**, 215–223 (2015)
57. Redondo, O., Prolongo, S.G., Campo, M., Sbarufatti, C., Giglio, M.: Anti-icing and de-icing coatings based Joule's heating of graphene nanoplatelets. Compos. Sci. Technol. **164**, 65–73 (2018)
58. Sánchez-Romate, X.F., Sans, A., Jiménez-Suárez, A., Prolongo, S.G.: The addition of graphene nanoplatelets into epoxy/polycaprolactone composites for autonomous self-healing activation by joule's heating effect. Compos. Sci. Technol. **213**, 108950 (2021)

59. Park, J.S., Kim, H.S., Thomas Hahn, H.: Healing behavior of a matrix crack on a carbon fiber/mendomer composite. Compos. Sci. Technol. **69**, 1082–1087 (2009)
60. Sánchez-Romate, X.F., Gutiérrez, R., Cortés, A., Jiménez-Suárez, A., Prolongo, S.G.: Multifunctional coatings based on GNP/epoxy systems: strain sensing mechanisms and joule's heating capabilities for deicing applications. Prog. Org. Coat. **167**, 106829 (2022)

Imparting Electrical Conductivity in Epoxy Resins (Chemistry and Approaches)

Negar Farzanehfar, Atefeh Nasr Esfahani, Mehdi Sheikhi, and Fatemeh Rafiemanzelat

Abstract Electrically conductive epoxy thermosets are getting widespread consideration due to the fast-growing advanced engineering material industry. There are known platforms for encapsulating semiconductors, equipment constituents, electric circuit board substances, aerospace, etc. Currently, various efforts are being made to manufacture conductive epoxy-based nanocomposites, and a systematic and comprehensive understanding is required to move the achievements a step ahead. The conduction mechanism appears as a result of conductive network formation created in the presence of a specific type of additives, namely electrically conductive fillers. Conductive fillers are powders, fibers, and other materials added to epoxy resin to make it easier for electrons to pass through. This chapter describes how the electrical conductance of epoxy thermosets is improved using different types of conductive fillers. The emphasis is on conventional electrically conductive agents (e.g., metals, carbonaceous fillers, and intrinsically conductive polymers) as well as green ionic mixtures, including multi-functioning ionic liquids and deep eutectic solvents. The latter category is important since ionic mixtures can play simultaneously as epoxy hardening compounds and curing catalysts, in addition to their role as electrically conductive agents. Numerous examples of recent and current research activities are given to introduce a complete background of achievement.

Keywords Epoxy resin · Conductive nanocomposites · Electrical conductivity · Conductive additives · Ionic liquids · Deep eutectic solvents

1 Introduction

In the developing industries, there is a growing demand for high-performance conductive polymer composite materials in many industrial sectors such as medical, aerospace, and automotive. Although insulating polymers have advantages in various applications, many cases require a conductive substrate for the intended electrical

N. Farzanehfar · A. Nasr Esfahani · M. Sheikhi · F. Rafiemanzelat (✉)
Polymer Chemistry Research Laboratory, Department of Chemistry, University of Isfahan, 81746-73441 Isfahan, Iran
e-mail: frafiemanzelat@chem.ui.ac.ir

N. Hameed et al. (eds.), *Multifunctional Epoxy Resins*, Engineering Materials,
https://doi.org/10.1007/978-981-19-6038-3_13

and electronic areas, including dissipation of electrostatic charge from rubber, transmission lines, electrical machines, artificial muscles, and biosensors. Due to these potentials, electrically conductive thermosets have gained intensive attention from academic and industrial researchers. Thus, material engineers have been seeking to find a sustainable way to induce electrical conductivity to be conventional, cheap, and easy to access with polymeric precursors and combine the conductivity of conducting agents with the versatility of thermosets. For this, they have persistently attempted to produce conductive platforms and modify their electrical properties as well [1, 2].

Epoxy resins are reactive polymer chains that can be useful industrial materials after they are cured by polymerization into three-dimensional networks. Thanks to their excellent thermal and chemical stability and mechanical characters, high stiffness, feasibility to tailor their properties by both polymerization and curing protocols, low creep, and very low cure shrinkage, they are widely used in high-performance engineering usages like tough adhesives, coatings, and paints along with components in aerospace and automobile manufacturing industries [3, 4]. They are also used as medium matrix for manufacturing composite materials for electronic components, construction, mining, capsulation of semiconductors, equipment parts, and electronic circuit boarding stuff [3]. In addition, given a medium conductance, epoxy thermosets are primary candidates for use in tools such as medical equipment, electronic boards, and cement. The low-level electric conduction of epoxy thermosets (about 10^{-7} to 10^{-14} S/m) is their limitation to employ as electrically conductive materials. Their low electrical conductivity imposes challenges, for example, in aircraft protection against lightning and interference of electromagnetic waves [5]. Also, good electrical conductivity is needed for having antistatic properties to protect mining and transport equipment, gas storage, and electrical and electronic devices against fire [6]. To address these issues, great attention has been paid to prepare polymeric nanocomposites or blends and manipulating their electrical characteristic as well as mechanical and physical properties by applying sustainable procedures, as will be discussed in this chapter.

This chapter first describes the general principles of conductive polymer composites, briefly emphasizing influential factors of conductivity. This is followed in Sect. 3 by the conduction mechanism as well as structural parameters capable of reducing the percolation threshold of the composites. Sections 2 and 3 are prerequisites for the following contents related specifically to conductive epoxy thermosets. Section 4 provides the main methods to fabricate conducting epoxy thermosets concerning the type of additives (metallic fillers, intrinsically conductive polymers, and ionic mixtures), especially green conducting materials developed recently as an innovative class of conductive additives. The design and efficiency of hybridized conductive epoxy nanocomposites as one of the interesting subjects in polymer science are discussed in this section as well. The common processes of incorporation and dispersion of fillers are reviewed in Sect. 5, which is followed by the manually tailorable factors to affect the performance of loaded fillers in the polymer matrix.

2 Conductive Polymer Composites (CPCs)

Electricity polymer composite conductors are defined as smart composites composed of dispersed hybrid or single conductive agents as fillers in nonconductive (or less conductive) polymer matrix, providing an electrically conductive material required for different applications. The conductivity value depending on the specific application of polymer can range from 10^{-12} to 10^{-8} S/cm for electrostatic discharge, 10^{-8} to 10^{-2} S/cm for partly conductive usages, and above 10^{-2} S/cm for shielding usages, etc. (Fig. 1) [7]. The key factor for the preparation of CPCs is how to disperse conducting additives into the matrix to obtain a continuous conductive network within the composite. Suppose the filler concentration gets to a critical amount, the nonconducting substance changes from an insulating to conducting state in the sense that the electric conduction exhibits a sharp increase. This critical volume fraction is specified as the percolation threshold and will be discussed in Sect. 3.1. Solution processing, melt blending, and in situ polymerizations are the conventional methods developed for the fabrication of CPCs and have been described carefully by Pang et al. Generally, CPCs are categorized into two types (isotropic and anisotropic) upon the direction of the conductance axis of a material which is in close relation with the filler type and composite fabrication method [7, 8].

2.1 Isotropic and Anisotropic CPCs

The main types of CPCs are isotropic and anisotropic conductive materials. The isotropic versions are electrically conductive materials that exhibit conductivity in all directions, while the anisotropic materials show a different conductivity behavior in different directions. To fabricate an isotropic CPCs, it is needed to incorporate

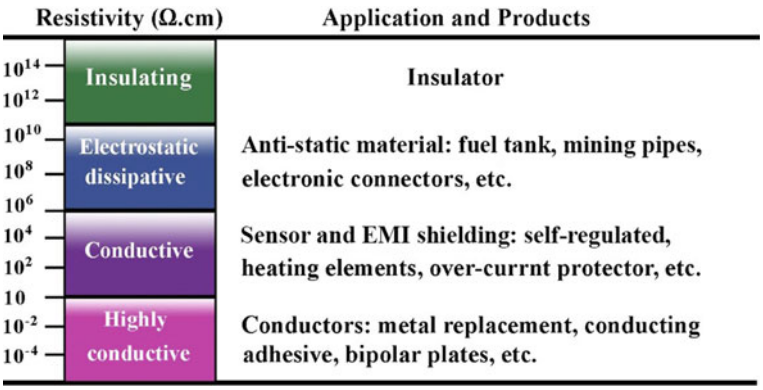

Fig. 1 Classifying of CPCs substances based on their electrical resistance and utilization scopes (Reproduced with permission from Elsevier [8])

a high concentration of conductive fillers into the polymer or resin through which a conductive network can be formed, and the material exhibits conductivity in all directions after manufacturing. The used thermoplastic or thermoset matrix precursor can be modified chemically so that the conducting agents are able to form mechanically or electrically interactions with the matrix [9, 10]. In contrast, for the fabrication of anisotropic CPCs, the filler concentration remains below the percolation threshold (around 5–20 vol%), which causes electrical conductivity only in one orientation or axis or in two orientations (unidirectional or bidirectional anisotropic). This is because of the imperfect network formation, which is formed at concentrations below the percolation threshold. Anisotropic conductive materials are produced as thermoset or thermoplastic substances or as liquids and pastes that, after processing, conductivity is finally achieved [10, 11].

3 Conduction Mechanisms

The general conduction mechanisms of CPCs are explained based on two models, i.e., electron tunneling and particle-to-particle connection (Fig. 2). A phenomenon through which the electrical conductivity can be achieved either by jumping of electrons between neighboring particles which are segregated by means of a tinny film of nonconducting polymer matrix or by crossing the matrix barrier is the electron tunneling model (Fig. 2a). The electrical conductivity via the second mechanism is achieved through the filler particles attached to each other. Contacting filler particles form conductivity pathways which facilitate making a conducting net in the matrix. Therefore, electrons are able to move from one particle to a neighboring particle [12–14] (Fig. 2b).

3.1 Percolation Threshold (PT)

As discussed, the least amount of conductor agents needed to create a conducting net is defined as the percolation threshold (Fig. 3). At the critical volumetric concentration of fillers, composite resistivity drops suddenly, and more links between filler components increase the number of paths that the electron can pass through the composite [14].

To predict the conduction of composites, numerous methods are developed based upon influential determinants, including specific conductance of the additive particles, volume portion of the conducting phase, the possibility of the formation of at least a one-directional conducting net, and the connections at the interfacing between the individual additive particles and the polymer matrix [17]. As shown in Fig. 3, three main regions of conductivity can be described depending on the number of particle arrangements involved in the formation of conducting pathway within the matrix. Region I is the state where the material is nonconductive, and particle concentration

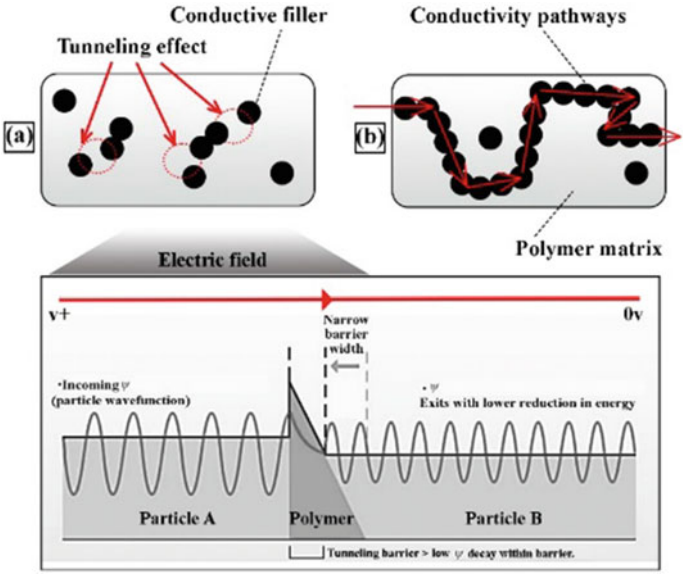

Fig. 2 **a** Tunneling effect between conductive fillers embedded in an insulator matrix and **b** schematic illustration of the possible conductivity pathways in CPCs. The filler particles produce a conductive pathway among each other which facilitates electrical current (Redrawn from Refs. [10, 13, 15])

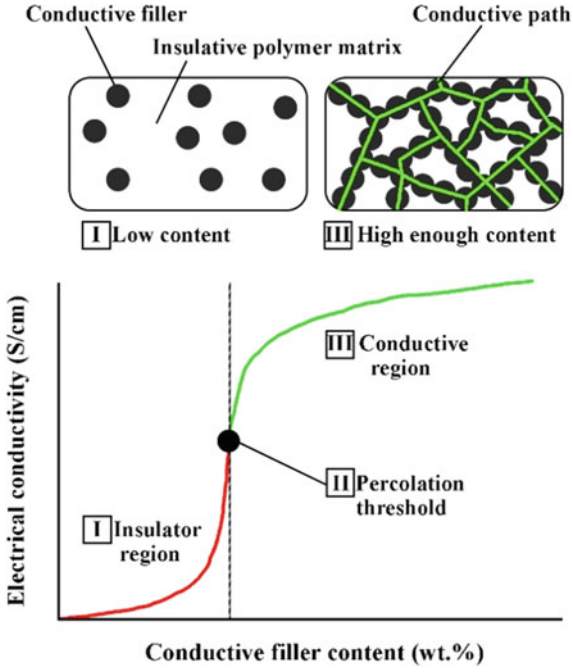

Fig. 3 Variation of composite conductivity versus filler concentration (Redrawn from Refs. [14, 16])

is not sufficient to form an electrically conductive path. Region II corresponds to the state where the conductivity exhibits a fast increase (resistivity decreases) due to a small variation of filler concentration [16]. The conductivity is produced by direct contacts of particles, tunneling effect, or both [10]. The space thickness (the width of nonconductive polymer) and level of the potential barrier affect the tunneling effect [18]. Finally, region III describes a conductive composite, and its conductivity is close to those of the conductive particles. In this case, the maximal conductivity is observed matching sufficiently numerous paths for the flow of electrons [19]. Usually, it is recommended that no more filler is added to avoid further increase in weight. At this stage, the conductivity of the composite can be calculated according to Eq. 1 (called percolation power law equation):

$$\sigma = \sigma_f (V_{\mathrm{f}} - V_{\mathrm{crit}})^t \tag{1}$$

in which σ and σ_f are the electric conductance of composite and pure additive, correspondingly [19]. V_{f}, V_{crit}, and t denote the filler volume fraction, the PT, and the critical exponent, respectively.

Numerous experimental investigations and mathematical modeling methods have been developed for the prediction of this critical concentration (PT) or (critical volume fraction, V_{c}), wherein dispersed particles in the composite form a conductive network. The probability of formation of such a network can be calculated through the statistical number mean average of connections between each neighboring particle. At the PT, the critical number of connections for each particle can be calculated via Eq. 2:

$$C_p = P_c Z \tag{2}$$

where P_{c} and Z are defined as the critical possibility of making a net system and the maximum number of probable connections per particle, respectively. The experimentally measured value of C_{p} is 1.5, which is a constant for spherical fillers dispersed in a composite [18, 20].

3.1.1 Factors Affecting PT

As mechanical and rheological characteristics of the composites are affected by means of the particle volume fraction, lower PT values are often desired. There are several factors that affect the magnitude of PT, the most important of which are morphological properties of the matrix, number of components involved in the composite, particle shape and size, pre-treatment of particle, and particle size distribution. In the following, we briefly discussed two important factors affecting the value of the critical concentration of conducting agents [21, 22].

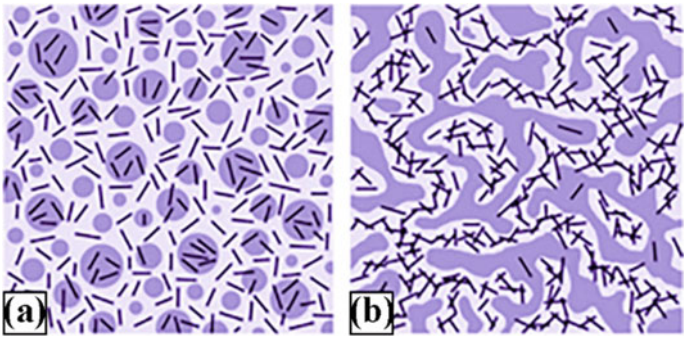

Fig. 4 Illustration of the influence of blend morphology on the creation of conducting net **a** droplet blends morphology and **b** co-continuous blend morphology resulting in double percolation phenomenon (Redrawn from Ref. [22])

Crystallinity and Morphology

A higher degree of polymer crystallinity moves a greater portion of conducting particles into the amorphous phase, facilitating the formation of a continual conductive pathway with a lower level of PT. This is owing to the optimal arrangement of additives inside the matrix and decrease of space among particles in the amorphous phase [23].

Polymer Blends

For the same reason discussed above, a conducting composite made from a nonhomogeneous polymer mixture might need fewer PT than composites made from each pure polymer. For a nonhomogeneous blend with a co-continual morphology (Fig. 4), the fillers preferably are located in polymer 1 phase, causing the forming of conducting paths at lower PT (double percolation phenomenon). For the double percolation phenomenon, the conductive additive phase should be continuous in the polymer 1 phase as well as the conducting phase (polymer 1+ filler) in the polymer 2 phase (Fig. 4b) [24].

The conductive additives can selectively concentrate in only one of the phases of the polymer blend or at the boundary among them. The latter situation results in lesser PT values. Processing or thermal treatment of the blend changes the droplet blend morphology (Fig. 4a) into the co-continuous morphology. Consequently, the fillers are located in one phase or at the boundary (Fig. 4b). By increasing the degree of crystallinity, fillers are excluded from the crystalline phase to the amorphous phase [22]. It must be added that in polymer blends, the filler tends to migrate to a more compatible polymer phase due to differences in interfacial tension between polymers and filler particles. Further, when the matrix is composed of two or more types of polymers, the filler particles might not be dispersed homogenously in the

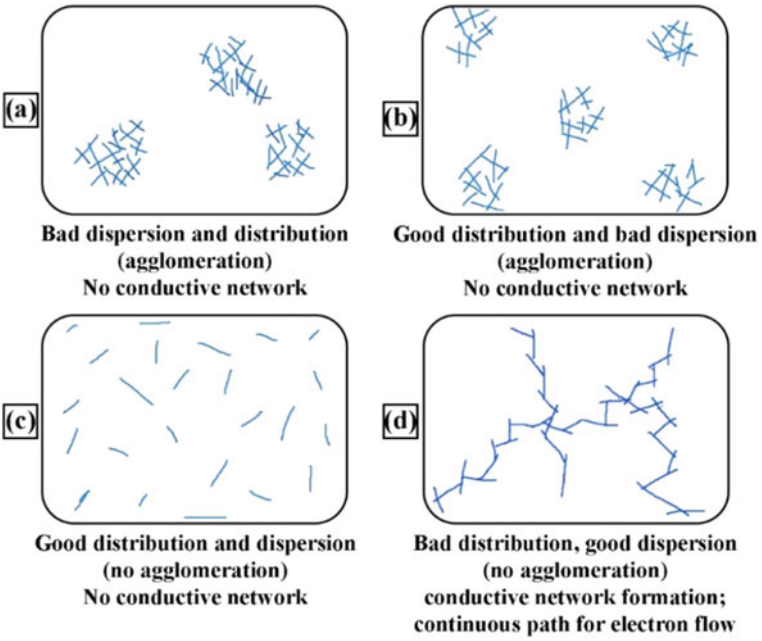

Fig. 5 Influence of dispersing and distributing of additives on polymer's conductance. **a**, **b** The poor filler dispersion inhibits network formation. **c** Complete distribution of well-dispersed fillers at low filler concentration increases the adjacent fillers distance and consequently inhibits network development. **d** The favored distributing of well-dispersed additives creates a conductive three dimensional network (Redrawn from Ref. [17])

system and are selectively located in the lower viscosity polymer phase. Thus, fabrication methods and processing conditions must be considered carefully before the incorporation of fillers into the matrix [24].

The concentration ratio of polymer blend and fillers affects the selective location of fillers, and the fractions of the polymers in a droplet morphology of the pure blend together with co-continuous morphology may be stabilized and refined [25, 26]. As shown in Fig. 5, besides achieving a good distribution of fillers, a good dispersion of them is a vital criterion for building a conductive network at lower PT in a nonconductive matrix.

4 Approaches to Impart Electrical Conductivity in Epoxy Resins

Conductive polymers are categorized into (I) intrinsically conducting polymers (ICPs), having a solid backbone made up of an extensively conjugated system, and (II) extrinsically conductive polymers (ECPs) made up of an ordinary insulating

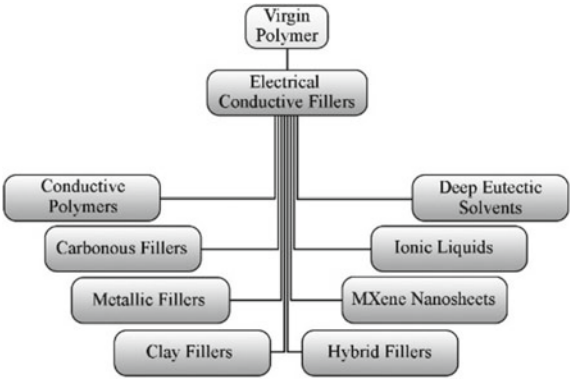

Fig. 6 Different kinds of additives for the production of conductive epoxy thermosets

matrix and external conductive agents. Epoxy resins are a member of nonconducting polymers that, by incorporating electrically conductive fillers, are converted into a conducting cured resin. To prepare advanced materials from epoxy resins, the addition of different forms of fillers can be a smart way to benefit from both additive and polymer properties. A wide spectrum of fillers and additives has been evolved to increase the mechanical, thermal, electrical, optical, magnetic, and flame retardant properties of the epoxy matrix each of which is realized by the application of special fillers. To impart conductivity properties in epoxy, several types of specific kinds of additives called conductive fillers are used. They include metals (conductive elements), carbonaceous fillers, ceramic fillers, inherently conductive polymers (ICP)s (e.g., blending of polymers), as well as ionic mixtures such as ionic liquids (ILs) and deep eutectic solvents (DESs) as a new generation of conducting fillers (Fig. 6) [27–29].

In the following, we discuss the application and performance of the most common conductive fillers based on their types which have received great attention in the preparation of conductive epoxy-based materials. These fillers are known owing to their superior multi-functioning properties compared with others. The conductive agents are also categorized in terms of their intrinsic conductivity and wherein metal-based materials exhibit much more conductivities (Fig. 7). It is worth mentioning that the size and geometry of filler particles are also important factors that one can categorize according to their shape characteristics [30].

4.1 Metallic Fillers

Metallic fillers integrated into the epoxy resins boost the composite's special properties such as thermal conductivity, thermal expansion, heat resistance, and shrinkage and have the potential to provide a conductive pathway within the insulator material. Metallic fillers are metal particles with less than 20 μm in diameter. To exceed the

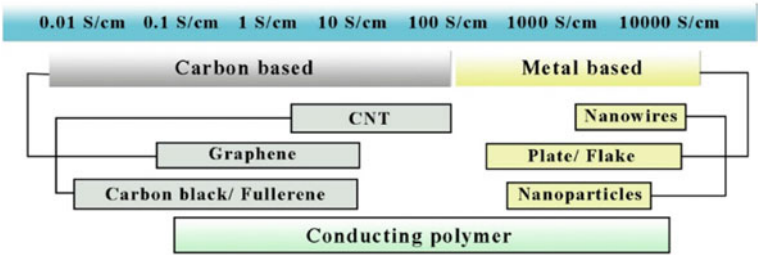

Fig. 7 General conductivity ranges of common fillers (Copied, with authorization from RSC [30])

PT, wide particle size distributions are usually preferred since a lower concentration of fillers is necessary to initiate electrical conductivity [28, 29]. Metal fillers involving gold (Au), silver (Ag), copper (Cu), and nickel (Ni) are the most known metal fillers applied in the preparation of nanocomposites. Metal oxides are a type of metallic fillers which are generally available, less expensive, and exhibit more cytocompatibility. Due to the feasibility of their preparation as well as their excellent properties, they are considered an alternative to metals and carbon materials in electrochemical applications. Despite their promising advantages, aggregation of metal oxide nanoparticles might reduce their active surface and subsequent performance as conducting agents. Therefore, it is suggested to treat virgin particles with chemical methods before application. Metal-based additives have been widely used in the fabrication of conductive nanocomposites, especially with epoxy resins. Among these, silver and copper are the most efficient fillers for preparing conductive epoxy thermosets [31].

4.1.1 Silver (Ag)

Ag nanoparticles are considered matchless fillers due to their great electric conductance and optical, thermal, and biological properties. Regardless of being expensive, they are broadly used due to their several benefits like easy forming and making in different sizes and shapes such as flakes, nano-powders, nanowires, and nanorods. The silver oxides possess excellent conductance that is commonly rare for other metals. Both Ag particles and their oxide derivatives provide a high level of electrical and thermal conduction that is usually difficult to achieve in the case of other metals. For instance, a 15–30 vol% of silver flakes loading is sufficient to prepare electrically conductive epoxy adhesives [32].

Silver particles are often applied in epoxy thermosets after hybridization with other conductive fillers, as will be discussed in Sect. 4.8. However, individual Ag particles have also been used as conductive agents, but the produced composites show some limitations, such as Ag agglomeration or migration, low thermal and electrical conductance, and poor impact resistance. The electrical characteristic of epoxy/Ag composites has been investigated after manipulating filler performance

through physical and chemical modifications [30]. For example, adding silica particles can increase both the electric conductance and the mechano-thermal properties of epoxy/Ag nanocomposites. The Monte Carlo simulation results disclosed that suitable intermolecular connections are formed among silver nanoparticles in the presence of silica, resulting in a conductive network formation at the same Ag concentration. Thus, the resistivity decreased from 10^4 Ω cm to 10^{-4} Ω cm with the addition of 1.5 vol% of silica particles (Fig. 8). The interactions among OH groups on the SiO_2 surface and functional groups of epoxy resin led to suitable dispersion of SiO_2 in the resin, reducing the number and extent of holes in the nanocomposite [33].

It should be stated that, despite the higher aspect ratio of nanomaterials which facilitates the conductive network formation, the overall resistance should also be considered. The overall resistance of a nanocomposite like epoxy/Ag includes the summation of the resistance of additives, the resistance among additives, and the resistance among additives and matrix (Fig. 9).

Jiang et al. treated Ag particles with five varied kinds of surfactants to reduce agglomeration by fewer connection points among the particles. The results showed that diacid functionalized Ag nanoparticles resulted in much more resistivity reduction than other surfactants [34]. Although these organic layers on the particles reduced the particle agglomeration, they created a nonconducting layer on the Ag particles, as

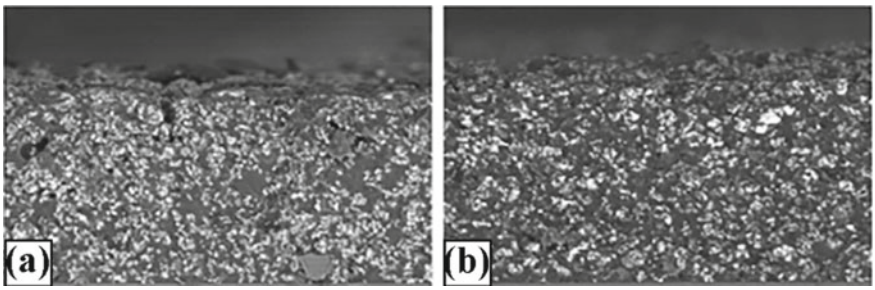

Fig. 8 SEM pictures of side view morphologies of epoxy/Ag nanocomposites (**a**) with and (**b**) without SiO_2 (Copied, with authorization from the American Institute of Physics Publishing [33])

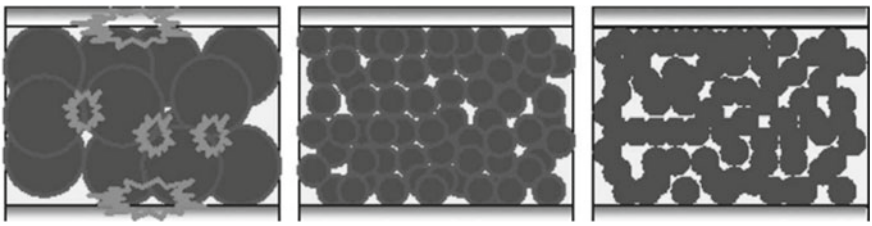

Fig. 9 Influence of particle size on contact points and subsequent resistivity (Reproduced with permission from Springer Nature [34])

reported by Lu et al. Ag flakes were made from Ag powders by mechanical grinding and coated with a tinny film of organic lubricant. This treatment resulted in the reduction of conductivities of epoxy/Ag flake nanocomposite. The most efficient results were obtained after removing the nonconductive lubricants by glycol butyl ether and poly(ethylene glycol) [30].

4.1.2 Copper (Cu)

Metallic copper is a cost-effective, flexible, and formable material with high electrical and thermal conductivity, which can be an alternative to the currently employed epoxy/Ag composites [35]. The challenge associated with their corresponding composite materials is the tendency of Cu to oxidize to copper oxide, then to cupric sulfide, and finally to copper carbonate under environmental circumstances [36]. Organic or inorganic copper coating, nitrogen-based copper treatment, and using solder powder in the composite process are the main techniques to prevent the corrosion and oxidation of Cu. Further, Cu can be modified by other conductive metals, such as silver, to improve its stability [37]. Nitrogen-based compounds such as benzotriazole and imidazole can also control the oxidation phenomenon through the formation of more stable Cu complexes [38]. Mohd et al. prepared cetyltrimethylammonium bromide (CTAB) stabilized epoxy/Cu nanocomposites. The composites exhibited conducting properties comparable with epoxy/Ag nanocomposites. They synthesized Cu nanoparticles in epoxy through the water to organic phase transfer method. In this method, a solution of epoxy in toluene was used as the organic phase. The solution of Cu^{2+} ions in water stabilized by CTAB was reduced to metallic Cu by $NaBH_4$ [39]. In another report with a similar purpose, copper powders after surface modification by silane linking reagent (SCA) were used for conductive epoxy/Cu adhesives. SCA can form a connection betwixt Cu particles and epoxy resin (Fig. 10), connecting two kinds of materials with complete unlike properties and enhancing the filler dispersion. It was found that when the SCA to Cu powder mass ratio was 3:100, the bulk resistance decreased to the lowest amount of 1.34×10^{-3} Ω cm. Then the bulk resistance increased again with an enhancement of SCA content [40].

The finding described above illustrated the potential of conductive fillers, especially Ag and Cu, to achieve electrically conductive epoxy thermosets. Although intact metal particles are known as sufficient conductive materials, incorporation within the epoxy matrix requires chemical or physical modifications [40].

4.2 Carbonaceous Fillers

Carbonaceous materials are made up of carbon atoms joined together, forming different shapes. They can be generally categorized into prevalent carbonaceous materials such as carbon black (CB) and activated nanostructures, including carbon nanotube (CNTs), graphene and graphene oxide (GO), fullerenes, etc. (Fig. 11) [41]

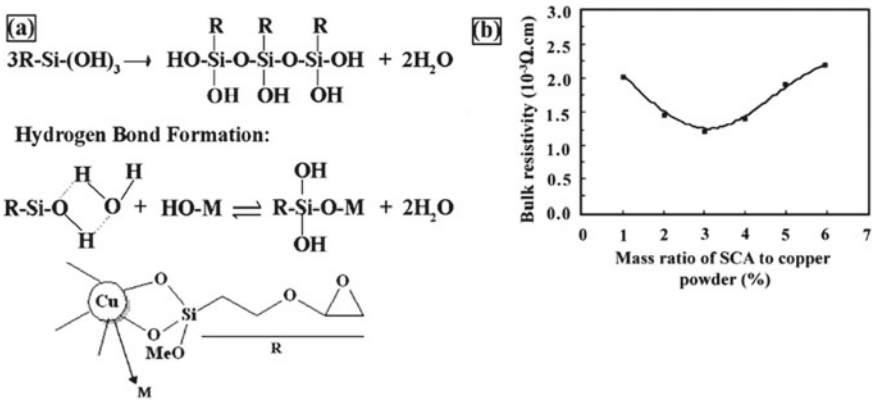

Fig. 10 **a** Correlative reaction for the copper-epoxy linking via Cu modified with SCA. **b** Variation of bulk resistivity versus SCA amount (Copied, with authorization from Elsevier [40])

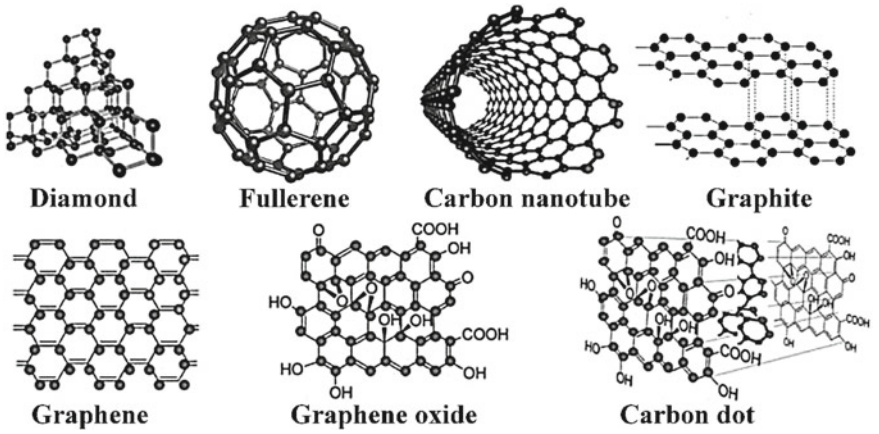

Fig. 11 Collage of different carbon nanomaterial structures and their nomenclature (Reproduced with permission from Elsevier [4])

These nanostructures have a great specific surface area, conductance, mechanical properties, high control on functionalization, and electrochemical stability.

4.2.1 Carbon Nanotubes (CNTs)

CNTs are hollow tubes made of carbon with typically nanometers diameters and are mainly categorized into mono-walled carbon nanotubes (SWCNT) and multi-walled carbon nanotubes (MWCNT)s. Due to attractive characteristics, such as excellent

aspect ratio, good electric and thermal conductance, small thermal expansion coefficient, and good tensile strength, they are regarded as promising agents for the preparation of materials with great functioning. Thanks to their good electric conduction (10^5 to 10^6 S/cm) and great surface area, CNTs are superior to ordinary additives to increase electric conductance and the mechanical properties of the nanocomposite at a fairly lesser amount of PT [4]. For example, the conductivity of MWCNT/epoxy nanocomposites initiates at a low PT (below 1.5 wt%) and reaches a high level of conductivity. Although CNTs provide a large surface area, the existence of strong van der Waals interactions within the structure can increase the probability of agglomeration, reducing their efficiency as time goes on. Consequently, different physical and chemical techniques have been established to disperse CNT particles more efficiently including ultrasonication, using surfactants, acid oxidation of CNTs, high shear mixing, and surface modifications [10]. Compared to SWCNTs, MWCNTs have been mainly utilized as conducting additives owing to lesser price and superior dispersion. Though, the greater intrinsic electrical conductance of SWCNTs causes and enhances the conductivity at lower PT. In this regard, a novel method is the predispersion of SWCNTs to ensure fine dispersion. Moisala et al. applied this treatment, and epoxy composites were made with low additive contents (0.005–0.5 wt%) [42].

Since the electrical performance of nanocomposites depends on processing conditions, different procedures have been developed by researchers. To facilitate increasing the efficient aspect ratio of CNTs, Rosca and Hoa used a three-roll milling method to disperse MWCNT particles within the epoxy resin. During the process, shear force and the number of rolling determined the quality dispersion of the nanotube. They showed that the composite conductance increased nearly 10× as the aspect ratio increased 5.5× [43].

Alignment methods of CNTs through which randomly dispersed rod-like fillers get an aligned structure under the application of electric and/or magnetic fields are other strategies to enhance the efficiency of filler conductivity. For example, Ma et al. applied a low magnetic field of 0.4 T and imposed CNTs alignment in the epoxy resin. The findings approved the role of a magnetic field as the electric conductance was improved by 6–8 orders of size (10^{-7} S/m) together with a reduced PT value [44]. Khan et al. showed the effect of electric field on epoxy/CNT nanocomposites. They applied DC current to align the MWCNT fillers in an epoxy matrix. Composites containing aligned CNTs showed better electric conductance and mechanical strength compared to the composite prepared with randomly dispersed CNTs. Also, composites containing aligned CNTs required lower PT (0.0031 vol%), while the PT was 0.034 vol% for the composite containing random-oriented CNTs [45].

4.2.2 Carbon Nanofibers (CNFs)

CNFs or vapor-grown carbon nanofibers (VGCNF) are hollow nanofibers with a diameter between 50 and 300 nm with substantial properties, for example, great mechanical and thermal properties, high stiffness, and electric conductance as high as metals (10^5 to 10^6 S/cm). Carbon fibers, due to their low density (much lower density

than steel) and high strength, can form lightweight materials with outstanding properties, especially in advanced applications of composites. Despite the superior properties of CNTs, due to the high-volume production of CNFs and their cost-effectiveness compared to CNTs, CNFs can be an outstanding substitute for CNTs. Many studies have been accomplished to increase the composites' electric and mechanical properties with the integration of CNFs in the polymer matrix, especially in epoxy composites. For example, Ladani and Wang used CNFs to increase the electric conductivity properties of epoxy nanocomposites. They used a surfactant followed by a three-roll grinder for dispersing of CNFs in a liquid resin. Then, the CNFs were oriented using an exterior AC electric field. By adding 1.6 wt% of CNFs, an enhanced electric conductance to around 7 orders of magnitudes to 10^{-2} S/m was detected and rupture energy enhanced to 1600% from 134 to 2345 J/m^2 [6]. In another study, Bal et al. applied different amounts of CNF up to 1 wt% and used them under refrigerated as well as at room temperature curing conditions to study the electrical and mechanical characteristics of epoxy nanocomposites. The data revealed that the conductivity of composites with 0.5–1.0 wt% CNF was 3 to 6 orders of magnitude more than pure epoxy, in the range of 2×10^{-4} S/m to 4×10^{-1} S/m. Refrigerated specimens showed improved dispersion and better conductivity at low amounts of CNFs, while room temperature cured samples showed higher conductivity at high amounts of CNFs due to the fiber alignment in the network structure [46]. Although CNFs have a high surface area and are a suitable and inexpensive alternative to CNTs, one of the challenges of using them is that their electrical and mechanical properties are lower when randomly oriented than in their align-oriented state. Therefore, many efforts have been made to align them, such as using mechanical stretching or applying electric or magnetic fields. In one study, Wu et al. coated CNFs with magnetic Fe_3O_4 nanoparticles and then used a weak magnetic field of ~ 50 mT to align them. According to the results, aligned nanocomposites exhibited higher electrical conductivity (over one order of magnitude) in comparison with randomly oriented epoxy nanocomposites [47].

4.2.3 Carbon Black (CB)

Most carbon black grades are incorporated into epoxy resins to impart electrical conductivity at lower volume fractions. Their efficiency varies dramatically depending on the size and geometry, preparation procedures, porosity, and surface chemistry, leading to the wide electrical conductivity ranges from 10^2 to 10^3 S/cm. The advantages of some CB grades, such as a low aggregation, good electrical conductivity, and less volatility, make them suitable candidates for the fabrication of electrically conductive composites. Particularly, CBs with a high aspect ratio are preferred since they facilitate the formation of conductive networks and require lower PT [4, 17]. In CB clusters, electron channeling is dominant for the movement of electrons as they flow among the particles that are firmly positioned near each other and surrounded by the polymer. The electrical conductivity rises with the size of the aggregate due to the facile leap of electrons through the polymer matrix [9].

Despite the advantages of CB as a filler of high-performance composites, the required concentration restricts its application. Typically, CB-based composites need a high level of CB to reach adequate electric conductance. The challenge arises when the higher loading of CB leads to an increase in viscosity and impairment of mechanical properties [48]. Several methods have been reported to decrease PT of CB filled composites, the most important of which is using a second filler to contribute with CB or preparing composites with polymer blends [49]. However, the latter suffers from the probability of polymers incompatibility. For example, Michaela et al. studied the electrical conductance of epoxy/silicone/CB blends. The three-component material showed a six times greater conductance compared to epoxy/CB composites at a similar level of CB [50].

4.2.4 Graphene, Expanded Graphite

Using graphene nanoparticles (GNPs) as an additive in the fabrication of polymer composites is a hot research topic because of its outstanding mechanical properties (hardness and Young's modulus) and great thermal conductivities (3000–5000 W/m K) and super electrical conductivity, etc. [51]. It is believed that graphene-based nanocomposites present a low PT due to the high aspect ratio, improving the electromagnetic interference shielding effectiveness of epoxy resins. Further, GNP can be applied as a more efficient toughening agent to enhance the toughness of epoxy thermosets and most properties of polymer [52, 53]. Although the aspect ratio of GNPs is higher than other nanofillers, the composite conductivity deteriorates over time owing to the inhomogeneous dispersing of graphene sheets inside the composite. To address this, several approaches have been developed to increase the long-term and stable dispersion of GNPs, including chemical and non-chemical functionalization, microwave exfoliating and surface modifying, etc., through which its aspect ratio, hydrophobicity, and π-π interactions are altered. Also, optimization of processing conditions has received immense consideration in facilitating electron flow and reduction of required filler concentrations [54]. Chandrasekaran et al. developed GO/epoxy nanocomposites with the use of two dispersion techniques, namely the three-roll mill method and sonication. An utmost conductance of 1.8×10^{-6} S/m was achieved by the three-roll mill method for 1.0 wt% of GNP [55]. Li et al. described a new method to enhance the surface conductivity of epoxy resins by applying carbon-based nanofillers. For this, they used sprayed GNPs and CNTs on the substrate instead of random dispersion of additives inside the matrix, resulting in a reduction of the surface resistivity of non-modified resin from 2 to 3 Ω/sq to resistivity $= 3 \times 10^{-4}$ Ω/sq in the case of composite material [56].

Another current research subject deals with the investigation of the synergistic influence of additives with unlike aspect ratios. As represented in Fig. 12, appreciable electrical conductivity values can be obtained by the combinations of carbonaceous fillers as well as by varying their concentration [57].

Han et al. incorporated graphene platelets (GnPs) into epoxy adhesives to improve lap shear strength and electric conductance. Besides the significant performance

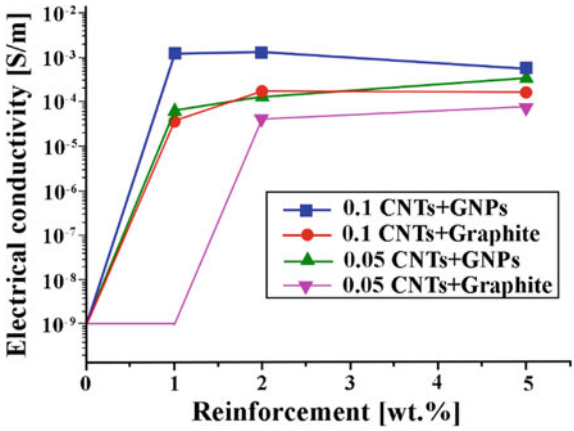

Fig. 12 Synergistic influence of additives mixture on the electric conductance of hybridized composites (Reproduced with permission from Multidisciplinary Digital Publishing Institute [57])

of GnPs, they reported that the simultaneous presence of GnPs and CNTs could generate a three-dimensional network, affecting the lap shear strength of composite dramatically in comparison with pure epoxy resin or the composite prepared from only one of the fillers. The PT of the composite comprising GnPs and CNTs was verified at 0.41 vol%, which was lesser than that of the composite loaded with only GnP (0.58 vol%) or CNTs (0.53 vol%) nanofillers [58].

4.3 MXene Nanosheets

Recently, MXene nanosheets have evolved as an innovative generation of transition metal carbide/nitride 2D nanostructured materials with the potential to be applied in various research fields owing to their outstanding chemical and structural characteristics. MXenes are known as encouraging conductive agents thanks to their inherent high conductance and unrivaled structure [59]. Since the surface atoms of MXenes are metals like Ti, they are able to bond easily to the oxygen atom of epoxy resins and are distributed well in the polymer matrix. Feng et al. prepared epoxy resin containing $Ti_3C_2T_x$ MXene nano-plates and obtained composites with outstanding conductance (4.52×10^{-4} S/m) and mechanical characteristics [60]. The calculated PT of the composite was about 0.28 vol% (0.85 wt%) (Fig. 13).

Song et al. loaded rGO and MXene nanosheets inside epoxy resin to prepare conductive honeycomb structural epoxy nanocomposites. They showed that the electric conductance improved with the rise of MXene content, whereas the epoxy nanocomposite with a maximum content of both additives presented the maximum electrical conductance [61].

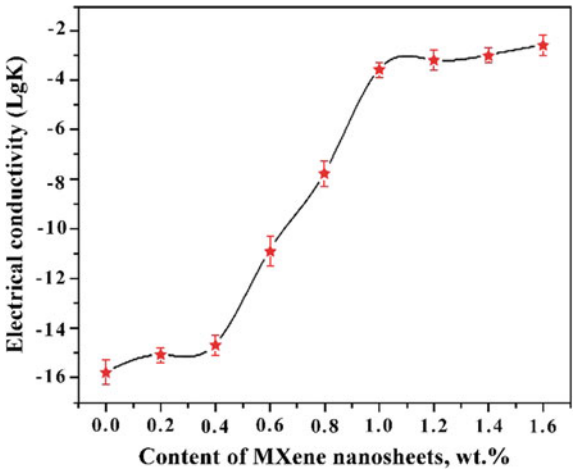

Fig. 13 Electric conductance of the epoxy/MXene composite at varying content of $Ti_3C_2T_x$ MXene nanosheets (Reproduced with permission from Multidisciplinary Digital Publishing Institute [60])

4.4 Clay

Clay is in the form of fine grains, a kind of natural soil. These particles are utilized in numerous electrochemical applications due to their advantages, such as excellent surface area, porous structure, and ability to transfer electrons. This filler is not usually used individually in electrical applications, and their hybridized nanostructures have gained immense attention in the fabrication of conductive epoxy thermosets [62].

4.5 Ionic Liquids (ILs)

ILs are described as salts in the liquid state. These liquids are commonly composed of bulky cations, which are stabilized through interaction with organic or inorganic anions. ILs have evolved as green alternatives to common organic solvents due to the advantages associated with these ionic mixtures. There is a wide range of precursors for the preparation of ILs, and therefore, one can easily tailor their major properties by changing the nature of ILs [63, 64]. Please refer to the excellent review written by Ghandi et al. for more detail [65]. In addition to the application of ILs as a component (as the solvent, catalyst, or reactant) in many composite materials, they are also considered promising compounds for the production of electroactive apparatus, for instance, lithium-ion batteries, capacitors, etc., thanks to their low viscosity, ionic nature, and excellent conductivity. In this context, the improvement of the electric conductance of epoxy composites has been reported by several research groups. Moreover, ILs can be applied as catalysts, hardeners, plasticizers, and lubricants in the fabrication of epoxy thermosets [66–68]. Zhang et al. applied 1-butyl-3-methylimidazolium iodide ([BMIM] [I]), which played simultaneously two roles as a catalyst of curing reaction and conducting agent. They observed that the electrical

resistance of the composite was reduced by nearly two times compared to epoxy resins cured in the presence of other imidazole-based compounds. Further, [BMIM][I] caused gelation of the resin at a lower level of the hardening processes, enhancing the development of a conducting network [69]. Another potential ILs was 1-ethyl-3-methylimidazolium *bis*(trifluoromethane sulfonyl) imide ([EMIm][TFSI]), acting as an excellent conducting agent for the epoxy resins cured by tetraethylenepentamine. This IL affected the composite's resistivity, mechanical strength, and morphology in terms of the applied concentration. At lower concentrations, the mobility of ions inside the matrix is confined due to the rigid and glassy nature of the network; however, the restriction was diminished at higher concentrations, showing higher conductivity values (84.0×10^{-2} S/m) [70].

Matsumoto et al. reported the synthesis of transparent epoxy thermosets conductor carrying a quaternary ammonium salt in the polymer's backbone. The network was produced via warming a mixture of different di-epoxide compounds, glycidyltrimethylammonium *bis*(trifluoromethanesulfonyl) imide, and diamine cross-linking reagent. In addition to good thermomechanical stability, the cross-linked polymers showed a range of conductance with the maximum conductivity in the case of poly (ethylene glycol)-based di-epoxide (1.0×10^{-3} S/m) used as one of the reactants [71]. To enhance the conductivity value and achieve a high level of functionality, Shirshova et al. added a mature *bis*(trifluoromethane) sulfonimide lithium salt (LiTFSI) and ethyl-3-methylimidazolium *bis*(trifluoromethylsulfonyl)imide ([EMIM][TFSI]) ILs to an epoxy thermoset. The conductivity was approached to 8.0×10^{-2} S/m, which was sufficient to apply thin films of material as separation membranes for Li-ion batteries [72]. In another work, Soares et al. investigated the influence of alkyl-phosphonium-based ILs decorated with altered anions on the morphology, ionic conductivity, and mechanical characteristics of epoxy networks cross-linked with Jeffamine-D230. The structure of ILs and conductivities at altered temperatures are presented in Fig. 14. The authors observed a substantial dependency between conductance and frequency, proving that the material had a semiconducting behavior. The calculated Arrhenius plots showed the influence of the temperature on the conductance, as presented in Fig. 14b. Samples having Phos-DCA and Phos-DBS showed a noteworthy relation between conductance and temperature, proposing the formation of more polar structures. The material composed of Phos-DCA exhibited the utmost conductance (10^{-6} S/cm), indicating the greater movement of the dicyanamide anion, possibly as a result of its enhanced dispersion in the epoxy matrix [73].

The incorporation of 1-decyl-3-methylimidazolium bromide ([DMIm][Br]) content as high as 50 wt% in the epoxy matrix caused solid and pliable electrolyte with great heat resistance and ionic conductance of about 0.1×10^{-2} S/m at RT that enhanced up to 10×10^{-2} S/m at 170 °C [74].

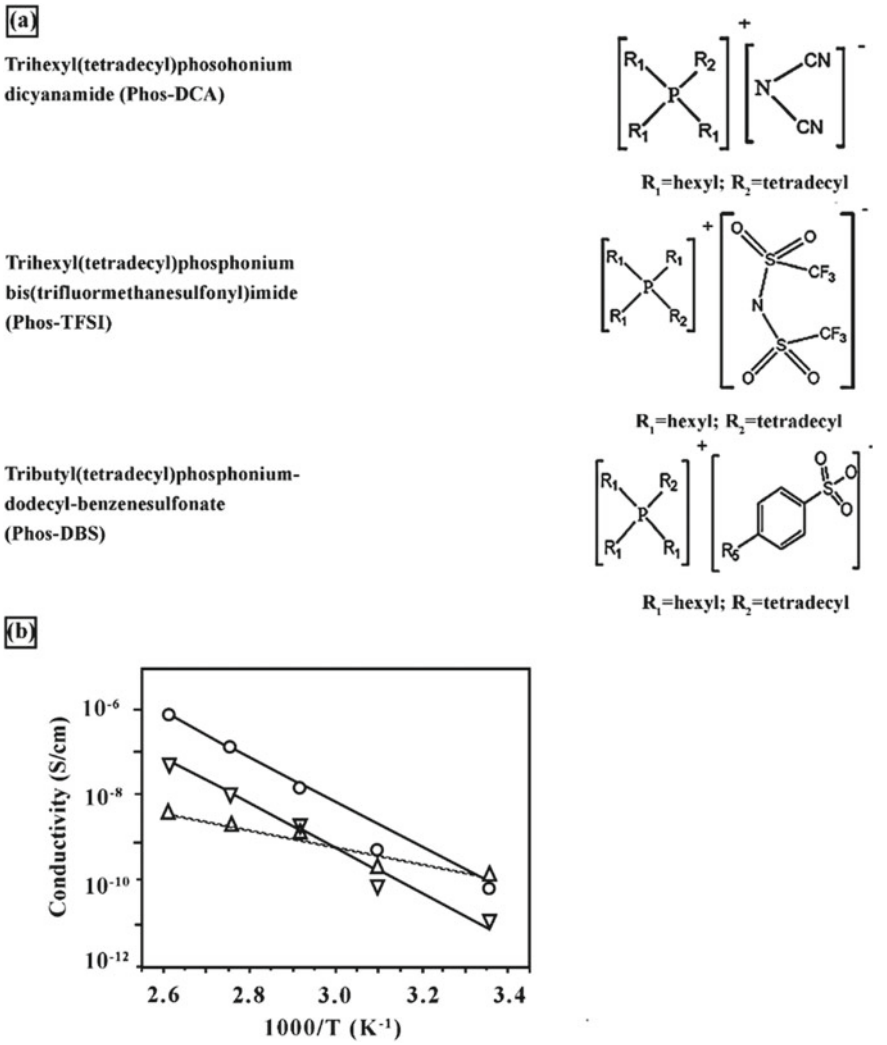

Fig. 14 **a** Structure of ionic liquids. **b** Variation of conductivities as the temperature (at a frequency of 1 kHz) reduces for thermosets having (O) Phos-DCA; (Δ) Phos-TFSI; (∇) Phos-DBS ILs (Reproduced with permission from Elsevier [73])

4.6 Deep Eutectic Solvents (DESs)

Unlike ILs with disadvantages, such as non-bioadaptability [75], multi-step purification procedures, and the unfeasibility to be used in bulk chemical processes [76], DESs are easily prepared in sheer form. They are non-active against H_2O, eco-friendly (once cautiously made from eco-benign compounds), and biodegradable [77]. DESs are used as a solvent, precursor, and green substitute for traditional

synthesis methods. Particular DESs comprise the components that cause exceptional properties in the resulting product or affect their morphology, molecular weight, conductance, and reaction speed [78]. Using DES as a green cross-linking agent, reduced the required amount of the amine conventional hardener. [79]. Furthermore, DESs cause the curing reaction to occur in homogeneous surroundings, affecting network morphology and ionic conductivity [64, 80]. Lately, the conductance of solid polymer electrolytes has been noticed as the main topic because of their great efficiency in electronic devices [81]. Due to the suitable electrical conductance and durability of DESs, their usage as gel electrolytes has been explored as eco-compatible substitutes to ILs. Actually, eutectic gels show good conduction and ductility in smart sensing and flexible electronics applications as a novel category of ionic gels [82]. Despite the good electrical conductivity and stability of DESs, their applications as conducting agents in epoxy polymers have been rarely studied. Lately, our research team has assessed the influence of natural DESs based on arginine (Arg) or glutamic acid (Glu) and ethylene glycol on the cure reaction kinetics, reaction progress, and electrical conductance of epoxy resin based on bisphenol-A diglicydylether (DGEBA) (Fig. 15a). The formed DESs played two roles as epoxy curing catalyst and conducting agents. The results revealed a noticeable influence of DESs on the course of epoxy-amine reaction based on hydrogen acceptor components of DES. Electrochemical impedance spectroscopy showed that higher concentrations of DESs can make a high level of conductivity. It is worth mentioning that the nature and content of DESs affected the amount of reaction progress, and, consequently, the trend of conductivity. DC conductivity increased with decreased monomer consumption or increased by increasing the DES dosage. In fact, the electrons flow rate in a matrix is limited due to the polymer chain's compactness of polymer chains and the enhanced charge movement in the cross-linked sample. We observed significant changes in the isothermal cross-linking reaction growth by using $[DES]_{Arg/Eg}$ and $[DES]_{Glu/Eg}$ compared to the conductive ILs and nonconductive common curing agents. It was shown that the presence of $[DES]_{Arg/Eg}$ led to a decrease in the E_{act} of epoxy curing reaction more efficiently than that of $[DES]_{Glu/Eg}$ [83].

4.7 Intrinsically Conductive Polymers (ICPs) as Filler

Conductive polymers or, more precisely, ICPs exhibit the electrical properties previously found only in metals. The electrical conductance of ICPs (10^{-10} to 10^{+5} S/cm) and their environmental stability against moisture, heat, and corrosion make them ideal candidates for various applications such as antistatic materials and commercial batteries and monitors [21]. These organic polymers can conduct electricity; however, their strength is not similar to commodity or engineering polymers. For a nonconductive polymer matrix, adding a small quantity of conducting polymers is a sustainable route for obtaining a conductive matrix. Combining a small weight fraction of conductive polymers like polypyrrole (PPy), polythiophenes (PTh), etc., with commercial polymers can fabricate a conductive reinforced material suitable

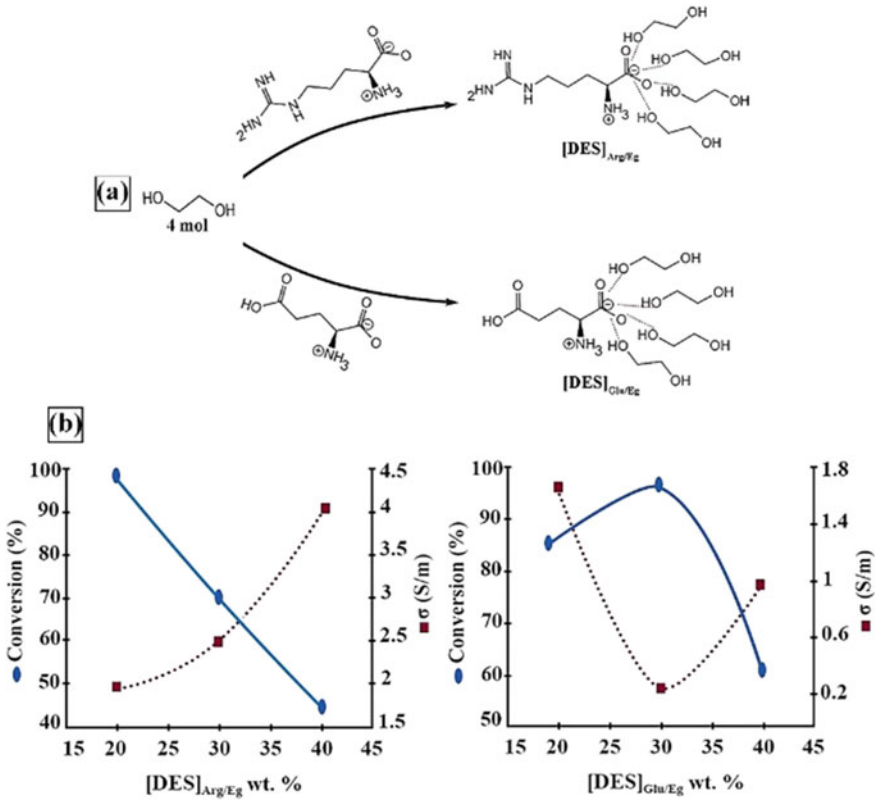

Fig. 15 **a** Synthesis course and suggested structure of DESs from their corresponding compounds. **b** Variation of DC conductance and reaction progress versus DESs content for the specimens cross-linked isothermally at 323 K (Reproduced with permission from Elsevier [83])

for different applications. Several blending methods have been developed, which can be classified into two general chemical and electrochemical methods. Paoli et al. reviewed the benefits of using blends in some technological applications rather than pure conductive polymers [84]. Newly, ICPs have been noticed as one of the motivating candidates to prepare conductive epoxy thermosets since they overcome some limitations and drawbacks of metal fillers. It should be noted that ICPs generate less electrical conductivity compared to carbonaceous and metal fillers [85]. In the following, we reviewed the recent research and achievements of the conductive epoxy networks by blending epoxy resin with ICPs.

4.7.1 Polypyrrole (PPy)

PPy has attracted significant attention due to its electrical conductivity (7.5×10^3 S/cm) and its fascinating thermal and physicomechanical properties. Its conductivity results in electrons jumping between the chains and the movement of cations or anions inside the matrix. Due to the aforementioned advantages, PPy is considered the main component in high-performance applications, including microelectronics, biosensors, as well as tissue engineering, and surgical instruments. However, PPy suffers irregularities in the polymer backbone due to probable redox reactions occurring in contact with moisture and oxygen, which ultimately deteriorates its conductivity [86, 87]. Through the contribution of PPy as a filler in the epoxy composites, Olivier et al. prepared an epoxy-based material reinforced in view of electrical and mechanical properties. They found that the matrix conductivity increased from 10^{-12} S/cm up to 2×10^{-5} S/cm by adding only 8.1 vol% of PPy particles in the epoxy resin. The result of mechanical–thermal analysis indicated that the PPy particles did not seem to have a mechanical reinforcement effect. In another work, Barrau et al. showed the enhancement of the conductance of PPy-epoxy composites by eight orders of magnitude (1×10^{-5} S/m) at 15 wt% PPy content in comparison with pristine epoxy. Further, they observed a continuous growth of the Tg with PPy amount as a result of the greater Tg of the PPy. However, they observed a downshift in Tg in the vicinity of PT, related to the increase of epoxy chain motion at this concentration, as shown in Fig. 16 [88].

The morphology of the applied PPy influences the range of conductivity values. To explore the influence of conductive additive geometry on the conductance of the polymer matrix, Zhang et al. applied fibrous and spherical PPy in the epoxy matrix. The results demonstrated that due to the higher aspect ratio, nanofibrous PPy resulted in lower PT compared to spherical PPy nanostructure [89].

Surface treatment of fillers is always considered a promising way to enhance the filler properties, subsequently increasing the end-use performance. In this context,

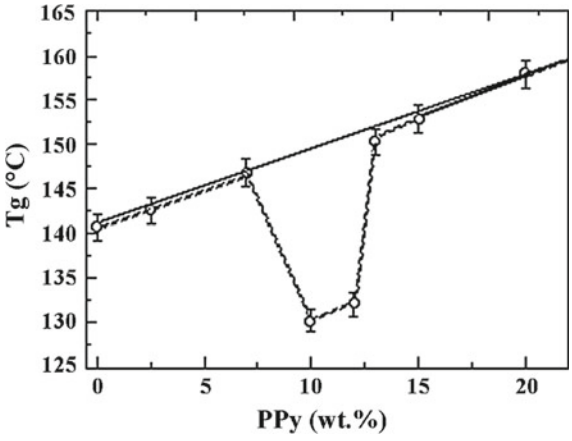

Fig. 16 Variation of Tg of PPy—epoxy blend versus PPy weight content (Copied, with authorization from John Wiley and Sons [88])

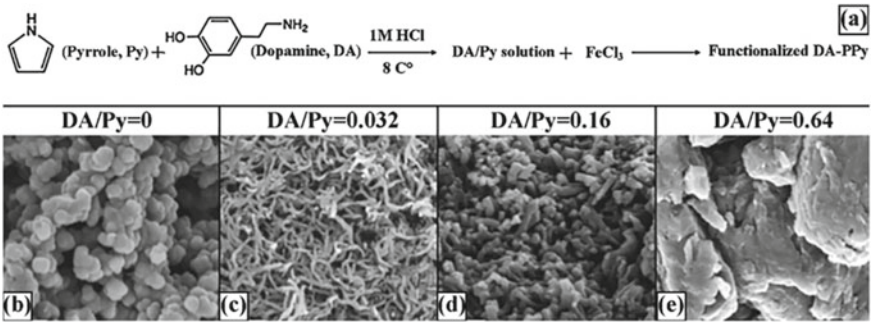

Fig. 17 **a** Synthesis path for the functionalization of PPy; SEM descriptions of DA-PPy with **b** spherical morphology, **c** fibrous morphology, **d** nanorod morphology, and **e** nanoflake morphology (Copied, with authorization from John Wiley and Sons [90])

Zhang et al. functionalized PPy with dopamine (DA) molecules and investigated the role of PPy modification on the conductivity of final epoxy-based adhesives. They observed a correlation between DA/PPy reacting mole ratio on the morphology of produced fillers so that several morphologies, such as nanosphere, nanofiber, nanorod, and nanoflake, can be achieved by easily changing the feed components, as displayed in Fig. 17. It was detected that the conductance increased to 24 S/m with adding of 3 wt% of DA-PPy, as a superior capacitance for supercapacitor application [90].

In a similar work of filler treatment, Guo et al. coated the PPy on magnetite (Fe_3O_4) nanoparticles and used them as a hardener of epoxy thermosets, as shown in Fig. 18. This resulted in enhanced conductivity and good distribution of Fe_3O_4 within the matrix. It was found that the conductance of the epoxy resin cured by modified particles increased seven times compared to the unmodified specimen [91].

4.7.2 Polyaniline (PANI)

PANI is a member of the conductive polymer family. In addition, PANI displays a relevant role in the development of high-performance nanocomposites. It has advantages over other conducting polymers, such as high-temperature resistance, good environmental stability, and excellent electrical conductivity. PANI is polymerized from cheap aniline monomer and can be classified into three oxidation states: a completely oxidized form pernigraniline, a completely reduced form leucoemeraldine, and partially oxidized form emeraldine base. The range of PANI conductivity depends on its oxidative state and can be increased up to 30 S/cm for emeraldine after protonation and the formation of charge carriers. The blending of PANI with a host nonconductive matrix (such as epoxy resin) is an ongoing research field conducted by the motivation for combination of electrical properties of PANI with great properties of matrix [92, 93]. The challenge arises when the amine functional groups of epoxy curing agents can reverse the protonation of PANI and reduce its conductance

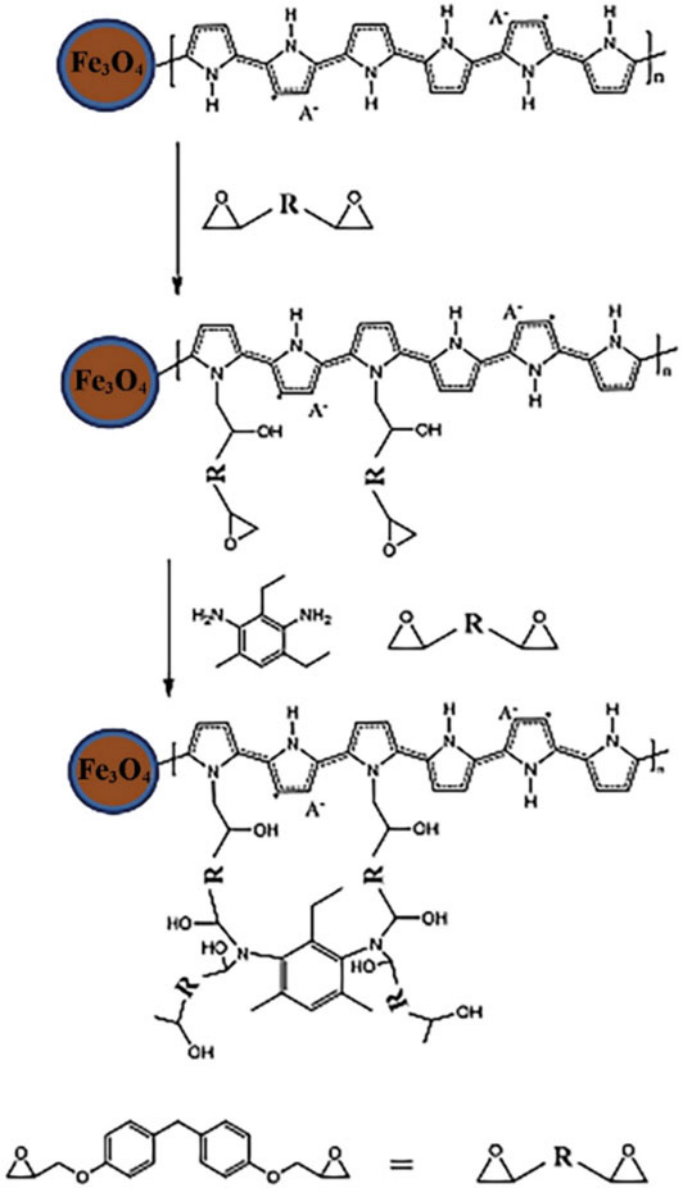

Fig. 18 Cross-linked structure formed by the epoxy resin and modified curing agent (Copied, with authorization from RSC [91])

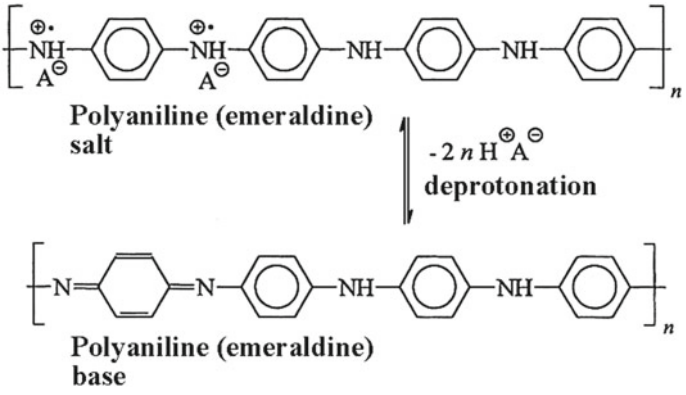

Fig. 19 De-protonation of conductive PANI by amine-based curing agents turns the polymer state into a nonconductive fashion (Reproduced, with permission from Pure and Applied Chemistry [94])

potential (Fig. 19). Therefore, the type and concentration of used hardener should be optimized to address this challenge [94].

In this regard, the type of protonating agent plays an important role in producing stable conductive forms so that the reverse reaction is not favored in a competing reaction. Researchers have used protonation of PANI with various acids, for example, *p*–CH_3–C_6H_4–SO_3H and HCl, wherein the PT was at quantities above 15 wt% of the conductive polyaniline salt [94]. A run-through of these diverse examinations showed that the doping agent of polyaniline, the grade of epoxy, and their blending method were the most influential parameters responsible for developing a high conductive polymer blend. Tsotra et al. studied the stability and final conductance of epoxy resin/PANI blend protonated with dodecylbenzenesulfonic acid (DBSA). In addition to the significant role of DBSA-PANI on the mechanical properties of the material, the PT value decreased to 2 wt% with a maximum conductivity of 2×10^{-7} S/cm for 10 wt% PANI-DBSA [95]. The structure of the DBSA-PANI component (Fig. 20) was responsible for the fine dispersion of filler and its stable nature as well, leading to the achieved electrical performance.

In complementary work, Jia et al. studied the influence of two kinds of PANI-DBSA, powder and paste (having additional DBSA), on the dispersion and following conductivity level. It was shown that paste form resulted in lesser PT in comparison with powder, owing to its superior dispersion in the resin. To enhance more, they applied PANI-DBSA coated mica particles and found excellent conductivity values for the composite due to good dispersion. The PANI-mica sticky stuff achieved a considerably improved dispersion in the epoxy resin than in powder form resulting in a much better reduction in composite resistivity in terms of filler concentration (Fig. 21) [96].

In the following, Soares et al. evaluated the result of physical blending and polymerization of DBSA doped PANI in an epoxy matrix on the conductivity of the

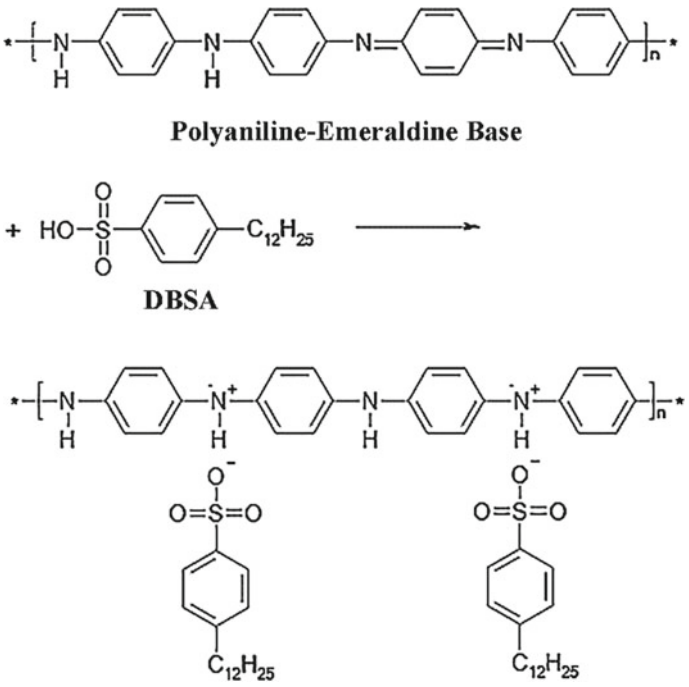

Fig. 20 Protonation of emeraldine base by acid–base reaction between PANI and DBSA (Copied, with authorization from Elsevier [95])

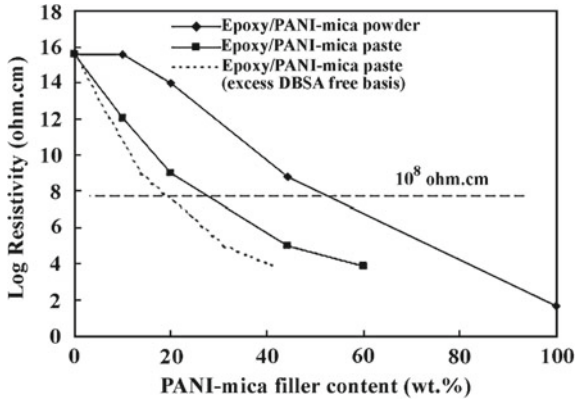

Fig. 21 Electrical resistivity of modified epoxy/PANI composites in terms of filler content (Copied, with authorization from Elsevier [96])

epoxy thermoset. A lower PT was gained at 2 wt% additive content for in situ polymerization method compared with physical blending (i.e., 10 wt%) with a maximum conductance of 10^{-3} S/cm at 12 wt% filler content [97].

4.7.3 Polythiophene (PTh)

PTh, a well-known electroluminescent, is the next widely used ICP in epoxy-based materials. Although PTh is a polymer with a low price and density along with suitable electrical conductivity and good environmental stability [98], its insolubility and poorer constancy in the p-doped conductive form are a challenge to its application and processability. Therefore, it is rarely used in polymer blends in comparison with two previous conductive polymers. However, researchers attempt to increase PTh performance in PTh–epoxy thermosets. Zabihi et al. prepared PTh nanoparticles and studied the electrical characteristic of the PTh-epoxy matrix. The electrical conductance was enhanced by adding PTh and got to 1×10^{-7} S/m at 20 wt% loading, with a PT of 0.5–1 wt%. To improve the dispersion of PTh within epoxy resin, other strategies have been developed as well. Khezri et al. prepared hybrid composites comprised of PTh enriched GO through polymerization of the thiophene monomer absorbed on GO surface. PTh-GO nanoparticles were well dispersed in the epoxy matrix owing to powerful interaction among functional groups on the GO surface and continuous phase (Fig. 22). With this modification, the aspect ratio of the PTh–GO increased and allowed to form a conductive pathway better than the PTh to afford a lesser PT quantity (1 wt%) [99]. Similar functional group alteration was also reported by Bazireh et al. with the difference that they used CNTs instead of GO. Electrical conductivity measurements revealed that the conductivity of material varied between 2.5×10^{-2} and 1.7 S/cm in terms of composite composition [99].

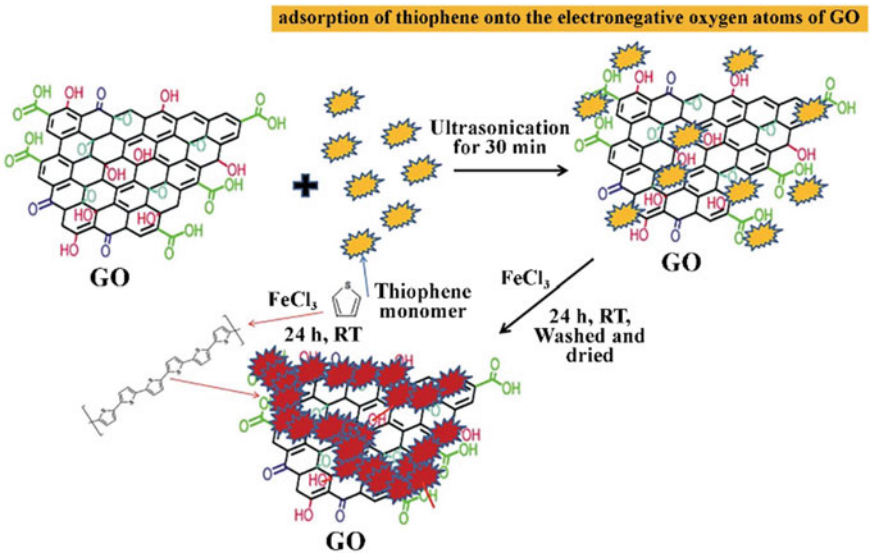

Fig. 22 Schematic illustration for the synthesis of PTh on GO nanosheets (Copied, with authorization from the Royal Society of Chemistry Publishing [99])

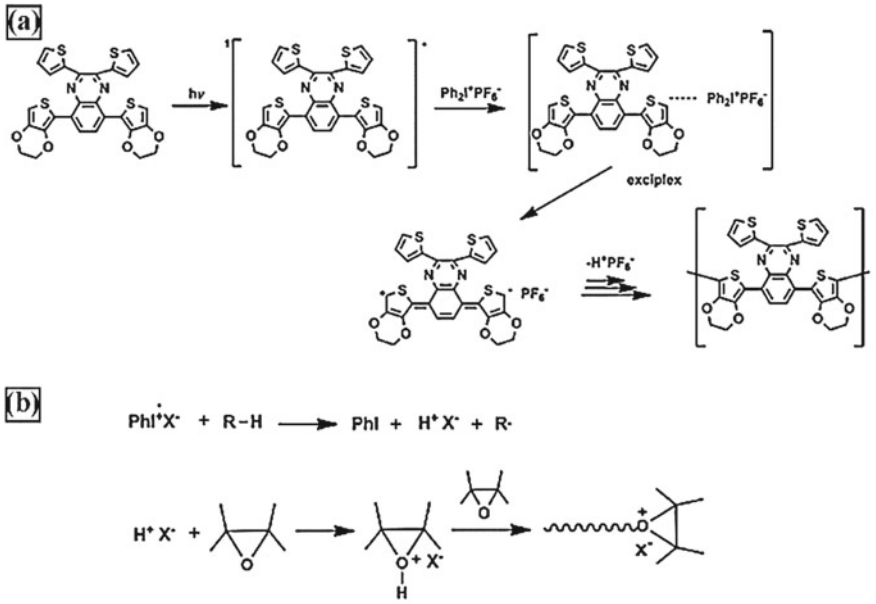

Fig. 23 **a** Photopolymerization of thiophenes to produce highly conjugated PTh. **b** Direct cationic polymerization of epoxides induced by light illumination (Reproduced, with permission from Elsevier [100])

Marco et al. developed a novel method to link conductive polymers with the epoxy networks to enhance the conductivity of material as well as the dispersal of conductive additives in the medium. In the process, an epoxy-PTh network was formed by light-stimulated concurrent polymerization of thiophene and a two-functional epoxy monomer, 1,6-hexanediol diglycidyl ether (HDGE). Polymerization of epoxy monomer was initiated by the liberated protons resulting from thiophene photopolymerization, as shown in Fig. 23. They illustrated that the applied methodology, in addition to PTh doping using iodonium salt, could significantly improve the conductivity of produced material [100].

4.7.4 Poly(3,4-ethylenedioxythiophene) (PEDOT)

PEDOT is another member of ICPs that is doped with a myriad of synthetic or biological compounds, with the most common being polystyrene sulfonate (PSS) [101]. The attraction toward PEDOT, especially in biomedical applications, arises from its potential to stimulate cells, visual translucency in its conductive state, great stableness, adequate band gap, and small oxidation–reduction potential [102]. The main disadvantage of PEDOT is low solubility in solvents which can be partially relieved by using counterions such as polystyrene sulfonate (PEDOT:PSS) or tetramethacrylate [103]. Current advances in PEDOT: PSS polymeric mixtures and composites

have been reviewed by Liu et al. [104]. In terms of epoxy-based materials, several reports directly used PEDOT: PSS to initiate conductivity for industrial application. Jian et al. enhanced the anticorrosive acting of epoxy coatings by incorporation of innately conductive PEDOT: PSS. The surface morphology studies ascertained that the erosion of coatings was reduced considerably by an increasing amount of PEDOT:PSS [105]. The report of Si et al. is another example of PEDOT commercial advantages for the reduction of silver content in epoxy thermosets. As discussed in Sect. 4.1.1, silver (Ag) is unique among affordable metals because of its high conductivity; however, the amount of silver must be reduced to allow its cost-effective application. It was observed that the use of dry PEDOT:PSS in epoxy-based adhesives decreased the quantity of Ag too much lower than that of conventional silver-based conductive adhesives [106]. In the following, they reported the use of water-based PEDOT: PSS nanogels for improving the conductivity level of the conventional conductive epoxy thermosets. The results indicated that CH_3OH as a solvent could contribute mainly to the distribution of PEDOT:PSS particles in epoxy and raise the conductivity among PEDOT:PSS and Ag particles [106].

4.8 Hybrid Composites Based on Epoxy Resin

Hybridization is a process of incorporating two or more organic or inorganic fillers inside a polymeric matrix to yield a higher active surface, strength, higher strength-to-weight ratio, and other properties required for high-performance applications [107]. To enhance the electrical conductivity of epoxy thermosets, multi-blending of additives with different physical characteristics, for example, particle geometry, surface chemistry, interfacial tension, etc., can be used [108, 109]. This section concerns the development of electroactive hybrid composites of epoxy resins, especially based on the combination of conductive polymers with carbonaceous or metal fillers.

A significant contribution has been made toward the hybrid composites of epoxy coatings with sufficient conductivity and corrosion inhibition. Yue et al. prepared epoxy-based composite coatings with enhanced electrical conductivity and corrosion resistance via the incorporative acting of PANI and titanium nitride (TiN). The results indicated that the corrosion potential ($E_{corr} = -0.338$ V) for PANI-TiN/epoxy composite was moved up by 0.235 and 0.120 V compared with the original epoxy matrix ($E_{corr} = -0.573$ V) and PANI/epoxy ($E_{corr} = -0.458$ V), respectively [110]. The corrosion inhibition of epoxy coatings was also reported by blending epoxy with PANI/ZnO and core-shell particles of polysulfide@urea–formaldehyde resin as a self-restoring factor. The coating composed of 7.5% core-shell particles exhibited corrosion protection. PANI not only operated as a physical wall against the corroding agents but also trapped the electrons released from the substrate (e.g., Al). These electrons can convert doped PANI to a de-doped state according to the reaction described in Fig. 24.

It is clear that the penetrations of corrosive species inside the matrix became more difficult with the addition of ZnO particles, and therefore, much more efficiency was

$$Al \rightarrow Al^{3+} + 3e$$

$$[PANI^{y+}(DBS^{-})_y]_n + nye \rightarrow (PANI)_n + nyDBS^{-}$$

doped dedoped

Fig. 24 De-doping of PANI induces a decrease in film conductivity (Reproduced with permission from Elsevier [111])

achieved [111]. We can also refer to the research reported recently by Pirhady et al. to increase the adhesion of fillers on the substrate. They replaced PANI/ZnO component with alumina/PANI core-shell nanoparticles doped with cerium nitrate inhibitor. Hybridization of PANI with AL_2O_3 was carried out through the adsorption of aniline monomer on the surface of Al_2O_3 and subsequent polymerization using $(NH_4)_2S_2O_8$ (APS) as an oxidation reagent. Results of electrochemical impedance spectroscopy demonstrated that the fabricated epoxy coatings provided excellent active protection against corrosion due to the formation of the Ce^{3+}/amine complex. Further, alumina nanoparticles enhanced the mechanical and blocking properties of the coating [112].

Other hybrid nanocomposites have also been evolved for different applications via a combination of PANI with carbonaceous fillers, especially CNTs. Imani et al. prepared conductive epoxy adhesives by incorporation of MWCNT and PANI doped with para-toluenesulfonic acid. The composite was prepared through in situ polymerization that resulted in suitable dispersal and great mixability of additives with the matrix. The PT values for epoxy/MWCNT, epoxy/PANI, and epoxy/PANI/MWCNT were calculated at 0.049, 0.043, and 0.026 wt%, indicating the synergistic effect of fillers [113]. Gu et al. reported the surface functionalizing of MWNTs with PANI (PANI/MWCNT) via an easy surface-initiation polymerization technique by means of the oxidizing of CNTs and later anilines by a Cr^{+6} oxidizing agent. This modification resulted in a more stabilized MWCNT upon loading in epoxy matrix compared to individual application of MWCNT particles. The electrical conductance of cross-linked epoxy incorporated with modified MWNTs was enhanced 5.5 times compared with pristine specimens [114]. In another work, Wang et al. fabricated a mixed conductor with a sandwich configuration, wherein PANI-coated CNT (PANI@CNT) was trapped between GO sheets (PANI@CNT-GO) by electrostatic and π-π stacking interactions (Fig. 25). The results indicated that the dielectric properties of PANI@CNT-GO/EP composites were not caused by the simple adding of its primary constituents but had an evident synergetic effect [115].

Another type of hybridized epoxy nanocomposites is based on the additives, wherein Ag is contributed as one of the main components. Luan et al. demonstrated an enhancement in the tunneling effect of Ag-nanowires (NW) upon the addition of chemically reduced graphene (CRG). In addition to the reduction of PT value from 30 to 10 wt%, the presence of CRGs also enhanced the heat resistance and mechanical strength of the composite via the formation of interactions between hardener and epoxy chains, as shown in Fig. 26 [116].

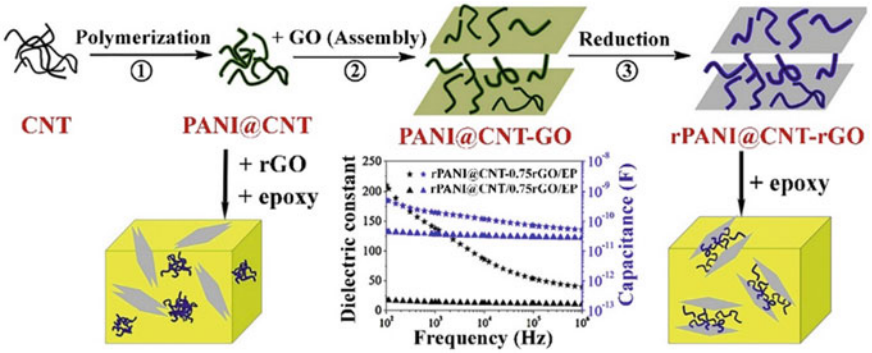

Fig. 25 Schematic preparation of PANI@CNT-GO hybrids (Reproduced with permission from Elsevier [115])

Zhang et al. hybridized CNT with Ag particles and used them as conductive agents. At low concentrations, the Ag particle is not able to interconnect with the next particle through a channel. Adding percentages above 65 wt% of Ag filler increased the conductivity by forming tunnels in the epoxy matrix. Initially, the composite contained only Ag filler, and gradually CNT filler was added to the system. As presented in Fig. 27, the electrical resistance of epoxy composite containing 65 wt% Ag was equal to 9.8×10^{-3} Ω cm, which was reduced to 9×10^{-4} Ω cm after the addition of 0.8 wt% CNT. As the CNT content exceeded the PT, the composite crossed the percolation area, and a change happened like a charge transfer from tunneling to partial metallic diffusing transference [117].

One of the problems of using fibers as a conductive filler is the electrical conductance of the composite in the direction of the sheet thickness. To solve this problem, two-dimensional and one-dimensional (or zero-dimensional) fillers can be used simultaneously. Kandare et al. used graphene filler as a two-dimensional filler and silver nanoparticles or silver nanowires as zero and one-dimensional fillers in epoxy, respectively. The results showed that the simultaneous use of these two types of additives improved the conductance of the composite in the direction of sheet thickness up to 70%. In contrast, the conductance of epoxy composite with one type of graphene filler increased by 55%. The reason for the further increase in the presence of two types of fillers, silver and graphene, was the increase in physical interactions and the creation of more pathways for electron transfer [118].

In another study, nano and microscale conductive fillers were utilized simultaneously to explore the influence of hybrid additive scale on the conductivity of the epoxy composite. Marcq et al. used two types of CNTs multi-wall carbon nanotubes (MWCNTs) and double-wall carbon nanotubes (DWCNTs) as nanofillers and silver flakes as microscale fillers. The outcomes indicated that the dispersion of CNTs and the agglomerates of silver particles in the polymer medium improved the conductivity of the epoxy composite owing to the combined effect of both additives at the micro and nanoscales. Different percentages of Ag filler and 0.4%

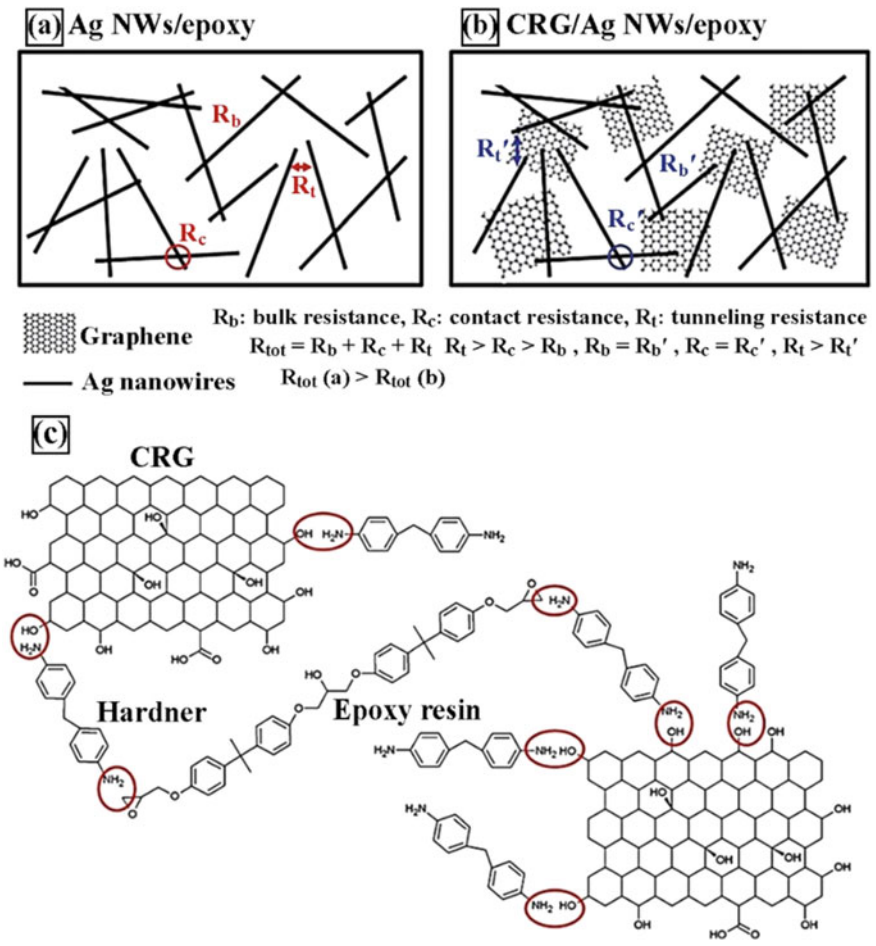

Fig. 26 Conductivity patterns of **a** the composite contained with Ag NWs lonely, **b** the CRG–Ag NWs mixed composite and **c** scheme of the interactions among the surface functional groups of the CRGs and curing agents in the epoxy matrix (Copied with authorization from the Royal Society of Chemistry [116])

vol CNTs were used to prepare conductive composites. According to Fig. 28, the penetration threshold for epoxy-containing Ag/MWCNT filler was 15% vol and for Ag/DWCNT filler was 17.5% vol, which increased the conductivity three and one times compared to epoxy/Ag composite, respectively. Also, at 25% vol, the conductance of epoxy/Ag/MWCNT was three times greater than that of epoxy/Ag/DWCNT [107].

Nowadays, an emerging trend is to prepare hybrid materials using nanoclay. Though different types of clay have been used, montmorillonite (MMT) is one of the most commonly used clay so far for the creation of hybrid substances. In the realm

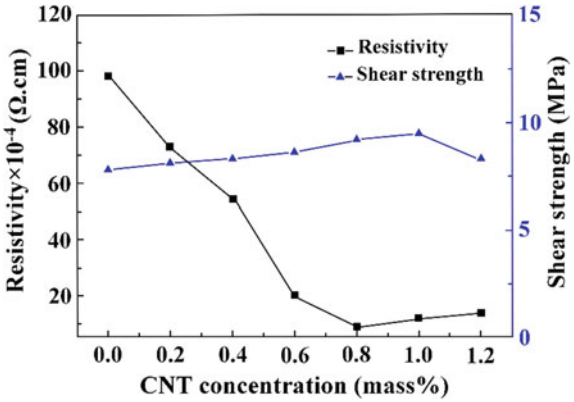

Fig. 27 Resistance and shear strength of the as cross-linked ECAs with varying CNT content (Copied, with authorization from Springer Nature [117])

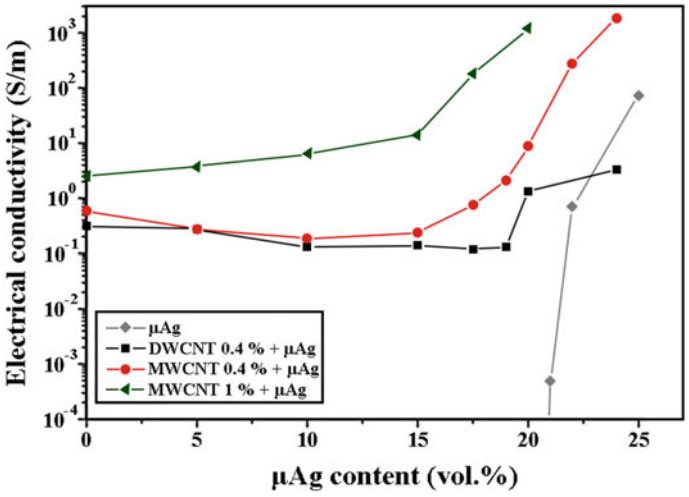

Fig. 28 Relation of the electric conductance of epoxy to the Ag flecks content for mixed composites. Data points are linked to direct the eye (Reproduced with permission from Elsevier [107])

of epoxy composites, great attention has been devoted to clay-based composites due to the advantages of these nanosheets. For example, clay significantly enhances the dispersion of CNTs and electrical properties in conductive epoxy. Sene et al. used simultaneously two types of fillers, MWCNT and MMT, and investigated the electric conductance of the product. In this study, in place polymerization technique was used to mix the fillers and epoxy matrix, and high-energy ultrasound (which does not require a solvent) was used to achieve a better dispersion. The outcomes revealed that

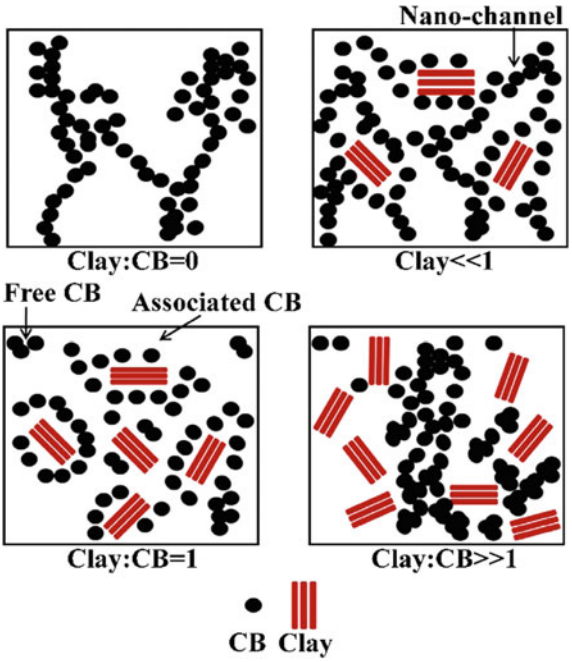

Fig. 29 Representation of micro-constructional progress in epoxy composites having various ratios of CB and clay (Reproduced with permission from Elsevier [120])

the use of these two fillers enhanced both the electric conductance and mechanical strength of the epoxy matrix and had a synergistic effect [119].

Etika et al. added clay filler to the epoxy resins containing different percentages of CB filler to increase its electrical conductance. They reported that by adding only 0.5 wt% of the clay to the system having 2.5–5.0 wt% CB, the electrical conductivity showed a sharp increase. The mechanism behind this phenomenon is the facile initiation of conductive network formation in the existence of both fillers simultaneously, as shown in Fig. 29 [120].

The findings described above indicated the excellent role of fillers hybridization on the performance of multi-functional materials. In addition to what we discussed above, there exists a wide spectrum of electrically conductive hybrid composites prepared with the combination of different fillers and novel approaches and treatments. For more details, the reader is suggested to read a great review recently published by Prunet et al. discussing hybrid conductive polymers used in flexible electronic devices [121].

5 Dispersion of Conductive Fillers and Incorporation Methods

Homogeneous filler distribution is considered the main challenge of composite formation. Filler dispersion becomes more difficult as the filler content increases since they are more likely to agglomerate, deteriorating the mechanical and electrical properties of the polymer. Thus, proper dispersing of fillers could facilitate the initiation of electrical conductance and reduce PT value [1, 55]. To achieve an idealized dispersion, sustainable methods are strongly demanded to disperse the fillers well, without degradation or geometry changes. For this, an interaction can be established between the filler and the surrounding polymer. Surface energy is a determining factor that affects the interaction of fillers and polymers and subsequently changes the quality of particle distribution. Further, these interactions directly influence the morphological and some other properties of the prepared composites [7].

Several techniques have been evolved for the proper dispersion of fillers in epoxy resins (Fig. 30). In these methods, a solvent might be used for viscosity reduction and better dispersion of the fillers. After mixing, the used solvent should be removed from the system, although, with the evaporation of the solvent, the agglomeration of fillers may occur again [13, 122].

5.1 Melt Processing

Melt processing or melt mixing has received immense attention as it is a solvent-free method. In this method, the fillers are mixed with a molten polymer using high shear mixing to disperse filler particles homogenously between polymer chains. The use of high shear mixing creates excellent dispersion for conductive fillers but can reduce the aspect ratio of fillers, resulting in undesirable properties in filler–polymer composites. Also, polymer chains experience a significant reduction in structural

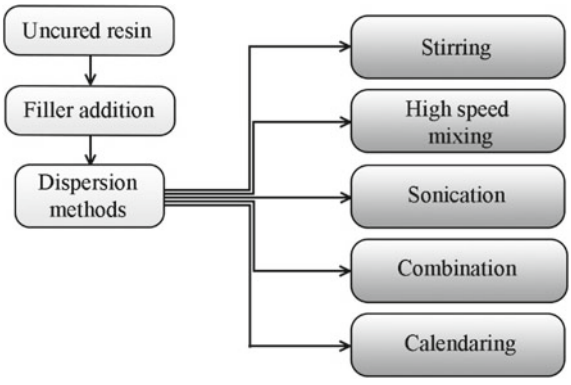

Fig. 30 Common methods of fillers dispersion in epoxy thermosets

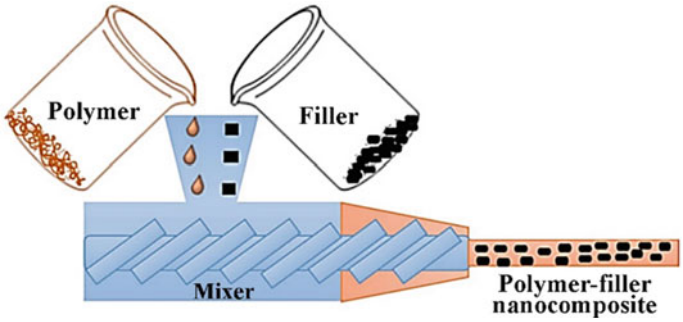

Fig. 31 Preparation of conductive polymer composites using melt mixing (Copied, with authorization from Elsevier [124])

entropy throughout this procedure. However, melt processing is desired for industrial processes due to its rate and easiness. This is a suitable technique for polymer blend formation [123].

The extrusion-based compounding process is the main method of melt processing. Twin-screw extruders are majorly applied to improve the efficiency of the mixing process. The screw consists of two intermeshing, co-rotating screws helping to increase of pumping rate as well as dispersion quality. For the composite, the components are fed into an extruder barrel, and following a homogeneous mixture is extruded to be fabricated. Different processing methods like injection molding and compression methods can increase the mechanical and electrical properties of the final product. Figure 31 shows the composite extrusion process schematically, wherein graphene-based nanocomposite is manufactured by application of a single-screw extruder [13].

5.2 Solution Blending

In the case of sheet and tube-shaped fillers such as graphene and CNTs, the solution mixing method is of interest. Here, a similar solvent (organic solvent or water) is first added to both the polymer and filler separately. Ultrasonication can also be used to increase the dispersal of fillers in the solvent. Finally, the polymer solution is added to the filler suspension, and then the solvent is removed after vigorous mixing, as shown in Fig. 32 [123].

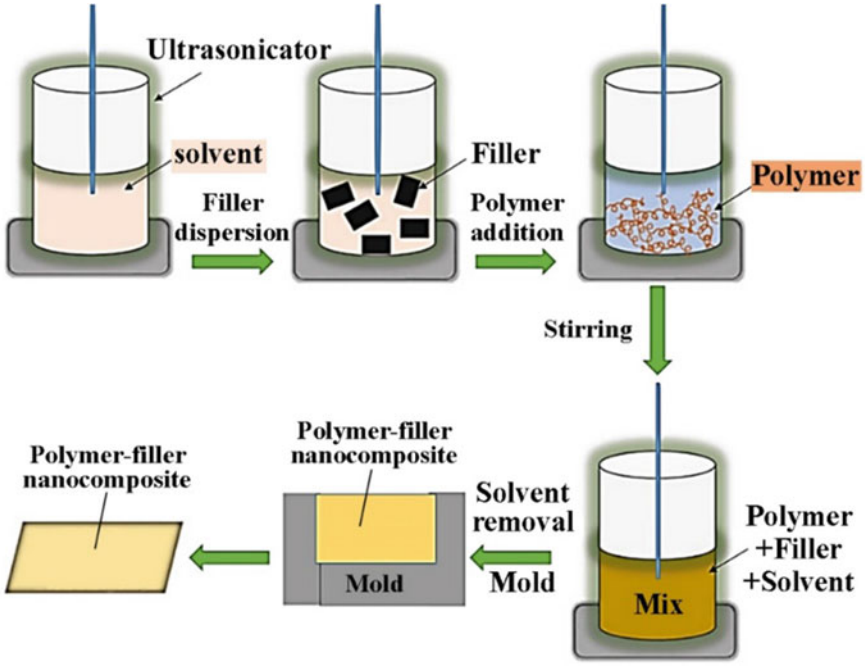

Fig. 32 Preparation steps of a composite containing filler via solution mixing method (Reproduced with permission from Elsevier [124])

5.3 In Situ Method

Upon this technique, the fillers are first blended with monomer or monomer mixtures, and then the polymerization begins in the presence of additive particles (Fig. 33). In this method, the probability of particle degradation or geometry changes is close to zero as the destructive mechanical shears are not applied. Further, there exists enough time for the particles to form secondary interactions with the polymer molecules. One of the problems associated with this procedure is the need for high electric power to disperse the additives, which makes it commercially unusable. Compared to other mixing methods, this procedure is appropriate for insoluble polymers that are not miscible in the solution processing method or for polymers that have low thermal resistance and have problems in the melt mixing method. Also, the composites prepared by this method showed enhanced mechanical properties, and lower PT value than that of other methods [123].

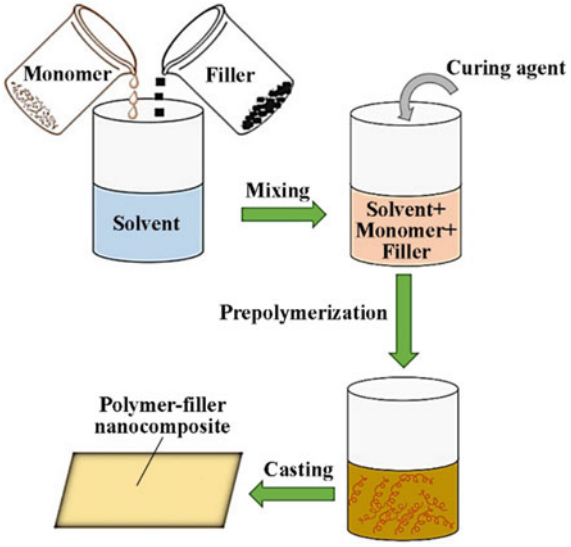

Fig. 33 Preparation of conductive polymer composites using in situ polymerization (Reproduced with permission from Elsevier [124])

5.4 Other Methods

The three methods mentioned above are the main methods of composites preparation techniques. However, there are some other methods like latex technology developed so far. In latex technology, filler particles first form an aqueous colloid, then merge with the associated polymer latex, and finally dry [21].

The common methods described above have their pros and cons, as listed in Table 1.

Table 1 Benefits and drawbacks of the three main techniques of composite construction [17]

Mixing techniques	Benefits	Drawbacks
Melt blending	Simplicity of method, usability in industry, creating good dispersion for fillers	Make changes and reductions in their dimensions, reduce other properties related to fillers
Solution mixing	Better dispersion of fillers (due to lower viscosity) than the melt mixing method	Unsuitable for use in the industry, requires special methods for dispersing fillers and affecting their dimensions
In situ polymerization	Creates good dispersion for fillers, lower PT than the other two methods	Requires a lot of energy to disperse fillers, not economical

6 Determinants Influencing the Electric Conductance of Polymer Composites

To prepare nanocomposites, various parameters must be considered. Regardless of the form of design, the producer requires to consider these factors when producing a novel polymer nanocomposite product. In general, these parameters can be divided into three main categories: parameters related to fillers, polymer matrix, and preparation of nanocomposites [125, 126].

6.1 Additive Characteristics

The geometric shape of the loaded conductive agents is an effective factor in the formation of isotropic and anisotropic structures. In anisotropic conductive materials, spherical fillers and oriented rod-like fillers are preferred to trigger conductivity only on Z-axis and restrict electrical contact on the X-Y axis. However, sheet (flake)-like fillers provide electrical conductivity in all directions when they are used at the same concentrations [109].

6.1.1 Additive Geometric Shape

The physical properties of fillers, such as different geometrical shapes, are critical factors affecting the conductivity of the final composite. The filler's geometries, such as shape (e.g., powder, fibers, etc.), dimension, and size, affect the range of conductivity. For example, although carbon fillers are the same materials, their electrical conductivity shows significant differences due to differences in their shape. Smaller filler sizes or higher length to diameter ratio (higher than 1) reduces the PT and thus increases the electrical conductivity of the composite [125, 126].

6.1.2 Size Polydispersity

The fillers may be exposed to changes in size or dimension during the preparation and processing steps. As mentioned, the geometry of the additive particles affects the conductivity of the composite, so the distribution of some filler characteristics such as length, diameter, and thickness can also affect the electrical conductivity [17].

6.1.3 Orientation

Some substance features are inherently orientation dependent, like electrical conductance, so how the filler particles are oriented within the matrix can directly increase

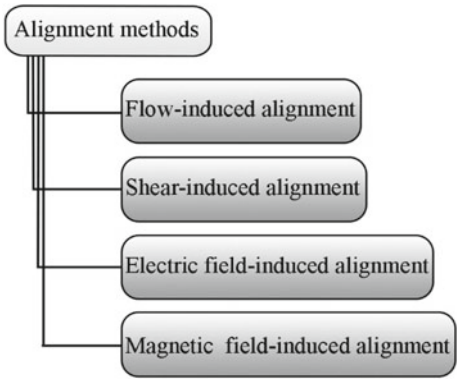

Fig. 34 Alignment methods for orientation of the nanofillers in nanocomposites

or decrease the filler's conductance efficiency. Orientation mode causes the fillers to experience a different number of contacts, subsequently making different electrical conductivity in the composite. Some successful alignment methods are shown in Fig. 34 [15, 125, 126].

6.2 Polymer Properties

The properties of the nonconducting polymer can also influence the final conductance of the composite. Polymer type, crystallization degree, viscosity, polarity, and even superficial tension of the polymer can affect the amount of filler required to conduct electricity. As mentioned earlier, the interaction between the conductive additive and the nonconductive polymer medium affects the distribution of fillers. For example, increasing the polarity of a nonconductive polymer decreases the PT due to the enhanced interactivity between the conductive additive and the polymer medium. Also, for a polymer with an amorphous phase, the required concentration of the filler is much more than a polymer with a semicrystalline phase [17].

6.3 Processing Conditions

As mentioned before, the processing conditions for conductive material fabrication are of great importance. For example, although intense mixing causes the fillers to distribute well, it might collapse the filler particles and affect the final conductivity. In methods such as injection molding and extrusion, the fillers pass through a nozzle or mold that causes them to orient in the same direction resulting in the formation of anisotropic conductive materials. Another influential factor is the pathway responsible for network formation. If the network possesses structural defects and voids, it means that the conductive fillers are absent there, subsequently restricting

the achievement of electric conductance in a specific route. It is deduced that the manufacturing condition is important to changing conductivity features of materials [5].

Ning et al. studied the influence of different factors of the fabrication process on the electrical properties of polymer/MWCNTs nanocomposites. They prepared epoxy/MWCNT nanocomposites via in situ polymerization method. They found that in situ polymerization was efficient in the production of the electrically conductive nanocomposites by adding a very small amount of CNT. It was found that curing at a high temperature increased the electric conductance of nanocomposites because of the easy formation of a macroscopic conductive network. The influence of blending rate and period was intricate, but moderate shear forces and less blending period were useful for the construction of macroscopic conductive networks of MWCNT, and no important aggregations of MWCNT were recognized for the samples. Substantial high shear forces and blending period could disintegrate the created conducting networks of MWCNTs [127].

7 Influence of Conductive Additives on Thermal and Mechanical Properties

The mixing of conductive fillers with epoxy alters its electrical conductance and affects other properties of the polymer, for example, mechanical and thermal properties. Composites containing conductive fillers show a higher Young's modulus than pure polymers. In general, various factors such as the amount of added fillers, the surface area of the fillers, their geometry and structure, as well as the interaction between the fillers and the polymer medium, change the mechanical properties of the composites [15].

8 Conclusions and Future Outlook

Epoxy resins, also known as polyepoxides, are a class of reactive prepolymers that are widely used as matrix materials for engineering composites. Since the first experiments of conductive nanocomposites were demonstrated using the embedding of conductive agents, many advances have been made to fabricate much more efficient conductive additives. The ultimate exploitation of the potential of different approaches will produce novel engineering composites. To achieve this, the synthesis of stable, high-efficient conducting agents, followed by designing a suitable manufacturing process, could be envisioned. One of the merging trends is the combination of diverse kinds of conducting agents to fabricate mixed additives. Hybrid materials with multi-functionality are strongly desired and are the subject of ongoing research. The next trend is the induction of specific orientation and morphologies for fillers,

especially rod-shaped additives, by application of external electric or magnetic fields. Moreover, epoxies cured in the presence of DESs playing as catalysts, hardeners, and conducting agents have not been explored carefully, and deep research is needed to develop more efficient mixtures.

References

1. Lee, B.-L.: Electrically conductive polymer composites and blends. Polym. Eng. Sci. (1992). https://doi.org/10.1002/pen.760320107
2. Fox, R.T., Wani, V., Howard, K.E., et al.: Conductive polymer composite materials and their utility in electromagnetic shielding applications. J. Appl. Polym. Sci. (2008). https://doi.org/10.1002/app.27317
3. Meng, Q., Han, S., Araby, S., et al.: Mechanically robust, electrically and thermally conductive graphene-based epoxy adhesives. J. Adhes. Sci. Technol. (2019). https://doi.org/10.1080/01694243.2019.1595890
4. Liu, S., Chevali, V.S., Xu, Z., et al.: A review of extending performance of epoxy resins using carbon nanomaterials. Compos. Part B Eng. (2018)
5. Aradhana, R., Mohanty, S., Nayak, S.K.: A review on epoxy-based electrically conductive adhesives. Int. J. Adhes. Adhes. (2020). https://doi.org/10.1016/j.ijadhadh.2020.102596
6. Ladani, R.B., Wu, S., Kinloch, A.J., et al.: Improving the toughness and electrical conductivity of epoxy nanocomposites by using aligned carbon nanofibres. Compos. Sci. Technol. (2015). https://doi.org/10.1016/j.compscitech.2015.06.006
7. Alemour, B., Badran, O., Hassan, M.R.: A review of using conductive composite materials in solving lightening strike and ice accumulation problems in aviation. J. Aerosp. Technol. Manag. (2019)
8. Pang, H., Xu, L., Yan, D.X., Li, Z.M.: Conductive polymer composites with segregated structures. Prog. Polym. Sci. (2014)
9. Mir, I., Kumar, D.: Recent advances in isotropic conductive adhesives for electronics packaging applications. Int. J. Adhes. Adhes. (2008). https://doi.org/10.1016/j.ijadhadh.2007.10.004
10. Kausar, A.: Application of polymer-based composites: conductive pastes based on polymeric composite/nanocomposite. In: Electrical Conductivity in Polymer-Based Composites: Experiments, Modelling, and Applications (2018)
11. Gao, J.F., Yan, D.X., Yuan, B., et al.: Large-scale fabrication and electrical properties of an anisotropic conductive polymer composite utilizing preferable location of carbon nanotubes in a polymer blend. Compos. Sci. Technol. (2010). https://doi.org/10.1016/j.compscitech.2010.07.019
12. Liu, M., Zhang, Q., Zhao, Y., et al.: Design and development of a fully printed accelerometer with a carbon paste-based strain gauge. Sensors (Switzerland) (2020). https://doi.org/10.3390/s20123395
13. Badrul, F., Abdul Halim, K.A., Mohd Salleh, M.A.A., et al.: Current advancement in electrically conductive polymer composites for electronic interconnect applications: a short review. In: IOP Conference Series: Materials Science and Engineering (2019)
14. Frigione, M., Lettieri, M.: Recent advances and trends of nanofilled/nanostructured epoxies. Materials (Basel) (2020)
15. Koncar, V.: Smart textiles for monitoring and measurement applications. In: Smart Textiles for In Situ Monitoring of Composites (2019)
16. Alemour, B., Yaacob, M.H., Lim, H.N., Hassan, M.R.: Review of electrical properties of graphene conductive composites. Int. J. Nanoelectron. Mater. (2018)
17. Gulrez, S.K.H., Ali Mohsin, M.E., Shaikh, H., et al.: A review on electrically conductive polypropylene and polyethylene. Polym. Compos. (2014)

18. Sancaktar, E., Bai, L.: Electrically conductive epoxy adhesives. Polymers (Basel) (2011). https://doi.org/10.3390/polym3010427
19. Gkourmpis, T.: Electrically conductive polymer nanocomposites. In: Controlling the Morphology of Polymers: Multiple Scales of Structure and Processing (2016)
20. Rahaman, M., Aldalbahi, A., Govindasami, P., et al.: A new insight in determining the percolation threshold of electrical conductivity for extrinsically conducting polymer composites through different sigmoidal models. Polymers (Basel) (2017). https://doi.org/10.3390/polym9100527
21. Kaur, G., Adhikari, R., Cass, P., et al.: Electrically conductive polymers and composites for biomedical applications. RSC Adv. (2015)
22. de Sousa, D.E.S., Scuracchio, C.H., de Oliveira, Barra, G.M., de Almeida Lucas, A.: Expanded graphite as a multifunctional filler for polymer nanocomposites. In: Multifunctionality of Polymer Composites: Challenges and New Solutions (2015)
23. Amarasekera, J.: Conductive plastics for electrical and electronic applications. Reinf. Plast. (2005). https://doi.org/10.1016/S0034-3617(05)70734-7
24. Gojny, F.H., Wichmann, M.H.G., Fiedler, B., et al.: Evaluation and identification of electrical and thermal conduction mechanisms in carbon nanotube/epoxy composites. Polymer (Guildf) (2006). https://doi.org/10.1016/j.polymer.2006.01.029
25. Amoabeng, D., Roell, D., Clouse, K.M., et al.: A composition-morphology map for particle-filled blends of immiscible thermoplastic polymers. Polymer (Guildf) (2017). https://doi.org/10.1016/j.polymer.2017.04.009
26. Salzano De Luna, M., Filippone, G.: Effects of nanoparticles on the morphology of immiscible polymer blends - Challenges and opportunities. Eur. Polym. J. (2016)
27. Grancarić, A.M., Jerković, I., Koncar, V., et al.: Conductive polymers for smart textile applications. J. Ind. Text. (2018)
28. Zhu, J., Abeykoon, C., Karim, N.: Investigation into the effects of fillers in polymer processing. Int. J. Light Mater. Manuf. (2021). https://doi.org/10.1016/j.ijlmm.2021.04.003
29. Amoabeng, D., Velankar, S.S.: A review of conductive polymer composites filled with low melting point metal alloys. Polym. Eng. Sci. (2018). https://doi.org/10.1002/pen.24774
30. Lu, D., Tong, Q.K., Wong, C.P.: A study of lubricants on silver flakes for microelectronics conductive adhesives. IEEE Trans. Components Packag. Technol. (1999). https://doi.org/10.1109/6144.796536
31. Tolinski, M.: Additives for modifying electrical properties. In: Additives for Polyolefins (2015)
32. Zhang, X.F., Liu, Z.G., Shen, W., Gurunathan, S.: Silver nanoparticles: synthesis, characterization, properties, applications, and therapeutic approaches. Int. J. Mol. Sci. (2016)
33. Nam, S., Woo Cho, H., Kim, T., et al.: Effects of silica particles on the electrical percolation threshold and thermomechanical properties of epoxy/silver nanocomposites. Appl. Phys. Lett. (2011). https://doi.org/10.1063/1.3615690
34. Jiang, H., Moon, K.S., Lu, J., Wong, C.P.: Conductivity enhancement of nano silver-filled conductive adhesives by particle surface functionalization. J. Electron. Mater. (2005). https://doi.org/10.1007/s11664-005-0202-6
35. Chan, K.L., Mariatti, M., Lockman, Z., Sim, L.C.: Effect of ultrasonication medium on the properties of copper nanoparticle-filled epoxy composite for electrical conductive adhesive (ECA) application. J. Mater. Sci. Mater. Electron. (2010). https://doi.org/10.1007/s10854-009-9991-3
36. Zhang, X., Cheng, X., Yin, H., et al.: Preparation of needle shaped nano-copper by microwave-assisted water system and study on its application of enhanced epoxy resin coating electrical conductivity. Appl. Surf. Sci. (2008). https://doi.org/10.1016/j.apsusc.2008.03.078
37. Mawaki, T., Teramoto, A., Ishii, K., et al.: Modification of copper and copper oxide surface states due to isopropyl alcohol treatment toward area-selective processes. J. Vac. Sci. Technol. A. (2021). https://doi.org/10.1116/6.0000618
38. Baharudin, L., Yip, A.C.K., Golovko, V.B., et al.: CO oxidation and the inhibition effects of carboxyl-modification and copper clusters on multi-walled carbon nanotubes. Appl. Catal. B Environ. (2020). https://doi.org/10.1016/j.apcatb.2019.118265

39. Mohd Hirmizi, N.H., Abu Bakar, M., Tan, W.L., et al.: Electrical and thermal behavior of copper-epoxy nanocomposites prepared via aqueous to organic phase transfer technique. J. Nanomater. (2012). https://doi.org/10.1155/2012/219073
40. Zhao, H., Liang, T., Liu, B.: Synthesis and properties of copper conductive adhesives modified by SiO_2 nanoparticles. Int. J. Adhes. Adhes. (2007). https://doi.org/10.1016/j.ijadhadh.2006.03.006
41. Wei, C., Akinwolemiwa, B., Yu, L., et al.: Polymer composites with functionalized carbon nanotube and graphene. In: Polymer Composites with Functionalized Nanoparticles: Synthesis, Properties, and Applications (2018)
42. Moisala, A., Li, Q., Kinloch, I.A., Windle, A.H.: Thermal and electrical conductivity of single- and multi-walled carbon nanotube-epoxy composites. Compos. Sci. Technol. (2006). https://doi.org/10.1016/j.compscitech.2005.10.016
43. Rosca, I.D., Hoa, S.V.: Highly conductive multiwall carbon nanotube and epoxy composites produced by three-roll milling. Carbon N Y (2009). https://doi.org/10.1016/j.carbon.2009.03.039
44. Ma, C., Liu, H.Y., Du, X., et al.: Fracture resistance, thermal and electrical properties of epoxy composites containing aligned carbon nanotubes by low magnetic field. Compos. Sci. Technol. (2015). https://doi.org/10.1016/j.compscitech.2015.04.007
45. Khan, S.U., Pothnis, J.R., Kim, J.K.: Effects of carbon nanotube alignment on electrical and mechanical properties of epoxy nanocomposites. Compos. Part A Appl. Sci. Manuf. (2013). https://doi.org/10.1016/j.compositesa.2013.01.015
46. Bal, S.: Experimental study of mechanical and electrical properties of carbon nanofiber/epoxy composites. Mater. Des. (2010). https://doi.org/10.1016/j.matdes.2009.11.058
47. Wu, S., Ladani, R.B., Zhang, J., et al.: Epoxy nanocomposites containing magnetite-carbon nanofibers aligned using a weak magnetic field. Polymer (Guildf) (2015). https://doi.org/10.1016/j.polymer.2015.04.080
48. Zhang, W., Dehghani-Sanij, A.A., Blackburn, R.S.: Carbon based conductive polymer composites. J. Mater. Sci. (2007)
49. Gubbels, F., Blacher, S., Vanlathem, E., et al.: Design of electrical conductive composites: key role of the morphology on the electrical properties of carbon black filled polymer blends. Macromolecules (1995). https://doi.org/10.1021/ma00109a030
50. Pelíšková, M., Kazantseva, N.E., Prokeš, J., et al.: Electrical conductivity of epoxy/silicone/carbon black composites: effect of composite microstructure. Polym. Compos. (2014). https://doi.org/10.1002/pc.22888
51. Mehrali, M., Sadeghinezhad, E., Latibari, S.T., et al.: Investigation of thermal conductivity and rheological properties of nanofluids containing graphene nanoplatelets. Nanoscale Res. Lett. (2014). https://doi.org/10.1186/1556-276X-9-15
52. Tarawneh, M.A., Saraireh, S.A., Chen, R.S., et al.: Mechanical reinforcement with enhanced electrical and heat conduction of epoxy resin by polyaniline and graphene nanoplatelets. Nanotechnol. Rev. (2020). https://doi.org/10.1515/ntrev-2020-0118
53. Meschi Amoli, B., Trinidad, J., Rivers, G., et al.: SDS-stabilized graphene nanosheets for highly electrically conductive adhesives. Carbon N Y (2015). https://doi.org/10.1016/j.carbon.2015.04.039
54. Li, Y., Tang, J., Huang, L., et al.: Facile preparation, characterization and performance of noncovalently functionalized graphene/epoxy nanocomposites with poly(sodium 4-styrenesulfonate). Compos. Part A Appl. Sci. Manuf. (2015). https://doi.org/10.1016/j.compositesa.2014.09.016
55. Chandrasekaran, S., Seidel, C., Schulte, K.: Preparation and characterization of graphite nanoplatelet (GNP)/epoxy nano-composite: mechanical, electrical and thermal properties. Eur. Polym. J. (2013). https://doi.org/10.1016/j.eurpolymj.2013.10.008
56. Li, Y., Zhang, H., Liu, Y., et al.: Synergistic effects of spray-coated hybrid carbon nanoparticles for enhanced electrical and thermal surface conductivity of CFRP laminates. Compos. Part A Appl. Sci. Manuf. (2018). https://doi.org/10.1016/j.compositesa.2017.10.032

57. Caradonna, A., Badini, C., Padovano, E., Pietroluongo, M.: Electrical and thermal conductivity of epoxy-carbon filler composites processed by calendaring. Materials (Basel) (2019). https://doi.org/10.3390/ma12091522
58. Han, S., Meng, Q., Pan, X., et al.: Synergistic effect of graphene and carbon nanotube on lap shear strength and electrical conductivity of epoxy adhesives. J. Appl. Polym. Sci. (2019). https://doi.org/10.1002/app.48056
59. Simon, P.: Two-dimensional MXene with controlled interlayer spacing for electrochemical energy storage. ACS Nano. (2017)
60. Feng, A., Hou, T., Jia, Z., et al.: Preparation and characterization of epoxy resin filled with $Ti_3C_2T_x$ MXene nanosheets with excellent electric conductivity. Nanomaterials (2020). https://doi.org/10.3390/nano10010162
61. Song, P., Qiu, H., Wang, L., et al.: Honeycomb structural rGO-MXene/epoxy nanocomposites for superior electromagnetic interference shielding performance. Sustain. Mater. Technol. (2020). https://doi.org/10.1016/j.susmat.2020.e00153
62. Emre, F.B., Kesik, M., Kanik, F.E., et al.: A benzimidazole-based conducting polymer and a PMMA-clay nanocomposite containing biosensor platform for glucose sensing. Synth. Met. (2015). https://doi.org/10.1016/j.synthmet.2015.06.015
63. Maka, H., Spychaj, T.: Epoxy resin crosslinked with conventional and deep eutectic ionic liquids. Polim./Polym. (2012). https://doi.org/10.14314/polimery.2012.456
64. Mąka, H., Spychaj, T., Kowalczyk, K.: Imidazolium and deep eutectic ionic liquids as epoxy resin crosslinkers and graphite nanoplatelets dispersants. J. Appl. Polym. Sci. (2014). https://doi.org/10.1002/app.40401
65. Ghandi, K.: A review of ionic liquids, their limits and applications. Green Sustain. Chem. (2014). https://doi.org/10.4236/gsc.2014.41008
66. Lefort, T., Duchet-Rumeau, J., Livi, S., et al.: Dielectric behaviour of an epoxy network cured with a phosphonium-based ionic liquid. Polymer (Guildf) (2021). https://doi.org/10.1016/j.polymer.2021.123645
67. Lemaoui, T., Darwish, A.S., Hammoudi, N.E.H., et al.: Prediction of electrical conductivity of deep eutectic solvents using COSMO-RS sigma profiles as molecular descriptors: a quantitative structure-property relationship study. Ind. Eng. Chem. Res. (2020). https://doi.org/10.1021/acs.iecr.0c02542
68. Capricho, J.C., Fox, B., Hameed, N.: Multifunctionality in epoxy resins. Polym. Rev. (2020)
69. Zhang, X., Sun, H., Yang, C., et al.: Highly conductive polymer composites from room-temperature ionic liquid cured epoxy resin: Effect of interphase layer on percolation conductance. RSC Adv. (2013). https://doi.org/10.1039/c2ra23027e
70. Matsumoto, K., Endo, T.: Confinement of ionic liquid by networked polymers based on multifunctional epoxy resins. Macromolecules (2008). https://doi.org/10.1021/ma801293j
71. Matsumoto, K., Endo, T.: Synthesis of ion conductive networked polymers based on an ionic liquid epoxide having a quaternary ammonium salt structure. Macromolecules (2009). https://doi.org/10.1021/ma900508q
72. Shirshova, N., Bismarck, A., Greenhalgh, E.S., et al.: Composition as a means to control morphology and properties of epoxy based dual-phase structural electrolytes. J. Phys. Chem. C (2014). https://doi.org/10.1021/jp507952b
73. Soares, B.G., Silva, A.A., Pereira, J., Livi, S.: Preparation of epoxy/jeffamine networks modified with phosphonium based ionic liquids. Macromol. Mater. Eng. (2015). https://doi.org/10.1002/mame.201400293
74. Oliveira da Silva, L.C., Soares, B.G.: New all solid-state polymer electrolyte based on epoxy resin and ionic liquid for high temperature applications. J. Appl. Polym. Sci. (2018). https://doi.org/10.1002/app.45838
75. El Achkar, T., Fourmentin, S., Greige-Gerges, H.: Deep eutectic solvents: an overview on their interactions with water and biochemical compounds. J. Mol. Liq. (2019)
76. Płotka-Wasylka, J., de la Guardia, M., Andruch, V., Vilková, M.: Deep eutectic solvents vs ionic liquids: similarities and differences. Microchem. J. (2020)

77. Kudłak, B., Owczarek, K., Namieśnik, J.: Selected issues related to the toxicity of ionic liquids and deep eutectic solvents—a review. Environ. Sci. Pollut. Res. (2015). https://doi.org/10.1007/s11356-015-4794-y
78. Del Monte, F., Carriazo, D., Serrano, M.C., et al.: Deep eutectic solvents in polymerizations: a greener alternative to conventional syntheses. Chemsuschem (2014). https://doi.org/10.1002/cssc.201300864
79. Azizi, N., Batebi, E.: Highly efficient deep eutectic solvent catalyzed ring opening of epoxides. Catal. Sci. Technol. (2012). https://doi.org/10.1039/c2cy20456h
80. Fernandes, P.M.V., Campiña, J.M., Pereira, C.M., Silva, F.: Electrosynthesis of polyaniline from choline-based deep eutectic solvents: morphology, stability and electrochromism. J. Electrochem. Soc. (2012). https://doi.org/10.1149/2.059209jes
81. Leclère, M., Livi, S., Maréchal, M., et al.: The properties of new epoxy networks swollen with ionic liquids. RSC Adv. (2016). https://doi.org/10.1039/c6ra08824d
82. Wang, J., Zhang, S., Ma, Z., Yan, L.: Deep eutectic solvents eutectogels: progress and challenges. Green Chem. Eng. (2021). https://doi.org/10.1016/j.gce.2021.06.001
83. Sheikhi, M., Rafiemanzelat, F., Sadeghpour, N., et al.: Deep eutectic solvents based on L-Arginine and glutamic acid as green catalysts and conductive agents for epoxy resins. J. Mol. Liq. (2021). https://doi.org/10.1016/j.molliq.2021.117568
84. De Paoli, M.A., Gazotti, W.A.: Conductive polymer blends: preparation, properties and applications. In: Macromolecular Symposia (2002)
85. Cassignol, C., Cavarero, M., Boudet, A., Ricard, A.: Microstructure-conductivity relationship in conducting polypyrrole/epoxy composites. Polymer (Guildf) (1999). https://doi.org/10.1016/S0032-3861(98)00349-8
86. Aradhana, R., Mohanty, S., Nayak, S.K.: Synergistic effect of polypyrrole and reduced graphene oxide on mechanical, electrical and thermal properties of epoxy adhesives. Polymer (Guildf) (2019). https://doi.org/10.1016/j.polymer.2019.02.006
87. Mir, I.A., Kumar, D.: Development of polypyrrole/epoxy composites as isotropically conductive adhesives. J. Adhes. (2010). https://doi.org/10.1080/00218461003704519
88. Barrau, S., Demont, P., Maraval, C., et al.: Glass transition temperature depression at the percolation threshold in carbon nanotube-epoxy resin and polypyrrole-epoxy resin composites. Macromol. Rapid Commun. (2005). https://doi.org/10.1002/marc.200400515
89. Zhang, X., Yan, X., Guo, J., et al.: Polypyrrole doped epoxy resin nanocomposites with enhanced mechanical properties and reduced flammability. J. Mater. Chem. C (2015). https://doi.org/10.1039/c4tc01978d
90. Zhang, W., Zhou, Y., Feng, K., et al.: Morphologically controlled bioinspired dopamine-polypyrrole nanostructures with tunable electrical properties. Adv. Electron. Mater. (2015). https://doi.org/10.1002/aelm.201500205
91. Guo, J., Zhang, X., Gu, H., et al.: Reinforced magnetic epoxy nanocomposites with conductive polypyrrole nanocoating on nanomagnetite as a coupling agent. RSC Adv. (2014). https://doi.org/10.1039/c4ra07359b
92. Stejskal, J., Gilbert, R.G.: Polyaniline. Preparation of a conducting polymer (IUPAC technical report). Pure Appl. Chem. (2002). https://doi.org/10.1351/pac200274050857
93. Stejskal, J., Sapurina, I.: Polyaniline—a conducting polymer. In: Materials Syntheses: A Practical Guide (2008)
94. Kathirgamanathan, P.: Curable electrically conductive resins with polyaniline fillers. Polymer (Guildf) (1993). https://doi.org/10.1016/0032-3861(93)90141-V
95. Tsotra, P., Friedrich, K.: Thermal, mechanical, and electrical properties of epoxy resin/polyaniline-dodecylbenzenesulfonic acid blends. Synth. Met. (2004). https://doi.org/10.1016/j.synthmet.2003.12.016
96. Gerasimova, A.V., Memetov, N.R., Tkachev, A.G., Yagubov, V.S.: Electrically conductive composites based on epoxy resin modified with graphene. Vektor Nauk Tol'yattinskogo Gos Univ. (2020). https://doi.org/10.18323/2073-5073-2020-3-19-25
97. Soares, B.G., Celestino, M.L., Magioli, M., et al.: Synthesis of conductive adhesives based on epoxy resin and polyaniline. DBSA using the in situ polymerization and physical mixing procedures. Synth. Met. (2010). https://doi.org/10.1016/j.synthmet.2010.07.021

98. Zabihi, O., Khodabandeh, A., Mostafavi, S.M.: Preparation, optimization and thermal characterization of a novel conductive thermoset nanocomposite containing polythiophene nanoparticles using dynamic thermal analysis. Polym. Degrad. Stab. (2012). https://doi.org/10.1016/j.polymdegradstab.2011.10.022
99. Khezri, T., Sharif, M., Pourabas, B.: Polythiophene-graphene oxide doped epoxy resin nanocomposites with enhanced electrical, mechanical and thermal properties. RSC Adv. (2016). https://doi.org/10.1039/c6ra16701b
100. Sangermano, M., Sordo, F., Chiolerio, A., Yagci, Y.: One-pot photoinduced synthesis of conductive polythiophene-epoxy network films. Polymer (Guildf) (2013). https://doi.org/10.1016/j.polymer.2013.02.026
101. Boehler, C., Aqrawe, Z., Asplund, M.: Applications of PEDOT in bioelectronic medicine. Bioelectron. Med. (2019). https://doi.org/10.2217/bem-2019-0014
102. Groenendaal, L., Zotti, G., Aubert, P.H., et al.: Electrochemistry of poly(3,4-alkylenedioxythiophene) derivatives. Adv. Mater. (2003)
103. Kirchmeyer, S., Reuter, K.: Scientific importance, properties and growing applications of poly(3,4-ethylenedioxythiophene). J. Mater. Chem. (2005). https://doi.org/10.1039/b417803n
104. Liu, Y., Zhang, L.: Recent progress on poly(3,4-ethyl-enedioxythiophene): polystyrenesulfonate-based flexible composite thermoelectric materials. Fuhe Cailiao Xuebao/Acta Mater. Compos. Sin. (2021)
105. Hou, J., Zhu, G., Xu, J., Liu, H.: Anticorrosion performance of epoxy coatings containing small amount of inherently conducting PEDOT/PSS on hull steel in seawater. J. Mater. Sci. Technol. (2013). https://doi.org/10.1016/j.jmst.2013.03.023
106. Si, P., Trinidad, J., Chen, L., et al.: PEDOT:PSS nano-gels for highly electrically conductive silver/epoxy composite adhesives. J. Mater. Sci. Mater. Electron (2018). https://doi.org/10.1007/s10854-017-8093-x
107. Marcq, F., Demont, P., Monfraix, P., et al.: Carbon nanotubes and silver flakes filled epoxy resin for new hybrid conductive adhesives. In: Microelectronics Reliability (2011)
108. Chang, D.D., Crawford, P.A., Fulton, J.A., et al.: An overview and evaluation of anisotropically conductive adhesive films for fine pitch electronic assembly. IEEE Trans. Components, Hybrids, Manuf. Technol. (1993). https://doi.org/10.1109/33.273681
109. Whalley, D.C., Williams, D.J., Ogunjimi, A.Y., et al.: Comparison of the behavior of isotropic and anisotropic conducting adhesives. In: American Society of Mechanical Engineers, Production Engineering Division (Publication) PED (1993)
110. Situ, Y., Ji, W., Liu, C., et al.: Synergistic effect of homogeneously dispersed PANI-TiN nanocomposites towards long-term anticorrosive performance of epoxy coatings. Prog. Org. Coat. (2019). https://doi.org/10.1016/j.porgcoat.2019.01.034
111. Najjar, R., Katourani, S.A., Hosseini, M.G.: Self-healing and corrosion protection performance of organic polysulfide@urea-formaldehyde resin core-shell nanoparticles in epoxy/PANI/ZnO nanocomposite coatings on anodized aluminum alloy. Prog. Org. Coat. (2018). https://doi.org/10.1016/j.porgcoat.2018.08.015
112. Pirhady Tavandashti, N., Molana Almas, S., Esmaeilzadeh, E.: Corrosion protection performance of epoxy coating containing alumina/PANI nanoparticles doped with cerium nitrate inhibitor on Al-2024 substrates. Prog. Org. Coat. (2021). https://doi.org/10.1016/j.porgcoat.2021.106133
113. Imani, A., Arabi, M., Farzi, G.: Effect of in-situ oxidative preparation on electrical properties of Epoxy/PANi/MWCNTs nanocomposites. J. Mater. Sci. Mater. Electron. (2016). https://doi.org/10.1007/s10854-016-5122-0
114. Gu, H., Tadakamalla, S., Zhang, X., et al.: Epoxy resin nanosuspensions and reinforced nanocomposites from polyaniline stabilized multi-walled carbon nanotubes. J. Mater. Chem. C (2013). https://doi.org/10.1039/c2tc00379a
115. Wang, T., Yuan, L., Liang, G., Gu, A.: Polyaniline coated carbon nanotube/graphene "sandwich" hybrid and its high-k epoxy composites with low dielectric loss and percolation threshold. Appl. Surf. Sci. (2015). https://doi.org/10.1016/j.apsusc.2015.10.115

116. Luan, V.H., Tien, H.N., Cuong, T.V., et al.: Novel conductive epoxy composites composed of 2-D chemically reduced graphene and 1-D silver nanowire hybrid fillers. J. Mater. Chem. (2012). https://doi.org/10.1039/c2jm16910j
117. Zhang, X.M., Yang, X.L., Wang, K.Y.: Electrical conductivity enhancement of epoxy by hybrid carbon nanotubes and self-made silver nanoparticles. Fibers Polym. (2019). https://doi.org/10.1007/s12221-019-8640-6
118. Kandare, E., Khatibi, A.A., Yoo, S., et al.: Improving the through-thickness thermal and electrical conductivity of carbon fibre/epoxy laminates by exploiting synergy between graphene and silver nano-inclusions. Compos. Part A Appl. Sci. Manuf. (2015). https://doi.org/10.1016/j.compositesa.2014.10.024
119. Sene, T.S., Ramos, A., Becker, D., Coelho, L.A.F.: Electrical conductivity behavior of epoxy matrix nanocomposites with simultaneous dispersion of carbon nanotubes and clays. Polym. Compos. (2016). https://doi.org/10.1002/pc.23332
120. Etika, K.C., Liu, L., Hess, L.A., Grunlan, J.C.: The influence of synergistic stabilization of carbon black and clay on the electrical and mechanical properties of epoxy composites. Carbon N Y (2009). https://doi.org/10.1016/j.carbon.2009.07.031
121. Prunet, G., Pawula, F., Fleury, G., et al.: A review on conductive polymers and their hybrids for flexible and wearable thermoelectric applications. Mater. Today Phys. (2021)
122. Ahmed, F., Lalia, B.S., Kochkodan, V., et al.: Electrically conductive polymeric membranes for fouling prevention and detection: a review. Desalination (2016)
123. Armstrong, G.: An introduction to polymer nanocomposites. Eur. J. Phys. (2015)
124. Gangarapu, S., Sunku, K., Babu, P.S., Sudarsanam, P.: Fabrication of polymer-graphene nanocomposites. In: Handbook of Polymer and Ceramic Nanotechnology (2020)
125. Akpan, E.I., Shen, X., Wetzel, B., Friedrich, K.: Design and synthesis of polymer nanocomposites. In: Polymer Composites with Functionalized Nanoparticles: Synthesis, Properties, and Applications (2018)
126. Polymer Composites with Functionalized Nanoparticles (2019)
127. Hu, N., Masuda, Z., Yamamoto, G., et al.: Effect of fabrication process on electrical properties of polymer/multi-wall carbon nanotube nanocomposites. Compos. Part A Appl. Sci. Manuf. (2008). https://doi.org/10.1016/j.compositesa.2008.01.002

Applications of Electrically Conductive Epoxy Adhesives

Jie Chen, Wenbin Li, and Xiaoan Nie

Abstract Electrically conductive adhesives (ECAs) mainly comprise the resin matrix, conductive particles, dispersion additives, and other additives. ECAs can effectively bond various materials and have conductive properties. The conductive mechanism of ECAs is considered to be the contact between conductive particles to form an electrical path. ECAs are widely used for microelectronic assembly, including the connection of thin wires with printed circuits, electroplating bottom plates, metal layers of ceramic adhere and metal chassis, bonding wire and tube base, bonding elements, and plane hole passing through printed circuits, bonding waveguide tuning, and hole repair. At present, much research has been done in epoxy-based conductive adhesives, including categories, conduction mechanisms, fillers, and applications.

Keywords Epoxy resin · Conductive adhesives · Conductive mechanism · Conductive fillers

1 Introduction

Electronic products continue to develop to the direction of miniature, flat, high sensitivity, and high reliability. With electric current conductivity and excellent bonding performance, electrically conductive adhesives (ECAs) are used in many electronics fields. As an alternative to tin/lead-based solders, ECAs have many excellent properties and are conductive composites applications owing to their environmental friendliness, low processing temperature, and high flexibility [1]. Normally, ECAs can be prepared by dispersing conductive fillers in an insulating polymer matrix or by physically blending conductive polymers with the matrix. Specifically, conductive fillers mostly include metals/metal-coated materials, carbons, and ceramic materials. Moreover, intrinsic conductive polymers mainly include polypyrrole, polyaniline,

J. Chen (✉) · W. Li · X. Nie
Institute of Chemical Industry of Forest Products, Jiangsu Province, Chinese Academy of Forestry, 16 Suojin Wucun, Nanjing 210042, People's Republic of China
e-mail: chenjie_hi@126.com; jiechen@icifp.cn

N. Hameed et al. (eds.), *Multifunctional Epoxy Resins*, Engineering Materials,
https://doi.org/10.1007/978-981-19-6038-3_14

polythiophene, and polyacetylene, which can be blended with an insulating matrix to achieve conductivity.

Depending on the morphology, filling rate, and performance, conductive adhesives can be roughly divided into isotropic conductive adhesives (ICAs) and anisotropic conductive adhesives (ACAs). The two categories conduct current equally in all directions and only in the Z-direction based on packing arrangement, respectively [2]. The conductive mechanism of conductive adhesives is that the contact between conductive particles forms an electrical pathway (a three-dimensional conducting network), which endows the conductive adhesives with electrical conductivity. Conductive adhesives contain solvents, and conductive particles are separated in the adhesives before curing or drying, so the particles do not continuously contact with each other and are insulating. After conductive adhesive curing or drying, due to the volatilization of solvent and adhesive curing caused by adhesive volume shrinkage, conductive particles stably and continuously contact with each other, showing electrical conductivity.

The electron tunneling effect can also produce a certain current path between conductive particles in the conductive adhesive. When the conductive particles do not contact each other, an isolation layer exists between the particles, which hinders the directional motion of free electrons in the conductive particles. According to the concept of quantum mechanics, for a microscopic particle, even if its energy is lower than the barrier energy, penetration in addition to reflection may occur, which is known as the tunneling effect. Electrons, which are microscopic particles, can pass through the barrier of conductive particle separation. The former mechanism and the latter concept are based on and relating to electrical conductivity, respectively [3]. Generally, applications of ICAs include electrical interconnections for connecting substrates (e.g., ceramics and plastics) and replacement solders for thermal-sensitive elements [4]. ACAs are applied into flat panel display, glass flip-chips, smart cards, and flip boards [5].

Epoxy resin-based ECAs are widely used in the field of electronics, such as die connection and weldless interconnection because they possess outstanding chemical, thermal and mechanical properties, adhesiveness, compatibility with diverse additives and substrates, and availability of solvent-free formulations [1]. However, epoxy resins have low electrical conductivity (10^{-7} to 10^{-14} S m^{-1}), which limits the use of ECAs. Because of this question, this chapter discusses the basic principles and limitations of various ECAs, and the main conductive mechanisms that contribute to conductivity of ECAs based on epoxy resins. Various conductive fillers in ECAs are discussed: metals, carbons, ceramics, metal coatings, polypyrrole, polyaniline, and polythiophene.

2 Electrically Conductive Adhesives

ECAs are generally deemed as conductive composite materials with an essentially clean and straightforward alternative to electronic applications. ECAs can provide an intrinsic adhesion when the polymer substrate is cured. When the concentration of

the conductive filler exceeds the critical level (the percolation limit), the composite conductivity rises suddenly. Namely, the conductive filler constitutes a conductive network by linking within the substrate, which provides a path for electron transport. In applications such as integrated circuits, conductive adhesives are a prospective alternative to lead-free tin–lead solders with six merits:

(1) lead-free;
(2) low environmental pollution;
(3) lower curing temperature than that of the solder;
(4) high dimensional stability;
(5) processability;
(6) adhesive ability for multi-material applications.

Conductive adhesives have many advantages for integrated circuits and various electronic applications, but still have some disadvantages, such as low conductivity, poor mechanical properties, easy migration, and unstable contact resistance between the adhesive and the component [6].

Diverse blends of conductive substrates and non-conductive substances were studied in the early twentieth century. A patent (1926) for electromechanical applications of conductive adhesives, a conducting varnish (1933), an electrically conductive composite comprising metal powder or graphite-reinforced Bakelite resin (1933), and a patent with electrically conductive adhesive were registered [1]. U.S. patent in 1956 proposed an application of conductive cement that uses a thermosetting polymer as a binding agent to fix semiconductor crystals to a metal substrate, which was regarded an early use of ECAs in electronics. Then, publications on experimental and theoretical research of conductive adhesives are increasing. ECAs are applied extensively in electronics because of low processing temperature and various low-cost fillers and are significantly superior over the existing interconnection technology. The adhesives have an apparent coefficient of thermal expansion owing to their high flexibility and advantages over solder alloy when bonding large chips on any substrate. In addition, MacDiarmid, Heeger, and Shirakawa won the Nobel Prize in 2000 for their discovery of inherently conductive polymers.

2.1 Types of ECAs

ECAs can be divided by the substrates into thermoplastic ECAs and thermosetting ECAs. The thermosetting substrates of ECAs are originally monomers and prepolymers undergoing polymerization reaction in solidification, forming a three-dimensional crosslinked structure in the polymer chain connection form with high-temperature stability. The substrates of thermoplastic ECAs are composed of very long polymer chains that contain a few branched chains, which and flow easily at high temperature and do not easily form a crosslinked three-dimensional network. At present, the substrates of most of commercial ECAs are thermosetting resins, of which epoxy resin is widely used owing to its excellent comprehensive performance.

Thermoplastic resins can also be added at appropriate temperature to improve the toughness and reprocessing performance of the system.

Depending on the curing system, ECAs can be separated into room-temperature-curing ECAs, medium-temperature-curing ECAs, high-temperature-curing ECAs, and UV-curing ECAs. Room-temperature-curing ECAs are unstable, and the volume resistivity easily changes when stored at room temperature. The metal particles easily oxidize during high-temperature curing of ECAs, and the curing time must be shorter to meet the requirements of ECAs. Medium-temperature-curing ECAs (below 150 °C) are used worldwide, and the temperature resistance of electronic components, the use of temperature matching, and mechanical properties are also better. UV-curable conductive adhesives combine the UV-curable technology with ECAs, which gives ECAs new properties and expands their application range. They can be used in the electronic display technology, such as electroluminescence of liquid crystal display.

Depending on the types of conductive fillers, conductive adhesives can also be divided into metal-filled ECAs, non-metal-filled ECAs, and other-filled ECAs. Metal-filled ECAs can also be separated into precious-metal-filled ECAs. The conductive fillers used are mainly gold, silver, and base metals. Conductive fillers include aluminum, copper, nickel, iron, and other metal powder, sheet, fiber. Nonmetallic conductive fillers mainly include carbon black, graphite, and carbon fiber. Other types of conductive fillers are mainly silver-coated glass fiber, silver-coated carbon powder, and metal oxides. Metal-filled ECAs, especially precious-metal-filled ECAs, have excellent conductive performance and high stability, but are limited by high costs. They are generally used for precise connection or connection in a more demanding environment. Non-metal-filled ECAs have poor conductivity and are mostly used for printing resistors, electromagnetic shielding, and switching contacts. Other-filled ECAs have good comprehensive properties and are one of the important research and development directions in the future.

According to the application fields, ECAs can be classified into ECAs for filling holes, ECAs for printing lines, and ECAs for connecting. The application of ECAs for plugging holes is mainly reflected in high-density interconnect multilayer boards. ECAs are used to fill the micro-holes, formed by photoimaging or laser, and play the role of conductive interconnection between layers. ECAs are used in printed circuits, mainly printed circuit boards, because the ECAs before solidification are commonly liquids or creams, and have a certain fluidity under the action of external force. Hence, the conductive adhesives can be put directly on the insulation layer with a net printing to draw the line. Consequently, circuit boards can be reasonably made to eliminate the chemical plating, plating, and etching, but do not produce pollution, which is good for the environment. ECAs are connected mainly in the manufacturing and assembly process of parts or parts and substrate conductives.

ECAs can also be classified by the conduction direction into isotropic conductive adhesives (ICAs) and anisotropic conductive adhesives (ACAs). The main difference is that ICAs are conductive in all directions, while ACAs are conductive in a direction-dependent way. ICAs are lead-free substitutes for solders because of their environmental friendliness, short assembly time, low cost effective, processing temperature,

and thermomechanical fatigue. ICAs can be widely used in non-solderable substrates and finer pitches. However, ICAs have some shortcomings, such as air trap, hygroscopicity, non-self-alignment, and ease of silver migration, which lead to low conductivity, low impact strength and instable contact resistance. ACAs become a research hotspot for fine pitch components thanks to their low cost and processing temperature, no cleaning, and lead-free formulations. However, ACAs rely on complicated methods and special bonding equipment, which limit the applications of ECAs.

2.1.1 Isotropic Conductive Adhesives (ICAs)

The ICA systems require a higher concentration of a filler to quickly meet the permeability percolation threshold, which can form a conductive network and conduct in all directions over this threshold. The matrix acting as the binder for the base material may be thermoplastic (e.g., polyvinyl acetate, polyvinyl chloride, polyvinyl alcohol ethers) or thermosetting (e.g., epoxy, cyanate ester, silicone, polyurethane) and may form mechanical or electric bonds with the base material. Especially, thermoplastic ICAs can be recycled or repaired and are more widely used in ECAs. However, ICAs have certain limitations, including the deterioration at high temperatures and poor strength. Polymer matrix resins mainly include epoxy resins, phenolic resins, polyimide, polyurethane, and thermoplastic plastics. The mechanical properties of epoxy resin include good thermal performance, low curing shrinkage rate, adhesive ability, and strong mechanical/thermal shock resistance. It can be used in various complex conditions (e.g., hot and humid, chemical corrosion) with strong resistance. Epoxy resin can also be cured at a lower temperature, and the formulation can be designed strongly. At present, thus, epoxy resin-based conductive adhesives are dominant in the conductive adhesive market.

In ICAs, conductive fillers as the main formulation component mainly consist of carbon, metal, and metal oxides, which are uniformly distributed in the resin matrix in spherical, sheet, or fibrous form and form conductive paths after curing. Different from the point-to-point contact of spherical metal particles in the conductive adhesives, sheet metal particles have better electrical conductivity because of their high horizontal to vertical ratio, which makes them have both point-to-point contact and face-to-face contact. Table 1 shows the conductivity of various conductive fillers, including Ag, Au, Ni, Cu, and C. Ag is widely used owing to its high conductivity, simple processing, and largest contact with flakes [7].

ICAs have been used for electrical interconnection of non-weldable substrates and welding replacement of thermal sensors with the help of ceramic and plastic properties. In these fields, they are usually called “polymer solders.” Some studies on epoxy-based conductive adhesives focus on obtaining high conductivity of ICAs under different conditions. For example, Sachdev et al. prepared ICAs using epoxy siloxane hybrid composites with excellent bonding strength, durability, low resistivity, and low tensile modulus. Wu et al. (2006) found the volume resistivity of epoxy-based ICAs filled with silver nanowires was remarkably lower at low filler loading (1.2×10^{-6} Ω m at 56 wt% Ag nanowire) [8].

Table 1 Electrical resistivity of common conductive fillers

Conductive filler	Resistivity (Ω cm)	Equivalent to the conductivity of mercury
Au	2.40×10^{-6}	39.6
Ag	1.62×10^{-6}	59.1
Cu	1.69×10^{-6}	56.7
Al	2.62×10^{-6}	36.1
Zn	5.92×10^{-6}	16.0
Fe	9.78×10^{-6}	9.8
Ni	7.23×10^{-6}	13.8
Sn	1.14×10^{-5}	8.3
Pb	2.06×10^{-5}	4.6
Bi	1.06×10^{-4}	0.8
C (graphite)	10^{-3}–1	0.000095–0.095

2.1.2 Anisotropic Conductive Adhesives (ACAs)

ACAs are composed of polymer resins, conductive particles, and other additives. Polymer resins provide conductive adhesives with the bonding ability and mechanical properties. Polymer resins include thermoplastic resins, thermosetting resins, and their mixtures. Thermosetting resins include acrylic resins, epoxy resins, and vinyl acetate copolymers, while thermoplastic resins include polyurethane. Conductive particles provide ACAs with Z-axis conductivity, including gold-plated-type polymer microspheres on the surface of core-shell structures, gold-plated-type metal particles, or solid metal particles. Curing agents react with thermosetting resins to form three-dimensional crosslinking structures and correspond to different thermosetting resins, but thermoplastic resins do not need a curing agent. Compared with ACAs based on thermoplastic resins, ACAs based on thermosetting resins have higher bonding strength and can work stably at higher temperature.

ACAs do not have a complete conductive network system because the conductive filler concentration (about 5–20 vol%) is below the percolation threshold. Thus, ACAs lead to current flow in one direction (Z-axis, unidirectional ACAs) or two directions (bidirectional ACAs) by exerting external forces. ACAs, as the main bonding materials for electronic packaging, are usually connected between the substrate and chip by hot pressing. The bonding process mainly includes three steps: preloading, bonding, and post-treatment. In preloading, the lower protective film of ACAs is removed and placed on the substrate to be bonded to soften ACAs at lower temperature and pressure than required for curing. The purpose of preloading is to make ACAs fully contact with the substrate and rearrange some conductive particles in preparation for bonding. The preloading process usually takes tens of seconds. In the bonding process, the upper protective film of ACAs is discarded, and conductive bumps and substrate circuit chip circuit are aligned. Then, after raising to the curing temperature, a part of the conductive particles under the action of external pressure

are sandwiched between the substrate and chip circuit in two conductive bumps, and an insulation layer of conductive particles is crushed. Then, the adhesive and curing agent of ACAs undergoes curing reactions, which achieve the connection between the chip circuit and the substrate circuit. In other directions, conductive particles do not form a conductive path with each other, thus achieving the anisotropic structure of insulation in other directions and conductivity in a single direction. Post-treatment can reduce the stress concentration and internal stress in the solidified colloid. Post-treatment can also prevent colloid solidification and improve the bonding stability in the hot-pressing process.

ACAs can also be divided into film anisotropic conductive pastes (ACFs) and gel anisotropic conductive pastes (ACPs). ACFs and ACPs work in the same principle, but the devices that can be bonded are different. ACFs are supplied in rolls and separated from each other by a protective film to avoid adhesion. ACPs are paste liquids. The biggest difference between ACFs and ACPs is that ACPs are used by dropping or brushing, while ACFs are used by hot pressing. ACFs can connect components in short time with simple hot-pressing equipment. ACPs cannot be easily stored, and gas discharge in large area hot pressing is hard. Even printing thickness and the distribution of conductive particles are uncontrollable. Therefore, ACPs have not been rapidly developed. ACFs can be used for flip-chip packaging, circuit board connection, and LCD connection. Although ACAs provide much convenience for modern bonding and basically meet the requirements, there are still many problems: (1) long-term stable storage problems; (2) low impact resistance of epoxy resin; (3) low stability at high temperature or high humidity.

2.2 Conduction Mechanisms in ECAs

Basically, ECAs comprise conductive fillers distributed in an insulation polymer. The conductive mechanism theories of ECAs are mainly divided into the percolation theory and the tunneling effect theory from macroscopic and microscopic perspectives. The former holds that the shrinkage of ECAs makes the conductive particles form a stable continuous contact and then induces conductivity. With an increase in the content of conductive particles, the resistance of the cured conductive adhesive is weakened first slowly and then sharply when the particle concentration reaches a critical level, which is called the percolation threshold. Initially, the composites are non-conductive until reaching the critical level. With a rise in filler concentration, conductive particle clusters are enlarged in size, forming conductive channels. The conductive filler is spread in the polymer matrix, and the conductivity of the conductive adhesive depends on the particle volume fraction. When the critical filling volume concentration is reached, the resistivity of the electrode suddenly decreases to a low order of magnitude.

The characterization of conductive channels is mainly based on two mechanisms: interparticle contact and electron tunneling. ECAs form a conductive network through physical contact or tunneling between conductive particles during the

packing. At the percolation threshold, an uninterrupted particle conductive chain exists in the adhesive formula, which leads to a significant reduction in resistivity. When the filler concentration exceeds the critical level, the particle volume fraction in the system rises, promoting the conduction. As the current carriers intensify the drift of polarized particles, they further combine, and the contact between particles becomes the dominant conduction mechanism of electron tunneling.

As for the conductive mechanism of ECAs, three situations are feasible: The conductive filler is separated, and the intrinsic conductivity of the filler plays a role; the conductive filler is in direct contact, and the electron tunneling between conductive particles is predominant. First, conductive fillers are mutually divided in the polymer; the internal conduction of the conductive fillers takes effect, and the conductivity of the ECAs increases. However, this increase is lower because the internal conductive fillers cannot wholly overcome the polymer barrier and blockage. Second, the conductive fillers of ECAs are in direct contact to constitute a continuous conductive network in the polymer matrix, which transmits electrons via the particle network through the conductance mechanism of metal particles. Last, electrons can be transferred between the conductive fillers by passing through the narrow gap (<10 nm) between the fillers when a thin insulating polymer matrix closely separates the fillers (electron tunneling effect). The alternating current/direct current (AC/DC) behavior of composites can distinguish between interparticle or band conduction and electron tunneling conduction. Moreover, band conduction and tunneling are associated with DC and AC conductivity, respectively.

2.3 Epoxy Resin-Based ECAs

Welding is generally considered a convenient way to connect two matrices, such as metals. Welding offers strong bonding and high conductivity along or across the matrix, but these methods have many troubles, such as the existence of harmful substances (e.g., lead), high processing temperature, the need for a cleaning solvent, and the inability to connect some materials (e.g., glass). To overcome the problems related to solders, many research groups have carried out much research. The first type of conductive cement is based on an epoxy resin composed of silver particles, which connect semiconductor crystals to metal substrates or supports. This material can be regarded as the first ECAs use in electronic technology. For example, the effect of the silver sheet lubricating layer on composite conductivity was studied to remove the lubricating layer with an ordinary solvent. Alternatively, an inherently conductive polymer is introduced to the epoxy matrix to improve electrical performances.

There are many studies on the preparation of conductive adhesives (conductive filler mixed with insulating matrix, and conductive polymer mixed with insulating polymer). For example, Jia et al. (2003) investigated a conductive epoxy-anhydride system involving polyaniline (PANI)-dodecylbenzenesulfonic acid (DBSA) and revealed the percolation threshold of PANI-DBSA filler-reinforced epoxy composites [9]. Choi et al. (2005) characterized the electrics of epoxy composites modified by

vapor-grown carbon nanofibers, and results show the electrical resistivity decreased with the filler content [10]. The mechanical and electrical properties of low-viscosity epoxy composites outperformed those of high-viscosity composites.

The conductive fillers integrated into the epoxy insulating substrate include metal, carbon, ceramic, and metal coatings. Ma et al. (2008) provide a simple way to decorate carbon nanotubes (CNTs) with silver nanoparticles (Ag–NPs) to strengthen conductivity [11]. Conductive polymer composites were prepared by adding Ag@CNTs as a conductive filler into epoxy resin. The conductivity of composites with 0.10 wt% Ag@CNTs was over four orders-of-magnitude higher than those with the same content of pristine or functionalized CNTs, which verifies the superiority of Ag@CNTs. Zhang et al. (2010) reported highly reliable, cheap ICAs—silver-coated Cu flakes—for electronic packaging and found the resistivity of ICAs (2.4×10^{-4} Ω cm) was identical to that of commercial Ag-filled ICAs [12]. Yim et al. (2010) reported a new type of ICAs with CNTs and low-melting-point alloys as fillers and found the CNT-filled ICAs had lower electrical resistance than those of common ICAs [13]. The effect of ceramic fillers on the electrical behaviors of epoxy resin-based adhesives was also studied. Zhao et al. (2014) used face-centered cubic (FCC) TiB ceramic powder as a conductive filler to prepare epoxy-based ceramic ECAs with the polymer matrix [14].

When the epoxy monomer of ECAs is mixed with an appropriate curing agent, the viscous liquid monomer or prepolymer is transformed into an insoluble three-dimensional (3D) network. The curing kinetics is mainly affected by the reaction activity and the migrability or flexibility of functional groups. The crosslinking reaction of epoxy resin is mainly affected by curing time, curing temperature, curing agent structure, and filler dosage. Therefore, in epoxy-based ECAs, the conductive filler can be used to catalyze the curing reaction, changing the curing rate, and finally affecting the properties of ECAs (e.g., crosslinking density, strength, bending modulus, hardness, conductivity, heating conductivity).

2.4 Conductive Fillers

ECAs are composed of a non-conductive polymer and a conductive filler. When the filler content exceeds its percolation threshold, a 3D conductive network is formed, which strengthens the conductivity of the polymer. Table 2 shows various conductive fillers.

2.4.1 Metal Fillers

Generally, a wide versus narrow particle size distribution calls for a lower filler concentration to surpass the percolation threshold in imbuing conductivity. The importance of particle size distribution is associated with the particle size and average particle size. Compared with any other metal, silver particles are unique with high

Table 2 Types of conductive fillers

Conductive fillers	Metal fillers	Ag
		Au
		Ni
		C
	Carbon fillers	Carbon nanotube
		Carbon nanofiber
		Carbon black
		Graphene
	Ceramic fillers	BN, TiC, SiC, TiB_2, TiN, TiB, BF
	Metal-coated fillers	Metal core
		Non-metal core

conductivity and thermal conductivity, and silver oxides also have higher conductivity than other metals. When the polymer matrix level is 15–30 vol%, the filler load of silver sheets is usually used to prepare ICAs. In addition to low cost and easy formation, they can be made into diverse shapes and sizes and be composed of silver sheets, particles, wires, and nanorods.

Lu et al. (1999) studied the conductivity of epoxy adhesive after removing the lubricating layer on the silver sheet, and successfully removed some solvents, resulting in higher conductivity of the composites [15]. Johnsen et al. (2012) probed into the conductivity (by current arrangement) of Ag-reinforced epoxy composites [16]. Due to the electronic arrangement, the volume conductivity of epoxy material rose by five orders of magnitude. The conductivity of isolated silver wires increased by 9–10 orders of magnitude as the particle alignment led to a transition from polymer- to silver-dominated conductivity [16]. Despite the high conductivity of silver particles, electrochemical composites made from silver-reinforced materials are limited in practical application by the disadvantages in conductivity, thermal conductivity, silver migration, and impact strength.

Nanosilver particles (e.g., Ag nanoparticles, nanowires, and nanorods) have superior conductivity. Cheng et al. (2007) prepared a UV-curable epoxy adhesive with nanosilver particles without a polymeric protector [17]. With a photosensitive mixture of $AgNO_3$ in ethylene glycol as example, the surface electrical resistivity of photocurable conductive adhesives may be decreased to $8.803 \times 10^6\ \Omega\ m^{-1}$ under 900 mJ cm^{-2} irradiation. Tee et al. (2007) used Ag-NPs as a conductive metal filler to prepare Ag-NPs-filled epoxy resin composites [18]. Electrical characterization showed the insulator transited to the conductor when the Ag content was 5% (vol/vol) because of the effective treatment with a silane coupling agent. As for the morphology, the filler dispersion of the composite system was significantly improved after the treatment. Xiong et al. (2014) prepared a typical epoxy resin-based conductive adhesive and studied the effects of curing processes on the conductivity of adhesives [19]. It was found the curing temperature dramatically influenced the

loading of 55% silver, and the volume resistivity of ICAs dropped from 1.0×10^{-3} at 180 °C to 4.7×10^{-3} at 250 °C. In addition, they discussed why the volume resistivity changed with temperature from the perspective of silver sheet dispersion in ICAs.

Gold particles are usually used as thin-layer coatings for electrical connectors in the electronic industry. They perform well in conductivity, corrosion resistance, oxidation resistance, non-chlorinated acid resistance, non-toxicity, and ductility. However, they also are easily affected by free chlorine and have high costs. Nickel, an essential component of various alloys, is a low-cost filler with high oxidation resistance in the atmosphere. It can maintain high corrosion resistance in a wide range of pH, but its conductivity is worse than that of silver and copper, so it is the preferred filler for electromagnetic shielding materials. Nickel is usually used for spherical particles in ACAs because it has a resistivity two orders-of-magnitude higher than that of Ag-filled adhesives, limiting its application in ICAs. The main reason for the high resistivity of nickel is its high hardness and difficulty in transforming into thin sheets with the best shape and size. Nickel has a wide size range, including spherical and narrow size distribution. Nickel can be plated with chemical gold to improve oxidation resistance.

Copper, a soft and changeable ductile metal, is widely applied as a conductive filler in the electronic industry thanks to its high conductivity, thermal conductivity, good electromigration properties, and economic benefits. Copper has higher electrical conductivity and lower cost than silver, but its oxidation resistance is weak, and it easily oxidized into non-conductive copper oxide, thus affecting the conductivity of the coating. Therefore, as a conductive metal filler, copper shall be modified to enhance its oxidation resistance. The main difficulty of using Cu-based electrochemical composites is to control copper oxidation and gradually reduce the electrical properties of adhesives. Generally, this problem can be solved via organic or inorganic coating of copper, N-based processing of copper, and incorporation of solder powder to the adhesive system. In addition, surface modification (plating conductive silver) of copper improves its stability, and the treatment (nitrobenzotriazole and imidazole) of copper can produce stable oxidation-controlled complexes.

2.4.2 Carbon Fillers

Carbon particles, mainly including carbon black (CB), CNTs, carbon nanofibers (CNFs), and graphene (GR), are a type of conductive fillers with more extensive application. They have abnormally high conductivity because of large surface volume ratio or aspect ratio. Some nanofillers have one- and two-dimensional structures, which are significantly recognized and used because of unique optical, chemical, electrical, thermal, mechanical, and properties.

CNTs featured with high strength, modulus, surface, thermal conductivity, current density, and thermal stability are considered excellent nanofillers to enhance the properties of polymers, adhesives, and composites. However, large specific surface areas and the inherently strong van der Waals force in structures lead to the agglomeration or aggregation of CNTs, limiting the ability of CNTs to strengthen the properties

of polymers. To address this problem, CNTs aggregates must be decomposed and completely dispersed in the substrates, which often results in an increase in the properties of adhesives or composites. Therefore, various methods have been proposed to enhance the dispersion of CNTs in the matrix, including high-shear mixing, ultrasound, surfactant, acid oxidation of CNTs, and other chemical approaches. Due to the high aspect ratio, CNTs can form an efficient conducting network with a low percolation threshold so as to make many polymers conductive. CNTs obtain a percolation threshold when the filler load is minimal, which provides high conductivity for the polymer matrix because the aspect ratio is proportional inversely to the volume fraction of the filler.

Material researchers have studied CNTs to improve the conductivity of various polymers. Jakubinek et al. (2015) added low load (nearly 1%, w/w) SWCNTs to raw aerospace-level epoxy resins to transfer conductivity while keeping structural adhesion, and thus developed structural and conductive adhesives [20]. It was found the composites' peel strength and lap shear strength did not vary with the introduction of 0.5 wt% SWCNTs, but increased by 30% and decreased by 10%–15%, respectively, after the addition of 1 wt% SWCNTs. For SWCNTs adhesive with 1 wt% addition, the conductivity of the composite was up to 10^{-1} S m^{-1}. High conductivity and uniform dispersion after the addition of 8 wt% MWCNTs were achieved by three-roll milling. Reportedly, the aspect ratio is among the critical parameters determining the conductivity and seepage behavior of composites, and when the aspect ratio rises by 5.5 times, the conductivity increases by nearly ten times [21]. Moreover, three-roll milling can induce the extended arrangement of MWCNTs with a high aspect ratio under medium load (2–4 wt%). The arrangement of CNTs greatly influences the conductivity of epoxy adhesives. Felisberto et al. (2012) reported the electrical properties of CNTs/epoxy composites filled with aligned and randomly oriented nanotubes [22]. It was found the percolation threshold of the composites with ordered CNTs was one order-of-magnitude smaller compared with those under random orientation (0.06–0.5 wt%). At the percolation threshold, the conductivity was 1.4×10^{-5} S/m.

CNFs or VGCNFs are cheap, hollow, discontinuous cylinders/filaments in diameter of 50–500 nm and length of several microns, providing a high-aspect ratio stacked cones (length/diameter > 100) and nanographene layers arranged in parallel along the axis. This arrangement is about 100 times smaller than standard carbon fibers [23]. CNFs or VGCNFs, featured with outstanding mechanical properties, physical properties, thermal conductivity, and conductivity, have interested researchers as ideal candidates for carbon-filled materials to prepare polymer matrix composites/nanocomposites. For example, the conductivity of nanocomposites is about 10^6 S m^{-1}, and the thermal conductivity is about 1900 Wm^{-1} K^{-1}. However, the performances of VGCNFs are better than CNTs because of their mass production from natural gases or coals and high cost-effectiveness compared with CNTs. VGCNFs are more widely used and easier-to-obtain, making them excellent substitutes for CNTs [23]. Due to the interaction of van der Waals forces between carbon fibers, VGCNFs tend to agglomerate, resulting in poor properties of composites. Therefore, improving the ultimate performance of reinforced

composites/nanocomposites is the only goal [23]. Smrutisikha et al. (2010) prepared CNF/epoxy composites with different CNF contents (up to 1 wt%) under different curing conditions and studied the electrical properties [24]. The conductivity of the insulating epoxy resin was improved by 3–6 orders of magnitude after the injection of CNF. In addition, the samples cured at room temperature had high conductivity, which was due to the network formed by nanofiber aggregation along the fiber arrangement direction.

CB is an amorphous carbon and pure para-crystalline carbon material as clusters. This light, loose, and fine black powder has a large surface area of 10–3000 $m^2\ g^{-1}$. CB results from incomplete burning or thermal degradation of carbonaceous materials (e.g., heavy oil, coal, fuel oil, and natural gas) under deficient air. According to records, China is one of the earliest countries to produce CB. The structure of CB is expressed by the degree of chain or grape-like aggregation between CB particles. CB comprises agglomerates in size and morphology, and the particle number in each agglomerate is named high-structure CB. The oil absorption value is indicative of structure, and a larger means a higher structure of CB, which easily forms a spatial network channel that is hard to destroy. High-structure CB has fine particles, dense mesh chains, large specific surface area, and many particles per unit mass, which contribute to the formation of a conductive chain structure in polymers. Among many CB varieties, acetylene CB is the best. CB particles with broad versus narrow particle size distribution can give more conductivity to the polymer, which can be explained by statistical methods.

The larger CB filling amount leads to the higher density and more conductive paths of dispersed CB particles or CB particle aggregates, the smaller average distance between particles, and the higher probability of mutual contact. A more polar blend system composed of polymers with different polarities, and CB contains a larger critical volume fraction of CB, meaning that the system conductivity decreases. Because the surface of CB contains strong polar groups, the polarity of the matrix is significant, and the effect is enhanced. At this time, the strength increases, but this hinders the aggregation of conductive particles, resulting in poor conductivity. However, in the blend system composed of a multi-component resin matrix and CB, the filled CB will produce segregation due to the varying polarities of different matrices. The conductivity relies on the concentration and layout of CB particles and the proportion of polymers both in the segregation phase.

In the example of CB, the dominant mechanism of electron tunneling is current driven because it involves the current between flowing particles that are closely located in the polymer matrix by the interlayer. The net increase in conductivity is due to electrons jumping easily within the whole matrix. Gonza'lez et al. (2005) tested the conductivity of commercial CB under compression and found the conductivity of carbon with small compressed volume rose with the decline of sample volume [25]. The increase of total conductivity is more significant for the densest carbon and less for the lightest carbon. The conductivity and its change under compression are positively correlated with carbon density. Tantawy et al. (2002) showed that epoxy composites were electrically and thermally stable at high CB content, giving them a broad application prospect in heating devices and conductive composites [26]. In

addition, the conductivity of the insulating epoxy resin matrix rose with the increase of CB content, and the conductivity (3.4×10^{-5} S m^{-1}) was above 7 wt% CB.

Studies show that CB will significantly impact the curing kinetics and conductivity of epoxy formulations. Trihotri et al. (2015) explored the impacts of curing conditions on the activation energy and dielectric properties of CB-epoxy (CB-EP) composites at varying temperatures and frequencies, and reported that room-temperature-cured CB-EP had higher activation energy and lower dielectric constant compared with heat-cured CB-EP [27]. In addition, with an increment of CB concentration in the composites, the activation energy of the curing system decreases, which may be ascribed to the higher polarization energy or charge carrier density.

GR with outstanding electrical, mechanical, and optical properties is formed by closely packing carbon atoms into a single-layer two-dimensional honeycomb lattice structure. GR is among the materials with the highest strength known. Graphene outperforms other nanofillers in terms of specific surface area and aspect ratio and can build an uninterrupted conductive network in the polymer matrix. However, due to the high aspect ratio, hydrophobicity, and π-π interaction of graphene layers, graphene is unevenly dispersed in the composite matrix, resulting in a reduction and deterioration of material properties. Therefore, researchers use different technologies (e.g., covalent/non-covalent functionalization, microwave stripping, surface modification) to evenly disperse graphene layers into polymers.

The conductivity of different graphene epoxy composite derivatives has already been studied with structural results. Liu et al. (2013) carried out marginal functionalization by Friedel Crafts acylation reaction between original graphite and 4-aminobenzoic acid to obtain 4-aminobenzoic acid-based functional fossil ink [28]. Functionalization mainly occurred in the edges of graphite, and the original graphene structure on the inner substrate was retained. Functional graphene sheets were used as nanoscale reinforcing materials to produce epoxy-based conductive composites for electrical interconnection. The conductivity of the composites increased by 31.3%, and the shear strength rose from 8.7 to 15.2 MPa after adding 0.6 wt% functional graphene. Bindu et al. (2014) prepared microwave stripping reduced graphene oxide (MERGO) was from natural graphite and synthesized epoxy nanocomposites from in-situ polymerization with triethylenetetramine (TETA) as a curing agent [29]. The AC conductivity of the nanocomposites was 10^{-5} S m^{-1}, and the dielectric constant was significantly improved. Preparing epoxy/MERGO nanocomposites from graphene is economical and straightforward and can be applied to the production of other MERGO-based polymer nanocomposites.

2.4.3 Ceramic Fillers

Ceramic materials are inorganic non-metal substances resulting from the forming and high-temperature sintering of natural or synthetic compounds. They have high melting point, hardness, and high wear and oxidation resistance. Ceramic materials are often used as fillers in ECAs owing to their large dielectric constant, low dielectric loss, and high thermal stability. Common ceramic materials include barium titanate

($BaTiO_3$), calcium cupric titanate (CCTO), calcium titanate ($CaTiO_3$), and titanium dioxide (TiO_2). Ceramics have a lower linear expansion index than metals do and have high dimensional stability upon temperature variation. Functional ceramics such as BN, TiC, SiC, TiB_2, TiN, and TiB usually have remarkable physical properties and are applied in many fields, including fillers for epoxy-based conductive adhesives.

Ceramic ECAs were prepared using face-centered cubic (FCC) TiB ceramic powder as a conductive filler and the polymer as a matrix. Also, the conductivity of the ceramic electrolytic capacitor was studied [30]. A percolation threshold was obtained at 60% FCC-TiB with the lowest resistivity of 1×10^{-3} Ω m at 75% loading. Some ceramics including BaFe, BN, TiB_2, TiN, and SiC have semiconductor properties. These materials are also considered secondary fillers of ECAs, which are usually used to enhance the conductivity and thermal conductivity of composites. Saad et al. (2015) prepared barium ferrite/polyaniline composites (Ba Ferrite/PANI) by in-situ polymerization, which were dispersed in a diglycidyl ether bisphenol A/carboxyl polyester hybrid powder coating system [14]. The filling amount of Ba ferrite/PANI was directly proportional to the conductivity of epoxy composites. Cui et al. (2013) prepared conductive adhesive (ECAs) by adding microsilver sheet and hexagonal boron nitride (BN) nanoparticles to the matrix resin [31]. The hexagonal BN nanoparticles well affected the reliability of electrochemical ceramics and improved the properties of the ceramics.

Some researchers synthesized ceramic nanomaterials for epoxy-based adhesives. Bouzidi et al. (2015) prepared indium tin oxide (ITO) nanopowders using the sol–gel method and prepared the ITO nanoparticles (ITO-EP-NCs) in the epoxy resin matrix [32]. The UV absorption performance of ITO-EP-NCs was enhanced under 2 wt% ITO load, and the absorption bandwidth reached 400 nm. The addition of ITO nanoparticles improved the UV and IR shielding properties of epoxy resin. Abenojar et al. (2009) probed into the curing and mechanical properties of an epoxy adhesive filled with boron carbide (B4C) [33]. The B4C-reinforced epoxy resin had high wear resistance and specific wear resistance against alumina. With the increase of B4C content, the reinforced epoxy resin showed good mechanical properties and fine particles. T_g decreased slightly after addition of B4C. Singh et al. (2017) reported the synergistic impact of hybrid BN and graphene on the thermal conductivity of epoxy adhesives [34]. The thermal conductivity increased to 1.65 W m^{-1} K^{-1} by about nine folds from the original epoxy resin. The activation energy declined with the incorporation of BN particles into the epoxy/graphene framework. Also, the curing speed of the epoxy/graphene/BN adhesive system surpassed that of the epoxy/graphene adhesive system.

Ceramic fillers are often used in ECAs because of their low dielectric loss and large dielectric constant and heating stability. Achieving a higher dielectric constant at a lower filling amount is difficult. In general, at above 50 wt%, although ceramic/polymer matrix composites have high dielectric constant, the ceramic packing is prone to reunition, leading to the formation of numerous holes and defects in the composite. Hence, the wear performance of the composite material will decline, leading to a conductance loss. The main reason is that the dielectric properties at the interface between the high-dielectric ceramic filler and the low-dielectric polymer

matrix are too different, resulting in the distortion of the electric field. Therefore, how to improve the interface compatibility between ceramic fillers and polymer substrates becomes a research focus in recent years. There are two main research directions: to form a core–shell structure on the filler surface and to graft organic polymers on the ceramic surface.

2.4.4 Metal-Coated Fillers

Compared with carbon-based fillers and ceramic fillers, some metal fillers have high conductivity and thermal conductivity. Among them, silver (Ag) is used in ECAs because of its easy processing, high conductivity, thermal conductivity, and chemical stability. However, its high cost hinders its wide application in many electronic fields. Therefore, Ag is usually mixed with other fillers to make coating fillers, which promotes high conductivity, and has a low cost. Copper with low electrical impedance, good electromigration, and low cost is widely used as an epoxy-based conductive filler. However, the main disadvantage of the copper filler is copper oxidation or corrosion, reducing the electrical performance of the electrolytic capacitor. Therefore, the copper filler needs surface modification to control oxidation, which can be achieved by coating other metals (e.g., silver) on the copper surface. On this basis, Nishikawa et al. (2010) coated a silver layer on the surface of copper particles to solve the problems due to high resistance and oxidation [35]. Curing and reliability tests showed the epoxy-based ECAs of the Ag-plated Cu filler were much lower and more stable than the pure Cu filler because the Ag coating over Cu prevented Cu oxidation. Zhao et al. [36] prepared sheet silver-plated copper-filled ICAs with epoxy resin as the matrix and tetraethylpentamine as a curing agent. The Ag content on the copper surface of the coating was up to 96.32%, and the flake Cu–Ag powder with high-content silver had high oxidation resistance. In addition, the percolation threshold of ICAS filled with flake Cu–Ag powder was only 40%.

The non-metal core of metal-coated epoxy conductive fillers mainly includes carbon filler, various polymers, or glasses with lower conductivity than metal particles. Carbon-based materials such as graphite or graphene, CNTs, and CFs have high aspect ratios and provide epoxy-based adhesives with mechanical strength and high thermal stability, but their conductivity is lower than metal fillers. Therefore, with the help of the high conductivity of some metal particles based on Ag and Au, conductive metal particles are coated on carbon-based fillers to improve their conductivity and save costs of ECAs. Wei et al. (2009) prepared nano-graphite from expanded graphite and silver-plated nano-graphite [37]. The Ag-plated nano-graphite conductive adhesive comprised an epoxy resin, a silver-plated nano-graphite conductive filler, triethanolamine, and other additives. The percolation thresholds of the conductive adhesive were 7 wt% and 17 wt%, respectively. When the conductive filler concentration was 20 wt%, the epoxy conductive adhesive had lower resistivity of 1.50×10^{-3} Ω cm and high thermal stability. Gallego et al. (2015) tested gold-functionalized graphene (Au-GNP) as a conductive filler in epoxy adhesives to study

the conductivity of ECAs [38]. The Au-GNP nanofiller was distributed into UV-curable epoxy resin. The addition of Au-GNP nanofiller significantly improved the conductivity by about four orders of magnitude relative to the epoxy nanocomposites with the same dose of bare graphene. Kim et al. (2014) showed that MWCNTs can enhance the conductivity by electroless nickel plating (Ni) and improve the electromagnetic interference shielding rate of Ni-MWCNTs-reinforced epoxy nanocomposites, suggesting a high Ni content raises surface conductivity [39]. The insulator was transformed into a conductor by coating metal particles on the surface of the polymer. It can control the overall cost of ECAS and improve the strength and elastic modulus of composites. Zeng et al. (2006) prepared conductive composites with epoxy resin (EP) as a matrix and nickel-plated polyethylene terephthalate (PET) fiber as a filler [40]. Compared with conventional nickel-plated PET/EP composites, ultrasonic electroless nickel-plated PET/EP composites contained more nickel and less phosphorus, showing higher electrical conductivity and better electromagnetic shielding effect.

2.5 Inherent Conductive Polymers

ICPs are organic materials with conductive properties owing to their unique structure, but they are fragile and cannot withstand any significant external load. ICPs show high conductivity (101 S m^{-1}, close to that of copper, 10^3 S m^{-1}) and low specific mass (1.2–1.7). In recent years, ICPs are regarded as promising conductive fillers because of their metal electronic and semiconductor optical properties, flexible mechanics, and processability of traditional polymers. Conductive polymers can be prepared by doping conjugated polymers, which becomes a trend. Generally, the conductivity of conductive materials formed by conjugated polymers is between 10^{-11} and 10^{-8} S m^{-1}, and can be increased by 6–9 orders of magnitude to 10^{-5} to 10^{1} S m^{-1} after doping. ICPs are filling materials to provide conductivity for adhesive formulation. However, compared with traditional conductive fillers (e.g., metal and carbon fillers), the conductivity of adhesive formulations prepared from conductive polymers is lower, while traditional conductive fillers-enhanced adhesive systems are usually sufficient to meet some applications. ICPs-reinforced conductive adhesives can be achieved by mixing two polymers (adhesive matrix and ICPs) or building an interpenetrating polymer network. When the adhesive matrix is mixed with ICPs, conductive polymer particles are added to the liquid polymer matrix and cured under thermal conditions. Another method of preparing conductive adhesive is to polymerize and compressed-mold a conductive polymer in an insulating matrix.

3 Prospects of ECAs

According to literature and policy reports, ECAs have an outstanding market prospect and opportunities in various industries. To meet the further requirements of ECAs, high conductivity can be achieved by several methods. New trends may include the integration of different conductive fillers (mainly nanofillers) to generate mixed fillers. Adding hybrid fillers into the insulating matrix can improve the conductivity and show the synergistic effect of the two fillers. The mixed filler promotes electron transport in the 3D electronic network because the secondary filler will be used as the primary filler between the bridges. In addition, the development of ICP fillers based on metal particle coatings may beneficially impact ECAs. The evolution of ICPs-coated carbon-based nanofillers can remarkably improve conductivity. Coating metal conductive particles into carbon-based nanofillers and changing the carbon fillers to strengthen the conductivity of epoxy composites is a sustainable and reliable method to prepare ECAs.

4 Summary

This chapter mainly introduces all aspects of epoxy-based conductive adhesive (ECAs) as economical substitutes of welding connection in many electronic packaging industries. It covers the basic principle of ECAs, especially categories (e.g., ICAs and ACAs) and the conduction mechanism. The mixing of a conductive filler and an epoxy resin matrix to transform an insulating material into a conductive one is elaborated. The conductive fillers introduced into the epoxy matrix include metal fillers, carbon fillers, ceramic fillers, and metal-coated fillers. Several inherently conducting polymers mixed with epoxy include polypyrroles, polyanilines, and polythiophene.

References

1. Aradhana, R., Mohanty, S., Nayak, S.K.: A review on epoxy-based electrically conductive adhesives. Int. J. Adhes. Adhes. **2020**, 99
2. Li, Y., Moon, K.S., Li, H., Wong, C.P.: Conductivity improvement of isotropic conductive adhesives with short-chain dicarboxylic acids. In: 54th Electronic Components and Technology Conference, Las Vegas, NV, Feb 03, 2004; Las Vegas, NV, 2004; pp 1959–1964
3. Pietila, M., Makela, T., Levon, K., Kivilahti, J., Isotalo, H.: Electrically conductive polyaniline adhesive. In: 4th International Conference on Adhesive Joining and Coating Technology in Electronics Manufacturing, Helsinki Univ Technol, Espoo, Finland, Jun 18–21, 2000; Helsinki Univ Technol, Espoo, Finland, 2000; pp 118–120
4. Mir, I., Kumar, D.: Recent advances in isotropic conductive adhesives for electronics packaging applications. Int. J. Adhes. Adhes. **28**(7), 362–371 (2008)

5. Yim, M.J., Paik, K.W.: Recent advances on anisotropic conductive adhesives (ACAs) for flat panel displays and semiconductor packaging applications. Int. J. Adhes. Adhes. **26**(5), 304–313 (2006)
6. Jouan, A., Constantinescu, A.: A modified dissipated energy fatigue criterion to consider the thermo-oxidative ageing of electrically conductive silicone adhesive joints. Int. J. Fatigue **116**, 68–79 (2018)
7. Li, Y., Wong, C.P.: Recent advances of conductive adhesives as a lead-free alternative in electronic packaging: materials, processing, reliability and applications. Mater. Sci. Eng. R-Rep. **51**(1–3), 1–35 (2006)
8. Wu, H.P., Liu, J.F., Wu, X.J., Ge, M.Y., Wang, Y.W., Zhang, G.Q., Jiang, J.Z.: High conductivity of isotropic conductive adhesives filled with silver nanowires. Int. J. Adhes. Adhes. **26**(8), 617–621 (2006)
9. Jia, W., Tchoudakov, R., Segal, E., Joseph, R., Narkis, M., Siegmann, A.: Electrically conductive composites based on epoxy resin with polyaniline-DBSA fillers. Synth. Met. **132**(3), 269–278 (2003)
10. Choi, Y.K., Sugimoto, K., Song, S.M., Gotoh, Y., Ohkoshi, Y., Endo, M.: Mechanical and physical properties of epoxy composites reinforced by vapor grown carbon nanofibers. Carbon **43**(10), 2199–2208 (2005)
11. Ma, P.C., Tang, B.Z., Kim, J.K.: Effect of CNT decoration with silver nanoparticles on electrical conductivity of CNT-polymer composites. Carbon **46**(11), 1497–1505 (2008)
12. Zhang, R.W., Lin, W., Lawrence, K., Wong, C.P.: Highly reliable, low cost, isotropically conductive adhesives filled with Ag-coated Cu flakes for electronic packaging applications. Int. J. Adhes. Adhes. **30**(6), 403–407 (2010)
13. Yim, B.S., Kim, J.M.: Characteristics of isotropically conductive adhesive (ICA) filled with carbon nanotubes (CNTs) and low-melting-point alloy fillers. Mater. Trans. **51**(12), 2329–2331 (2010)
14. Zhao, J.C., Hu, J.D., Jiao, D.N., Tosto, S.: Application of face centred cubic TiB powder as conductive filler for electrically conductive adhesives. Trans. Nonferrous Met. Soc. China **24**(6), 1773–1778 (2014)
15. Lu, D.Q., Tong, Q.K., Wong, C.P.: A study of lubricants on silver flakes for microelectronics conductive adhesives. IEEE Trans. Compon. Packag. Technol. **22**(3), 365–371 (1999)
16. Johnsen, G.K., Knaapila, M., Martinsen, O.G., Helgesen, G.: Conductivity enhancement of silver filled polymer composites through electric field alignment. Compos. Sci. Technol. **72**(15), 1841–1847 (2012)
17. Cheng, W.-T., Chih, Y.-W., Yeh, W.-T.: In situ fabrication of photocurable conductive adhesives with silver nano-particles in the absence of capping agent. Int. J. Adhes. Adhes. **27**(3), 236–243 (2007)
18. Tee, D.I., Mariatti, M., Azizan, A., See, C.H., Chong, K.F.: Effect of silane-based coupling agent on the properties of silver nanoparticles filled epoxy composites. Compos. Sci. Technol. **67**(11–12), 2584–2591 (2007)
19. Xiong, N., Li, Z., Li, J., Xie, H., Wang, Y.: Influence of curing procedures on the electrical properties of epoxy-based isotropic conductive adhesives. In: 15th International Conference on Electronic Packaging Technology (ICEPT), Chinese Inst Elect, Chengdu, Peoples Republic of China, 2014 Aug 12–15, 2014; Chinese Inst Elect, Chengdu, People's Republic of China, 2014; pp 373–377
20. Jakubinek, M.B., Ashrafi, B., Zhang, Y.F., Martinez-Rubi, Y., Kingston, C.T., Johnston, A., Simard, B.: Single-walled carbon nanotube-epoxy composites for structural and conductive aerospace adhesives. Compos. Part B-Eng. **69**, 87–93 (2015)
21. Rosca, I.D., Hoa, S.V.: Highly conductive multiwall carbon nanotube and epoxy composites produced by three-roll milling. Carbon **47**(8), 1958–1968 (2009)
22. Felisberto, M., Arias-Duran, A., Ramos, J.A., Mondragon, I., Candal, R., Goyanes, S., Rubiolo, G.H.: Influence of filler alignment in the mechanical and electrical properties of carbon nanotubes/epoxy nanocomposites. Phys. B-Condens. Matter **407**(16), 3181–3183 (2012)

23. Cardoso, P., Klosterman, D., Covas, J.A., van Hattum, F.W.J., Lanceros-Mendez, S.: Quantitative evaluation of the dispersion achievable using different preparation methods and DC electrical conductivity of vapor grown carbon nanofiber/epoxy composites. Polym. Test. **31**(5), 697–704 (2012)
24. Bal, S.: Experimental study of mechanical and electrical properties of carbon nanofiber/epoxy composites. Mater. Des. **31**(5), 2406–2413 (2010)
25. Sanchez-Gonzalez, J., Macias-Garcia, A., Alexandre-Franco, M.F., Gomez-Serrano, V.: Electrical conductivity of carbon blacks under compression. Carbon **43**(4), 741–747 (2005)
26. El-Tantawy, F., Kamada, K., Ohnabe, H.: In situ network structure, electrical and thermal properties of conductive epoxy resin-carbon black composites for electrical heater applications. Mater. Lett. **56**(1–2), 112–126 (2002)
27. Trihotri, M., Dwivedi, U.K., Khan, F.H., Malik, M.M., Qureshi, M.S.: Effect of curing on activation energy and dielectric properties of carbon black-epoxy composites at different temperatures. J. Non-Cryst. Solids **421**, 1–13 (2015)
28. Liu, K.H., Chen, S.L., Luo, Y.F., Jia, D.M., Gao, H., Hu, G.J., Liu, L.: Edge-functionalized graphene as reinforcement of epoxy-based conductive composite for electrical interconnects. Compos. Sci. Technol. **88**, 84–91 (2013)
29. Sharmila, T.K.B., Nair, A.B., Abraham, B.T., Beegum, P.M.S., Thachil, E.T.: Microwave exfoliated reduced graphene oxide epoxy nanocomposites for high performance applications. Polymer **55**(16), 3614–3627 (2014)
30. Saad, G.R., Ezz, A.A., Ahmed, H.A.: Cure kinetics, thermal stability, and dielectric properties of epoxy/barium ferrite/polyaniline composites. Thermochim. Acta **599**, 84–94 (2015)
31. Cui, H.W., Li, D.S., Fan, Q., Lai, H.X.: Electrical and mechanical properties of electrically conductive adhesives from epoxy, micro-silver flakes, and nano-hexagonal boron nitride particles after humid and thermal aging. Int. J. Adhes. Adhes. **44**, 232–236 (2013)
32. Bouzidi, A., Omri, K., El Mir, L., Guermazi, H.: Preparation, structural and optical investigations of ITO nanopowder and ITO/epoxy nanocomposites. Mater. Sci. Semicond. Process. **39**, 536–543 (2015)
33. Abenojar, J., Martinez, M.A., Velasco, F., Pascual-Sanchez, V., Martin-Martinez, J.M.: Effect of boron carbide filler on the curing and mechanical properties of an epoxy resin. J. Adhes. **85**(4–5), 216–238 (2009)
34. Singh, A.K., Panda, B.P., Mohanty, S., Nayak, S.K., Gupta, M.K.: Synergistic effect of hybrid graphene and boron nitride on the cure kinetics and thermal conductivity of epoxy adhesives. Polym. Adv. Technol. **28**(12), 1851–1864 (2017)
35. Nishikawa, H., Mikami, S., Miyake, K., Aoki, A., Takemoto, T.: Effects of silver coating covered with copper filler on electrical resistivity of electrically conductive adhesives. Mater. Trans. **51**(10), 1785–1789 (2010)
36. Zhao, J., Zhang, D.M.: Epoxy-based adhesives filled with flakes Ag-coated copper as conductive fillers. Polym. Compos. **38**(5), 846–851 (2017)
37. Lin, W., Xi, X.R., Yu, C.S.: Research of silver plating nano-graphite filled conductive adhesive. Synth. Met. **159**(7–8), 619–624 (2009)
38. Martin-Gallego, M., Lopez-Manchado, M.A., Calza, P., Roppolo, I., Sangermano, M.: Gold-functionalized graphene as conductive filler in UV-curable epoxy resin. J. Mater. Sci. **50**(2), 605–610 (2015)
39. Kim, B.J., Bae, K.M., Lee, Y.S., An, K.H., Park, S.J.: EMI shielding behaviors of Ni-coated MWCNTs-filled epoxy matrix nanocomposites. Surf. Coat. Technol. **242**, 125–131 (2014)
40. Zeng, W., Tan, S.T.: Preparation and EMI shielding properties of nickel-coated PET fiber filled epoxy composites. Polym. Compos. **27**(1), 24–29 (2006)